Loughborough
University

Experimental and Computational Fluid Dynamics Studies on Spray-Freeze-Drying and Spray-Drying of Proteins

by

Chinnaswamy Anandharamakrishnan

Department of Chemical Engineering

A Doctoral Thesis submitted in partial fulfilment of the
requirements for the award of the degree of Doctor of
Philosophy of Loughborough University

2008

Abstract

This thesis presents an experimental and computational fluid dynamics (CFD) study of spray-drying, spray-freezing and spray-freeze-drying of whey proteins. The effects of varying feed concentration (20 - 40% w/v) and outlet temperature (60°C - 120°C) on whey protein denaturation (determined by DSC) and solubility at pH 4.6 (by Kjeldhal and RP-HPLC methods) have been investigated in a pilot-scale co-current spray dryer. The study confirms that low outlet gas temperatures (60°C and 80°C) produce the lowest amount of denaturation, with almost complete denaturation observed at 120°C. Slightly more denaturation was found with a 40% feed concentration. A reversed phase HPLC technique has been applied to measure the loss of solubility of α-lactalbumin and β-lactoglobulin. Significantly higher losses in solubility were observed for β-lactoglobulin compared to α-lactalbumin. Increasing the feed concentration at higher outlet temperatures also caused noticeable increases in insolubility. The reversed phase HPLC results were consistent with those obtained from total protein nitrogen content (Kjeldhal) analyses. This comparative study suggests that the protein solubility can also be calculated from RP-HPLC technique.

Spray-freeze drying is an alternative approach to spray drying, which is less likely to cause protein denaturation and loss of solubility. Conventional freeze-drying involves high capital and operating costs, due to the low temperatures, high vacuum and very long drying times. One solution to this problem is to reduce the dimensions of the material being dried. This is the basis of the spray-freeze-drying technique, involving atomisation of a liquid to form droplets, freezing the droplets and subliming off the ice at low temperature and atmospheric pressure in a fluidised bed. However, the quantities of gas required for atmospheric freeze-drying are prohibitively expensive. A pilot-scale spray-freeze-drying process was investigated, in which fluidisation was performed at sub-atmospheric pressures, allowing rapid freeze-drying (in about one hour) but using much less gas. This was demonstrated using whey protein which yields a product with a highly porous structure, with little loss of protein solubility. This process has potential to produce high-value-added food and pharmaceutical products more quickly and cheaply than is currently possible by commercial vacuum freeze-drying processes.

CFD simulations were developed for short and tall form spray-dryers to study the particle velocity, temperature and residence time during drying. These simulation results agreed well with the published experimental data. The tall-form spray dryer model predictions showed that more particles impact on the cylindrical wall position and this may affect the protein denaturation and solubility. This study suggests that a short form dryer with a bottom outlet is more suitable for drying of proteins. Similarly, a CFD simulation for the spray-freezing operation was developed to study the gas flow pattern and particle trajectories and histories. This CFD model also includes the latent heat effects during the phase change. The simulation predictions agreed reasonably well with the experimental results. A comparison of simulations for a solid and a hollow cone spray suggested that the latter yields lower particle temperatures with low particle collection efficiency. A modified chamber geometry was proposed and the simulation showed that the new design could achieve higher particle collection efficiencies.

Dedication

to my Parents

to my Wife and Son.

Acknowledgements

First of all, I would like to thank my supervisors Professor Chris Rielly and Dr. Andy Stapley for their supervision and unflinching support over the past three years.

I am deeply grateful to Prof. Chris Rielly for his never ending inspiration and guidance right from my application stage of Commonwealth Scholarship. He has shown extreme patience in helping me to understand the concepts of CFD modelling. I admired him for his wide stretched knowledge in Chemical Engineering subject. I thank him for his meticulous approach in reviewing my work that helped me to improve my research contributions. I learnt many skills from him especially, research approach, numerical modelling, technical writing and planning, which will definitely be helpful for my remaining research career. I appreciate his help in guiding me to overcome my research and other problems.

I sincerely thank Dr. Andy Stapley for his help and support. He was always present to help me during the SFD experiments even at midnight. I am confident that this SF+VFBFD process will be commercialised in near future with his hard work, energy and knowledge. I am also thankful to him for due diligence in proofreading of this thesis.

I gratefully acknowledge the Commonwealth Scholarship Commission, UK for awarding of a Commonwealth Scholarship to me and financial support, which enabled this work to be carried out. I also thank Ministry of HRD, Government of India as they nominated me for Commonwealth Scholarship.

I thank all the technicians and staff in the Chemical Engineering Department especially, Chris Manning, Graham Moody, Kim Winfer, Dave Smith, Jim Muddimer, Paul Izzard, Sean Creedon, Tony Eyre and Yasmin Kosar for their help in completing my research.

A special thanks to my dear friend Julious Gimbun for his help during CFD simulation work and also thanks to Mu, Hamant, Abhijeet and all other friends in the Chemical Engineering Department. I would also like to thank Dr. Immanuel Sebastine and Dr. Vaidhyanathan for their encouragement.

At this point, I would like to thank all my teachers especially Dr. KSMS. Raghavarao, Prof. C.M. Lakshmanan, Dr. Nagendra Gandhi and Prof. Krishnasamy for the foundation they helped to lay in shaping my research career. I also thankful to my home institute Central Food Technological Research Institute (CFTRI), Mysore, India and Dr. M.C. Varadaraj, Dr. B.S. Jena and Dr. P.S. Negi for their help and support.

I would sincerely like to thank my parents and my sister Ghandhimathi for their prayers, love, encouragement and support right from the beginning.

This work would not have been possible without my wife Shashikala and my son Nishanth, I appreciate their sacrifice, patient and morale support throughout my research.

Finally, I pray and thank GOD for all.

Anandharamakrishnan
December 2007

Table of Contents

List of figures

List of Tables

Nomenclature

a_w	water activity (equilibrium relative humidity)
A_p	surface area of the particle
$C'g$	maximum solute concentration
C_D	drag coefficient
c_s	specific heat of sample
c_p	specific heat of particle
c_g	specific heat of gas
c_w	specific heat of water
c_{wv}	specific heat of water vapour
$D_{i,m}$	diffusion coefficient of water vapour in the gas phase
$\bar{d}$	mean diameter
d_p	diameter of the particle
E	internal (thermal) energy
h	heat transfer coefficient
h_j	is the enthalpy of species *j*
h_{fg}	latent heat
k	turbulence kinetic energy
K	calibration factor
k_c	mass transfer coefficient
k_{eff}	effective conductivity
k_t	turbulent thermal conductivity
k_{ta}	thermal conductivity
l	length scale of turbulence
M	the mass of sample
M_a	mass flow rate of gas
m_p	mass of the particle
M_s	mass flow rate of dry solid in the feed liquid/slurry
n	spread parameter
p	pressure gradient
Q_{ai}	heat flow of inlet gas to dryer
Q_{ao}	heat flow of outlet gas from dryer

Q_L	heat loss from the dryer
Q_R	heat flow rates to the reference sample
Q_S	heat flow rates to the sample
Q_{si}	heat flow of dried product leaving dryer
Q_{si}	heat flow of feed liquid entering dryer
T	temperature
T_c	*collapse* temperature
T_d	denaturation temperature
T_g	glass transition temperature
T_{g1}	inlet gas temperature to the furnace
T_{g2}	inlet gas temperature to the dryer
T_{g3}	outlet gas temperature from the dryer
T_m	melting temperature
T_p	particle temperature
T_{p1}	inlet feed temperature
T_{p2}	outlet particle temperature
T_R	reference sample temperature
T_s	sample temperature
t_f	total time taken for freezing
u_b	bubble rise velocity
u_{mf}	minimum fluidisation velocity
$\underline{u}_p$	particle velocity
$\underline{v}$	velocity vector
W_s	moisture content of the feed
$W_{s\,o}$	moisture content of the dried product
Y_1	absolute inlet gas humidity to the furnace
Y_2	absolute inlet gas humidity to the dryer
Y_3	absolute outlet gas humidity from the dryer
Y_g	gas humidity
Y_j	mass fraction of species j
Y_s^*	saturation gas humidity
ΔH	enthalpy of denaturation

Greek

μ	viscosity
μ_g	viscosity at glass transition temperature T_g
μ_t	turbulent (or eddy) viscosity
g	gravitational force
ε	turbulence dissipation rate
θ_f	freezing temperature
λ	latent heat of sublimation
ρ_g	density of the gas
ρ_p	density of the particle
$\underline{\tau}$	stress tensor

Subscripts

bl	base line
D	drag
dry	dry solid
g	gas
mf	minimum fluidisation
N	nozzle
p	particle
wet	wet solid

Dimensionless groups

Pr	Prandtl number = $\frac{c_p\mu}{k_{ta}}$
Nu	Nusselt number = $\frac{hd_p}{k_{ta}}$
Sh	Sherwood number = $\frac{k_c d_p}{D_{i,m}}$
Sc	Schmidt number = $\frac{\mu}{\rho_g D_{i,m}}$
Re	Reynolds number = $\frac{\rho_g vd}{\mu}$

Abbreviations

2-D	Two-dimensional
3-D	Three-dimensional
AFBFD	Atmospheric fluidised bed freeze drying
AFD	Atmospheric freeze-drying
BSA	Bovine serum albumin
CFD	Computational fluid dynamics
DPM	Discrete phase model
DSC	Differential scanning calorimetry
DSD	Drop size distribution
FD	Conventional vacuum freeze-drying
HPLC	High performance liquid chromatography
LN_2	Liquified nitrogen
PDA	Phase Doppler Anemometer
PDCAAS	Protein digestibility corrected amino acid score
PEEK	Polyether-ether-ether-ketone
PSI-Cell	Particle source in cell
RNG	Renormalization group
RP-HPLC	Reversed phase high performance liquid chromatography
RR	Rosin-Rammler
RSM	Reynolds Stress Model
RT	Residence time
RTD	Residence time distribution
SEM	Scanning electron microscope
SFD	Spray freeze drying
SFL	Spray-freezing into liquid
SFV	Spray-freezing into vapour
SFV/L	Spray-freezing into vapour over liquid
TFA	Tri fluoroacetic acid
VFBFD	Vacuum fluidised bed freeze drying
WPC	Whey protein concentrate
WPI	Whey protein isolate

Chapter 1

Introduction

1.1 The background to this research

Drying is the removal of moisture by evaporation of liquid or sublimation of solid to the vapour phase by a combination of heat and mass transfer. Drying is the oldest method of preserving food, and dried products have useful attributes in terms of good storage stability, economical way of transport and unique structural qualities. Drying is one of the most important unit operations and has probably the widest applications in the food and pharmaceutical industries. There are three common drying methods used to create particles from solutions namely freeze-drying, spray-drying and drum drying.

Freeze-drying is a popular method of producing shelf-stable particulate products, and is of particular value for drying thermally-sensitive materials (usually biologically based), which can be heat damaged by higher temperature methods. Porous structures are formed from the creation of ice crystals during the freezing stage, which subsequently sublime during the drying stage and this often leads to good rehydration behaviour of the powdered product. However, the freeze-drying process has some disadvantages including high capital and operating costs due to the very low drying rates and consequently long drying times. It has been found that the rate controlling step of freeze-drying is the diffusion of water vapour through the solid, and thus reducing the particle size can be an effective way of speeding up the process (Malecki, 1970; Heldman, 1974). This is the basis of the spray-freeze-drying technique.

Spray-freeze drying (SFD) is a technique which involves a liquid or solution being atomised into droplets, solidified by contact with a cold fluid and ice subliming at low temperature and pressure. (Leunenberger, 2002). Although the technique was first developed in the 1950's (Meryman, 1959), it does not appear to have had widespread use. Mumenthaler and Leuenberger (1991) (see also Leuenberger, 2002) used cold dessicated gas to first freeze and then dry the spray in an integrated fluidised bed at atmospheric pressure. A problem with the atmospheric spray-freeze-drying process is the very large quantities of cold dry gas that need to be circulated through the bed with high velocity. This leads to particles being swept out of the fluidised bed (Mumenthaler and Leuenberger, 1991). An alternative method to avoid circulating large mass flow rates of dry gas, which does not appear to have been considered in the literature, is to apply a partial vacuum to the process. That means spray-freezing at atmospheric conditions, followed by freeze-drying in a fluidised bed at sub-atmospheric pressure. A number of researchers have studied fluidised bed drying from a theoretical and experimental point of view. However, fluidisation under reduced pressure has been largely overlooked although vacuum fluidisation can be used at much lower operating temperatures than at atmospheric pressure (Llop *et al.*, 1996). This thesis reports on the vacuum fluidised bed freeze-drying (VFBFD) which is a dehydration technique for removal of ice by sublimation, so that the quality of product is very high and also it requires a smaller volume of cold gas compared to atmospheric conditions. The published literature on spray-freeze drying is very limited. SFD process have been related to spraying a solution into a cold medium (dry gas or liquid), and freeze-drying the resultant frozen particles by contacting with a cold, dry gas stream, typically at atmospheric pressure in a fluidised bed or conventional lyophilization to remove the water (Gombotz and Brown, 1990; Maa *et al.*, 1999; Rogers *et al.*, 2003; Wang *et al.*, 2006). Spray-freezing coupled with freeze-drying in a VFBFD is an alternative to traditional freeze drying techniques. In this background, as none of the existing techniques have been found to be completely effective, there is scope for developing more efficient methods for drying of heat sensitive material such as proteins, enzymes, vitamins, bacteria and biopharmaceutics.

Spray-drying is one of the well established method for producing dry powders and is the direct opposite to the spray-freeze-drying technique, i.e. an atomised spray is contacted with hot gas which is used as the drying medium. Evaporation takes place to yield dried particles, which are subsequently separated from the gas stream by a variety of methods (Masters, 1991). Currently, spray drying is the preferred method for producing whey proteins in powder form. Normally, it comes at the end-point of the processing line, as it is an important step to control the final product quality. It has some advantages such as, rapid drying rates, a wide range of operating temperatures and short residence times. Although, a large number of studies have been carried out on spray drying, so far, relatively little work has been reported on the effects of spray drying operating conditions on denaturation and solubility of proteins.

Computational fluid dynamics (CFD) is the numerical simulation of fluid motion. CFD is increasingly used in the design, scale-up, optimization and trouble-shooting of spray columns, because measurements of air flow, temperature, particle size and humidity within the drying chamber are very difficult and expensive in large scale spray dryers (Langrish and Fletcher, 2001). Crowe *et al.* (1977) proposed the particle source in cell (PSI-Cell) model to the spray drying process. This PSI-Cell model implements two-way coupling between the gaseous drying medium and the spray droplets (It is currently used by most of the CFD software packages) using the Eulerian-Lagrangian particle tracking or discrete phase modeling (DPM) approach. In DPM, the gas phase is considered as a continuous phase (Eulerian approach) and the spray is represented by a number of discrete computational 'particles'. Individual particles are tracked through the flow domain from their injection point until they escape the domain (Lagrangian approach) (Nijdam *et al.* 2006).

Many researchers have studied the CFD simulation of spray drying (Langrish and Zbicinski, 1994; Kieviet, 1997; Huang *et al.*, 2006). All the published CFD models focused on the gas temperature and velocity profiles. Notably, the histories of the particle velocity, temperature, residence time and final recovery of particles have been totally overlooked. One exception was Kieviet (1997), who developed a 2-D CFD model for particle residence time in a short-form spray dryer. However, their axi-symmetric geometry did not fully represent the outlet pipe line, which is a major factor causing air re-circulation. Moreover, the distribution of particles impact position on walls is also important for spray chamber design and the drying of heat sensitive materials such as proteins.

Similarly, knowledge of droplet/particles diameter, velocity, temperature and final end-points are important for designing and operating the spray-freezing process. However, it is difficult to measure these variables during the experiments at very low temperature, due to rapid cooling and fog formation. Thus, CFD simulations of the spray-freezing operations were performed. In this context, this thesis aims to address particles behaviour during spray drying and spray-freezing processes.

1.2 Objectives of the study

1. To study the effects of process variables on the denaturation and solubility of whey proteins during spray-drying and examine the physical, functional and morphological properties of the particulate product materials.
2. To investigate the effects of temperature on drying rate during spray-freeze-drying and examine the physical, functional and morphological properties of whey protein powders.
3. To develop a three-dimensional CFD model to study the gas flow pattern, particles velocity, temperature and residence time during spray-drying operations. This model prediction will be compared with the published experimental results.
4. To develop a CFD model to examine the gas flow pattern, droplets velocity, particle temperature, residence time and recovery of final products during spray-freezing operations with experimental validation.

1.3 Outline of this thesis

This thesis consists of two main parts. The first part is concerned with experimental studies of spray-drying and spray-freeze-drying of whey proteins. The second part looks at the CFD simulations of spray drying and spray freezing. The experimental part is contained in the chapters 3 to 6 and chapters 7 and 8 describe the CFD simulations. A schematic of the thesis outline is presented in figure (1-1), and the individual chapters are briefly described in the remainder of this chapter.

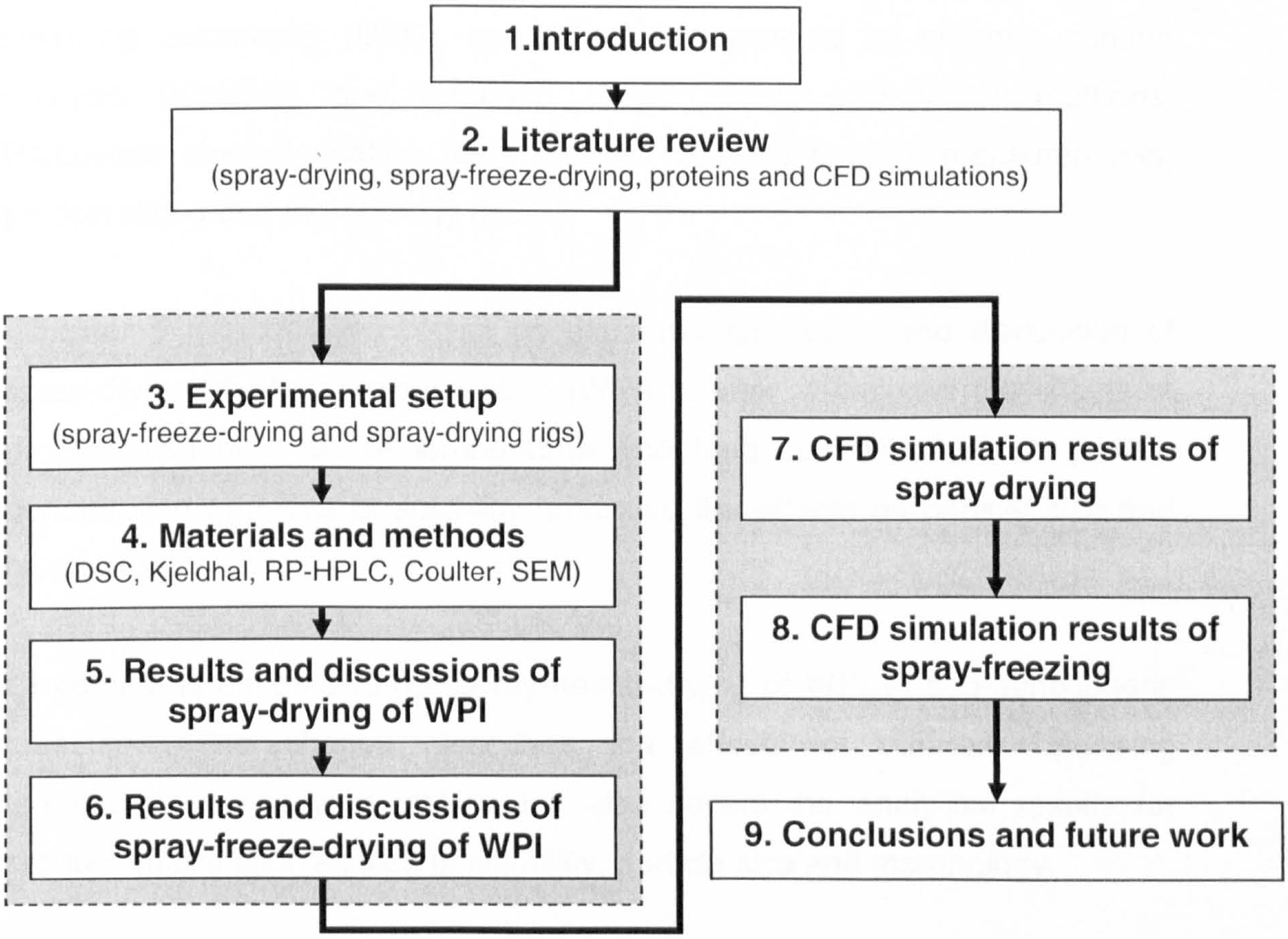

Figure 1-1: Road map for the thesis.

Chapter 2 is a literature review of spray-drying and spray-freeze-drying operations including the related fields of freeze-drying and atmospheric freeze-drying. It also covers the functional properties of proteins, and the technological challenges involved in the drying of whey proteins. The final section of the chapter covers the introduction of CFD with relevant spray drying models.

Chapter 3 describes the experimental rigs used in this research such as, the spray-freezing rig, the spray drying rig and the vacuum fluidised bed freeze dryer rig. The instrumentation and operating procedures are also explained.

Chapter 4 describes the various materials used in this research and the methods of characterising the samples and standards. It includes product quality analysis techniques such as denaturation analysis by differential scanning calorimetry (DSC), solubility measurements by nitrogen content analysis (Kjeldhal) and reversed phase HPLC (RP-HPLC) methods. Particulate characterisation tests include moisture content measurements, particle sizing and morphology (SEM).

Chapter 5 is a detailed report on experimental results and discussion of spray-drying of whey protein isolate (WPI) powder. It includes the effects of process variables (outlet temperature and feed concentration) on protein denaturation and loss of solubility, and also the effects on particle size and morphology.

Chapter 6 is devoted to the spray-freeze-drying of WPI at sub-atmospheric pressures. The chapter describes the effects of different operating temperatures on drying rate and it also covers the analytical results for product quality such as loss of solubility, particle size and morphology.

Chapter 7 describes the CFD modelling and simulations for spray drying operations. The first section of the chapter is focussed on the comparative study on a short-form spray dryer simulation with published experimental and prediction results. This is followed by tall-form spray dryer simulations relevant to the spray dryer used for the experiments reported in Chapter 5.

Chapter 8 opens the door for CFD simulations for spray-freezing operations. The first section of the chapter compares simulations on spray freezing with experimental data. The second section discusses the use of two different types of spray methods, namely solid and hollow cone spray. The final section explores the possibilities of a new spray-freezing chamber design using CFD simulation.

Chapter 9 gives a brief description of the main findings of the above work and recommendations for future work.

Chapter 2

Literature review

2.1 Introduction

Drying is the oldest method of preserving food. In ancient times man froze seal meat on ice in frozen climates and in tropical climates he dried foods in the sun. Whilst there is little recorded history of dehydration of foods, sun-drying and the smoking of foods over a hot fire are mentioned in the Bible. The first artificial drying of food was recorded in the 18th century. A British patent on drying of vegetables was issued in 1840 and dried vegetables produced in Canada were shipped to South Africa for the British forces in the Boer War in 1899-1902 (Vanarsdel and Copley, 1963). During World War II, rotary drum drying was used for producing whey, buttermilk and tomato powders. Since then, numerous drying methods have been designed and developed for specific products, such as tunnel drying, drum drying, bin-drying, air-suspension drying, spray drying, vacuum drying, freeze-drying, fluidised bed drying, microwave drying, solar drying and spray-freeze-drying.

A literature survey is presented here to describe the processes of spray drying and spray-freeze-drying along with the related techniques of freeze drying and fluidised bed drying. This includes the numerical and computational fluid dynamics modelling studies for these drying systems. In addition, the nature and characteristics of whey proteins and its applications are discussed.

2.2 Spray drying

Spray drying is the process of transforming a feed (solution or suspension) from a fluid into a dried particulate form by spraying the feed into a hot drying medium. Spray drying is a widely used industrial process for the continuous production of dry powders. In 1888 the first patent covering the spray drying concept was filed by La Mont (Masters, 1991). Later Percy (1872) filed a patent with a detailed description of spray drying. In 1901, Stauff patented a spray dryer for blood serum and this patent was purchased in 1905 by the American company, Merril Soul, who developed the first commercial spray dryer for milk. Since then there has been significant progress in both the design and techniques of spray drying (Masters, 1991).

2.2.1 Applications of Spray drying

Spray drying is widely used in the food and pharmaceutical industries for producing high quality powders with low moisture content (Charm, 1971; Masters, 1991). Spray drying is used for a wide range of products such as proteins, vitamins, bacteria, enzymes, yeast, flavours, milk, eggs, soups, beverages, fruit juices, vegetables and encapsulated products. Several studies and patents on spray drying have been summarized by Masters (1991).

2.2.2 Principles of spray drying

As shown in figure (2-1), spray drying involves three stages of operation: (1) atomisation of liquid feed into a spray chamber, (2) contact between the spray and the drying medium and (3) separation of dried products from air stream.

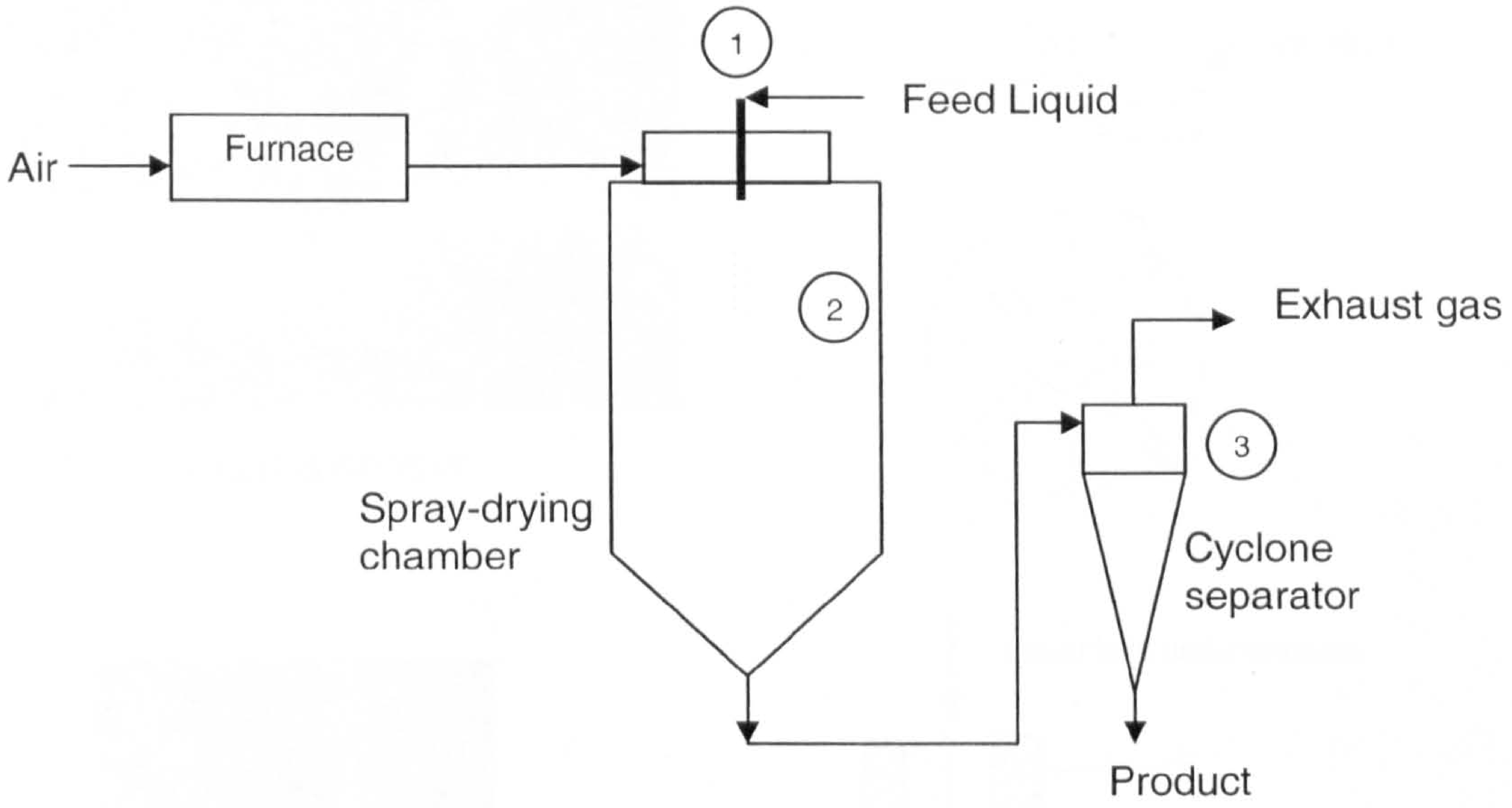

Figure 2-1: The process stages of spray drying (Masters, 1991).

2.2.2.1 Atomisation

Atomisation is a process, where the bulk-liquid breaks up into a large number of small droplets. The choice of atomiser is most important in achieving economic production of high quality products (Fellows, 1998). The different types of atomiser (Masters, 1991) are:

Centrifugal or rotary atomiser (figure 2-2.a). Liquid is fed to the centre of a rotating wheel with a peripheral velocity of 90-200 m/s. Droplets are produced typically in the range of 30-120 μm sizes. The size of droplets produced from the nozzle varies directly with feed rate and feed viscosity and inversely with wheel speed and wheel diameter.

Pressure nozzle atomiser (figure 2-2.b). Liquid is forced at 700-2000 kPa pressure through a small aperture. Here the size of droplets is typically in the range of 120-250 μm. The droplet size produced from the nozzle varies directly with feed rate and feed viscosity and inversely with pressure.

Two-fluid nozzle atomiser (figure 2-2.c). Compressed air creates a shear field, which atomises the liquid and produces a wide range of droplet sizes.

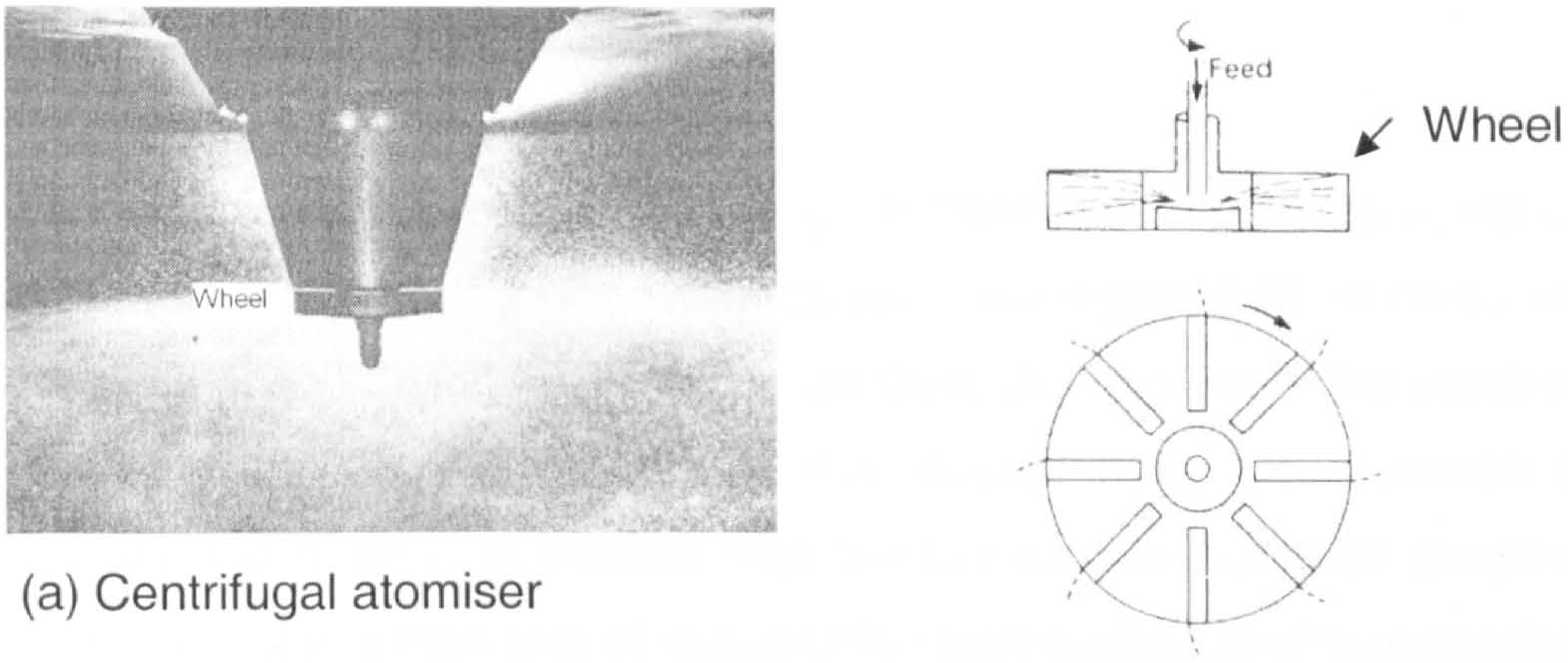

(a) Centrifugal atomiser

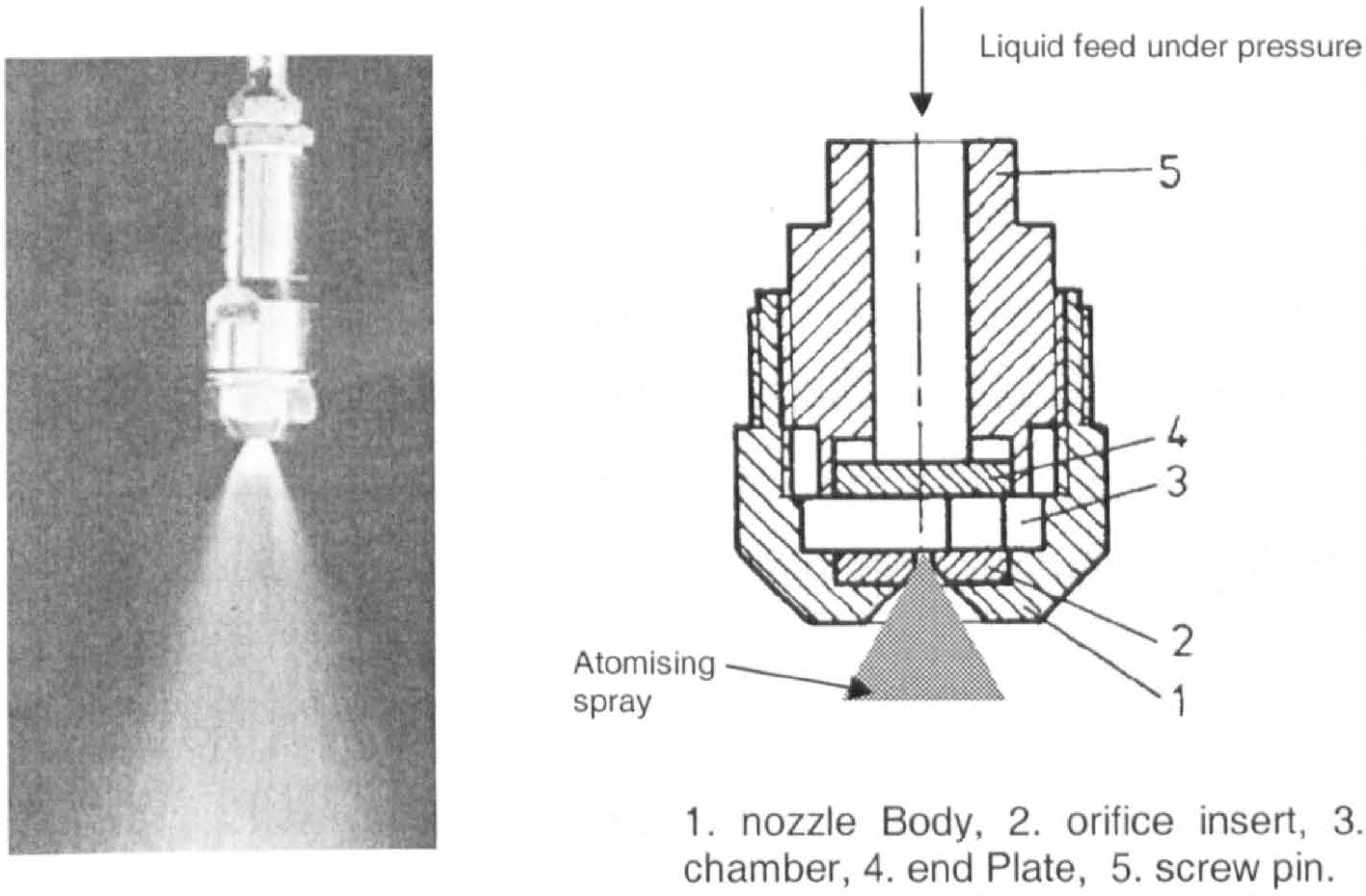

1. nozzle Body, 2. orifice insert, 3. swirl chamber, 4. end Plate, 5. screw pin.

(b) Pressure nozzle

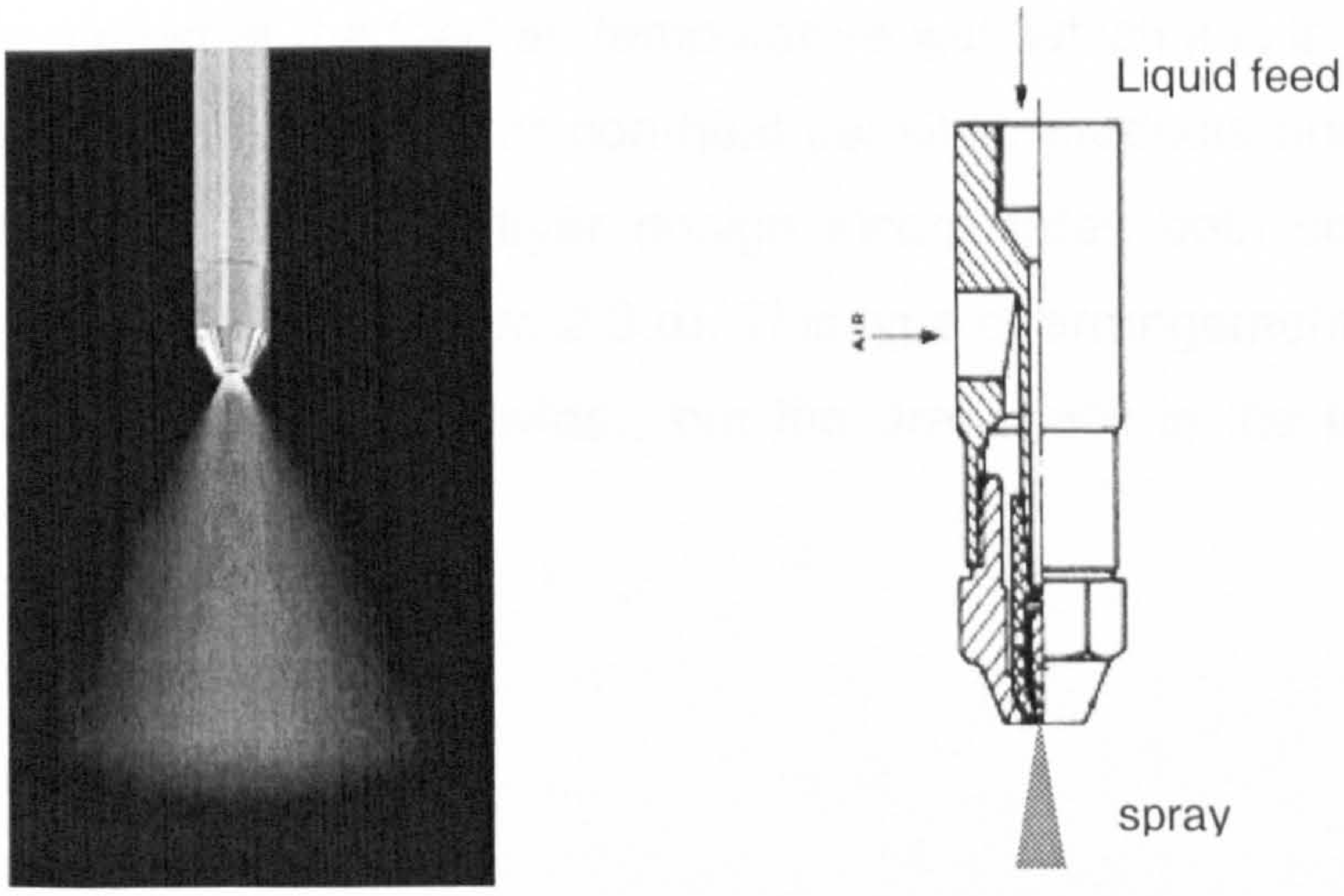

(c) Two-fluid nozzle

Figure 2-2: Spray nozzles: (a) Centrifugal atomiser, (b) Pressure nozzle atomiser and (c) Two-fluid nozzle (Masters, 1991).

2.2.2.2 Spray-air contact

During spray-air contact, droplets usually meet hot air in the spraying chamber either in co-current flow or counter-current flow (figure 2-3). In co-current flow, the product and drying medium passes through the dryer in the same direction as shown in figures (2-3 a-b). In this arrangement, the atomised droplets entering the dryer is in contact with the hot inlet air but their temperature is kept low due to a high rate of evaporation taking place and is approximately at the wet-bulb temperature. As the droplets pass through the dryer the moisture content decreases, the air temperature also decreases and so the particle temperature does not rise substantially as the particle dries and the effect of evaporation cooling diminishes (Mujumdar, 1987). The temperature of the products leaving the dryer is slightly lower than the exhaust air temperature. This co-current configuration is therefore very suitable for the drying of heat-sensitive materials. The advantages of co-current flow process are rapid spray evaporation, shorter evaporation time and less thermal degradation of the products (Masters, 1991).

In contrast, in the counter-current configuration, the product and drying medium enter at the opposite ends of the drying chamber (see figure 2-3 c). Here the outlet product temperature is higher than the exhaust air temperature and is almost at the feed air temperature with which it is in contact. This type of arrangement is used for non-heat sensitive products only. In another type called mixed flow, the dryer design incorporates both co-current flow and counter-current flow (figure 2-3 d). This type of arrangement is used for drying of coarse free-flowing powder, but the draw back is the temperature of the product is high.

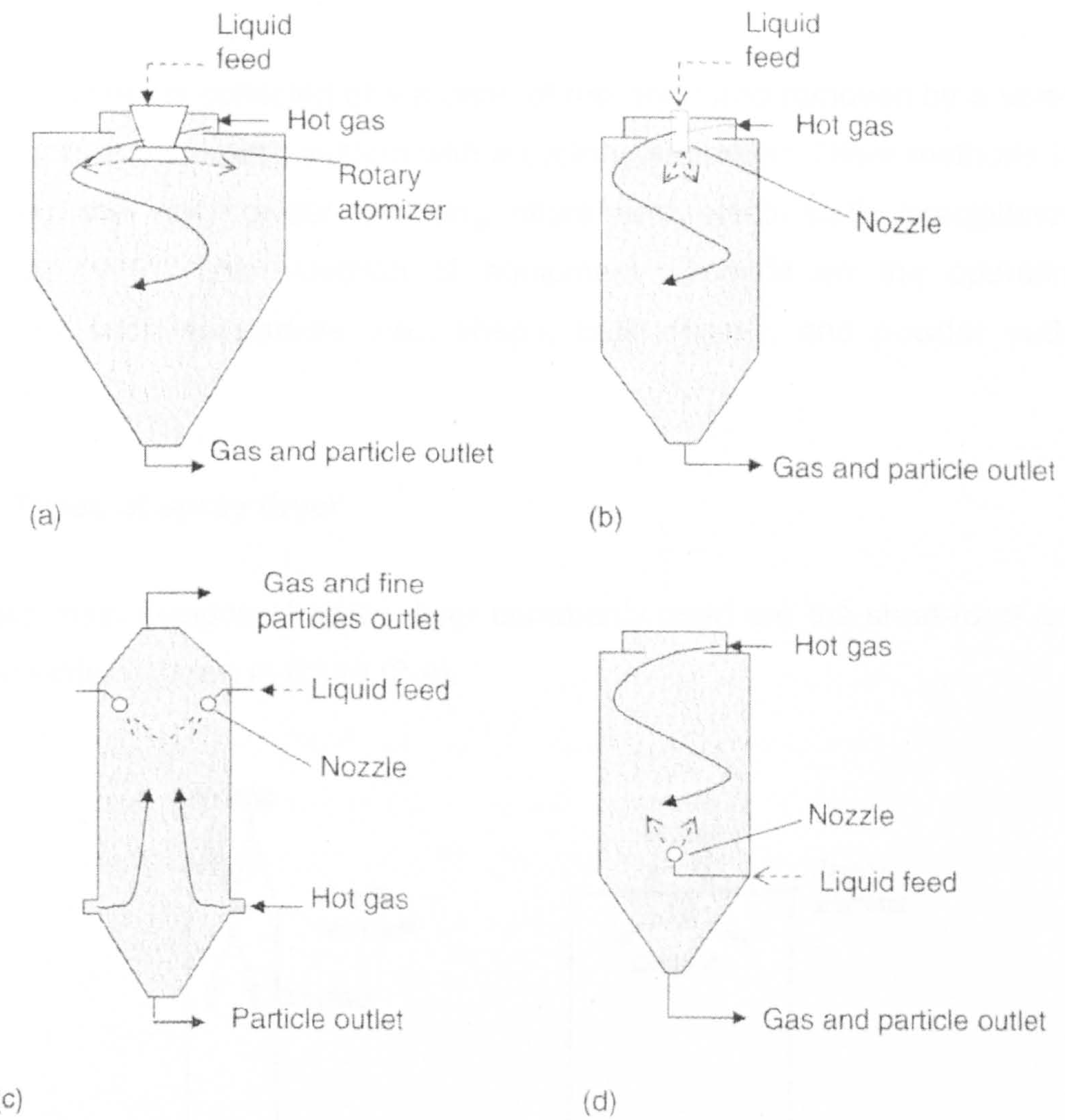

Figure 2-3: Spray dryer configurations: (a) co-current with rotary atomiser; (b) co-current with nozzle; (c) counter current with pressure nozzle; (d) mixed flow with pressure nozzle (Crowe, 2006).

When droplets come in contact with hot air, evaporation of moisture takes place from their surfaces. The large surface area of the droplets leads to rapid evaporation rates, keeping the temperature of the droplets at the wet-bulb temperature (Mujumdar, 1987). In this period different products exhibit different characteristics such as, expansion, collapse, disintegration and irregular shape (detailed discussion in 2.2.5). Methods for calculating the changes in size, density and studies of droplet drying are described by Masters (1991).

2.2.2.3 Separation of dried products

The dry powder is collected at the base of the dryer and removed by a screw conveyor or a pneumatic system with a cyclone separator. Other methods for collecting the dry powder are bag filters and electrostatic precipitators (Fellows, 1998). The selection of equipment depends on the operating conditions such as particle size, shape, bulk density, and powder outlet position.

2.2.3 Types of spray dryer

The two main designs of spray dryer commonly used are the short-form and tall-form driers shown in figure (2-4).

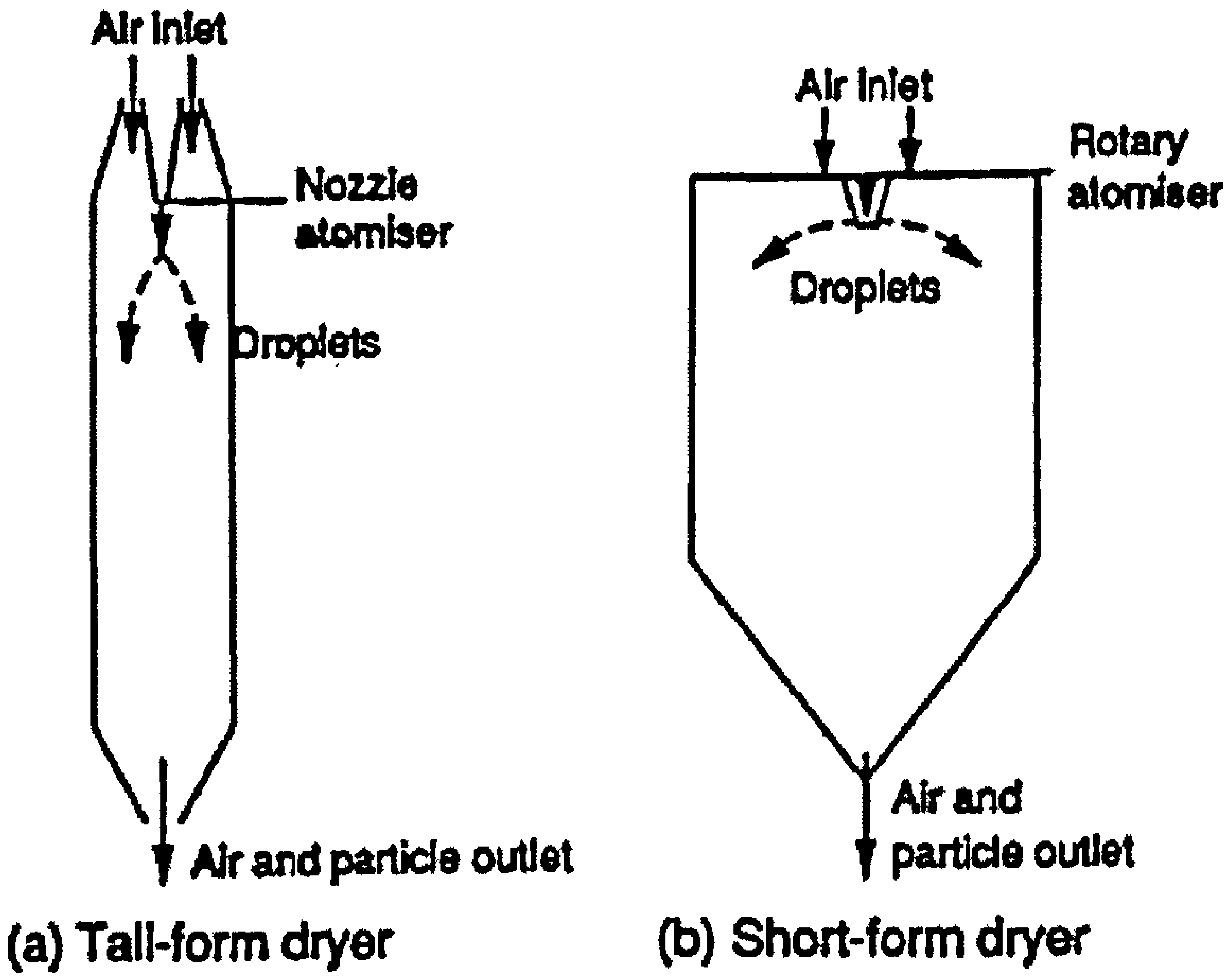

(a) Tall-form dryer (b) Short-form dryer

Figure 2-4: Schematic diagrams of the main types of spray-dryer (Langrish and Fletcher, 2001).

Tall-form designs are characterised by height-to-diameter aspect ratios of greater than 5:1. Short-form dryers, have height-to-diameter ratios of around 2:1. The short-form dryers are the most widely used as they accommodate the comparatively flat spray disk from a rotary atomiser (Masters, 1991). The flow patterns observed in short-form dryers are more complex than those in tall-form dryers, with many dryers having no plug-flow zone and a wide range of gas residence times (Langrish and Fletcher, 2001).

2.2.4 Processing problems

The major problems in spray dryer operations are stickiness and thermal degradation of the products. The following sub-sections describe these problems and their solutions.

2.2.4.1 Stickiness

Stickiness is the main problem that limits the spray drying of various food products. The glass transition temperature (T_g) is the major indicator of stickiness. The glass transition temperature is a temperature and time-dependent change in physical state from the glassy to rubbery viscous liquid without phase change (Jeremiah, 1995). The rubbery state is associated with stickiness, whereas the glassy state is not. The amorphous sugars in foods are stable below T_g and at this state, amorphous material exist as solid "*glass*" and above T_g as "*rubber*" (Blanshard and Lillford, 1993). The changes from the glassy state to the rubbery state occur at a glass transition temperature. The amorphous state in a food is often formed during drying, freezing, extrusion and baking by rapid cooling from melt or by a removal of water during freezing. It is a non-equilibrium metastable state which shows a high degree of hygroscopicity (Bhandari *et al.*, 1997).

Materials containing high sugar and/or organic acid contents have a low glass transition temperature (T_g) and therefore are more likely to exhibit sticky behaviour (determined by whether the T_g is below the actual temperature of the material). This problem could be avoided by using additives (e.g. glucose syrup, maltodextrin) which increase the glass transition temperature (Truong *et al.*, 2004) allowing drying operations to occur below the glass transition temperature.

The T_g value can be determined by Differential Scanning Calorimetry (DSC) (detailed discussion in chapter 6). The following Gordon and Taylor equation can be used to predict T_g for a binary mixture of water and a single solute (Miao and Roos, 2004).

$$T_g = \frac{w_1 T_{g1} + c w_2 T_{g2}}{w_1 + c w_2} \qquad \text{Eq (2-1)}$$

where, w_1 and w_2 are mass fraction of solute and water , T_{g1} and T_{g2} are glass transition temperatures (K) of solute and water (138 K) respectively and c is the ratio of specific heat change of solute to water at the glass transition temperature. Jouppila and Roos (1994) proposed the state diagram as shown in figure (2-5) of T_g function of water activity a_w and sorption at 24 °C temperature with the use of Gordon and Taylor equation (2-1). They used experimental values for fitting the prediction of T_g of lactose and Guggenheim–Anderson–De Boer (GAB) sorption isotherm model for skim milk powder. Figure (2-5) also indicates that decrease in water content bring down the T_g value to the ambient temperature of 24 °C.

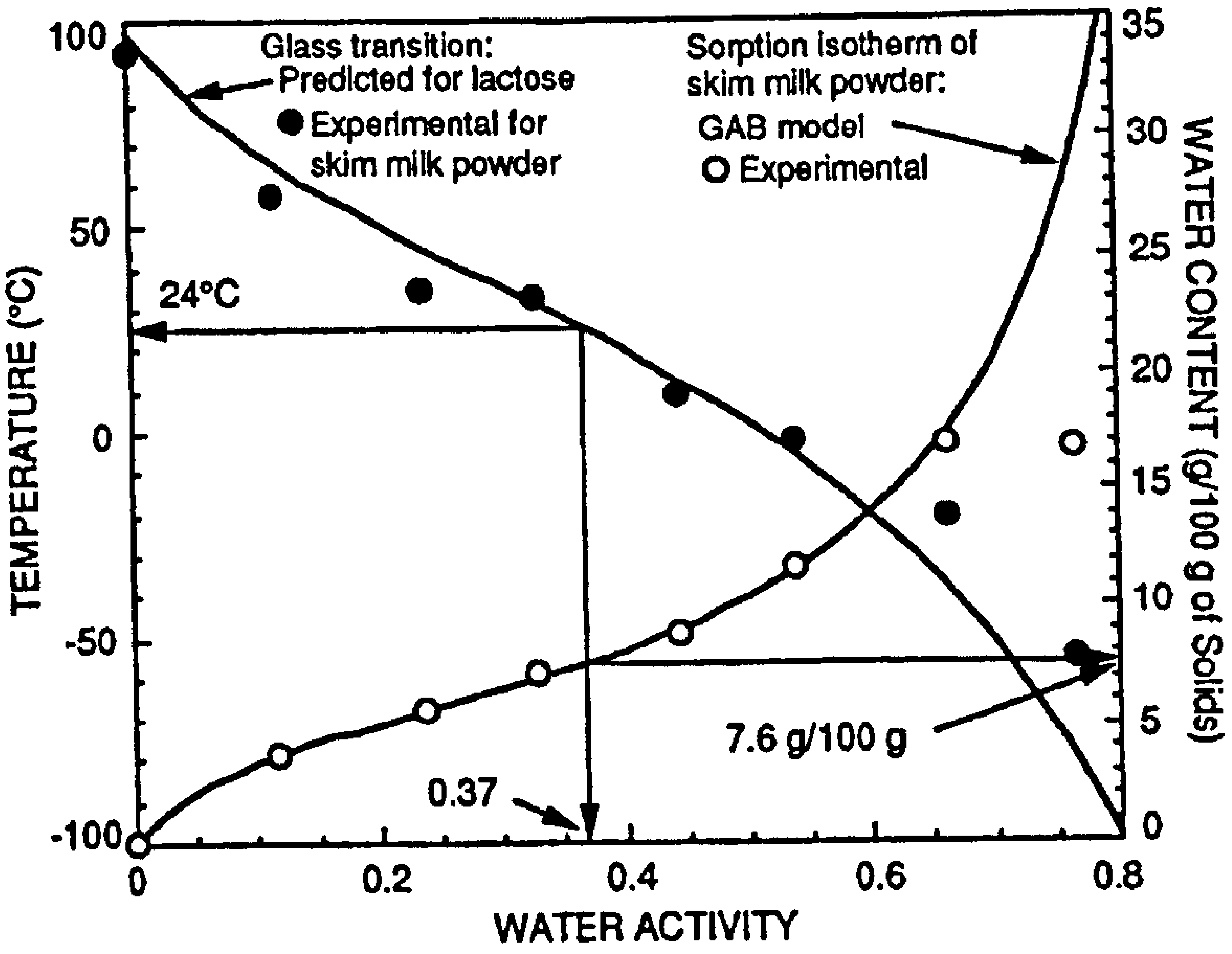

Figure 2-5: State diagram for glass transition temperature function of water activity and sorption isotherm (Jouppila and Roos, 1994).

Table (2-1) represents physical properties of sugars and stickiness behaviour during spray drying (Bhandari *et al.*, 1997). The glass transition temperatures of most of the water soluble food components (carbohydrate and proteins) are high and increase with increasing molecular weight. In dairy products, stickiness is caused by the presence of lactose (T_g = 101°C) and glucose and fructose also shown higher degree of hygrocopicity.

Table 2.1: Physical properties of sugars and stickiness behaviour during spray drying (Bhandari *et al.*, 1997).

Sugars	Hygroscopicity	Melting point (°C)	Solubility in water at 60ºC (%w/w)	T_g (°C)	Stickiness
Lactose	+	223	35	101	+
Maltose	++	165	52	87	++
Sucrose	+++	186	71	62	+++
Glucose	+++++	146	72	31	+++++
Fructose	++++++	105	89	5	++++++

+ symbol indicates the relative degree of hygrocopicity or stickiness

2.2.4.2 Thermal degradation of heat sensitive materials

Most biological based products (proteins, enzymes, antioxidants, vitamins and bacteria) are heat sensitive. During spray drying, inactivation or denaturation occurs to these products due to their exposure to high temperatures. These effects can be minimized by using small droplets, with low outlet air temperature or by adding encapsulating materials (wall materials) to protect these heat sensitive products (Etzel, *et al.,* 1996; Couin, 2004). A detailed discussion on the thermal denaturation of proteins is described in section 2.6.2.

2.2.5 Drying of single droplets

Spray drying is a simple drying method, where a large surface area is available for heat and mass transfer as a result of atomising the liquid into a very large number of small droplets (≈100 μm). The rates of heat and mass transfer are functions of temperature, humidity and the transport properties of the air surrounding the droplets (Perry, 1984). In a single droplet drying process, the constant rate period continues for a short period depending on the moisture content nature of the droplet. In this stage, the droplet temperature is initially close to the wet-bulb temperature of the air and gradually increases to reach the dry-bulb temperature during the falling rate period where the evaporation rate is dependent upon the rate of water vapour diffusion through the dried surface shell (Farid, 2003).

Etzel *et al.* (1996) used a mathematical model to predict the enzyme inactivation in a spray dried products and found that increasing the outlet temperature leads to an increase in bubble volume. A schematic model diagram is shown in figure (2-6).

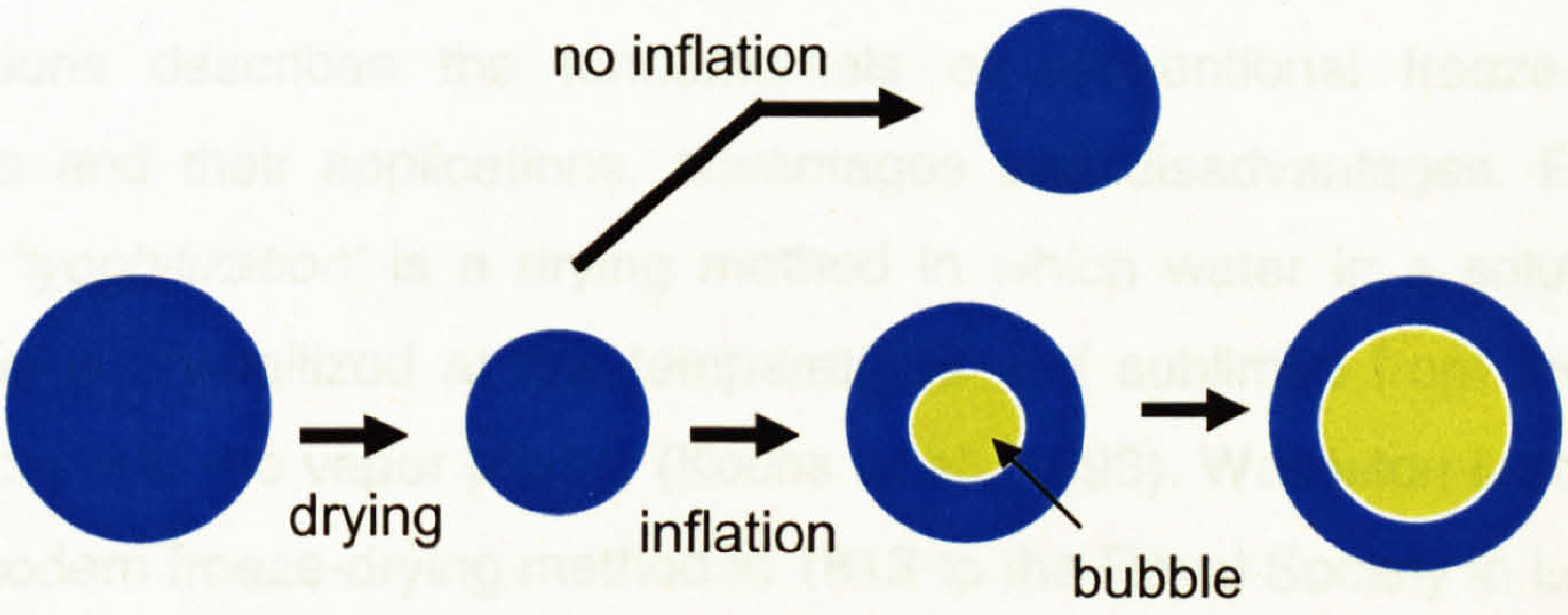

Figure 2-6: Schematic diagram of the modelled process of bubble formation during spray drying (Etzel *et al.*, 1996).

During the falling rate period, a crust was formed and the droplet temperature rose towards the dry-bulb temperature of the air. If the partial pressure of moisture vapour at the droplet centre exceeded ambient pressure and thus resulted in a bubble formation and increase in temperature the droplet inflated to an outer radius and finally yields in irregular random shape particles (Etzel *et al.*, 1996). They also observed from the experimental results that bubble volumes were sometimes larger than the dry solids volume and increased with increasing outlet-air at 120 °C.

2.2.6 Advantages and disadvantages of spray drying

The advantages of the spray drying process are: continuous operation, wide range of operating temperatures, short residence times, production of a powdered product, suitability for both heat-sensitive and heat-resistant materials and rapid drying (Keey, 1972; Katta and Gauvin, 1975; Masters, 1991; Fellows, 1998). However, the quality of spray dried products often suffers from denaturation of proteins, inactivation of enzymes and bacteria, loss of volatile flavour and aroma component (the degree of volatile loss is depends upon the droplet size and flavour oil boiling point). Moreover, spray-drying processes require high capital costs.

2.3 Freeze-drying

This sections describes the fundamentals of conventional freeze-drying techniques and their applications, advantages and disadvantages. Freeze-drying or *'lyophilization'* is a drying method in which water in a solution or suspension is crystallized at low temperatures and sublimed from the solid state directly into the vapor phase. (Kochs *et al.*, 1993). Wallaston introduced the first modern freeze-drying method in 1813 to the Royal Society in London. The freeze-drying process was developed during World War II as a technique for the preservation of human plasma. During the 1930s, the Low Temperature Research Station in Cambridge was involved in fundamental research on the freeze-drying of biologicals and an apparatus was built by Greaves for the freeze-drying of blood serum (Oetjen, 1999). The first large scale process for the freeze-drying of instant coffee was developed in 1938 (Roehrig and Wright, 1972). Merymann (1959) experimentally proved that the freeze-drying of biological products was possible at atmospheric pressure (a detailed discussion follows in section 2.4.3). Thereafter a lot of modifications and improvements have take place in this field.

The quality of freeze dried products is very high in comparison with that of products dehydrated using other techniques, due to the prevention of heat damage (King, 1970). A freeze-drying process provides a product which is stable (dry form), rapidly soluble (large surface area) and elegant (uniformly colored cake). The freeze-drying process consists of four steps as follows:

Freezing: freezing a substance to from crystallized ice. The crystallization depends on the cooling rate, initial concentration and end temperature of cooling. Most of food components remain in an amorphous, glassy state (i.e. do not crystallize), but the water component does crystallise.

Primary drying: ice is removed by sublimation at low temperature and low pressure. Sublimation occurs at the interface between the frozen and dry material and this starts at the ice surface.

Secondary drying: unfrozen water is removed by desorption. This step typically takes one third of the drying time. The final moisture content for foodstuffs is 2 to 10% and for biological products is 0.1 to 3%.

Final treatment: the drying chamber is filled with an inert gas (nitrogen for foodstuffs, argon for biological products) for preserving the products after drying.

2.3.1 Principles of freeze-drying

During the *freezing* step, sensible heat is first removed to reduce the temperature of the products, followed by removal of the latent heat of crystallization to form ice crystals.

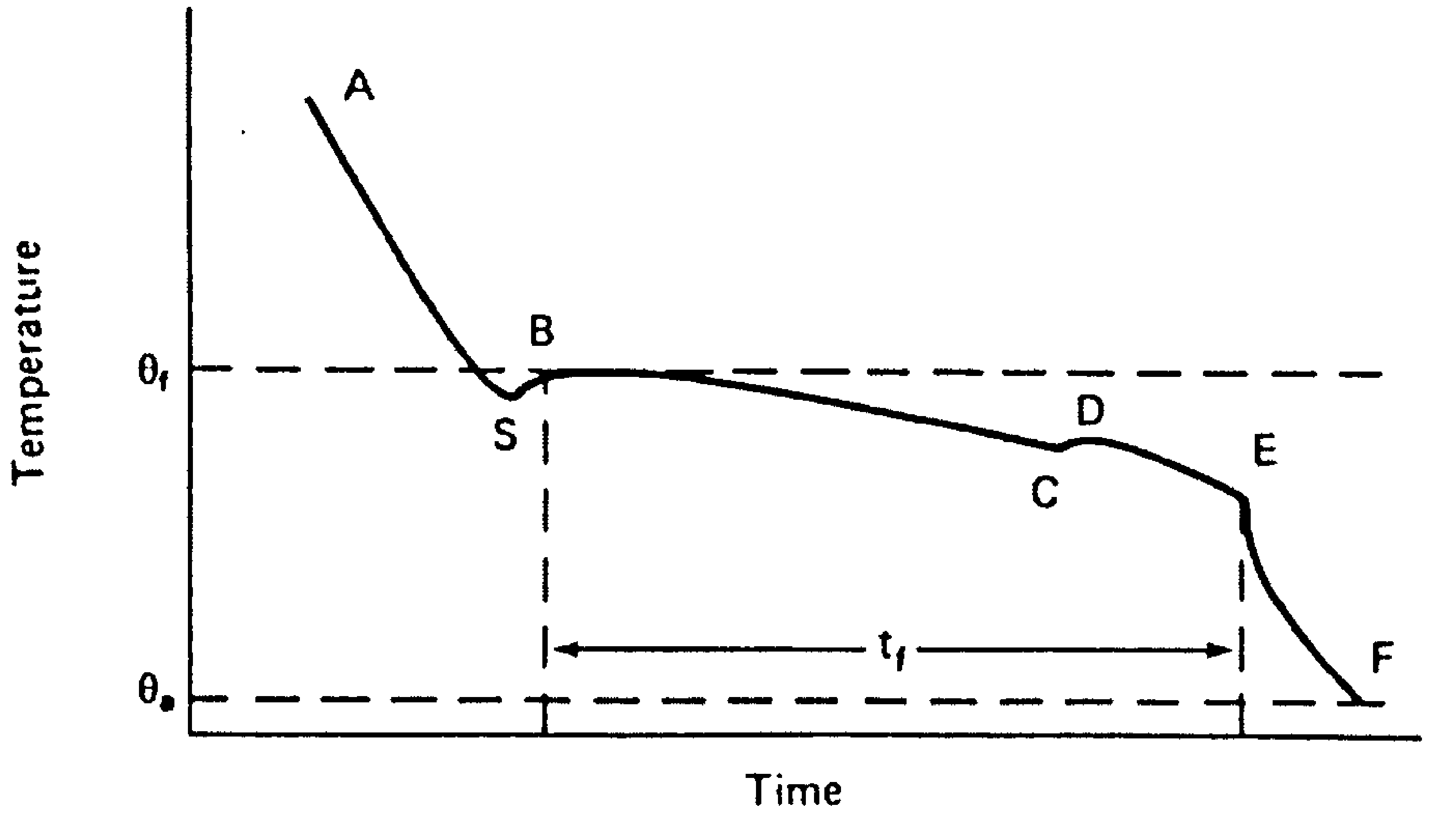

Figure 2-7: Time-temperature data during freezing (Fellows, 1998).

Figure (2-7) shows a typical time-temperature relationship for foods during the freezing step (Fellows, 1998). From the graph:

AS: The food is cooled to below its freezing temperature (θ_f) but water remains in the liquid state.

SB: ice crystals begin to form and their latent heat of crystallization is released.

BC: the majority of the ice is formed along with a slight fall in temperature.

CD: the temperature rises to the eutectic temperature (maximum allowable product temperature) of the solute.

DE: crystallization of water and solute continues. (t_f is the total time taken for freezing).

EF: the temperature of ice-water mixture falls to the temperature of the freezing chamber (θ_a).

During the freezing of foods, the temperature decreases and water is removed from the food in the form of ice and the solutes present in the unfrozen products are freeze-concentrated. The phase diagram of the food material system is shown in figure (2-8).

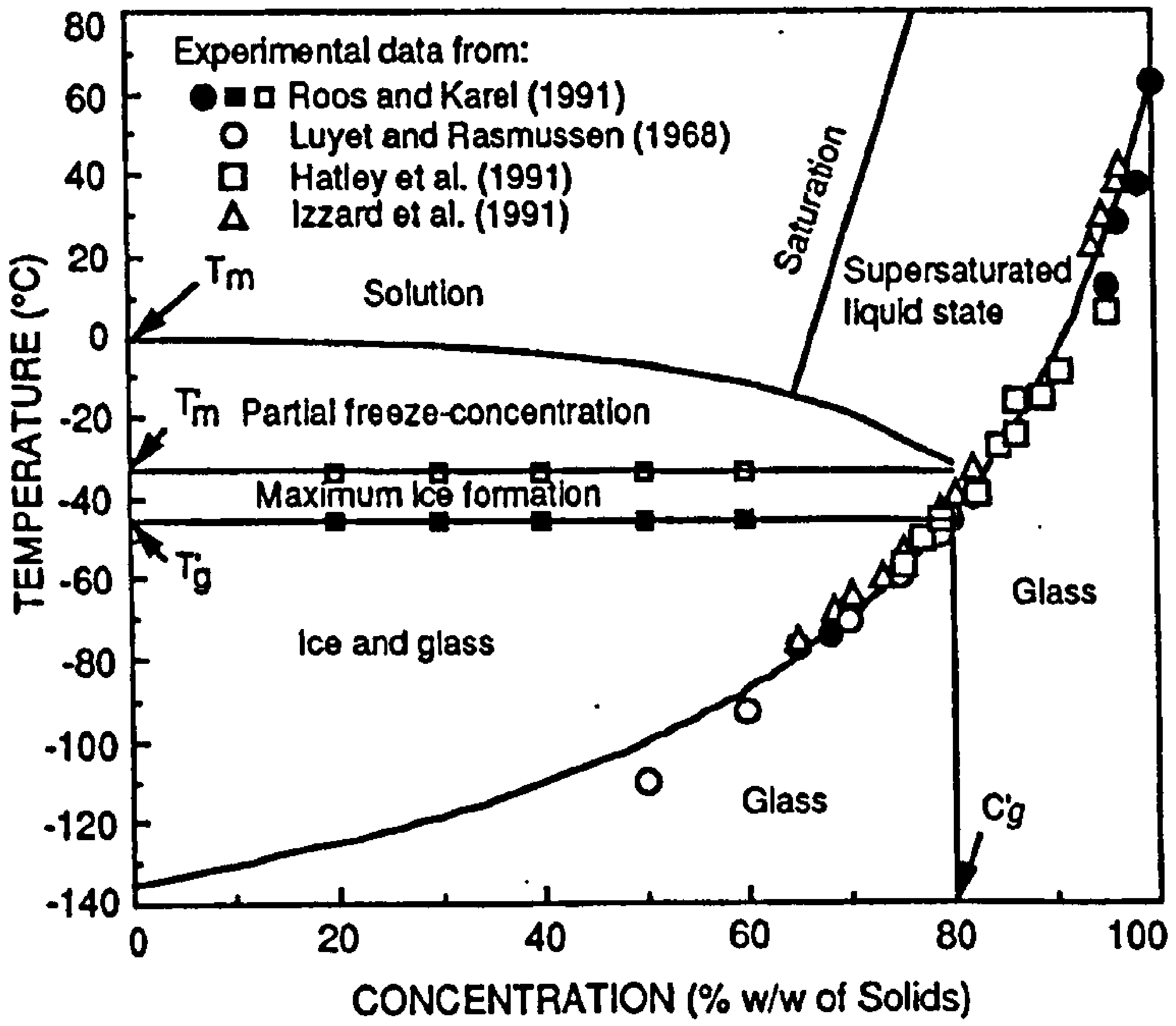

Figure 2-8: Phase diagram of food materials (Roos, 1996).

In the glassy state below the glass transition temperature (T_g) amorphous materials are assumed to be stable. Materials with solute concentrations lower than that in the maximum solute concentration (C'*g*) shows ice formation below the equilibrium melting temperature (T_m), but maximum ice formation is achieved only below the melting point of ice in contact with the maximally freeze-concentrated solute (T'_m), but above the T_g of the freeze-concentrated solute (T'_g) (Blanshard and Lillford, 1993; Roos, 1996).

Hindmarsh *et al.* (2003) measured the temperatures when freezing single distilled water droplets on a thermocouple junction and recorded the images of freezing droplet using high magnification video camera. They observed all the stages in figure (2-7), but with an expanded recalescence stage (SB). Experimental results were well correlated with their numerical model.

A problem in the primary drying step is that '*collapse*' can occur, which is when the viscosity of the structural material is reduced to a level at which it cannot support its weight against gravity (Bhandari *et al.*, 1997). The term *collapse* has been used to describe loss of structure, reduction in pore size and volumetric shrinkage in dried food materials (Levi and Karel, 1995), resulting from a time, temperature and moisture dependent viscous flow that results in loss of structure

The *collapse* temperature (T_c) decreases with decreasing molecular weight and it also decreases with increasing moisture content (Oetjen, 1999). T_c can be related to the glass transition temperature. When the temperature (T) higher than T_g, the amorphous matrix viscosity decreases. This decrease is a function of (T-T_g) and this was described by the William-Landel-Ferry (WLF) relationship (equation 2-2) (Bhandari and Howes, 1999).

$$\log_{10}\frac{\mu}{\mu_g} = -\frac{17.4(T-T_g)}{51.6+(T-T_g)} \qquad \text{Eq (2-2)}$$

where, μ is the viscosity, μ_g is the viscosity at glass transition temperature (T_g) and T is the temperature (K). Example for some the food materials collapse temperature (T_c) are listed in the table (2-2) (Kudra and Strumillo, 1998). The collapse temperature is often lower than those applied during drying. This can be prevented by increasing the molecular weight by adding materials such as dextran, fructose, glucose, maltose, polyethylene glycol etc.

Table 2-2: *Collapse* temperature of selected beverages.

Material	**Initial dissolved solid content % mass**	**Collapse temperature (T_c) °C**
Coffee extract	25	-20.0
Orange juice	23	-24.0
Grapefruit juice	16	-30.5
Sweetened concord grape juice	16	-33.5
Prune extract	20	-35.0
Lemon juice	9	-36.5
Apple juice	22	-41.5
Pineapple juice	10	-41.5
Concord grape juice	16	-46.0

After freeze-drying, structural properties (particle density, bulk density and porosity) of apple, banana, carrot and potato were investigated by Krokida *et al.* (1998). These authors found that the physical properties of freeze-dried materials depend on temperature during freeze-drying and *collapse* occurred above the glass transition temperature. Increase in frozen material temperature resulted in a structural collapse and therefore a reduction of the final porosity. Hence, freeze-drying should be operated below its glass transition temperature.

Levi and Karel (1995) studied *collapse* in freeze-dried carbohydrates above their glass transition temperature and observed that T_c depends on the duration of the experiment, even though the theoretical glass transition temperature (T_g) was independent of time. Knopp *et al.* (1998) studied the *collapse* temperature (T_c) of sucrose solution and found that T_c was equal to the glass transition temperature (T_g).

These reports also revealed that collapse in freeze-dried matrices may adversely affect the properties of the freeze-dried material such as, loss of volatiles during storage, poor rehydration capabilities, uneven moisture distribution and extensive caking in the final product.

2.3.3 Advantages and disadvantages of freeze-drying

Freeze-drying is well known and widely used in the food and pharmaceutical industries. The process operates at low temperature which reduces thermal damage to the products and reduces volatile losses. There is little perceived loss in sensory qualities and the porous structured product exhibits good rehydration properties, yielding high quality products (Jeremiah, 1995; Cohen and Yang, 1995). The most common commercial examples of freeze dried food products are (Stapley, 2008):

- (i) Freeze dried tea and coffee
- (ii) Freeze dried meat and vegetables
- (iii) Freeze dried fruits such as strawberries, cranberries and raspberries
- (iv) Freeze dried herbs
- (v) Freeze dried pet foods for dogs (meat), for cats (fish) and for fish (krill, worms)

In the pharmaceuticals industry the freeze-drying process is widely used to produce a powder form of vaccines, enzymes and bacteria. However, freeze-drying is an expensive dehydration process because of low drying rates (due to the low temperature) and high capital and energy cost due to the refrigeration and vacuum units (Franks, 1998).

2.4 Fluidisation

This section describes the principles and applications of fluidisation, because in spray-freeze-drying process, the drying step was performed using vacuum fluidised bed freeze-drying (VFBFD) method. Hence, knowledge of fluidisation is important for the design and operation of the fluidised bed freeze-dryer.

> "The arrival time of a space probe traveling to Saturn can be predicted more accurately than the behavior of a fluidised bed chemical reactor"
>
> \- Geldart, 1986

Even today this quotation may be true, because of the difficulties in defining and measuring the fundamental variables such as size, shape and density of the particles. These variables play an important role in the prediction of the dynamic behaviour in fluidised beds.

Fluidised-bed reactors have been used on an industrial scale for over fifty years. Fluidisation as a technique has been recorded as being used in the early sixteenth century. The patent on a form of fluidisation was issued in 1910 to Phillips and Bulteel. The first commercial scale fluidised unit was developed by BASF in Germany in 1921 and the first large scale fluidisation application for catalytic cracking of oil vapors was developed by Murphree and coworkers in the United States in 1943 (Leva, 1959) . The first major use in the food industry was for the quick freezing of foods in England in 1950 (Shilton and Niranjan, 1993).

2.4.1 Principles of fluidisation

Fluidisation is a phenomenon which occurs when a fluid (gas or liquid) flows upward through a bed of particles with a sufficient velocity to support the weight of the particles, without carrying them away in the fluid stream (Geldart, 1986). The minimum fluid velocity required to support the bed is known as the minimum fluidisation velocity (u_{mf}) and its value depends on the physical properties of the fluid and solid particles. In gas-solid fluidisation, increasing the gas velocity above the u_{mf} results in the formation of bubbles (like gas bubbles in a boiling liquid). At these velocities the bed is divided into an emulsion phase and a bubble phase. A further increase in gas velocity leads to more vigorous bubbling, with larger and larger bubbles (the diameter of the bubble approaches the vessel diameter). At this stage the bed behaviour is known as *slugging.* Still higher gas velocities result in more and more particles being thrown into the *freeboard* (the space above the bed). When the gas superficial velocity exceeds the terminal velocity of the particle, the solids will be carried over (entrainment or elution) and out of the system as shown in figure (2-9). (Yates, 1983; Geldart, 1986; Howard, 1989; Kunii and Levenspiel, 1991).

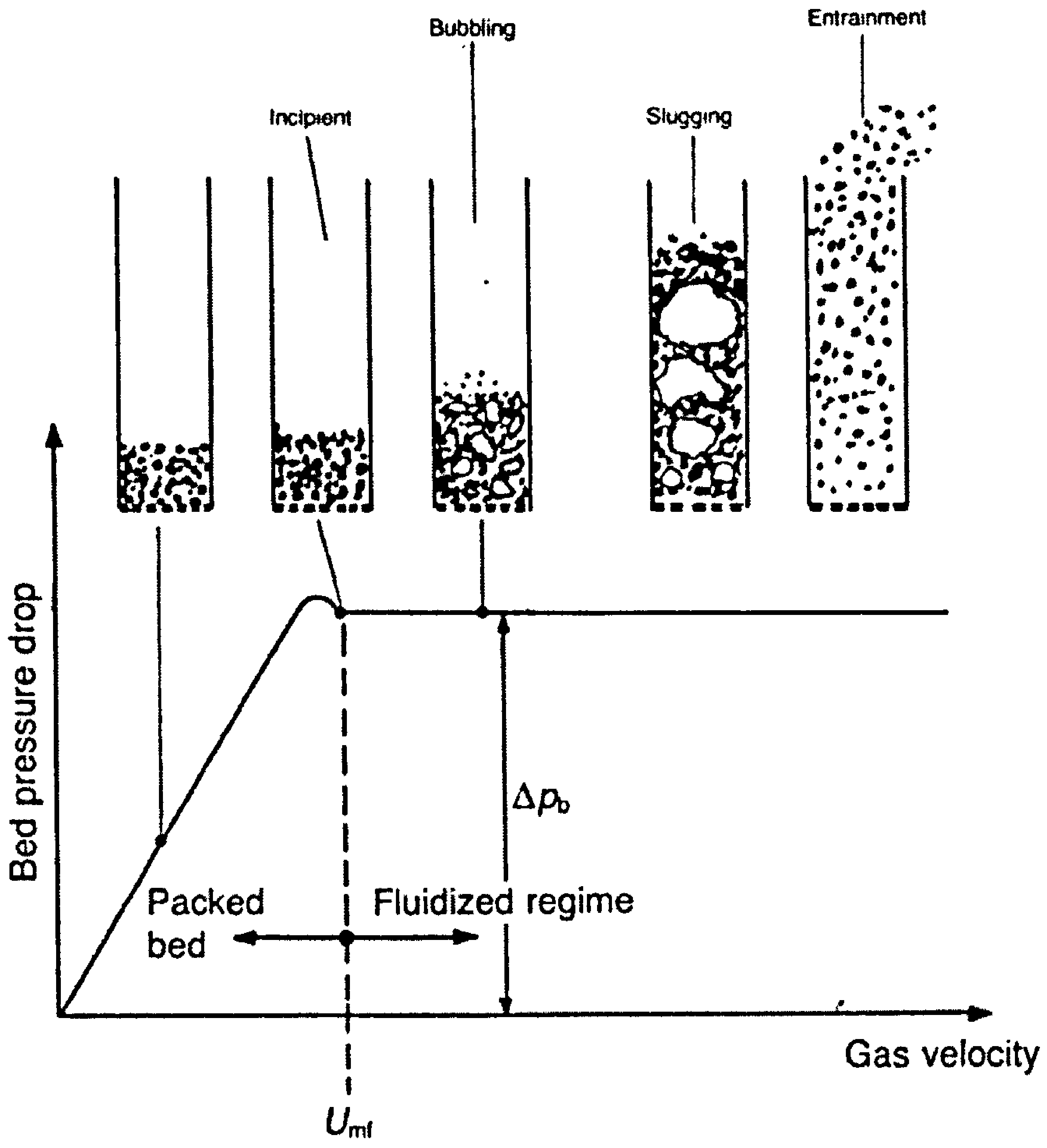

Figure 2-9: Bed behaviour with gas velocity changes (Howard, 1989).

The velocity at which the bubbles first form is known as the minimum bubbling velocity (u_b). Some types of particles cannot be fluidised satisfactorily (e.g.

cohesive particles). A convenient classification of powders in a gas fluidised bed at atmospheric conditions, according to the way they behave, was suggested by Geldart (1986). Figure (2-10), shows how he arranged the various powders into four groups: Group A (low density particles, diameter of the particle d_p= 30-150 μm), Group B (sand like particles, d_p= 150-500 μm), Group C (cohesive or very fine powders, d_p < 30 μm) and Group D (very large size or very dense particles).

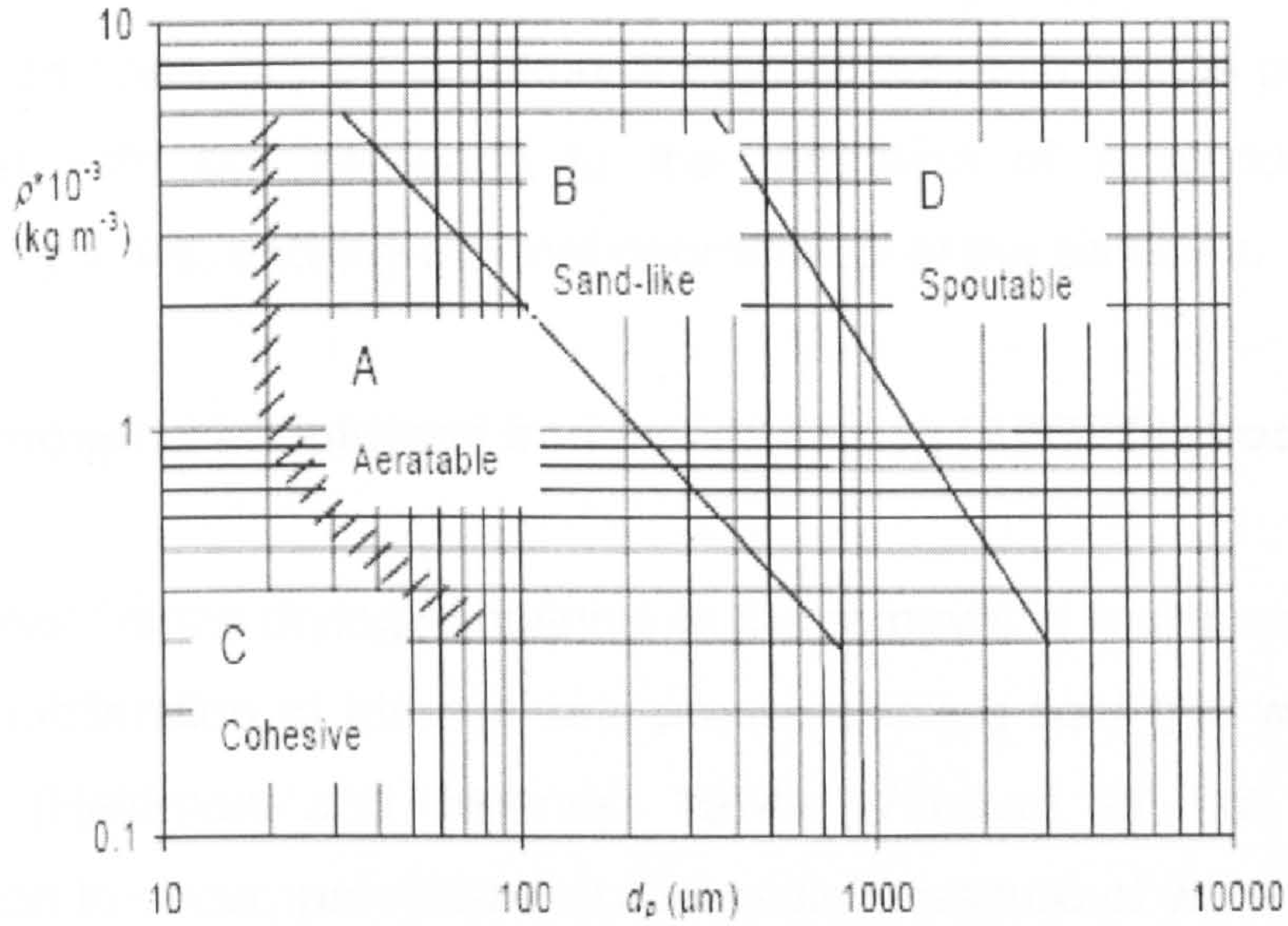

Figure 2-10: Geldart classification of particles at atmospheric conditions (Geldart, 1986).

Many different designs of fluidised bed have been proposed for the drying of particulate materials, including mechanically agitated dryers, vibratory fluidised beds, centrifugal fluidised beds, continuous centrifugal fluidised beds, whirling fluidised beds, beds with internal baffle and spouted beds (Senadeera *et al.*, 2000). In the fluidised bed drying process three different tasks have to be accomplished by the fluidising gas; (i) to establish good dynamic fluidisation conditions (ii) to provide enough heat (iii) to remove all evaporated moisture without saturation (Kozanoglu *et al.*, 2002).

2.4.2 Advantages and disadvantages of fluidised bed drying

Fluidised bed drying has been successfully used in many chemical processing industries. The fluidised bed has the advantages of excellent heat and mass transfer (good contact between particles and fluids), suitability for large-scale operations, rapid mixing of solids (leading to fast drying of the particles) and low capital cost of construction. However, there are some disadvantages to this process: (i) it is suitable for easily fluidised particles only, (ii) a wide distribution of residence times (in continuous dryers) leads to non-uniform drying of particles, (iii) evaporation of organic solvents (in the pharmaceutical industries) with hot air leads to the formation of a mixture within the flammability limits, and (iv) thermal degradation of the particles.

2.4.3 Atmospheric fluidised bed freeze drying (AFBFD) process

Atmospheric freeze drying is defined as the removal of moisture from a frozen food by sublimation at atmospheric pressure using cold gas with a very low humidity (Heldman and Hohner, 1974). Vacuum is not essential for sublimation to occur, provided that the partial pressure of water vapour in the gas phase is kept below the saturation value and the temperature is kept below the water triple point (see figure 2-11).

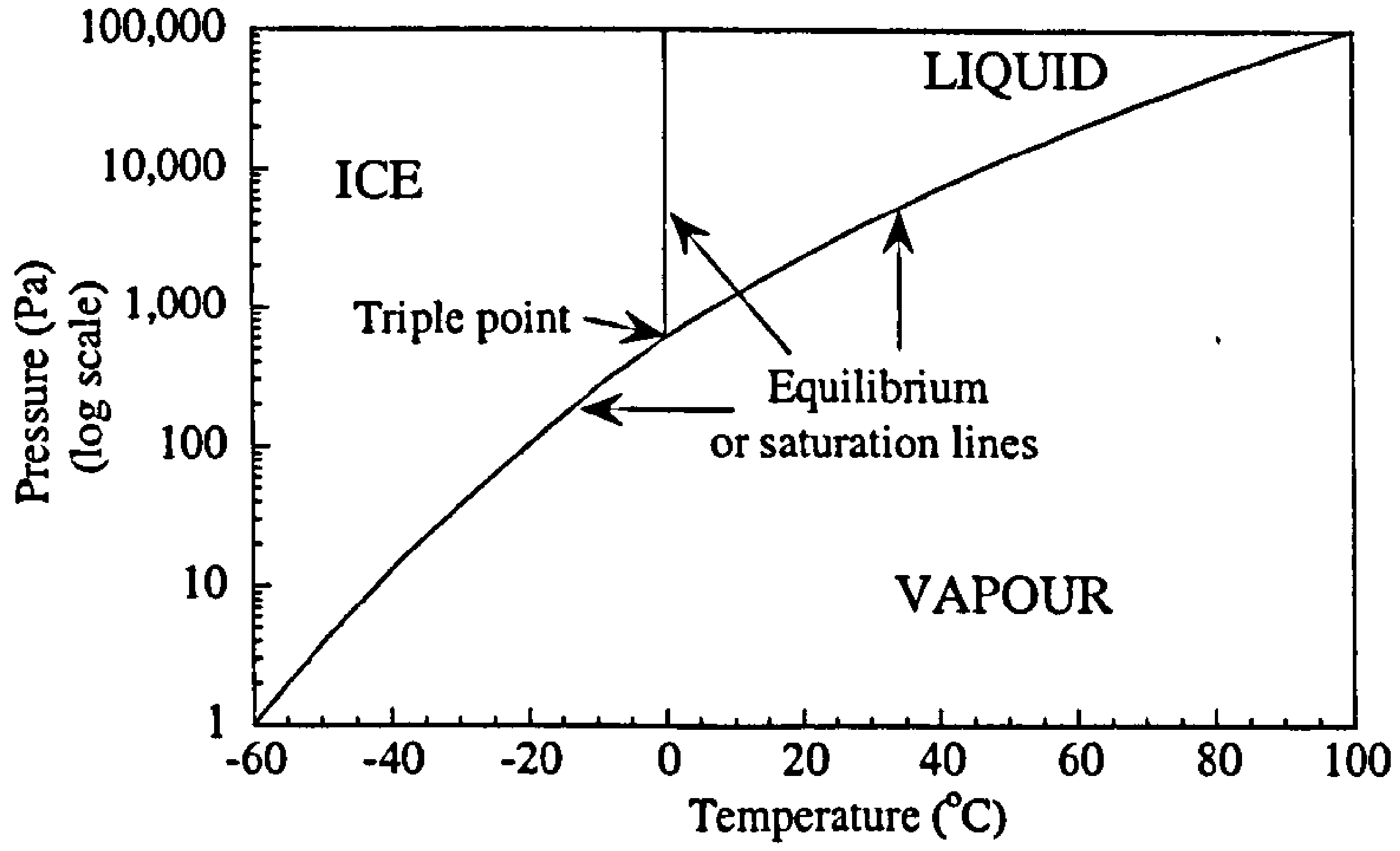

Figure 2-11: Phase diagram for water and representation of the corresponding phase-transition processes (data adopted from standard bookd.

The best example of this condition can be seen in Antarctica, where ice sublimation occurs on a very large scale at atmospheric pressure. During strong winds, surface ice is blown loose, becomes airborne and sublimes (Mann, 1998). In another example, clothes put out to dry on a frosty day freeze like boards but yet dry perfectly.

Various studies have been performed on the atmospheric fluidised bed freeze drying (AFBFD) process. The advantages of the AFBFD processes include better retention of volatile flavours, true freeze drying (entire process held below the freezing temperature of the products) and the use of simple equipment. One of the first studies on AFBFD process was performed by Malecki *et al.* (1970) using apple juice and egg albumin solution. They found that AFBFD process using pure apple juice was not feasible due to the slow drying rate (0.6% weight loss per hr at -34°C temperature) but egg albumin had a quick drying rate (6.5% weight loss per hr at -26°C temperature). The reason was that apple juice has a low glass transition temperature, where as egg albumin does not. Boeh-Ocansey (1988) found 98% retention of β-carotene (an antioxidant known to inhibit carcinogenesis) in carrots using AFBFD process, compared to 95%, obtained with the normal freeze drying process (cited by Shilton and Niranjan, 1993) and it indicates that both the process were yield similar quality products.

Atmospheric pressure freeze-drying with a fluidised adsorbent (to collect the water vapour given off at sublimation) was described by Wolff and Gilbert (1990). They found that the freeze-drying time was longer than for a vacuum freeze drying method and also they encountered difficulties in the separation of freeze-dried products from the adsorbent. Boeh-Ocansey (1983) studied and compared the fluidised bed freeze drying of liquid foods (milk, orange juice, lemon juice and coffee extract) using adsorbent under atmospheric and vacuum conditions and concluded that vacuum conditions were better for small diameter particles (≤3 mm). Lombrana and Villaran (1997) studied the influence of pressure and temperature on freeze-drying in an adsorbent fluidised bed at atmospheric pressure, as well as under vacuum. These authors showed that under vacuum, the drying time was reduced by 50%

compared to the atmospheric conditions. Matteo *et al.* (2003) studied heat and mass transfer during atmospheric freeze drying of foods (potato in cylindrical shape) in a fluidised bed. They observed that the fluidisation velocity had no effect on dehydration rates, but that decreases in particle size increased the freeze-drying rate. They also found that the process incurred lower operating cost than the conventional freeze drying process.

In conclusion, AFBFD process requires very long times and using an adsorbent in fluidised bed freeze-drying reduces the drying time, but it is a problem to separate the product from the adsorbent. Fluidised bed freeze-drying under reduced pressure is faster than at atmospheric pressure, but it needs more attention on the equipment design and vacuum seal. Therefore, the vacuum fluidised bed freeze-drying (VFBFD) process is an alternative to atmospheric condition, and this condition is suitable for food and pharmaceutical products due to its very low operating temperature with short drying time.

2.5 Spray-Freeze-Drying

Spray-freeze-drying involves spraying a solution into a cold medium (dry gas/liquid), and freeze-drying the resultant frozen particles by contacting with a cold, dry gas stream, typically at atmospheric pressure in a fluidised bed or conventional lyophilization to remove the solvent (water). This enables much faster drying rates than are usually possible by conventional freeze-drying, due to the small particle sizes involved.

Spray-freeze-drying has many existing and potential applications in the food and pharmaceutical industries. In the pharmaceutical industries, powder production and handling has been an integral part of pharmaceutical processing, because of the wide use of oral dosage forms. The mechanical milling, precipitation and spray drying methods are mainly used for powder preparation (Maa *et al.*, 1999). Biopharmaceutical (protein) powders find an increasing number of applications in the pharmaceutical industries due to large number of new biological actives for disease treatment and also it is used for dry powder inhalation and sustained drug delivery system (Leuenberger *et al.*, 2006). Spray drying is a widely used method for producing dry and aerosol powders. However, it has some limitations due to the sensitivity of certain proteins to the processing environment and it has low cyclone efficiency whereby fine particles may be lost.

The atmospheric fluidised bed freeze-drying (AFBFD) process and its applications are discussed in section 2.4.3. In the late 1980s, the AFBFD concept was used by Leuenberger (1986) and he filed a US/PCT patent on the combination of spray-freezing with fluidisation drying at atmospheric condition. At present, three types of techniques (figure 2-12) are used for spray-freezing: (i) spray-freezing into vapour (SFV), (ii) spray-freezing into vapour over liquid (SFV/L) and (iii) spray-freezing into liquid (SFL). All these methods and processes are discussed in the following sub-sections.

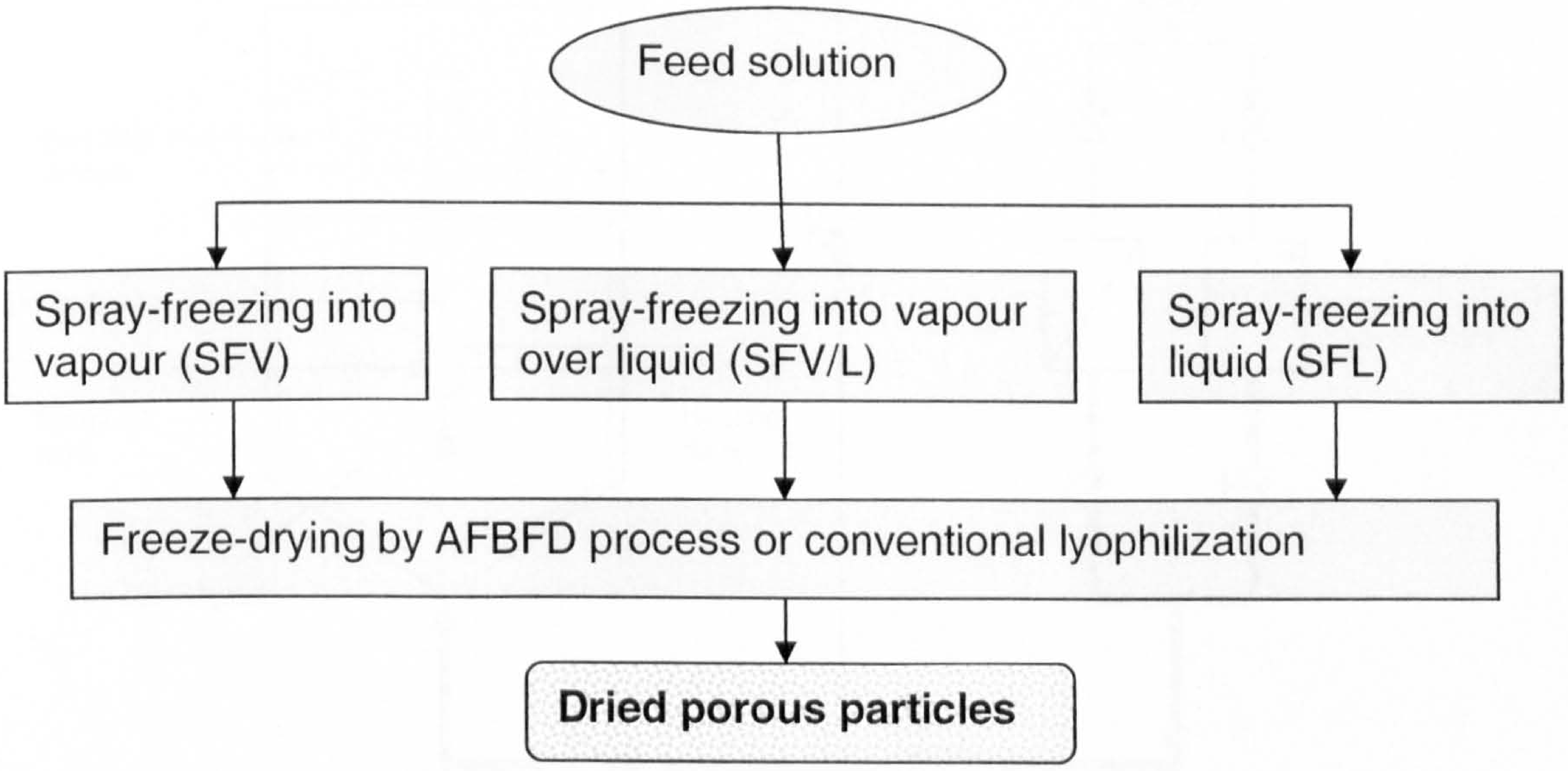

Figure 2-12: Spray-freeze-drying processes.

2.5.1 Spray-freezing into vapour

Spray-freezing into vapour (SFV) involves atomisation of a feed solution into a cold dry gas and freeze-drying by fluidisation or lyophilization to remove the solvent (water). Mumenthaler and Leuenberger (1991) used cold desiccated gas to first freeze and then dry the frozen particles in an integrated fluidised bed at atmospheric pressure as shown in figure (2-13). They observed, high aroma retention in food products, free-flowing powders, short drying times and improved cost effectiveness compared to the freeze drying method. Again, Leuenberger's (2002) group successfully produced an instant water-soluble (increases the bioavailability of the substances) drug (10-30 μm size) using the SFV technique at atmospheric pressure. This process is a batch process and used counter current flow of drying medium and feed liquid. This process is very suitable for heat sensitive materials because it produces a porous structure with a high surface area and increases the bioavailability of the substances. However, the counter current operation leads to particles elutriation and Leuenberger (2002) also observed the elutriation of particles and it caught by a gas-filter.

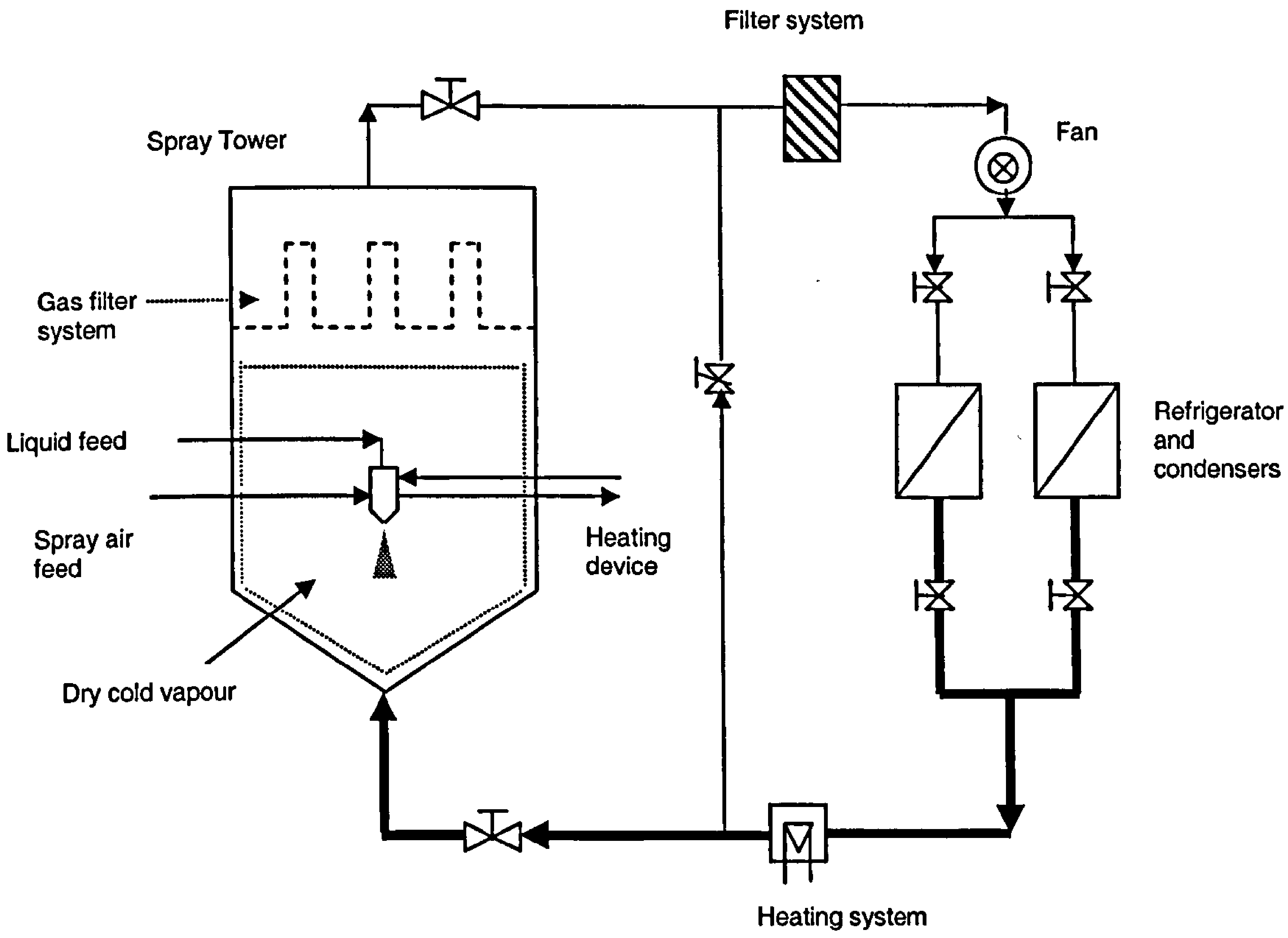

Figure 2-13: Schematic diagram of the atmospheric spray-freeze-drying apparatus (Leuenberger, 2002).

Recently, another type of atmospheric SFV process was developed by Wang *et al.* (2006) for the drying of proteins (BSA). In this process, nitrogen gas was passed through a cooling coil (submerged in liquid nitrogen) and into a spray-freezing chamber (see figure 2-14). The feed solution was atomised within the chamber and frozen particles were collected on the exit filter disc and dried at atmospheric pressure using the same dry cold gas stream. In this co-current flow process, they able to avoid the particle elutriation which occurred in the experiments performed by Leuenberger (2002).

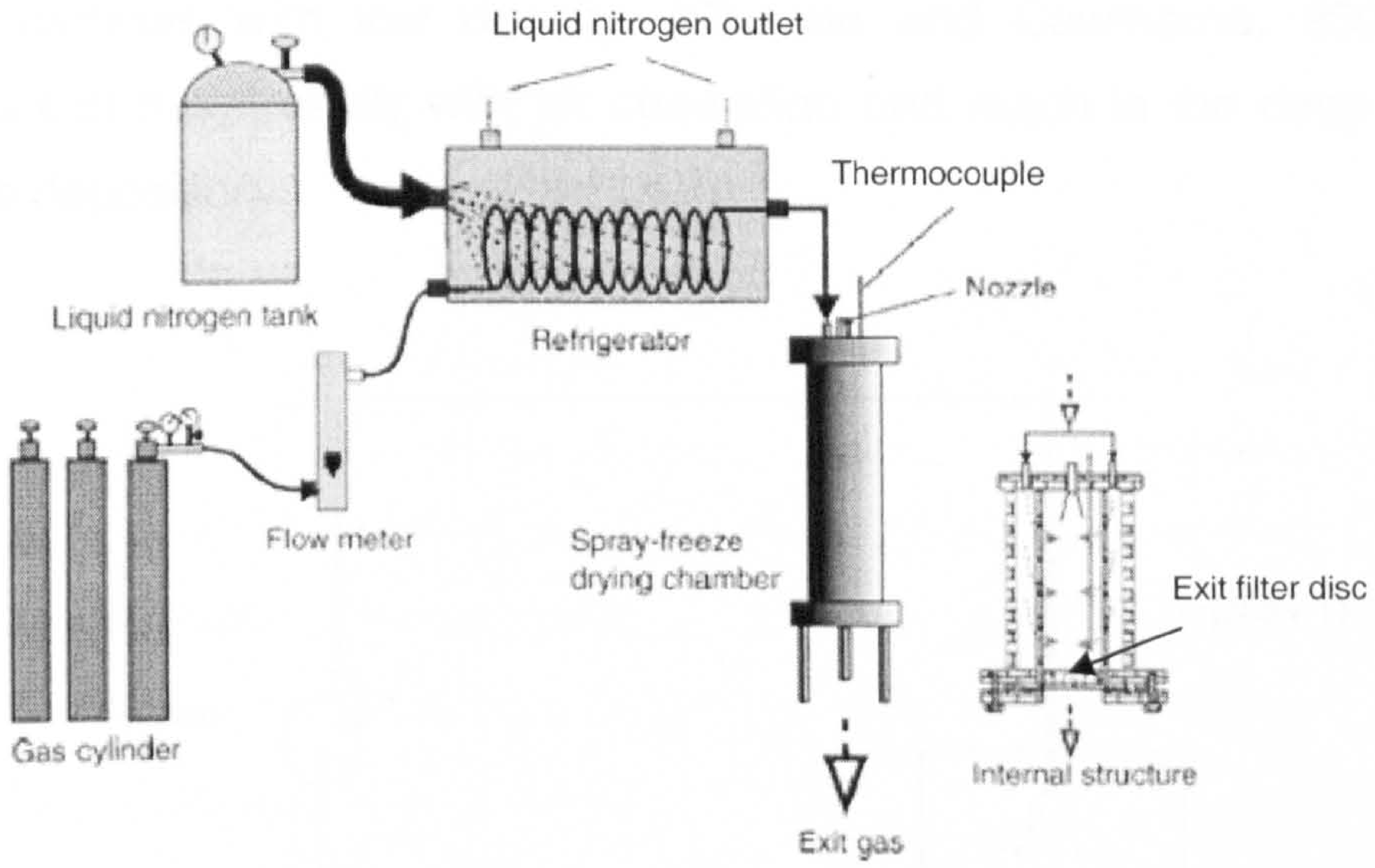

Figure 2-14: Schematic diagram of the atmospheric spray-freeze-drying apparatus (Wang *et al.*, 2006).

2.5.2 Spray-freezing into vapour over liquid

In spray-freezing into vapour over liquid (SFV/L) process (figure 2-15), the feed solution is atomised for the nozzle positioned at distance above the refrigerant (liquid nitrogen). The atomised droplets starts to freeze in the vapour phase before they contact the surface of the cryogenic liquid and the suspended frozen particles are separated from the liquid nitrogen followed by conventional lyophilization process to remove the solvent (Rogers *et al.*, 2003).

In the pharmaceutical industries, powder production for dry powder inhaler (DPI) is a fast growing area. Research on insulin administration via pulmonary delivery by the inhalation method is currently undergoing clinical trials. The absorption of insulin into the deep lung (alveoli) may be possible using a dry powder inhaler (DPI). The jet milling, spray drying and crystallization are currently used methods for inhaled dried powder preparations. However, all these methods have some limitations due to the sensitivity of certain pharmaceutical ingredients to the processing environment, and also poor control on particle size. Spray-freeze-drying is a potential alternative to these conventional processes, having greater control on particle size and produces porous particles with low density. (Shoyele and Cawthorne, 2006). The particles can travel easily with air streamline and reach in the deep lung for effective deposition.

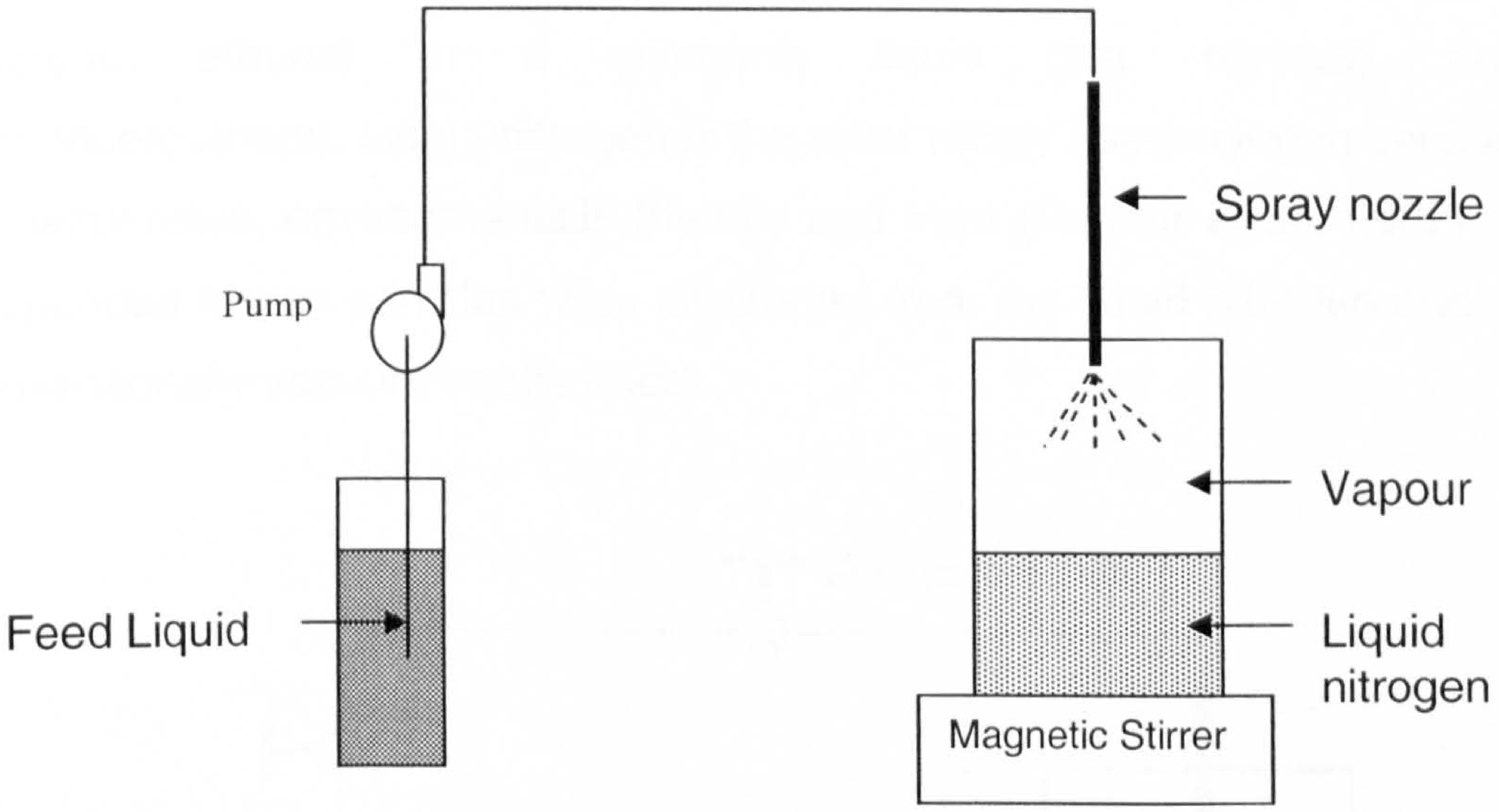

Figure 2-15: Schematic diagram of the spray-freezing into vapour over liquid (SFV/L).

Maa *et al.* (1999) manufactured a protein inhalation powder by spraying the liquid protein through a two-fluid nozzle into a round bottom flask containing liquid nitrogen. The flask was submerged in liquid nitrogen and agitated by a magnetic stirrer. The protein powder was separated and dried by a conventional freeze drying method. They found that spray-freezing in liquid nitrogen produced porous particles of lower density than from the spray drying method.

Sonner *et al.* (2002) studied trypsinogen (model protein) stability using the SFV/L method. They used an ultrasonic nozzle to atomise the feed liquid into the circular metal bowl (containing liquid nitrogen and conical metal cover used to minimize the loss of liquid nitrogen. They effectively produced protein (trypsinogen / trehalose) loaded particles (size range 20-80 μm) for epidermal delivery used.

2.5.3 Spray-freezing into liquid

Figure (2-16) shows the spray-freezing into liquid (SFL) process and it involves the atomisation of a feed solution into a compressed liquid (e.g. CO_2, propane, ethane) or a cryogenic liquid (e.g. nitrogen, argon, hydrofluoroethers). Liquid nitrogen is the most widely used cryogen because it is inexpensive, environmentally friendly and inert (Rogers *et al.*, 2002). The suspended frozen particles were separated from the liquid nitrogen and then conventionally vacuum freeze dried.

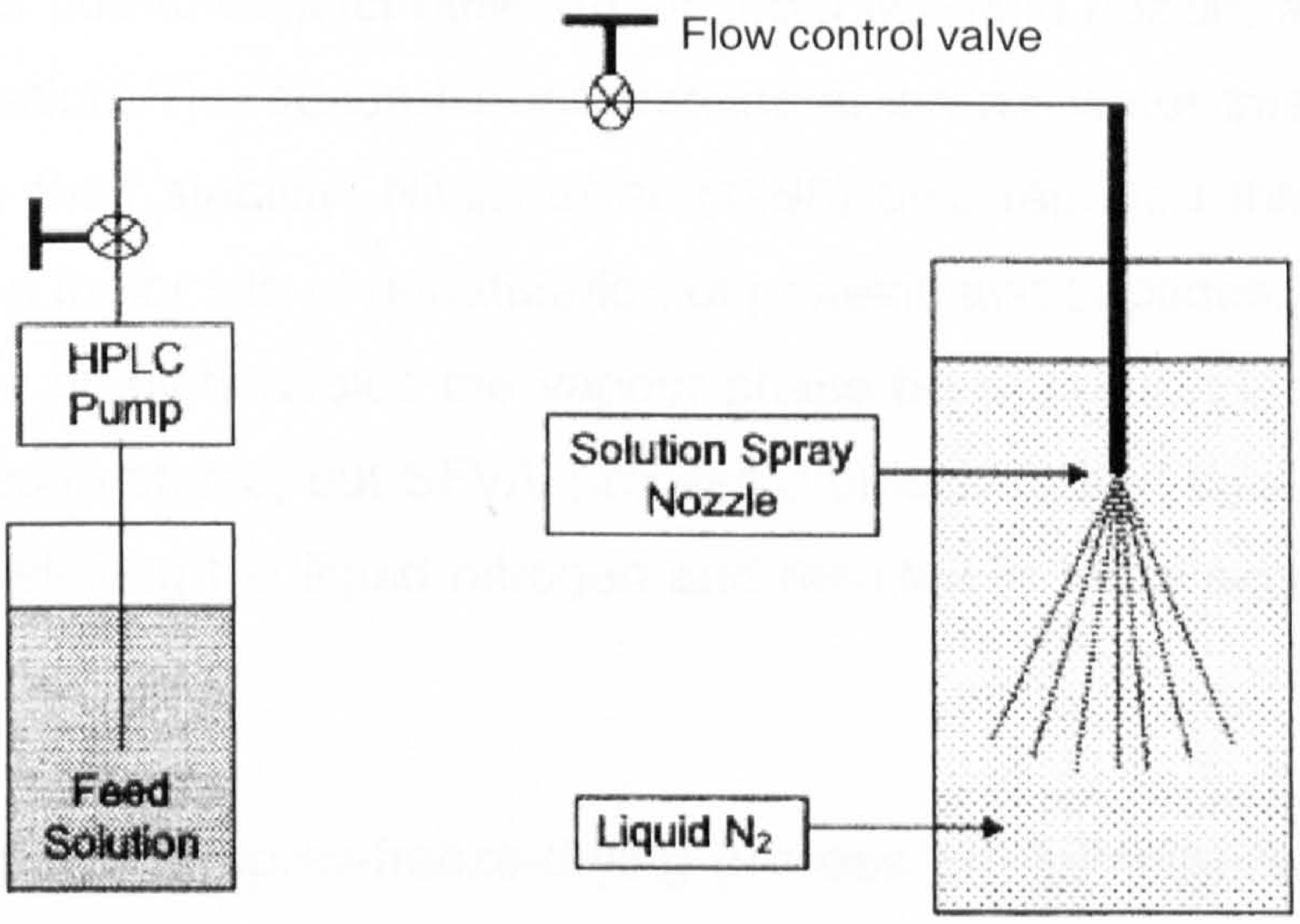

Figure 2-16: Schematic diagram of the spray-freezing into liquid (SFL) (Rogers *et al.*, 2002).

Costantino *et al.* (2000) studied the spray-freeze drying of bovine serum albumin (BSA) as a model protein and examined the effects of atomisation conditions on the particle size and stability using the SFL technique. These authors revealed that the initial release of protein [encapsulated in poly(lactide-co-glycolide) microspheres] occurs from the smallest size of particles. On the other hand, an increase in the particle size caused a reduction in the drying rate. Costantino *et al.* (2002) also reported the effect of formulation variables (addition of surfactants or mannitol) on microencapsulated proteins using the SFL technique. Rogers *et al.* (2002) used polyether-ether-ether-ketone (PEEK) nozzle (63.5 μm diameter) to atomise the feed solution (pharmaceutical ingredient) into the liquid nitrogen surface at constant pressure (5000 psi). The PEEK nozzle has excellent chemical resistance, high strength and can withstand very low and high temperatures. The frozen particles were collected by sieving and finally a conventional freeze-drying method was used for drying. They also studied a pilot-scale SFL process, where a 127 μm diameter PEEK nozzle was used.

Yu *et al.* (2006) compared the SFL and SFV/L process in the context of protein aggregation and they concluded that the SFL process yields a smaller degree of protein aggregation and less loss of enzyme activity relative to SFV/L process due to contact between air (from two-fluid nozzle) and droplet during atomisation. The adsorption of proteins at the air–water interface may also influence their stability. Niven *et al.* (1996) also reported that air-water interface was a major site of denaturation of proteins and peptides. In the SFL process, water droplets avoids the vapour phase because nozzle was within the liquid nitrogen phase, but SFV/L process droplets passed through vapour phase before striking the liquid nitrogen and resulted in more aggregation of proteins.

The developments of spray-freeze-drying process are summarized in Table (2-3). It clearly indicates that the equipment development and applications of SFD technology is used in wide range of products from food to pharmaceuticals. However, all the published and patented processes are based on spray cooling in liquid nitrogen/vapour under atmospheric conditions followed by conventional freeze-drying or atmospheric fluidised bed freeze-drying.

Table 2-3: Developments of spray-freeze-drying process

Year	Researchers	Process*	Focus
1959	Merymann	SFV+FD	Drying of mouse kidney tissue
1963	Woodward	AFBFD	Drying of low sugar foods
1970	Malecki *et al.*	AFBFD	Drying of apple juice, liquid egg and orange juice
1974	Helman and Hohner	AFBFD	Equipment development
1983	Boeh-Ocansy	AFBFD with adsorbent	Equipment development
1986	Leuenberger	SFV+ AFBFD	Equipment development
1990	Wolff and Gibert	AFBFD with adsorbent	Equipment development
1991	Leuenberger	SFV+ AFBFD	Drying of manitol
1999	Maa *et al.*	SFV/L+FD	Production of protein inhalation powder
2000	Costantino *et al.*	SFL+FD	Drying of proteins (BSA)
2002	Rogers *et al.*	SFL+FD	Drying of pharmaceutical ingredients
2002	Sonner *et al.*	SFV/L+FD	Production of protein loaded particles for epidermal delivery
2003	Hu *et al.*	SFL+FD	Drying of pharmaceutical ingredients
2004	Yu *et al.*	SFL+FD	Drying of proteins (BSA)
2004	Maa *et al.*	SFV/L+FD	Development of a process for preparation of influenza vaccine dry powder formulation.
2005	Sweeney *et al.*	SFL+FD	Production of liposomal ciprofloxacin powder for inhaled aerosol drug delivery.
2006	Wang *et al.*	SFV+AFD	Drying of proteins (BSA)
2006	Anandharamakrishnan *et al.*	SFV+VFBFD	Equipment development and drying of proteins

* SFV - spray-freezing into vapour
SFV/L - spray-freezing into vapour over liquid
SFL - spray-freezing into liquid
AFBFD - atmospheric fluidised bed freeze-drying
AFD - atmospheric freeze-drying
FD - conventional vacuum freeze-drying
VFBFD - vacuum fluidised bed freeze-drying

Relatively, little has been published on the SFV technique to date, yet the potential for generating protein products with controlled microstructures renders this an exciting area for development in the food and pharmaceutical industries, particularly for proteins, which are susceptible to heat damage by the currently used spray drying method. In this context, the SF+VFBFD is an alternative to conventional spray drying and freeze-drying methods for producing proteins in powder form.

2.6 Proteins

This section provides an overview of proteins in general and whey proteins in particular, including their functional properties and problems that can arise as a result of processing such as, denaturation and loss of solubility.

The term "protein" comes from the Greek word "proteios" which means of "*primary importance*" Proteins are an important class of biochemical molecules. They are high molecular mass organic compounds that consist of amino acids joined by peptide bonds. Proteins are essential to the structure and function of all living organisms. Proteins were discovered by Jons Jakob Berzelius who mentioned the word '*protein*' in a letter he sent to Gerhardus Johannes Mulder on 10th July 1838, where he wrote:

> "The name **protein** that I propose for the organic oxide of fibrin and albumin, I wanted to derive from πρωτειoξ (the Greek word), because it appears to be primitive or principal substance of animal nutrition"

Proteins are natural polypeptides in chain form, synthesized with different amino acids within the cell. These polypeptide chains have the characteristics of folding into unique 3D structures, which are stabilized by a combination of electrostatic and hydrophobic interactions, along with multiple hydrogen bonds that are formed between the side chains of the amino acids (Creighton, 1992; Branden and Tooze, 1999). The functional properties of proteins depend upon their three-dimensional structure, which is determined by the particular sequences of amino acids in polypeptide chains (primary structure), and builds over structural levels as shown in figure (2-17).

The protein structural levels are described as:

Primary: The ordering of amino acids within the polypeptide chain.

Secondary: The bending or twisting of polypeptide chains into alpha-helix, beta-pleated and random coil structures.

Tertiary: As a results of bonding between "side chains" causing folds, bends and loops in the protein chain.

Quaternary: Occurrence of more than one polypeptide chain in a protein.

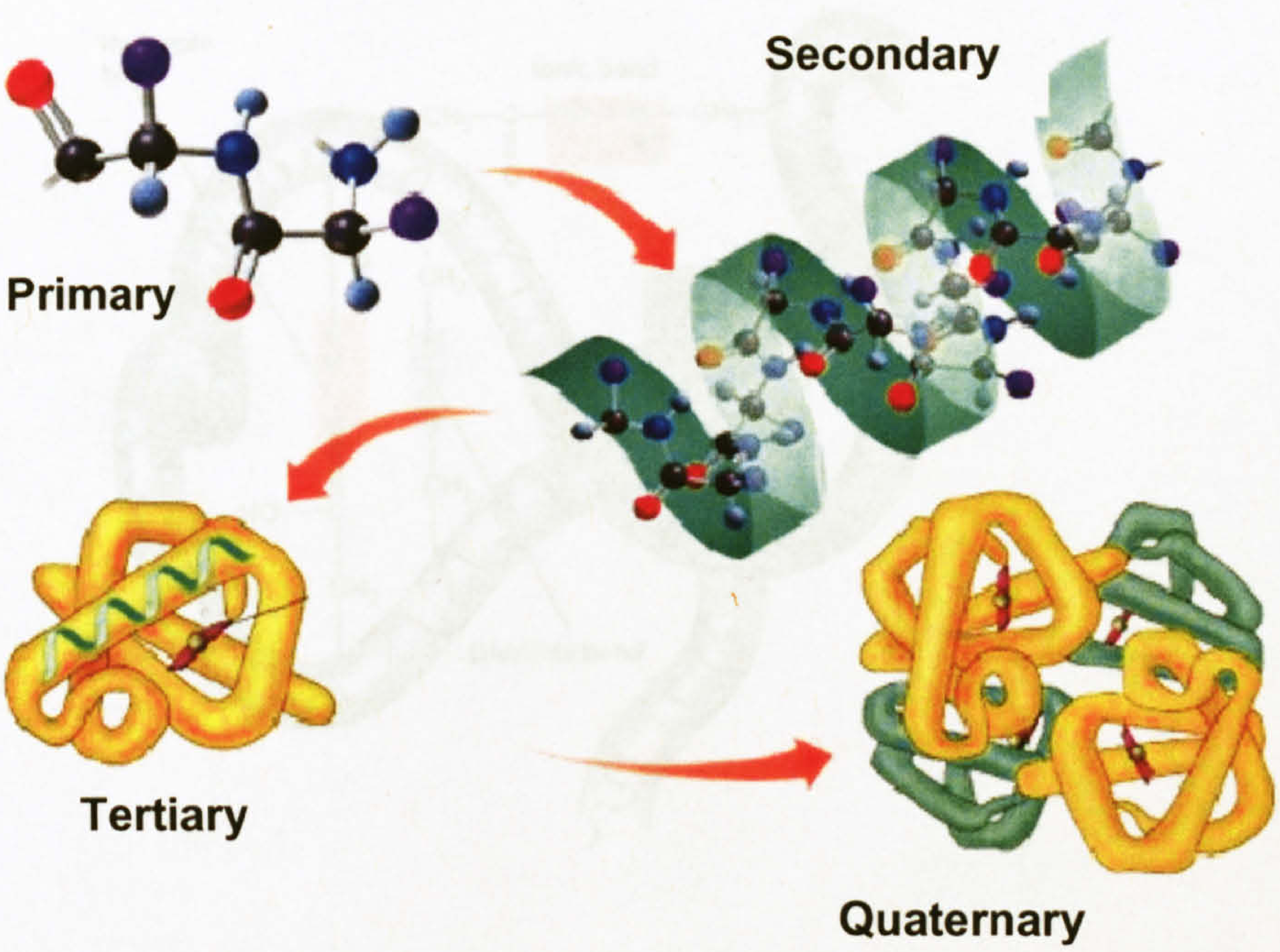

Figure 2-17: Protein structural levels (Branden and Tooze, 1999).

2.6.1 Denaturation of proteins

Denaturation is a process, which involves the disruption and destruction of bonds in the secondary, tertiary and quaternary protein structures. In their native state, interactions between the polypeptide chains stabilize the protein structure and are sufficient to maintain its conformation over a range of environmental conditions. A change in the environmental conditions disrupts the normal alpha-helix and beta sheets in a protein (biologically active folded molecules in their native state) into an unfolded random shape (a biologically inactive denatured state) (Creighton, 1992). Figure (2-18) shows an example of a single polypeptide chain in the native form. Its structure is dictated by the presence of hydrogen, ionic and covalent (disulphide bonds). The nature of the environmental changes causes denaturation by the disruption of different bonds between the side chains. For example, (1) *heat and organic compounds* break apart H bonds and disrupt hydrophobic interactions; (2) *acid and bases* break H bonds between polar R groups and disrupts ionic bonds; (3) *heavy metal ions* react with S-S bonds to form solid; (4) *agitation* such as by whipping stretches the chains until the bonds break.

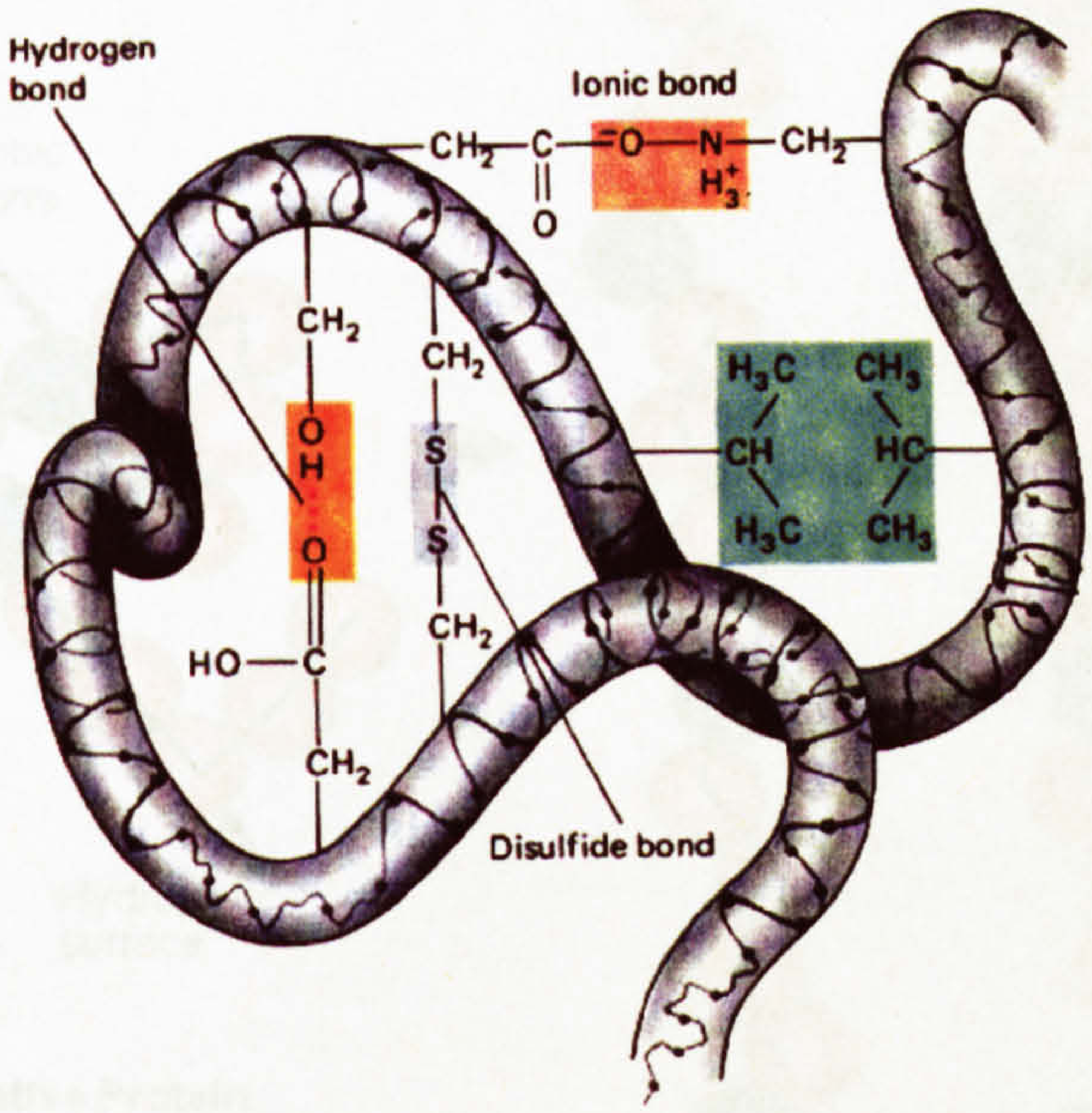

Figure 2-18: A polypeptide chain in native form.

2.6.2 Thermal denaturation of proteins

In drying operations, protein denaturation mainly occurs as a result of thermal treatment. Figure (2-19) shows the different states of polypeptide chains that can arise during processing. In aqueous media the strong bonds (hydrogen and ionic) produce a compact globular molecule with a tightly packed hydrophobic core this is the native form. These hydrophobic groups are buried inside the polypeptide chain and hydrophilic groups are exposed at the surfaces. Exposing the proteins to temperatures above their denaturation temperature, the hydrophobic interactions break and alter the native folded state into an inactive unfolded state. The unfolded protein states allow cross-linking interactions between protein molecules mainly due to hydrophobic interactions. These interactions result in aggregation, coagulation and finally precipitation (loss of solubility). The best example of this reaction is transparent egg white, which becomes non-transparent during heating on a hot plate, as denatures and subsequently gels.

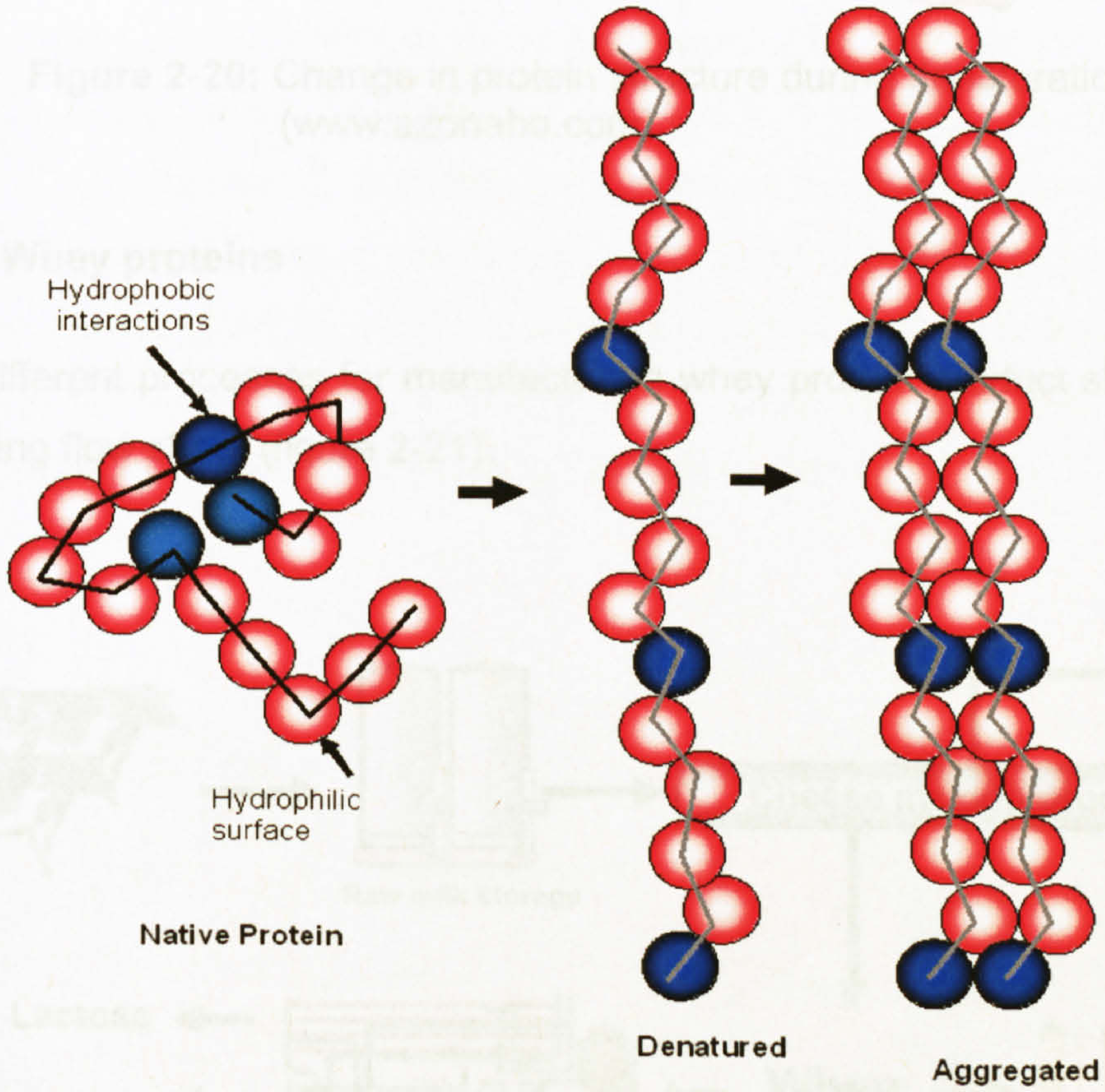

Figure 2-19: A polypeptide chain in the native, denatured and aggregated states.

Enthalpy, entropy and temperature determine the free energy difference between the native and the denatured state. The enthalpy difference between the native and denatured states can reach several hundred J/mol. The entropy of the native state is lower as the chains are highly ordered, whereas in the denatured state it is disordered with many different conformations of the protein molecule (Branden and Tooze, 1999). During denaturation, the size of the protein increases to a value consistent with a random coil polymer of the same molecular weight and the denatured proteins start to aggregate with other denatured proteins. This is illustrated in figure (2-20).

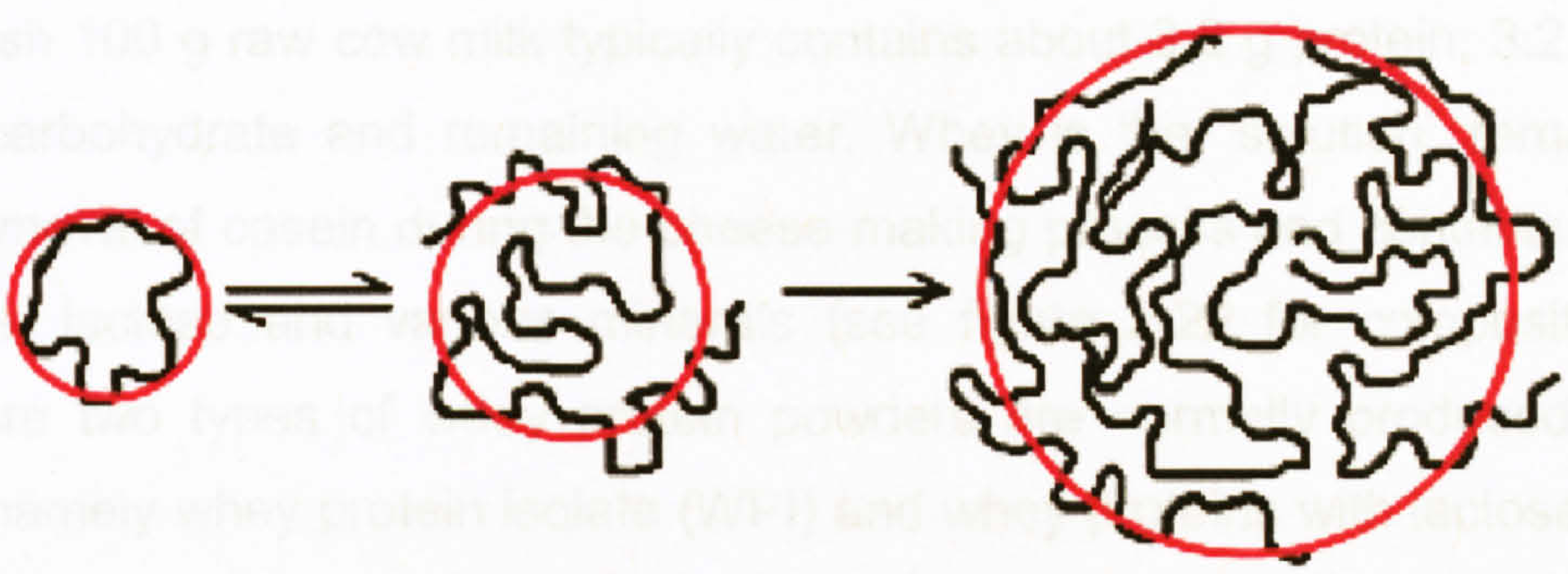

Figure 2-20: Change in protein structure during denaturation (www.azonaho.com).

2.6.3 Whey proteins

The different processes for manufacturing whey protein product shown in the following flow sheet (figure 2-21).

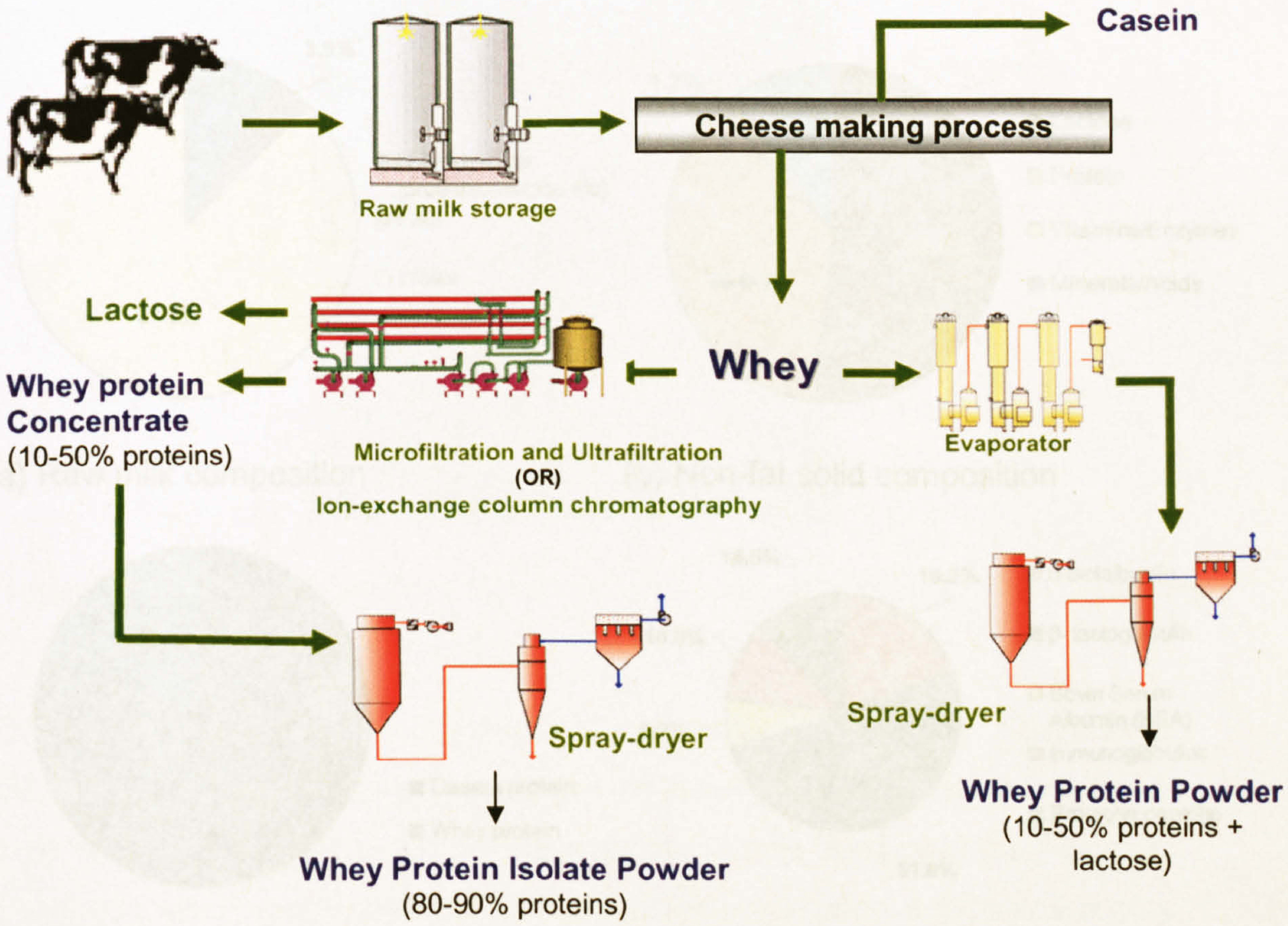

Figure 2-21: Process flow diagram of different forms of whey proteins.

The fresh 100 g raw cow milk typically contains about 3.2 g protein, 3.2 g fat, 3.7 g carbohydrate and remaining water. Whey is the "solution" remaining after removal of casein during the cheese-making process and contains whey proteins, lactose and various minerals (see figure 2-22 for compositions). They are two types of whey protein powders are normally produced from whey, namely whey protein isolate (WPI) and whey proteins with lactose. The whey protein isolate (WPI) powder is produced by removal of lactose and minerals using either ion-exchange adsorption separation or microfiltration followed by spray drying methods and it contains nearly 90% proteins (Walsh, 2002). The spray dried concentrated whey products are whey protein with lactose powder (10-50% proteins). As the concentration of lactose increases the protein concentration decreases. The figure (2-22) shows the typical composition of whey proteins in milk (McKenzie, 1971).

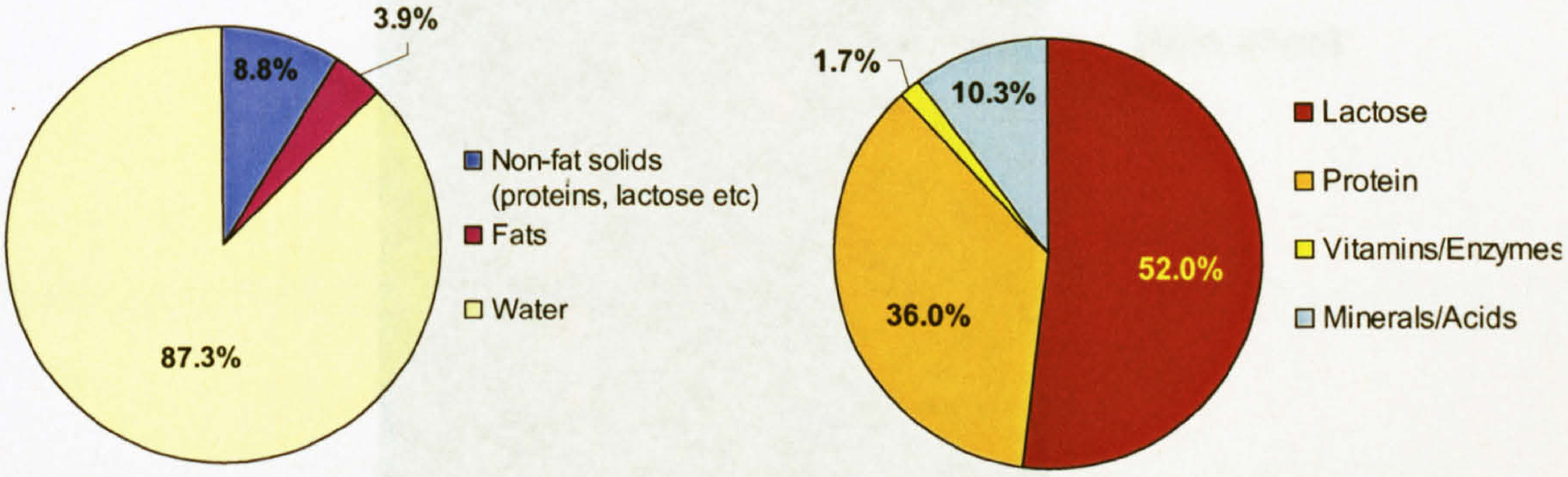

(a) Raw milk composition (b) Non-fat solid composition

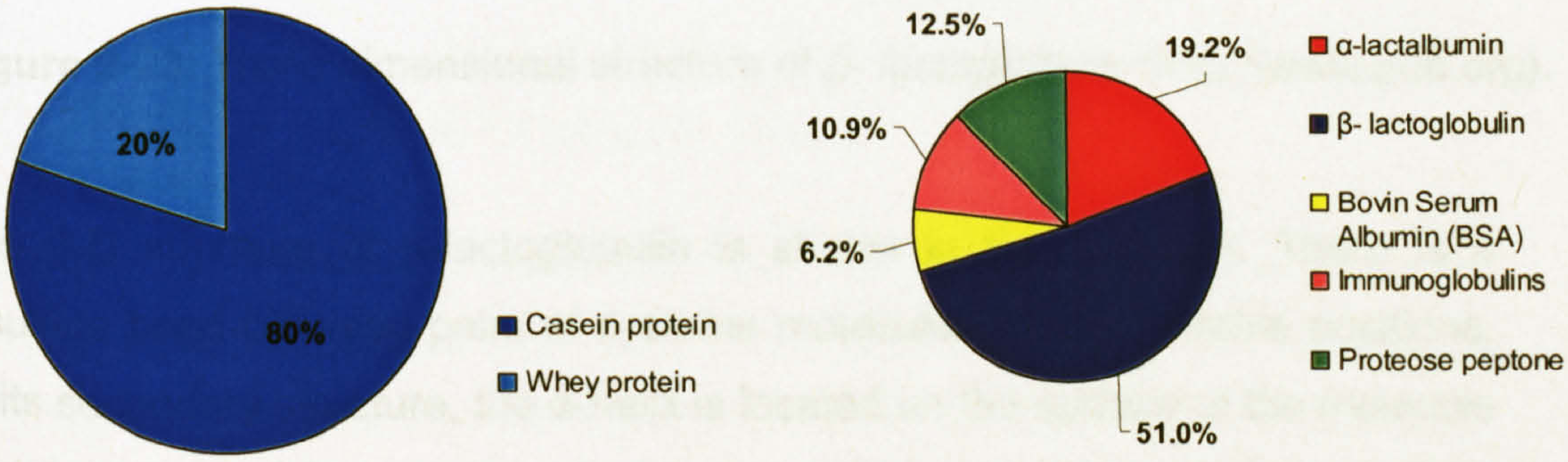

(c) Protein composition (d) Whey protein composition

Figure 2-22: Milk protein compositions.

The two major proteins in whey proteins are β-lactoglobulin and α-lactalbumin. The biochemical and physicochemical properties of both these proteins have been extensively studied and their primary, secondary, tertiary and quaternary structures are well documented. These are now described.

2.6.3.1 β-lactoglobulin

The main constituent of whey is β- lactoglobulin and it is a very stable and well studied protein. It constitutes the major protein (51%) in whey and hence the nature of whey protein depends greatly upon its properties. It plays an extremely important role in the food industry as a result of its gelation and emulsification properties (Schokker *et al.*, 2000; Anema *et al.*, 2005). β-lactoglobulin has 162 amino acids with a molecular weight of about 18300 Da (Kay *et al.*, 1990).

Figure 2-23: Three dimensional structure of *β- lactoglobulin* (http://www.pdb.org).

The 3-D structure of β-lactoglobulin is shown in figure (2-23). There is a disulfide bond between pairs of cysteine molecules at two variable positions. In its secondary structure, the α-helix is located on the surface of the molecule and 8 strands of β-structure out of 9 are arranged to form a β- barrel with a hydrophobic centre.

2.6.3.2 α-lactalbumin

The second main (19%) constituent of whey is α-lactalbumin with 123 amino acids and a molecular weight of 14200 Da. α-lactalbumin is stabilised by four disulphide bonds and does not contain a free thiol group. (Boye *et al.*, 1997; Permyakov and Berliner, 2000). The thiol groups are important in the formation of disulfide linked aggregates (Oldfield *et al.*, 2005). Alpha helices are shown in the structure (figure 2-24).

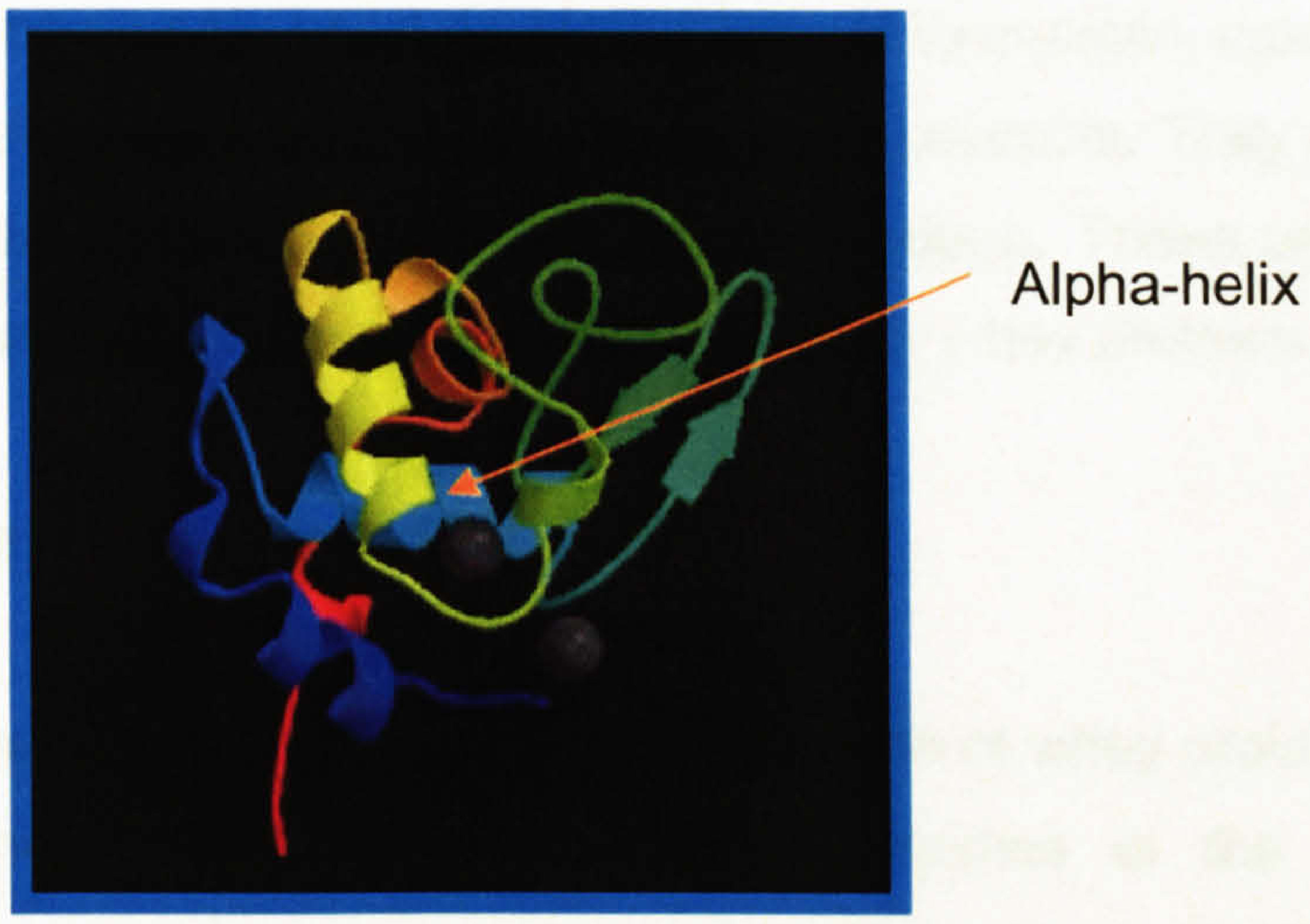

Figure 2-24: Three dimensional structure of α-lactalbumin (http://www.pdb.org).

α-lactalbumin is considered to be the most heat-stable whey protein. Calcium (Ca^{2+}) forms intermolecular ionic bonds with α-lactalbumin, which gives an added resistance to thermal denaturation or unfolding (Boye *et al.*, 1997).

2.6.4 Nutritional benefits of whey proteins

An essential amino acid is an amino acid that cannot be synthesized by the humans organism and therefore must be supplied in the diet. Amino acids are "*building blocks*" of healthy bodies. Compared to any other protein on a gram to gram basis, whey protein isolate delivers more essential amino acid to the body without fat or cholesterol. Whey proteins have the highest possible Protein Digestibility Corrected Amino Acid Score (PDCAAS) of 1.0, which is an indicator of their ability to supply all the essential amino acids to the body.

Whey proteins have an excellent amino acid balance, including both essential and sulphur containing amino acids. Whey proteins help to prevent muscle breakdown and spare glycogen during exercise. Whey protein contains many of the same components found in human breast milk and for this reason, is a key ingredient in a wide variety of infant formulas, including those for premature babies. It also helps to control the blood pressure and also increases insulin sensitivity. Recently, it has been found to inhibit the growth of several types of cancer tumours.

Whey proteins are commonly used as ingredients in formulated foods, such as dairy foods, bakery products, beverages and meat products. They are also used as encapsulating agents for pharmaceutical products. These properties highlight the nutritional quality and cost-effectiveness of whey proteins.

2.6.5 Whey protein denaturation and solubility

Several studies have been reported on the denaturation of whey protein in the aqueous state. One of the earliest calorimetric studies of the thermal denaturation of whey proteins was carried out by Rugg *et al.* (1977), using differential scanning calorimetry (DSC) to study thermal transitions of whey proteins and enzymes in milk ultrafiltrate solution. These authors found that α-lactalbumin, lysozyme, ribonuclease and xanthine oxidase were relatively thermally stable compared to other milk proteins. Ibanoglu (2005) studied the thermal denaturation of bovine serum albumin (BSA), lysozyme and whey protein isolate (WPI) in the presence of hydrocolloids (pectin, guar gum). WPI was observed to be relatively stable at acidic pH (4.0) but denatured at a lower temperature at an alkaline pH (9.0). The highest thermal stability obtained was in presence of pectin.

There are numerous studies of the effects of thermal treatment on the denaturation of whey proteins during the heating of milk (Dannenberg and Kessler, 1988; Anema, 2000; Oldfield *et al.*, 2000; Ferreira *et al.*, 2001; Anema, 2001) but very few works have reported on the effect of solids concentration on the denaturation of whey protein. Guy *et al.* (1967) and Law and Leaver, (1997) observed that for a given thermal process, whey protein denaturation was at a minimum for a low total protein concentration in milk. In contrast, McKenna and O'Sullivan (1971) found that increasing the total solid concentration reduces the denaturation of protein during the heating of milk at 80°C.

Although a large number of studies have been carried out on the spray drying of whey powder, so far, relatively little work has been reported on the effects of spray drying conditions on the denaturation of whey proteins. However, an exception is Guyomarch *et al.* (2000) who found that denaturation (determined by precipitation at pH 4.6) of whey proteins takes place during the pasteurisation stage, whereas during spray drying of skim milk, denaturation occurs only to a small extent at 160-190°C inlet and 65-90°C outlet air temperatures. Recently, Oldfield *et al.* (2005) observed that varying the inlet and outlet gas temperatures (from 160 to 200 °C and 89 to 101 °C, respectively) did not affect the amount of whey protein denaturation (analysed by mini-gel electrophoresis method). However, in their experiments, they found that most of the whey proteins had already been denatured during concentration of the skimmed milk by preheating from 70°C to 120°C for 52 s, prior to feeding to the spray drier.

Solubility is an important property for the functional behaviour of whey proteins. Soluble proteins impart emulsion, foam, gelation and whipping properties; a decrease in solubility affects the protein functionality. The solubility depends on whether the proteins are in their native or denatured state and also on environmental factors such as pH and temperature. However, denaturation alone is not enough to cause a measurable loss of solubility, as the proteins must also aggregate (Pelegrine *et al.*, 2005). The solubility of whey protein concentrate (WPC) gels with honey and wheat flour was studied by Yamul and Lupano (2005) who found that wheat flour interacts with WPC through noncovalent bonds and disulphide bonds, which leads to thermal stability of the proteins.

2.7 Computational fluid dynamics (CFD)

CFD simulations were performed as part of the work of this thesis in order to understand particle behaviours during the spray-freezing and spray-drying processes. This section describes the principles of CFD with different methods used in the literature for spray drying simulations.

> "All the mathematical sciences are founded on relations between physical laws and laws of numbers, so that the aim of exact science is to reduce the problems of nature to the determination of quantities by operations with numbers"
>
> -James Clerk Maxwell, 1856

This approach (the use of supercomputers to solve aerodynamic problems) was used by NASA in 1970s for developing the HiMAT aircraft, but problems could be solved limitations in computer speed and storage meant that only two-dimensional flow (Anderson, 1984). By the 1990s, advances in computing power produced a similar boom in software development and solutions. Since then CFD has been used extensively by the scientific community worldwide. The reason for this interest is justified by the fact that it is possible to model computationally the physical fluid phenomena that are expensive and time consuming to measure directly.

Computational Fluid Dynamics (CFD) is a simulation tool, which uses powerful computers in combination with applied mathematics to model fluid flow situations and aid in the optimal design of industrial processes (Anderson, 1984; Versteeg and Malalasekera, 1995). The role of CFD in engineering has become so strong that today it may be viewed as a new third dimension of fluid dynamics (the other two dimensions are classical cases of pure experiment and pure theory). The method comprises solving equations for the conservation of mass, momentum and energy, using numerical methods to give predictions of velocity, temperature and pressure profiles inside the system. It powerful graphics can be used to then show the flow behaviour of fluid with 3D images (Scott and Richardson, 1997).

2.7.1 CFD Analysis

CFD analysis involves following three main steps. The first step is *Pre-processing*, which includes problem definition, geometry, meshing (this can usually be done with the help of a standard CAD programme) and generation of a computational model. The second step is *Processing,* which uses a computer to solve the mathematical equations of fluid flow. The final step of *Post-Processing* is used to evaluate and visualize the data generated by the CFD analysis (Xia and Sun, 2002) and validate the simulation results with experimental data.

2.7.2 Numerical simulations of gas-particle interactions

A general overview of the methods used for numerical simulation of gas-particle flows is presented in this sub-section. The primary problem in spray drying/spray cooling modelling is the coupling of equations in mass, momentum and energy between the gas and the droplets. These coupling phenomena of mass transfer from droplet to gas was coupling by evaporation, momentum exchange via drag and energy coupling by heat transfer, which are schematically shown in figure (2-25).

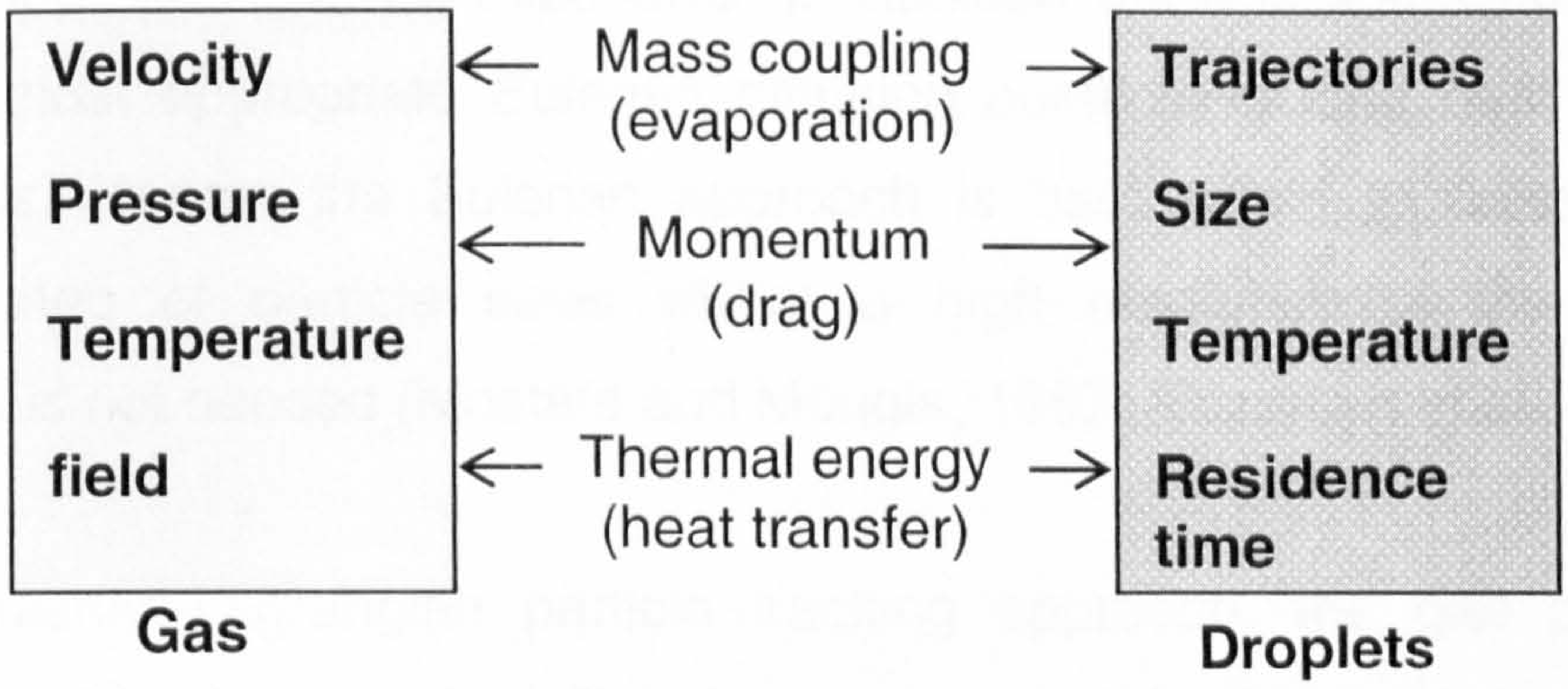

Figure 2-25: Gas-droplet coupling phenomena (Crowe *et al.*, 1977).

Heat is transferred from the gas phase to the droplets convectively and this leads to a decrease in temperature of the gas this affects the viscosity and density of the gas, which in turn may affect the gas flow field. This then affects the droplet trajectories and the heat transfer rate between the droplets and the gas (Crowe *et al.*, 1977). Hence, all three equations (mass, momentum and energy) are interdependent and should be included in the gas-droplets interactions.

2.7.2.1 Reference frames

The two most general two-phase modelling methods are the Eulerian-Eulerian and the Eulerian-Lagrangian methods. In the Eulerian-Eulerian method, the dispersed phase (droplets) are treated as a continuous (Eulerian) phase, i.e. there are two Eulerian phases, one for the gas another for droplets, which are interacting and interpenetrating continua (Mostafa and Mongia, 1987). Each computational cell contains certain fractions of gas and droplets, and the transport equations are written in such a way that the volume fractions of gas and liquid sum to unity. If the computational cell consists of just a single phase, the transport equations for the two phases revert to the conventional single-phase system. The advantages of the Eulerian-Eulerian approach are that it is usually relatively cheap in terms of computational demands for one additional set of equations and turbulence can be modelled fairly simply. However, if a separate set of transport equations is solved for each particle size (single particle diameter was used for the dispersed phase) then the Eulerian approach can be expensive. In addition there is some uncertainty over the most appropriate Eulerian diffusion coefficients and heat transfer coefficients. Hence, the Eulerian approach is best suited to flows with a narrow range of particle sizes where a high resolution of the particle properties is not needed (Mostafa and Mongia, 1987; Jakobsen *et al.*, 1997).

In the Eulerian-Lagrangian particle tracking approach, the gas phase is modelled using the standard Eulerian approach described above and the spray is represented by a number of discrete computational 'particles'. Individual particles are tracked through the flow domain from their injection point until they escape the domain in a Lagrangian frame work (Nijdam *et al.* 2006). The Eulerian-Lagrangian model has the advantage of being computationally cheaper than the Eulerian-Eulerian method for a large range of particle sizes. It can also provide more details of the behaviour and residence times of individual particles and can potentially approximate mass and heat transfer more accurately. On the other hand, the approach can be expensive if a large number of particles have to be tracked and it is best when the dispersed phase does not exceed 10% by volume of the mixture in any region (Bakker, 2002).

In both the Eulerian-Eulerian and the Eulerian-Lagrangian methods, the exchange of momentum between particles and gas needs to be modelled. This exchange can consist of several forces such as, drag, lift, virtual mass, lubrication and wall forces. Mostafa and Mongia (1987) concluded that the Eulerian approach performs better than Lagrangian method. In contrast, a recent study by Nijdam *et al.* (2006) found that both Eulerian and Lagrangian modelling approaches gave similar predictions for turbulent droplet dispersion and agglomeration of sprays for a wide range of droplet and gas flows. The two models were found to require similar computing times for a steady axi-symmetric spray. However, the authors preferred the Lagrangian models because of their wider range of applicability.

2.7.3 Turbulence models

Four turbulence models are commonly used for simulating sprays: (i) standard k-ε (k- turbulence kinetic energy and ε- turbulence dissipation rate) (ii) RNG k-ε, (iii) realizable k-ε, (iv) Reynolds Stress Model (RSM). Three models (standard, RNG, and realizable k-ε) have similar forms, with transport equations for k and ε. The standard k-ε model focuses on the mechanisms that affect the turbulent kinetic energy. It can be used over a wide range of turbulent flows due to its robustness and reasonable accuracy. In the realizable k-ε model, the term "realizable" means that the model satisfies certain mathematical constraints on the normal stresses, consistent with the physics of turbulent flows. It provides better prediction for flows involving rotation, boundary layers under strong adverse pressure gradients, separation, and recirculation (Anderson, 1984; Fletcher, 2000).

The RNG-based k-ε turbulence model is derived from the instantaneous Navier-Stokes equations, using a mathematical technique called "renormalization group" (RNG) methods. The analytical derivation results in a model with constants different from those in the standard k-ε model and additional terms and functions in the transport equations for k and ε. The effect of swirl on turbulence is included in the RNG model, which enhancing accuracy for swirling flows.

The Reynolds Stress Model has the same general form as the instantaneous Navier-Stokes equations, with the velocities and other solution variables ensemble-averaged (or time-averaged). The RSM is clearly superior for problems where anisotropy of turbulence has a dominant effect on the mean flow (e.g. highly swirling flows) (Fluent, 2005). Huang *et al.* (2004) showed that RNG k-ε model prediction was better for swirling two-phase flow in the spray drying chamber compared to standard k-ε, realizable k-ε and Reynolds stress models. However, this work spray drying and spray-freezing operations has no swirling flow inside the chamber.

2.7.4 CFD modelling and simulation of spray drying operations

In recent years, a rapid development in the application of CFD in food processing operations has been witnessed (Anandharamakrishnan, 2003; Norton and Sun, 2006). Figure (2-26) evidence the growth of this emerging field by the steady increase in peer-reviewed journal papers over the years on CFD applications in the food industry.

In the spray-drying field, CFD simulation tools are increasingly used because, measurements of air flow, temperature, particle size and humidity within the drying chamber are very difficult and expensive in large scale spray dryers. Langrish and Fletcher (2001) and Fletcher *et al.* (2003) comprehensively reviewed the applications of computational fluid dynamics in spray drying operations, to predict the flow patterns and temperature distributions of gas and droplets.

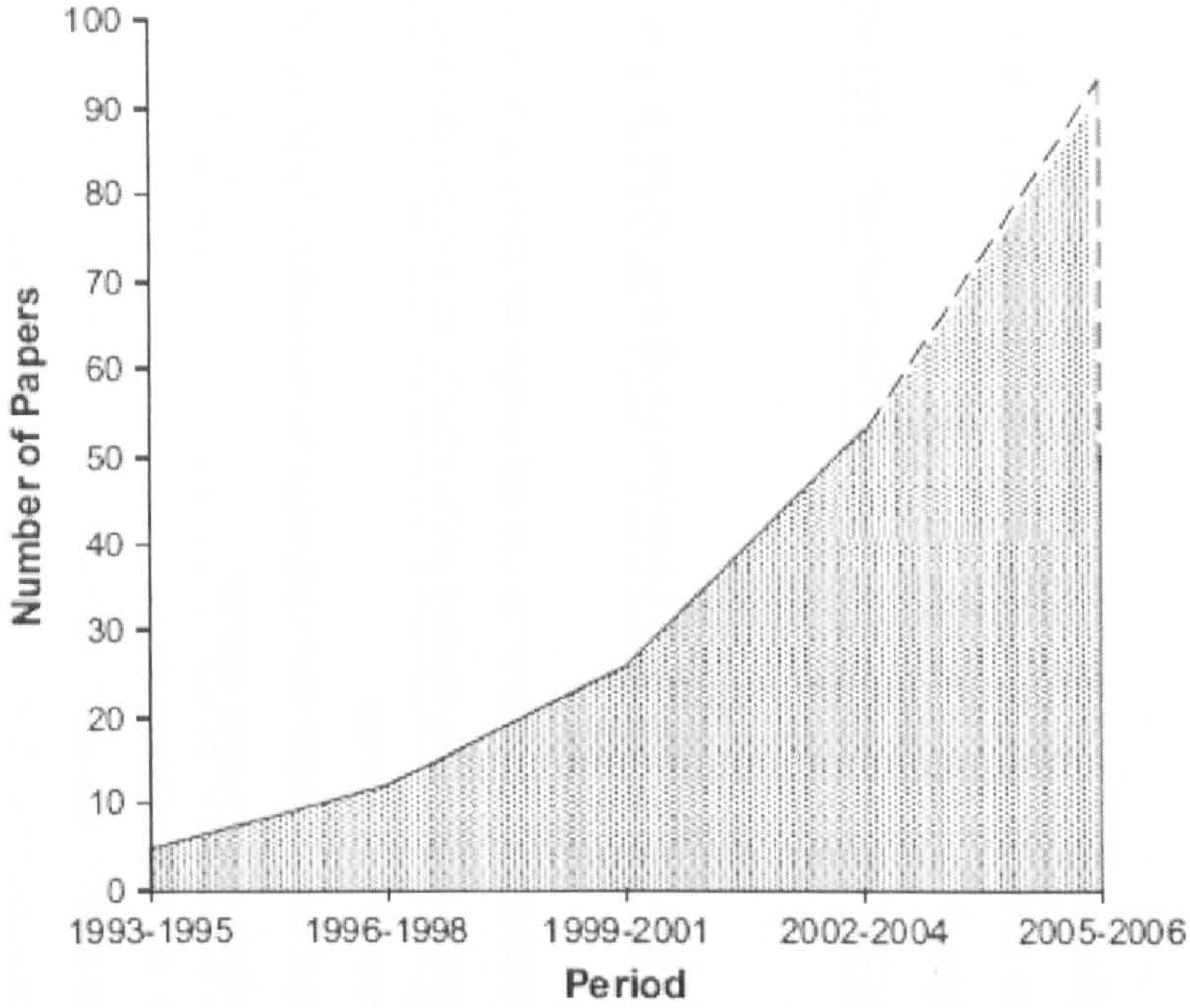

Figure 2-26: The number of published peer-reviewed papers with CFD applications in the food industry (Norton and Sun, 2006).

Crowe *et al.* (1977) first proposed the "*particle source in cell*" (PSI-Cell) model (see detailed discussions in Chapter 7) which includes two-way coupling between the drying gas and the spray droplets. The PSI-Cell model was used by Papadakis and King (1988) and they found good agreement between the model and experimental results in a concurrent spray dryer. Moreover, this PSI-Cell model is the basis for popular discrete phase modelling (DPM) and the DPM model is used for most of the commercial CFD software packages. A number of works have been studied on spray drying, which are summarized in the Table 2-5.

Table 2-4: Published spray-drying CFD models and their findings.

Authors	Problem descriptions	Model geometry	Turbulence Model	Software	Findings
Oakley and Bahu (1993)	Simulation of airflow pattern with experimental validation.	2D	standard k-ε and RSM	FLOW3D	Non-swirling flow spray chamber, the k-ε model gives good predictions of gas velocity profiles, whereas, for swirling flows RSM model gives better accurate predictions.
Langrish *et al.* (1993)	Simulation of airflow pattern to find out the oscillations in the flow field.	2D	standard k-ε	FLOW3D	Strongest oscillations occurs. Good agreement between hot-wire anemometer velocity measurements and simulation results.
Langrish *et al.* (1994)	Effects of the air inlet geometry and spray cone angle on wall deposition rates.	2D	standard k-ε	CFX	High swirl in the inlet air and large spray cone angle gave the lowest wall deposition rates in both the experiments and simulation.
Zbicinski (1995)	Simulation of airflow and particle trajectories in the tall-form dryer with experimental validation.	2D	standard k-ε	CFX	Good agreement between measurements and simulation results.
Kieviet (1997)	Simulation of airflow pattern, temperature, humidity, particle trajectories and resistance time in a co-current spray dryer fitted with a pressure nozzle. Experimental validation.	2D	standard k-ε	CFX	Model prediction agreed well with his experimental measurements such for velocity, temperature and humidity. Kieviet used the hot-wire anemometry (HWA) method for velocity measurements.
Southwell *et al.* (1999)	Simulation studies on the effects of increased turbulence in inlet air flow.	2D	standard k-ε	CFX	An increase in the amount of evaporation resulted directly from enhanced inlet turbulence.

Straatsma *et al.* (1999)	Temperature and moisture content of the air with the trajectories of the particles.	2D	standard k-ε	NIZO-DrySim	The drying of droplets is influenced by particles surface to surrounding air and diffusion within the particles. Diffusion process was included in their DrySim simulation
Huang *et al.* (2003)	investigating the airflow pattern, temperature, velocity and humidity profile at different spray dryer chamber configuration.	2D	standard k-ε	Fluent	The optimal chamber geometry will depends on the feed properties, atomiser type and drop size distribution
Langrish *et al.* (2004)	Experimental and simulation studies of inlet air swirl on the stability of the flow pattern in a spray dryers.	3D	RSM	CFX 5.6	Comparison of with and without spray showed that the introduction of spray has significant effect on the flow behaviour. An increase in swirl angle changes the internal flow pattern.
Huang *et al.* (2004)	Simulation of a spray dryer with rotary atomizer. Kieviet's (1997) spray dryer geometry was used.	3D	standard k-ε, RNG k-ε, Realizable k-ε and RSM	Fluent 6.1	Realizable k-ε cannot be used to simulate highly swirling two-phase flow. RNG k-ε turbulent model gives adequate accuracy at reasonable computational time.
Huang *et al.* (2006)	Simulation of a spray dryer with pressure nozzle and rotary atomiser. Kieviet's (1997) spray dryer geometry was used.	3D	RNG k-ε	Fluent 6.1	Their simulation results agreed well with Kieviet (1997) experimental results.
Ullum (2006)	Simulation of a spray dryer with rotary atomiser.	3D	RANS	Fluent 6.2	Rotary atomiser has a big influence on the flow pattern in pilot scale spray dryer, but its influence decreases with increase in size of spray dryer.

All the models mentioned in the table (2-4) were developed for gas temperature and velocity profiles but, particles histories such as, particles velocity, temperature, residence time and final recovery of particles have been totally overlooked. One exception was Kieviet's (1997), who studied the airflow pattern, temperature, humidity, particle trajectories and resistance time in a co-current spray dryer fitted with a pressure nozzle (detailed prediction and experimental results are given in chapter 7). Moreover, the same Kieviet's (1997) experimental data and the spray dryer geometry was used in this thesis work. Figure (2-27) depicts the air flow velocity profiles and it also shows the air recirculation zone created by product outlet pipe. However, in a axi-symmetric model does not give the actual primary particle residence time as total recirculation zone was not considered. Moreover, understating of particle trajectories in a tall and short form spray dryers with distribution of impact of the particle on walls are important for drying of heat sensitive materials like proteins.

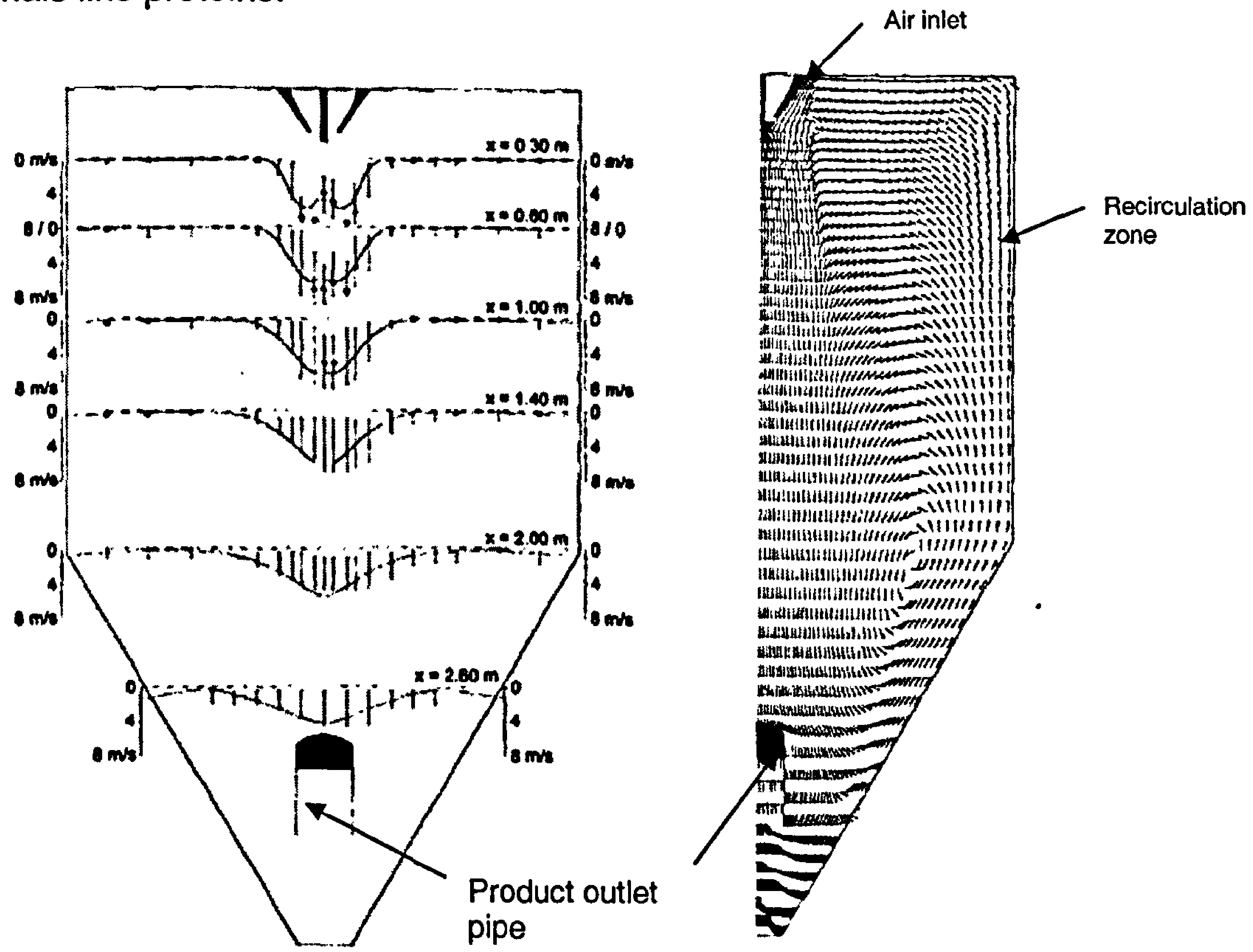

(a) (b)

Figure 2-27: Kieviet (1997) experimental (▪) and 2D simulation profiles (a) predicted and measured velocities (b) air flow pattern.

To date, no CFD simulations have been performed for spray-freezing operations, so there is a scope to explore a CFD model for spray-freezing process.

2.8 Conclusions

Spray Freeze-Drying (SFD) is a novel technique for generating products with controlled microstructures. This method is very suitable for the drying of heat sensitive materials, because of the very low operating temperatures and short processing times. So far, very few studies have been reported on the application of spray freezing into vapour (SFV) process. The literature study can be summarized in terms of gaps and scopes in the literature as follows:

Spray drying is a fast drying method, but it needs to be optimised with respect to processing variables such as, feed liquid concentration, outlet/inlet temperatures and gas flow rate for heat sensitive materials.

Freeze-drying is the most convenient and successful method for preserving micro-organisms and thermolabile materials. However, drying rates can be very slow, lasting 24h or more. Moreover, it is a very expensive process.

Protein denaturation occurs during spray drying and the published literature on denaturation studies is very limited. Moreover, a study on protein powder quality during spray drying and SFD is very much needed for developing high quality products.

Protein solubility is an important functional property of whey protein. For protein solubility analysis, most of the published articles have used a total nitrogen content analysis. This method is time consuming and difficult as well. There is a need for a simpler analytical method for solubility analysis to be developed.

Fluidised bed freeze drying is a unique method and is a suitable method for biomaterials. Very little work has been reported on freeze drying, coupled with fluidisation, with and without using an adsorbent.

Published spray-drying CFD models are related to the gas velocity, temperature profiles. Relatively little has been published on, particle histories such as particle temperature, velocity, residence time, and impact position on walls, which are the main factors for predicting product quality. ***CFD simulations*** are available for spray drying process; So far, no articles have been reported describing CFD simulations on spray-freezing operations.

Chapter 3

Experimental setup

3.1 Introduction

The spray-drying and spray-freeze drying concepts and their applications were discussed in Chapter 2. The main advantage of the spray-freeze-drying technique over conventional spray-drying and freeze-drying techniques is that the SFD process combines both the high quality powder product (e.g. less denaturation, highly porous particles) with short drying times.

The spray-freeze-drying unit operation at atmospheric pressure technique is the recently developed pilot scale process (discussed in Chapter 2, section 2.5.1). However, the quantities of gas required for atmospheric freeze-drying are prohibitively expensive. As freeze-drying must be performed below the collapse temperature of the material (which can be as low as -30°C) the ice phase exerts an extremely low vapour pressure (e.g. 38.96 Pa at -30°C). Even if freeze-drying had a negligible resistance for mass transfer from within the particle to the gas phase such that the exit gas of the fluidised bed was at the saturation value of the particle temperature, it would require (from the Ideal Gas Law) approximately 4200 kg of bone dry gas to pass through the bed in order to sublime 1 kg of ice. Although this can be partly offset by recirculating (and drying) the gas, this is a huge quantity of gas to have to be supplied to the process. The refrigeration and drying requirements for such a mass of gas to meet the required specification are considerable and severely harm the economics of the process. A further consideration is that to pass this mass of gas through the bed in a reasonable time (say a few hours) requires a very large gas volume flow rate and hence velocity. This leads to particles being swept out of the fluidised bed where they must be caught by a gas-filter (as observed by Mumenthaler and Leuenberger, 1991). Although this is a feasible means of drying the particles, it does render the fluidised bed (with its high heat and mass transfer ability) redundant. Alternative to avoid circulating large mass flow rates of dry gas, which does not appear to have been considered in the literature, is to apply a partial vacuum to the process. That means spray-freezing operation at atmospheric condition followed by drying at sub-atmospheric pressure.

Thus lower pressures are desirable as they decrease the mass of gas required and reduce the number of particles being swept from the bed. Thus the higher the vacuum the better, and this would suggest approaching the pressures used in conventional freeze-drying (with effectively no gas in the system). Conventional freeze dryers, however, have a source of heating to supply the latent heat of sublimation. This form of heating is not well suited to the uniform heating of powders as it does not make use of the high surface area to volume ratios, as it will only directly heat exposed surfaces. In the process proposed here the aim is to supply the latent heat from the fluidizing gas, but this will not be available if the pressure is too low. Thus one can postulate that there might be an optimum pressure of operation, which is low enough such that a small mass of gas is used, and high enough that the particle temperatures can be maintained.

The aim of this research is to demonstrate the ability to spray-freeze-drying and investigate the effect of different processing conditions on the quality of spray dried and spray freeze dried products. The chapter will describe the spray-drying and spray-freeze-drying experimental rigs used in this study, including instrumentation and operating procedures.

3.2 Spray-drying experimental set up

Figure (3-1) depicts a simple flow diagram of the spray-drying operations. A tall-form co-current spray dryer (figure 3-2) of 2.88 m height x 0.9 m diameter (Spray Processes, Bedford UK) was employed for the spray drying process (full spray chamber geometry is given in section 7.8). A peristaltic pump (Watson-Marlow 510U) was used to deliver the feed (whey protein) solution to the atomiser. The atomisation was performed by a twin-fluid nozzle, using compressed air at 45 psig as the atomising gas. Ambient air was directly heated in a burner using natural gas, allowing control of the inlet air temperature.

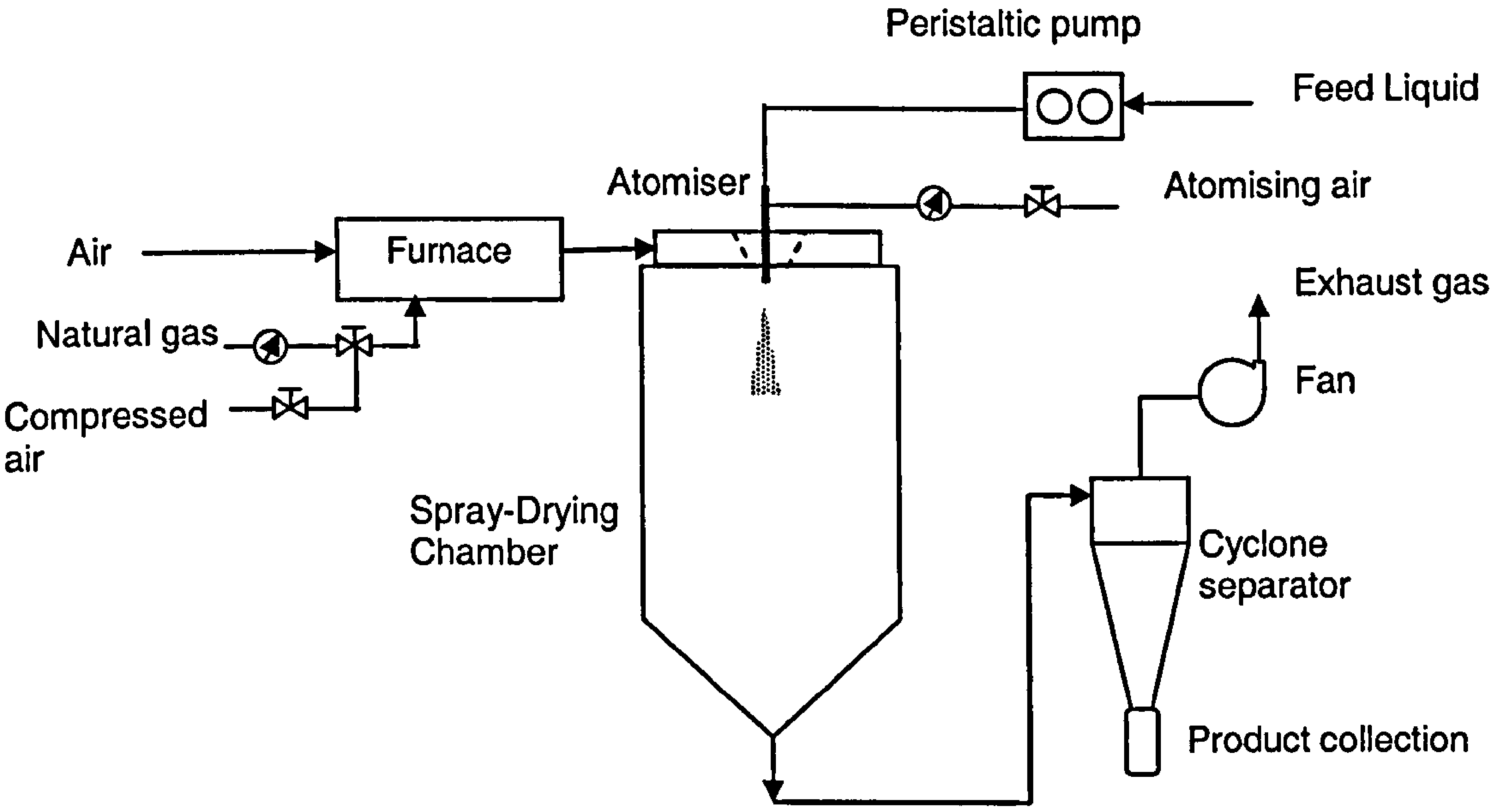

Figure 3-1: Flow diagram of spray-drying operation.

The flow velocity of the ambient air was measured at the inlet to the burner using a rotary vane anemometer (Airflow LCA 6000VT, Airflow Developments Ltd, High Wycombe, UK). It was found that the gas flow rate was approximately constant at 227 kg/hr for all experimental conditions (discussed in section 5.3). The humidity of the inlet air was measured using a handheld digital psychrometer (model RH-83, Omega). The aim of the spray drying study is to find out the effects of process variables (feed concentration and outlet temperature) on whey denaturation. Four different outlet temperatures of 60°C, 80°C, 100°C and 120°C were used for three feed concentrations (20%, 30% and 40% w/v) of solids.

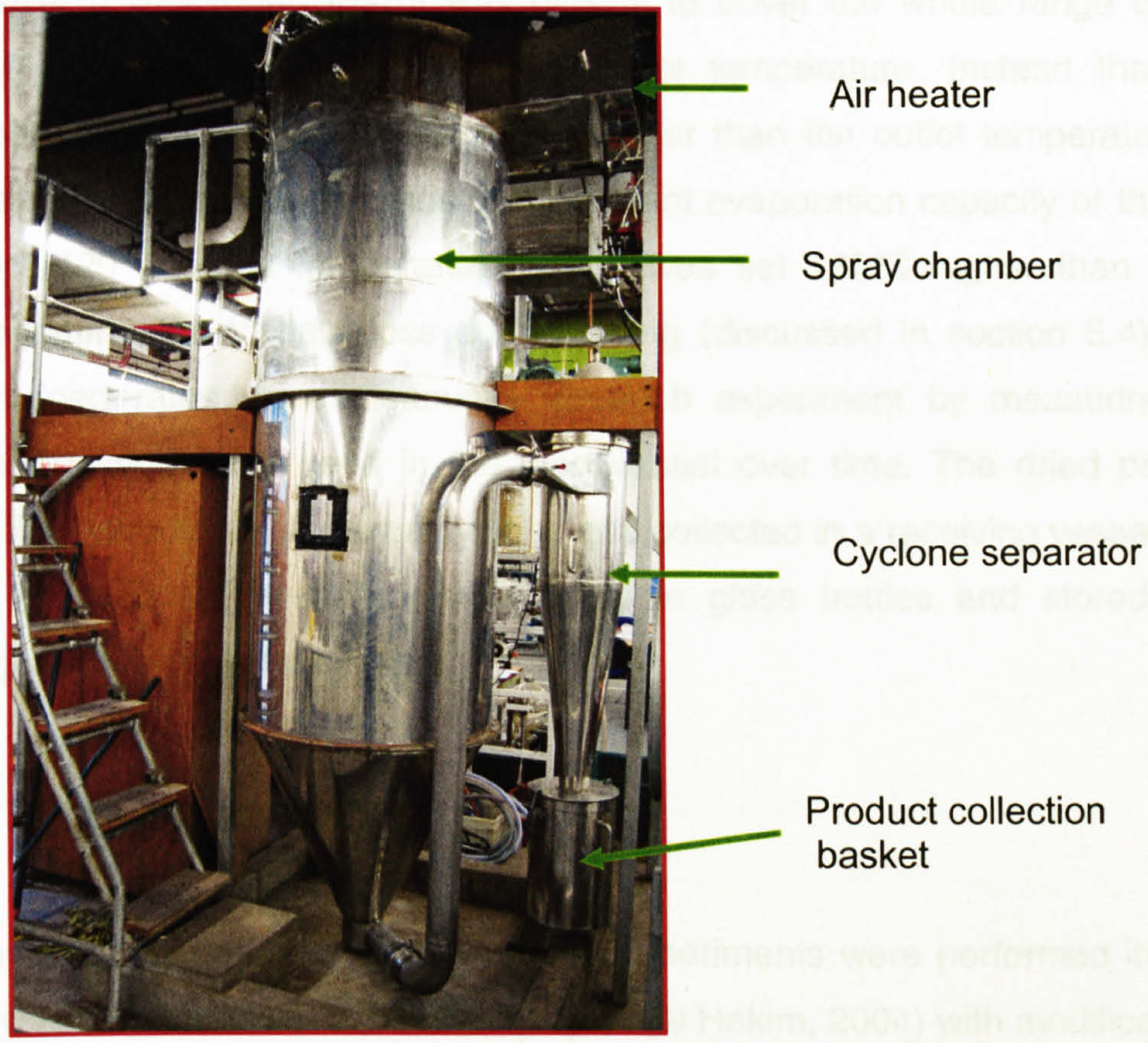

Figure 3-2: Photograph of the pilot-scale spray-dryer experimental rig.

3.2.1 Pilot scale spray drying rig operating procedure

The spray drying operation was initiated by passing hot air through the chamber for 15 minutes to warm up the chamber. This was followed by feeding distilled water through the atomiser and the outlet temperature was then set by adjusting the liquid feed rate (approx. 5 minutes). Once the required outlet temperature was reached the whey protein solution was fed into the drying chamber. The different feed concentrations of whey protein solution were spray dried over a range of gas inlet and outlet temperatures. The outlet temperature was effectively regulated by variation of the liquid feed flow rate. Four different outlet temperatures of 60°C, 80°C, 100°C and 120°C were used for each feed concentration. It was decided to use inlet temperature as the second controlled variable as it could be set more easily and reproducibly than the liquid feed flow rate for a given outlet temperature. However it was found that it was difficult to cover the whole range of gas outlet temperatures with a fixed gas inlet temperature. Instead the inlet temperature was generally set 100°C higher than the outlet temperature as this approximately corresponds to a constant evaporation capacity of the gas except 120°C outlet temperature, which was set 120°C higher than outlet temperature due to heat loss during drying (discussed in section 5.4). The liquid feed rates were measured for each experiment by measuring the change in volume of feed in the feed vessel over time. The dried product particles were separated by a cyclone and collected in a receiving vessel. The final products were sealed immediately in glass bottles and stored in a refrigerator for later analyses.

3.3 Spray-freeze-drying

Spray freezing and spray freeze drying experiments were performed in a rig that was constructed in a previous project (Al Hakim, 2004) with modifications. The spray-freeze drying experimental setup is divided into two experimental rigs namely, (i) the spray-freezing chamber and (ii) the vacuum fluidised bed freeze-dryer (VFBFD). Figure (3-3) depicts a block flow diagram of the spray-freeze-drying process.

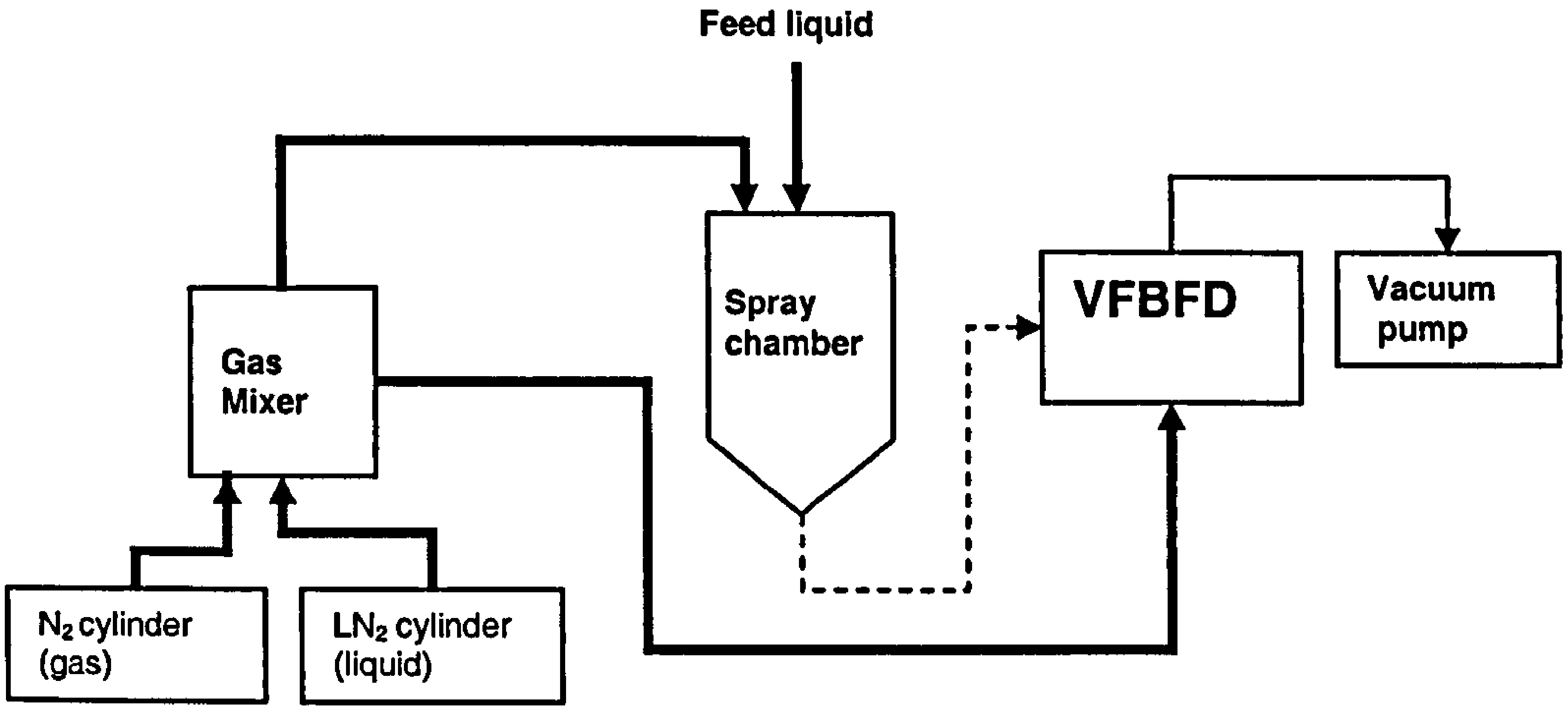

Figure 3-3: Block flow diagram of spray-freeze-drying operation.

Spray-freeze-drying was carried out in a two stages. Spray frozen particles are first formed by spraying the feed solution through a heated hydraulic nozzle into a cold nitrogen vapour at atmospheric pressure. This method is called spray-freezing into vapour (SFV) (discussed in section 2.5.1). The frozen particles were collected from the outlet of the chamber in cooled expanded polystyrene cups placed in a polystyrene box. The cups were then quickly covered and weighed. The particles were then loaded into the VFBFD unit, which consisted of a polycarbonate cylinder inside a stainless steel vacuum vessel. The cold gas from the gas mixer was used as a fluidising medium and the dried particles were collected from the polycarbonate cylinder at the end of the operation. All these unit operations are discussed in more detail in the following sections.

3.4 Spray-freezing chamber

A flow diagram of the spray-freezing operation is shown in figure (3-4).

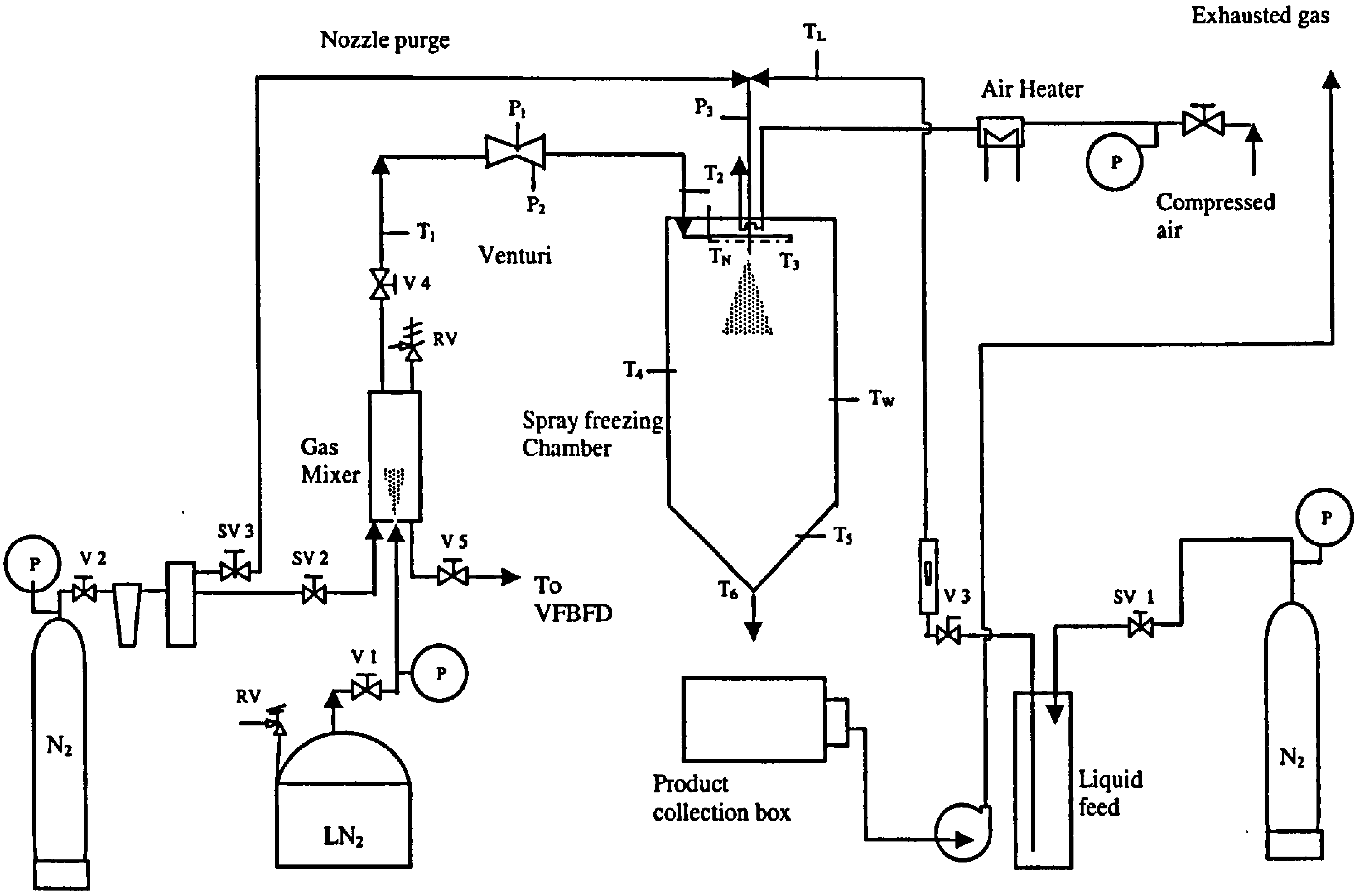

Figure 3-4: Flow diagram of spray-freezing operation.

The spray-freezing chamber is a cylindrical vessel of 2.01 m height and 0.8 m diameter with five removable vertical windows (1 m x 0.1 m) (the detailed geometry is given in Chapter 8, figure 8-1). The following temperatures and pressures were routinely recorded during each experiment.

T_1 - temperature of the LN_2 gas supply
T_2 - inlet temperature of the LN_2 gas
T_3 - gas temperature at spray point
T_4 & T_5 - gas temperature inside the chamber
T_6 - gas temperature at the outlet
T_N - nozzle body temperature
T_L - liquid feed temperature
T_W - chamber wall temperature
P_1 & P_2 - gas pressures
P_3 - nozzle pressure

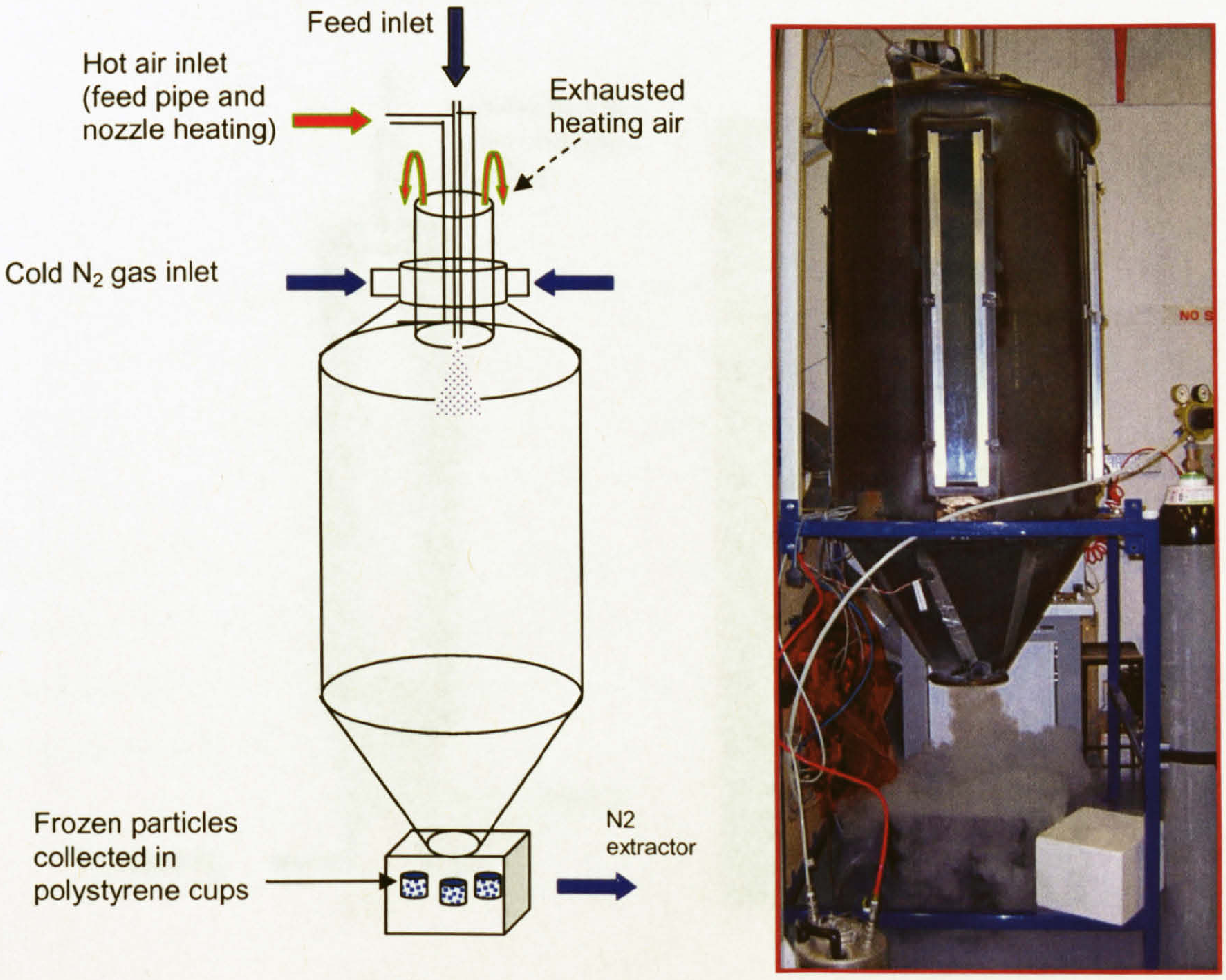

Figure 3-5: Spray-freezing chamber.

The chamber was made of 1 mm thick mild steel sheet with the inside of the vessel coated by matt-black acrylic paint. This was to protect the chamber from corrosion and to absorb light from previous PDA (Phase Doppler Anemometry) laser measurements to minimise the health and safety risk. The top cone section of the chamber has a N_2 gas inlet on either side. The particle collection box was kept below the bottom of the chamber and the nitrogen extractor unit also kept near to the chamber outlet as in figure (3-5). The frozen particles were collected from the outlet of the chamber in the polystyrene cups.

3.4.1 Gas Feed

Liquified nitrogen (LN_2) was used as the cooling medium, since it has the following advantages: low-cost, flexibility, very low humidity and high cooling power. The gas-mixer atomises (see figure 3-6) the liquid nitrogen, which is supplied from an external dewar as shown in figure (3-4).

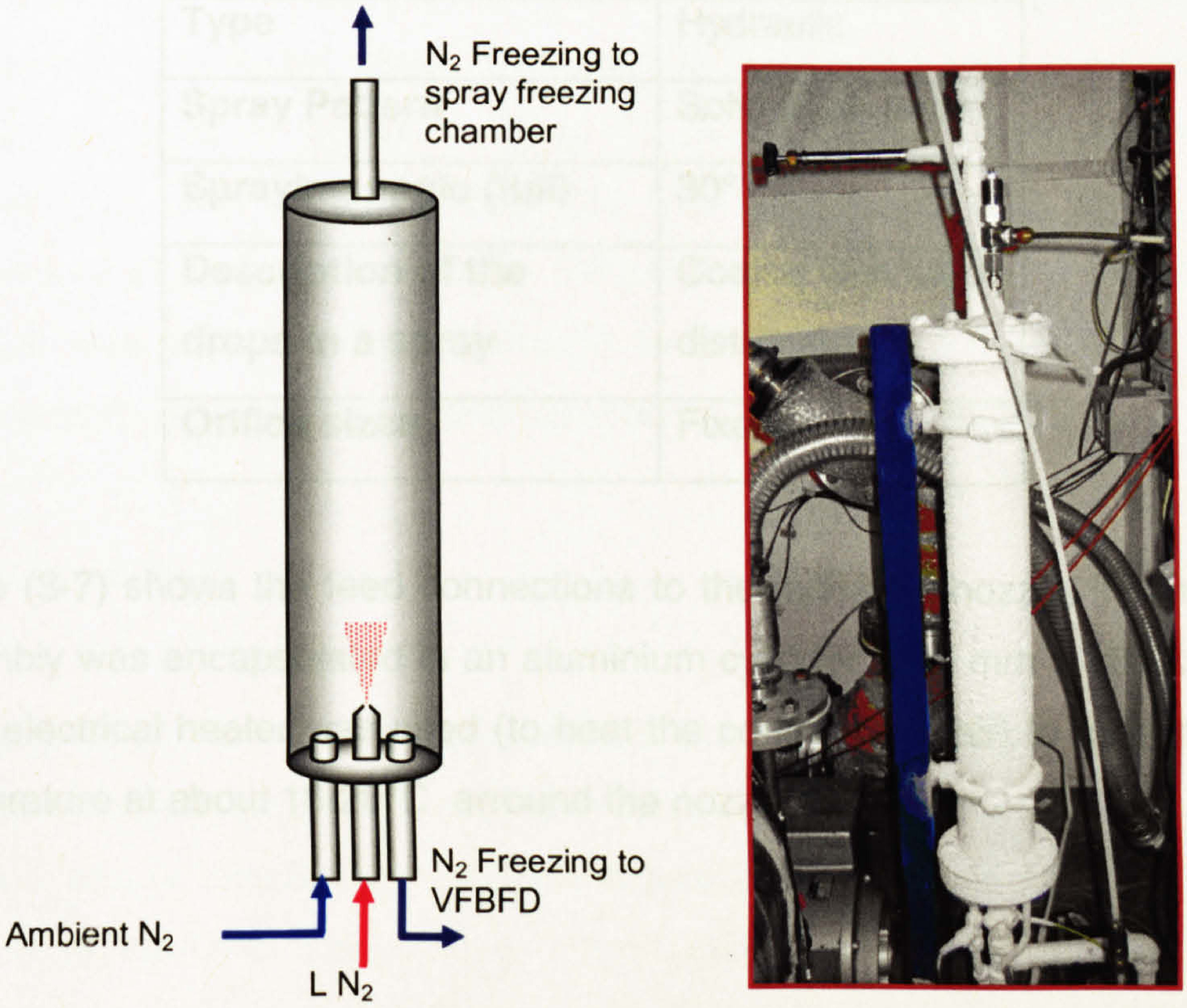

Figure 3-6: Gas mixer/ vaporiser.

The gas flow and the temperature were regulated by using a manual needle valve. This gas flowed through the Venturi and perforated copper pipes (rows of 3 mm orifices) to the spraying chamber.

3.4.2 Atomisation

Three different types of atomisers (pneumatic nozzle, hydraulic nozzle and rotary atomiser) are normally used in spraying operations. The selection of the atomiser depends on the operating conditions and product requirements (as discussed in chapter 1). In this research, the hydraulic nozzle atomiser (WL Series) was used for wide range of droplet size distributions. The nozzle was supplied by BETE Ltd, Lewes, East Sussex, UK. The general description of the spray nozzle is given in the Table (3-1).

Table 3-1: Spray nozzle descriptions (BETE Ltd).

Model	WL 0.253
Type	Hydraulic
Spray Pattern	Solid (Full) cone
Spraying angle (full)	30°
Description of the drops in a spray	Coarse with wide distribution
Orifice sizes	Fixed

Figure (3-7) shows the feed connections to the hydraulic nozzle. The nozzle assembly was encapsulated in an aluminium cylinder (700 mm x 100 mm). A small electrical heater was used (to heat the compressed air) to maintain the temperature at about 16-20°C arround the nozzle.

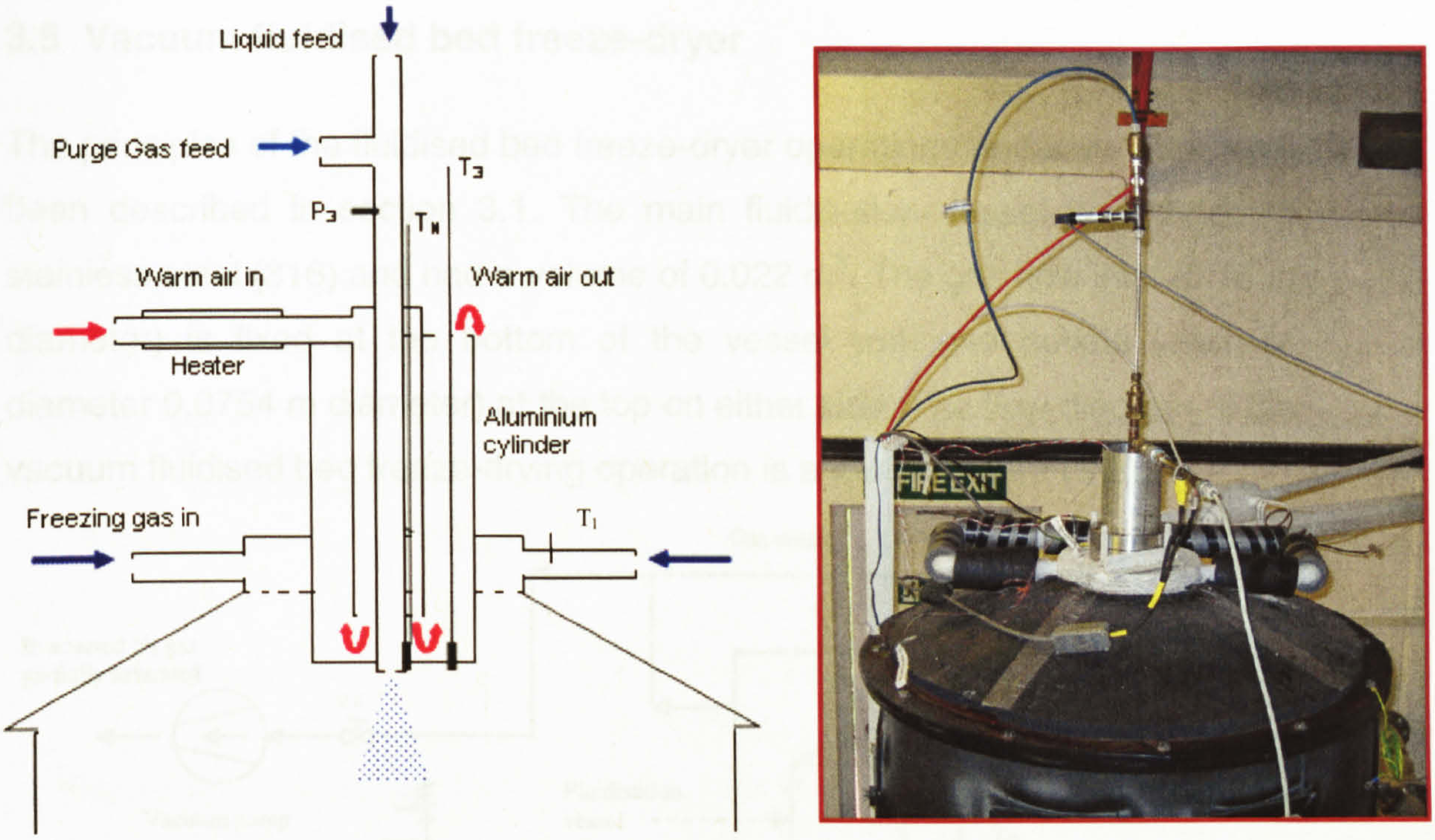

Figure 3-7: Feed connections to the nozzle.

The nozzle purge gas was supplied from compressed nitrogen gas cylinder (6 bar) through a solenoid valve. The liquid feed was fed from a pressurised vessel. The cylinder contains “Type T” thermocouples (supplied by RS Components, UK) for measuring the inlet gas feed (T_2), spray point temperature (T_3) and nozzle body temperatures (T_N). The inlet liquid feed pressure was measured by a pressure transducer (P_3). The position of the thermocouples and pressure transducer are shown in figure (3-7).

3.4.3 Liquid feed

The feed liquid from the pressure vessel flows to the spraying chamber by passing nitrogen gas from a pressurised cylinder (figure 3-4). This gas pressure can be regulated by a manual operating valve and solenoid valves are used as switches. The capacity of the feed pressure vessel is 20 litres and the pressure limit is up to 100 psi (Millipore, UK). The pressure of the feed liquid at the nozzle was recorded by a pressure transducer (D-20, Druck), which was connected to the data acquisition system described in section 3.6.

3.5 Vacuum fluidised bed freeze-dryer

The principles of the fluidised bed freeze-dryer operations under vacuum have been described in section 3.1. The main fluidisation vessel was made of stainless steel (316) and had a volume of 0.022 m^3. The gas flow inlet (0.15 m diameter) is fixed at the bottom of the vessel with two outlets (each of diameter 0.0754 m diameter) at the top on either side. The flow diagram of the vacuum fluidised bed freeze-drying operation is shown in figure (3-8).

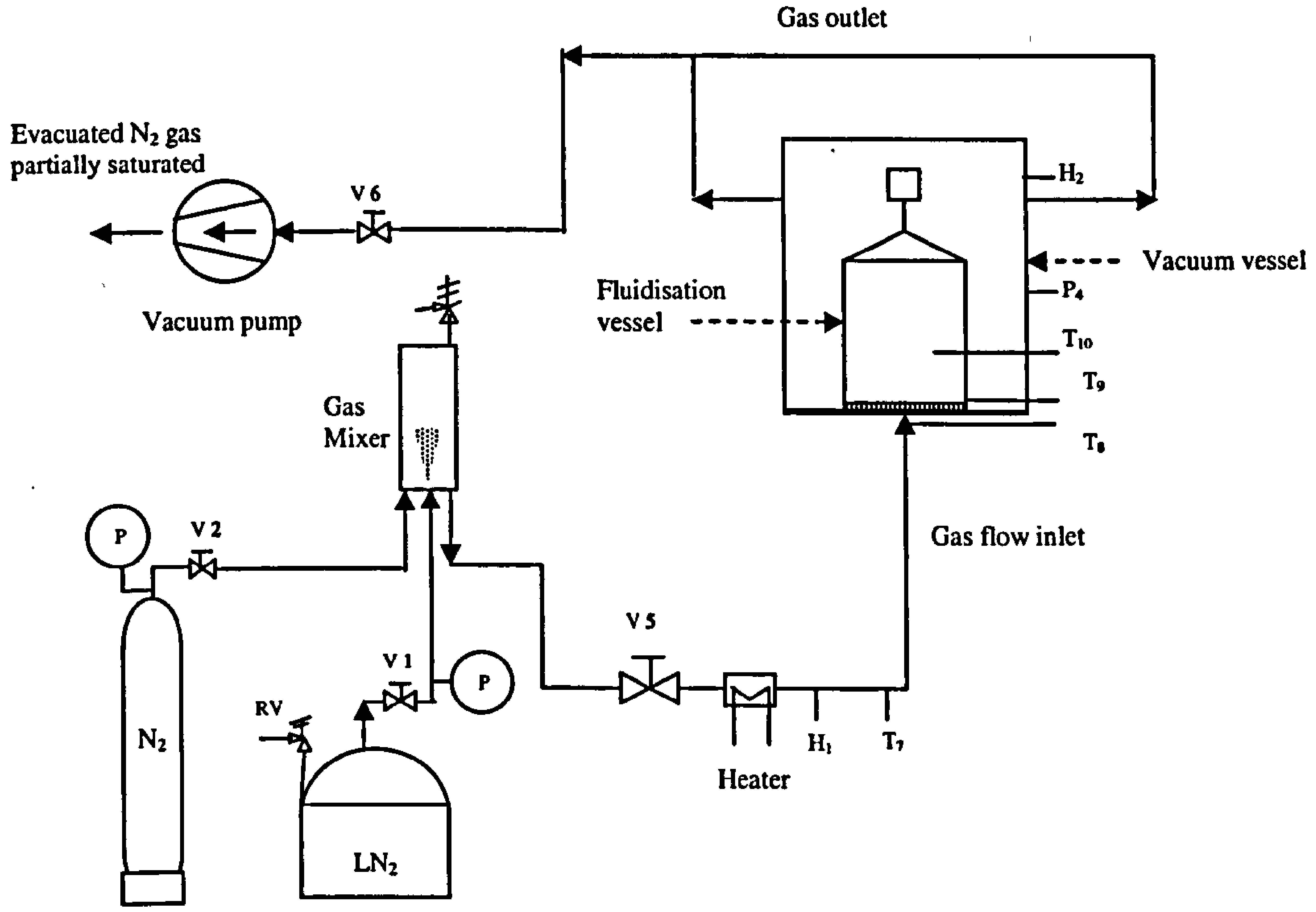

T_7 – temperature of N_2 supply
T_8 – temperature of inlet gas
T_9 – temperature of particles
T_{10} – temperature of outlet gas
H_1& H_2 – humidity of inlet and outlet gas
P_4 – pressure in fluidisation system

Figure 3-8: Flow diagram of vacuum fluidised bed freeze-drying operation.

Liquid nitrogen gas from the gas mixer passed into the fluidisation vessel. Inlet gas temperature was effectively controlled by recently designed and constructed annular heat exchanger by varying the heater temperature and the compressed air flow rate. A rotary-vane oil-sealed vacuum pump (Werner Rietschle-Germany, model CLF100) was used to extract the gas and create a partial vacuum. The operating capacity of the pump was 100 m^3/hr. The fluidised bed freeze drying vessel is shown in figure (3-9).

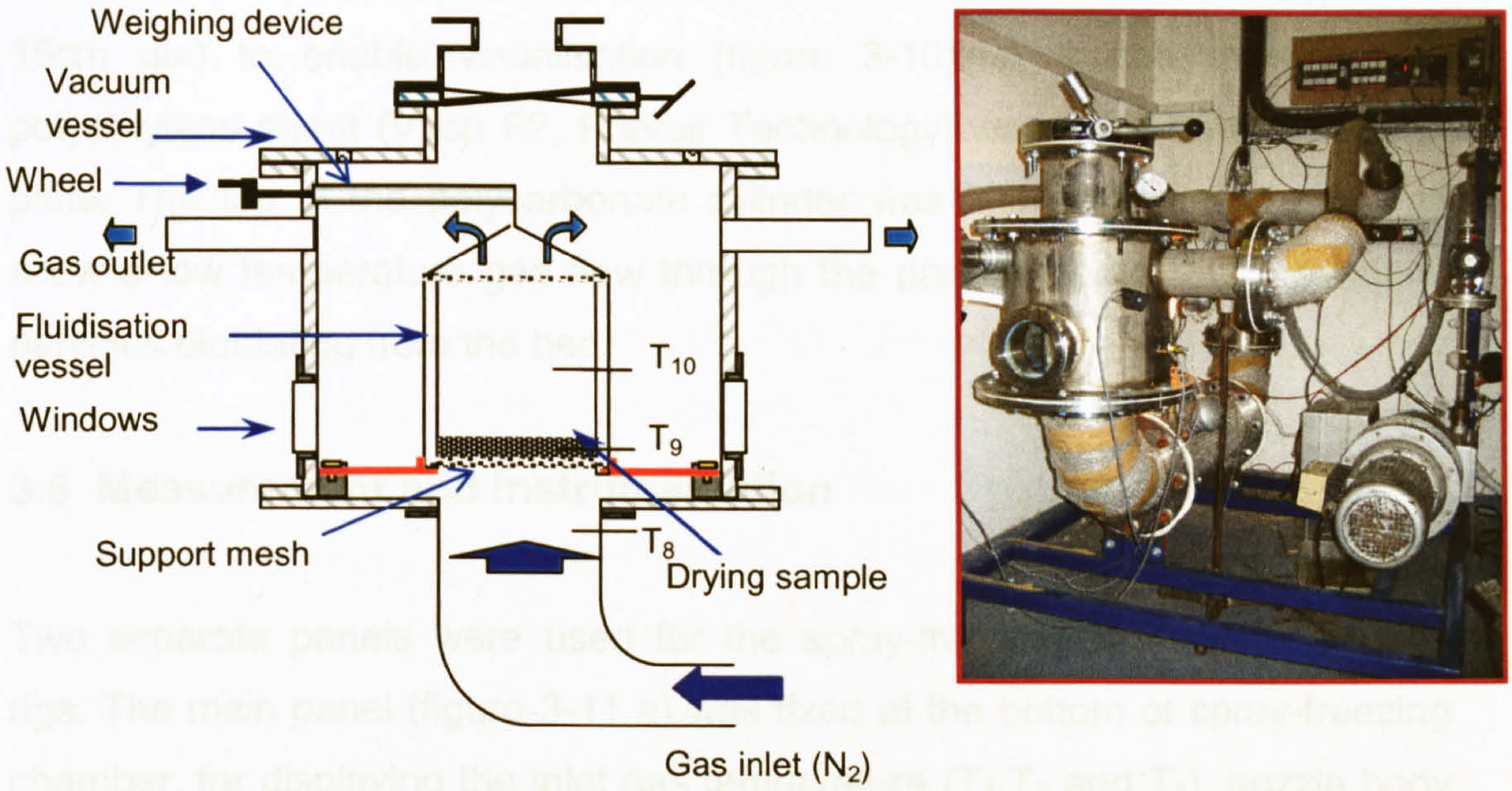

Figure 3-9: Schematic diagram of the vacuum fluidised bed freeze dryer.

The fluidisation unit was suspended from a spring balance to measure the sample mass (see figure 3-9), which was fixed to the hand operated wheel. During operation the hand operated wheel can be press down on the fluidisation unit to prevent gas escaping up the sides of the tube due to a high pressure drop across the bed. However, the measurement system proved to be unreliable and therefore was not used to provide data in the experiments reported in this thesis.

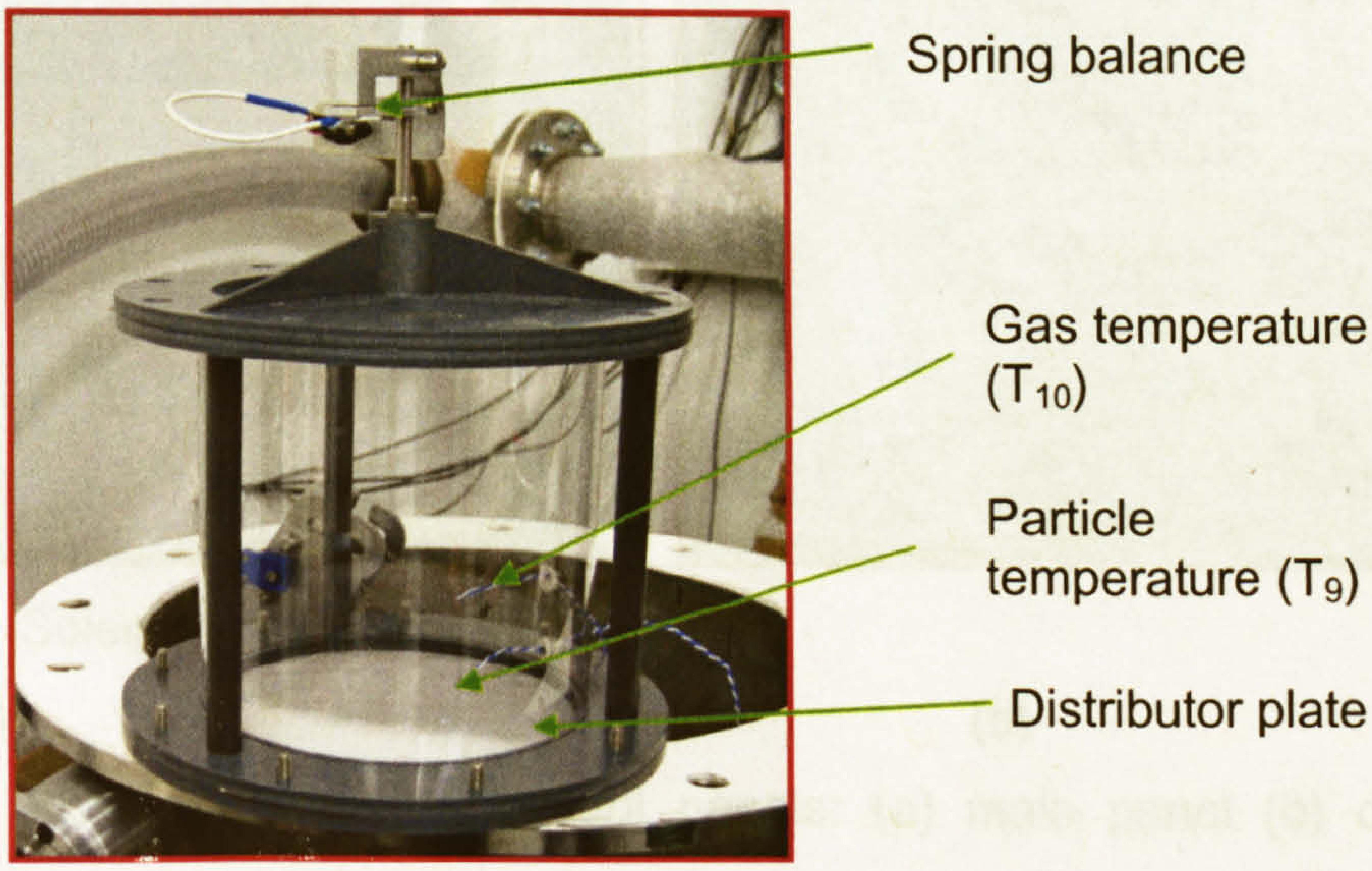

Figure 3-10: Photograph of fluidisation vessel.

The fluidisation vessel is made up of polycarbonate tube (16 cm height and 15cm dia) to enable visualisation (figure 3-10). A 2 mm thick porous polyethylene sheet (Vyon F2, Porvair Technology) was used as a distributor plate. The top of the polycarbonate cylinder was fitted with a fine mesh to allow a low temperature gas flow through the particle bed whilst preventing particles elutriating from the bed.

3.6 Measurement and Instrumentation

Two separate panels were used for the spray-freezing and the fluidisation rigs. The main panel (figure 3-11 a) was fixed at the bottom of spray-freezing chamber, for displaying the inlet gas temperature (T_1,T_2 and T_3), nozzle body temperature (T_N), chamber wall temperature (T_4) and gas outlet temperature (T_5). Two heating controls were also fixed at the main panel for controlling temperature around the hydraulic nozzle and for the feed gas to the VFBFD. The main panel has three solenoid valves for controlling (on-off) the feed liquid, purge gas to clear the nozzle after spraying is complete and the flow of cylinder N_2 gas to the gas mixer for purging the chamber.

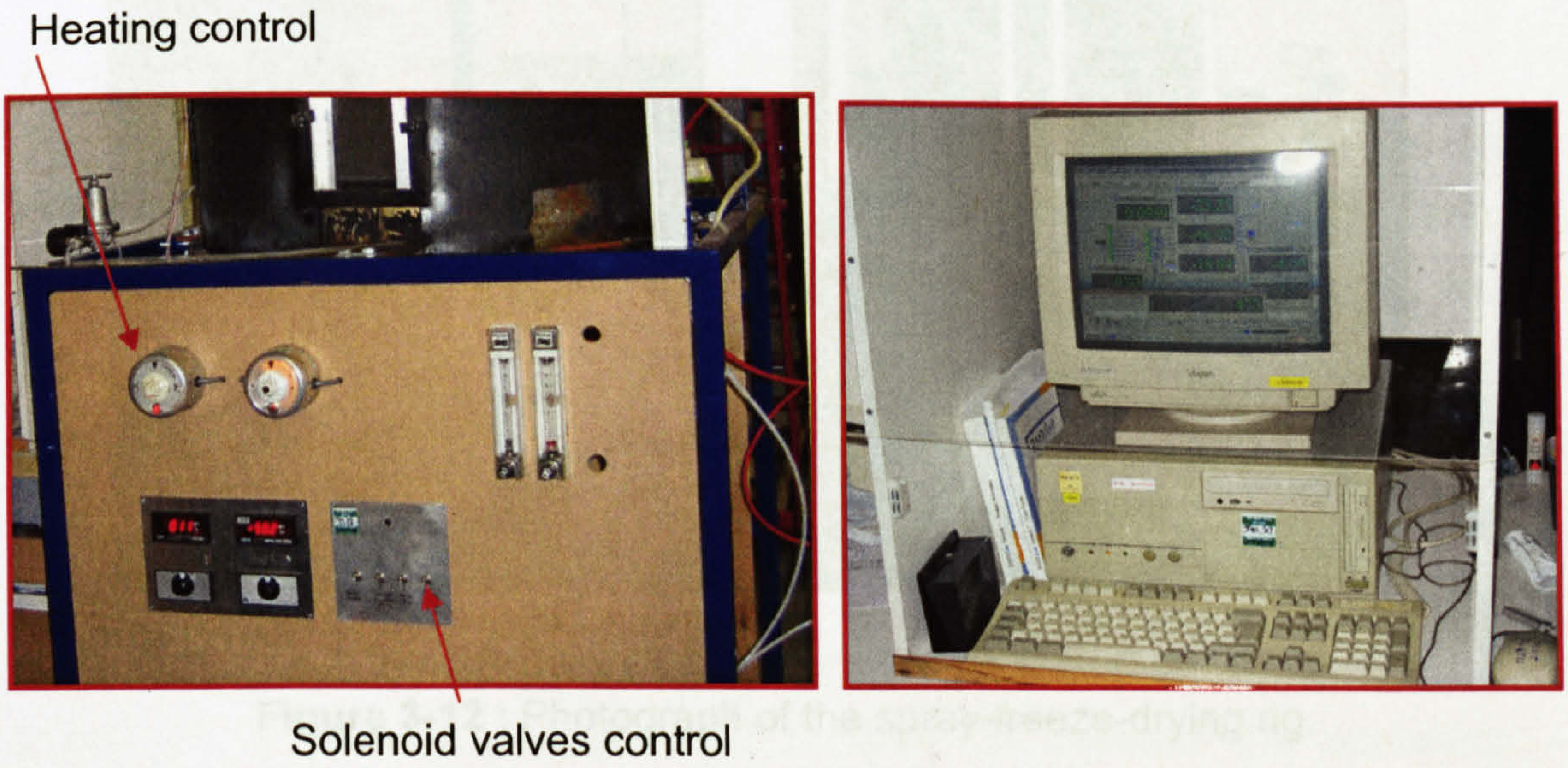

(a) (b)

Figure 3-11: Photograph of the control panels: (a) main panel (b) data acquisition system.

For spray freezing with water, five Type T thermocouples (RS Components, UK) were fixed within the spray freezing chamber for temperature measurements for validation of CFD simulation (see detailed discussion in section 8.2.1). In the fluidisation rig, three Type T thermocouples (T_8, T_9 and T_{10}), PT-100 probe, humidity sensors (H_1, H_2) (Michell Instruments, UK), and pressure transducer (P_4) (Druck PMP4070) were logged to a data acquisition hardware (Data Scan 7321&7050) into PC (operating using DasyLab software) as shown in figure (3-11b). This arrangement gave online measurements of temperature, humidity and pressure during the process. Photographs of the spray-freezing and VFBFD experimental rigs are shown in figure (3-12).

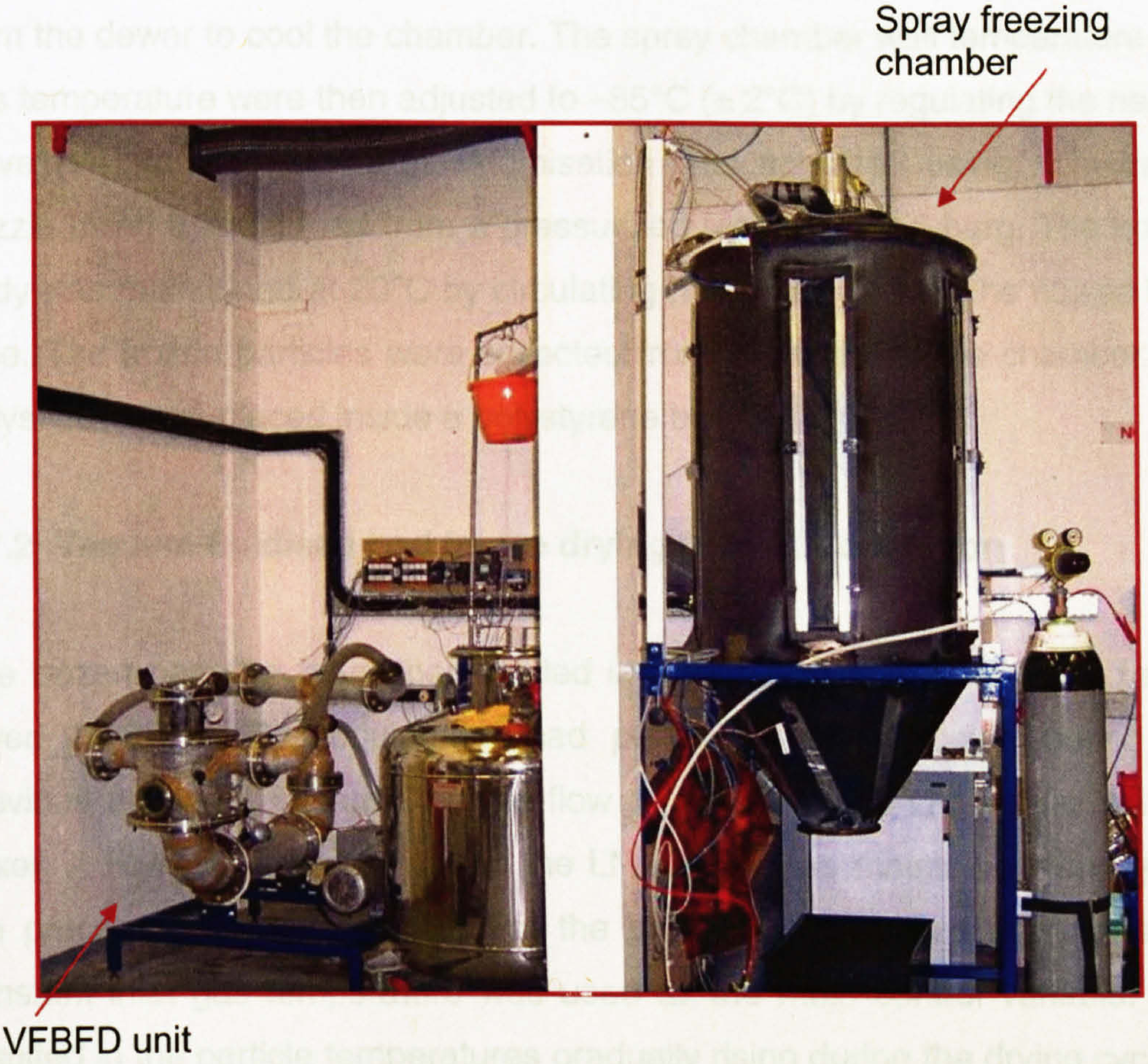

Figure 3-12 : Photograph of the spray-freezing-drying rig.

3.7 Pilot scale spray-freeze-drying rig operating procedure

Spray-freeze-drying was carried out as a two stage operations such as spray-freezing followed by drying. The operating procedures are given in the following sub-sections.

3.7.1 Spray-freezing operation

Spray frozen particulates are first formed by spraying the concentrate through a heated hydraulic nozzle into a cooled spray chamber. The chamber was first purged with nitrogen gas from a cylinder before introducing liquid nitrogen from the dewar to cool the chamber. The spray chamber wall temperature and gas temperature were then adjusted to –85°C (± 2°C) by regulating the needle valve (V4) at the gas mixer. Atomisation was achieved using a hydraulic nozzle using a liquid feed from a pressurized feed tank at 6 barg. The nozzle body was maintained at 20°C by circulating heated air around the nozzle feed pipe. The frozen particles were collected from the outlet of the chamber in a polystyrene cup placed inside a polystyrene box.

3.7.2 Vacuum fluidised bed freeze drying (VFBFD) operation

The frozen particles were then loaded into the vacuum fluidised bed freeze dryer (VFBFD). The equipment had previously been cooled during the previous 20 minutes period by the flow of gas from the LN_2 dewar via gas mixer. A flow of the nitrogen from the LN_2 dewar was maintained throughout the process (see figure 3-10). For the production of freeze dried whey, a constant inlet gas temperature was used as the main control variable. This resulted in the particle temperatures gradually rising during the drying cycle. A period of 10 minutes was required in order to stabilise the operating conditions at the beginning of the process (as the particles enter the chamber at a much colder temperature). The chamber was maintained under a partial vacuum (absolute pressure of 0.1 bar) by adjusting a combination of the needle valve V5 and gas valve V6 (see figure 3-8). The valve V6 was usually fully open to enable the full extraction capacity of the vacuum pump to be realised. Once the particle temperature stops rising, process was stopped and particles were collected in a glass bottle and stored in the refrigerator.

Chapter 4

Analytical materials and methods

4.1 Introduction

This chapter describes the materials used in this research and the methods of characterizing the untreated (feed material or solution) samples, final dried products and analytical standards. The analytical methods are divided into two categories related to (i) product characteristics and (ii) product quality. The product quality was assessed alongside the feed material characteristics. An overview of the various analytical methods is presented in figure (4-1).

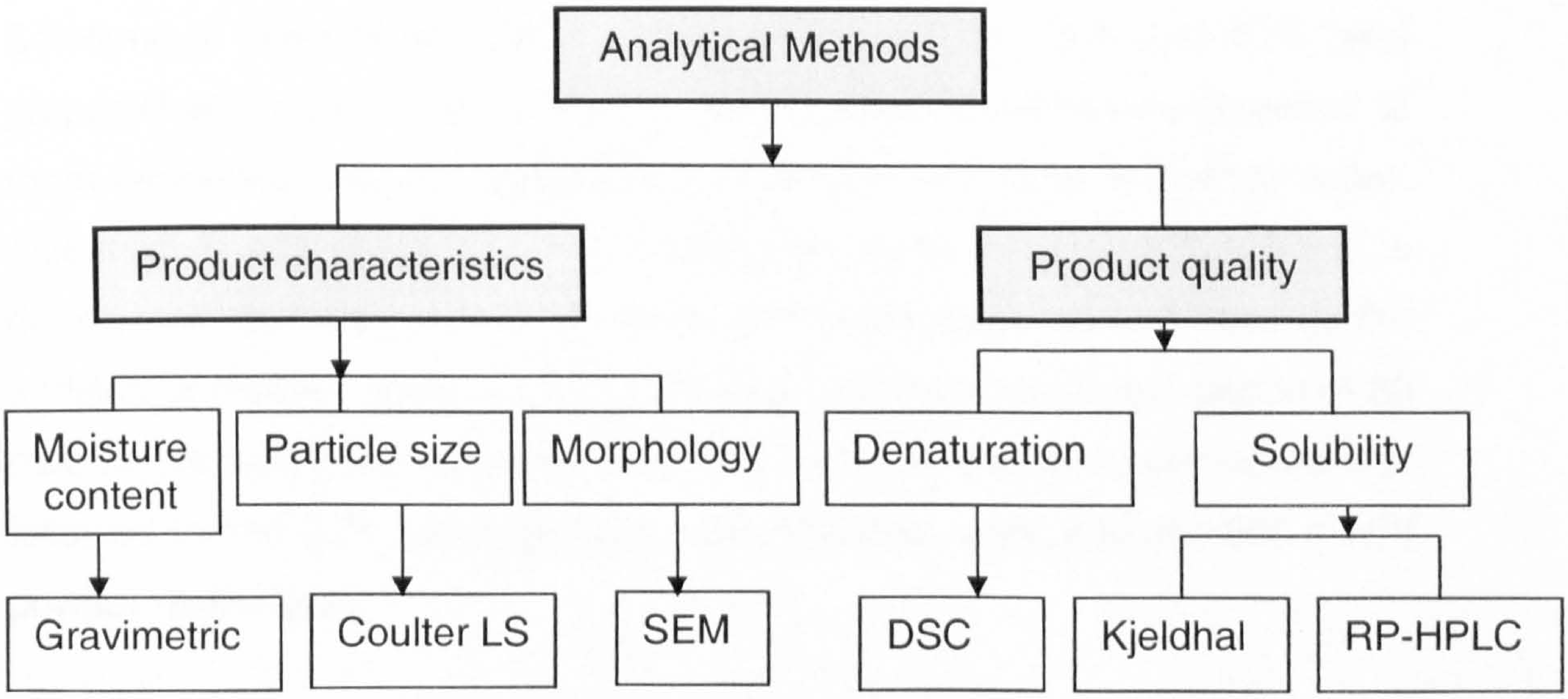

Figure 4-1: Structure of chapter 4.

4.2 Materials used for drying process and analysis

4.2.1 Whey protein isolate powder

Whey protein isolate (WPI) powder was obtained from Ultimate Nutrition (Fleetwood, Lancashire, UK). This is a lactose-free product and the manufacturer claims that 99% of the whey proteins are undenatured. The WPI powder is produced by using microfiltration followed by spray drying. The following compositional information is supplied by the manufacturer.

Table 4-1: WPI powder composition.

	(Mass per 100g of dry powder)
Protein	92.0g
Carbohydrate	3.0g
of which sugars	3.0g
Fat	3.0g
Fiber	1.0g
Sodium	Nil
Calcium Content	200mg
Lecithin (E322)	400mg

4.2.2 Whey protein solution preparation

Solutions of whey proteins with concentrations of 20%, 30% and 40% (w/v) prepared as follows: The 20% (w/v) whey protein solution was prepared at room temperature by dissolving 400 g of powder in 2 litres of distilled water. This mixture was gently stirred in a laboratory mixer (Silverson) for 10 min to dissolve all the whey proteins in water and finally made up to 2 litres by the addition of distilled water. The mixture was kept for a consistent period of 30 min, before spray drying for the protein to hydrate. The same procedure was followed for the 30% and 40% (w/v) concentrations, using 600 and 800 g WPI powder respectively.

4.2.3 Protein standards

α-lactalbumin (product L6010, approximately 85% purity as per manufacturer) and β- lactoglobulin (product L2506, approximately 80% purity as per manufacturer) were obtained from the Sigma Chemical Co. (Poole, UK) and were used as protein standards for reversed phase HPLC analysis.

4.2.4 Chemicals for the solubility analysis

Tri-fluoroacetic acid (TFA) and acetonitrile (HPLC grade) were purchased (Fisher Scientific, UK) and used for reversed phase HPLC (RP-HPLC) gradients. Kjeldhal catalyst (copper), sodium hydroxide solution (48%), ammonium sulphate, concentrated hydrochloric acid, concentrated sulfuric acid, boric acid and sodium chloride were obtained (Fisher Scientific, UK) and used for protein solubility analysis.

4.3 Methods of Characterisation

4.3.1 Moisture content analysis

The average moisture content of the spray-dried or spray-freeze-dried powdered product was measured gravimetrically. A known mass of sample (approximately 0.5 g) was placed in a glass sample bottle and dried in a vacuum oven at 105 ± 2°C for a period of 24 hours. The sample was then removed and immediately weighed to limit water absorption from the atmosphere. The initial and final weights were then used to calculate the wet basis moisture content based on following equation.

$$\%\ Moisture\ \ Content = \left(\frac{Initial\,Mass - Final\ \ Mass}{Initial\,Mass}\right)\times 100 \qquad \text{Eq (4-1)}$$

The measurements were carried out in duplicate for each sample and an average value calculated.

4.3.2 Differential Scanning Calorimetry

Differential Scanning Calorimetry (DSC) is an experimental technique for measuring the energy (heat) absorbed or released by a sample as it is heated or cooled at a constant temperature rate (Ford and Timmins, 1989). Two types of differential scanning calorimeters are commonly available: heat flux DSC and power compensation DSC. In this study, heat flux DSC was used and figure (4-2) shows the schematic representation of this technique. The sample pan (containing whey protein sample) and the reference pan (empty pan) are located in a furnace and heated or cooled by a controlled temperature program. Thermocouples are placed directly beneath the pans to provide a measurement of the sample and reference temperatures. If the sample absorbs heat because of melting the sample cools relative to the reference, and the temperature difference is detected by the DSC as an endothermal event. During crystallization, energy is released by the sample and an exothermal DSC event is recorded.

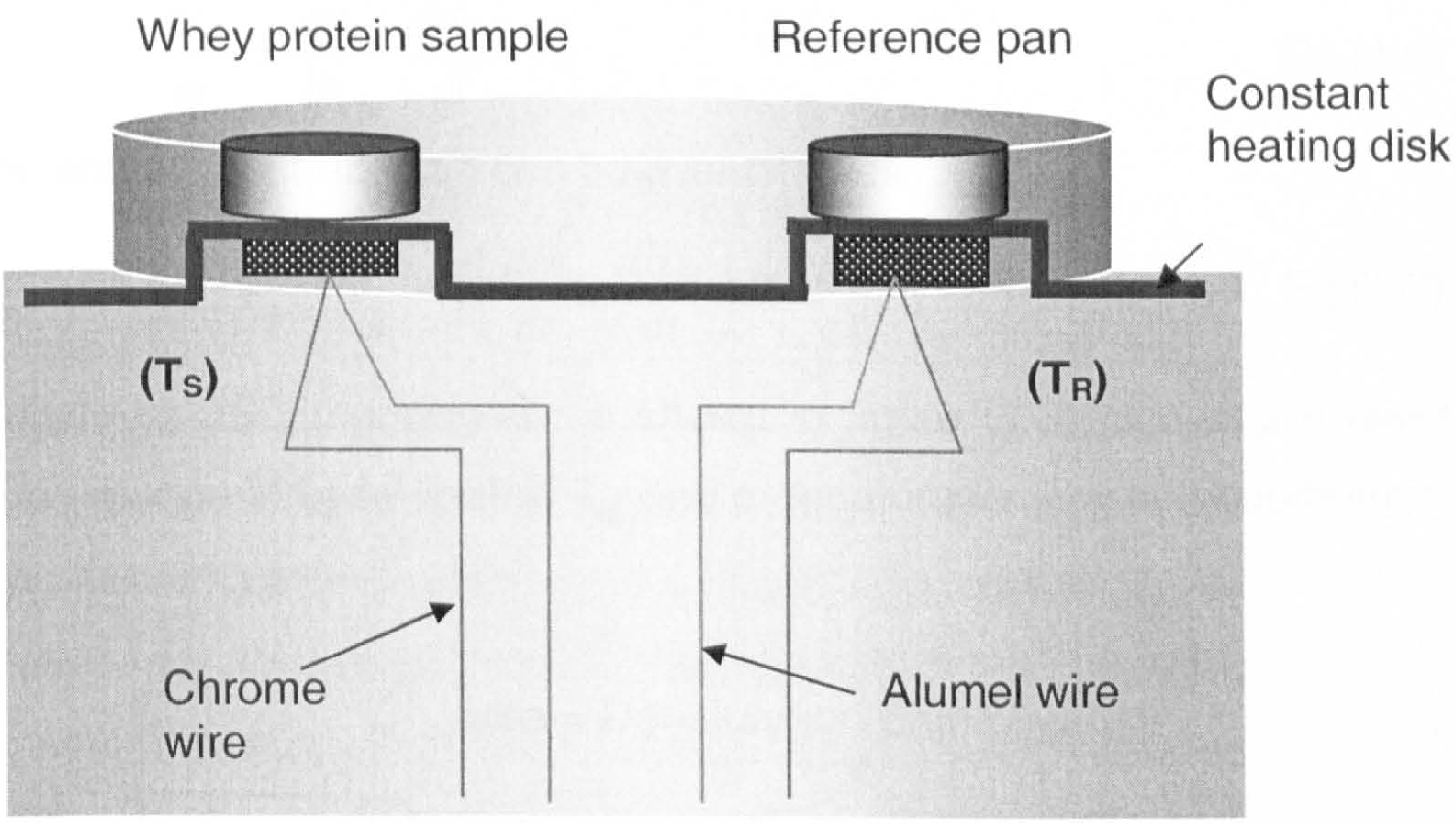

Figure 4-2: Schematic diagram of Heat Flux DSC.

The DSC can be calibrated to determine the heat flow into or out of the sample from the measured temperature difference as the differential temperature signal is approximately proportional to the difference between the heat flow rates to the sample (Q_S) and to the reference sample (Q_R).

$$Q_S - Q_R = -K(T_s - T_R) \qquad \text{Eq (4-2)}$$

where, K is the calibration factor. This differential heat flow is related to the rate of change of enthalpy of the sample.

$$Q_S - Q_R = \frac{dH}{dt} \qquad \text{Eq (4-3)}$$

For a sample with known heat capacity (c_s) and constant heating rate, this can be expressed

$$Q_S - Q_R = c_s \frac{dT}{dt} = \frac{dH_{bl}}{dt} \qquad \text{Eq (4-4)}$$

where, H_{bl} is the baseline (no reaction or transition in the sample). This appears as a flat "*baseline*" on a DSC thermogram, change in sample heat capacity (such as from passing through the glass transition) appears as a change in the "*baseline*" power. Any thermal transition manifests itself as a peak superimposed on the top of the baseline power.

$$\frac{dH}{dt} = \frac{dH_m}{dt} + \frac{dH_{bl}}{dt} \qquad \text{Eq (4-5)}$$

$$\frac{dH_m}{dt} = \frac{dH}{dt} - \frac{dH_{bl}}{dt} \qquad \text{Eq (4-6)}$$

Thus the enthalpy of transition can be evaluated as

$$\Delta H_m = \int dH_m = \int \left(\frac{dH}{dt} - \frac{dH_{bl}}{dt} \right) dt \qquad \text{Eq (4-7)}$$

An example of DSC thermogram is shown in figure (4-3), showing a glass transition (change in base line) at T_g, and a denaturation event (endothermic) at T_d.

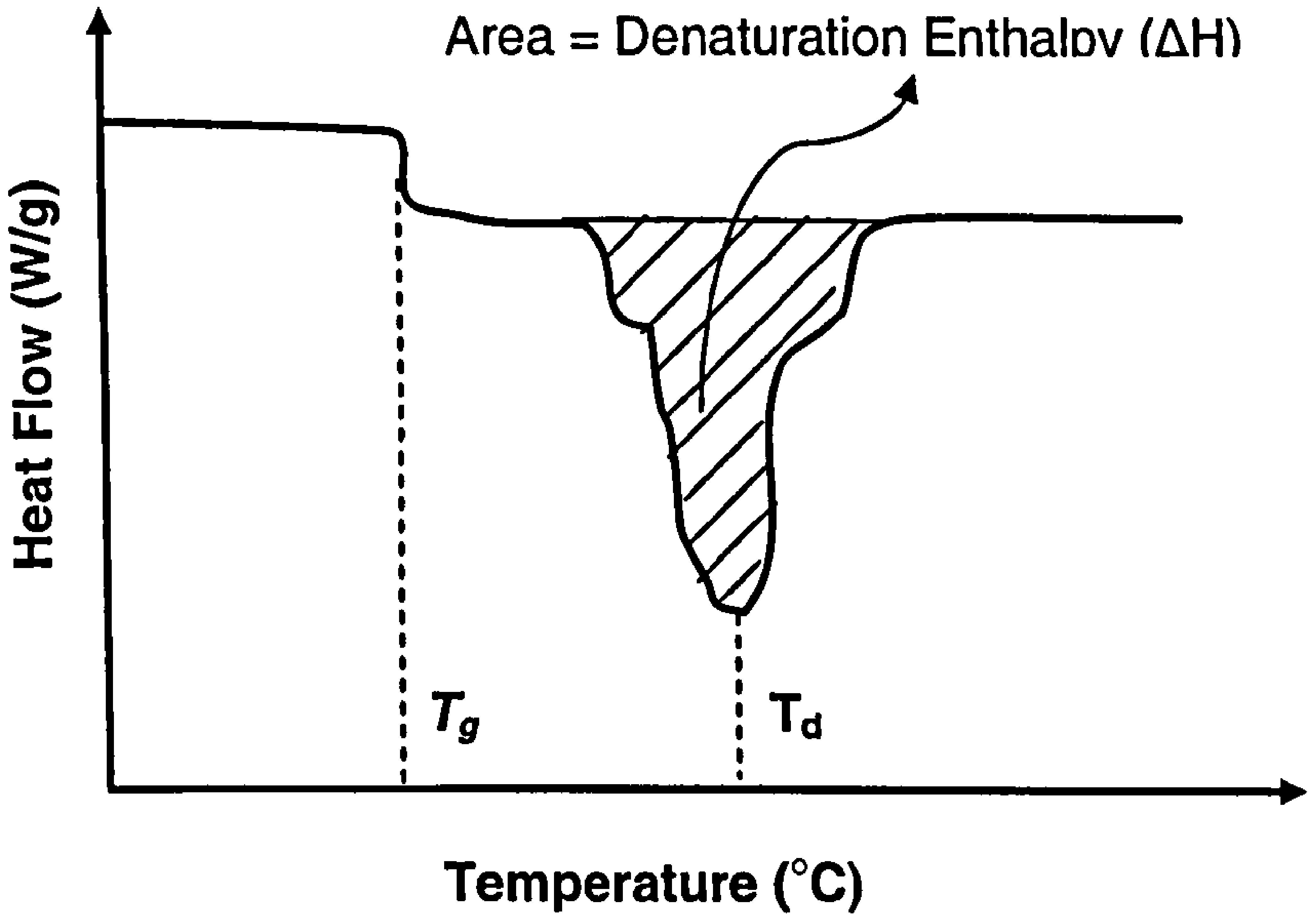

Figure 4-3: An example of DSC thermogram.

The characteristic terms of DSC curves are illustrated in figure (4-4) and the definitions are given below

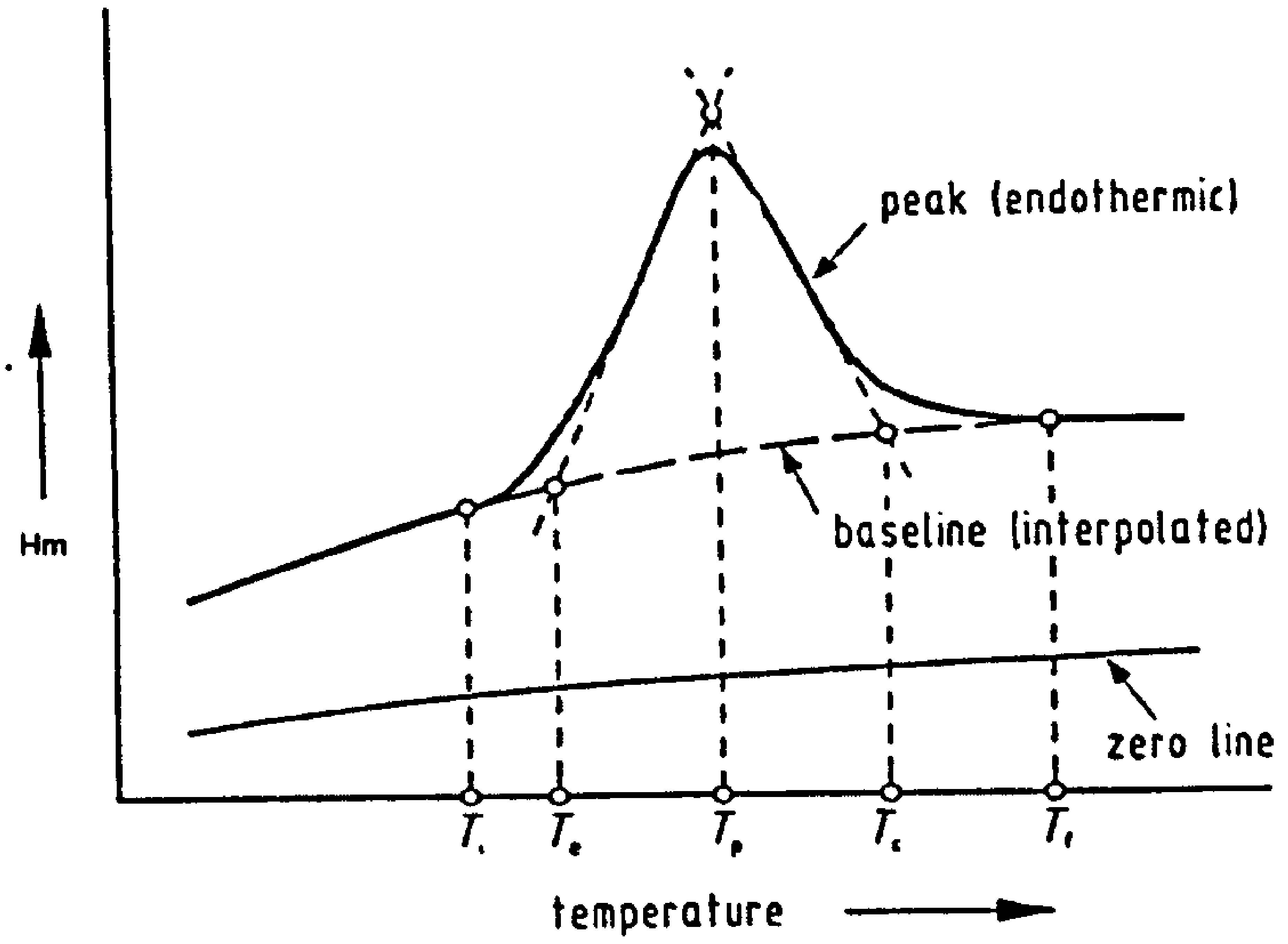

Figure 4-4: Characteristics of DSC thermogram (Hohne, 2003).

Zeroline - the curve measured without sample and sample pans, or with the sample and reference pans both empty

Baseline - the curve produced during steady state conditions (no transition in the sample)

Endothermic peak - steady state is disturbed by thermal transition in the sample.

T_i - initial peak temperature

T_e - extrapolated peak onset temperature (the auxiliary line through the ascending peak slope intersects the base line)

T_p - peak maximum temperature (e.g. denaturation temperature)

T_c - extrapolated peak offset temperature (the auxiliary line through the descending peak slope intersects the base line)

T_f - final peak temperature

4.3.2.1 DSC experimental procedure

A sample of 0.5 g spray dried whey protein powder was dissolved in 1.25 ml distilled water (40% w/v concentration) and gently mixed. A pipette was used to sample 15-23 mg of the solution, which was placed in a pre-weighed DSC pan. The pan was then hermetically sealed and weighed to 0.1 mg accuracy. The sample was placed in a Q10 DSC (TA Instruments, USA) and scanned from 20°C to 100°C at a programmed heating rate of 5°C/min. An empty pan was used as a reference. All DSC measurements were carried out in duplicate. The DSC instrument was calibrated for enthalpy and temperature using an indium standard at the same scan rate. During the DSC analysis, the remaining undenatured protein in the spray dried powder undergoes denaturation, and thus the enthalpy of denaturation (ΔH) is a measure of the amount of undenatured protein remaining in the sample after spray drying. After rapid cooling and rescanning of the same sample, no transition peaks were found at the same transition temperatures, which is evidence that complete protein denaturation has taken place in the DSC on the previous scan (only denatured proteins are presence in that sample) as shown in the figure (4-5). An example of spray dried powder of 30% liquid feed concentration at 80°C outlet temperature, the enthalpy values for the heat of denaturation (ΔH) were calculated from the area under a line extending from 50°C to 90°C and the values were normalised to give enthalpies per gram of *dry* protein, using the measured moisture contents. The peak temperature of denaturation (T_d) was computed from each thermal curve.

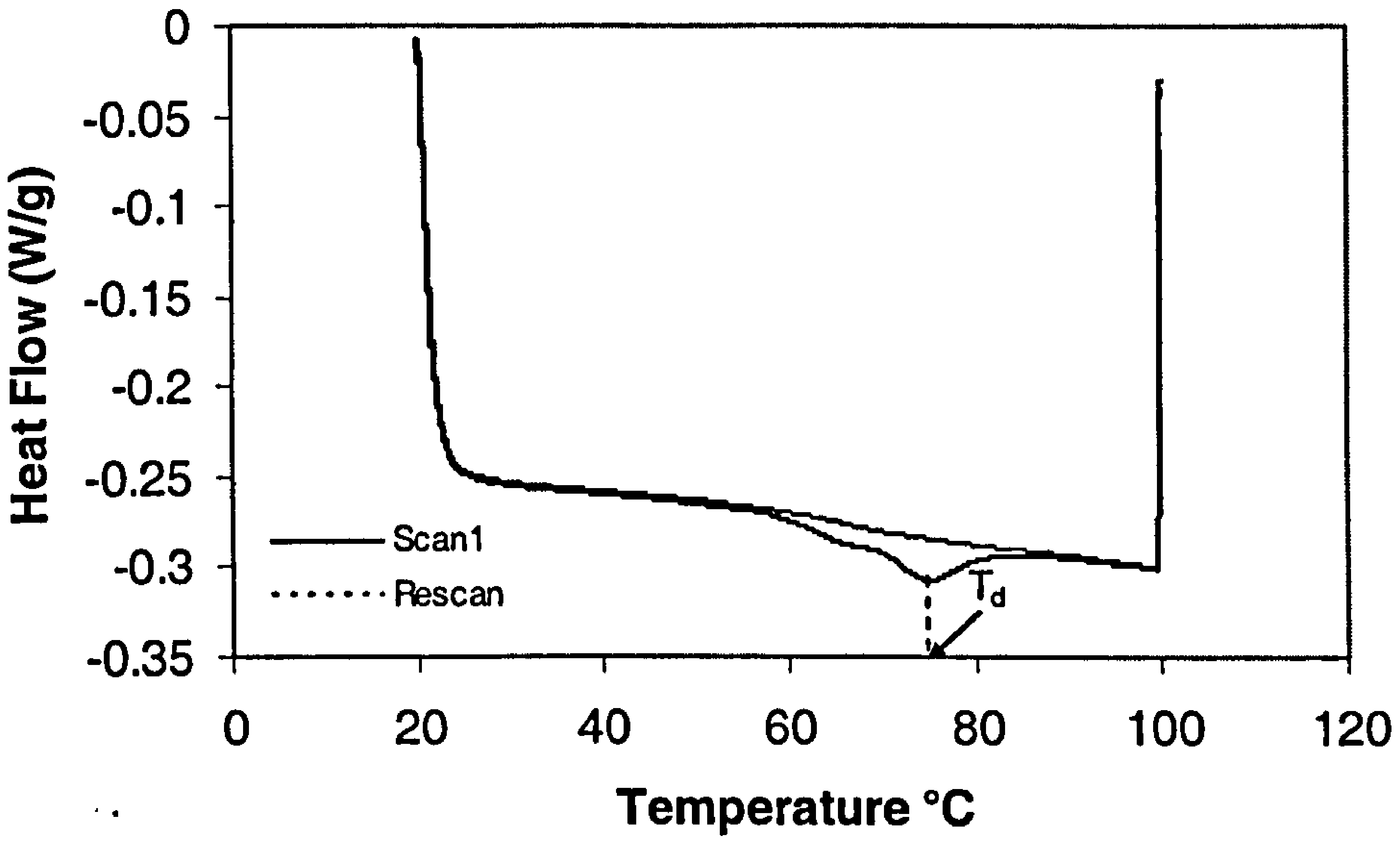

Figure 4-5: DSC thermograms of whey protein solution that has been spray dried from 30% (w/v) protein feed solution and an outlet temperature of 80°C.

4.3.3 Protein solubility analysis

Whey protein solubility was determined by a procedure described by Morr *et al.* (1985). The same method has been followed by a number of researchers, for example, Diaza *et al.* (2004); Fachin and Viotto (2005); Pelegrine and Gasparetto (2005).

4.3.3.1 Solubility experimental procedure

A sample of 500 mg of spray dried/spray-freeze-dried whey proteins was accurately weighed into a 100 ml beaker and a small amount of 0.1 M NaCl solution was then added to form a smooth paste. A further 40 ml of 0.1 M NaCl solution was then added to the paste. The beaker was placed on a magnetic stirrer and agitated vigorously. The dispersion was adjusted to pH 4.6 (the whey protein isoelectric point) (Pelegrine and Gasparetto, 2005) with 0.1 M HCl solution and gently stirred for 30 min. The pH of the dispersion was monitored and maintained at 4.6 throughout the stirring period. The dispersion was then transferred to a 50 ml volumetric flask, diluted to the mark with addition of 0.1 M HCl solution and mixed by shaking. The dispersion was then centrifuged for 30 min at 20,000 g and the resulting supernatant fraction was filtered through Whatman No.1 filter paper. The protein content of the supernatant was determined by a standard Kjeldahl method.

4.3.3.2 Kjeldahl method

The Kjeldahl method was developed in 1883 by a brewer called Johann Kjeldahl. When food containing protein is digested with a strong acid it releases nitrogen, which can be determined by titration. The amount of protein present is then calculated from the nitrogen content. The same basic approach is still used today. This method has been tested for a wide range of substances and is approved by various scientific associations including, AOAC International, Association of American Cereal Chemists, American Oil Chemists Society, Environmental Protection Agency, International Standards Organization and United States Department of Agriculture.

(a) Analytical Procedure

The Kjeldahl analytical method has three stages: (i) digestion, (ii) distillation and (iii) titration. A block diagram of the procedure is shown in figure (4-6).

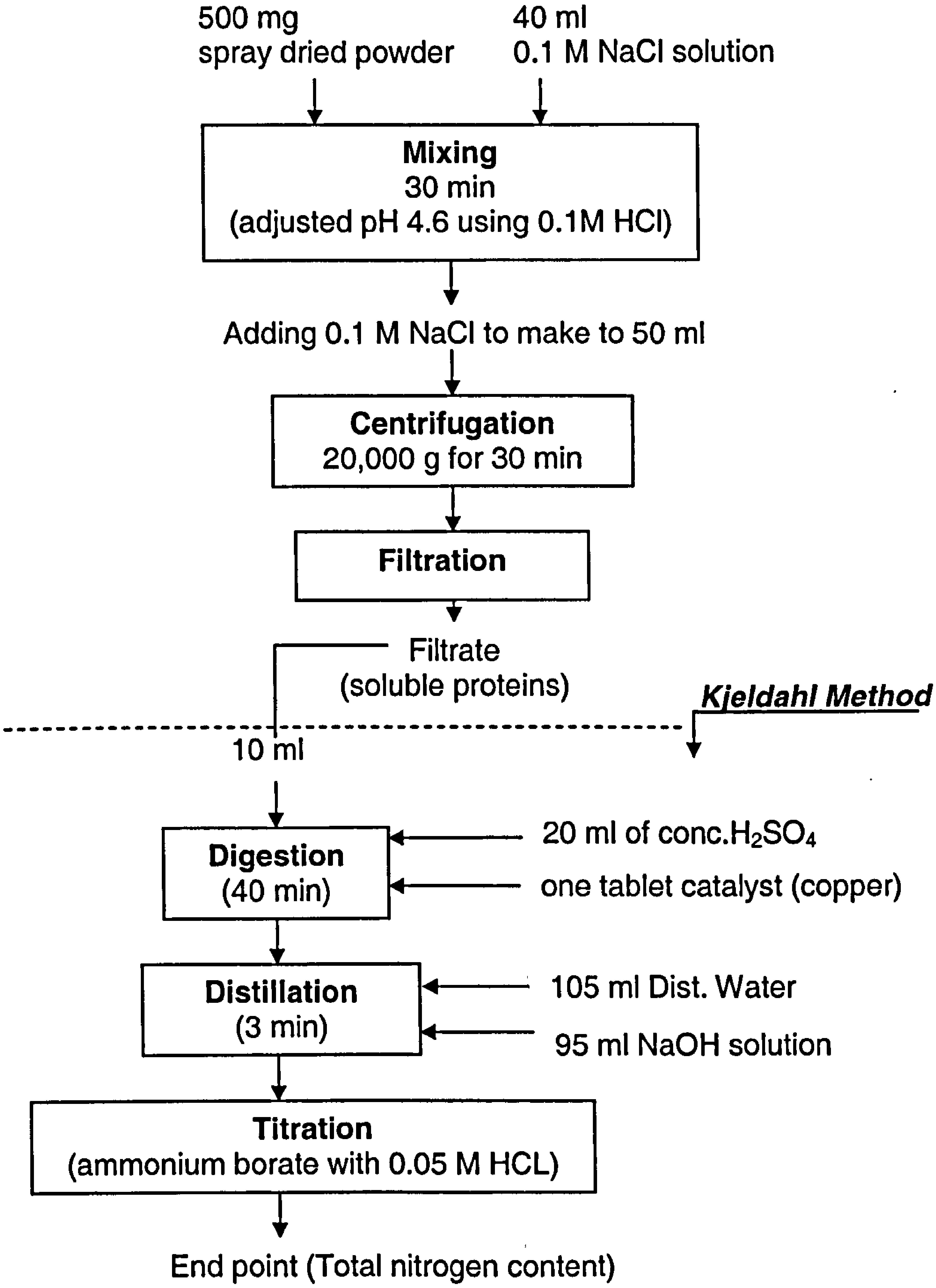

Figure 4-6: Block diagram of Kjeldahl procedure.

(i) ***Digestion***: 10 ml of filtrate (soluble whey proteins), 20 ml of concentrated H_2SO_4 (an oxidizing agent which digests the proteins) and one tablet of catalyst (copper) were added into Kjeldahl tube and then allowed to digest by heating for about 40 min. This digestion was carried out in digester units in a fume cupboard. Digestion converts any nitrogen in the sample (proteins) into ammonia and other organic matter to CO_2 and H_2O. Ammonia gas is not liberated in an acid solution because the ammonia is in the form of the ammonium ion (NH_4^+) which binds to the sulfate ion (SO_4^{2-}) and thus remains in solution.

$$\text{N (proteins)} + H_2SO_4 \rightarrow (NH_4)_2SO_4 + H_2O + CO_2 + \text{by-products} \qquad \text{Eq (4-8)}$$

(ii) ***Distillation***: After digestion has been completed the digestion tube and receiving conical flask (containing 5 ml of 20% boric acid) were connected to a steam distillation unit and volume of water and NaOH, distillation time were fixed in the distillation unit as follows: Distillation water = 105 ml; NaOH = 95 ml; Distillation time = 3 min.

The solution in the digestion tube was then made alkaline by the addition of 95 ml NaOH solution, which converts the ammonium sulfate into ammonia gas and changes the colour of the solution to dark brown.

$$(NH_4)_2SO_4 + 2\ NaOH \rightarrow 2NH_3 + 2H_2O + Na_2SO_4 \qquad \text{Eq (4-9)}$$

The ammonia gas moves out of the digestion tube into the receiving conical flask. The low pH of the solution in the receiving flask converts the ammonia gas into the ammonium ion and simultaneously converts the boric acid to the borate ion.

$$NH_3 + H_3BO_3\ \text{(boric acid)} \rightarrow NH_4^+ + H_2BO_3^-\ \text{(borate ion)} \qquad \text{Eq (4-10)}$$

(iii) ***Titration***: The receiving conical flask was removed and the nitrogen content was then determined by titration of the ammonium borate with 0.05 M HCl solution using a control indicator to determine the end-point (pink colour) of the reaction.

$$H_2BO_3^- + H^+ \rightarrow H_3BO_3 \qquad \text{Eq (4-11)}$$

The concentration of hydrogen ions (in moles) required to reach the end-point is equivalent to the concentration of nitrogen that was in the original sample.

(b) *Calculations*

The following equations were used to determine the protein solubility of a sample

$$\%N = \frac{14.01 \times (\textit{ml of titrant of sample} - \textit{ml of titrant of blank}) \times \textit{Molarity of standard acid}(0.05)}{\textit{Mass of sample}(g) \times 10}$$

$$\%\ \text{Protein} = \%\ \text{N x specific factor (= 6.38 for whey proteins)} \qquad \text{Eq (4-12)}$$

$$\text{Protein solubility (\%)} = \frac{(SP_C \times 50)}{TP} \times 100 \qquad \text{Eq (4-13)}$$

where, SP_C is the protein concentration of the supernatant (mg/ml) and TP is the weight of the protein (mg) in the original solution (mg). The degree of denaturation is finally determined from

$$\%\ \text{degree of denaturation} = \left(1 - \frac{SP_c}{SP_u}\right) \times 100 \qquad \text{Eq (4-14)}$$

where, SP_C is the soluble protein concentration of spray-dried products (mg/ml) and SP_U is the soluble protein concentration of the untreated sample (mg/ml). The experiments were carried out in duplicate for each sample and average values were taken to calculate the solubility at pH 4.6.

4.3.4 Reversed phase high performance liquid chromatography (RPHPLC) analysis

High performance liquid chromatography (HPLC) is known to be a powerful separation method as it can separate mixtures of large numbers of similar analytes in a short space of time. It also allows sample components to be identified by their retention time and their quantity to be determined by the peak area (Meyer, 1999).

HPLC is the principal technique for analysing milk proteins. A large number of different HPLC methods are available such as, ion-exchange chromatography, gel electrophoresis, gel filtration chromatography and reversed phase HPLC (RP-HPLC). In this study, the RP-HPLC method was used to determine the degree of soluble fraction of whey proteins in the spray dried power. This technique has biological significance as the separation is based on hydrophobic interactions, which are the main forces that stabilize the three-dimensional structure of proteins (Ferreira *et al.*, 2001). Thus further denaturation does not occur during analysis.

4.3.4.1 Principles of reversed phase HPLC

Reversed phase HPLC is the term used to describe conditions in which the stationary phase is less polar than the mobile phase (as opposed to the HPLC method, where the stationary phase is more polar) (Mant and Hodges, 1991; Meyer, 1999). Chemically bonded octadecylsilane, an n-alkane with 18 carbon atoms and cyclohexyl and phenyl groups is frequently used as the stationary phase. A schematic diagram of the RP-HPLC unit that was used is shown in figure (4-7). In a high-pressure gradient system, two pumps are used to convey eluents (solvents) at a particular ratio to the solvent mixer. The flow rate of each pump can be varied linearly with time. The sample is injected into the column by an auto-injector and the column is enclosed in a thermostat for temperature control.

The separations are based on the differential solubility in aqueous and organic media. Gradient elutions start with a predominantly aqueous mobile phase (water) and move gradually to a more organic mobile phase (acetonitrile). RP-HPLC separation is based on hydrophobicity (hydrophobic= water-repellent) and it correlates approximately with carbon number. The smaller molecules with lowest carbon numbers (less hydrophobic) elute first. A UV detector measures the absorbance of the eluate.

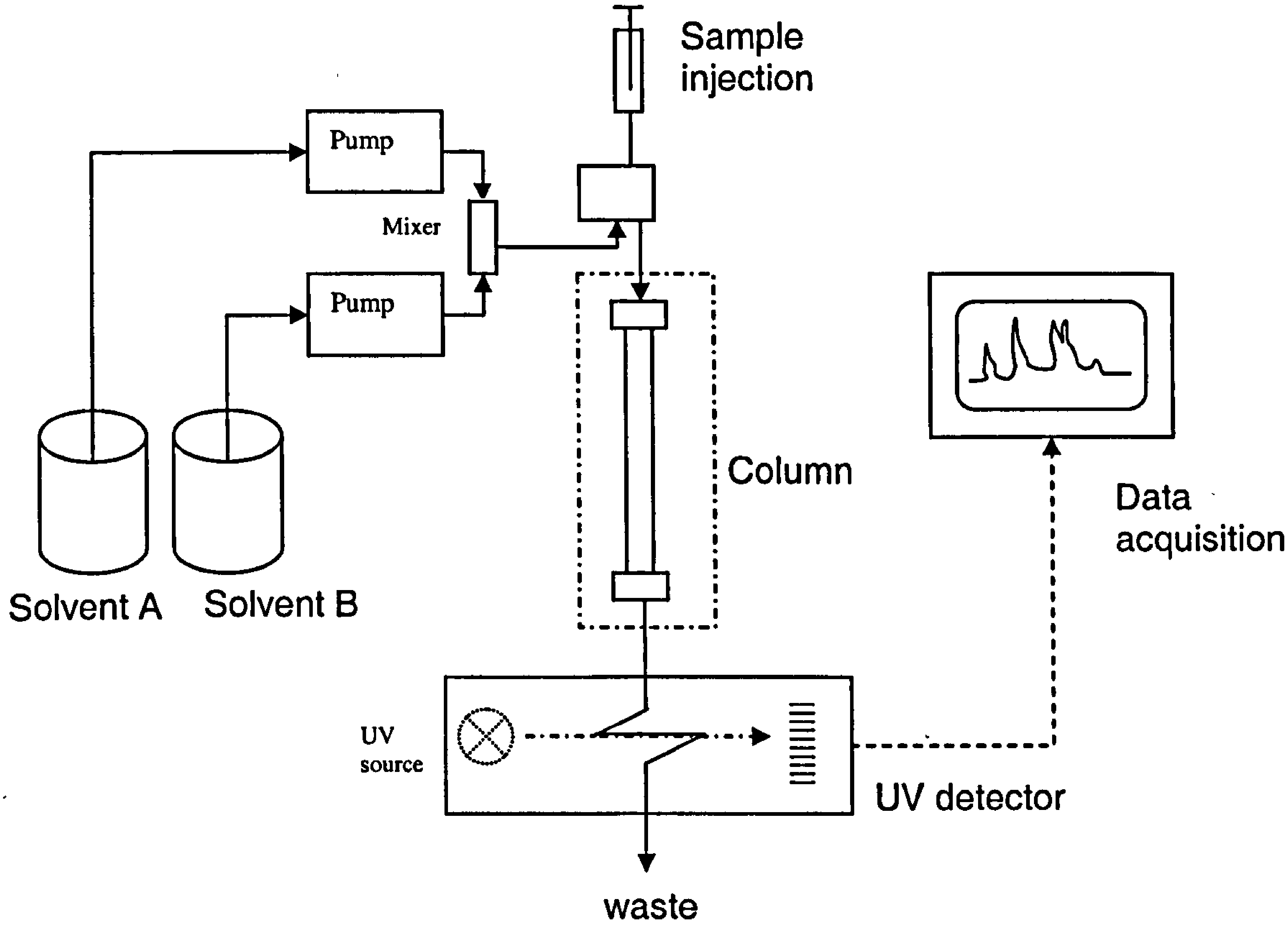

Figure 4-7: Schematic diagram of an RP-HPLC unit.

The degree of absorption resulting from passage of the light beam through the detection cell is a function of the molar absorptivity (ε), molar concentration of the compound (c) and length of the cell (d). The product of ε, c and d is known as the absorbance A (a dimensionless number),

$$A = \varepsilon cd \qquad \text{Eq (4-15)}$$

The signals are computed and produce the results in the form of peak retention time, height, width, area and % of area.

4.3.4.2 RP-HPLC analytical procedure

The amounts of native α-lactalbumin and β-lactoglobulin in the soluble fraction at pH 4.6 (whey protein isoelectric point) were determined by using reversed phase HPLC, based on the method described by Parris and Baginski (1991), Ferreira *et al.* (2001) and Ferreira and Cacote (2003). A sample of 500 mg of spray dried/spray-freeze-dried whey protein was accurately weighed into a 100 ml beaker and a small amount of ultra-pure Milli-Q water was added to form a smooth paste. A further 40 ml water was then added to the paste. The beaker was placed on a magnetic stirrer and agitated vigorously. The dispersion was adjusted to pH 4.6 (the whey protein isoelectric point) with 0.1 M HCl solution and gently stirred for 30 min. The pH of the dispersion was monitored and maintained at 4.6 throughout the stirring period. The dispersion was then transferred to a 50 ml volumetric flask, diluted to the 50 ml mark with the addition of water and mixed by shaking. The dispersion was then centrifuged for 30 min at 20,000g and the resulting supernatant fraction was filtered through Whatman No.1 filter paper. The filtrate was diluted in water (1:1). Prior to RP-HPLC analysis, all samples were centrifuged in a microfuge at 15000g for 3 min to remove any insoluble material.

An analytical HPLC (Agilent 1100) unit equipped with a binary pump was used for the HPLC analysis. A 20 μl sample was auto-injected into a polymeric reversed phase column containing a polystyrene-divinylbenzene copolymer-based packing (column length 250 mm; column diameter 4.1 mm; particle size 10μm, pore size 10nm). Gradient elution was carried out with a mixture of two solvents. The elution gradient was set as shown in the following table (4-2) and gradient elution profile is shown in the figure (4-8):

Eluant A : 0.1% trifluoroacetic acid (TFA) with 99.9% water
Eluant B : 0.1% trifluoroacetic acid (TFA), 19.9% water and 80% acetonitrile.

Table 4-2: Gradient elution profile.

Time (min)	Eluant A (%)	Eluant B (%)
20	→ 64-44	→ 36-56
10	→ 44-40	→ 56-60
5	→ 40-64	→ 60-36
3	Column re-equilibrium	

The total flow rate was fixed at 0.5 ml/min and the column temperature was maintained at 45°C. Concentrations were determined from the UV absorbance at a wavelength of 215 nm.

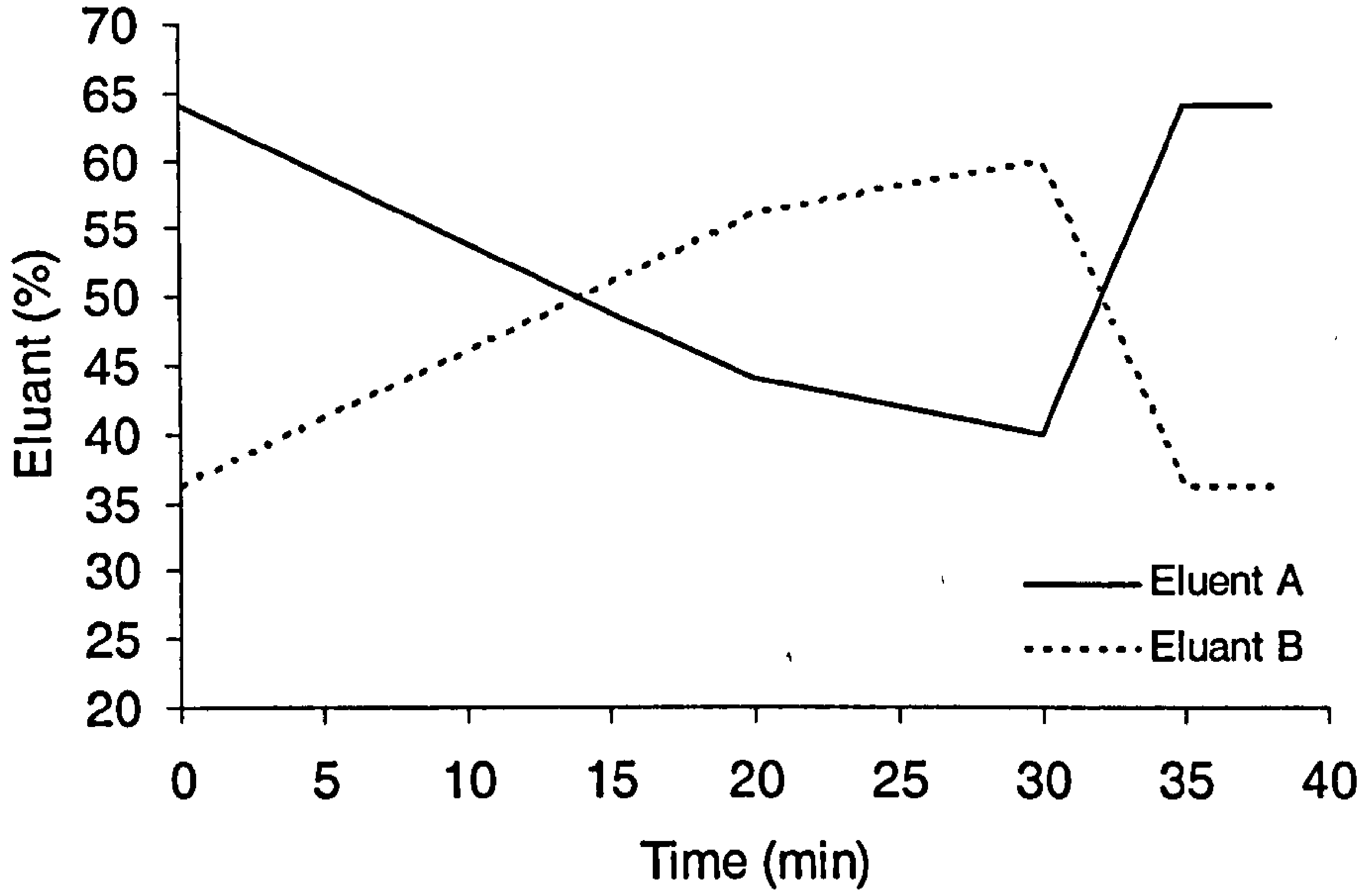

Figure 4-8: Gradient elution profile.

4.3.4.3 Protein Standard Calibrations

The RP-HPLC conditions were optimised for elution gradient, sample size, concentration and flow rate. The whey proteins were identified by means of the retention time and peaks were quantified by comparing peak areas with the results of a calibration series with pure native standards for bovine α-lactalbumin in the range of 0.375 to 3 mg/ml and bovine β-lactoglobulin in the range of 0.65 to 5 mg/ml as shown in figures (4-9) and (4-10).

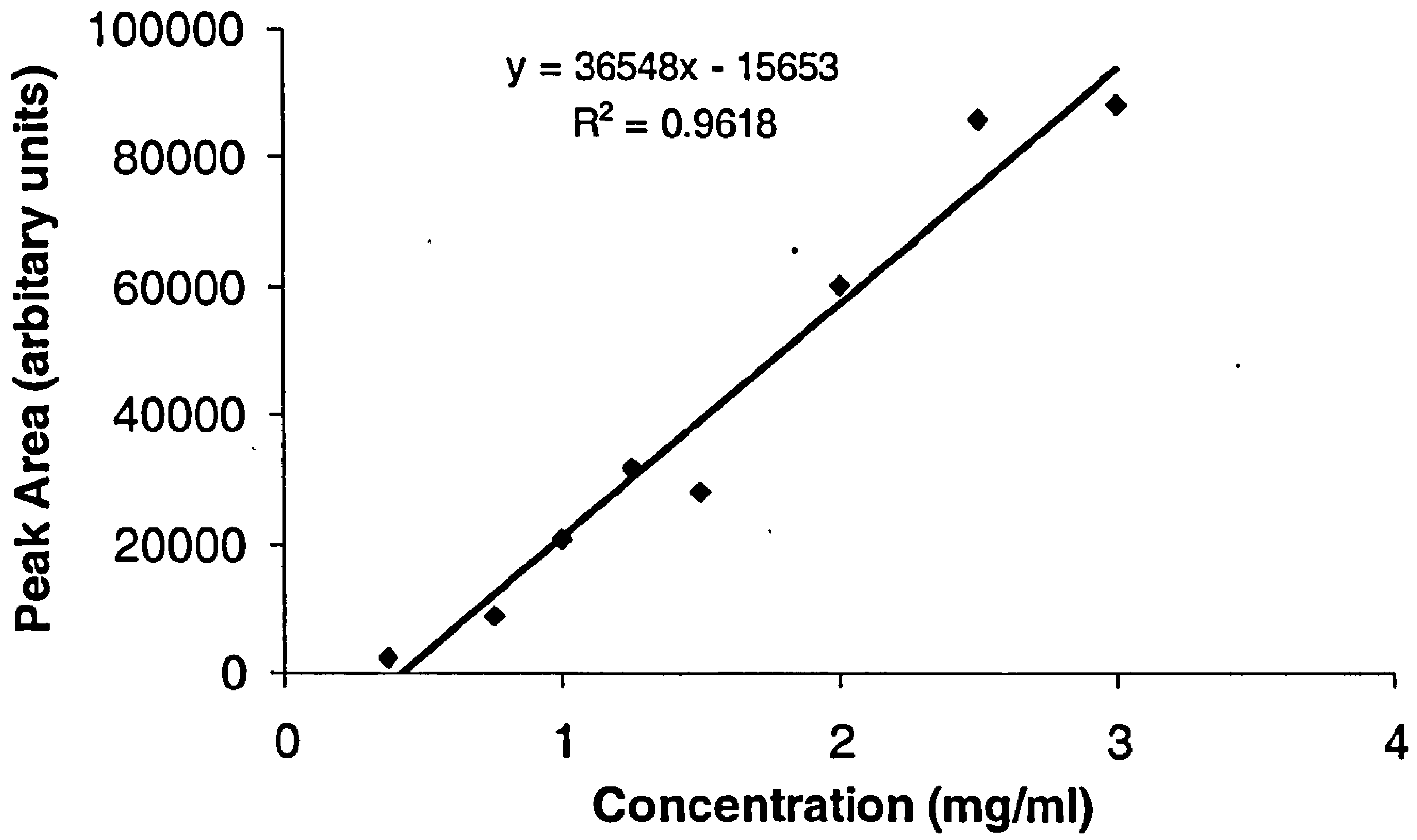

Figure 4-9: Calibration plot of bovine α-lactalbumin standard.

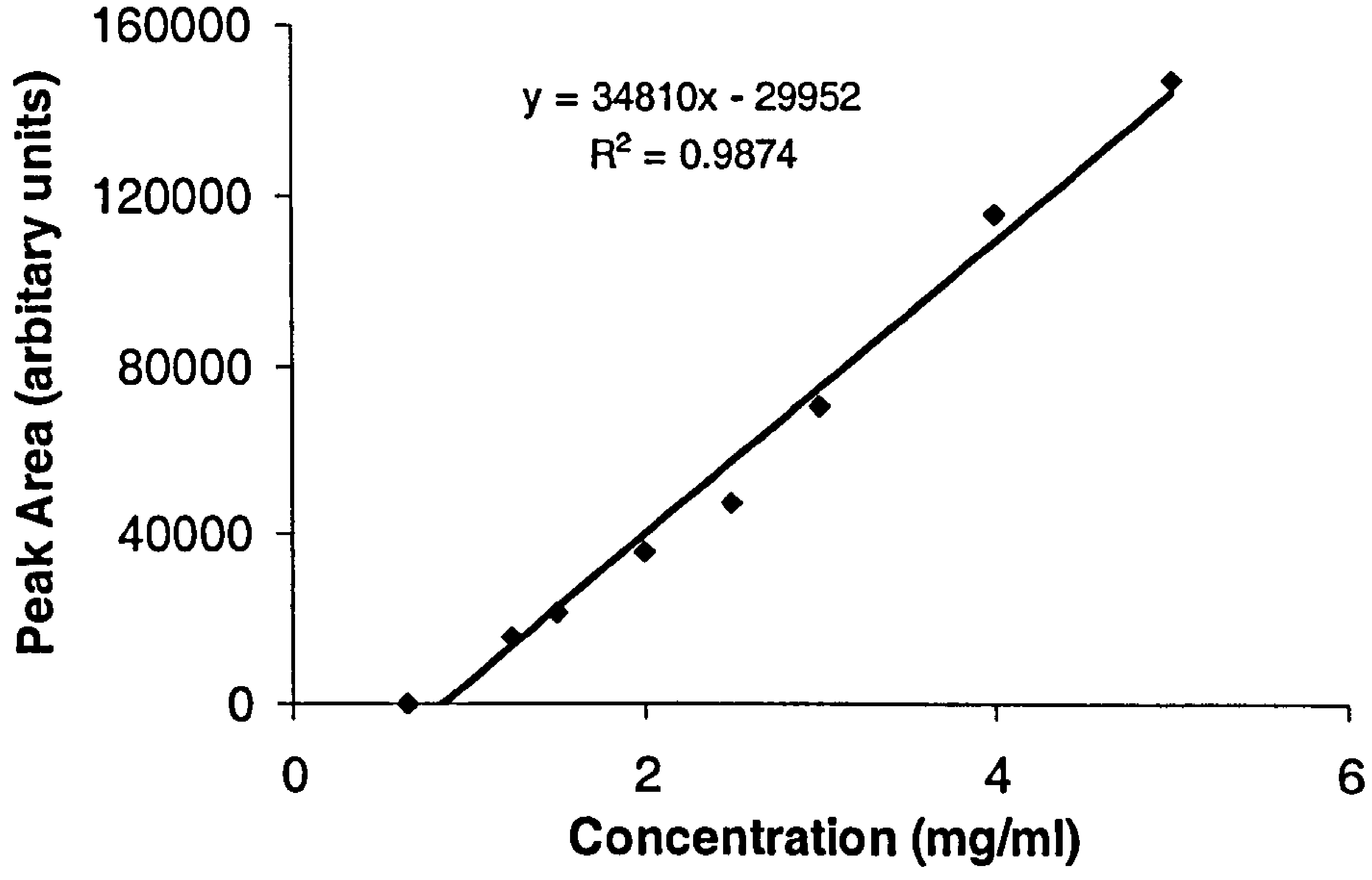

Figure 4-10: Calibration plot of bovine β-lactoglobulin standard.

Figure (4-11) shows the chromatographic patterns of the α-lactalbumin, β-lactoglobulin and mixture of these standards. The proteins were clearly resolved with retention times of (i) ~20 min one peak for α-lactalbumin; (ii) ~24 and ~25 min with two peaks for β-lactoglobulin B (β-lgB) and β-lactoglobulin A (β-IgA) respectively. The injection solvent was separated at 5 min. The same trend of separation was observed in other reports (e.g. Ferreira *et al.*, 2001& 2003; Elgar *et al.*, 2000).

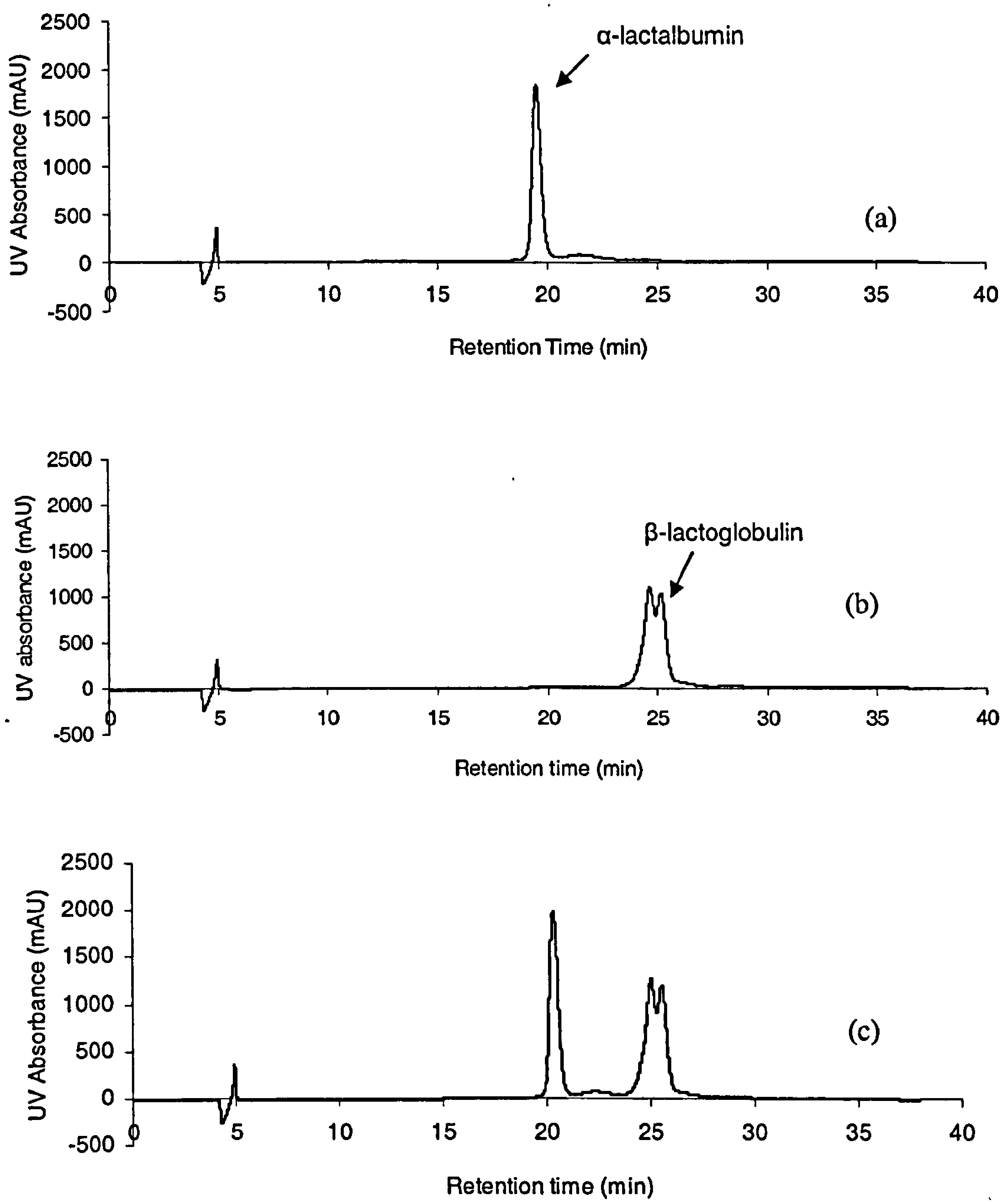

Figure 4-11: Chromatogram pattern of protein standards (a) α-lactalbumin, (b) β-lactoglobulin and (c) mixture of α-lactalbumin and β-lactoglobulin (1:2).

The spray dried whey protein sample chromatograms also exhibited similar retention time to the α-lactalbumin and β-lactoglobulin native standards. An example of chromatogram of whey protein spray dried from a 20 %(w/v) feed concentration with a 60°C outlet temperature is shown in figure (4-12).

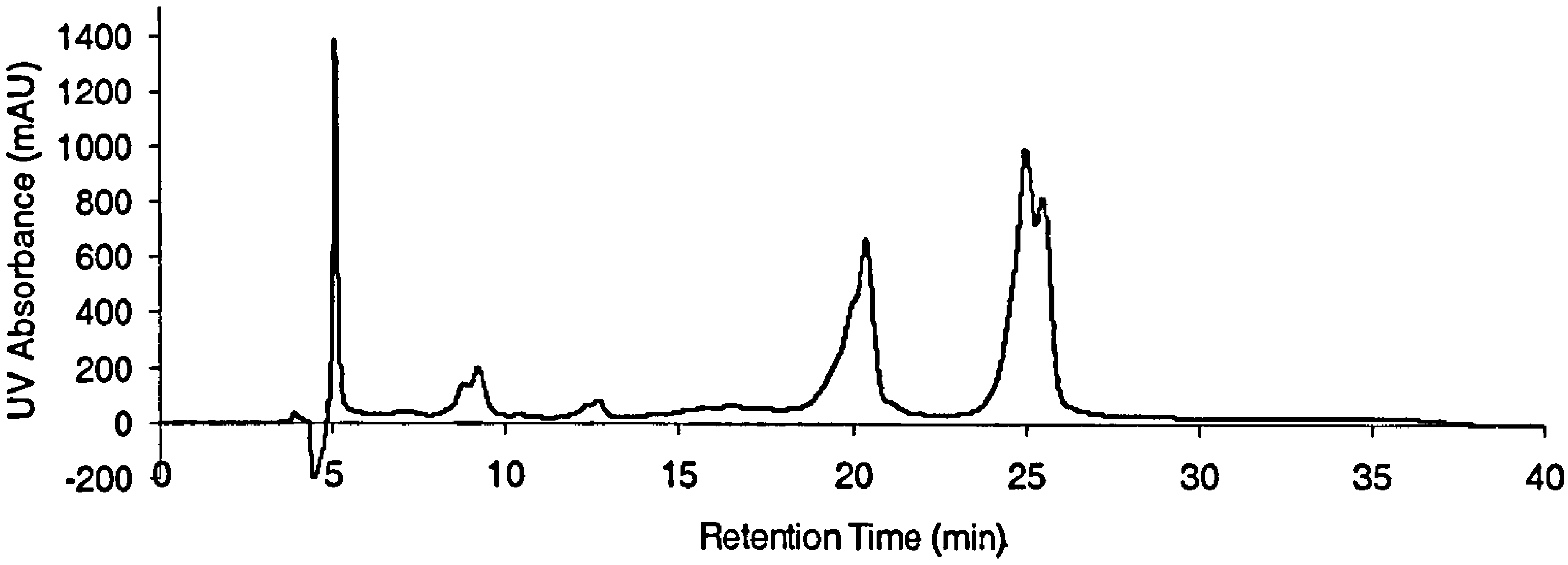

Figure 4-12: Chromatogram for whey protein spray dried from a 20% (w/v) feed solution with a 60°C outlet temperature.

The HPLC analyses were carried out in triplicate for each sample and average values were taken to calculate the degree of denaturation from the following equation:

$$\%\,\text{Loss of solubility} = \left(1 - \frac{SP_c}{SP_u}\right) \times 100 \qquad \text{Eq (4-16)}$$

where, SP_c is the soluble protein in the spray-dried or spray-freeze-dried sample and SP_u is the soluble protein in the untreated sample. These values were normalised to original protein mass using the measured moisture content.

4.3.5 Particle size analysis

The spray-dried and spray-freeze-dried product particle size distributions were determined by a Coulter LS 130 (Coulter Corporation, USA). This instrument uses laser diffraction to give particle size measurements in the range of 0.1 to 800 μm. The Coulter LS 130 uses a solid state laser at a wavelength of about 750 nm. The particles are dispersed in a cell containing a fluid, which is sealed with a circular side glass. The particles are mixed within this cell using a magnetic stirrer. The particle motion interrupts the path of a laser beam intermittently. The laser beam is focused by a Fourier lens and the diffraction pattern is recorded by photo detectors as indicated in figure (4-13).

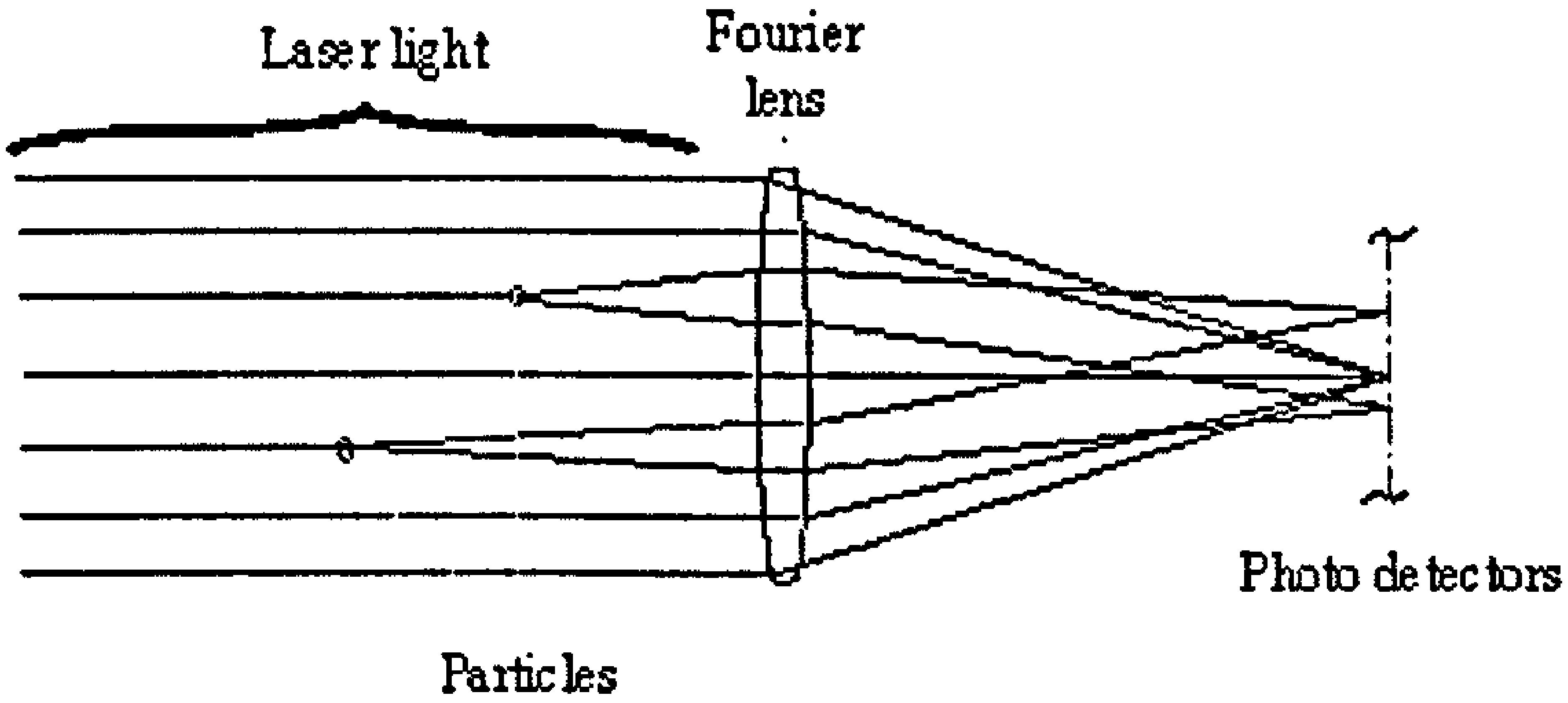

Figure 4-13: Schematic diagram of the particle measurements in Coulter LS130, Fourier lens focusing.

The signals were computed in the COULTER, which used a mathematical model based on Fraunhofer diffraction theory to produce the results in the form of particle mean diameter, median and standard deviation of the particle size. The particle dispersing fluid has to be transparent, non-viscous, non-dissolving of the sample particles, consistent, and have a density lighter than that of the sample particles. Commonly used dispersion liquids for milk and milk products are iso-butanol, iso-butanol+dethylphtalate and iso-amyl alcohol (Bornhardt, 1994).

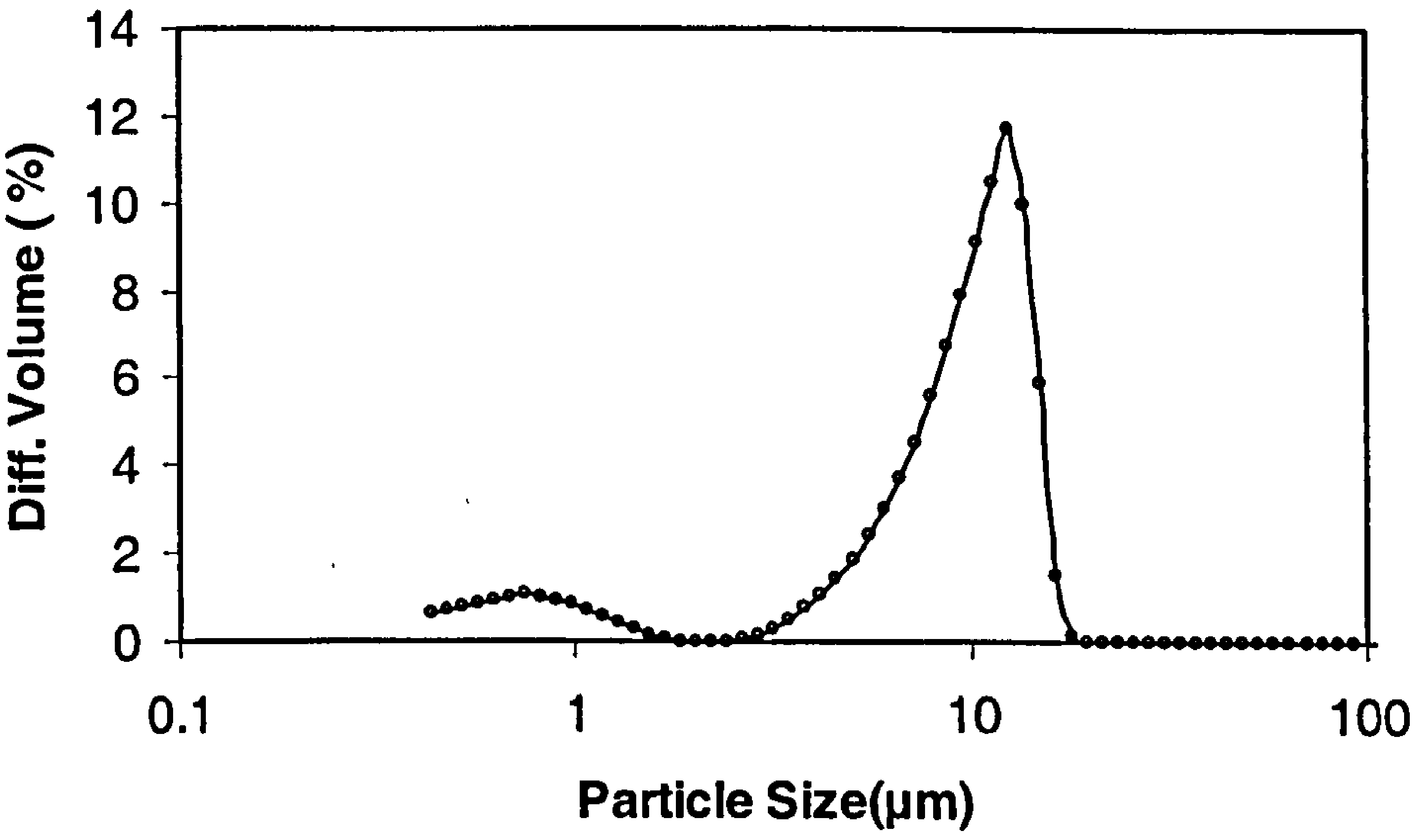

Figure 4-14: Particle size distribution of spray dried powder.

For these experiments, spray-dried/spray-freeze-dried samples were dispersed in a isobutanol solvent to perform the measurements. The particle sizes are presented as Sature mean diameters (d_{32}), and are the average of three independent measurements. An example particle size distribution of spray dried power from a 20%(w/v) liquid feed solution with a 80°C outlet temperature is shown in figure (4-14).

4.3.6 Scanning Electron Microscopy (SEM)

The Scanning Electron Microscope (SEM) is a commonly used instrument to probe the microstructure of materials, and provides information relating to topographical features, morphology, compositional differences, crystal structures and orientation. SEM is a microscope that uses electrons rather than light to form an image. In SEM, an electron beam is generated by an electron gun, which is accelerated to moderately high energy and positioned onto the sample by electromagnetic fields. The electrons interact with atoms in the specimen and generate a signal. The electron beam hits each spot on the sample and secondary electrons are emitted from its surface. A detector counts these electrons and sends the signals to an amplifier. The final image is built up from the number of electrons emitted from each spot on the sample.

There are many advantages of using the SEM instead of a light microscope. It has a large depth of field, which allows a large amount of the sample to be in focus at one time. It also produces images of high resolution, which means that closely spaced features can be examined at a high magnification. Preparation of the samples is relatively easy since most SEMs only require the sample to be conductive. This can be accomplished by coating the sample with a very thin layer of gold.

The Scanning Electron Microscope images of the spray-dried/spray-freeze-dried samples were examined using a Cambridge Stereo Scan 360 UK. Images were taken by Mr. Frank Page at the Institute of Polymer and Material Engineering (IPTME) department at Loughborough University.

Chapter 5

Experimental studies on spray-drying of whey proteins

5.1 Introduction

In spray drying operations, the main operating variables are: feed concentration, feed rate, air flow rate, atomisation pressure, and inlet and outlet temperatures. Although a large number of studies have been carried out on spray drying operations, the effect of process variables on whey protein powder quality has been largely overlooked. An exception is Oldfield *et al.* (2005) who observed that varying the inlet and outlet gas temperatures (from 160 to 200°C and 89 to 101°C, respectively) did not affect the amount of whey protein denaturation. However, in their experiments, they found that most of the whey proteins were denatured during concentration of the skimmed milk by preheating from 70 to 120°C for 52 s, prior to feeding to the spray dryer. In this study, the impact of varying gas outlet temperature up to a higher temperature of 120°C and of varying feed concentration on the denaturation and solubility of the dried whey protein product has been studied in a co-current operation. The various analytical method results and discussions are presented as illustrated in figure (5-1). The first part of the chapter describes about the product characteristics such as, moisture content, particle size and morphology. The second part of the chapter describes about the product quality in terms of protein denaturation and solubility.

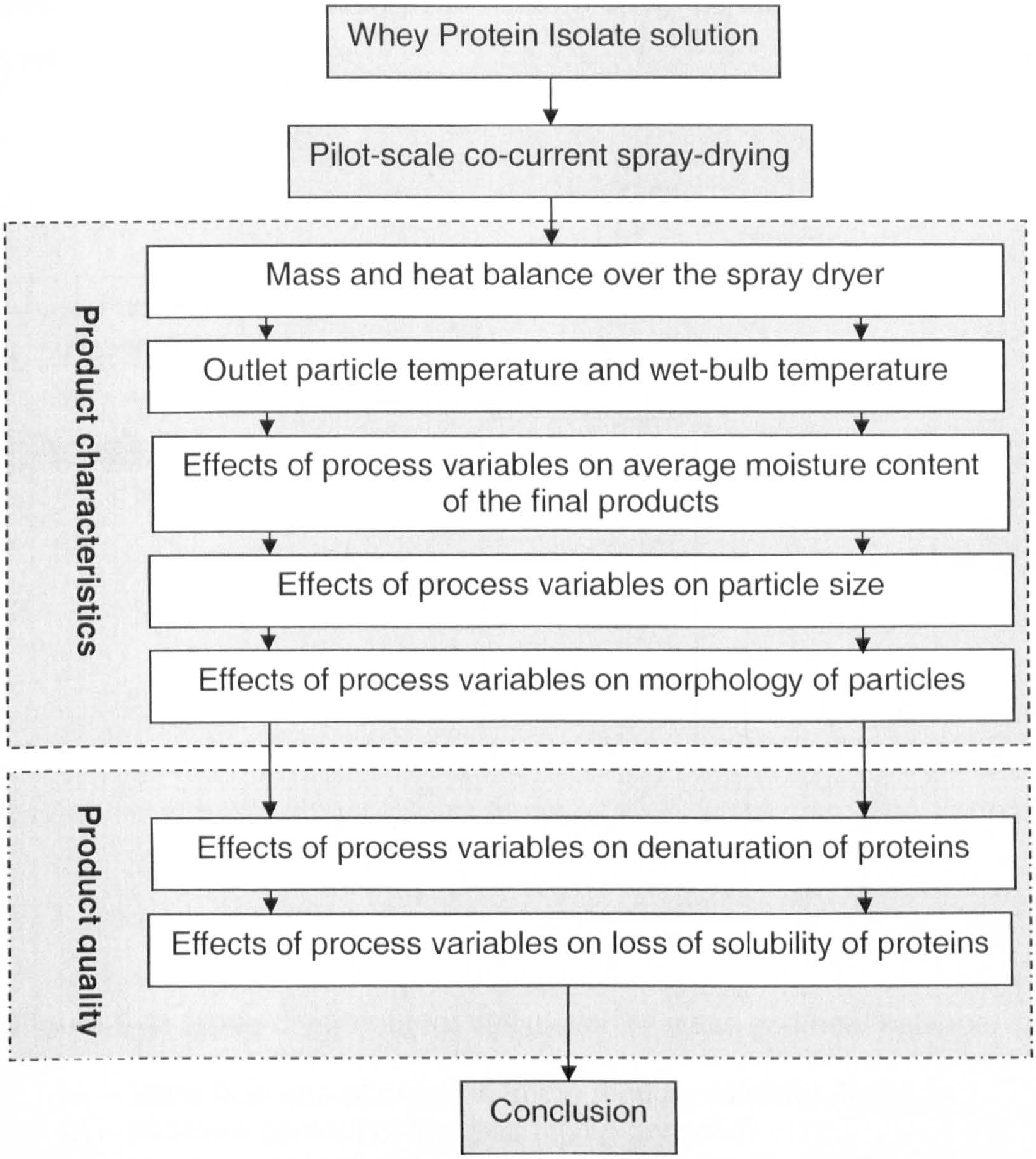

Figure 5-1: Structure of Chapter 5.

5.2 Experimental details

The feed liquid solution preparation method is described in Chapter 4, (section 4.2.2) and the methods of sample analysis are given in the same chapter, in section 4.3.

5.3 Mass and heat balance over spray dryer

The spray dryer outlet gas humidity and particle temperatures can be obtain from the mass and heat balance data. These calculations are important to find out the heat loss during the operation and help to understand the drying process. Mass and heat balances are drawn up in the following sub-sections with reference to figure (5-2).

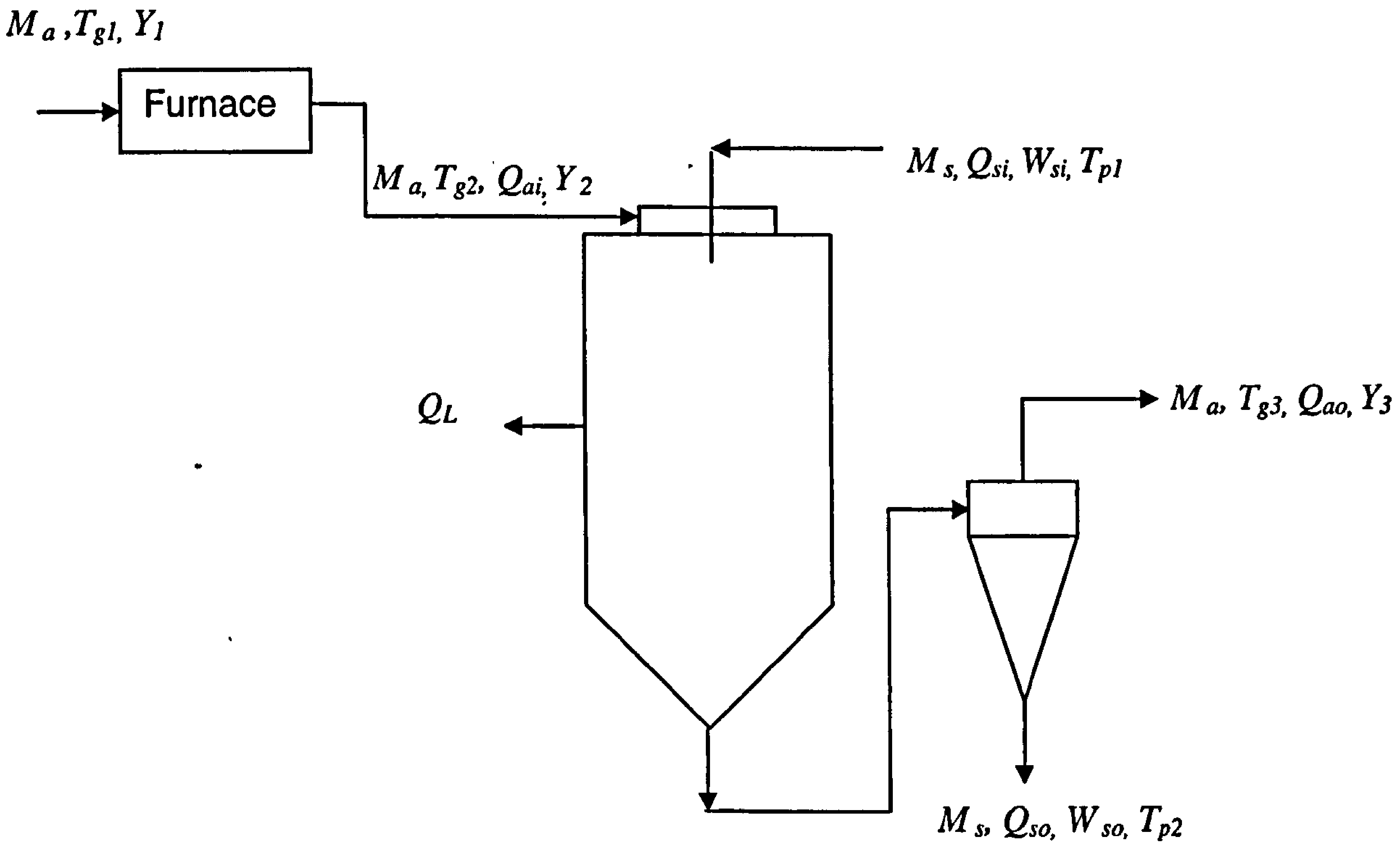

Figure 5-2: Spray dryer data for calculation of mass and heat balance.

M_s – Mass flow rate of dry solid in the feed liquid/slurry (kg/h)
W_{si} – Moisture content of the feed (kg/kg dry solid)
W_{so} – Moisture content of the dried product (kg/kg dry solid)
M_a – Mass flow rate of gas (kg/h)
Q_{ai} – Heat flow of inlet gas to dryer (J/h)
Q_{ao} – Heat flow of outlet gas from dryer (J/h)
Q_{si} – Heat flow of feed liquid entering dryer (J/h)
Q_{so} – Heat flow of dried product leaving dryer (J/h)
Q_L – Heat loss from the dryer (J/h)
Y_1 – Absolute inlet gas humidity to the furnace (kg/kg dry air)
Y_2 – Absolute inlet gas humidity to the dryer (kg/kg dry air)
Y_3 – Absolute outlet gas humidity from the dryer (kg/kg dry air)
T_{g1} – Inlet gas temperature to the furnace (K)
T_{g2} – Inlet gas temperature to the dryer (K)
T_{g3} – Outlet gas temperature from the dryer (K)
T_{p1} – Inlet feed temperature (K)
T_{p2} – Outlet particle temperature (K)

5.3.1 Mass balance

In a continuous steady-state operation, the mass flow rate of water in the inlet air and feed liquid equals the mass flow rate of water in the outlet streams. The individual stream flows (per hour) are as follows

Moisture entering in feed $= M_s W_{si}$
Moisture entering in gas $= M_a Y_2$
Moisture leaving the dryer in the dried product $= M_s W_{so}$
Moisture leaving the dryer in the exhaust drying air $= M_a Y_3$

If there is no product accumulation in the chamber, then

Input=output

$$M_s W_{si} + M_a Y_2 = M_s W_{so} + M_a Y_3 \qquad \text{Eq (5-1)}$$

Hence,

$$M_s (W_{si} - W_{so}) = M_a (Y_3 - Y_2) \qquad \text{Eq (5-2)}$$

i.e. the mass of water evaporated from the liquid feed equals that taken up by the air and rearranging equation (5-2) in terms of outlet air humidity,

$$Y_3 = Y_2 + \left[\frac{M_s}{M_a}\right](W_{si} - W_{so}) \qquad \text{Eq (5-3)}$$

The first term on the right hand side in equation (5-3), the absolute inlet gas humidity to the dryer (Y_2) was calculated from the combustion reaction of natural gas based on measured inlet air humidity (detail calculations in Appendix. A) and the remaining terms were measured and so this enables the outlet air humidity to be calculated (Table.5-1).

Table 5-1: Mass balance of the spray dryer.

T_{g1} (°C)	Ms kg/h	W_{si} kg/kg dry solid	Ma kg/h	Y_2 kg/kg dry air	W_{so} kg/kg dry solid	Y_3 kg/kg dry air
161	2.28	4.0	226.9	0.017	0.119	0.056
180	1.21	4.0	227.3	0.018	0.111	0.038
206	1.01	4.0	227.3	0.019	0.083	0.036
255	0.93	4.0	227.8	0.021	0.075	0.037
160	4.26	2.3	226.9	0.017	0.190	0.056
181	2.20	2.3	227.3	0.018	0.093	0.039
203	1.64	2.3	227.3	0.019	0.056	0.035
250	1.45	2.3	227.8	0.021	0.053	0.035
160	7.00	1.5	226.9	0.017	0.181	0.057
184	3.64	1.5	227.3	0.018	0.129	0.040
202	2.27	1.5	227.3	0.019	0.099	0.033
252	2.07	1.5	227.8	0.021	0.075	0.034

5.3.2 Energy balance

In a continuous steady-state the various heat flows in and out of a dryer operation must be balance. The individual heat flows are:

Enthalpy flow of air entering dryer $= M_a Q_{ai}$
Enthalpy flow of feed liquid entering dryer $= M_s Q_{si}$
Enthalpy flow of air leaving dryer $= M_a Q_{ao}$
Enthalpy flow of product leaving dryer $= M_s Q_{so}$
Heat loss from the dryer $= Q_L$

Hence, the heat balance can be written

$$M_aQ_{ai} + M_sQ_{si} = M_aQ_{ao} + M_sQ_{so} + Q_L \qquad \text{Eq (5-4)}$$

Rearranging equation (5-4) in terms of heat loss (Q_L),

$$Q_L = M_a(Q_{ai} - Q_{ao}) + M_s(Q_{si} - Q_{so}) \qquad \text{Eq (5-5)}$$

The heat flows associated with each stream are based on following equations:

$$Q_{ai} = (c_g + c_{wv}Y_2)(T_{g2} - T_o) + h_{fg}Y_2 \qquad \text{Eq (5-6)}$$
$$Q_{ao} = (c_g + c_{wv}Y_3)(T_{g3} - T_o) + h_{fg}Y_3 \qquad \text{Eq (5-7)}$$
$$Q_{si} = c_p(T_{p1} - T_o) + W_{si}c_w(T_{g2} - T_o) \qquad \text{Eq (5-8)}$$
$$Q_{so} = c_p(T_{p2} - T_o) + W_{so}c_w(T_{g3} - T_o) \qquad \text{Eq (5-9)}$$

Specific heat of wet gas (J/kg K) $c_{wg} = c_g + c_{wv}Y_2$ Eq (5-10)

where, c_g = specific heat of gas = 1012 J/kg K
c_{wv} = specific heat of water vapour = 1914 J/kg K
c_p = specific heat of solid particles =2500 J/kg dry solid K
c_w = specific heat of water = 4185 J/kg K
h_{fg} = latent heat of vaporization of water at T_0 = 2502000 J/kg
T_0 = reference temperature=298 K

Substituting the experimental data from Trial 1 experiments into equations (5-1) to (5-10) gives mass and heat balance of the spray dryer as depicted in Table 5-2. Detailed calculations are given in *Appendix. A.*

Table 5-2: Mass and heat balance of the spray dryer.

T_{g2} °C	T_{g3} °C	**Ms** kg/h	**Ma** kg/h	Y_2 kg/kg dry air	Y_3 kg/kg dry air	T_{p2} K	W_{si} kg/kg dry solid	W_{so} kg/kg dry solid	Q_{ai} x10^5 J/kg dry air	Q_{ao} x10^5 J/kg dry air	Q_{si} x10^5 J/kg dry solid	Q_{so} x10^5 J/kg dry solid	Q_L x10^5 J/hr	Q_L x10^3 J/kg
161	60	2.28	226.9	0.017	0.056	331	4	0.119	2.10	2.06	3.85	1.74	13	5.7
180	80	1.21	227.3	0.018	0.038	332	4	0.111	2.32	1.83	3.85	1.75	115	51
206	100	1.01	227.3	0.019	0.036	338	4	0.083	2.63	1.99	3.85	1.85	148	65
255	120	0.93	227.8	0.021	0.037	347	4	0.075	3.21	2.23	3.85	2.08	226	99
160	60	4.26	226.9	0.017	0.056	325	2.3	0.190	2.09	2.08	2.43	1.71	4.5	2
181	80	2.20	227.3	0.018	0.039	334	2.3	0.093	2.33	1.84	2.43	1.76	113	50
203	100	1.64	227.3	0.019	0.035	350	2.3	0.056	2.59	1.95	2.43	2.11	147	65
250	120	1.45	227.8	0.021	0.035	355	2.3	0.053	3.15	2.18	2.43	2.23	223	98
160	60	7.00	226.9	0.017	0.057	326.5	1.5	0.181	2.09	2.11	1.76	1.71	-4.4	-2
184	80	3.64	227.3	0.018	0.040	331	1.5	0.129	2.37	1.86	1.76	1.76	115	51
202	100	2.27	227.3	0.019	0.033	334	1.5	0.099	2.58	1.89	1.76	1.78	157	69
252	120	2.07	227.8	0.021	0.034	346	1.5	0.075	3.18	2.14	1.76	2.05	235	103

5.4 Estimation of particle drying parameters

The spray-dryer experimental set up and operating procedure has already been described in Chapter 3, section 3.2. Four different outlet temperatures of 60°C, 80°C, 100°C and 120°C were used for each feed concentration (20%, 30% and 40%). The inlet temperature was generally set 100°C higher than the outlet temperature as this approximately corresponds to a constant evaporation capacity of the gas. The exception was the 120°C outlet temperature which could not be achieved with an inlet temperature of 220°C and so an inlet temperature of 250°C was used instead. This is due to much greater heat losses at 120°C, estimated at 100 kJ/kg dry air based on a heat balance, compared with a heat loss of only 50 kJ/kg for an outlet temperature of 80°C (see calculations presented in section 5.3 and Table 5-2). The measured liquid feed flow rates and inlet and outlet air temperatures are given in the Table (5-3). The mean gas residence time was calculated based on a dryer volume of 1.714 m^3.

Three experiments were then repeated twice each in two separate trials (Trial 2 and Trial 3) using all three concentrations at an outlet temperature of 80°C to assess the reproducibility and repeatability of results. However, these additional trials were performed with a different batch of whey feed material to Trial 1. This may affect results as milk composition varies throughout the dairying season, which can leads to different WPI properties (Oldfield *et al.*, 2005). The full set of experimental operating conditions and results are presented in Table (5-3). The results for each measurement variable will be discussed in the following subsections.

Table 5-3: Experimental conditions used in the spray drying experiments (*Trial 2 and ** Trial 3 - same conditions of first trial, but with different batch of feed material).

Feed concentration (w/v)	Inlet air temp. (°C)	Outlet air temp. (°C)	Liquid feed rate (kg/h)	Residence time (s)
20%	161±0.2	60±0.9	11.4	26
	180±1.6	80±0.4	6.1	24
	180±0.2*	80±0.5	6.8	24
	180±0.5**	80±1.0	6.3	24
	206±0.3	100±0.2	5.1	23
	255±1.0	120±1.0	4.7	21
30%	160±0.9	60±0.6	14.7	26
	181±0.9	80±0.5	7.3	24
	180±1.0*	80±0.4	8.5	24
	180±0.2**	80±0.5	8.9	24
	203±0.8	100±0.9	5.4	23
	250±0.5	120±0.5	4.8	21
40%	160±0.4	60±0.4	17.5	26
	184±0.6	80±1.0	9.1	24
	180±0.1*	80±0.5	10.1	24
	180±0.1**	80±0.4	9.7	24
	202±0.5	100±0.8	5.7	23
	252±1.5	120±1.0	5.2	21

5.4.1 Estimation of wet-bulb and outlet particle temperatures

For trial 1 experiments, gas flow rate, wet-bulb temperature and estimated outlet particle temperature quantities were calculated using inlet air (post burner) humidities of 0.017, 0.018, 0.019 and 0.021 kg/kg for inlet air temperatures of 160°C, 180°C, 200°C and 250°C respectively, based upon the underlying ambient room humidity and the calculated humidity increase arising from the water combustion product in the gas air heater. A slight increase in these values (by 0.0028 kg/kg) was obtained for Trials 2 and 3 due to a slightly higher ambient room humidity. The outlet gas humidity and heat loss were estimated from overall mass and energy balances on the dryer (see section 5.3.). The wet bulb temperatures were read from the wet-bulb lines corresponding to the inlet gas conditions (see figure 5-3).

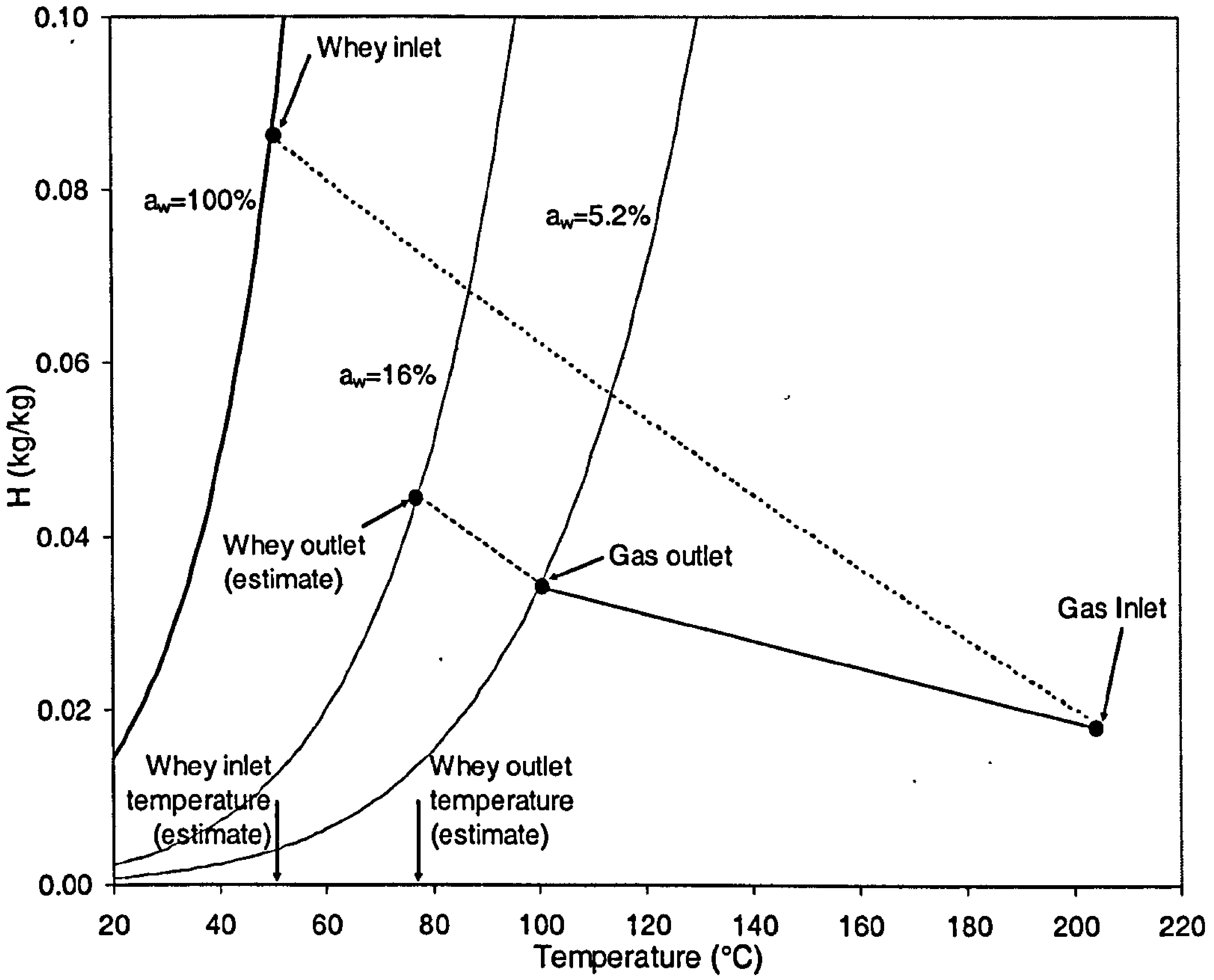

Figure 5-3: Psychrometric chart showing typical gas and particle inlet and outlet conditions. The wet bulb temperature is constant along the dotted lines. Curved lines of constant water activity, a_w, are also shown: 5.2% corresponds to the relative humidity of the outlet gas, and 16% is the equilibrium relative humidity corresponding to the whey product bulk moisture content.

The outlet particle temperatures were calculated from wet-bulb line, which can be explained as follows:

Mass transfer rate from particle = $-m^{\bullet} = k_c A_p (Y_s^{\bullet} - Y_{air})$ Eq (5-11)

Heat transfer rate from particle = $-h_{fg} m^{\bullet} = h A_p (T_{air} - T_p)$ Eq (5-12) where, k_c is the mass transfer coefficient (m/s), h is the heat transfer coefficient (W/m^2 K) and Y_s* is the water activity at surface of the particles.

Combining the equations (5-11) and (5-12) gives

$$hA_p(T_{air} - T_p) = k_c A_p h_{fg} (Y_s^* - Y_{air}) \qquad \text{Eq (5-13)}$$

Hence, wet-bulb line is, $Y_s^* - Y_{air} = \frac{h}{h_{fg} k_c}(T_{air} - T_p)$ Eq (5-14)

The outlet particle temperatures were estimated by following the wet-bulb lines from the gas outlet conditions to the relative humidity line corresponding to an estimate of the water activity (equilibrium relative humidity), a_w, on the surface of the whey powder product. The latter was determined from the moisture sorption isotherm of WPI powder (figure 5-4) at 50°C reported by Foster *et al.* (2005) using the measured product moisture content.

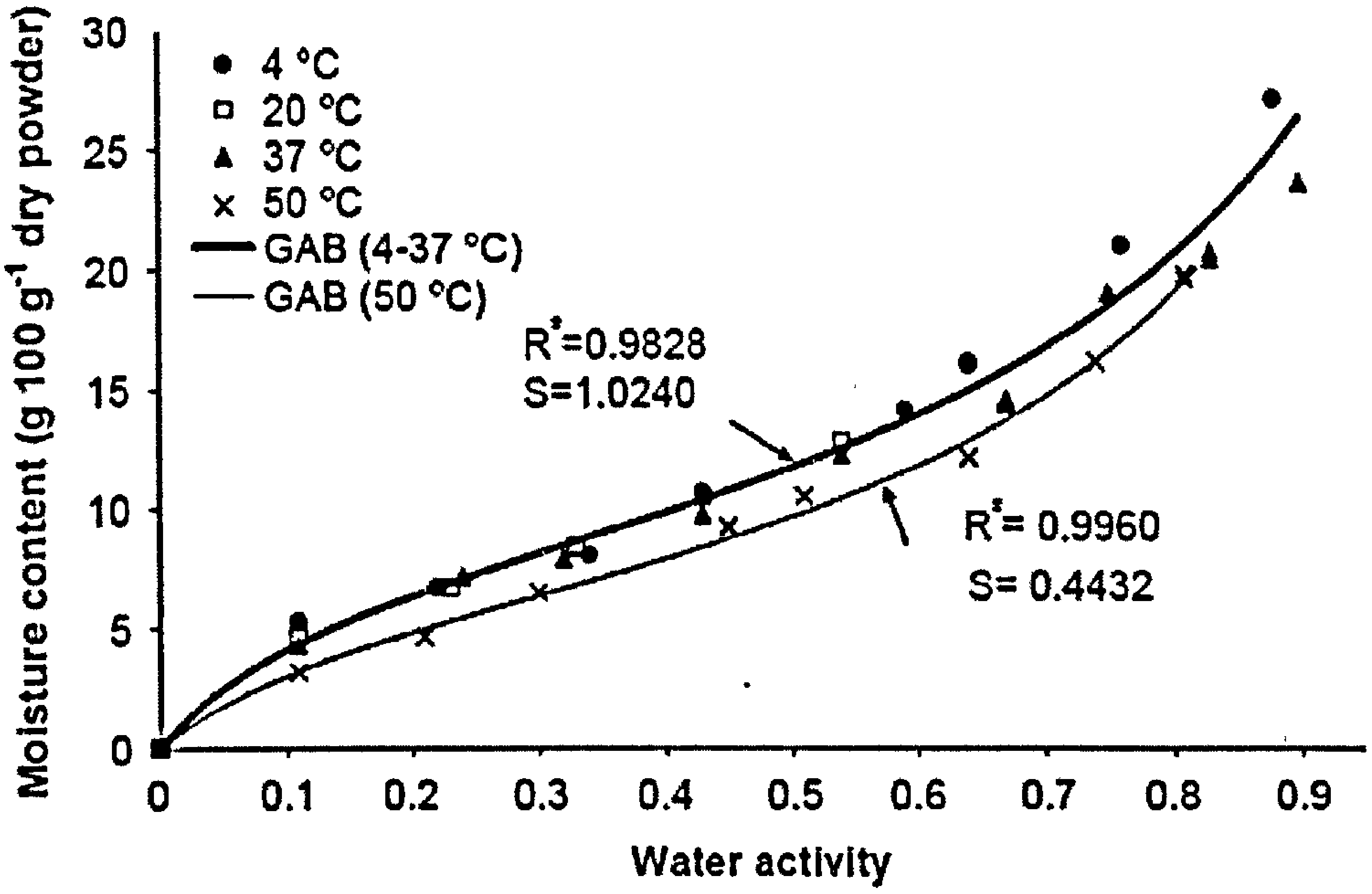

Figure 5-4: Moisture sorption isotherm of a WPI powder (Guggenheim–Anderson–De Boer (GAB) sorption isotherm model data) (Foster *et al.*, 2005).

This is only an approximate method to find the outlet particle temperature as it assumes that (i) the WPI used in this study has a similar desorption isotherm, (ii) there is no significant effect of temperature, and (iii) the measured moisture content is representative of the surface moisture content as the particles exit the spray dryer. In practice, the surface moisture content will almost always be lower than the average moisture content and thus the estimated particle outlet temperatures are lower bound estimates. Finally the equilibrium moisture contents of the particles corresponding to the relative humidity of the outlet gas were estimated using the same isotherm. The above quantities and calculation method (shown for 30% feed concentration at 100°C outlet temperature) are illustrated on a schematic of a psychrometric chart in figure (5-3) (based on ASAE data). The full psychrometric chart is shown in Appendix-B.

Table (5-4) shows various calculated quantities such as gas flow rate, wet-bulb temperature and estimated outlet particle temperature, equilibrium moisture content, bulk moisture content, which are useful to help understand and interpret the results.

Table 5.4: Spray drying operating conditions and various calculated quantities (* Trial 2 and ** Trial 3 - same conditions of first trial, but with different batch of feed material).

Feed Conc. (w/v)	Inlet conditions		Outlet conditions				
	Inlet air temp. (°C)	**Wet-bulb temp. (°C)**	**Outlet air Temp. (°C)**	**Outlet particle temp. (°C)**	**RH %**	**Equilibrium moisture content (%)**	**Average bulk moisture content (%)**
20%	161±0.2	44.5	60±0.9	58.5	44.0	10.5	10.6
	180±1.6	46.0	80±0.4	65.0	30.9	4.8	10.0
	180±0.2*	48.0	80±0.5*	68.1	32.0	8.2	8.1
	180±0.5**	48.0	80±1.0**	80.0	19.0	6.2	6.2
	206±0.3	51.0	100±0.2	72.5	30.0	2.6	7.7
	255±1.0	52.5	120±1.0	80.0	24.0	2.0	7.0
30%	160±0.9	44.5	60±0.6	52.5	67.5	10.0	16.0
	181±0.9	46.5	80±0.5	69.0	34.0	5.0	8.5
	180±1.0*	48.0	80±0.4*	77.0	22.0	6.9	6.9
	180±0.2**	48.0	80±0.5**	81.0	18.0	5.8	5.8
	203±0.8	51.0	100±0.9	87.5	16.0	2.5	5.3
	250±0.5	52.5	120±5.0	94.5	15.0	1.9	5.0
40%	160±0.4	44.6	60±0.4	53.0	65.0	10.5	15.3
	184±0.6	48.0	80±1.0	61.5	50.0	5.1	11.4
	180±0.1*	48.0	80±0.5*	70.0	49.0	11.2	11.2
	180±0.1**	48.0	80±0.4**	69.0	31.0	8.5	8.4
	202±0.5	50.0	100±0.8	69.5	37.5	2.5	9.0
	252±1.5	53.5	120±1.0	83.5	24.0	1.8	7.0

5.5 Effect on moisture content

The average bulk moisture contents (kg water/kg total) of the product powders are given in Table (5-4). The results of Trial 2 and Trial 3 show similar trends to Trial 1; the average standard deviation for the repeated results is 1.6%, which may be attributed to variations is spray dryer set-up (particularly in sealing the chamber) and differences in the WPI batches for Trial 1 and Trials 2 and 3. The moisture content values are plotted in figure (5-5), which reveals that increasing the outlet gas temperature (and inlet temperature) reduces the moisture content of the final products for all feed concentrations.

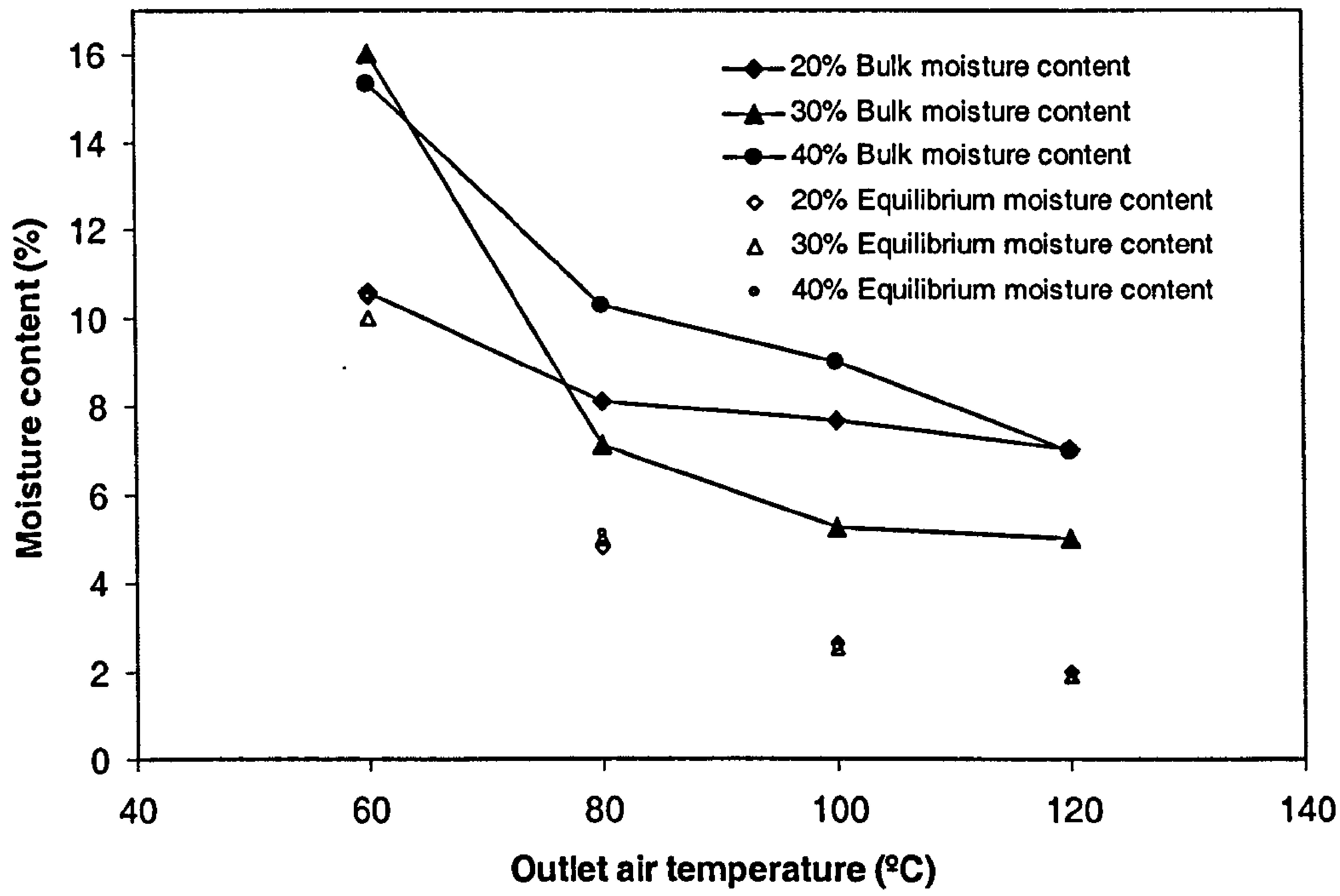

Figure 5-5: Effect of spray dryer outlet air temperature on the bulk and equilibrium moisture content of the spray dried product (average values of Trials 1, 2 and 3 are given for 80°C; the averaged standard deviations for the repeated runs was 1.6 %).

Higher outlet and inlet gas temperatures provide a greater driving force for heat and mass transfer from the particles, which yields a drier product material. This can be also be seen in the lower equilibrium moisture contents calculated from the outlet gas humidity. Thus the predominant effect shown in figure (5-5) is of changing the gas outlet temperature; the same trend was shown in other published reports (Samborska *et al.*, 2005; Etzel *et al.*, 1996). In these experiments, the gas mass flow rate was almost constant. Due to differences in gas density with temperature this resulted in slightly different volumetric flows and so the gas mean residence time for drying of the particles varied between 21-25 s over all experiments (Table 5-3). Thus gas mean residence time differences are only minor.

A secondary effect in figure (5-5) is due to changes in the feed concentration. One might expect that the feeds with the highest solids content would produce the driest product, as less moisture removal is required. However, the reverse appears to be true. Although the effect is small and comparable to the error in the repeatability experiments, it is consistently observed. This suggests that the drying of the 40% feed concentration solutions may somehow be impeded and the 20% feed concentrations yields higher moisture content than 30% feed concentration (except 60°C outlet temperature) because of higher water content in the feed. This could occur if the crust formed dries to such an extent that water vapour diffusion is hampered by a severe reduction in diffusivity at 40% feed concentration. Although the lower bound (equilibrium) estimates of the surface moisture content (also shown in figure 5-5) are similar for different feed concentrations at the same temperature it could reasonably be suggested that that the difference between surface moisture content and bulk moisture content (highest for the 40% feed concentration) could also be a good indicator of crust formation.

5.6 Effect on particle size

The Sauter mean particle diameters of all the spray dried powders are in the range of 8.5 to 19.9 μm (Table 5-5). The largest diameter are all found for the case where the feed concentration is 20% and at higher outlet temperatures (figures 5-6, 5-7, 5-8 and 5-9) for all three feed concentrations.

Table 5-5: Effect of spray dryer outlet temperature and feed concentration on the particle size.

	20 % Feed concentration	**30 % Feed concentration**	**40 %Feed Concentration**
Outlet gas temperature (°C)	Mean particle size (µm)	Mean particle size (µm)	Mean particle size (µm)
60	15.2	10.9	9.1
80	16.0	9.0	9.9
100	19.9	12.0	8.5
120	17.5	14.6	10.8

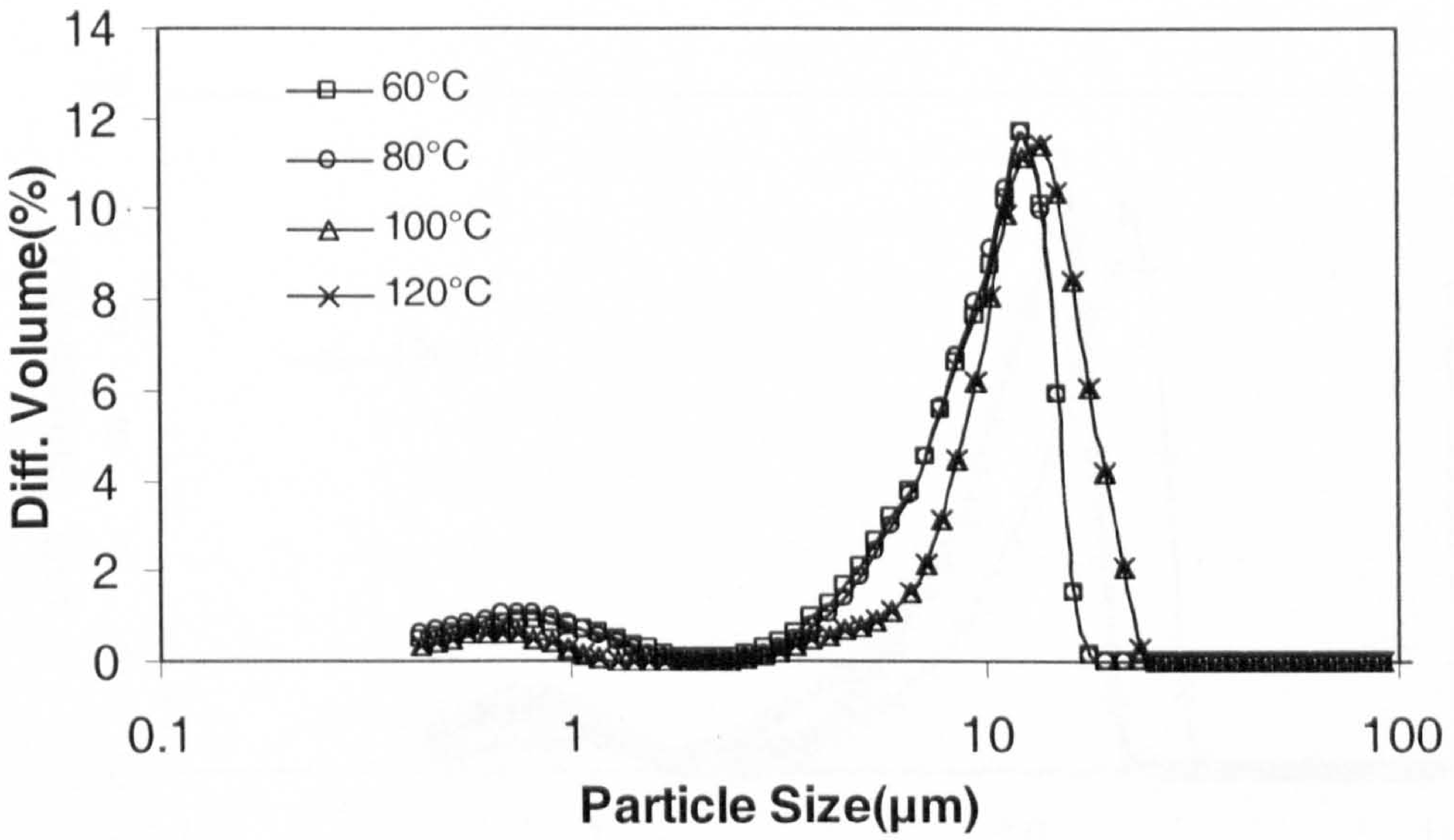

Figure 5-6: Effect of spray dryer outlet temperature and 20% (w/v) feed concentration on the particle size.

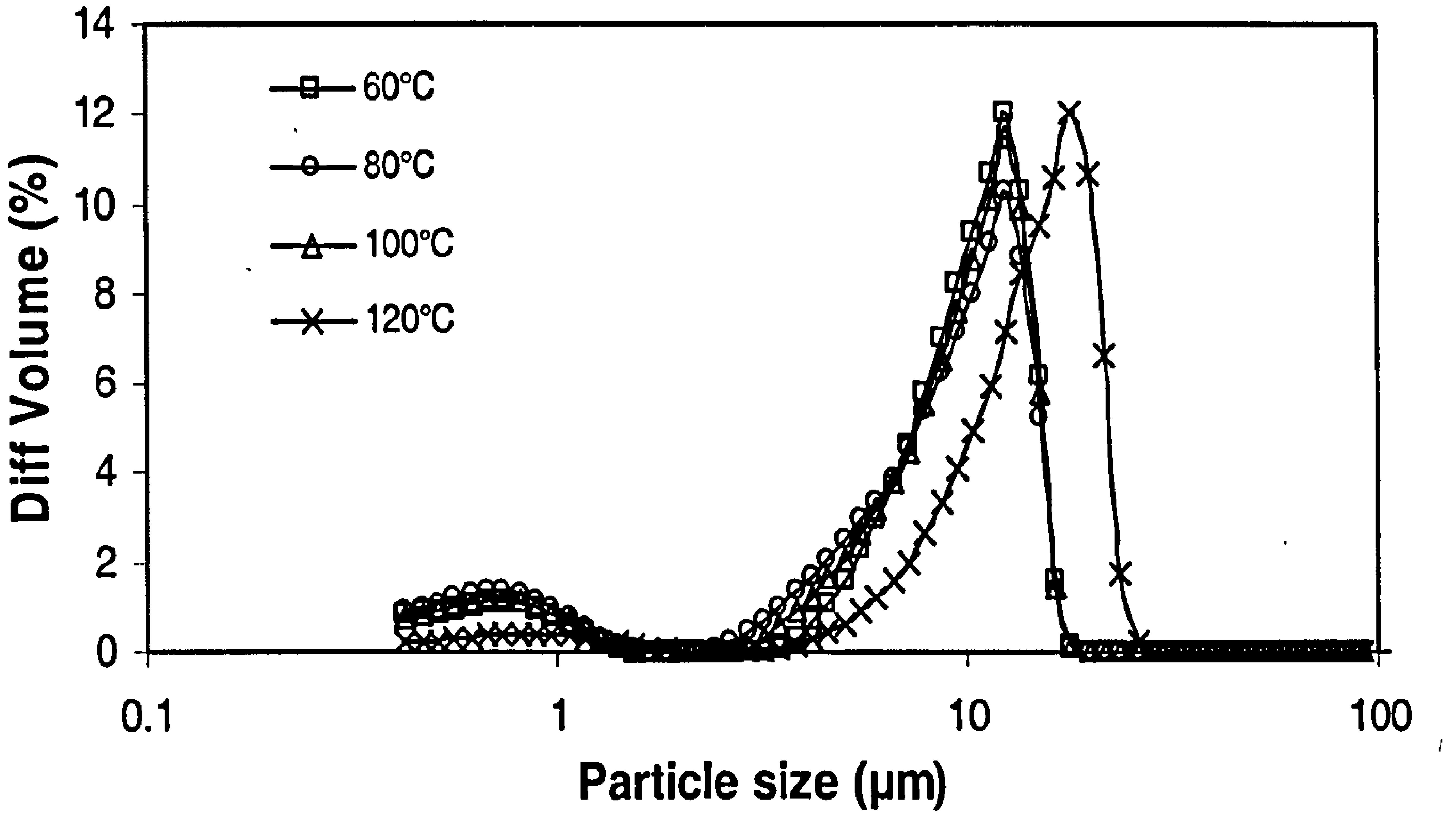

Figure 5-7: Effect of spray dryer outlet temperature and 30% (w/v) feed concentration on the particle size.

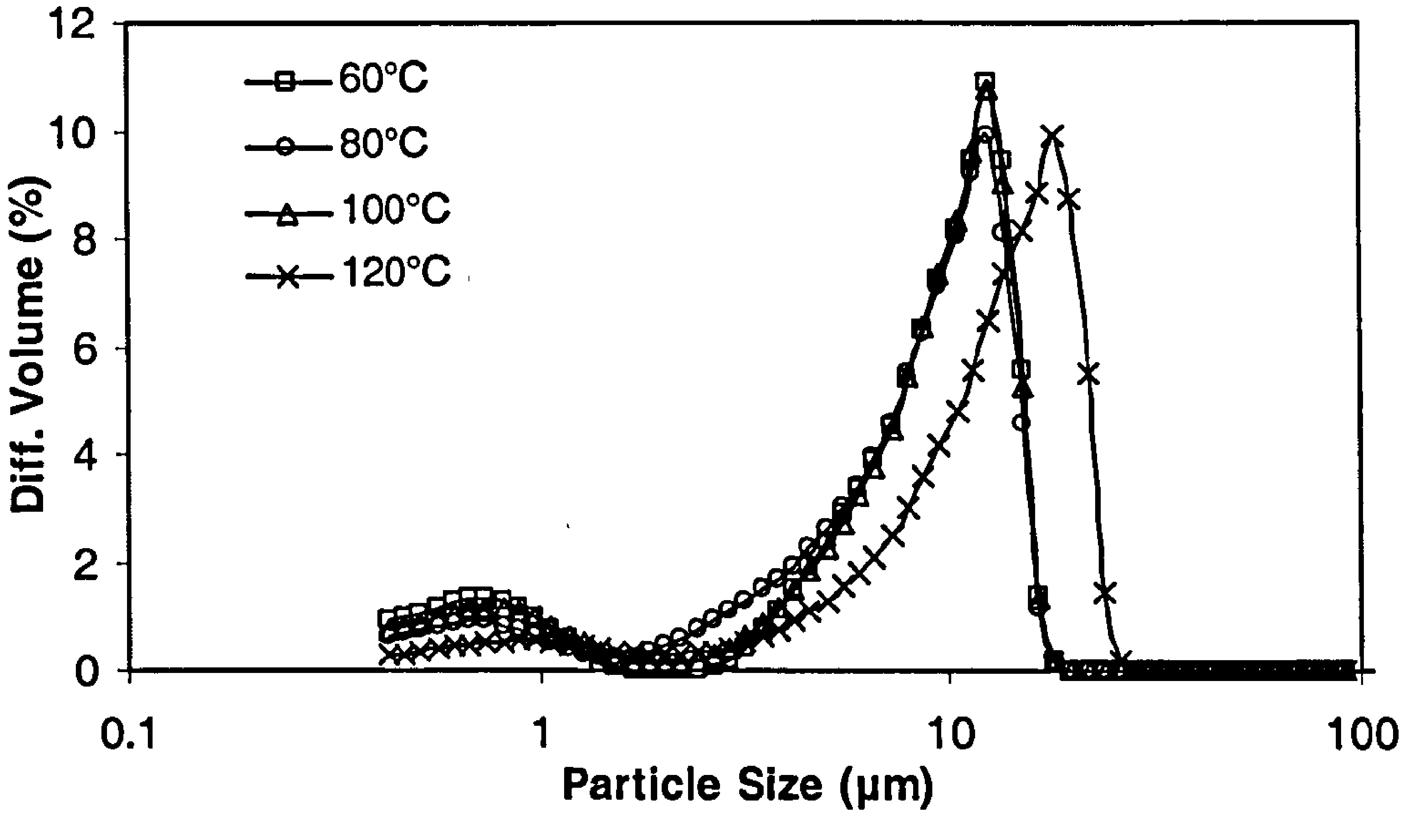

Figure 5-8: Effect of spray dryer outlet temperature and 40% (w/v) feed concentration on the particle size.

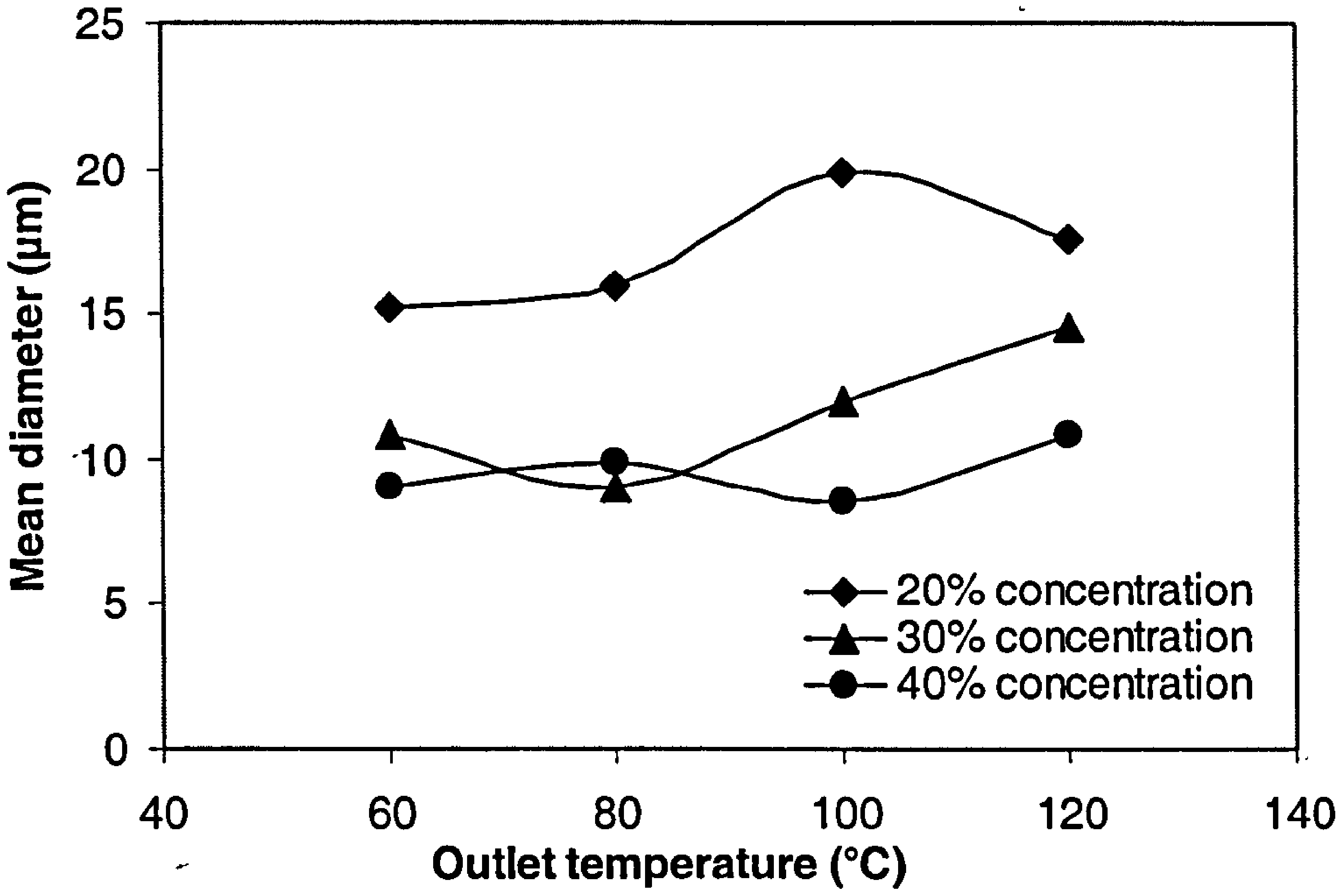

Figure 5-9: Effect of spray dryer outlet temperature and feed concentration on the particle size (Sauter mean diameter).

The variation in mean diameter may be due to two effects: (i) higher liquid feed rates for higher feed concentration (or viscosity) may cause smaller particle sizes due to finer atomisation (Master,1991; Stahl *et al.*, 2002), and/or (ii) bubble inflation of particles may take place (Etzel *el al.*, 1996). There is little evidence to suggest that liquid feed rate is responsible, as large changes in feed rate do not appear to drastically affect particle size. However, there is a possibility that bubble inflation may be more prevalent with a 20% feed concentration, as there is more water available to evaporate and also the surface may be soft enough to allow the particle to expand. If the partial pressure of moisture vapour at the droplet centre exceeded ambient pressure, the bubble volume increases (Etzel *et al.*,1996). In the case of higher outlet temperatures, a crust is believed to forms and the impermeable crust restricts the particle expansion due to bubble inflation and thus results in higher moisture content with irregular shape particles. A schematic model diagram (figure 2-6) of bubble inflation is discussed in section (2.2.5).

5.7 Effect on powder morphology

Micrographs obtained from the scanning electron microscopes are displayed in figures (5-10, 5-11 and 5-12), which shows the smooth skin-forming behaviour, which is typical of whey and skimmed milk products (Sheu and Rosenberg,1998; Al-Hakim and Stapley, 2004).

The micrographs of spray dried particles suggest a wide distribution of particle size, with apparently a low degree of particle aggregation for all the feed concentrations and outlet temperatures. In general, but with the exception of high feed concentrations and high temperatures, the dried particles are spherical in shape. However, at the lowest temperatures (60-80°C) some particles appear to have caved-in. As the outlet temperature increases (100-120°C) the 20% and 30% concentrations maintain a spherical shape whereas the 40% concentrations show irregularly shaped particles at higher outlet temperature due to strong crust (explained in the figure 5-32) and shown in figures 5-12 d and f.

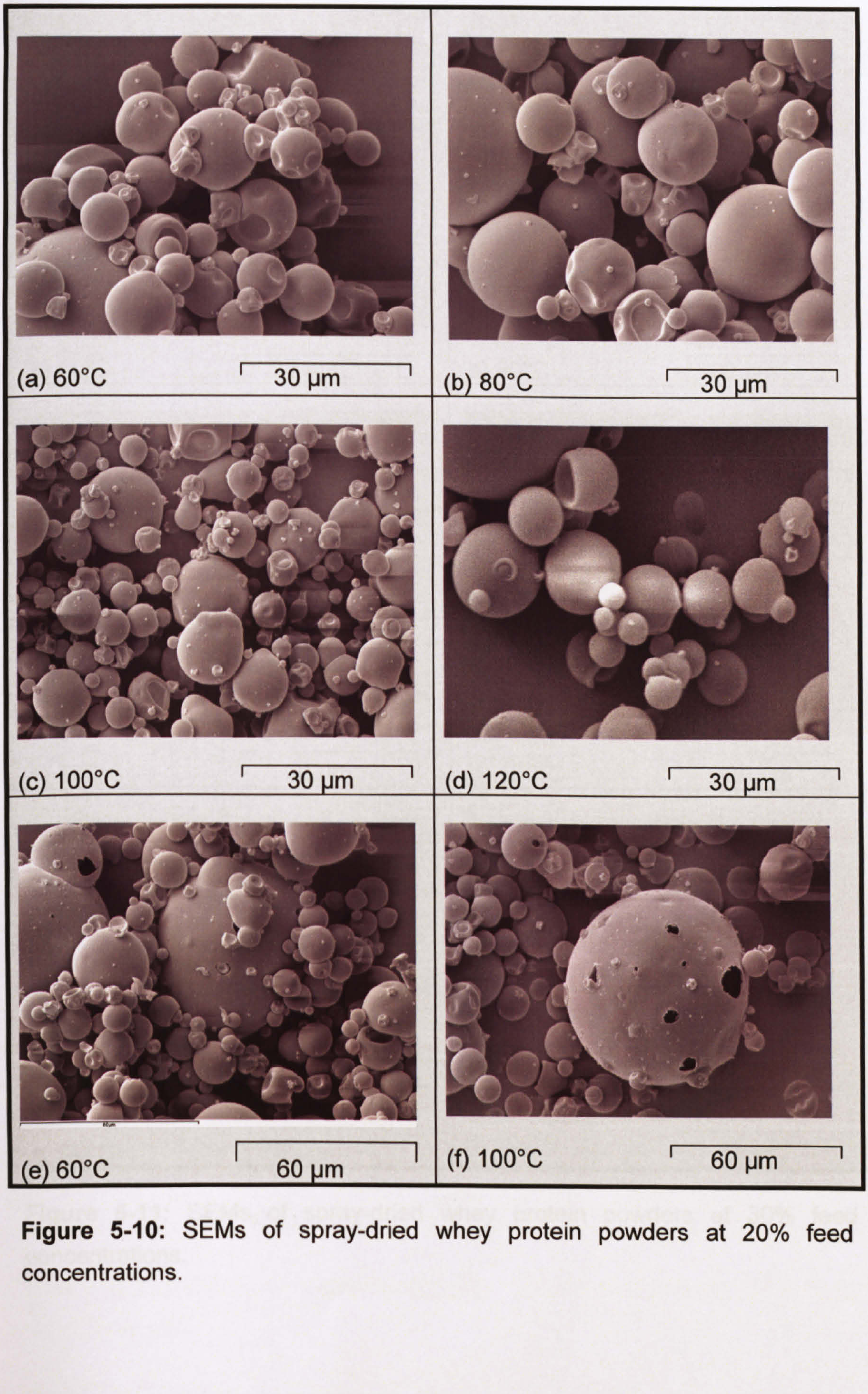

Figure 5-10: SEMs of spray-dried whey protein powders at 20% feed concentrations.

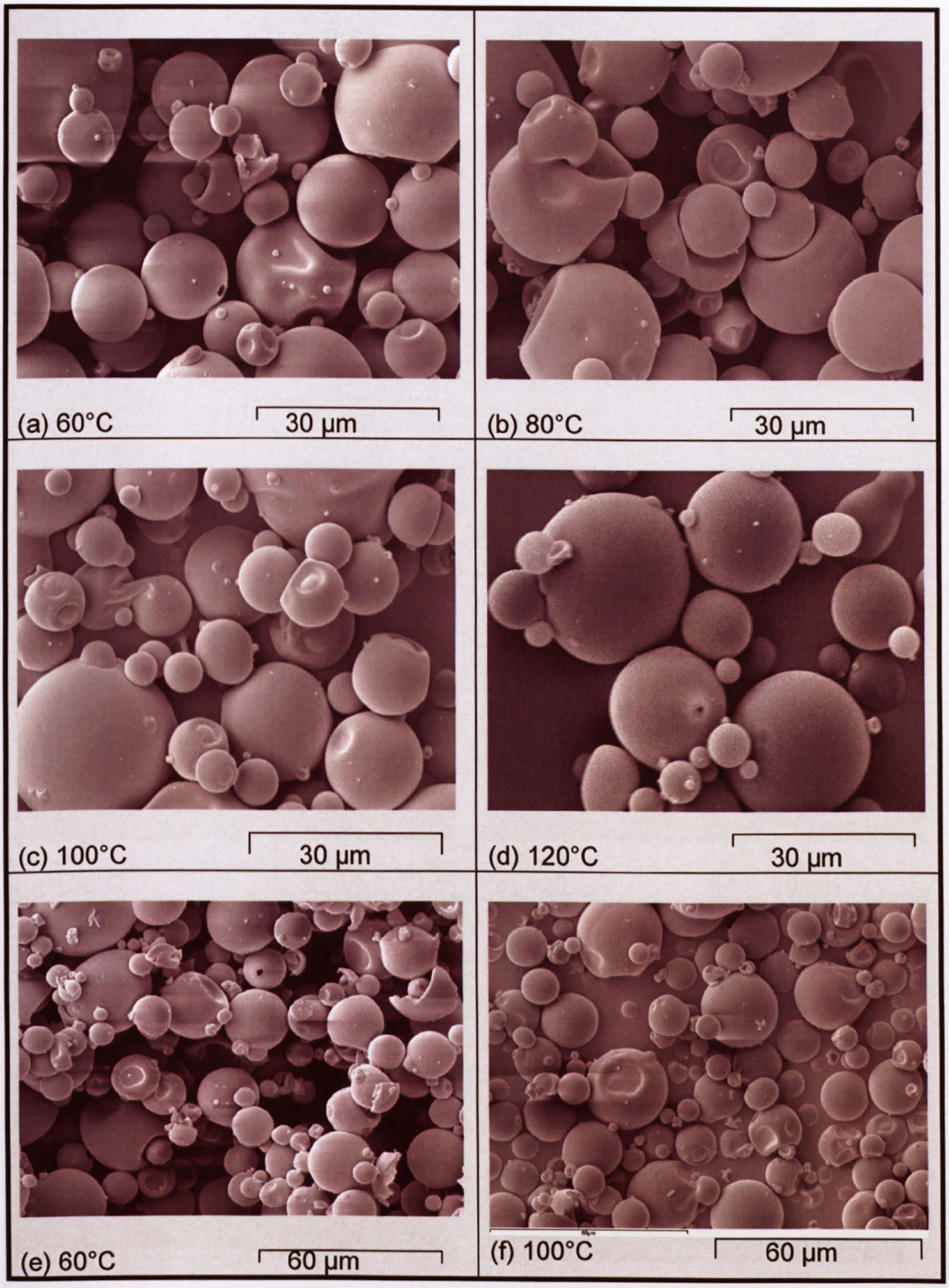

Figure 5-11: SEMs of spray-dried whey protein powders at 30% feed concentrations.

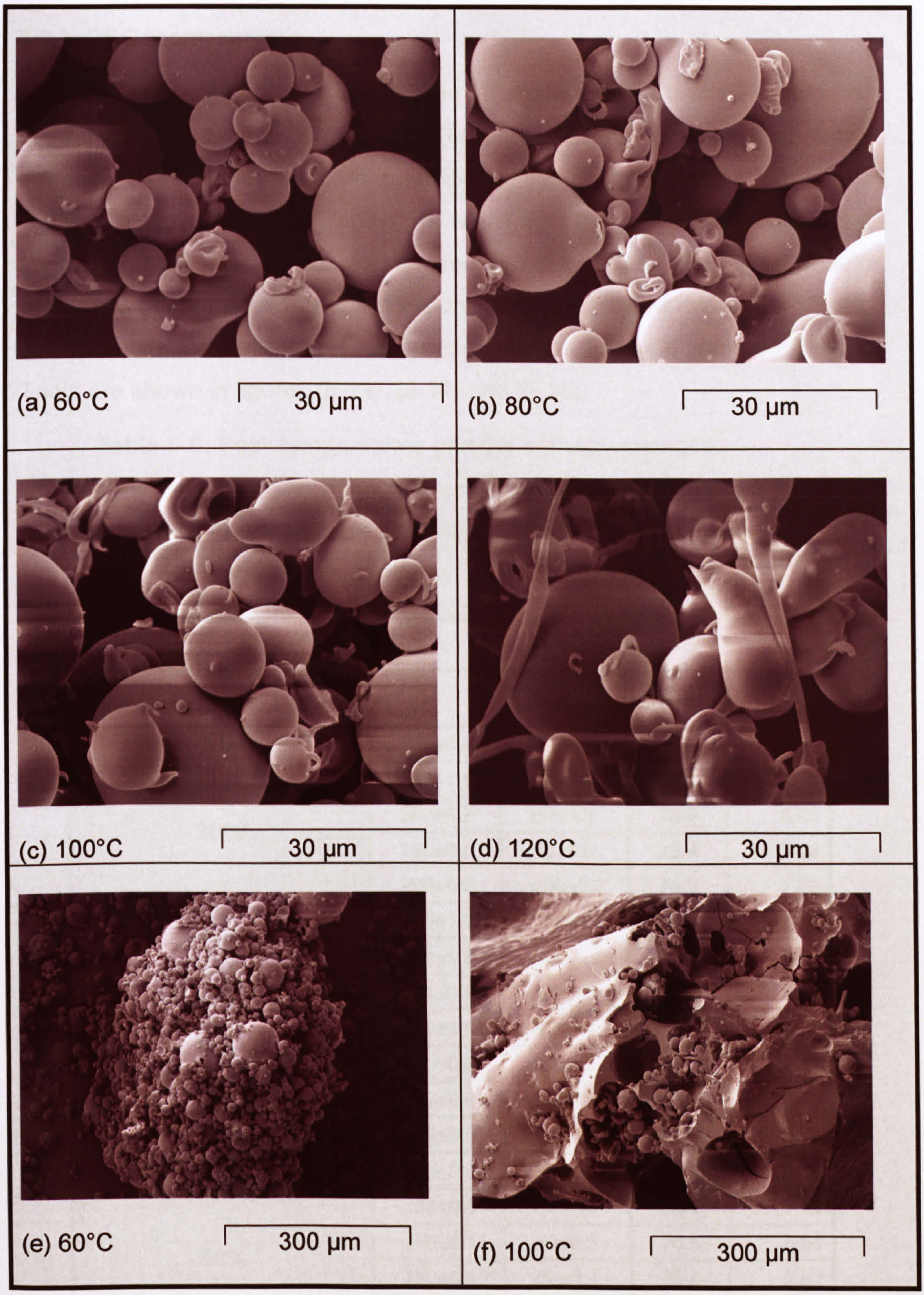
(a) 60°C

(b) 80°C

(c) 100°C

(d) 120°C

(e) 60°C

(f) 100°C

Figure 5-12: SEMs of spray-dried whey protein powders at 40% feed concentrations.

5.8 Effect on thermal denaturation of proteins

5.8.1 DSC thermograms

The DSC analysis performs further thermal processing on a small quantity of dried material resulting in denaturation of any remaining native proteins within the sample, as the temperature is ramped upwards (the analytical procedure is given in section 4.3.2.1). Table (5-6) represents the peak temperatures and the enthalpy changes for thermal denaturation of the spray dried whey protein product, as determined from the DSC thermogram. The repeated Trial 2 and Trial 3 results also reflect the Trial 1 observations. The DSC thermograms for Trial1 are shown in figures (5-13), (5-14) and (5-15).

Table 5-6: Peak temperatures and the enthalpy changes.

Feed concentration (w/v)	**Inlet air temp. (°C)**	**Outlet air temp. (°C)**	**T_d (°C)**	**ΔH (J/g)**
WPI (untreated)-Trial 1	–	–	74.5	13.67
WPI (untreated)-Trials 2 &3			75.1	11.01
20%	161±0.2	60±0.9	75.6	8.72
	180±1.6	80±0.4	75.2	10.12
	180±0.2*	80±0.5	75.6	8.26
	180±0.5**	80±1.0	75.4	7.62
	206±0.3	100±0.2	76.2	7.23
	255±1.0	120±1.0	76.8	2.89
30%	160±0.9	60±0.6	75.1	8.84
	181±0.9	80±0.5	74.9	9.12
	180±1.0*	80±0.4	75.7	7.72
	180±0.2**	80±0.5	75.7	7.22
	203±0.8	100±0.9	75.8	7.18
	250±0.5	120±0.5	76.8	3.36
40%	160±0.4	60±0.4	75.8	8.13
	184±0.6	80±1.0	75.2	7.91
	180±0.1*	80±0.5	75.5	6.64
	180±0.1**	80±0.4	75.5	6.47
	202±0.5	100±0.8	76.7	5.03
	252±1.5	120±1.0	79.3	0.76

All the DSC thermograms showed two transition with peak temperatures (T_d) in the range of 62-66°C and 74-80°C respectively. The mid point peak temperature is given in Table (5-6). The untreated WPI solution also showed the same thermal transitions at 65 and 74.5°C, which agreed with the results presented by Ibanoglu, (2005).

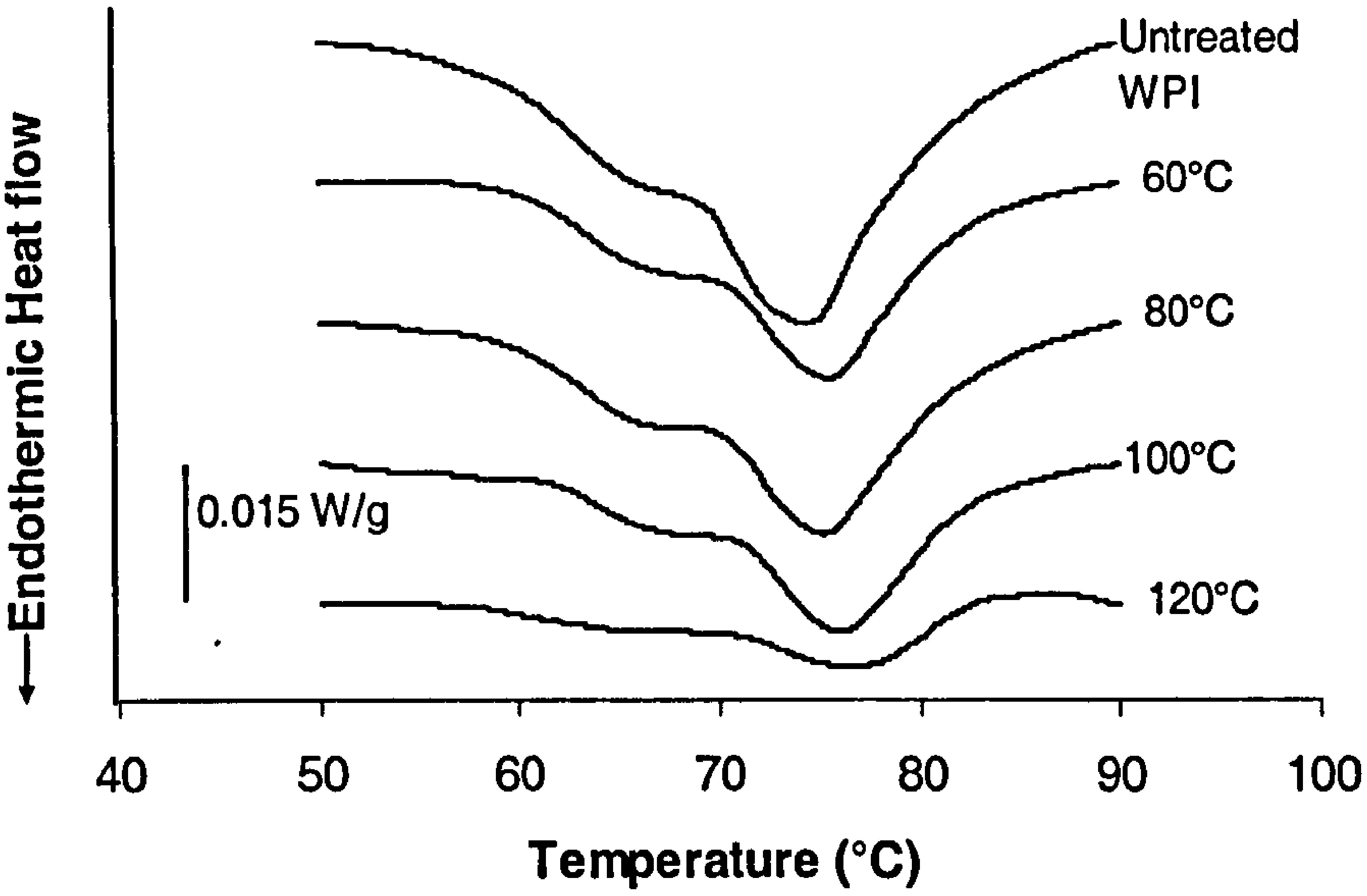

Figure 5-13: DSC thermogram of spray dried whey protein (20% w/v concentration) after spray drying with different outlet temperatures.

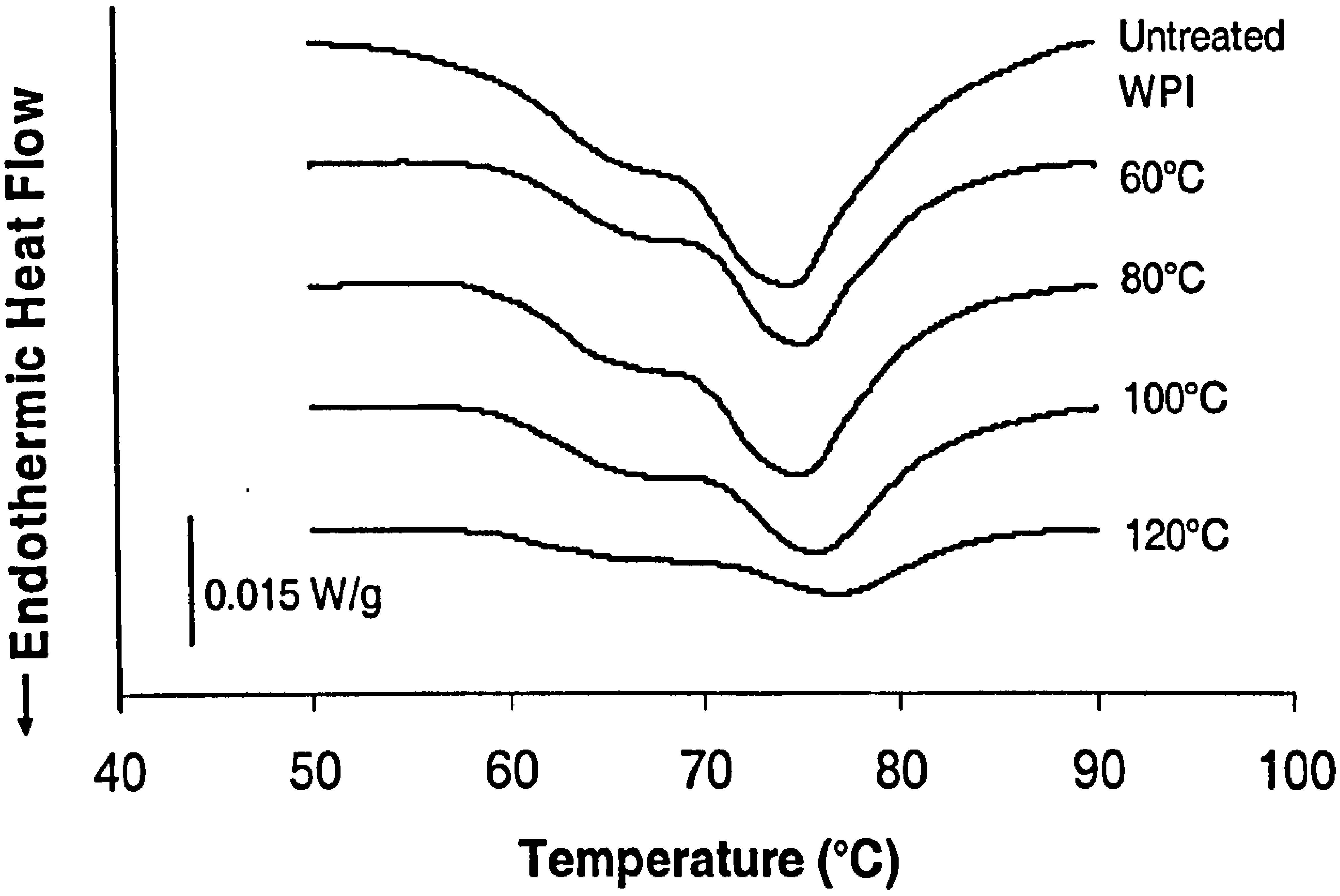

Figure 5-14: DSC thermogram of spray dried whey protein (30% w/v concentration) after spray drying with different outlet temperatures.

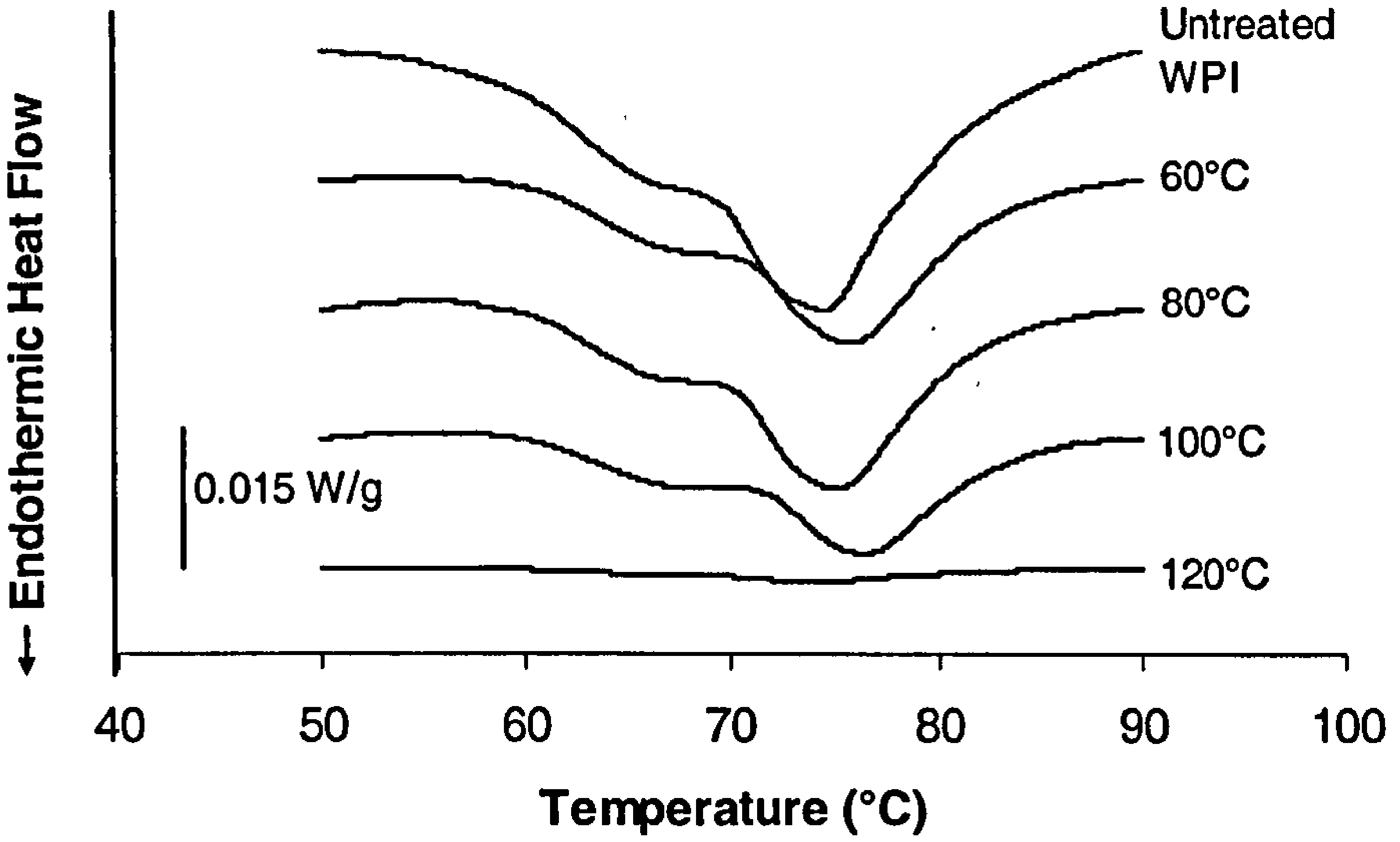

Figure 5-15: DSC thermogram of spray dried whey protein (40% w/v concentration) after spray drying with different outlet temperatures.

5.8.2 Denaturation Enthalpy

The percentage variation of denaturation of the spray dried powders with spray drying conditions are shown in figure (5-16).

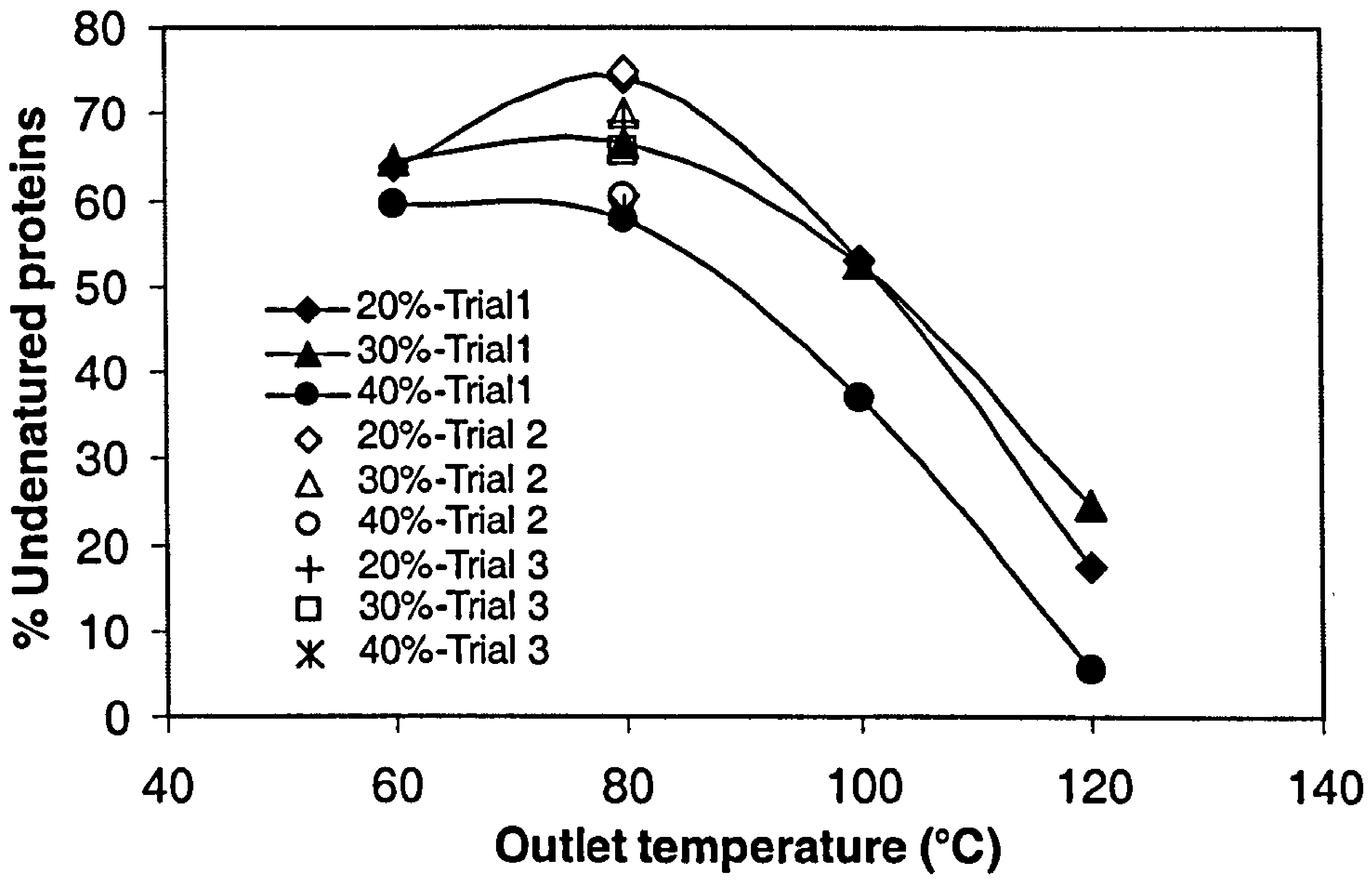

Figure 5-16: Effect of spray dryer outlet temperature and feed concentration on the denaturation of the spray dried product as determined by DSC.

Figure (5-16) indicates the amount of undenatured protein that remain in the spray dried product. At the highest outlet temperatures (100 °C and 120 °C) and the maximum feed concentration (40%) the denaturation enthalpy, ΔH, is the lowest, which indicates that only a small amount of undenatured proteins are present in the spray dried product, *i.e.* the spray drying operation has resulted in a significant amount of denaturation. Comparison of the ΔH values for these conditions with the peak enthalpy for the untreated WPI reveals that more than 70% of the proteins in the feed have been denatured during spray drying. Higher enthalpy values corresponding to reduced product denaturation are observed at outlet temperatures of 60°C and 80°C, which is consistent with Oldfield *et al.*'s (2005) findings. The results in figure (5-16) also show that the 20% and 30% feed solutions at an outlet temperature of 80°C gave the least denaturation compared to that of the untreated WPI, *i.e.* only about 30% of the feed proteins have been denatured.

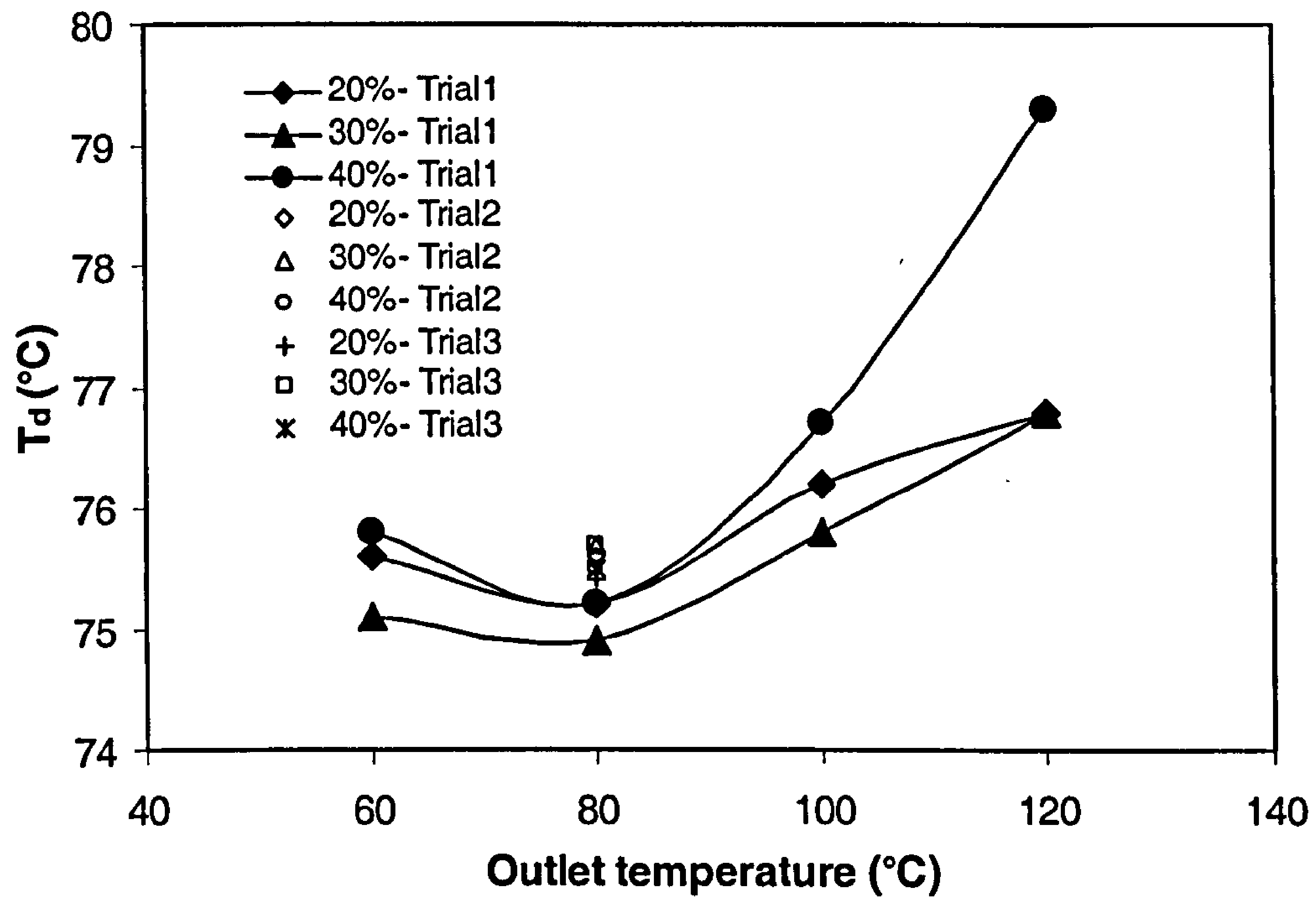

Figure 5-17: Effect of spray dryer outlet temperature and feed concentration on the peak temperature (T_d) for protein denaturation recorded in subsequent DSC experiments.

For spray drying gas outlet temperatures of 60°C and 80°C and all feed concentrations, the transition temperatures (T_d) for protein denaturation were in the range 74.9 to 75.8°C, which is constant within the experimental error. Trial 2 and Trial 3 also exhibited the same range of peak temperatures (see Table 5-6). However, an increase in the gas outlet temperature from 80°C to 120°C results in a small increase in the transition temperature of proteins in the range of 75.8 to 79.3°C (figure 5-17), indicating that the remaining undenatured proteins from higher outlet temperature runs show slightly greater thermal stability.

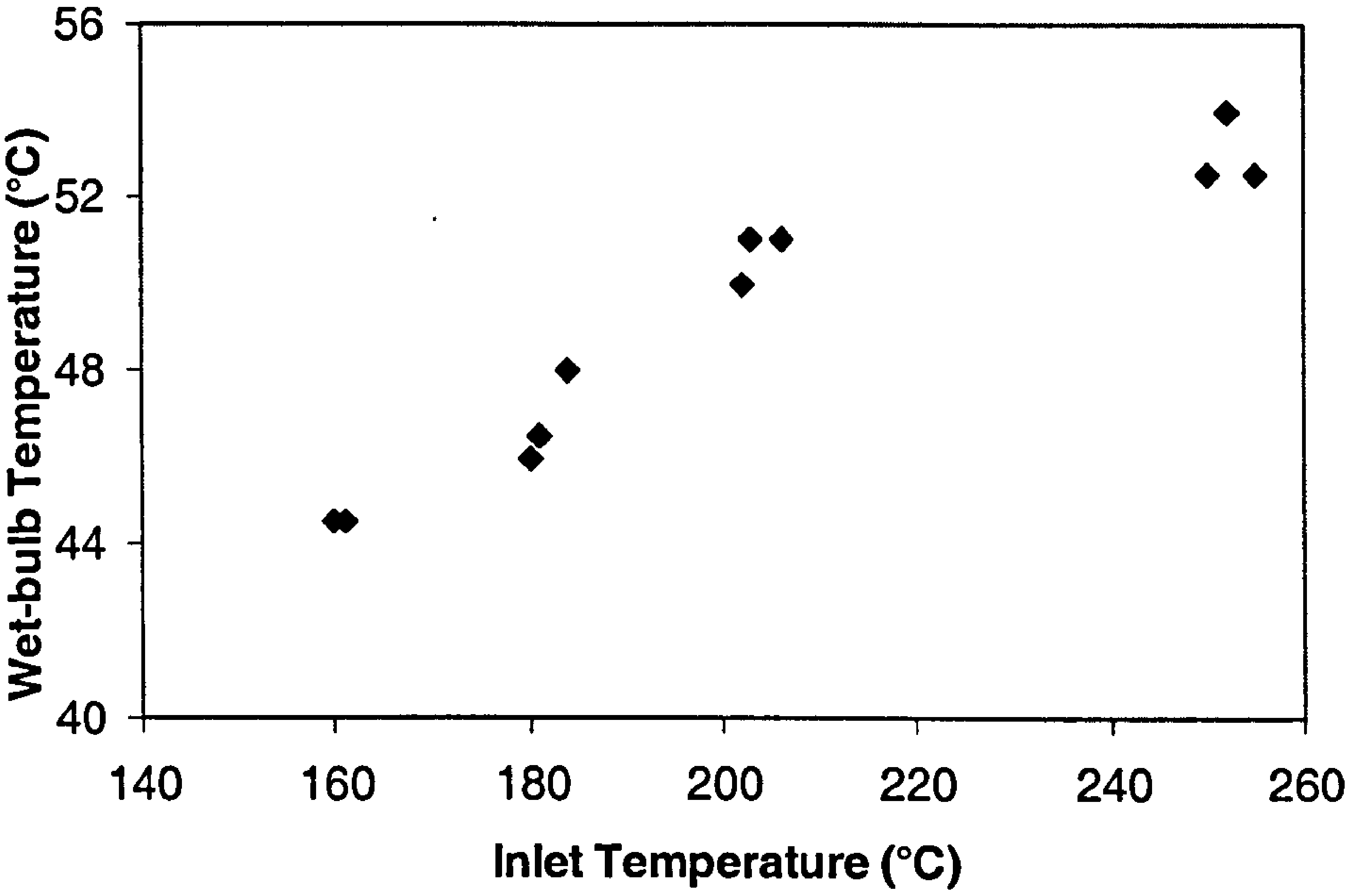

Figure 5-18: Effect of spray dryer inlet temperature on the wet-bulb temperature of the gas.

After atomisation, the liquid droplets contact the inlet hot air and water evaporation takes place rapidly from the droplet surface, cooling the droplets to their wet bulb temperature, as well cooling the surrounding hot air (Oldfield *et al.*, 2005). Figure (5-18) reveals that the wet-bulb temperatures (44-54°C) are below the temperatures generally required for denaturation as determined by DSC (i.e. 75°C). It is likely that most denaturation occurs later on, as the particle temperature approaches the gas outlet temperature. Hence, these later stages controls the final product quality (Maio *et al.*, 2004) and thus the gas outlet temperature can be seen to play a key role.

The published literature indicates that enzymes and proteins are more resistant to thermal denaturation at low moisture conditions (Terebiznik *et* al., 1997; Meerdink and van't Riet, 1995). A decrease in the moisture content reduces the freedom of movement of the protein molecules and thus prevents conformational changes and denaturation (Terebiznik *et al.*, 1997). For denaturation to occur, therefore, the whey proteins needs to be both hydrated and exposed to temperatures above at least 70°C at the same time.

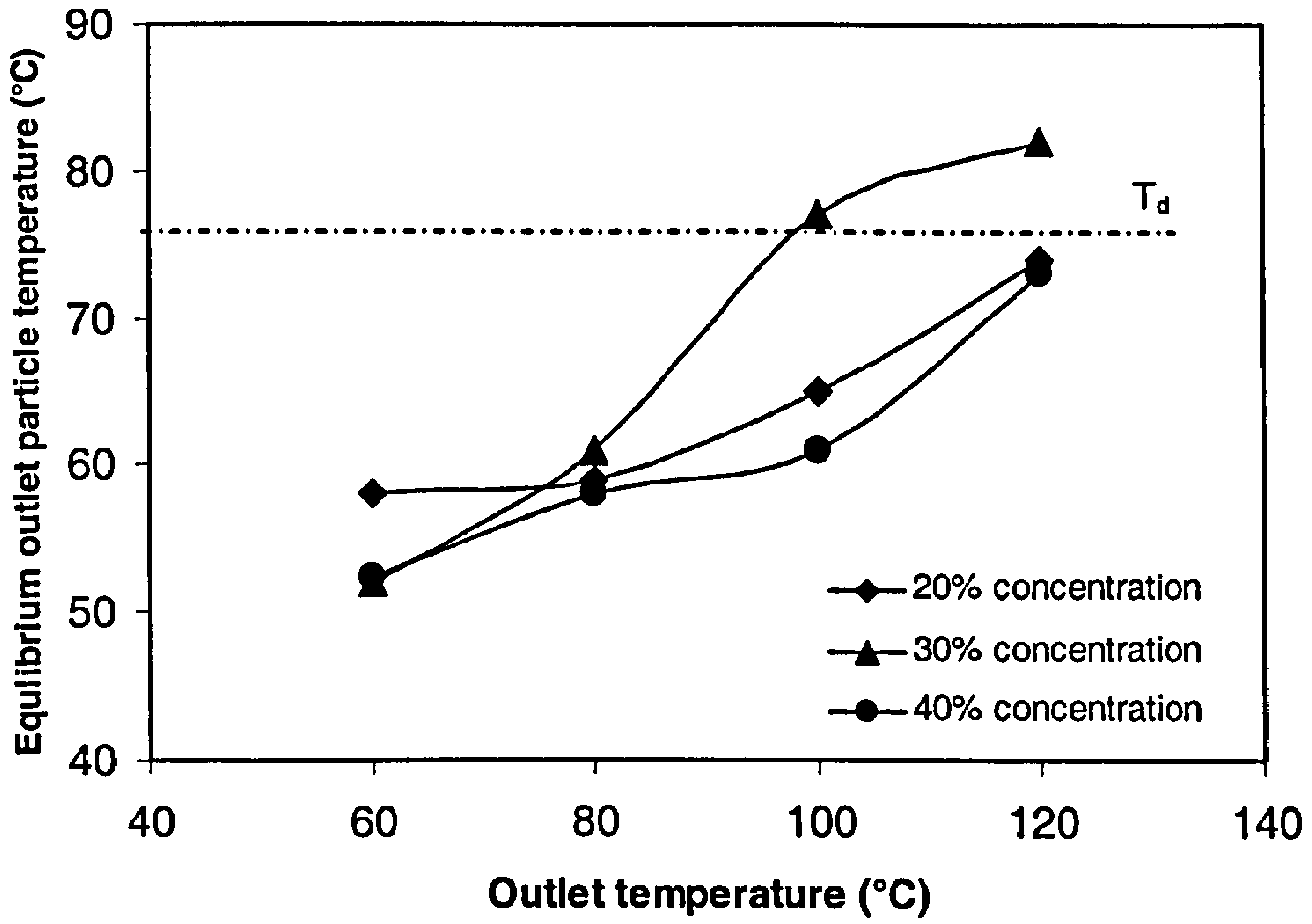

Figure 5-19: Effect of spray dryer outlet temperature and feed concentration on the lower bound estimate of outlet particle temperature (T_d - whey protein denaturation temperature).

As previously mentioned, this is unlikely to occur just after atomisation, as the droplets will be close to the wet-bulb temperature, which is well below 70°C, even with the hottest inlet gas. However, if the surface of the particles quickly dries out to leave a surface crust, the temperature will rise whilst still maintaining a relatively high level of moisture in the core, and denaturation might well then occur. The estimated (lower bound) particle outlet temperatures (based on the construction shown in figure 5-3) are plotted in figure (5-19), but the majority of these are below the denaturation temperature T_d. This therefore suggests that in many cases (particularly with 40% feed concentration) the surface moisture content must have been significantly lower than the bulk moisture in order for significant denaturation to have occurred. It was hypothesised earlier that crust formation might be favoured with higher solids content in the feed, and this could explain the higher levels of denaturation in the 40% solids experiments.

5.9 Effect on protein solubility

This section reports solubility analysis of spray dried whey proteins by using nitrogen content (Kjeldhal) (analytical procedure given in section 4.3.3.2) and reversed phase HPLC (section 4.3.4.2) methods. The loss of solubility at its isoelectric point can also be used to estimate protein denaturation (Fachin and Viotto, 2005). The proteins are more soluble at low pH (acidic) or high pH (alkaline) values as the molecules are charged and repel each other. When the pH approaches the isoelectric point (pI) the protein charges are progressively neutralised, reducing the repulsive forces, which in turn allows protein aggregation to occur more easily (Pelegrine and Gasparetto, 2005).

5.9.1 Nitrogen content (Kjeldhal) analysis

Figure (5-20) shows the results obtained from the nitrogen content analysis (Kjeldhal) for protein solubility at the different feed concentrations and outlet temperatures. The maximum protein solubility was found at the lower outlet temperatures (60°C and 80°C) as well as lower feed concentrations (20% and 30%). At higher temperature the solubility reduces significantly. Increasing the feed concentration resulted in slightly reduced values of protein solubility at each temperature.

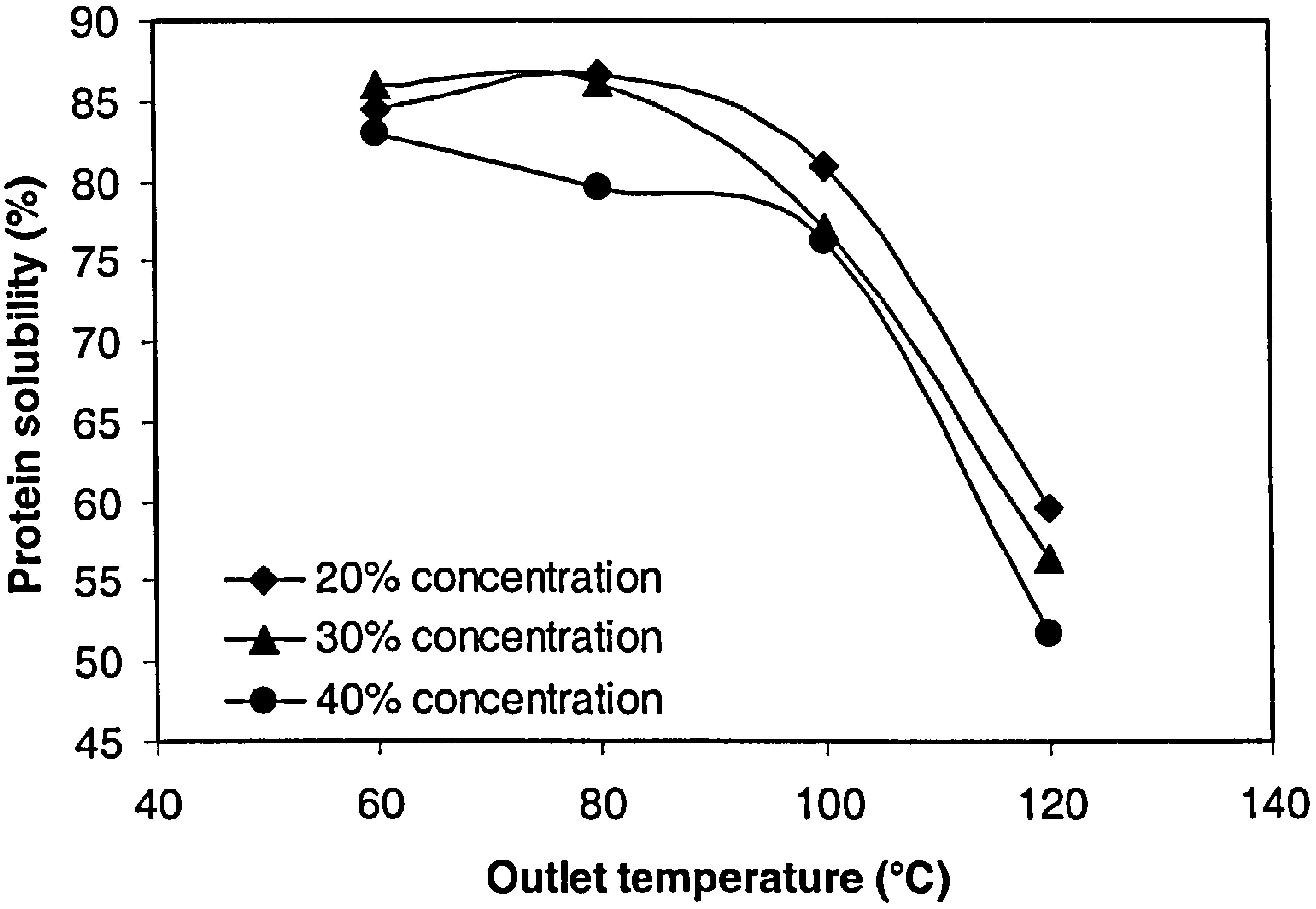

Figure 5-20: Effect of spray dryer outlet temperature and feed concentration on the solubility of the spray dried product.

There were only small effects on the solubility up to 80°C outlet temperatures, with 160-180°C gas inlet temperatures for all the feed concentrations. There were significant solubility differences at outlet temperatures above 80°C. These higher outlet temperatures were obtained by reducing the feed rate, leading to drier particles and higher equilibrium particle temperatures above the protein denaturation temperature, i.e. about 75°C (shown in figure 5-19).

5.9.2 RP-HPLC analytical methods

Whereas the Kjeldhal provides a measure of the overall loss of solubility, the RP-HPLC method is able to track the solubility of individual proteins. The loss of solubility of α-lactalbumin and β-lactoglobulin resulting from the spray drying of whey protein isolate solution has been studied by using reversed phase HPLC at pH 4.6. The RP-HPLC conditions were optimised for elution gradient, sample size, concentration and flow rate. The chromatographic system was calibrated by the external standard method, with pure native standards for bovine α-lactalbumin and bovine β-lactoglobulin (discussed in section 4.3.4). The proteins were separated with retention times of (i) ~20 min for α-lactalbumin; (ii) ~24 and ~25 min (two peaks) for β-lactoglobulin B (β-lgB) and β-lactoglobulin A (β-lgA), respectively. The same trend of separation is observed in other reports (*e.g.* Elgar *et al.*, 2000; Ferreira *et al.*, 2001 and Ferreira and Cacote, 2003). The spray dried whey protein samples also exhibited similar retention times to the α-lactalbumin and β-lactoglobulin native standards (see figure 4-12).

The chromatograms of spray dried whey protein at 20%, 30% and 40% (w/v) feed concentrations and at different outlet temperatures are compared with the untreated sample in figures (5-21, 5-22 and 5-23). The chromatogram of the untreated sample (feed solution) shows only two major peaks (α-lactalbumin and β-lactoglobulin) and thus indicates that other minor whey protein were denatured previously during the manufacturing process.

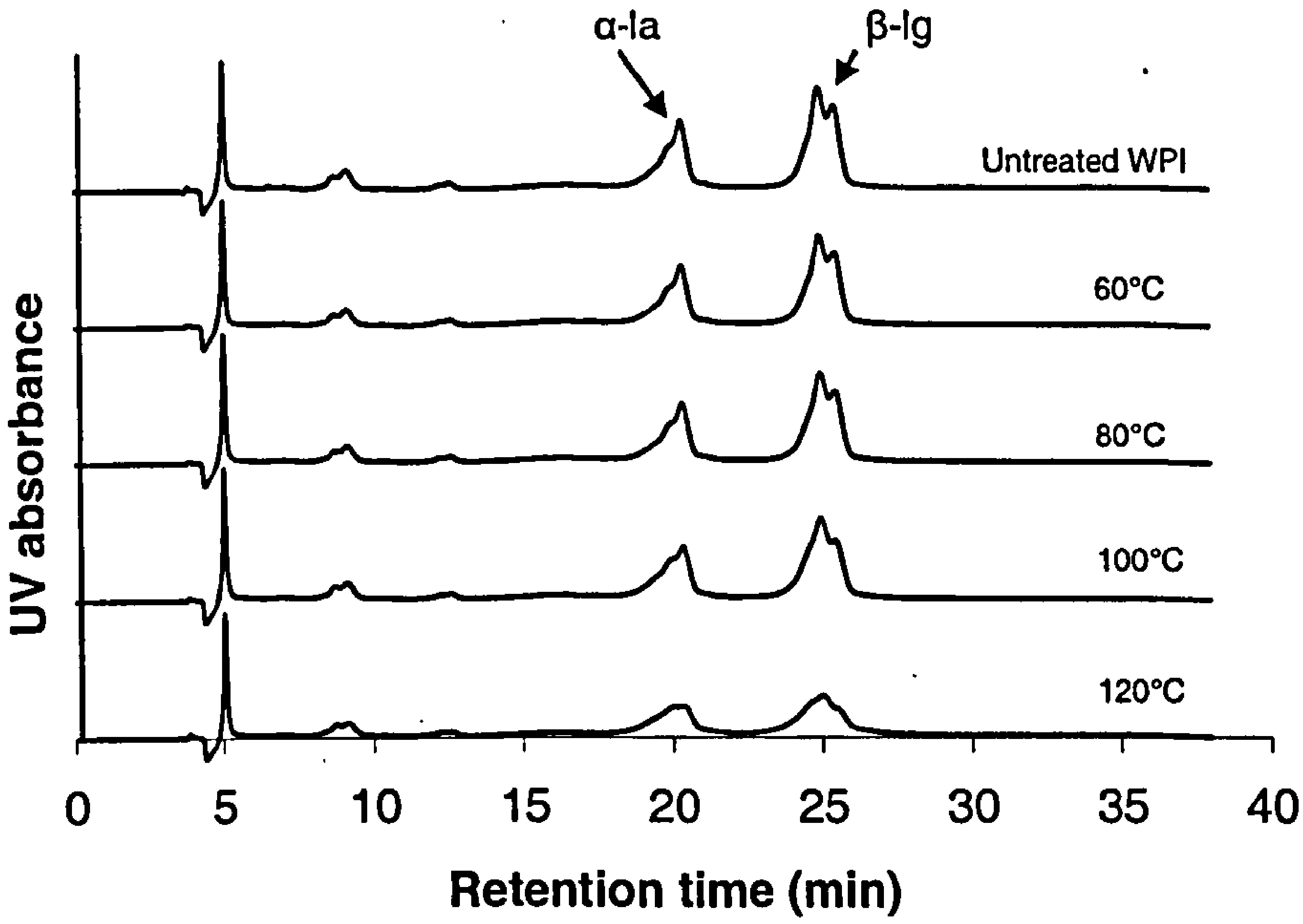

Figure 5-21: RP-HPLC Chromatograms of spray dried whey protein powder at 20% (w/v) feed concentration after spray drying with different outlet temperatures.

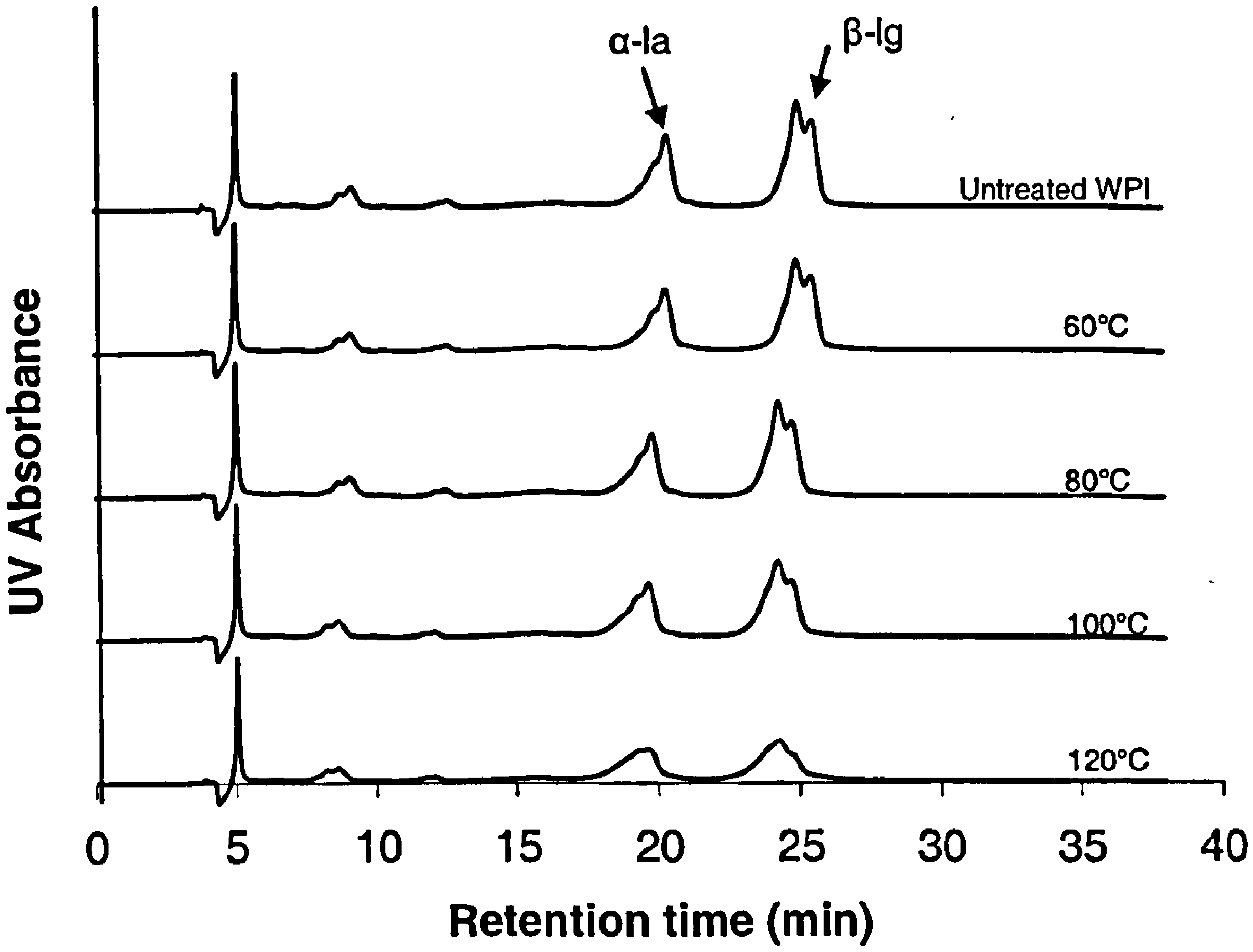

Figure 5-22: RP-HPLC Chromatograms of spray dried whey protein powder at 30% (w/v) feed concentration after spray drying with different outlet temperatures.

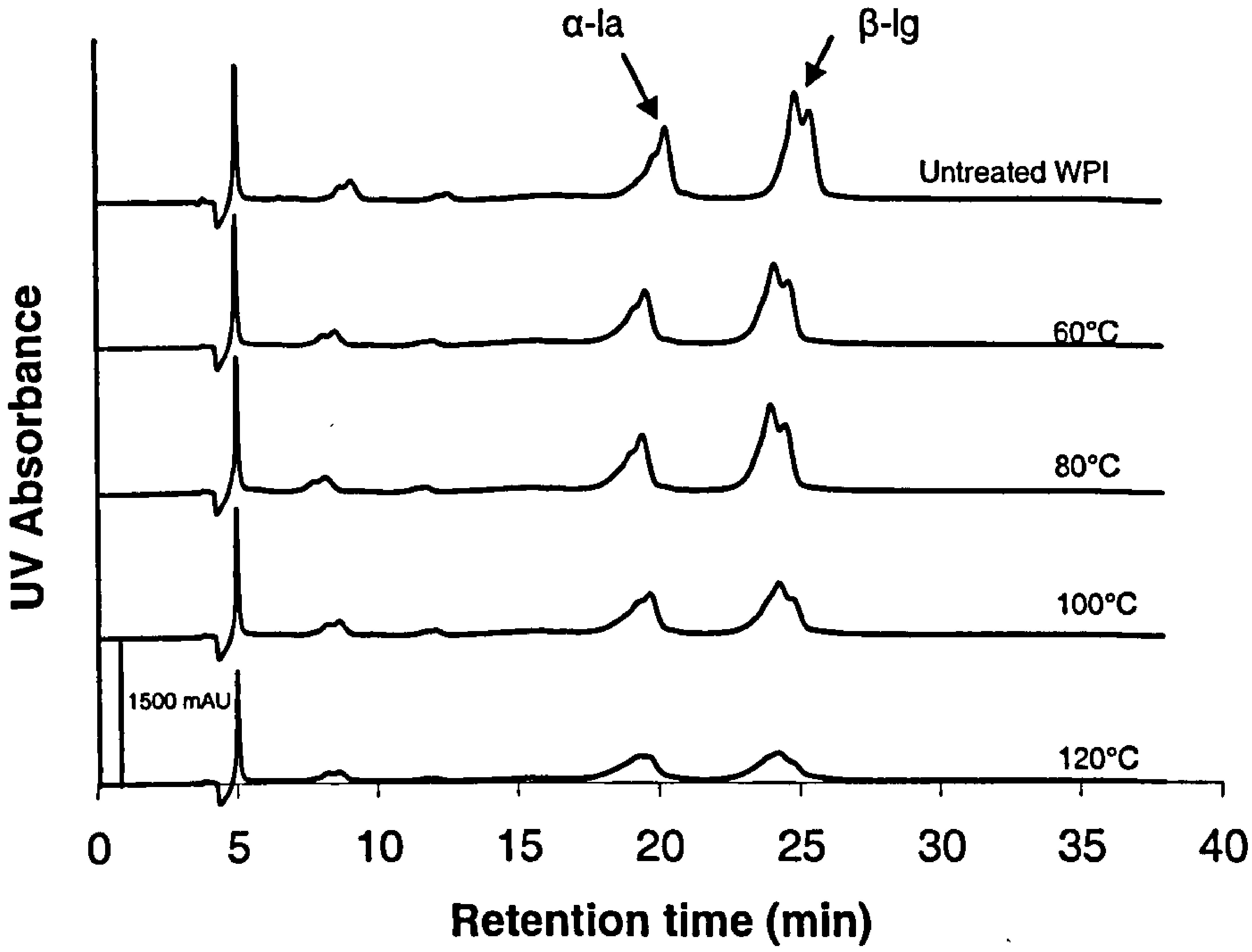

Figure 5-23: RP-HPLC Chromatograms of spray dried whey protein powder at 40% (w/v) feed concentration after spray drying with different outlet temperatures.

The decrease in the peak area in the RP-HPLC results shown in figures (5-21, 5-22 and 5-23), for the native whey proteins (α-lactalbumin and β-lactoglobulin), indicates a decrease in solubility at higher outlet temperatures, even when the feed flow rate remained approximately constant (which was the case for the 100 and 120 °C outlet temperatures – see Table 5-3).

Table 5-7: Experimental conditions used in the spray drying experiments and their effect on soluble native whey protein content.

Feed Concentration (w/v)	**Inlet air temp.** (°C)	**Outlet air temp.** (°C)	**Individual soluble whey protein content** (g per 100g of dry powder)	
			□-la	**□-lg**
WPI (untreated, Trial 1)	–	–	23.5	46.4
WPI (untreated, Trials 2&3)			22.5	46.4
20%	161±0.2	60±0.9	22.8	45.1
	180±1.6	80±0.4	23.2	45.2
	180±0.2 *	80±0.5	21.4	44.3
	180±0.5 **	80±1.0	21.3	44.7
	206±0.3	100±0.2	22.2	42.7
	255±1.0	120±1.0	17.2	29.9
30%	160±0.9	60±0.6	22.7	45.5
	181±0.9	80±0.5	23.0	45.4
	180±1.0 *	80±0.4	21.3	44.6
	180±0.2 **	80±0.5	21.6	44.6
	203±0.8	100±0.9	21.7	40.4
	250±0.5	120±0.5	18.2	29.8
40%	160±0.4	60±0.4	22.7	45.0
	184±0.6	80±1.0	22.5	43.9
	180±0.1 *	80±0.5	21.4	43.1
	180±0.1 **	80±0.4	21.4	42.1
	202±0.5	100±0.8	20.1	33.4
	252±1.5	120±1.0	15.2	25.5

Table (5-7) represents the amount of soluble native α-lactalbumin and β-lactoglobulin present in the spray dried product, as determined from the RP-HPLC method. The data for loss of solubility of α-lactalbumin and β-lactoglobulin at different outlet temperatures and feed concentrations are plotted in figures (5-24, 5-25 and 5-26).

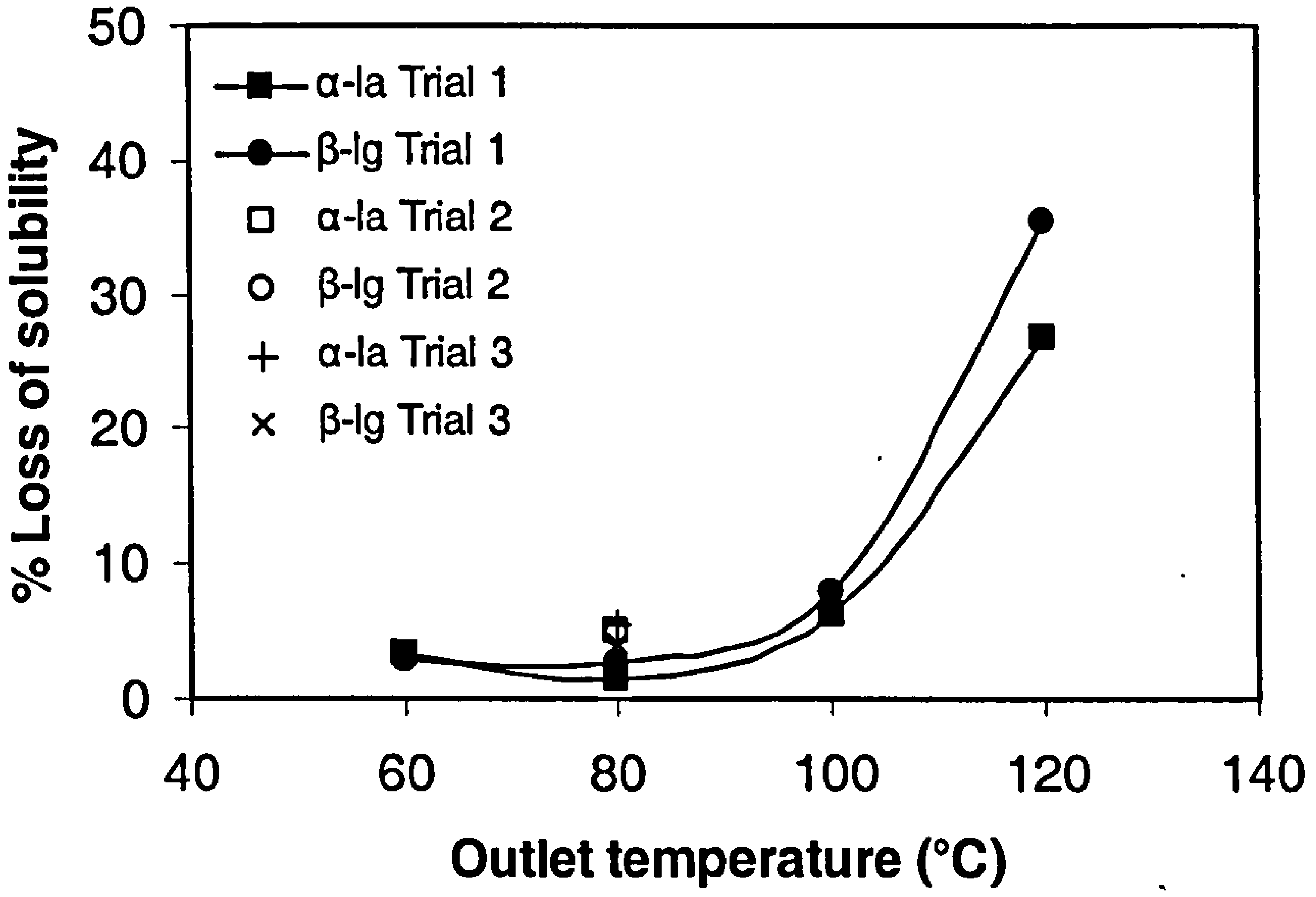

Figure 5-24: Effect of spray dryer outlet temperature on the loss of solubility of α-lactalbumin and β-lactoglobulin at 20% feed concentration.

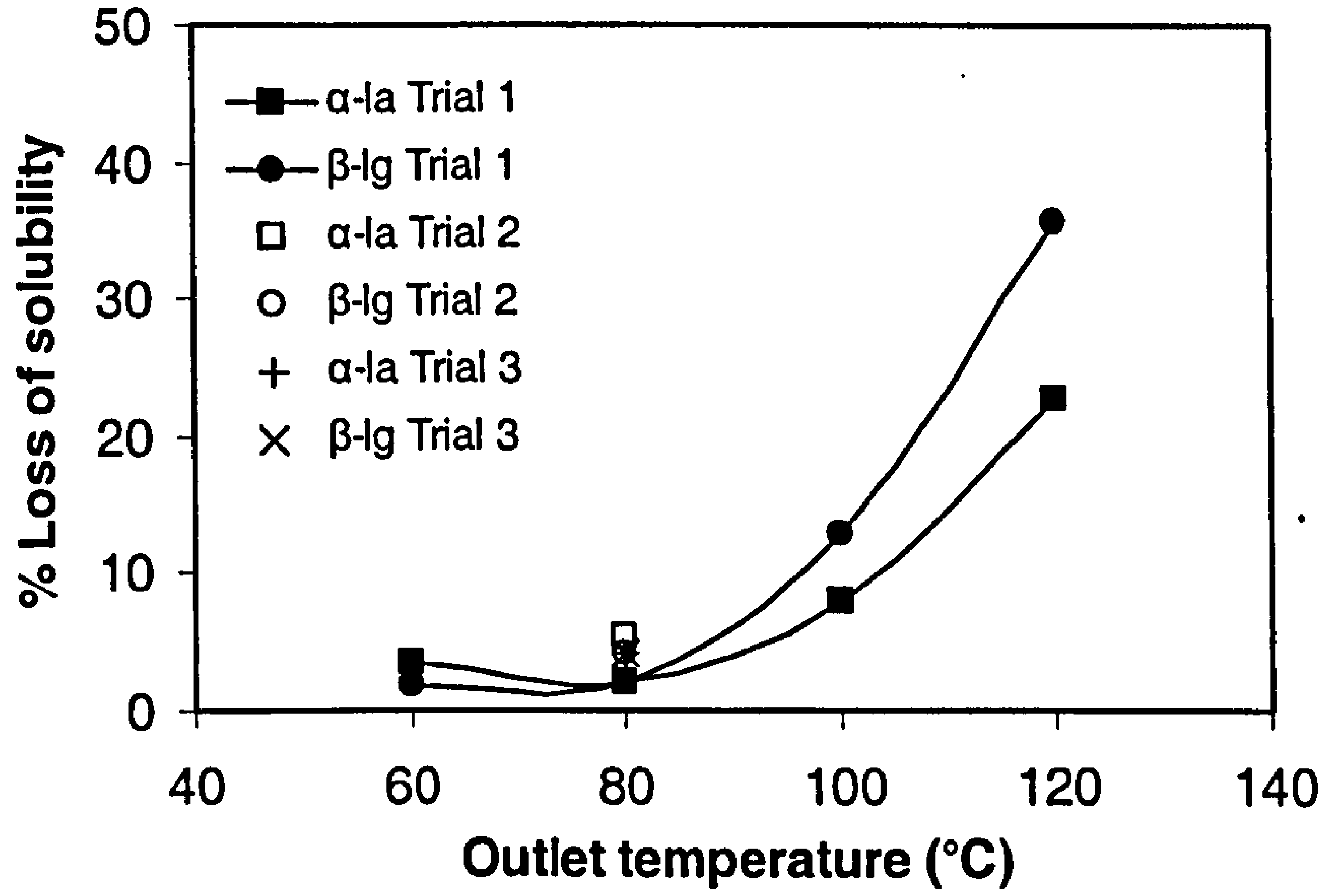

Figure 5-25: Effect of spray dryer outlet temperature on the loss of solubility of α-lactalbumin and β-lactoglobulin at 30% feed concentration.

The greatest loss in solubility of both α-lactalbumin and β-lactoglobulin is observed at the highest gas outlet temperatures (100 °C and 120 °C). Greater losses in solubility were found for β-lactoglobulin compared to α-lactalbumin (figures 5-24, 5-25 and 5-26). In contrast, the lower outlet temperatures (60°C and 80°C) had less effect on protein insolubility. The repeated Trials 2 and 3 results also reflect the Trial 1 observations.

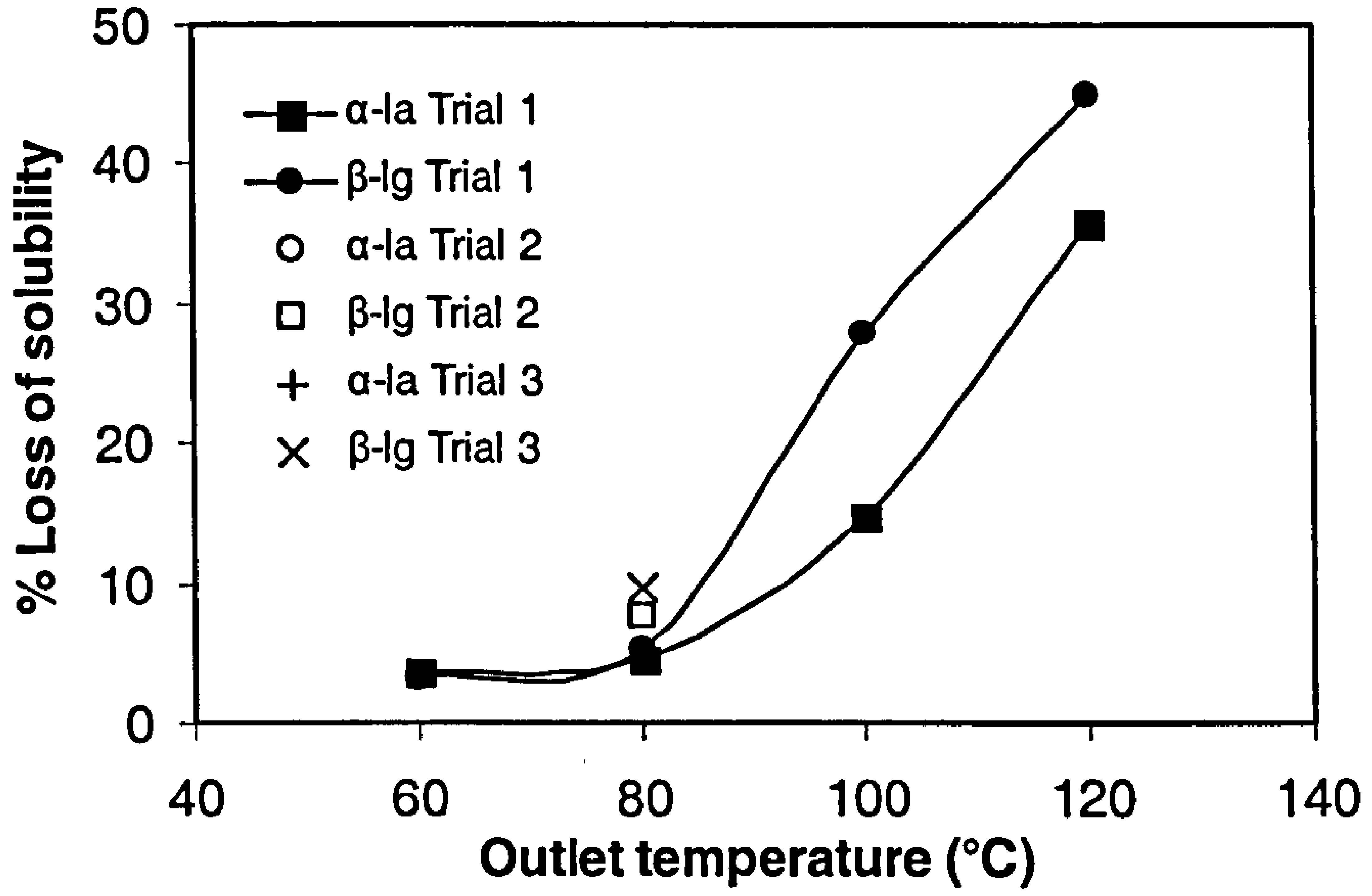

Figure 5-26: Effect of spray dryer outlet temperature on the loss of solubility of α-lactalbumin and β-lactoglobulin at 40% feed concentration.

The loss of solubility of α-lactalbumin and β-lactoglobulin at different feed concentrations is plotted in figures (5-27) and (5-28). This study reveals that the loss of solubility of both α-lactalbumin and β-lactoglobulin increases (by about 10%) with these increases in liquid feed concentration at the higher outlet gas temperatures (100 and 120 °C) but, at lower temperatures this effect is difficult to distinguish. The repeated Trials 2 and 3 results also shown similar trends to the Trial 1 observations.

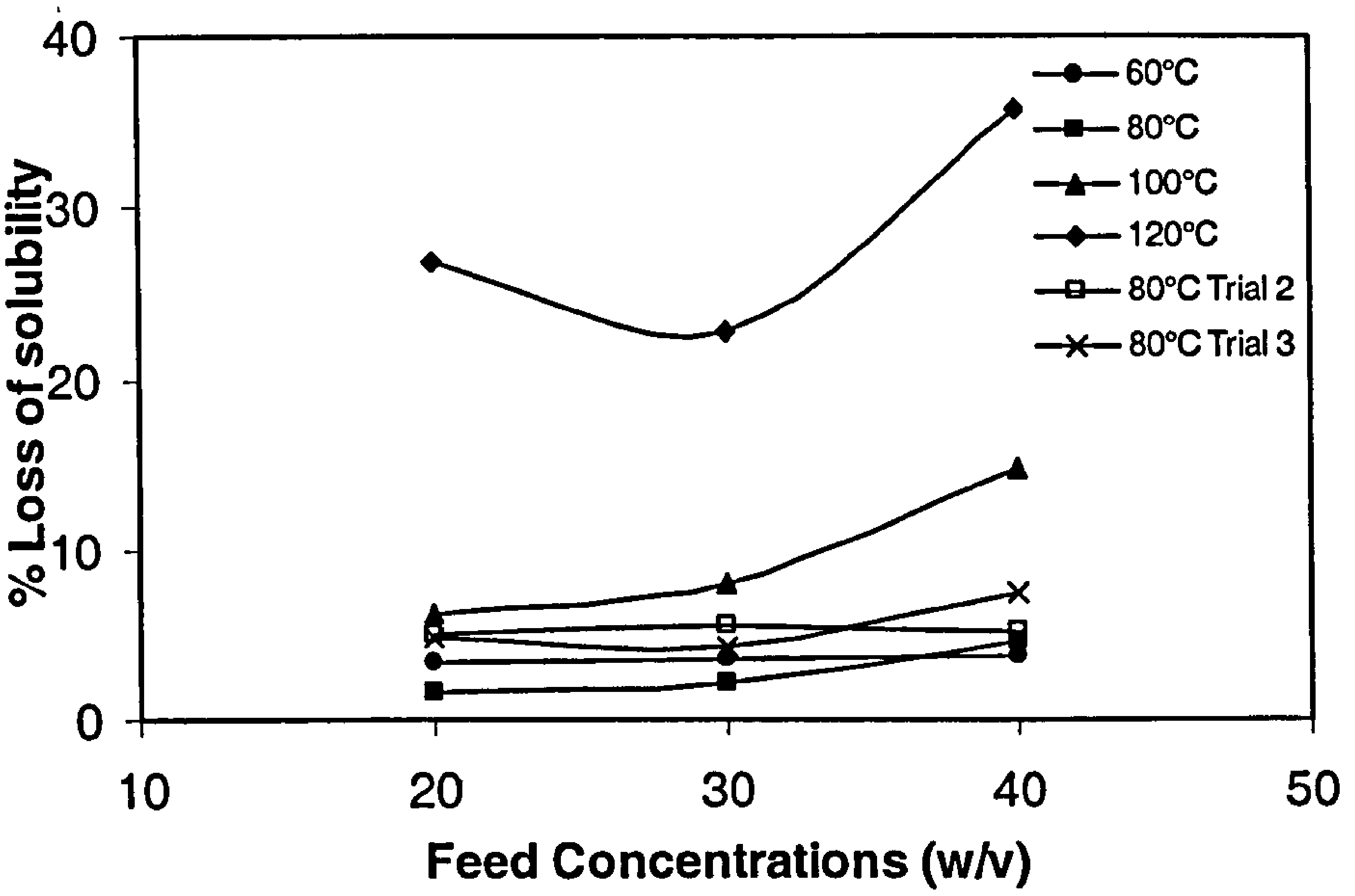

Figure 5-27: Effect of spray dryer feed concentration on loss of solubility of α-lactalbumin.

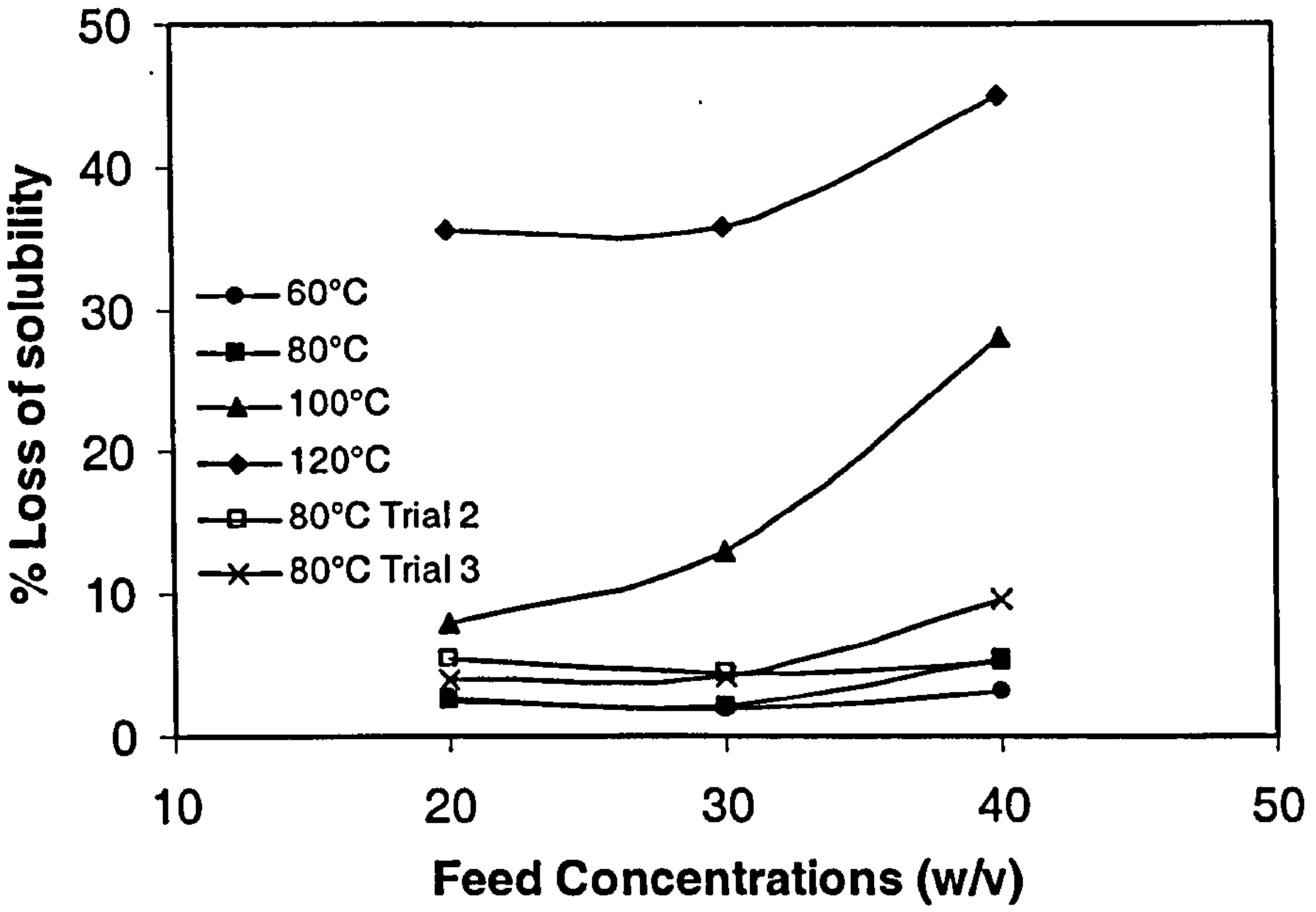

Figure 5-28: Effect of spray dryer feed concentration on loss of solubility of β-lactoglobulin.

The RP-HPLC analysis results reveal that β-lactoglobulin consistently suffers a greater loss in solubility than α-lactalbumin during these spray drying experiments. α-lactalbumin is reported to be the more heat stable whey protein (Ferreira *et al.*, 2001), as it is the only milk protein which binds with the Ca^{2+} ion (present in the whey used in these experiments) and this binding increases the stability of α-lactalbumin at higher temperatures (Permyakov and Berliner, 2000). Dissociation of the Ca^{2+} ion is indeed one of the steps in the denaturation process of α-lactalbumin (Boye *et al.*, 1997). Furthermore, it has been found that α-lactalbumin does not aggregate by itself but relies on forming aggregates with β-lactoglobulin (Schokker *et al.*, 2000).

5.10 Comparison of *DSC, Kjeldhal* and *RP-HPLC* analytical methods

This section, deals with comparison of three analytical methods such as DSC, total nitrogen content (Kjeldhal) and RP-HPLC methods. This is the first analytical comparison of its kind performed for whey protein denaturation and solubility studies. Moreover, this is the first time the RP-HPLC method has been applied to whey protein powder solubility analysis. Figure (5-29) shows the percentage denaturation and figures (5-30) and (5-31) depicts the loss of solubility during the spray drying of whey proteins.

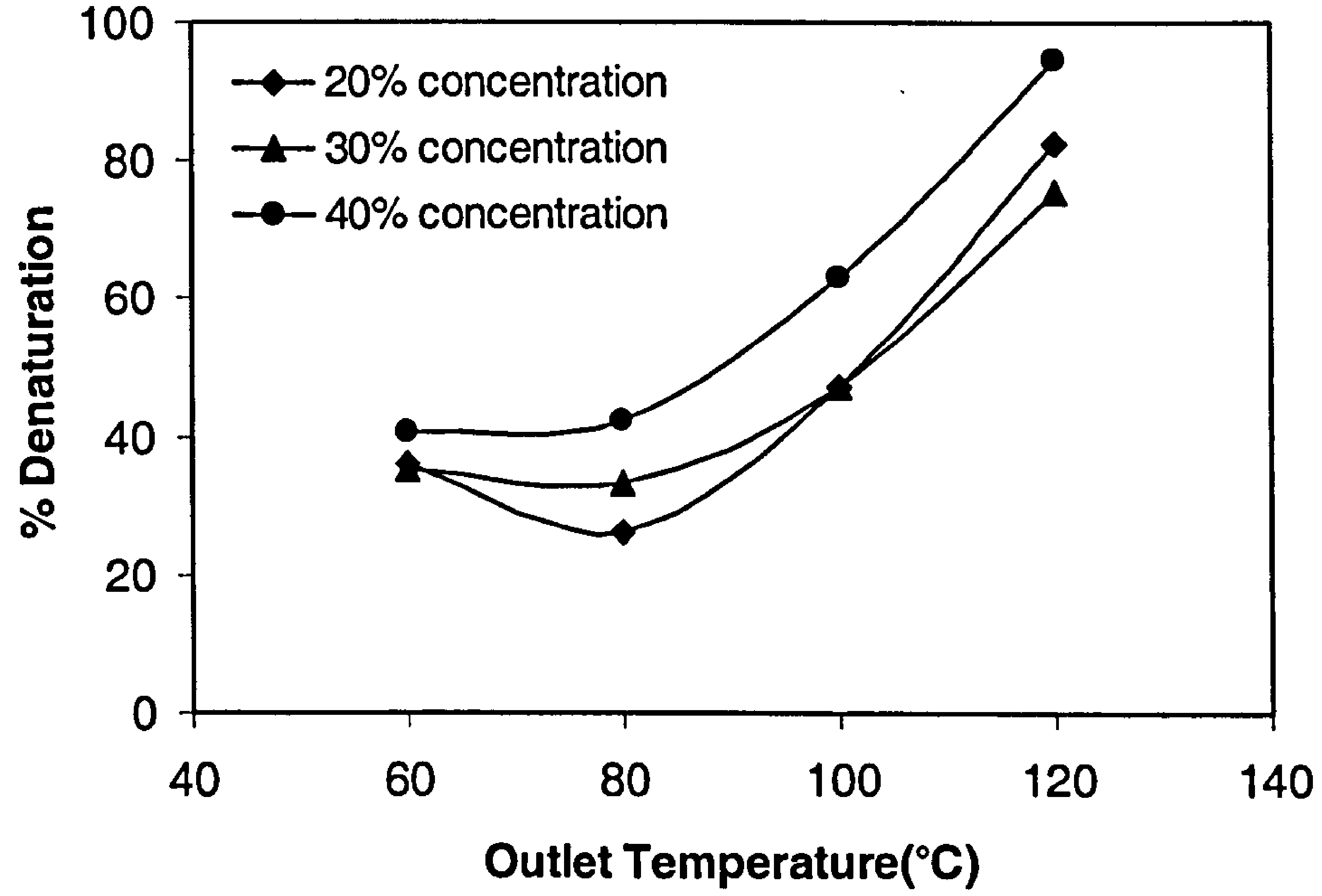

Figure 5-29: Effect of spray dryer outlet temperature and feed concentration on the % denaturation based on *DSC analysis.*

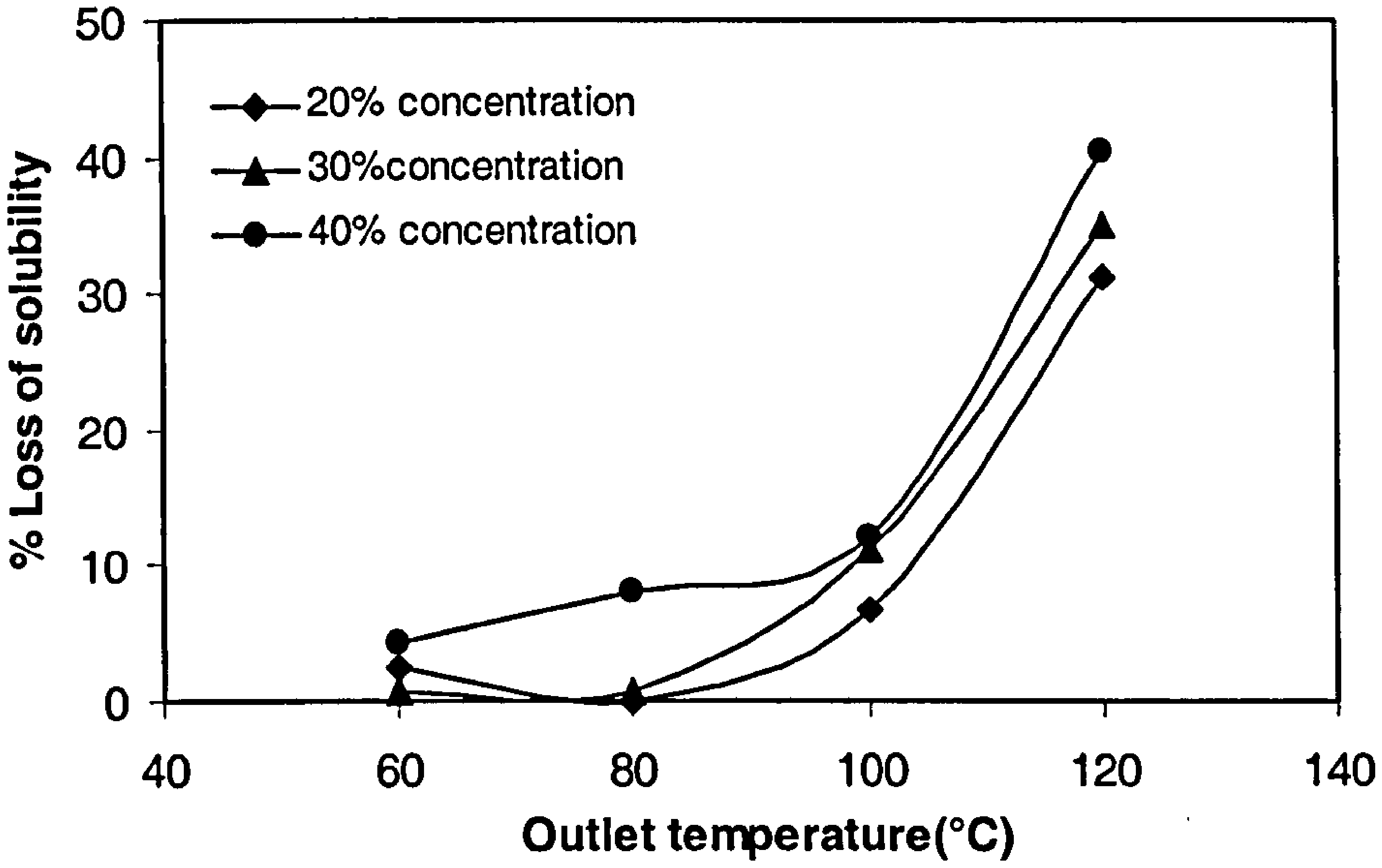

Figure 5-30: Effect of spray dryer outlet temperature and feed concentration on the % loss of solubility based on *nitrogen content analysis.*

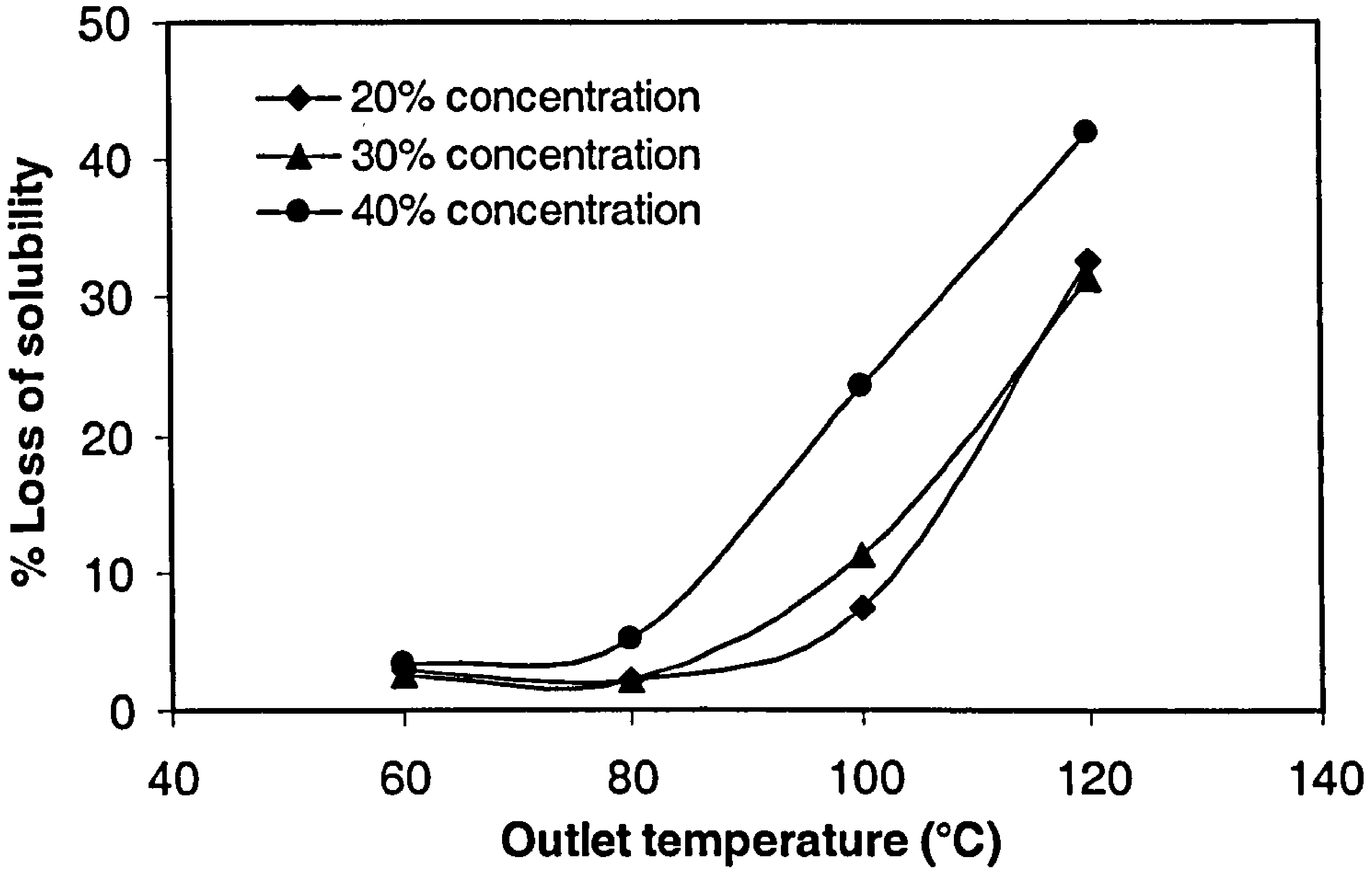

Figure 5-31: Effect of spray dryer outlet temperature and feed concentration on the % loss of solubility based on *RP-HPLC analysis.*

These results were obtained from the DSC, total nitrogen content and RP-HPLC methods respectively. The trends obtained from DSC analysis were qualitatively in agreement with the nitrogen content analysis and reversed phase HPLC separation observations. Here, high protein solubility values were observed to correspond with high denaturation enthalpy values, *i.e.* both quantities are measures of the amount of undenatured protein remaining in the dried product. Proteins, which have undergone denaturation without aggregation, remain soluble. Hence both denaturation *and* aggregation need to occur to produce insolubility, which can explain the less dramatic effect of thermal processing in figure (5-29), than in figure (5-30) or (5-31). For example, under the severest conditions (40% solids feed concentration and 120°C outlet temperature) the denaturation enthalpy is barely 5% of the original value, whereas solubility has only dropped by less than 50%. This may be because both protein denaturation *and* subsequent protein aggregation need to occur to produce insolubility, and aggregation may only be occurring to a limited extent. It has also been found that slightly higher temperatures are needed to induce aggregation (72°C) compared to denaturation (70°C), which may delay aggregation compared to denaturation (Anema *et al.*, 2005).

The reversed phase HPLC results were consistent with those from total protein nitrogen content analysis. The similarity of the results for RP-HPLC and total nitrogen give confidence to the RP-HPLC method of analysing protein solubility. This comparative study suggests that the protein solubility can also be calculated from RP-HPLC analysis. The RP-HPLC method also has distinct advantages in that it is much quicker, more straightforward and can resolve individual proteins.

The strongest influence on denaturation and solubility is undoubtedly temperature. High outlet (120°C) and inlet gas (250°C) temperatures produce very significant losses of the order of 40%, although it is the outlet temperature that provides the better indication of the temperatures experienced by the droplet during spray drying (Oldfield *et al.*, 2005). The published literature indicates that the degree of denaturation of proteins increases with increasing temperature and holding time (Dannenberg and Kessler, 1988; Law and Leaver, 1997). Oldfield *et al.* (2005) found that the rates of denaturation (measured by a gel electrophoresis method) of both α-lactalbumin and β-lactoglobulin substantially increased over the range 80-120°C during the preheating of skim milk. They also found that spray drying between 89°C and 101°C produced only small amounts of denaturation. As denaturation is a prerequisite for solubility loss, these results are in agreement with the trends found here.

Noticeable variations in solubility were found when the inlet feed concentration was varied. In general, feed concentrations of 40% produced the greatest amount of denaturation and loss in solubility. Two factors may be causing this: (i) a direct effect of concentration on denaturation and loss of solubility and/or (ii) an indirect effect from droplets of different initial concentrations undergoing different temperature histories during drying.

A direct effect of concentration on loss of solubility could either be caused by an influence on denaturation or on aggregation. Law and Leaver (1997) found that the rate of denaturation of whey protein (based on their loss of solubility at pH 4.6) increased with increasing total whey protein concentration in milk. Kessler *et al.* (1992) also observed the same trend in heated milk. However, Anema (2001) also found that α-lactalbumin denaturation was unaffected by varying solid concentration from 10 to 39% in skimmed milk during heating at the range of 75 to 100 °C for 15 minutes using native poly acrylamide gel electrophoresis (native-PAGE) method. Anema (2000) even found that increased concentration had a retardation effect on the denaturation of β-lactoglobulin in milk, but this may be influenced by the presence of lactose. Protein-bound lactose groups increase the active radius of the β-lactoglobulin molecules and thus leads to decrease in thiol-disulfide exchange reaction rate which in turn the irreversible denaturation of β-lactoglobulin. The same trend was shown by (McKenna and O'Sullivan, 1971) who found that increasing the concentration of skim milk solids from 9% to 40% during heating at 80°C for 20 minutes reduced the degree of denaturation.

The two apparently contradictory results can be reconciled by noting that Law and Leaver in fact measured solubility, and this is influenced by aggregation as well as denaturation. Aggregation, however, is more likely to be affected by concentration, as aggregation requires neighbouring molecules to collide (Law and Leaver, 1997). The protein molecules are able to aggregate in the denatured state as the hydrophobic and thiol groups are exposed, which were previously buried inside the molecules (Hoffmann and van Mil, 1997). Anema (2000) observed that although β-lactoglobulin denaturation was retarded at higher milk solid concentrations, decreases in solubility were observed.

There may also be a second indirect effect of feed concentration on denaturation and solubility from its effect on the particle temperature. Upon atomisation, the liquid droplets contact the inlet hot gas and water evaporation takes place rapidly from the droplet surface, cooling the droplets initially to their wet bulb temperature (44-54°C), as well as cooling the surrounding hot gas (Oldfield *et al.*, 2005). This stage of drying is believed to last only for a relatively short period of time. A crust is then likely to form on the surface of the droplet, which reduces the surface water activity and increases the droplet temperature.

It is likely that the more concentrated feed will form a dry crust more quickly and this will elevate the particle temperature away from the wet-bulb temperature. There is evidence for greater crust formation at 40% feed concentration as drier product was obtained in experiments with 30% feed concentration (see figure 5-32). As mentioned earlier that 40% feed concentration produced a higher moisture content. This could occur if the crust that forms dries to such an extent that water diffusion is hampered by a severe reduction in diffusivity. Thus, to summarise, the effect of increasing the feed concentration would be to promote crust formation, which would raise particle temperatures and lead to greater levels of denaturation and aggregation.

5.11 Main findings

This study confirms that low outlet gas temperatures (60-80°C) are required to avoid excessive denaturation of proteins, as determined by DSC. The DSC results are supported by protein solubility tests, which show qualitatively similar results, but a less dramatic fall-off at higher temperatures. Varying the feed concentration had a minor effect on whey protein denaturation and insolubility during spray drying, with higher feed concentrations, resulting in slightly more denaturation.

This comparative study suggests that the protein solubility can also be calculated from RP-HPLC analysis. Moreover, the RP-HPLC solubility analysis method is straightforward and requires less analytical time than the nitrogen content analysis method. The extent of protein denaturation can be estimated from the loss of solubility at its isoelectric point, but both protein denaturation *and* subsequent protein aggregation need to occur to produce insolubility.

It was observed that α-lactalbumin is more stable than β-lactoglobulin. At higher outlet gas temperatures and higher feed concentrations, there was a sharp increase in loss of solubility of α-lactalbumin and β-lactoglobulin, which was associated with occurrence of insolubility of the powders and at this stage extensive conformational changes followed by aggregation of protein took place. The literature indicates that both high temperatures and moist conditions are needed for denaturation to take place. It is hypothesised that as shown in figure (5-32), in spray drying this is most likely if a dry crust forms on the surface of the particle, whilst the core remains wet.

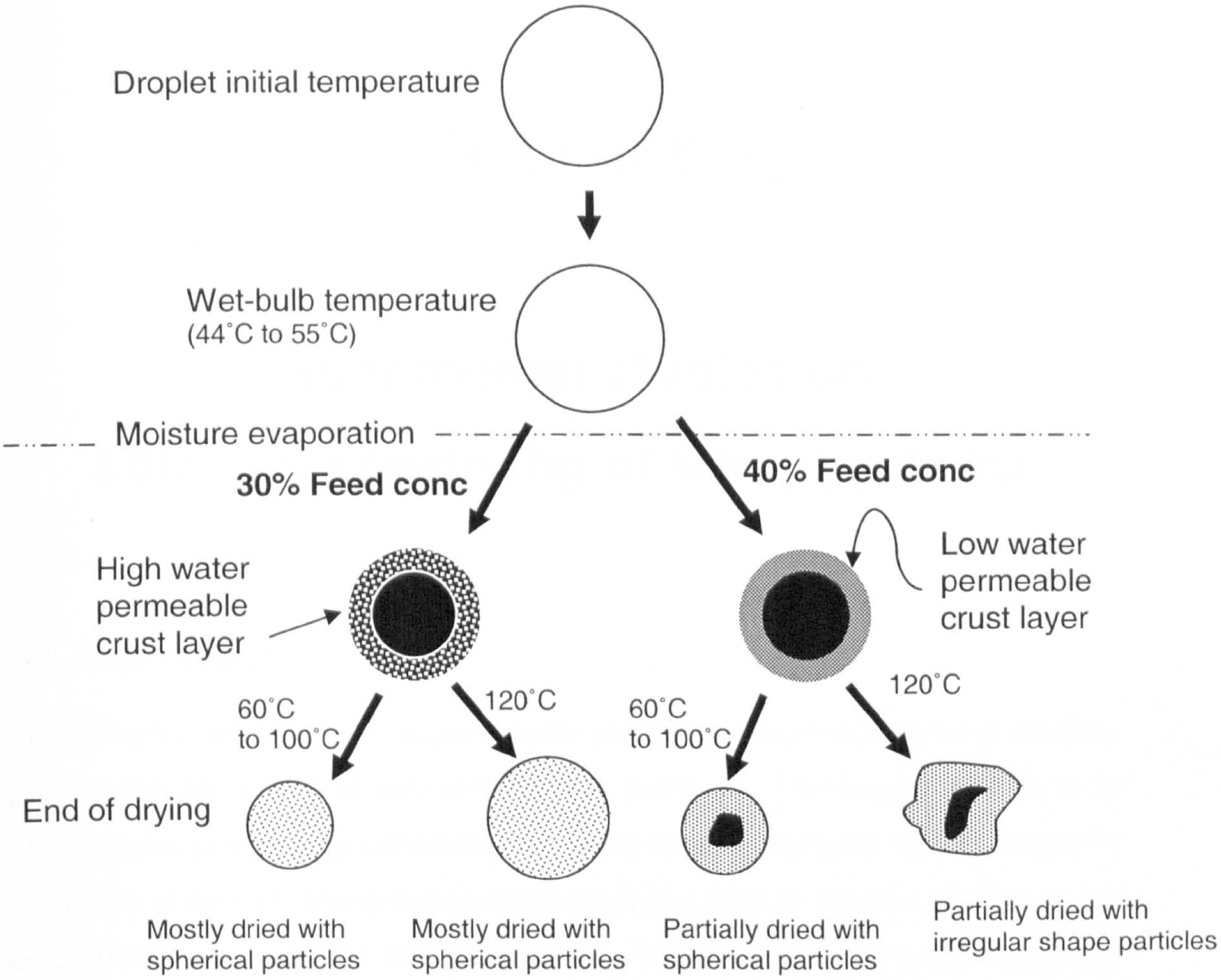

Figure 5-32: Schematic diagram of crust formation.

Results from moisture content analysis and particle size analysis of the dried product both suggest that higher feed concentrations result in a stronger crust, and this may explain the slightly greater denaturation and loss of solubility found for experiments using a feed concentration of 40%. Increasing the outlet gas temperature has the twin effect of increasing particle temperatures by shifting the wet-bulb lines, but perhaps more importantly by promoting the rapid formation of a dry crust whilst the inner core is still wet.

Chapter 6

Experimental studies on spray-freeze-drying of whey proteins

6.1 Introduction

This chapter deals with an experimental study on spray-freeze-drying of whey protein isolates (WPI) at sub-atmospheric pressure. The main objective is to find suitable processing conditions for spray-freeze-drying of WPI and also to study the effects of drying temperature on the quality of protein powders such as solubility, particle size and morphology. The experimental methods results and discussions are presented in the following sections, beginning with a preliminary DSC study to measure the glass transition temperature of frozen WPI solutions.

6.2 Glass transition temperature (T_g) of whey protein isolate

The main problem encountered in the freeze-drying of food products is "*collapse*". The term "*collapse*" has been used to describe the loss of structure, reduction in pore size and volumetric shrinkage in freeze dried food materials which are clearly undesirable (discussed in Chapter 2, section 2.3.1). Hence, the freeze-drying operation should be performed below the *collapse* temperature of the materials. Knopp *et al.* (1998) studied the *collapse* temperature (T_c) and found that T_c was equal to the glass transition temperature (T_g) for sucrose solutions. As there is an unavailability of data for the *collapse* temperature and/or glass transition temperature of whey proteins in the open literature, it was decided to find out the glass transition temperature of frozen whey protein solutions using the DSC method, as described by Roos and Karel (1991).

The DSC analysis used the following methods. Whey protein isolate powder (0.5 g) was dissolved in 1.25 ml of distilled water (40% w/v concentration) and gently mixed. A pipette was used to sample 15-20 mg of the solution, which was placed in a pre-weighed aluminium DSC pan. The pan was then hermetically sealed and weighed to 0.1 mg accuracy. The sample was placed in a Q10 DSC (TA Instruments, USA) and scanned from 20°C to -80°C at a programmed cooling rate of 10°C/min. An empty pan was used as a reference. After cooling, the sample was heated at 10°C/min to -40°C and held isothermally for 15 minutes. Again, the sample was recooled to -80°C at 5°C/min and scanned from -80°C to 20°C at 10°C/min. The DSC measurements were carried out in duplicate. The DSC instrument had previously been calibrated for temperature using an indium standard at the same scan rate of 5°C/min.

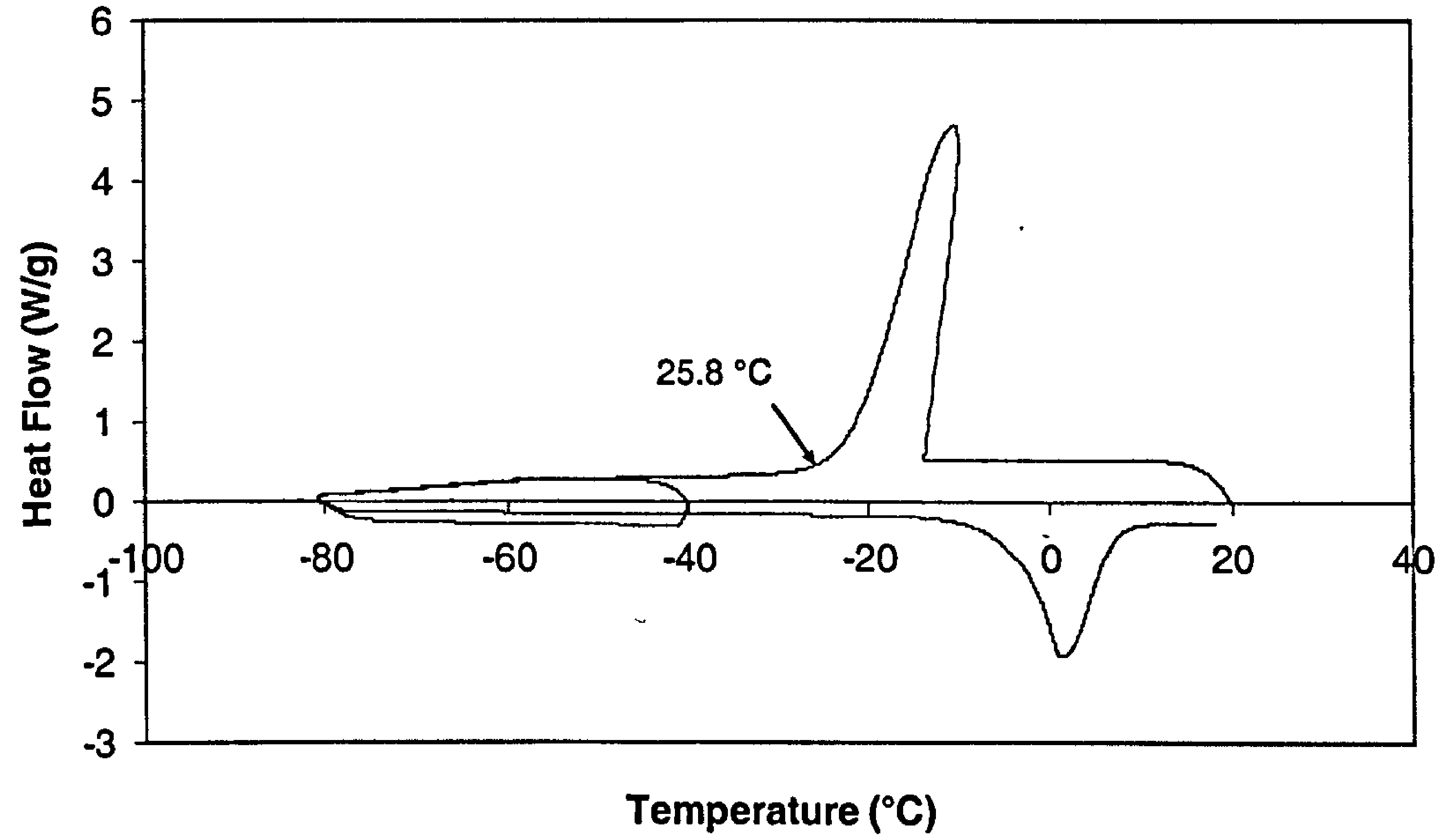

Figure 6-1: Thermal behaviour of whey protein isolate solution.

Figure (6-1) shows the thermal behaviour of whey protein isolate (WPI) solution. It is very difficult to find out the glass transition state from the thermogram. Hence, the temperature of -25.8°C was considered as glass transition state of WPI, where crystallization process was stopped as shown in figure 6-1.

6.3 Experimental details

The feed solution preparation method is described in Chapter 4 (section 4.2.2) and the methods of sample analysis are given in the same chapter, in section 4.3. The spray-freeze-drying (SFD) operations has two steps: (1) spray-freezing, the atomisation of WPI solution into cold vapour at atmospheric pressure, followed by (2) vacuum fluidised bed freeze drying (VFBFD).

6.4 Spray-freezing of whey proteins

The spray-freezing experimental set up and operating procedure is given in Chapter 3 (section 3.4 and 3.7). In the spray-freezing operation, the main operating variables are: feed concentration, feed pressure, cold gas flow rate and chamber temperature. The same chamber temperature (-85±2°C) at the start of spraying and feed concentration (20 % w/v) were used for all spray freezing trials. The liquid feed rates were measured for each experiment by measuring the change in volume of feed in the feed vessel over time. The measured liquid feed flow rate for all the trials was 0.0125 kg/s. The frozen particles were collected from the bottom of the spray-freezing chamber in an insulated container and weighed before transferred to the VFBFD rig.

6.5 Vacuum fluidised bed freeze drying (VFBFD) of whey proteins

The important operating variables of VFBFD process are the fluidised bed pressure and feed inlet gas temperature. The experimental set up and operating procedure are given in Chapter 3, section 3.5. Three different inlet gas temperatures of -10°C, -15°C and -30°C were used for all the trials. The inlet gas temperature was effectively controlled by a recently designed and constructed double pipe heat exchanger by varying the heater temperature and the air flow rate to the heater. Preliminary experiments were performed at chamber pressures of either 0.1 bara or 0.05 bara. However, it was found that at 0.05 bara pressure, there was no fluidisation of the particles due to insufficient drag on the particles. Hence, 0.1 bara pressure was used for all the trials.

6.5.1 Effect of temperature on moisture content

The average bulk moisture contents (kg water/kg total) of the product powders at the end of drying are given in Table (6-1), which shows that all the trials have produced acceptably dried products, except at -10°C inlet temperature. This may be due to agglomeration of particles during the drying process at that temperature.

Table 6-1: Experimental conditions used in the VFBFD experiments and their effect on moisture content.

Inlet gas temperature (°C)	**VFBFD chamber pressure (bar)**	**Trials**	**Feed in (g)**	**Average moisture content (wet basis) (%)**	**Average moisture content (dry basis) (%)**
-10± 1.0 °C	0.1	Tr 1	11.6	20.9	26.4
-15± 1.0 °C	0.1	Tr 1	7.2	9.5	10.5
		Tr 2	3.9	7.2	7.7
-30± 1.0 °C	0.1	Tr 1	5.3	14.0	16.3
		Tr 2	7.7	12.9	14.8
WPI (U)				7.5	8.1

6.5.2 Temperature measurements during VFBFD

Figure (6-2) shows an example of the time variation of the inlet and outlet gas temperatures and particle bed temperatures at a system pressure of 0.1 bar, and using a constant gas inlet temperature of -30°C. The temperature measurement locations are shown in Chapter 3 (figure 3-9). It can be seen that there is a significant "*wet-bulb*" depression of the particle temperature below the gas temperature, and a significant change in temperature of the gas as it passes through the bed. This indicates that a significant rate of drying is taking place as convective heat transfer from the gas to the particles must be taking place to overcome sublimative cooling. Indications from other experiments suggest that the difference between the particle and gas temperatures increases as the system pressure is reduced. This is because the pressure influences the thermal mass of the fluidising gas per unit volume and the heat transfer coefficient between the gas and the particle bed.

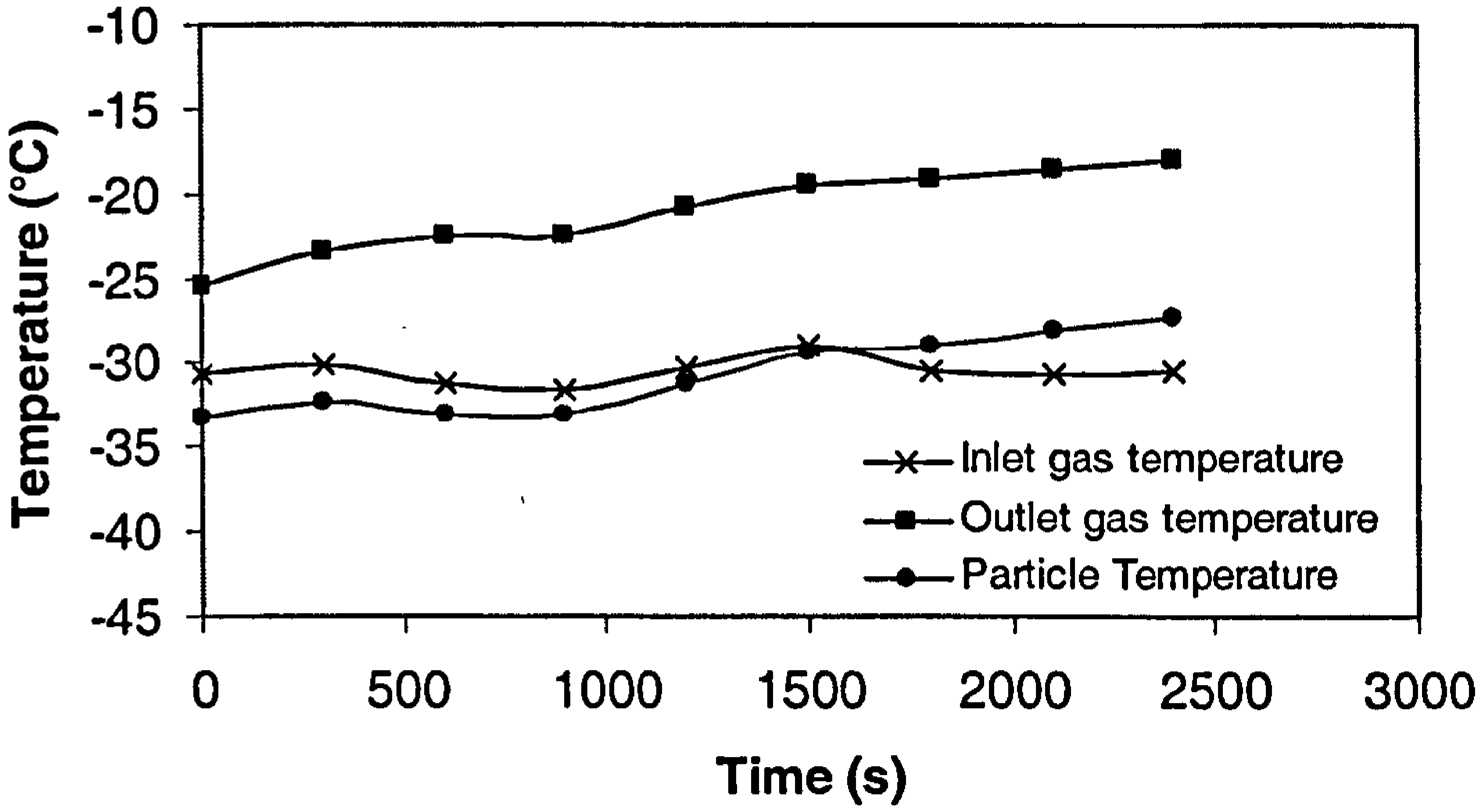

Figure 6-2: Temperature measurements of -30°C (Trial 1) gas temperature.

The outlet gas temperature is higher than the inlet gas temperature (defying the first law of thermodynamics) due to poor insulation of the chamber. This results in warming of the gas within the fluidising chamber.

6.5.3 Effect of temperature on drying rate

The variation of the rate of drying with time can be inferred from the temperature measurements by assuming that the heat transfer coefficient and heat transfer surface area are constant during drying. A heat balance on the particles may be written as:

$$-\frac{dM}{dt}=\frac{hA_p(T_g-T_p)}{\lambda} \qquad \text{Eq (6-1)}$$

where, A_p is the surface area of the particles, h is the heat transfer coefficient, λ is the latent heat of sublimation, T_p is the particle temperature, M is the mass of sample and T_g is the gas temperature in contact with the particles. The gas temperature T_g needs to be corrected by an amount ΔT_{offset} obtained at zero drying rate due to warming of gas in the fluidising chamber.

$$T_g = T_{inlet} + \Delta T_{offset} \qquad \text{Eq (6-2)}$$

$$\Delta T = T_g - T_p = T_{inlet} + \Delta T_{offset} - T_p \qquad \text{Eq (6-3)}$$

As the mass of dry whey also remains constant, the above equation can be expressed in terms of dry basis moisture content, i.e.

$$W = \frac{M}{M_{dry}} \Rightarrow \frac{dW}{dt} = \frac{1}{M_{dry}}\frac{dM}{dt} \qquad \text{Eq (6-4)}$$

$$-\frac{dW}{dt} = k(T_g - T_p) \qquad \text{Eq (6-5)}$$

where, k is the constant,

$$k = \frac{hA_p}{\lambda M_{dry}} \qquad \text{Eq (6-6)}$$

Integrating equation (6-5) over the whole time of the experiment yields:

$$W_i - W_f = k\int_0^{t_f}(T_g - T_p)dt \qquad \text{Eq (6-7)}$$

where, W_i is the initial dry basis moisture content and W_f is the final dry basis moisture content, Thus evaluating the area under the curve of T_g-T_p versus t (figure 6-3), combined with a knowledge of the initial (2.0 kg/kg) and final dry basis moisture contents enables the value of k to be determined.

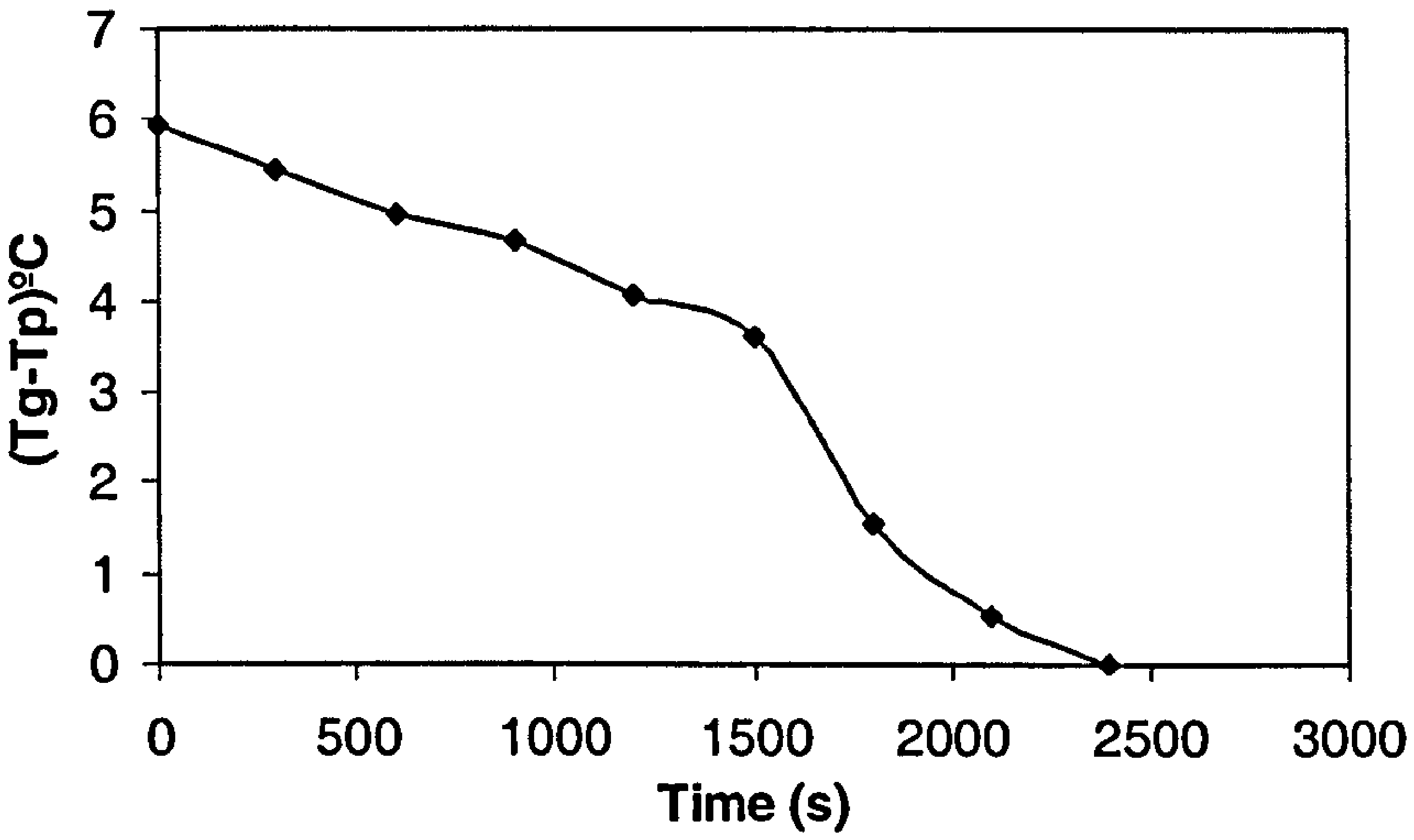

Figure 6-3: "Wet bulb" depression (difference of outlet gas and particle temperature) versus time during the freeze drying of whey at 0.1 bara.

Integrating equation (6-5) to intermediate times yields:

$$W_i - W = k\int_0^t (T_g - T_p)dt \qquad \text{Eq (6-8)}$$

Equation (6-7) thus offers a means of obtaining a basic drying curve for the material. This assumes that the material in contact with the particle bed thermocouple is representative of the bed as a whole. The drying curve obtained from this analysis is shown in figure (6-4), which shows a gradually decreasing rate of drying.

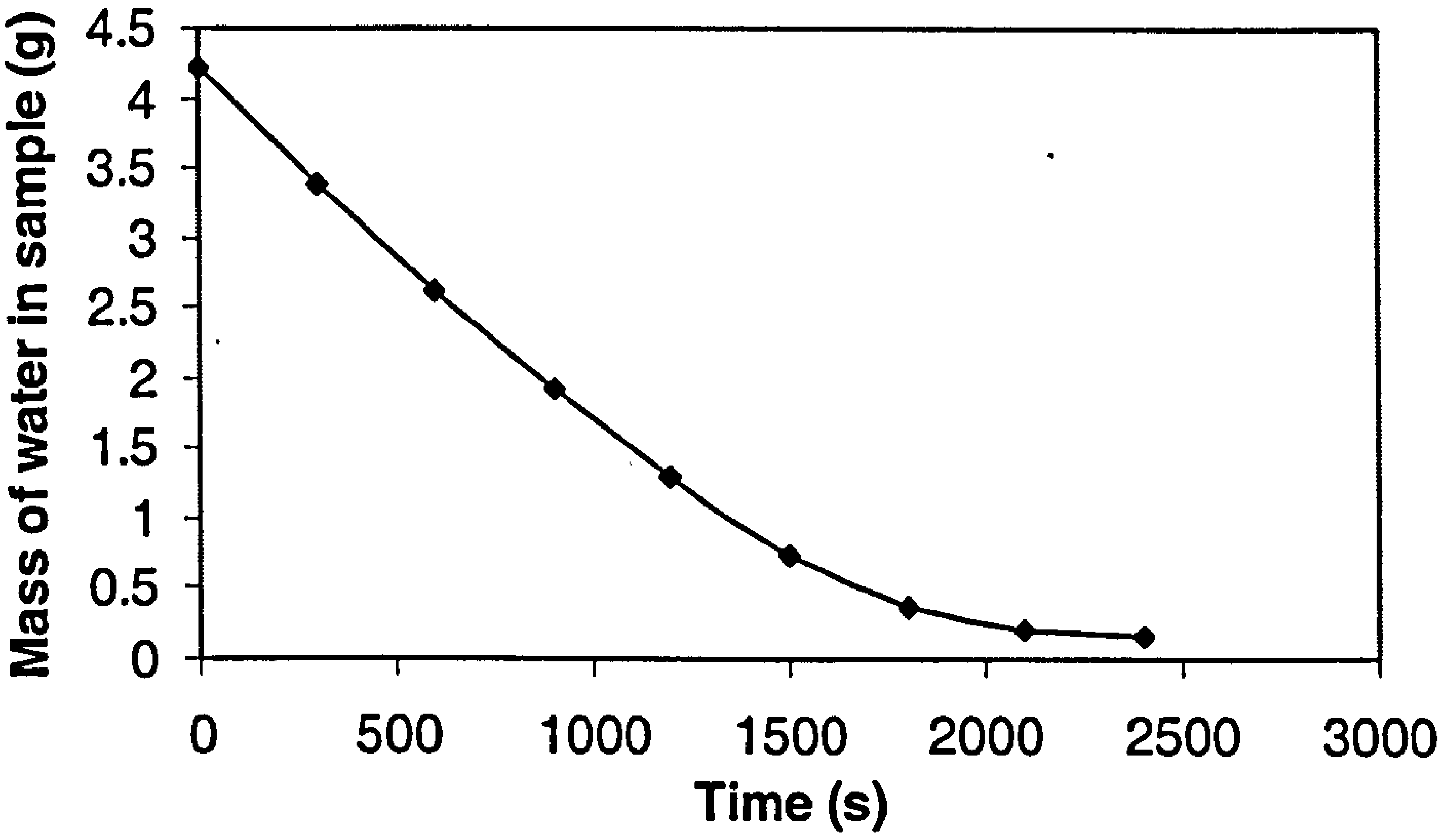

Figure 6-4: Drying curve calculated from the temperature data shown in figure (6-3).

The difference of outlet gas and particle temperature versus time during the freeze drying of all the trials are given in the figures (6-5).

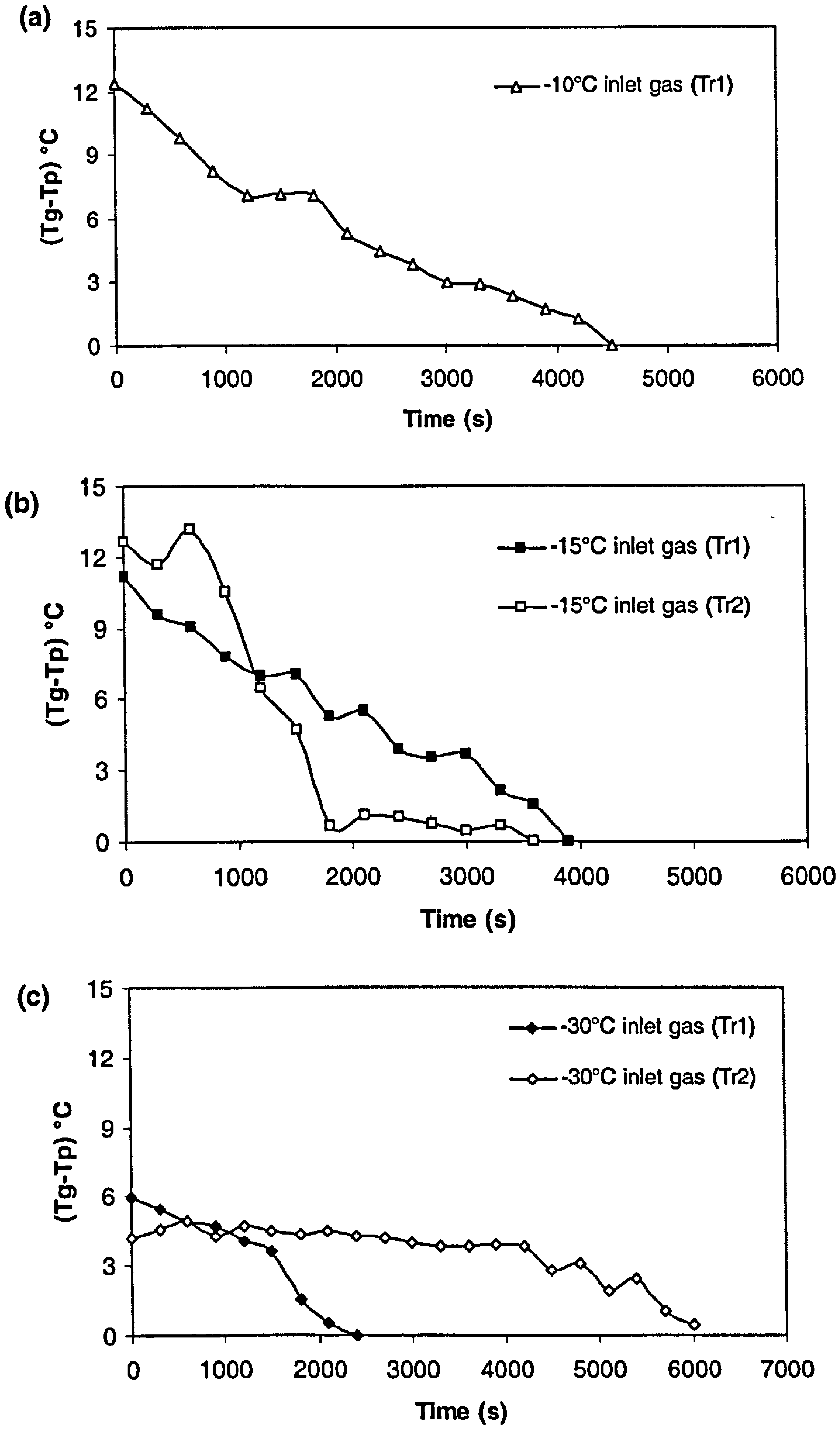

Figure 6-5: "Wet bulb" depression versus time during the freeze-drying of whey at 0.1 bara at (a) -10°C, (b) -15°C and (c) -30°C inlet gas temperatures.

The drying curves were obtained for the other trials using the same method and are shown in figure (6-6).

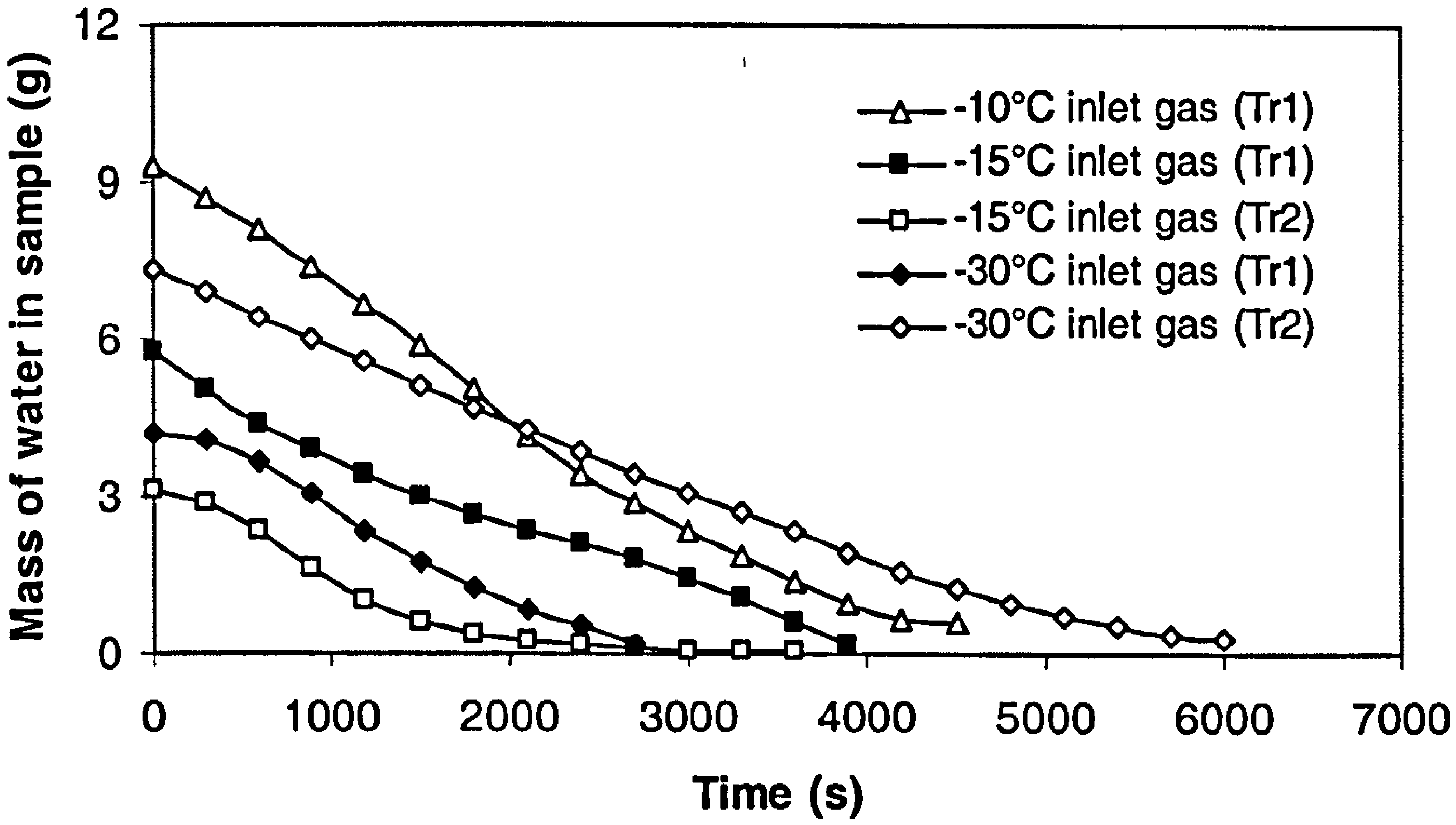

Figure 6-6: Drying curves of all the trials.

The drying rates of various trials in figure (6-6) were calculated from different initial masses, because of the difficulties in transferring reproducible quantities to the fluidised bed unit. The trials at higher inlet gas temperatures have show moderately higher drying rates; low initial mass trials also have showed higher drying rates, with drying times of less than an hour.

Table (6-2) shows the experimental and theoretical minimum drying times, obtained by assuming that the gas leaving the dryer is saturated. This is almost certainly likely to be untrue, but it puts a lower bound estimate on the drying time. The large difference between lower bound estimate and experimental drying times indicates that the limiting factor is not the supply of gas to the system, but rather internal or particle/gas mass transfer resistances.

Table 6-2: Theoretical estimated and experimental drying time.

Inlet gas temperature (ºC)	Trials	Feed (g)	Initial water mass (g)	Theoretical minimum time to dry * (s)	Experimental drying time (s)
-10± 1.0 °C	Tr 2	11.6	9.3	156	4500
-15± 1.0 °C	Tr 1	7.2	5.7	150	3900
	Tr 2	3.9	3.1	78	3600
-30± 1.0 °C	Tr 1	5.3	4.2	450	2700
	Tr 2	9.1	7.3	774	6000

* assuming saturated outlet gas and vacuum pump operating at 100 m^3/hr

6.6 Solubility analysis

The RP-HPLC chromatograms for whey protein isolate before and after spray freeze drying are shown in figures (6-7 a) and (6-7 b) respectively. The chromatograms can clearly resolve the individual peaks for α-lactalbumin and β-lactoglobulin. From the areas of these peaks, it was determined that there was no detectable loss of solubility of α-lactalbumin, whereas 2 % loss of solubility of β-lactoglobulin was shown during spray-freeze-drying of WPI in all trials. Thus only mild loss of solubilities in β-lactoglobulin occurs during spray-freeze-drying.

(a)

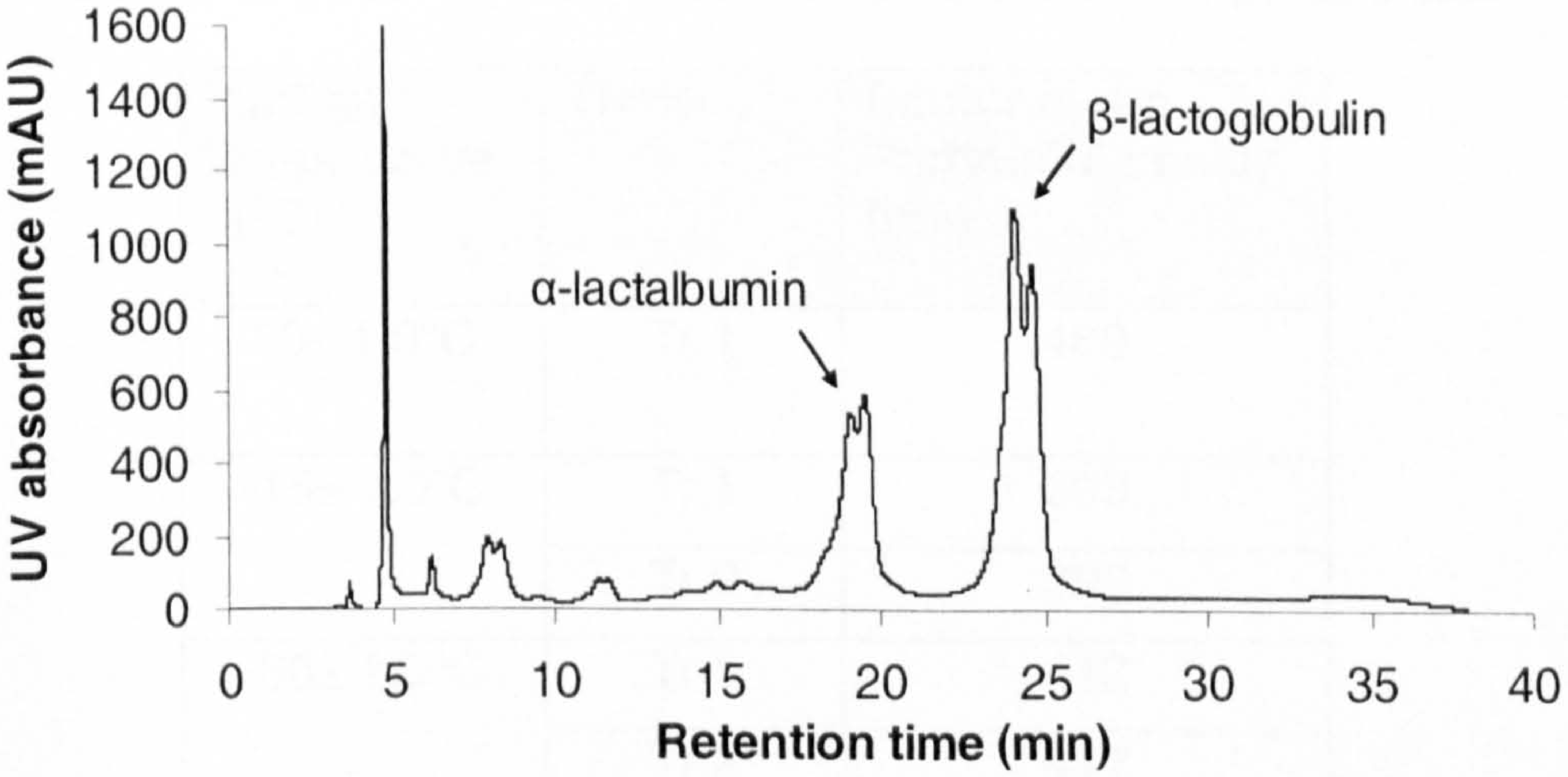

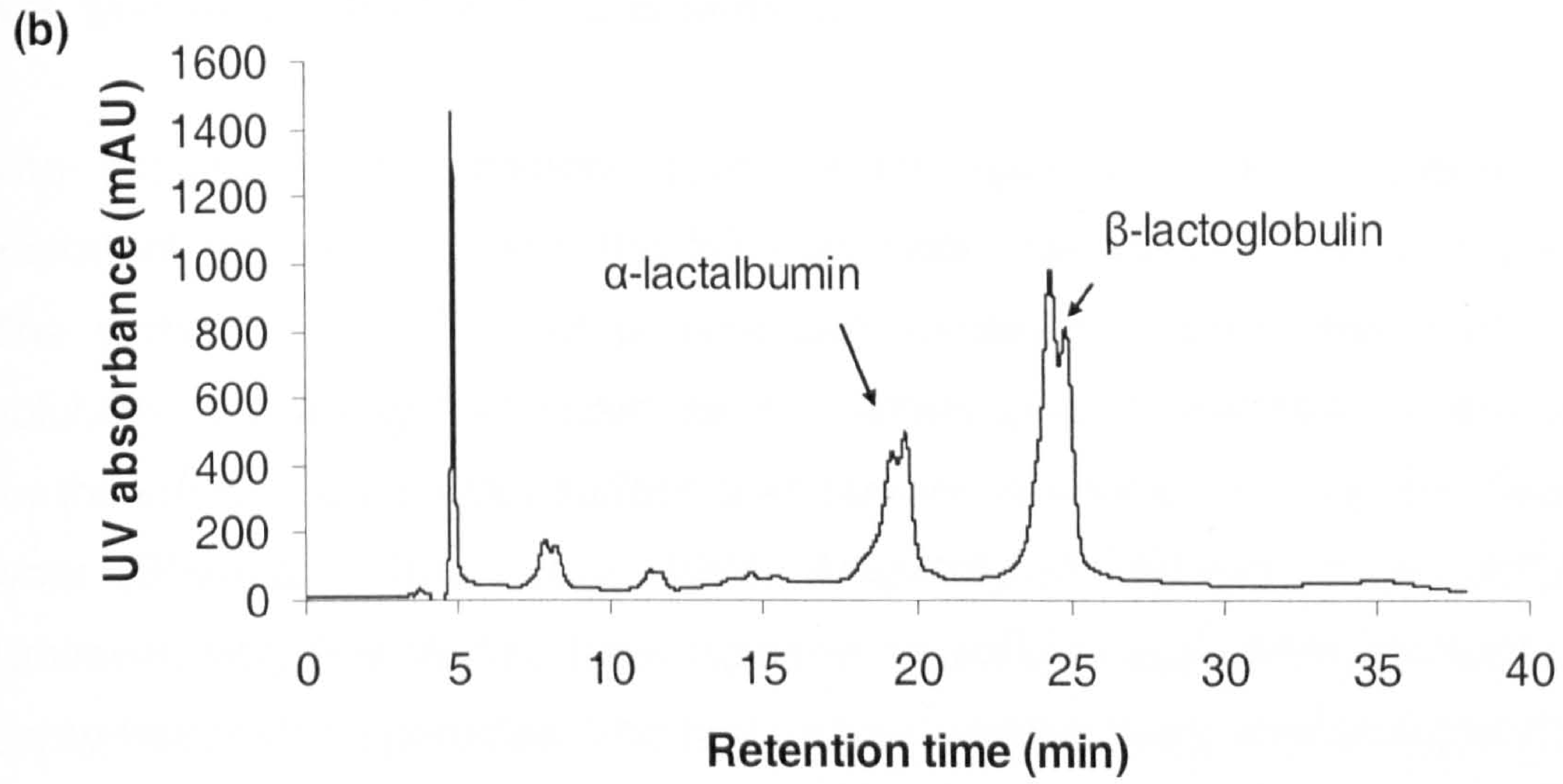

Figure 6-7: RP-HPLC chromatograms of spray-freeze-dried whey protein isolate (a) untreated WPI sample, (b) spray-freeze-dried WPI.

6.7 Particle size analysis

The Sauter mean particle diameters of all the spray-freeze-dried powders were in the range of 393 to 489 µm (Table 6-3). Larger diameter particles were found when an inlet temperature of -10°C was used. However, all the trials have shown significantly larger particle sizes. The variation in the mean diameter (Table 6-3) is due to agglomeration of the particles during drying that increases the particle size.

Table 6-3: Effect of VFBFD inlet temperature on the particle size.

Inlet gas temperature (°C)	Trials	Sauter mean Particle diameter (µm)
-10± 1.0°C	Tr 1	489
-15± 1.0°C	Tr 1	393
	Tr 2	396
-30± 1.0°C	Tr 1	412
	Tr 2	417

6.8 Microstructure of SFD powders

The analysis of the microstructure of the spray-freeze-dried product is important for understanding the SFD process and products characteristics. The surface composition of powder can influence its properties such as, solubility, flow ability and stickiness. Numerous studies have been performed for the spray-dried powder surface and internal structures including this thesis work (Sheu and Rosenberg, 1998; Anandharamakrishnan *et al.*, 2007). However, very few studies have reported on surface and micro structures of spray-freeze-dried particles. The first particle surface study was performed by Al-Hakim and Stapley (2004) with cryo-SEM images of spray-freeze dried whey protein powders and recently, MacLeod *et al.* (2006) studied cryo-SEM images of frozen droplets and conventional freeze-dried coffee and Hindmarsh *et al.* (2007) studied the surface and internal structure of frozen droplets of sucrose solution by adding anhydrous milk fat and whey protein concentrate. The present work focuses on the surface and internal structure of spray-freeze-dried WPI powders.

Figures (6-8, 6-9 and 6-10) show the SEM images of whey protein powders produced by spray-freeze-drying at -10°C, -15°C and -30°C inlet gas temperatures, respectively. At -10°C feed gas temperature (figures 6-8 a-b) there are many broken particles, with some irregular shapes, compared with the -30°C trial (see Figure 6-10 a). This may be due to *collapse*, the WPI glass transition temperature (T_g) was evaluated and found to be -25.8°C, as suggested by the DSC measurements of section 6.2.

Some areas of the figures have been marked to aid interpretation as follows:

A - is the surface of the particles
B - is the pores structure created during ice sublimation
C - is the inside core region of the particles

The surfaces of the particles (figures 6-8 c, 6-9 b and 6-10 b) are generally smooth (*A region*) containing small pores and an occasional surface blemish.

A magnification of one of these blemishes surface is shown in figure (6-9 e-f), which reveals a porous structure inside the particle (*C region*). This is to be expected from a freeze dried product, and is a consequence of ice crystal formation during the freezing step, which sublimes during freeze drying to leave a porous structure. Due to the very fast rates of freezing at this size scale the ice crystals – and hence pore sizes – are much smaller than normally found in freeze dried products. Figures (6-10 c-d) shows this at greater magnification. Figures (6-8 c, 6-9 b, 6-10 b-d) shows a similar surface nature for the particles from all the trials.

Figures (6-8 d, 6-9 c-d, 6-10 e-f) shows the internal pore structure created by the ice sublimation route (*B region*). Examples of the pore route are shown in figures (6-10 b and e) with circular marks. These micro structures are very similar to those found by Hindmarsh *et al.* (2007) in their cryo-SEM images of frozen droplets. During the freezing stage, whey proteins were absorbed on the ice/liquid interface and during the drying stage, when ice was removed it left voids at the centre core; hence WPI particles appears as a perforated shell wall, as shown in figures (6-10 c-d). Figures [6-8 d (marked C), 6-9 (marked C), 6-10 (marked C)] show hollow cavities that suggest the formation of gas bubbles inside the particles. These bubbles are likely to result from dissolved gas being releasing during atomisation, as the feed is held under pressure (6 bar) using compressed nitrogen in the feed chamber. Yu *et al.* (2006) also reported that small bubbles were generated during atomisation and they also observed bubbles were presented in the particles during SFV/L process.

The SEM image in figure (6-8 a-b) shows the agglomeration of the particles. However, freeze-drying operation should be operated below the material collapse temperatures. Based on the DSC experiment (section 6.2), freeze-drying of whey proteins should be operated below -25.8°C to avoid structural collapse. Hence, an inlet gas temperature of -30°C is suitable for drying of

WPI. Nevertheless, SFD process needs to be optimised to produce a large quantity of the powders without any agglomeration.

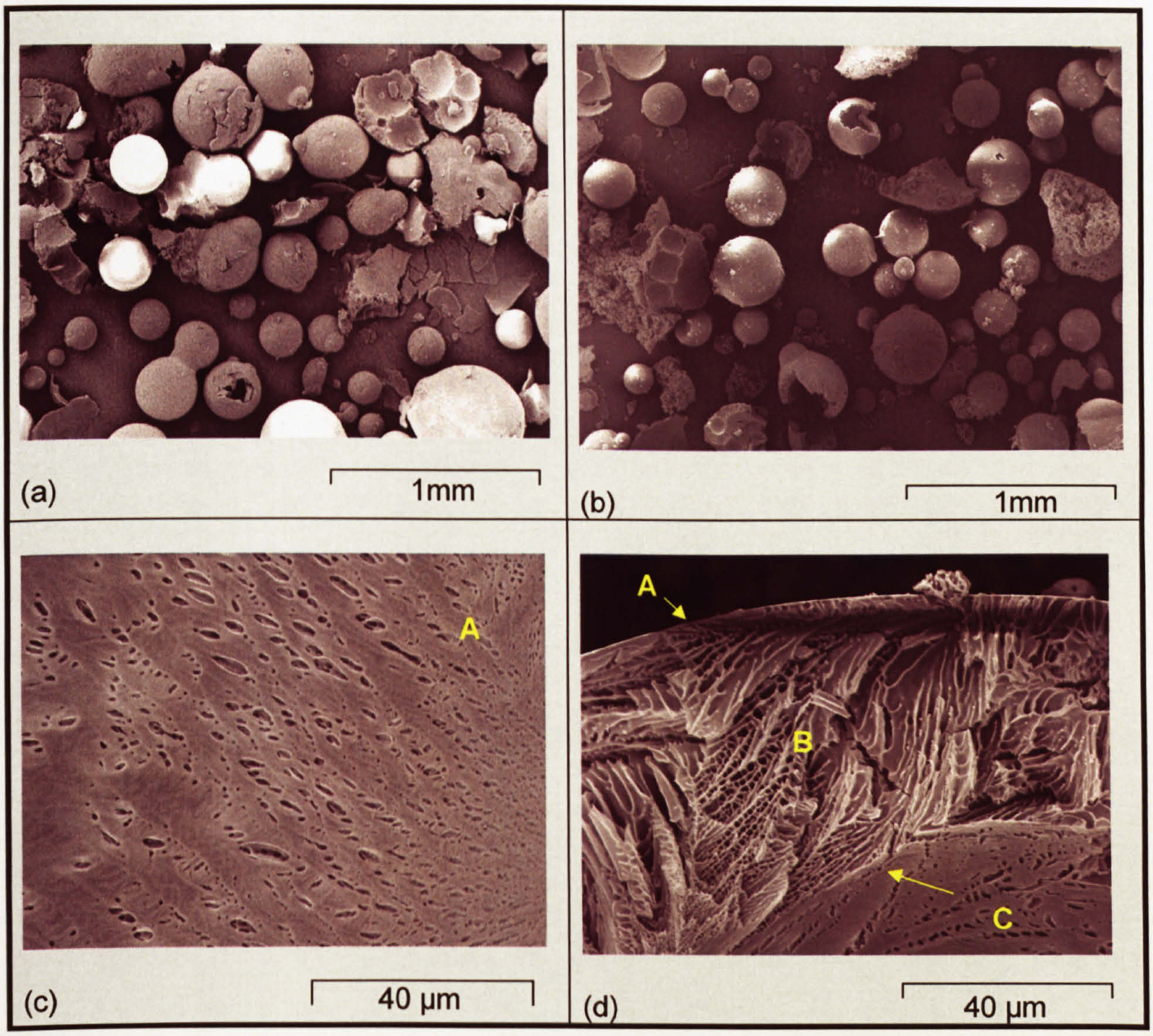

Figure 6-8: SEMs of spray-freeze-dried whey protein powders at -10°C inlet gas temperature (A - surface of the particles, B - pore structure created following ice sublimation, C - inside core region of the particles).

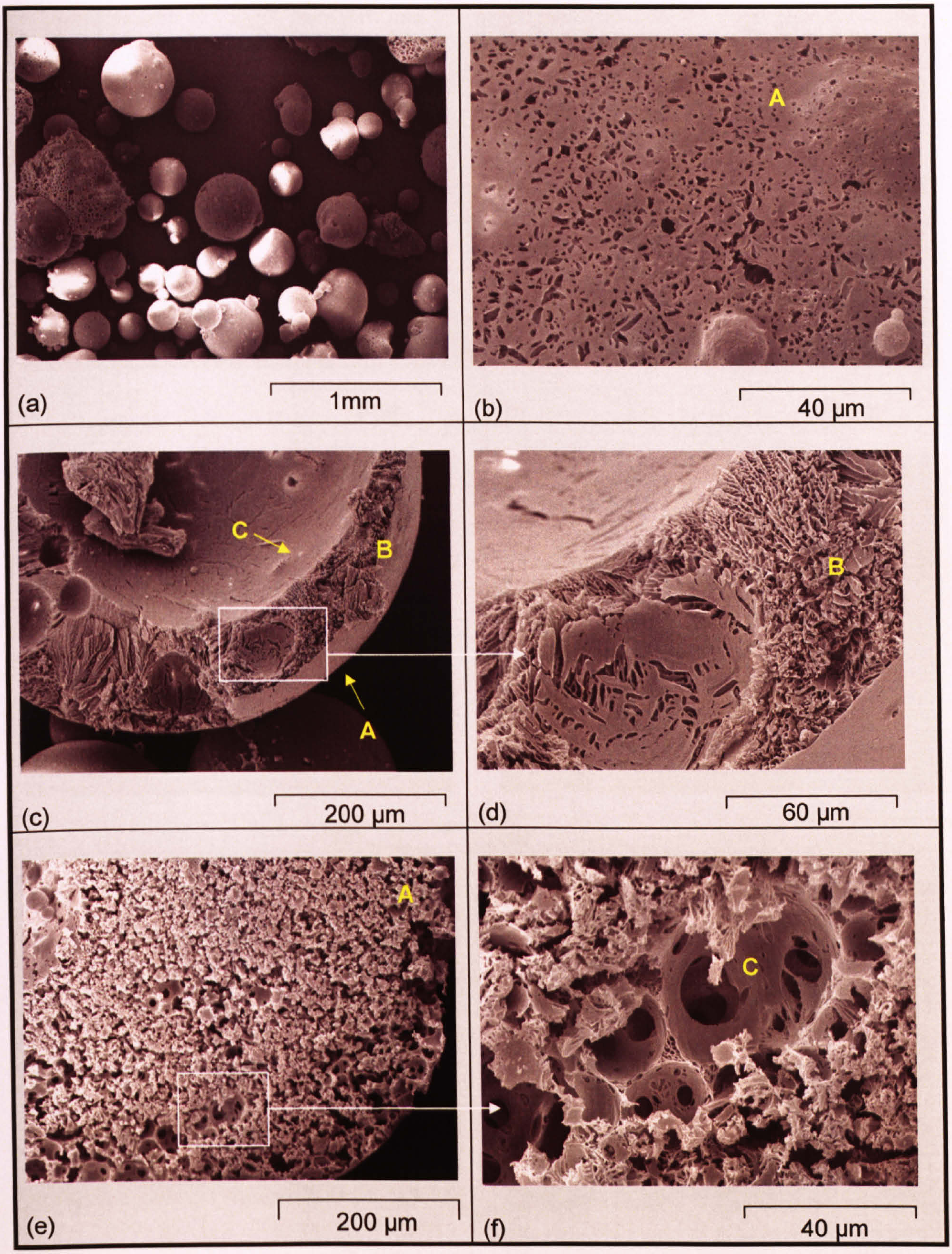

Figure 6-9: SEMs of spray-freeze-dried whey protein powders at -15°C inlet gas temperature (A - surface of the particles, B - pores structure created following ice sublimation, C - inside core region of the particles).

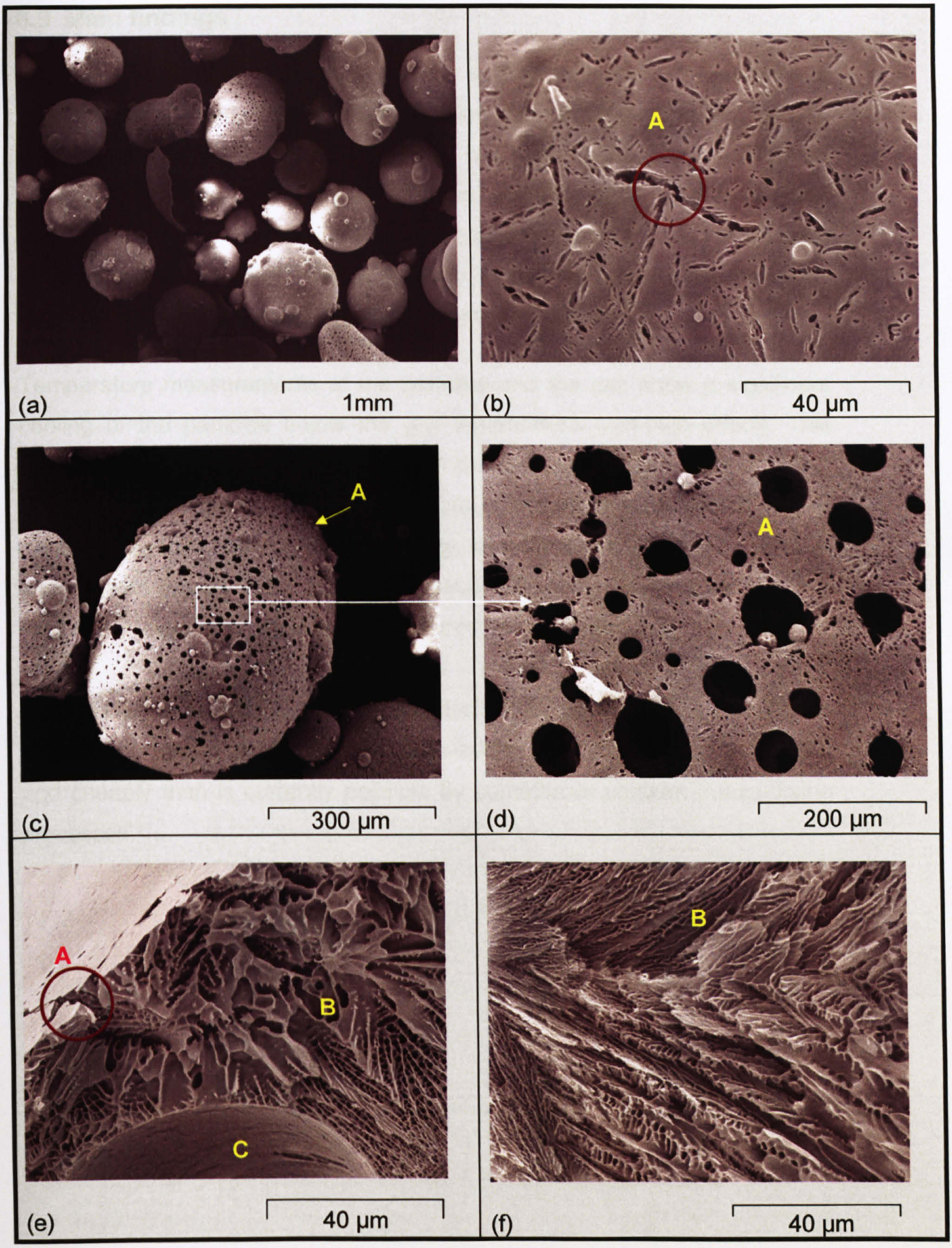

Figure 6-10: SEMs of spray-freeze-dried whey protein powders at -30°C inlet gas temperature (A - surface of the particles, B - pores structure created following ice sublimation, C - inside core region of the particles).

6.9 Main findings

The results presented here show that the spray-freeze-drying technique has been shown to work well when performing the freeze-drying step at sub-atmospheric pressures (0.1 bar). Not only has rapid drying been obtained (of the time scale of one hour), but the particles were not eluted from the fluidised bed. The technique has been shown to produce acceptable drying times even at temperatures of -30°C, which is likely to be below the glass transition temperature of the maximally freeze concentrated WPI matrix.

Temperature measurements of the particles and the gas show a significant cooling of the particles below the gas temperature (wet-bulb effect). This gradually diminishes during drying and can be used to construct a drying curve. The resulting product is highly porous and there is no loss of protein solubility for α-lactalbumin and very little loss for β-lactoglobulin. The SEM images also have shown a fine pore structure within the particles and this study also reveals that bubble formation occurs during atomisation.

Spray-freezing combined with VFBFD technique therefore has potential to produce pharmaceutical and high-value-added food products more quickly and cheaply than is currently possible by commercial vacuum freeze-drying processes.

Chapter 7

Computational Fluid Dynamics (CFD) simulation studies of spray drying

7.1 Introduction

This chapter deals with the development of a Computational Fluid Dynamics (CFD) model for the gas flow pattern and particle time histories such as, velocity, temperature and residence time during the spray-drying operation. The initial sections of this chapter cover the principles of CFD and the spray drying simulation methodology, followed by results and discussions of two different case studies performed using the Fluent 6.3 CFD package:

> ***Case A***: Short-form spray dryer simulation using the same geometry and boundary conditions as a simulation that has been published in the literature along with experimental results.
>
> ***Case B***: Tall-form spray dryer simulation (the spray drying rig described in Chapter 3 and Chapter 5).

The strategy is to use *Case A* to validate the simulation methods used here. The same methods will then be used to explore the spray drying operation studied in Chapter 5.

7.2 Problem description

The problem associated with simulating the spray drying process is to predict the particle temperature, thermal denaturation and size and shape of the particles during the drying operation. Moreover, modelling these variables is very difficult. Several numerical models have been developed in the past decades (Parti and Palancz, 1974; Katta and Gauvin 1975; Gauvin and Katta, 1976; Masters, 1991). However, most of the numerical models have neglected variations in air temperature, residence time and also flow of air and particles. Now it is possible to model spray-air mixing by combining airflow and particle trajectories using CFD packages. The co-current spray dryer configuration is preferred to counter-current operation for protein systems, as high rates of evaporative cooling from the wet droplet are able to maintain droplet temperatures far below those of the hot inlet gas. However, the particle (proteins) recirculation within the chamber may lead to denaturation, as dried particles will be exposed to the higher inlet air temperature. Against this background, it is important to understand the particles histories such as temperature, velocity, residence time and particles impact positions on the chamber wall during spray-drying to improve the product quality.

7.3 Theory of CFD modelling

CFD is a numerical technique for the solution of the equations governing the flow of fluids inside a defined flow geometry. The flow of any fluid can be described using the following transport equations (7-1 to 7-17) (Bird *et al*, 1960; Versteeg and Malalasekera, 1995; Bakker, 2002; Fluent 2005). These equations are derived by considering mass, momentum and energy balances in an element of fluid, resulting in a set of partial differential equations. They are completed by adding other algebraic equations from thermodynamics such as the equation of state for density and a constitutive equation to describe the rheology (Fletcher, 2000).

(a) Conservation of mass equation

The continuity equation describes the rate of change of density at a fixed point resulting from the divergence in the mass velocity vector $\rho\underline{v}$. Equation (7-1) is the steady, three-dimensional, mass conservation or continuity equation for the simplified case of a constant density fluid (incompressible fluid).

$$\nabla \cdot \underline{v} = 0 \qquad \text{Eq (7-1)}$$

where, ∇ has the dimensions of reciprocal length:

$$\nabla = \frac{\partial}{\partial x} i + \frac{\partial}{\partial y} j + \frac{\partial}{\partial z} k \qquad \text{Eq (7-2)}$$

(b) Momentum equation

The principles of the conservation of momentum is an application of Newton's Second Law of Motion to an element of fluid and states that a small volume of element moving with the fluid is accelerated because of the force acting upon it.

$$\rho_g \frac{D\underline{v}}{Dt} = -\nabla p + \nabla \cdot \underline{\underline{\tau}} + \rho_g \underline{g} \qquad \text{Eq (7-3)}$$

In equation (7-3), the convection terms are on the left side and the right hand side are the pressure gradient (p), source terms of gravitational force ($\underline{g}$) and stress tensor ($\underline{\underline{\tau}}$), which is responsible for diffusion of momentum.

(c) Energy equation

The first law of thermodynamics states that the time rate of change of internal energy plus kinetic energy is equal to the rate of heat transfer less the rate of work done by system. Fluent solves the energy equation in the following form.

$$\frac{\partial}{\partial t}(\rho E) + \nabla . \left[\underline{v}(\rho E + p) \right] = \nabla . \left[k_{eff} \nabla T - \sum_j h_j \underline{J}_j + (\underline{\underline{\tau}} . \underline{v}) \right] \qquad \text{Eq (7-4)}$$

where, E is the internal (thermal) energy, k_{eff} is the effective conductivity (k_{ta}+ k_t , where, k_{ta} is thermal conductivity and k_t is turbulent thermal conductivity), T is the temperature, $\underline{\underline{\tau}}$ is stress tensor and $\underline{J}_j$ is the diffusion flux of species j, h_j is the enthalpy of species j. The three terms on the right-hand side of the equation represent energy transfer due to conduction, species diffusion and viscous dissipation respectively.

7.3.1 Turbulence model

Most commercial CFD codes use turbulence models that are based on the splitting up of instantaneous quantities into a time-averaged and a fluctuating part by a process known as Reynolds decomposition. For turbulent flows, the standard k-ε model (k- turbulence kinetic energy and ε- turbulence dissipation rate) is the most commonly used, because it converges considerably better than Reynolds stress model (RSM) (Versteeg and Malalasekera, 1995) (see detailed discussions in section 2.7.3). In this work, spray-drying and spray-freezing operations have no swirling flows inside the chamber, hence the standard k-ε turbulence model was used. The transport of the turbulence kinetic energy k and its dissipation rate ε is given as follows:

$$\frac{\partial}{\partial t}(\rho k)+\nabla\cdot(\rho k\underline{v})=\nabla\cdot\left[\left(\mu+\frac{\mu_t}{\sigma_k}\right)\nabla k\right]+G_k-\rho\varepsilon \qquad \text{Eq (7-5)}$$

and

$$\frac{\partial}{\partial t}(\rho\varepsilon)+\nabla\cdot(\rho\varepsilon\underline{v})=\nabla\cdot\left[\left(\mu+\frac{\mu_t}{\sigma_\varepsilon}\right)\nabla\varepsilon\right]+C_{1\varepsilon}\frac{\varepsilon}{k}(G_k)-C_{2\varepsilon}\rho\frac{\varepsilon^2}{k}$$

Eq (7-6)

G_k is the generation of kinetic energy due to the mean velocity gradients. The quantities σ_k and σ_ε are the turbulent Prandtl numbers for k and ε, respectively and $C_{1\varepsilon}$, $C_{2\varepsilon}$, are constant. The turbulent (or eddy) viscosity, μ_t is calculated from k and ε as follows

$$\mu_t=\rho C_\mu\frac{k^2}{\varepsilon} \qquad \text{Eq (7-7)}$$

The model constants $C_{1\varepsilon}$, $C_{2\varepsilon}$,, C_μ σ_k and σ_ε took the following values (Launder and Spalding, 1972):

$$C_{1\varepsilon}=1.44,\ C_{2\varepsilon}=1.92,\ C_\mu=0.09,\sigma_k=1.0 \text{ and } \sigma_\varepsilon=1.3$$

For calculating an approximate solution of fluid flow equations, the equations have to be made discrete. For this, the flow domain is divided into number of control volumes. This is called a *grid* and at each *grid* cell approximate solutions for the Navier-Stokes and the continuity equations are calculated.

7.3.2 Particle tracking

Both the Eulerian-Eulerian and Eulerian-Lagrangian methods have been used in published simulations of spray drying (discussed in section 2.7.2). However, the Eulerian-Lagrangian frame work was selected for this work, because it provides residence times of individual particles with a large range of particle sizes. Crowe *et al.* (1977) first proposed the particle source in cell (PSI-Cell) model. This is the basis for the discrete phase model (DPM).

In the DPM, the flow field is divided into a grid defining computational cells around each grid point. Each computational cell is treated as a control volume for the continuous phase (gas phase). The droplets are treated as sources of mass, momentum and energy inside the each control volume. The gas phase is regarded as a continuum (Eulerian approach) and is described by first solving the gas flow field assuming no droplets are present. Using this continuous phase flow field, droplet trajectories together with size and temperature histories along the trajectories are calculated. The mass, momentum and energy source terms for each cell throughout the flow field are then determined. The source terms are evaluated from the droplet equation and are integrated over the time required to cross the length of the trajectory inside each control volume. The results are multiplied (scaled up) by the number flow rate of drops associated with this trajectory (Crowe *et al.*, 1977; Papadakis and King, 1988; Fluent 2005).

The gas flow field is solved again, incorporating these source terms and then new droplet trajectories and temperature histories are calculated. This approach provides the influence of the droplets on the gas velocity and temperature fields. The method proceeds iteratively calculating gas and particle velocity fields. The computational scheme of the PSI-Cell model is shown as a flow chart in figure (7-1).

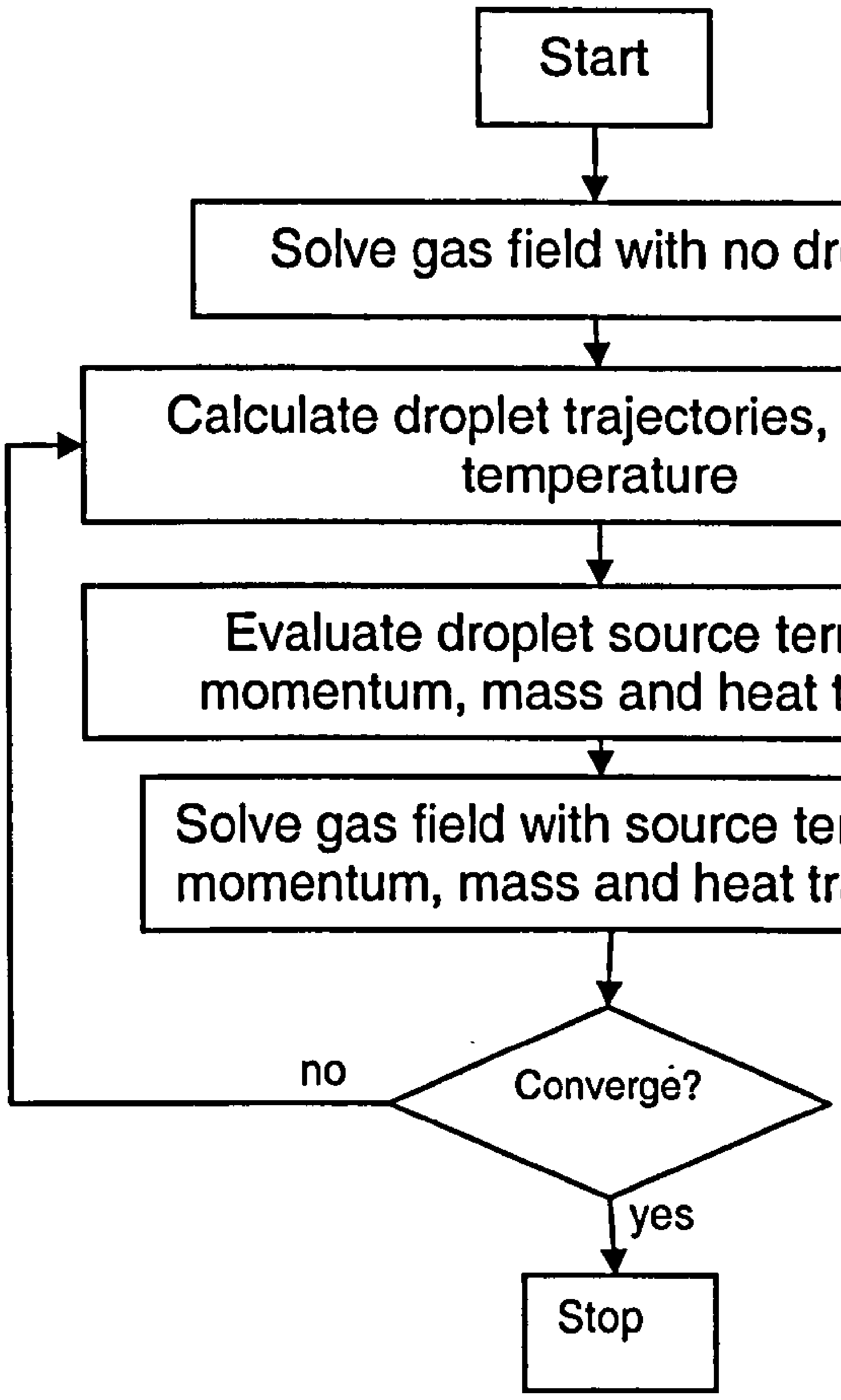

Figure. 7-1: Flow chart of PSI-Cell computational scheme (Crowe *et al.*, 1977).

The range of droplet sizes produced by the atomiser is represented by a number of discrete droplet sizes. Each initial droplet size is associated with one trajectory, along which the number flow rate of drops is constant, assuming that no coalescence or shattering occurs. Once the air velocities, temperatures, and humidities are postulated, the transport equations for the droplets of each size are integrated over time and position to yield droplet trajectories, velocities, sizes and temperatures. Calculations for droplets of each initial size continue until the volatile fractions (e.g. water) in the droplets evaporate completely, exit the column, or impact the column wall (Papadakis and King, 1988; Fluent, 2005).

7.4 Spray drying CFD simulation methodology

In this work, the CFD code Fluent 6.3 was used to simulate the three-dimensional configuration of a co-current flow spray-dryer fitted with a pressure nozzle for *Case A* and air blast atomiser for *Case B*. Two-way coupling between the drying medium and droplet was considered, where the DPM model was used. The finite volume method has been used to solve the partial differential equations of the model using the SIMPLE (Semi-Implicit Pressure-Linked Equations) method for pressure-velocity coupling and a Second Order Upwind scheme to interpolate the variables on the surface of the control volume; the standard k-ε turbulent model was used. The species transport model was selected with DPM and it gives the prediction of simultaneous heat and mass transfer during the drying process.

The combined Eulerian and Lagarangian model is used to obtain particle trajectories by solving the force balance equation:

$$\frac{d\underline{u}_p}{dt} = \frac{18\mu}{\rho_p d_p^{\,2}} \frac{C_D \mathrm{Re}}{24} (\underline{v} - \underline{u}_p) + \underline{g}\left[\frac{\rho_p - \rho_g}{\rho_p}\right] \qquad \text{Eq (7-8)}$$

where, $\underline{v}$ is the fluid phase velocity, $\underline{u}_p$ is the particle velocity, ρ_g is the density of the fluid and ρ_p is the density of the particle.

The particle force balance (equation of motion) includes discrete phase inertia, aerodynamic drag and gravity. The slip Reynolds number (Re) and drag coefficient (C_D) are given in the following equations.

$$\mathrm{Re} = \frac{\rho_g d_p |\underline{u}_p - \underline{v}|}{\mu} \qquad \text{Eq (7-9)}$$

$$C_D = a_1 + \frac{a_2}{Re} + \frac{a_3}{Re^2} \qquad \text{Eq (7-10)}$$

where, d_p is the particle diameter, and a_1, a_2 and a_3 are constants that apply to smooth spherical particles over several ranges of Re given by Morsi and Alexander (1972).

The velocity of particles relative to air velocity was used in the trajectory calculations (equation 7-8). Turbulent particle dispersion was included in this model as discrete eddy concept (details in Fluent manual, 2005). In this approach, the turbulent air flow pattern is assumed to be made up of a collection of randomly directed eddies, each with its own lifetime and size. Particles are injected into the flow domain at the nozzle point and envisaged to pass through these random eddies until they impact the wall or leave the flow domain through the product outlet. In this study, particle stickiness and particle-particle collisions (agglomeration) were not considered.

The heat and mass transfer between the particles and the hot gas is derived following the motion of the particles.

$$m_p c_p \frac{dT_p}{dt} = hA_p(T_g - T_p) + \frac{dm_p}{dt} h_{fg} \qquad \text{Eq (7-11)}$$

where, m_p is the mass of the particle, c_p is the particle specific heat, T_p is the particle temperature, h_{fg} is the latent heat, A_p is the surface area of the particle and h is the heat transfer co-efficient

The heat transfer coefficient was (h) obtained from the Ranz-Marshall (1952) equation.

$$Nu = \frac{hd_p}{k_{ta}} = 2 + 0.6(Re_d)^{1/2}(Pr)^{1/3} \qquad \text{Eq (7-12)}$$

where, Prandtl number (Pr) is defined as follows

$$Pr = \frac{c_p \mu}{k_{ta}} \qquad \text{Eq (7-13)}$$

where, d_p is the particle diameter, k_{ta} is the thermal conductivity of the fluid, μ is the molecular viscosity of the fluid.

The mass transfer rate (for evaporation) between the gas and the particles is calculated from the following equation.

$$\frac{dm_p}{dt} = -k_c A_p \left(Y_s^* - Y_g\right) \qquad \text{Eq (7-14)}$$

where, Y_s^* is the saturation humidity, Y_g is the gas humidity and k_c is the mass transfer co-efficient and it can be obtained from Sherwood number

$$Sh = \frac{k_c d_p}{D_{i,m}} = 2 + 0.6(\mathrm{Re}_d)^{1/2}(Sc)^{1/3} \qquad \text{Eq (7-15)}$$

where, $D_{i,m}$ is the diffusion coefficient of water vapour in the gas phase and Sc is the Schmidt number, defined as follows

$$Sc = \frac{\mu}{\rho_g D_{i,m}} \qquad \text{Eq (7-16)}$$

The values of vapour pressure, density, specific heat and diffusion coefficients were obtained from various sources (Perry, 1984; Incropera, 2007) and used as piece-wise linear functions of temperature in this model.

When the temperature of the droplet has reached the boiling point and while the mass of the droplet exceeds the non-volatile fraction. The boiling rate model was applied (Fluent manual, 2005).

$$\frac{d(d_p)}{dt} = \frac{4k_{ta}}{\rho_p c_g d_p}(1 + 0.23\sqrt{\mathrm{Re}})\ln\left[1 + \frac{c_g (T_g - T_p)}{h_{fg}}\right] \qquad \text{Eq (7-17)}$$

where, k_{ta} is the thermal conductivity of the gas and c_g is the heat capacity of the gas.

7.5 *Case A* : Short-form spray dryer

In order to validate the CFD simulation methodology with experimental results, Kieviet's (1997) experimental conditions were used. He employed a co-current, cylinder-on-cone short-form dryer chamber.

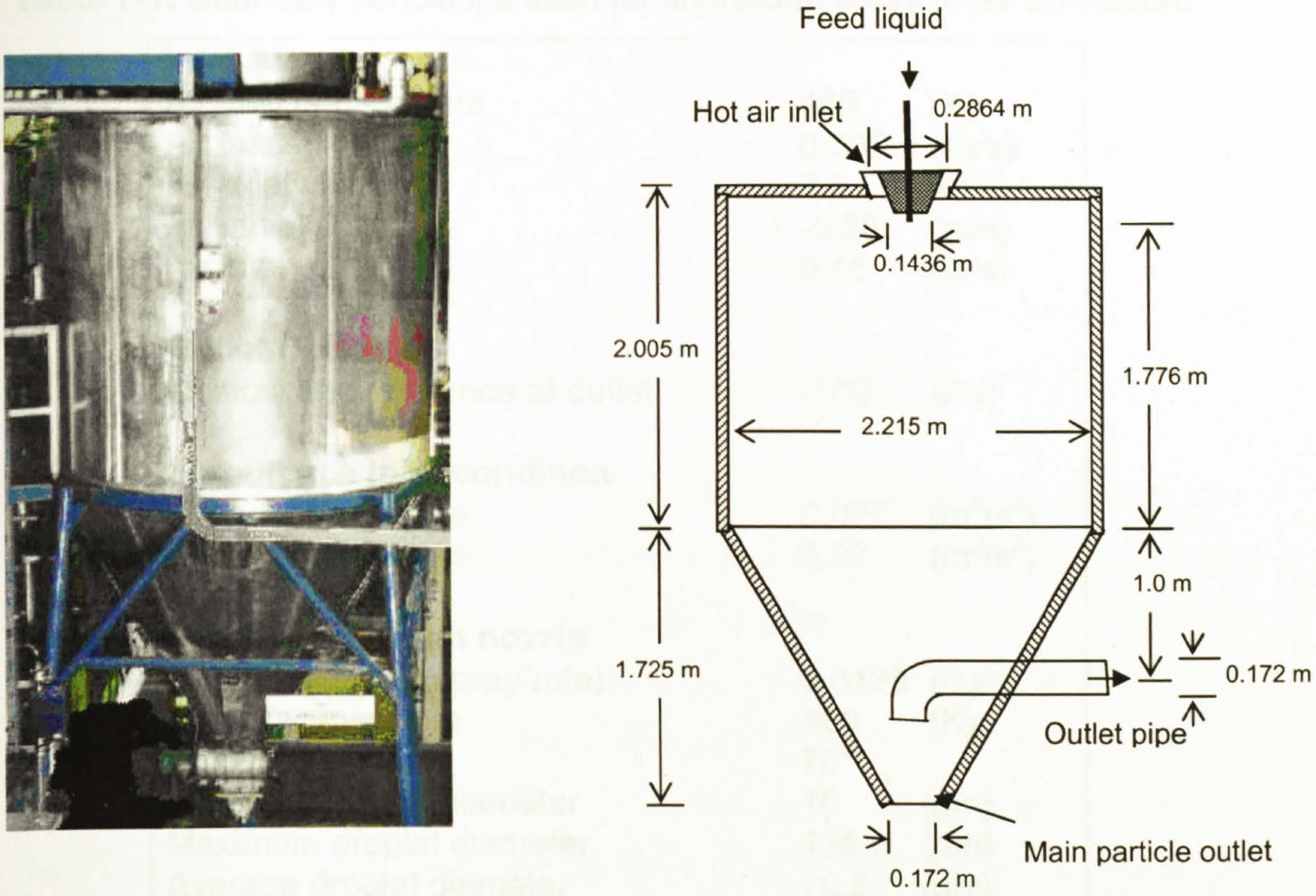

Figure 7-2: Spray-dryer geometry (Kieviet, 1997).

The geometry is shown in figure (7-2), with the pressure nozzle atomiser located at the top of the chamber and the drying air enters through an annulus. The outlet air line is a bent pipe mounted at the cone centre and is connected to the cyclone to separate the particles from the gas stream.

7.6 Boundary conditions

In order to compare this simulation results with experimental data and simulations of previous workers (Kieviet, 1997; Huang *et al.*, 2006), the same boundary conditions were used in this simulation. The feed liquid was 42.5% solids maltodextrin suspension. The remaining boundary conditions are given in Table (7-1). The outlet pressure was set as -100 Pa relative to the inlet (this assumes that a fan draws air out from the drying chamber). The CFD simulation was performed with a dual processor Xeon 3.8 GHz Genie workstation with 512 cache-memory, 3 GB RAM-memory and 400 GB hard disc memory. The running time of all the simulations took approximately 20 hrs.

Table 7-1: Boundary conditions used for short-form spray dryer simulation.

Inlet Air		
Air inlet temperature	468	(K)
Air mass flow rate	0.336	(kg/s)
Air axial velocity	7.5	(m/s)
Air radial velocity	-5.25	(m/s)
Air total velocity	9.15	(m/s)
Outlet Condition		
Outflow and reference at outlet	-100	(Pa)
Turbulence inlet condition		
Turbulence k-value	0.027	(m^2/s^2)
Turbulence ε-value	0.37	(m^2/s^3)
Liquid spray from nozzle		
Liquid feed rate (spray rate)	0.0139	(kg/s)
Feed Temperature	300	(K)
Spray angle	76°	
Minimum droplet diameter	10	(μm)
Maximum droplet diameter	138.0	(μm)
Average droplet diameter	70.5	(μm)
Droplet velocity at nozzle exit	59	(m/s)
Rosin-Rammler parameter	2.05	
Chamber wall conditions		
Chamber wall thickness	0.002	(m)
Wall material	Steel	
Overall wall-heat transfer co-efficient	3.5	(W/m^2K)
Air temperature outside wall	300	(K)
Interaction between wall and droplet	Escape	

Kieviet (1997) used experimental air inlet velocities to estimate k and ε values. The k and ε values were calculated using the following equations given by Langrish and Zbicinski (1994) and the calculated values are given in Table (7-1).

$$k_{inlet} = \frac{3}{2}(v_{inlet} I)^2 \qquad \text{Eq (7-18)}$$

where, I is the intensity of turbulence at the inlet. The intensity value was estimated from the following equation

$$I = 0.2 Re^{-1/8} \qquad \text{Eq (7-19)}$$

where, Re is the Reynolds number of the inlet pipe. The energy dissipation value was estimated from the following equation.

$$\varepsilon_{inlet} = \frac{C_\mu^{3/4} k_{inlet}^{3/2}}{l} \qquad \text{Eq (7-20)}$$

where, l is the length scale of turbulence (assuming to be the diameter of the inlet opening to the chamber), v_{inlet} is the inlet gas velocity, C_μ is a constant.

The spray "injection" conditions are specified in Table (7-1). The particle size distribution was modeled using the Rosin-Rammler distribution. Thirty particle sizes were chosen to represent the spray ranging from 10 to 138 μm. The total number of particle tracks was selected as 1500. In the Fluent code, a particle which hits the wall of drying chamber can be assumed to be either "*trapped*", "*escaped*" or "*reflected*". In this work, the "*escape*" boundary condition was used, where by the particles are lost from the calculation at the point of impact with the wall. The overall wall heat transfer coefficient was determined experimentally from an energy balance over the dryer. In Case A, the total heat loss was 7 kW and this leads to a heat transfer coefficient of 3.5 W/m^{2}K.

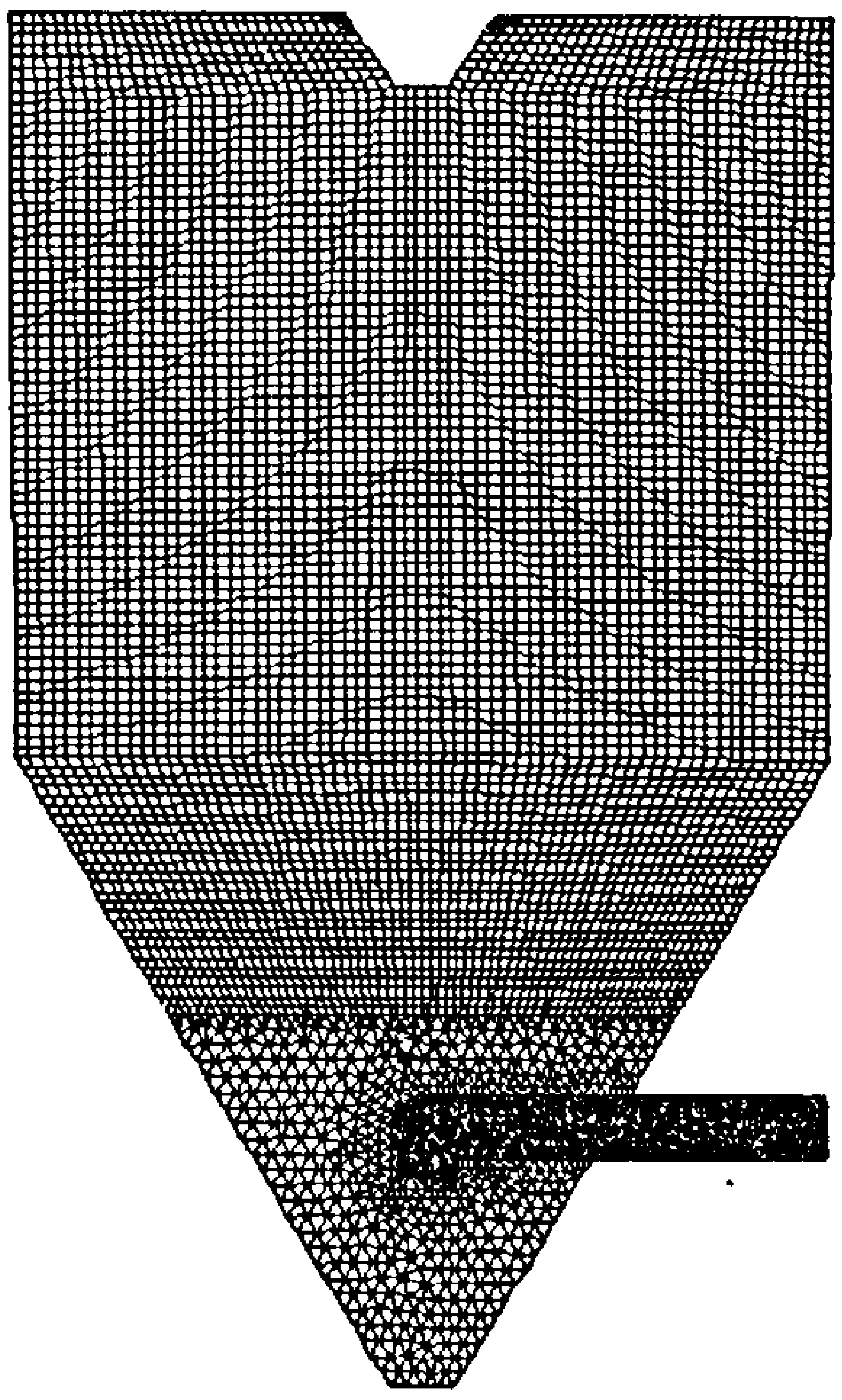

Figure 7-3: Grid used in the short-type spray dryer simulation.

In the 3D-model a hexahedral mesh (typical mesh size 0.001 m) was used for the cylindrical part of the drying chamber and at the bottom of cone chamber, a tetrahybrid mesh was used (mesh size also 0.001 m) due to meshing problem in outlet pipe line. The number of grid cells used for the geometry was 295,090 and is shown in figure (7-3).

7.7 *Case A:* Simulation results and discussion

In this work, CFD model predictions are compared with Kieviet's (1997) experimental results and Huang *et al's* (2006) simulations. The results obtained from the CFD model are presented in the following sub-sections in terms of gas velocity magnitude, temperature, humidity profiles and particle characteristics. The axial positions for comparison of measurements and simulation are shown in figure (7-4).

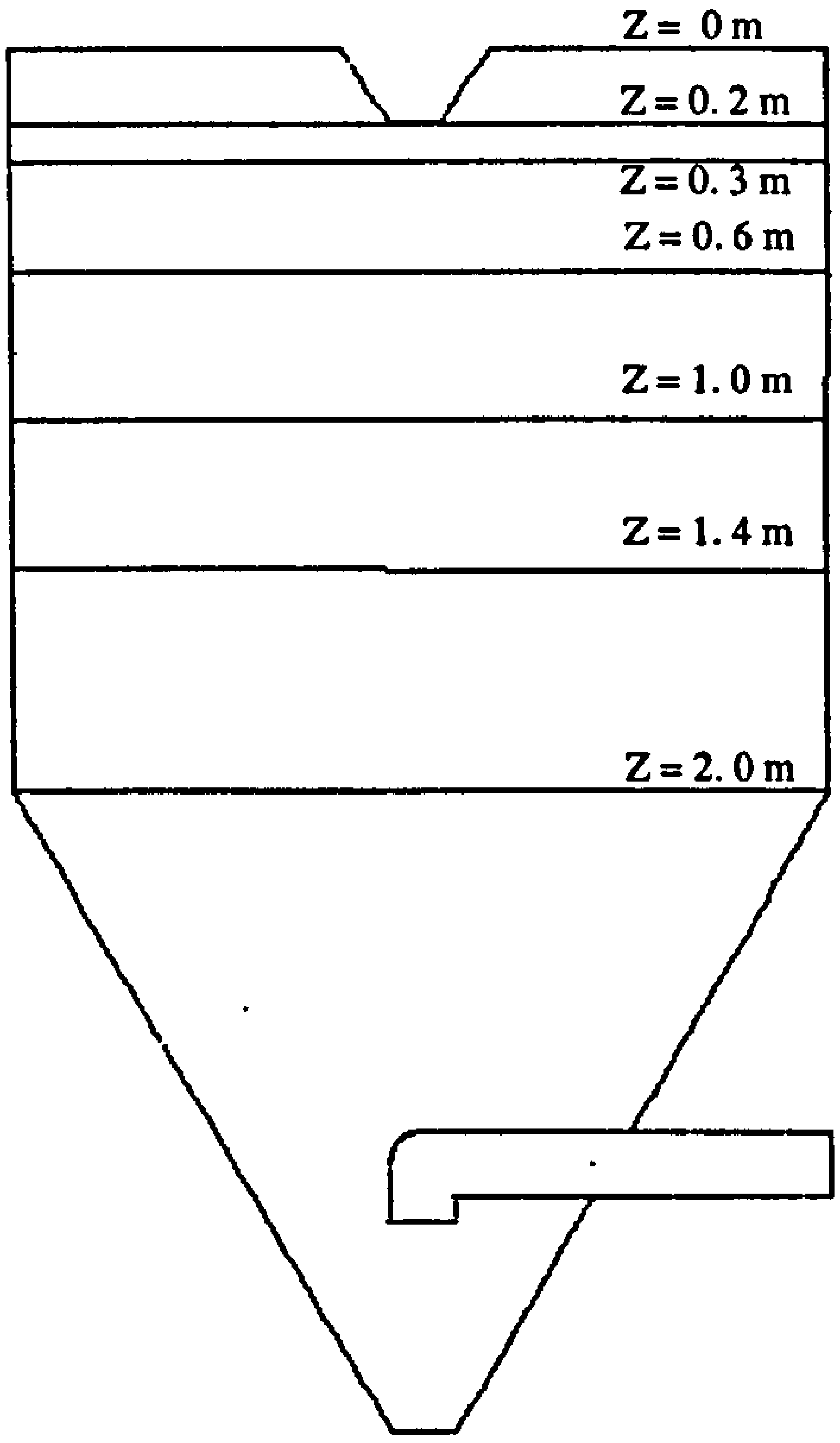

Figure 7-4: Axial positions for comparisons of measurements and simulations.

7.7.1 Gas flow Pattern

The first step in this simulation was to obtain the gas flow field in the absence of spray injection. Figures (7-5) shows the flow pattern of gas without and with spray injections. The flow pattern without spray injection shows two distinct zones, a fast flowing core zone and a slow circulation zone around the core. The air velocity decreases down to the outlet line. Kieviet (1997), observed the same trend in a two-dimensional axi-symmetric CFD model. In the gas velocity profiles with spray injection, it can be readily seen that there is a non-uniform velocity distribution in the core region of the chamber. A re-circulation zone is observed at the top and bottom of the chamber, as well as adjacent to the spray area. The re-circulation zone at the bottom of the chamber can cause small particles to be sent back up the chamber, which leads to an increase in the residence time of the particles. This re-circulation is likely to cause thermal degradation of the particles, as dried particles are exposed to the higher inlet gas temperatures. Moreover, an increase in particle re-circulation also results in higher wall deposition rates (Langrish and Zbicinski, 1994).

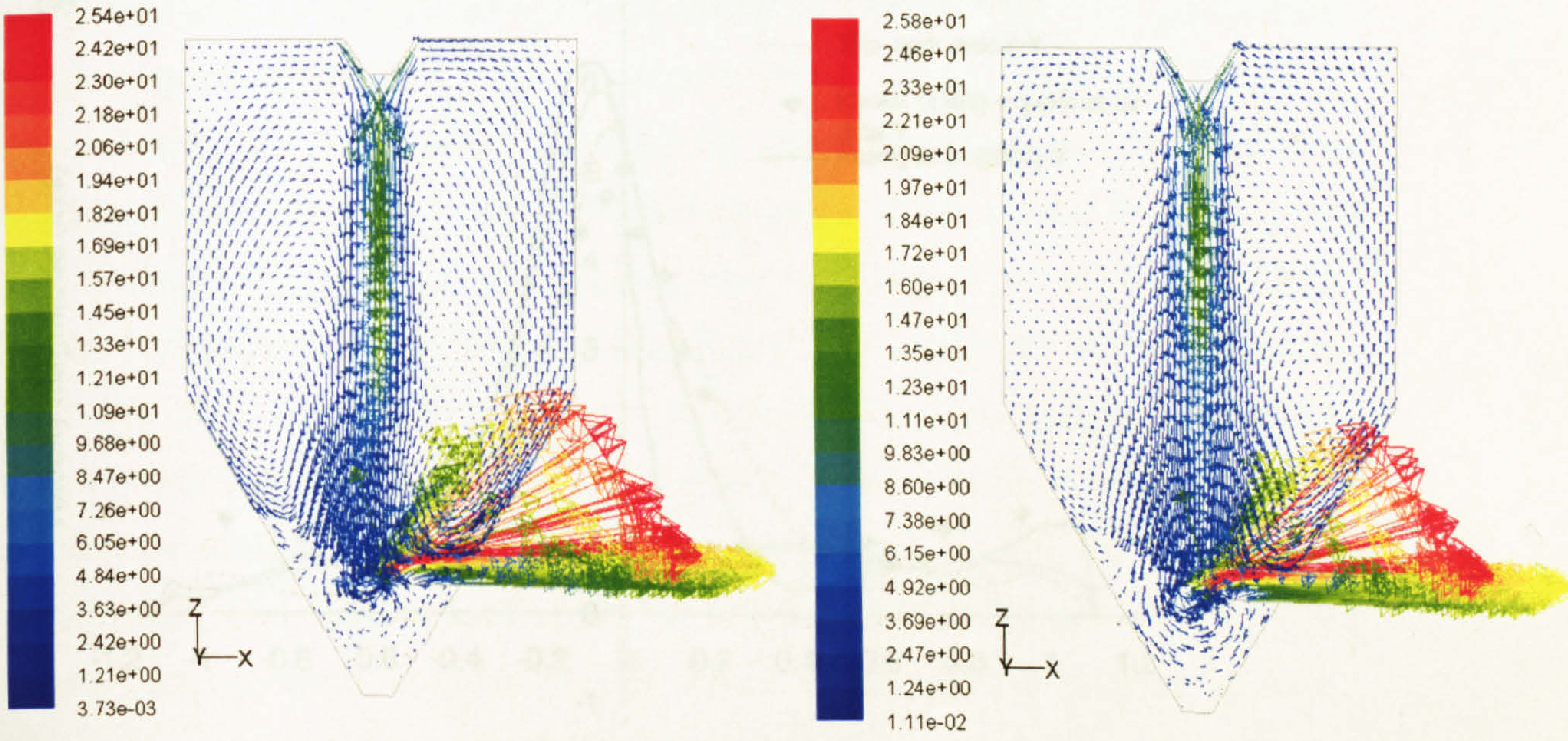

(a) (b)

Figure 7-5: Velocity magnitude vector (m/s) profiles of gas (a) without spray injection, and (b) with spray injection.

7.7.2 Comparison of the gas velocity profile without the spray injection

The gas velocity magnitude profiles are plotted in figures (7-6 a-b) at two different heights (z = 0.3 m and 2.0 m from the top of chamber) and compared with Kieviet's (1997) experimental measurements and Huang *et al*'s (2006) simulation predictions. Data obtained in the X-Z planes are labeled as X and Y-Z planes are labeled as Y in the figures (7-6 a-b).

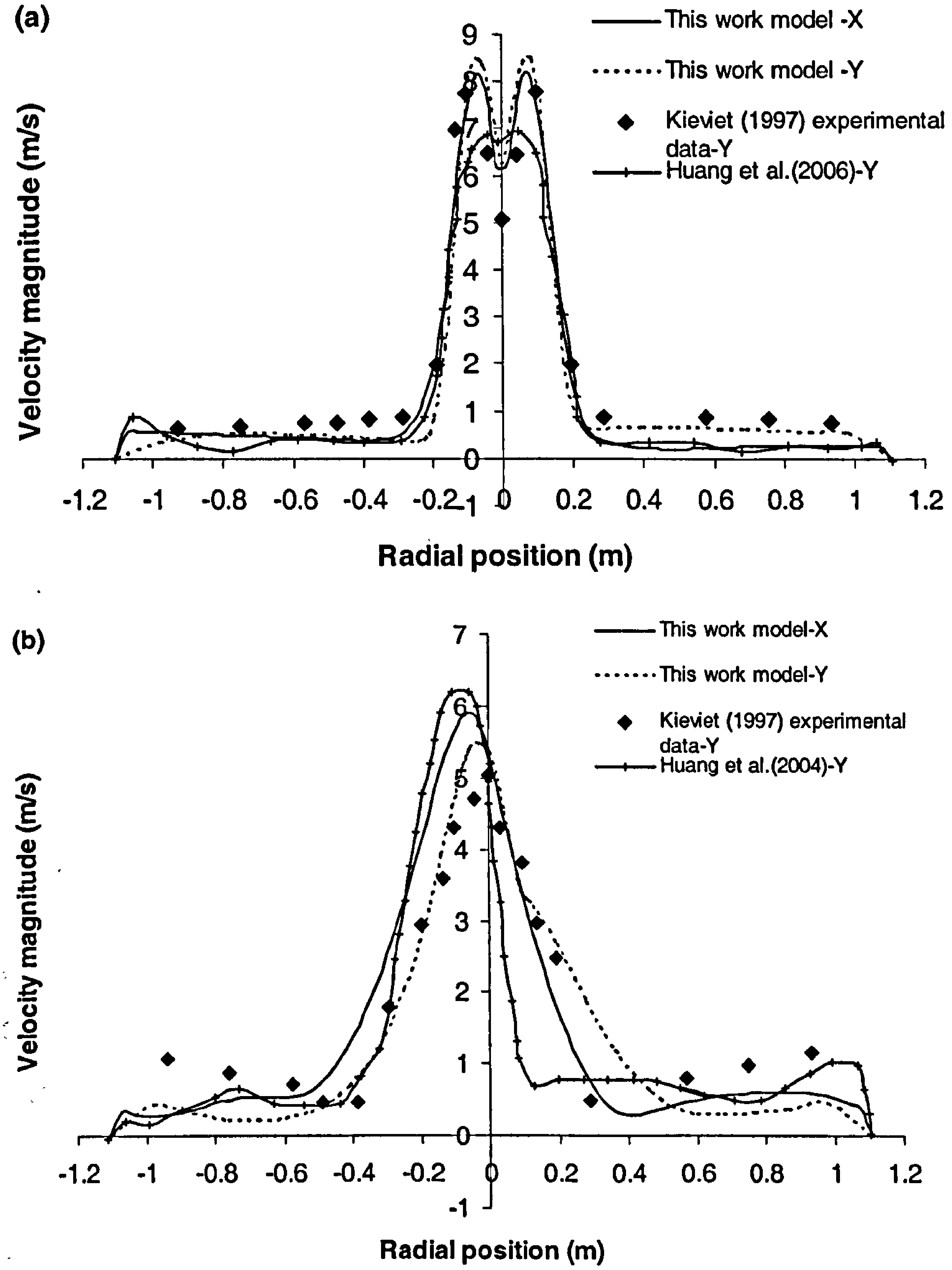

Figure 7-6: Comparison of gas which velocity magnitude between this work model with Kieviet's (1997) measurements and Huang *et al's* (2006) predictions at (a) z = 0.3 m and (b) z = 2 m distance.

The prediction from the current simulation agreed well with Kieveit's (1997) experimental results but, disagreed with Huang *et al*s (2006) predictions, especially at the 0.3 m level (7-6). In the core region of the chamber, the Kieviet's (1997) measured velocity (z = 0.3 m) was higher (8 m/s), whereas, Huang *et al's.* (2006) prediction shows a slightly lower velocity (7 m/s). The velocity is reduced as the gas stream goes downwards in the chamber, for example, at z = 0.3 m level the highest velocity magnitude is about 8 m/s, whereas, at z = 2.0 m level it is only 6 m/s. The gas flow patterns were almost symmetric at the upstream level of 0.3 m (figure 7-6 a), but asymmetric velocity profiles were found at the 2.0 m level (figure 7-6 b). This may be due to the bent outlet pipe which reduces the area for gas to go through at one side of the drying chamber. Hence, for the spray drying simulations there is a need to use 3D geometry inserted of axi-symmertic 2D.

7.7.3 Comparison of the gas temperature profile with spray injection

Figures (7-7 a-b) shows the radial profiles of gas temperature predictions at axial distances from the top of the chamber of z = 0.2 m and 1.4 m, and compares with Kieveit's (1997) experimental measurements. The predictions were in good agreement with the experimental results. In Kieveit's (1997) experiments, the feed was atomised by using pressure nozzle and this produced a hollow-cone spray. The temperature at the centre line axis was low and core region (0 < r< 0.2 m) was very high (figure 7-7 a), because this position was above the spray point (see figure 7-4). However, at the z = 1.4 m level this trend was not shown due to re-circulation of gas (figure 7-7 b). The same prediction was shown by Huang *et al*s (2006) model. A slight variation of gas temperature was found outside the core region (r > 0.3 m) except near to the wall. The temperature contours are depicted in figures (7-8), which shows that a large volume of the spray dryer has an almost uniform temperature, hence most of the drying takes place in the core region. For a given liquid feed flow rate, a higher atomiser pressure gives greater initial droplet momentum and thereby draws more hot air into the spray core region, which leads to more rapid drying (Papadakis and King, 1988). Moreover, the velocity of the gas flow in the volume outside the core was low and it appears that the particles do not penetrate into this zone (see figure 7-13). This was also observed by Kieviet (1997) and Huang *et al.* (2006).

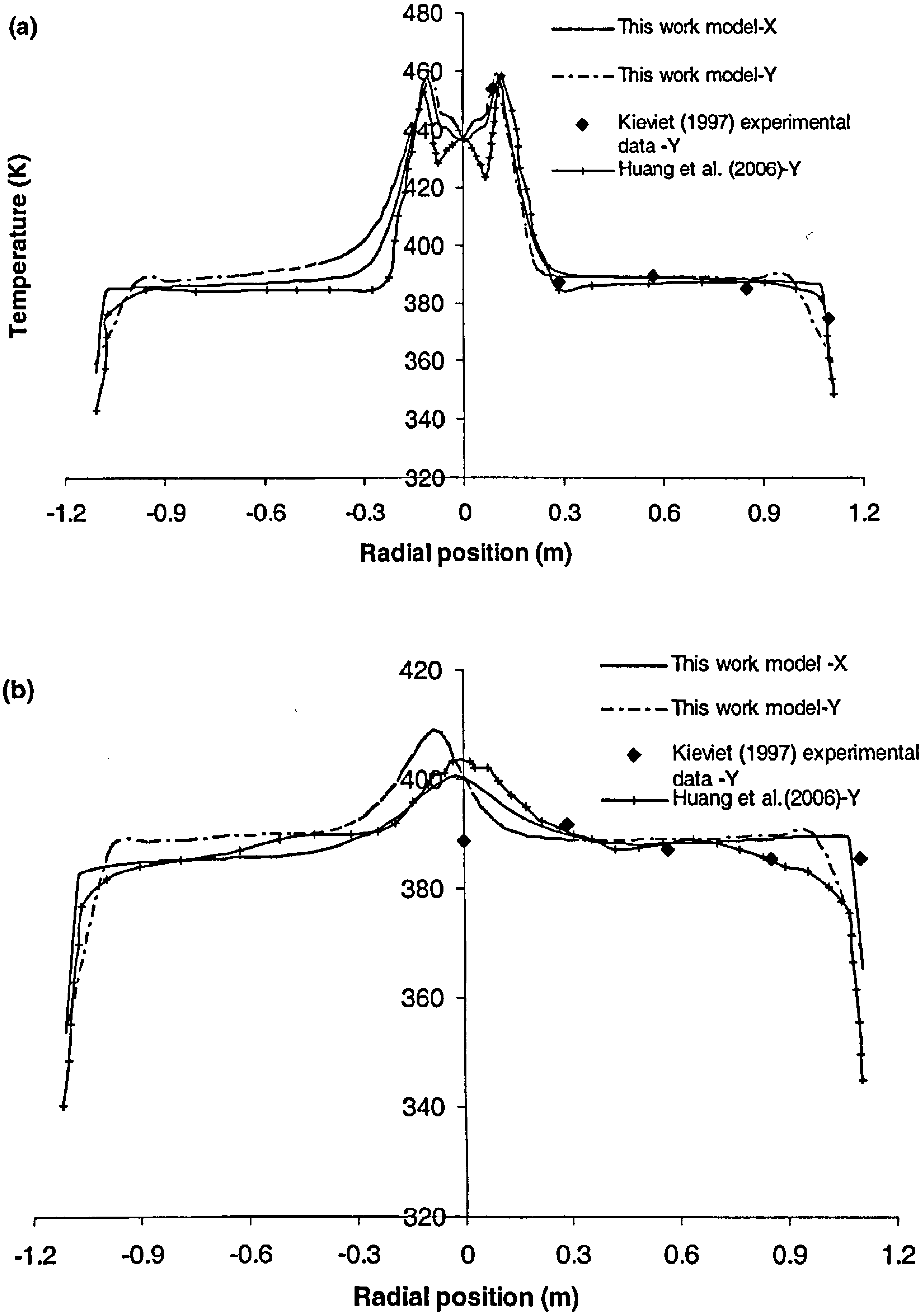

Figure 7-7: Comparison of gas temperature profiles between this work model with Kieviet's (1997) measurements and Huang *et al's* (2006) predictions at (a) z = 0.2 m and (b) z = 1.4 m distance.

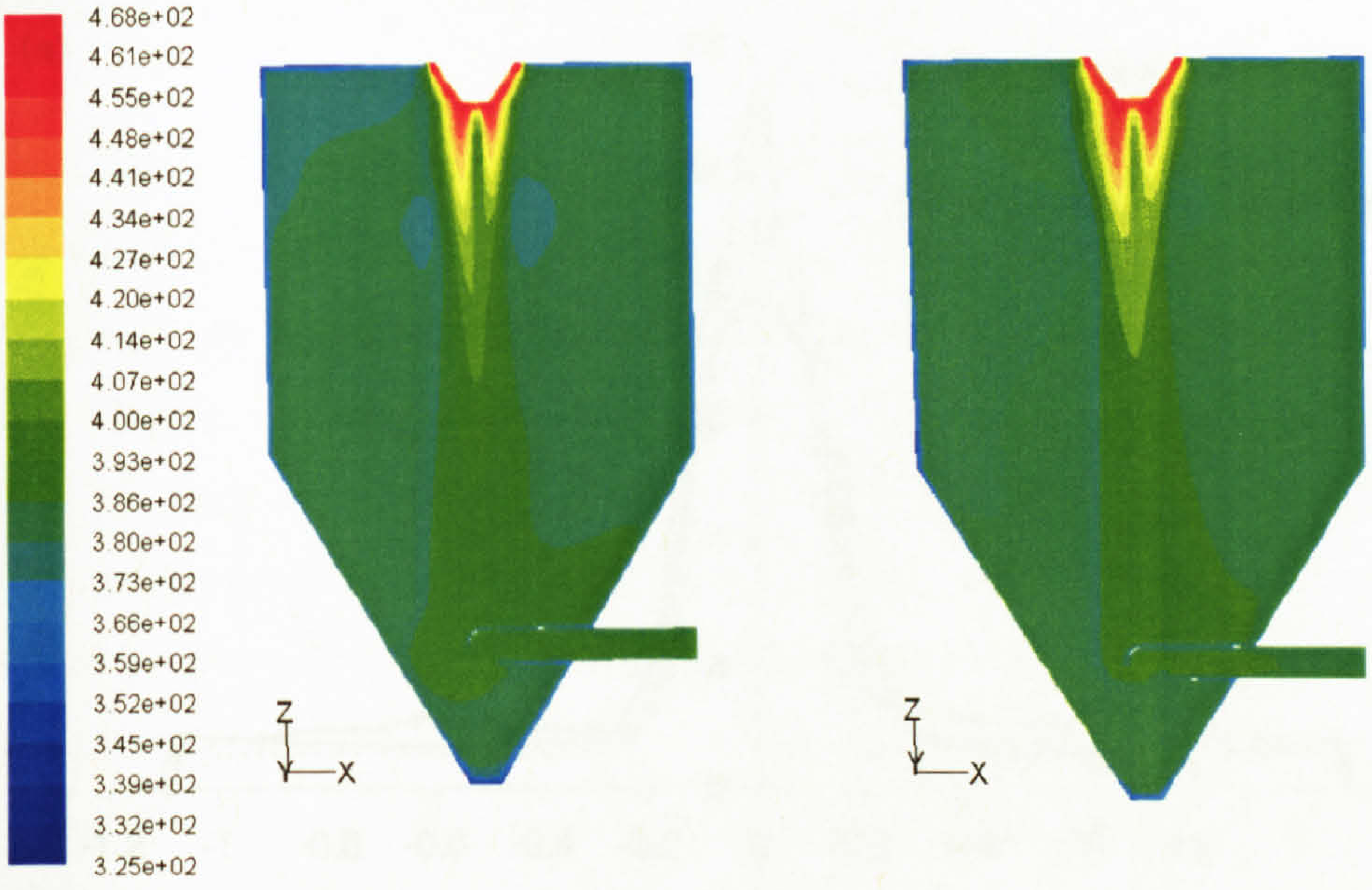

(a) (b)

Figure 7-8: Temperature (K) contours of gas (a) without spray injection, and (b) with spray injection.

The predicted outlet gas temperature for this simulation is 391 K, which is very close to Kieviet's experimental measurements of 389 K.

7.7.4 Comparison of gas velocity profiles with spray injection

The gas velocity magnitude profiles with the spray injection predictions is shown in figures (7-9). In this work, predictions of the velocity magnitude agreed well with Kieviet's (1997) axi-symmetric CFD model (not shown in figures). However, it does not agree well with Huang *et al*'s (2006) model (figures 7-9 a-b), where, in the core region higher velocity (11 m/s) were predicted. Kieviet's (1997) experimental results for the case without spray injection have shown that the core region has maximum velocity of 8 m/s (see figure 7-6 a). With spray injection, it should predict higher velocity than without spray injection. But, Huang *et al*'s (2006) results shows only 8 m/s in the spray region (figure 7-6). This is presumably Huang *et al* (2006) used solid cone spray inserted of hollow cone spray (see spray pattern in figure 7-6 a).

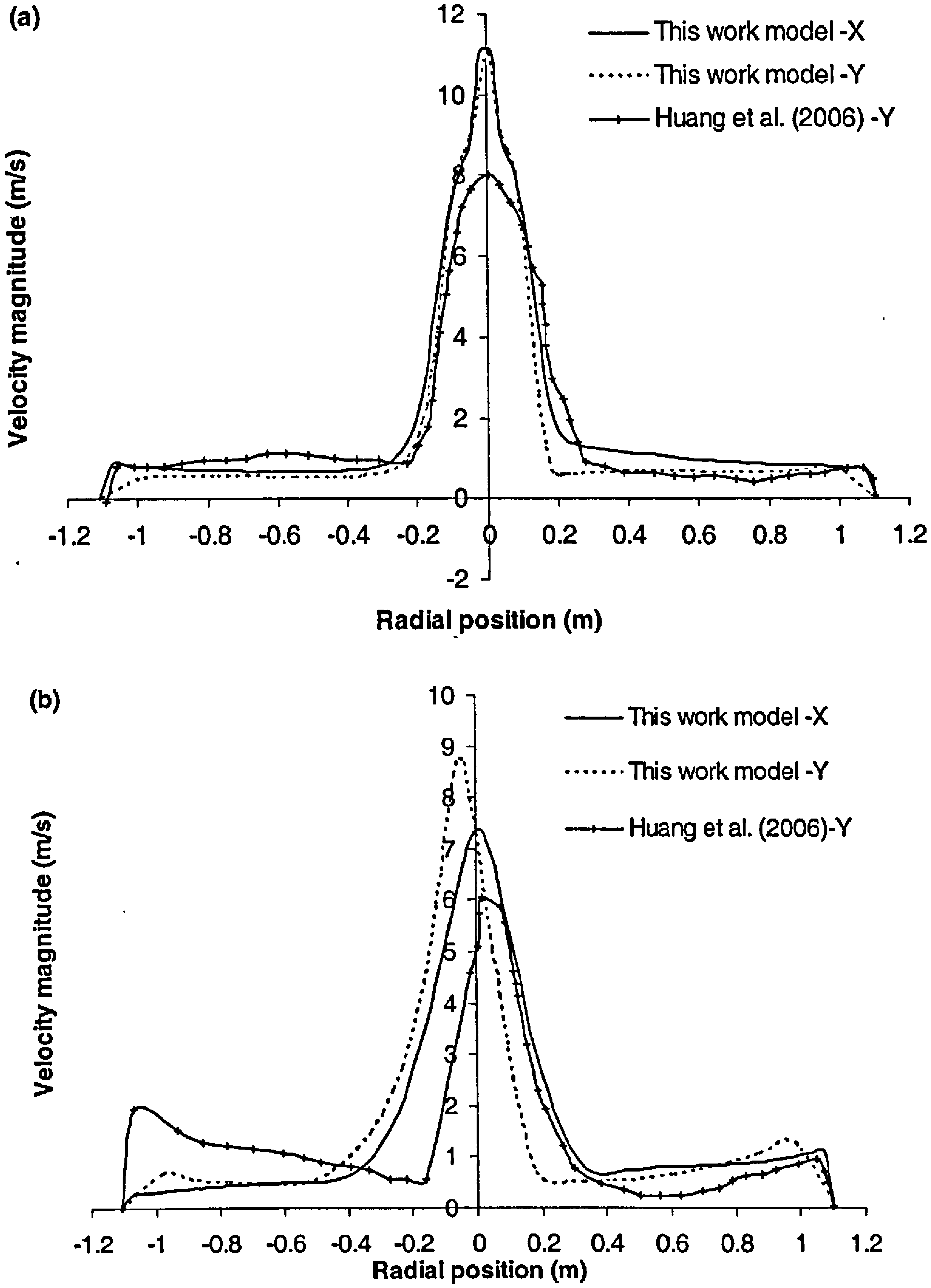

Figure 7-9: Comparison of gas velocity magnitude between this work and Huang *et al's.* (2006) predictions at (a) z = 0.3 m and (b) z = 1.4 m distance.

Figures (7-9 a-b) shows almost asymmetric velocity profiles and also that outside the core region, the axial velocity is low (< 1 m/s). The gas flow is significantly altered by including a spray injection, which adds downwards momentum to the flow. Therefore using a single phase assumption to model flow pattern is not appropriate.

7.7.5 Comparison of gas humidity profiles with spray injection

In figures (7-10), radial profiles of gas humidity, expressed as water vapour mass fraction are presented. The humidity profiles were similar in form to the gas temperature profiles, but inverted due to simultaneous heat and mass transfer. The humidities at core region (0< r< 0.2 m) were low at z = 0.2 m, because this was above the spray point (see figure 7-4). The predicted results were in good agreement with experimental results at z = 0.6 m and 1.0 m levels, but at z = 0.2 m and 1.4 m levels the predictions were slightly greater than the measured humidities (figures 7-10 a-d). However, its very difficult to predict humidity profiles accurately, because this CFD model considered the evaporation of moisture from the surface of drops to be at a constant drying rate. However, droplets may not always be in constant drying rate regime especially towards the end of drying. Hence, inter particle diffusion and/or water desorption factors may also be important to predict humidity.

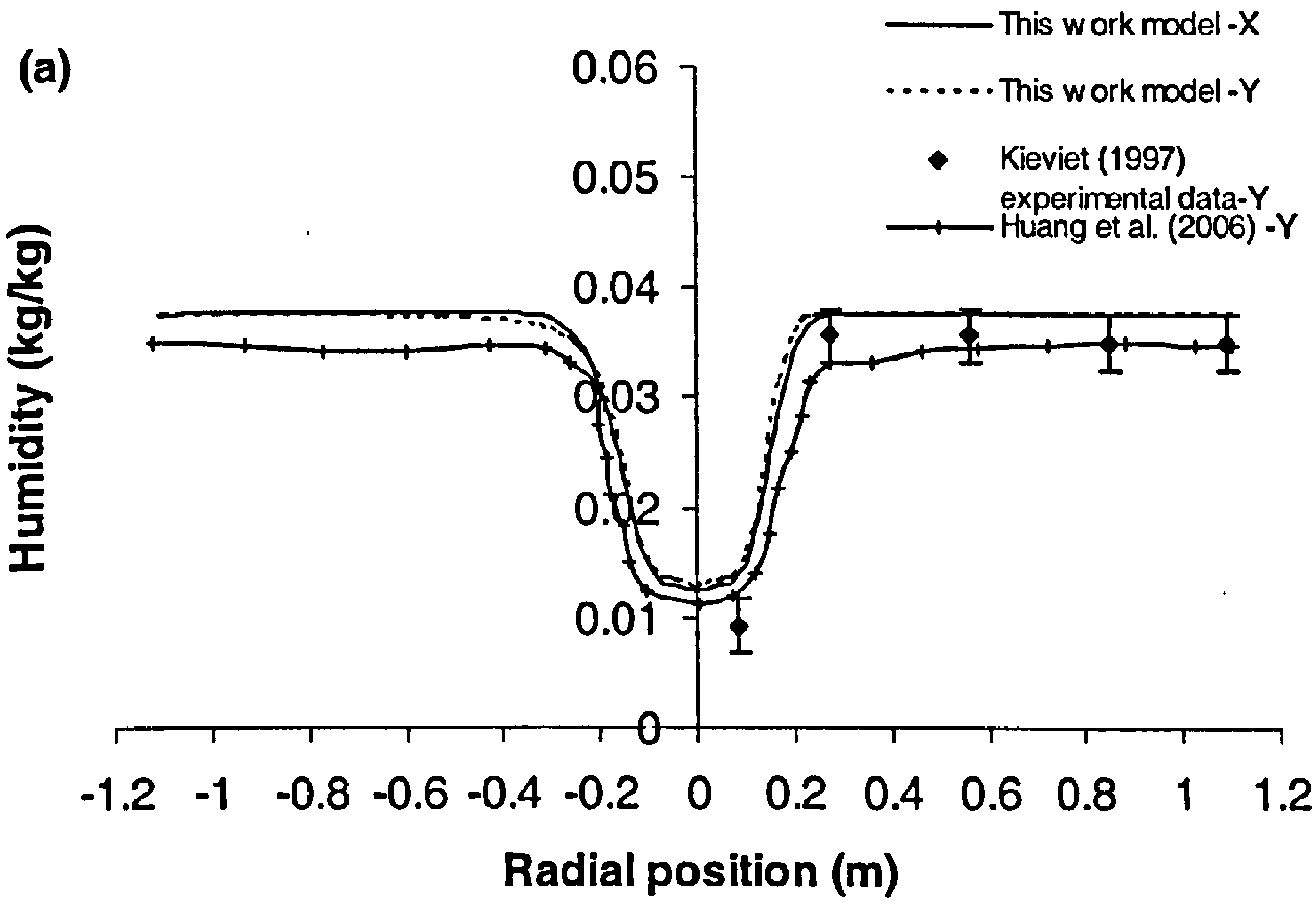

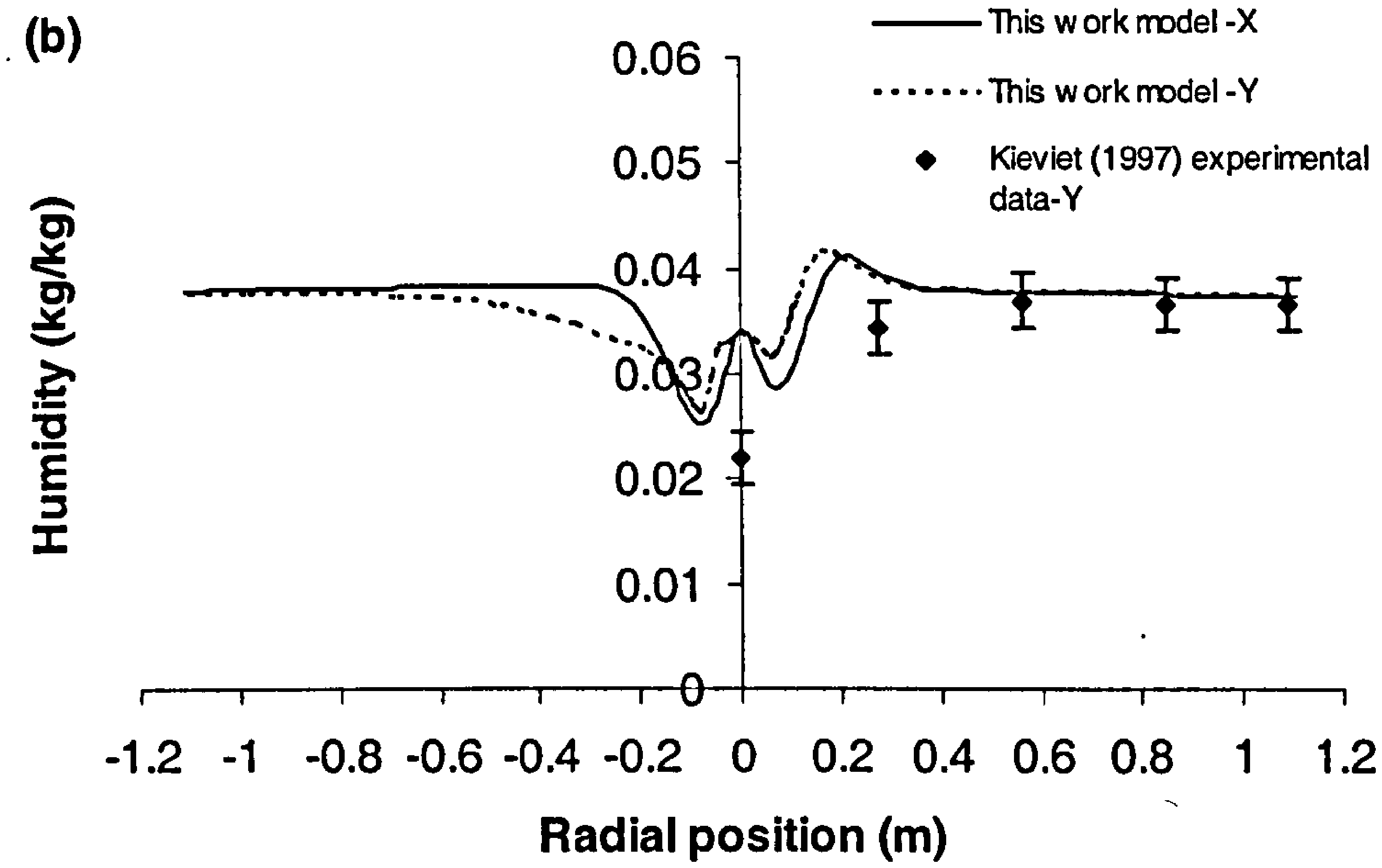
(b)
This work model -X
This work model -Y
Kieviet (1997) experimental data-Y
Humidity (kg/kg)
0.06
0.05
0.04
0.03
0.02
0.01
0
-1.2
-1
-0.8
-0.6
-0.4
-0.2
0
0.2
0.4
0.6
0.8
1
1.2
Radial position (m)

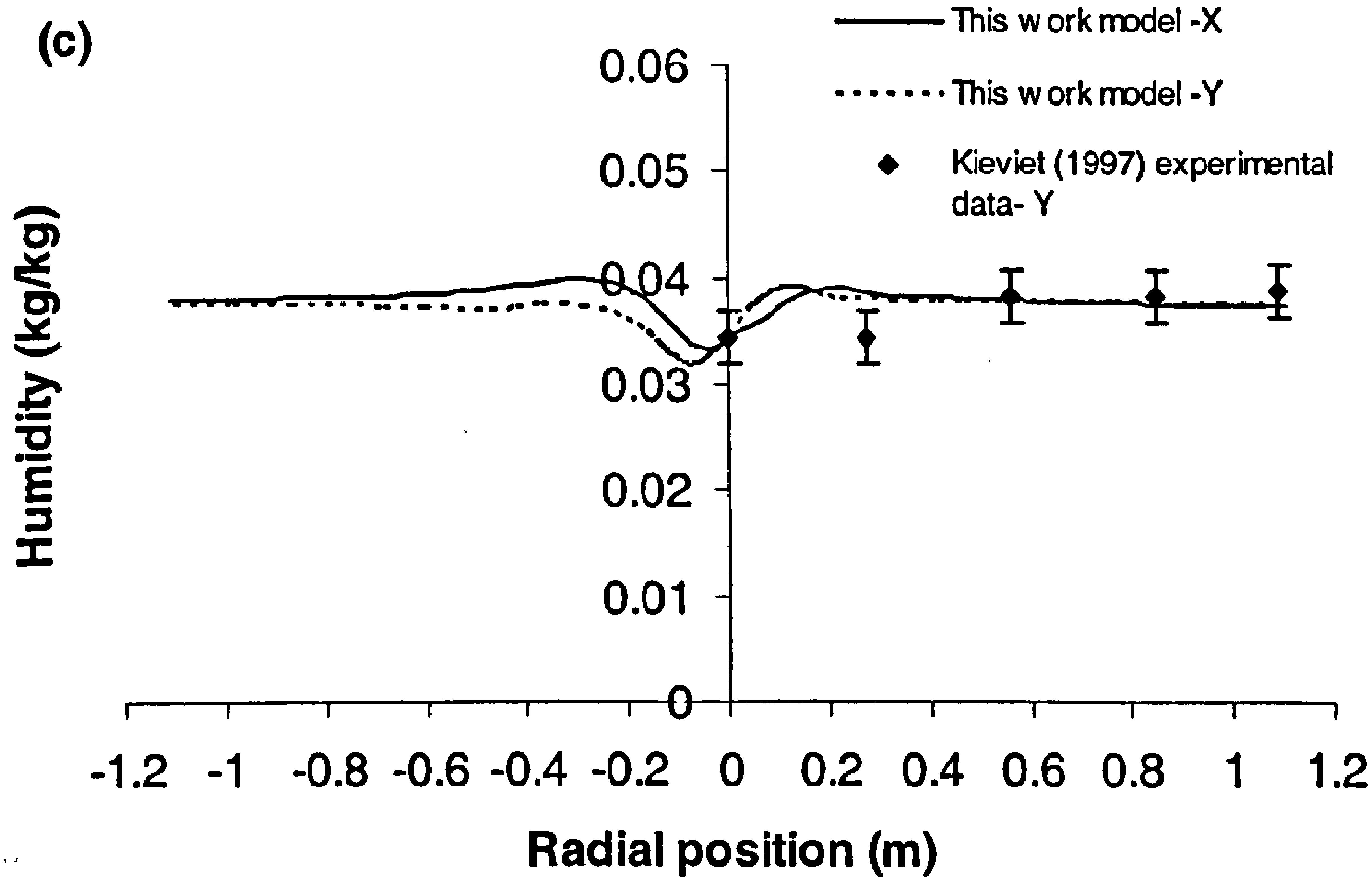
(c)
This work model -X
This work model -Y
Kieviet (1997) experimental data- Y
Humidity (kg/kg)
0.06
0.05
0.04
0.03
0.02
0.01
0
-1.2
-1
-0.8
-0.6
-0.4
-0.2
0
0.2
0.4
0.6
0.8
1
1.2
Radial position (m)

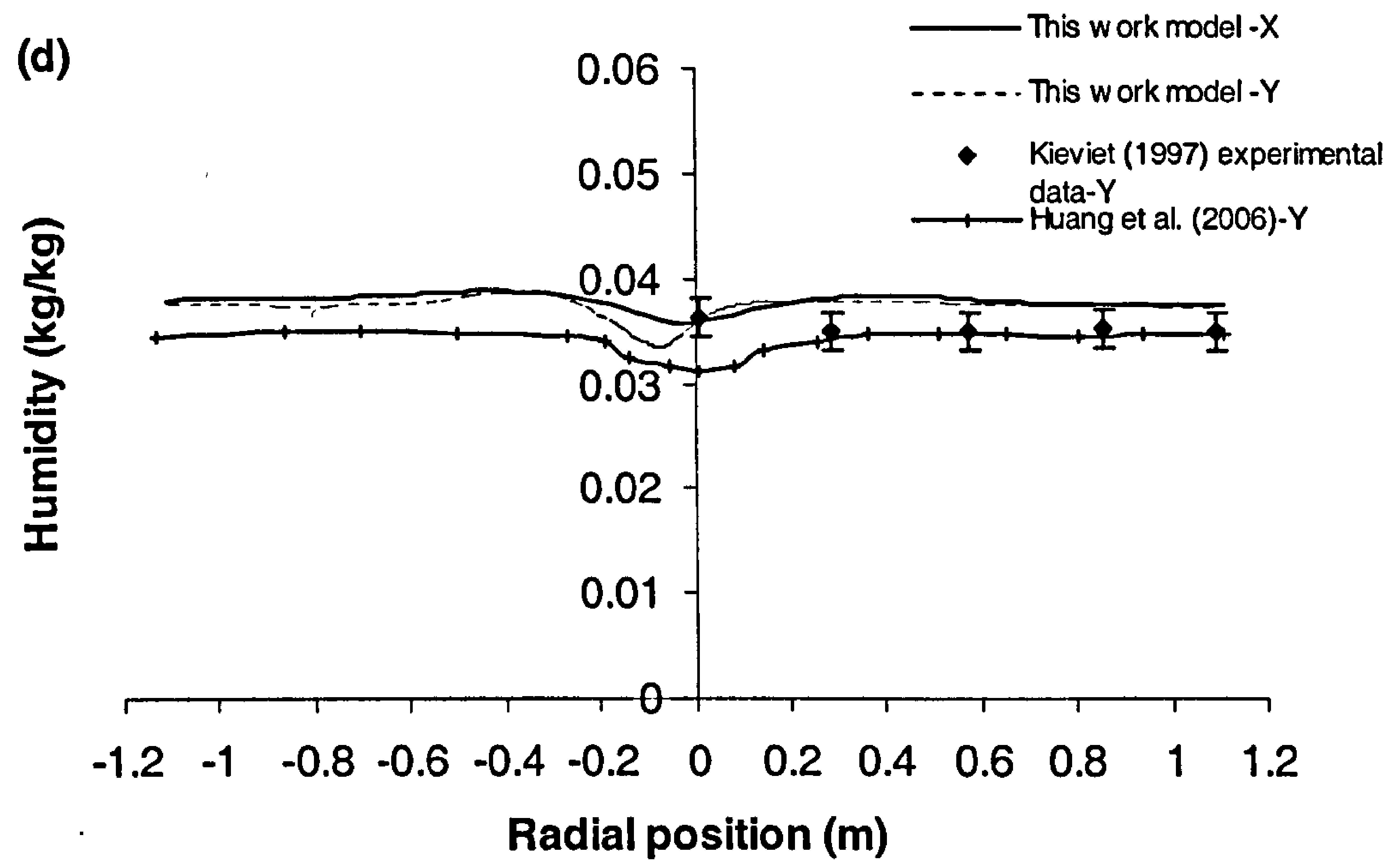

Figure 7-10: Comparison of gas humidity between this work, Kieviet's (1997) measurements and Huang *et al*'s (2006) predictions at (a) z = 0.2 m, (b) z = 0.6 m, (c) z = 1.0 m and (d) z = 1.4 m.

7.7.6 Particles histories

The particle histories for velocity and temperature, the particle residence time distribution (RTD) and the particles impact position on the wall are described in the following sub-sections. In this model, the Rosin-Rammler droplet distribution was used (Table 7-1) with 30 particles size ranges from 10 μm to 138 μm, but four particle diameters of 17 μm, 50 μm, 75 μm and 100 μm were selected to represent the behaviour of different particle sizes. The results and discussions of predicted radial profiles of particle axial velocity and temperatures at axial distance of z = 0.6 m, 1.0 m and 2.0 m level from chamber top are described in the following sub-sections. There are certain control volumes, where no droplets pass (mainly near to nozzle at radius 0 < r < 0.2 m), for the hollow cone spray injection.

The particles histories data presented in the following sub-sections were extracted from the simulation results using the in-house-developed post-processing computer program as these options are not available in the present commercial CFD codes.

7.7.7 Radial profiles of particle axial velocity

The predicted radial profiles of particle axial velocity at z = 0.6 m, 1.0 m and 2.0 m are shown in figures (7-11 a-c). The particle axial velocities are almost equal to the gas velocities at r > 0.4 m. In the core region of the chamber, no data are shown for particle velocities, because insufficient number of particles entered this region due to the hollow cone spray with 76° spray angle (figure 7-11 a-b). However, at the bottom of the chamber, figure (7-11 c) shows slightly higher axial velocities of the particles than the gas. The particles velocity can only be deducted from a small no of trajectories that passed through a given control volume and hence figure (7-11 c) shown almost same results. The larger particles have more momentum than smaller once and maintain their velocity to a greater extent (Crowe, 1977). The smaller size particles decelerate more rapidly towards their terminal velocities and terminal velocity is directly proportional to the square of the drop diameter (Papadakis and King, 1988).

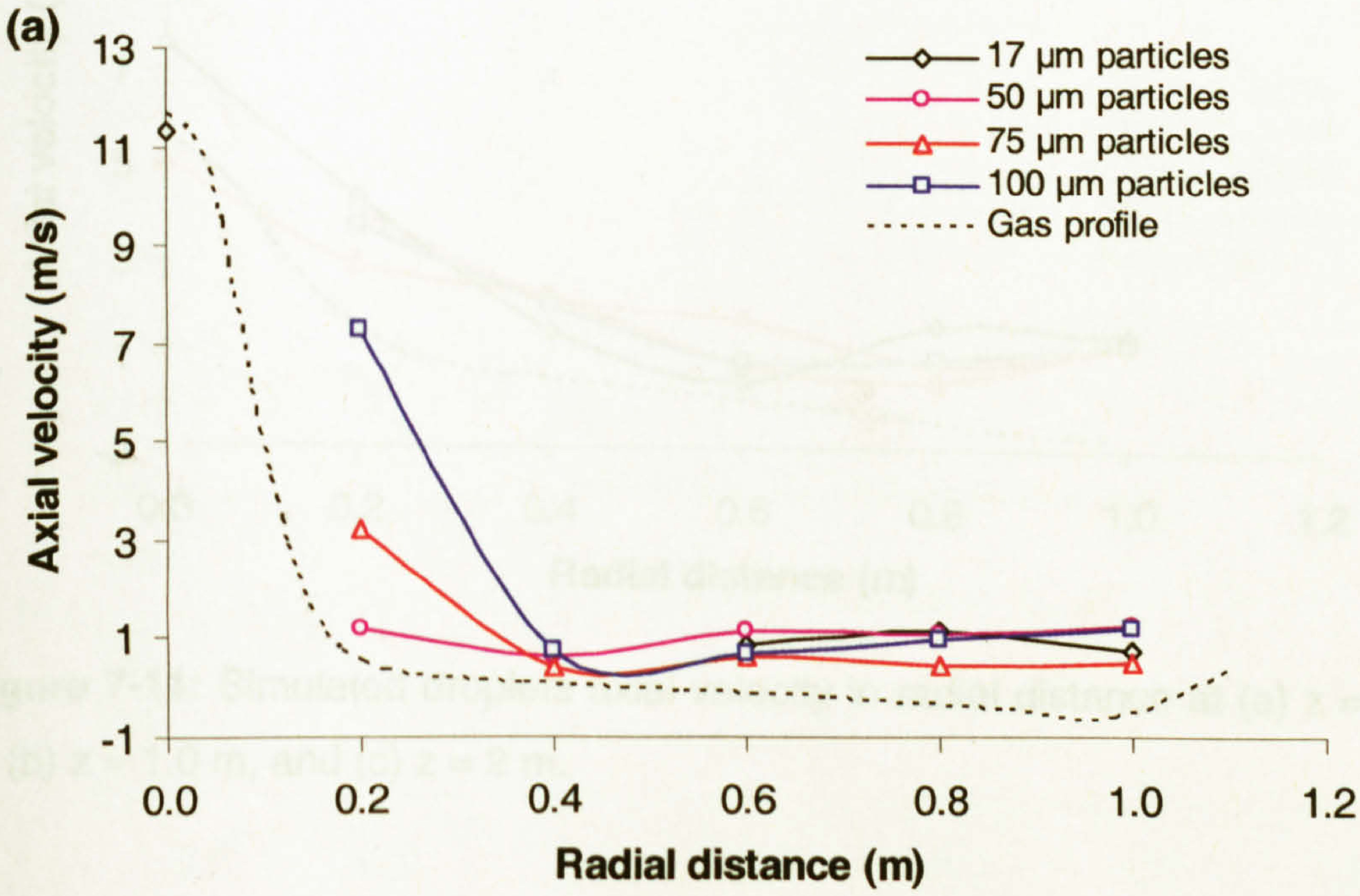

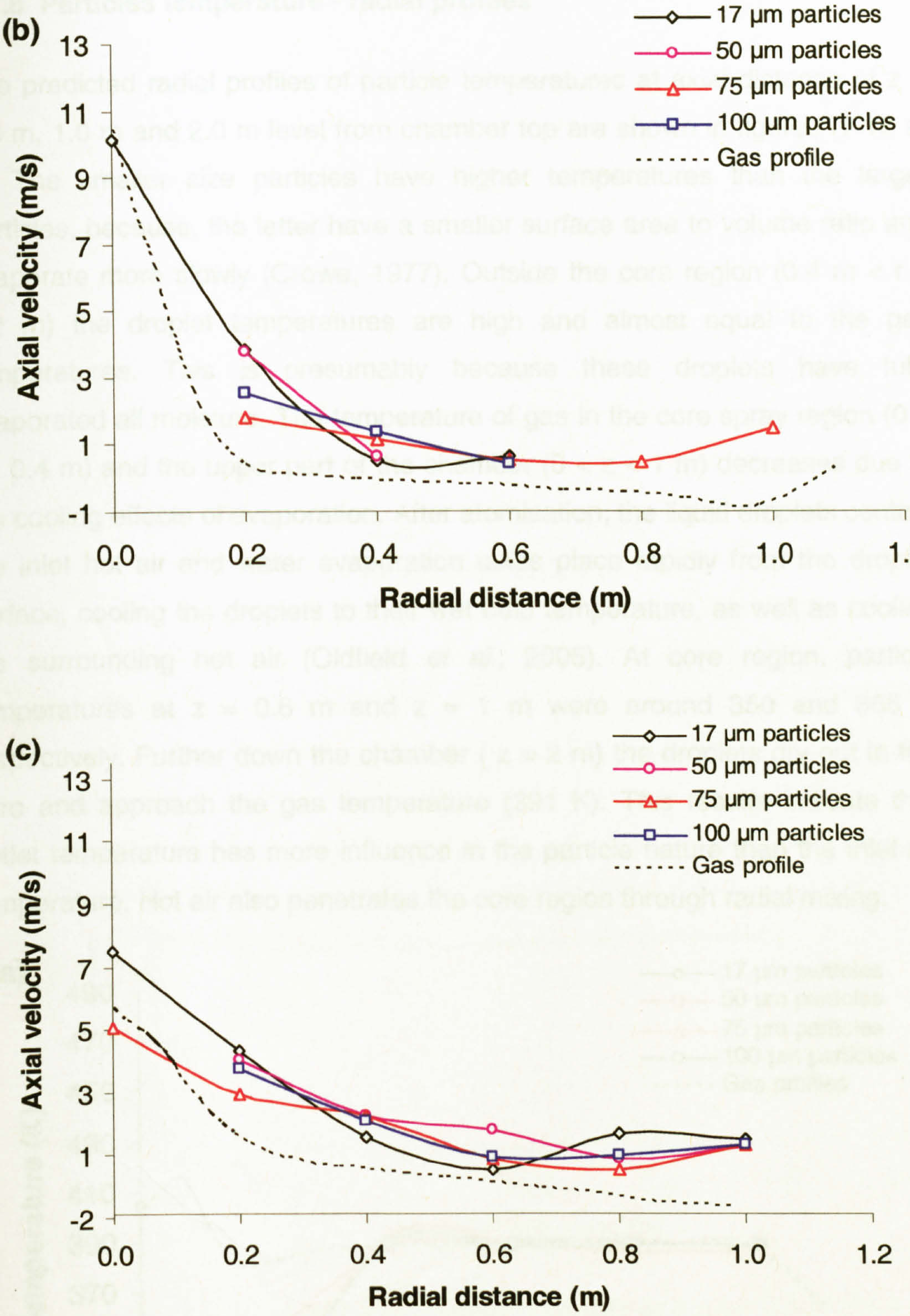

Figure 7-11: Simulated droplets axial velocity in radial distance at (a) z = 0.6 m (b) z = 1.0 m, and (c) z = 2 m.

7.7.8 Particles temperature - radial profiles

The predicted radial profiles of particle temperatures at axial distance of z = 0.6 m, 1.0 m and 2.0 m level from chamber top are shown in figures (7-12 a-c). The smaller size particles have higher temperatures than the larger particles, because, the latter have a smaller surface area to volume ratio and evaporate more slowly (Crowe, 1977). Outside the core region (0.4 m < r < 1.2 m) the droplet temperatures are high and almost equal to the gas temperatures. This is presumably because these droplets have fully evaporated all moisture. The temperature of gas in the core spray region (0 < r < 0.4 m) and the upper part of the chamber (0 < z < 1 m) decreases due to the cooling effects of evaporation. After atomisation, the liquid droplets contact the inlet hot air and water evaporation takes place rapidly from the droplet surface, cooling the droplets to their wet bulb temperature, as well as cooling the surrounding hot air (Oldfield *et al.*, 2005). At core region, particle temperatures at z = 0.6 m and z = 1 m were around 350 and 365 K respectively. Further down the chamber (z = 2 m) the droplets dry out in the core and approach the gas temperature (391 K). This results indicate that outlet temperature has more influence in the particle nature than the inlet air temperature. Hot air also penetrates the core region through radial mixing.

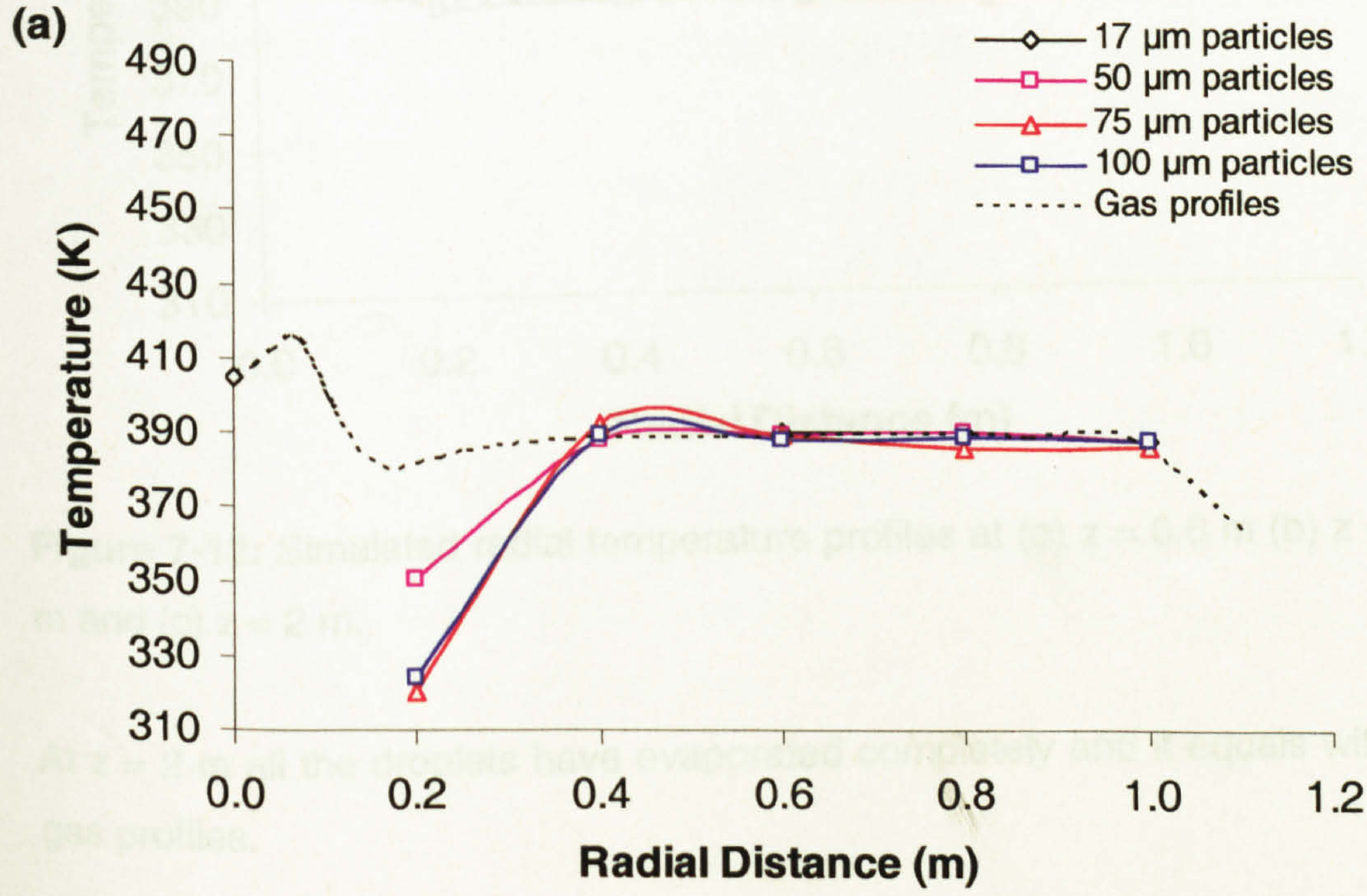

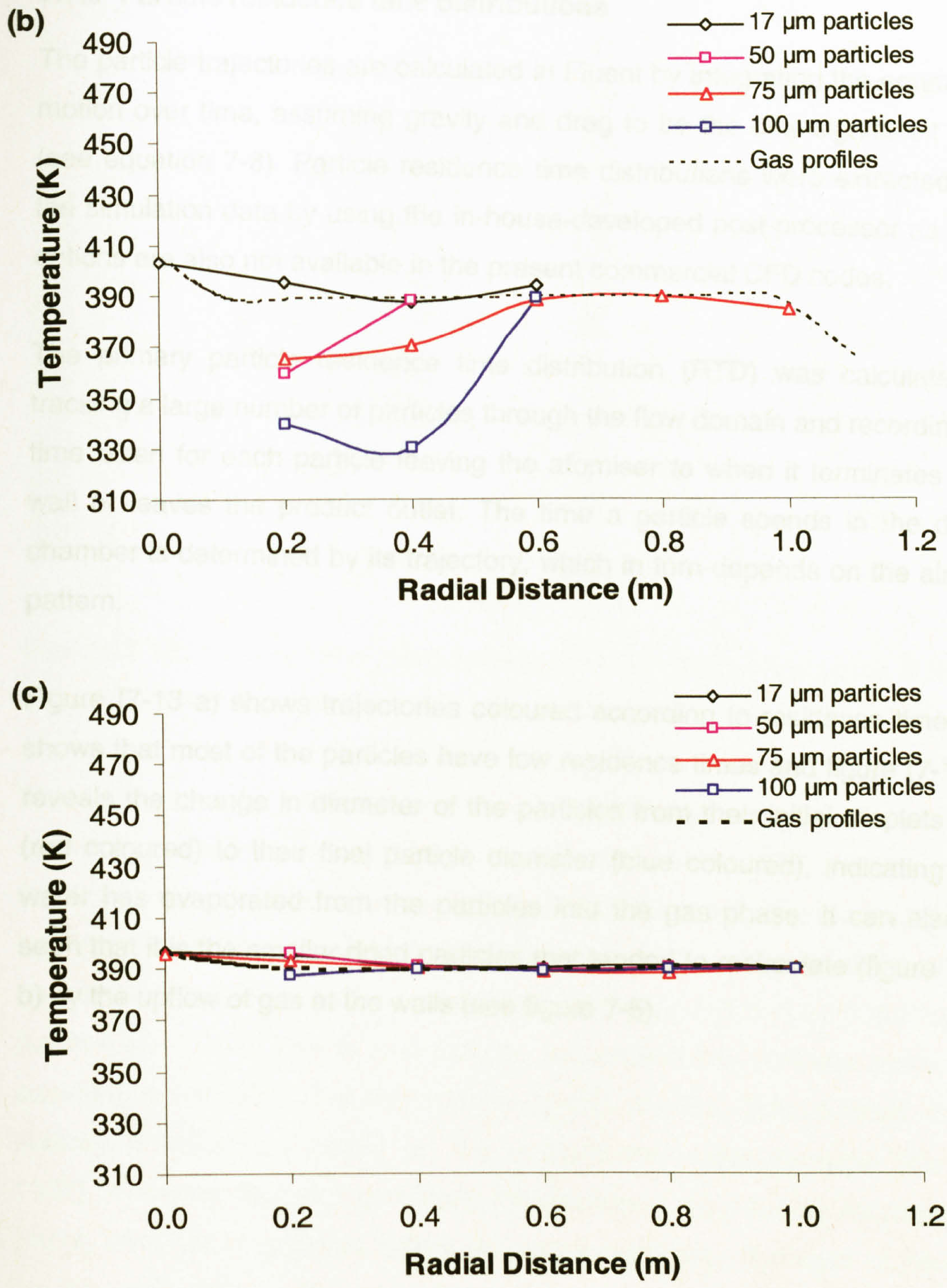

Figure 7-12: Simulated radial temperature profiles at (a) z = 0.6 m (b) z = 1.0 m and (c) z = 2 m.

At z = 2 m all the droplets have evaporated completely and it equals with the gas profiles.

7.7.9 Particle residence time distributions

The particle trajectories are calculated in Fluent by integrating the equation of motion over time, assuming gravity and drag to be the only significant terms (see equation 7-8). Particle residence time distributions were extracted from the simulation data by using the in-house-developed post-processor as these options are also not available in the present commercial CFD codes.

The primary particle residence time distribution (RTD) was calculated by tracking a large number of particles through the flow domain and recording the time taken for each particle leaving the atomiser to when it terminates on a wall or leaves the product outlet. The time a particle spends in the drying chamber is determined by its trajectory, which in turn depends on the air flow pattern.

Figure (7-13 a) shows trajectories coloured according to residence time and shows that most of the particles have low residence times and figure (7-13 b) reveals the change in diameter of the particles from their initial droplets size (red coloured) to their final particle diameter (blue coloured), indicating that water has evaporated from the particles into the gas phase. It can also be seen that it is the smaller dried particles that tended to recirculate (figure 7-13 b) by the upflow of gas at the walls (see figure 7-5).

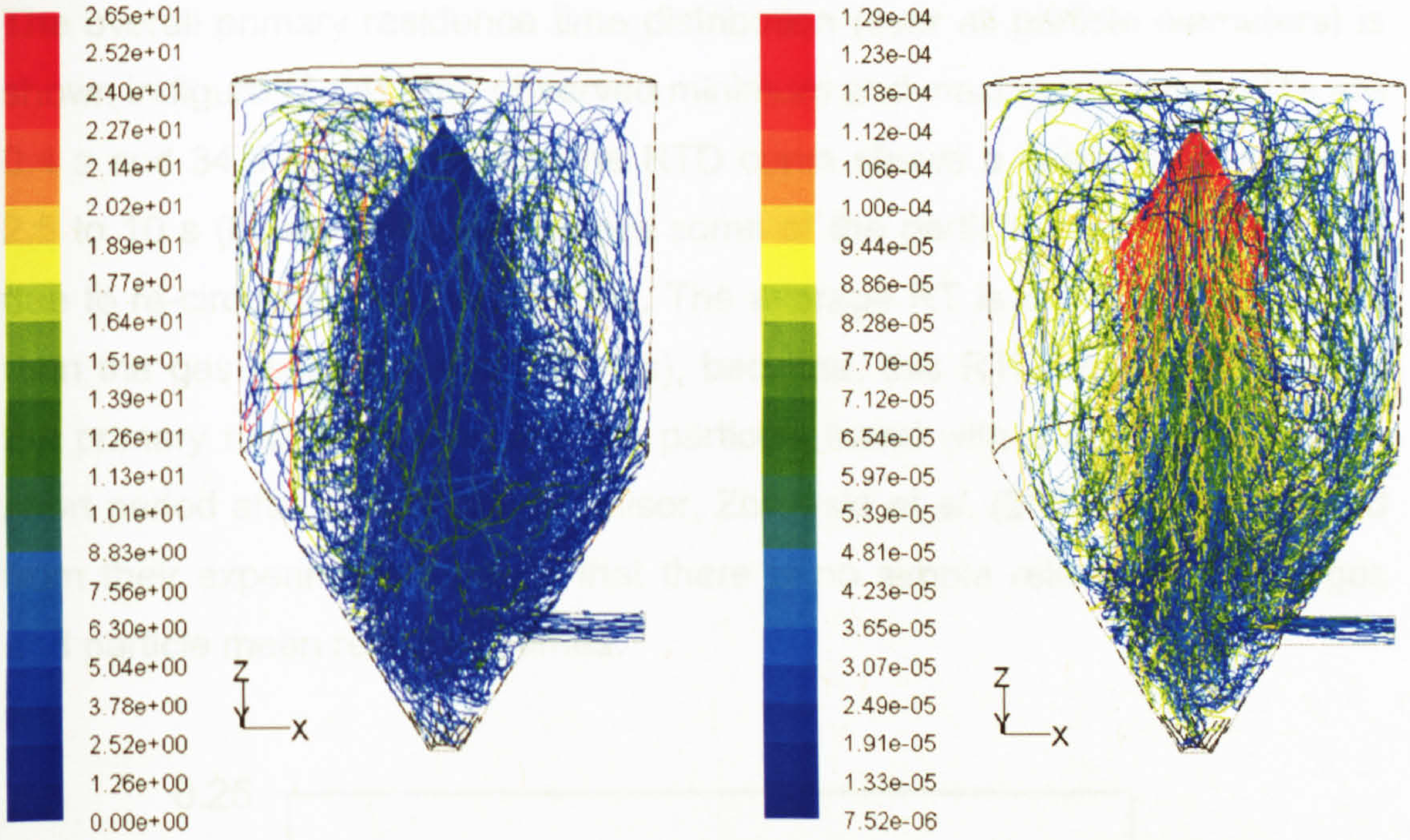

(a) (b)

Figure 7-13: Particle trajectories coloured by (a) particle residence time (s), and (b) particle diameter (m).

The residence time (RT) can be divided into two parts namely, primary and secondary residence times. The primary RT is calculated from the time taken for droplets leaving from nozzle until the particles impact on the wall or leave by the outlet. For particles that hit the wall a secondary residence time can be defined as the time taken for a particle to slide along the wall from the impact position to the exit. This is based on an assumption that particles move with constant velocity along the wall from the impact position. This constant sliding velocity is calculated based on the experimental measurements (Kieviet, 1997). However, this sliding velocity measurement may not be accurate, as sliding behavior of powders differs at various positions. The layer of powder on the wall grows with intermittent detachment of pieces of the layer. Moreover, two mechanical hammers are also often used to tumble the powders, so it is very difficult to calculate a representative constant sliding velocities of the particles. Hence, only primary RT results are given in this study.

The overall primary residence time distribution (over all particle diameters) is shown in figure (7-14). The observed minimum and maximum particle RTs are 0.4 s and 34.5 s respectively. The RTD curve shows a sharp peak between 2.5 to 10 s (figure 7-14) also shows some of the particles having a long RT, due to re-circulation of the particles. The average RT is 3.3 s, which is lower than the gas residence time (22.4 s), because, this RTD was calculated for the primary residence time and the particles travel with a high velocity for a short period after leaving the atomiser. Zbicinski *et al.* (2002) also concluded from their experimental results that there is no simple relation between gas and particle mean residence times.

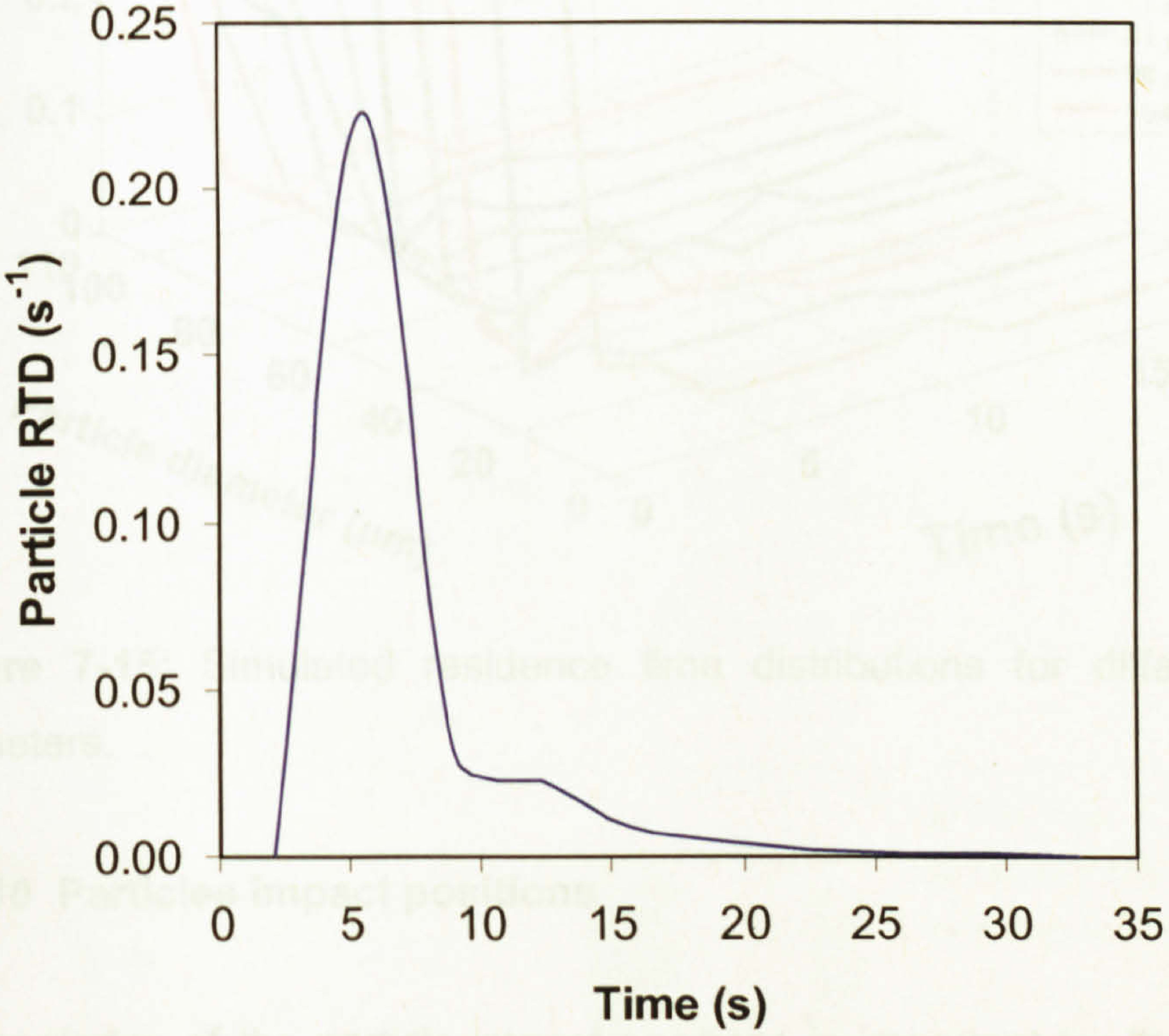

Figure 7-14: Particle overall primary RTD.

The RTDs of the different size particles are shown in figure (7-15). It is observed that larger diameter particles have longer residence times than smaller particles. The same trend was observed by Kieviet (1997), who also found that there was an enormous difference between measured and predicted results due to particle wall depositions and sliding movement. However, no direct measurement of primary residence time are available to confirm these predictions. These measurements are very difficult to make and are an interesting challenge for future research.

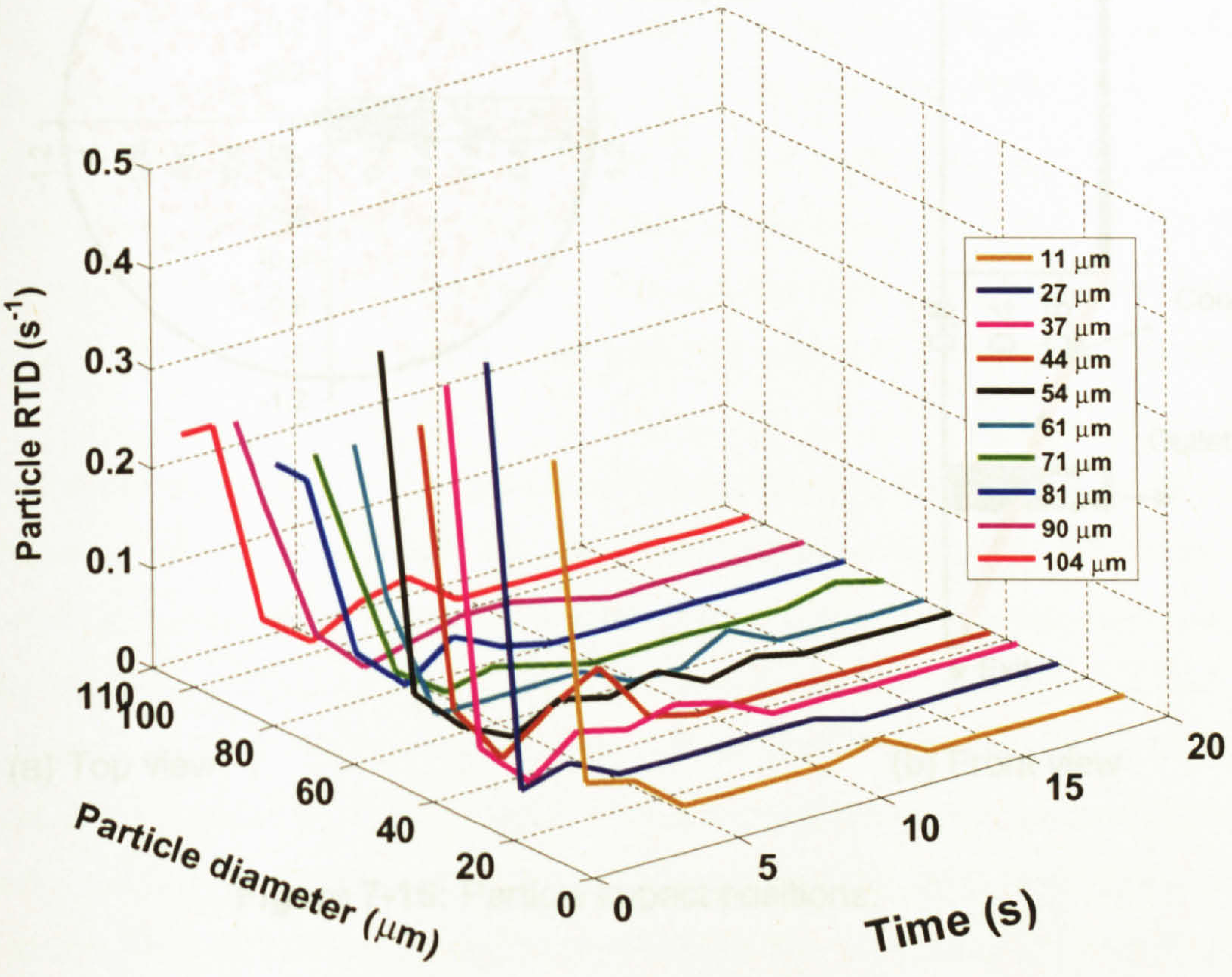

Figure 7-15: Simulated residence time distributions for different particle diameters.

7.7.10 Particles impact positions

A knowledge of the particle impact positions is important for the design and operation of spray-dryers and also influences the quality of the products. Particles impact positions on wall results were extracted from the simulation data using the in-house-developed post-processor.

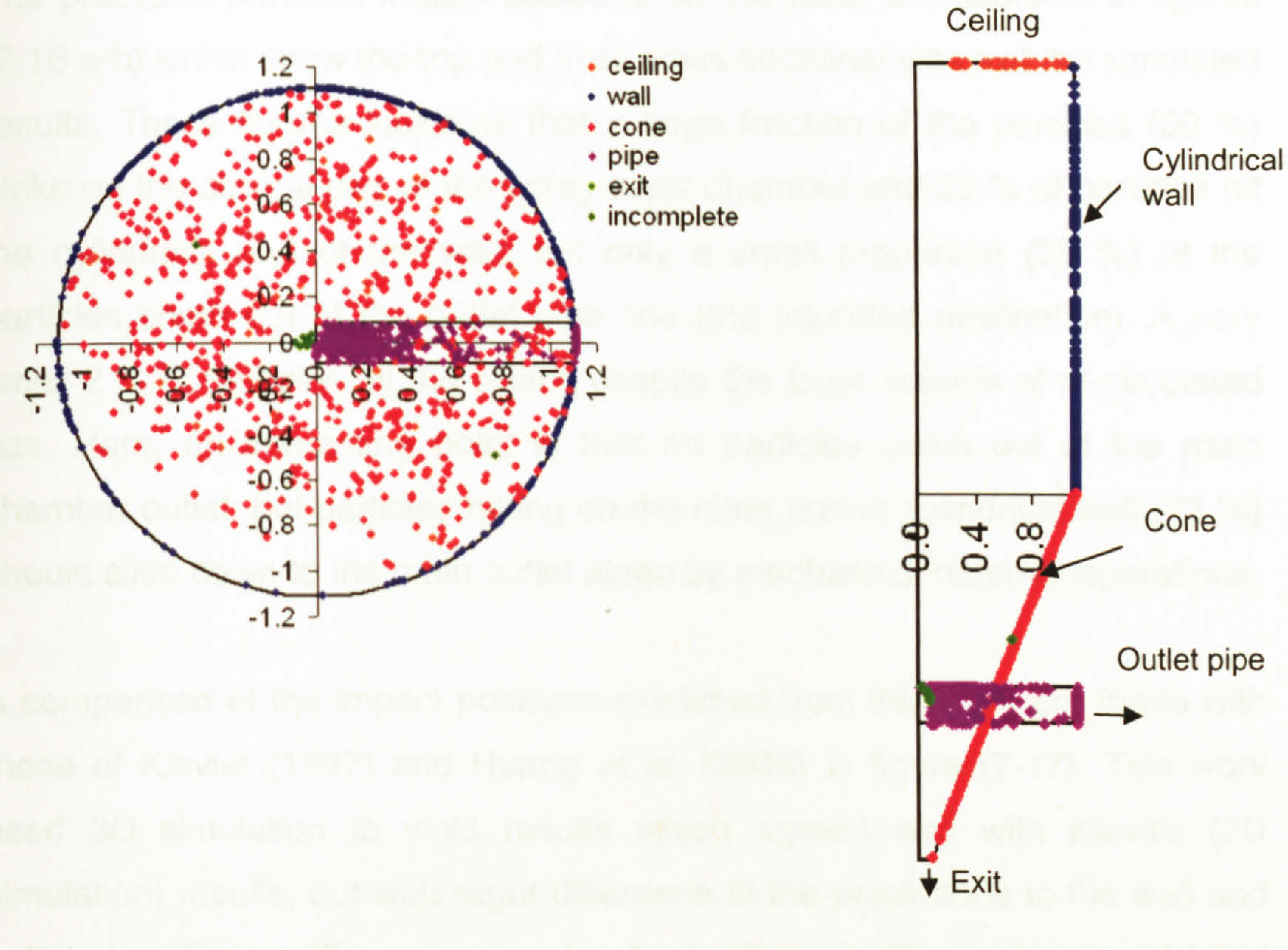

(a) Top view (b) Front view

Figure 7-16: Particle impact positions.

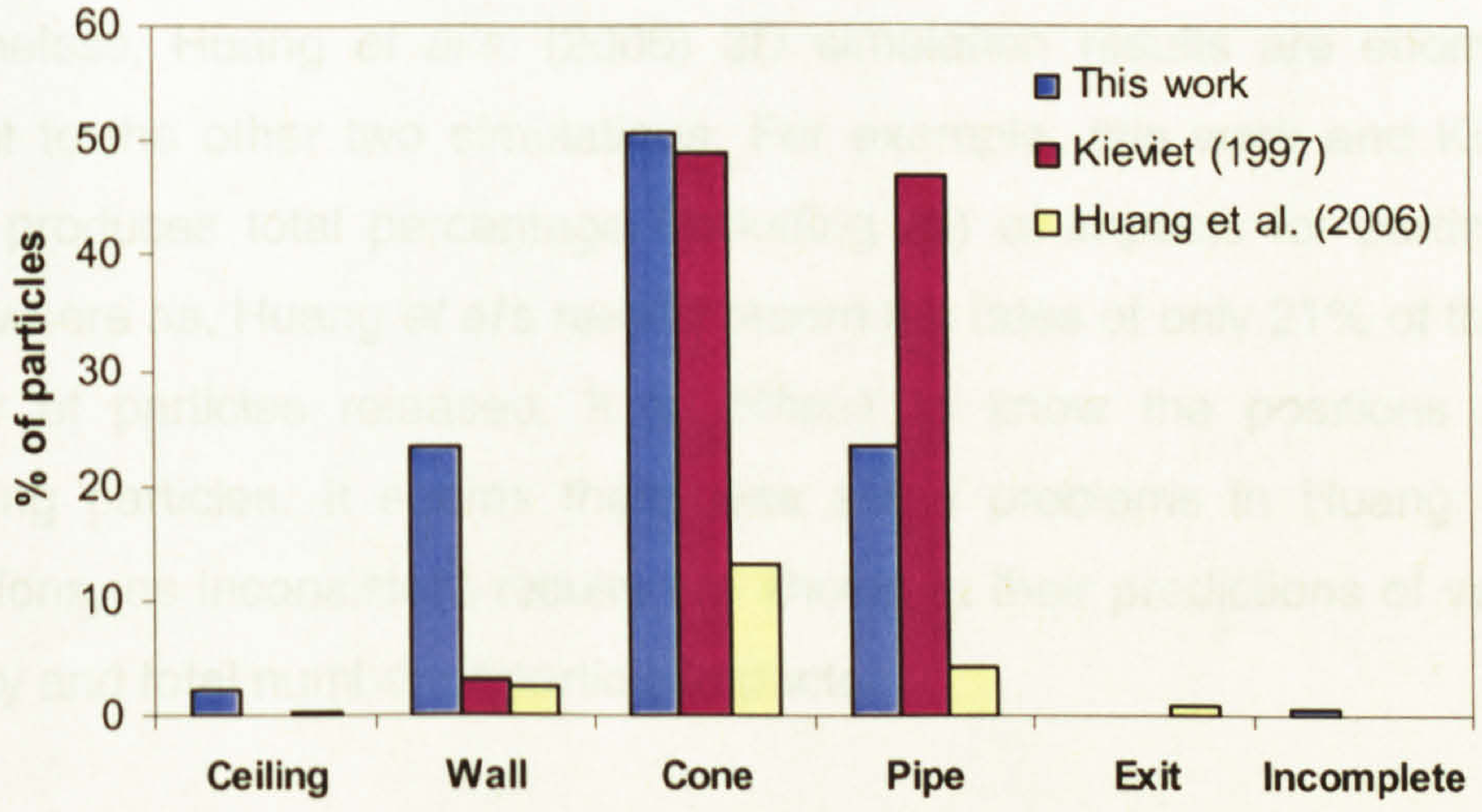

Figure 7-17: Comparison of particle impact positions.

The predicted particles impact positions on the walls are depicted in figures (7-16 a-b) which show the top and front cross-sectional views of the simulated results. These figures indicates that a large fraction of the particles (50 %) strike on the conical part of the spray-dryer chamber and 23 % of particles hit the cylindrical part of the wall, but only a small proportion (25 %) of the particles come out of the outlet pipe line (the intended destination). A very small 2 % of particles hit the ceiling despite the large volume of re-circulated gas. Here, an interesting point is that no particles come out of the main chamber outlet, but particles hitting on the cone and/or cylindrical wall (73 %) should slide down to the main outlet aided by mechanical hammer operations.

A comparison of the impact positions predicted from this work are made with those of Kieviet (1997) and Huang *et al.* (2006) in figure (7-17). This work used 3D simulation to yield results which agreed well with Kievit's (2D simulation) results, but with slight difference in the predictions to the wall and outlet pipe. These differences may be due to Kieviet's 2D simulation which did not fully consider the outlet pipe region (their geometry was selected from the front section of the pipe inserted of full length of the pipe, see figure. 2-27). Hence, the effect of re-circulation of gas from the outlet pipe line was high and resulted in more particles impacting on the cylindrical wall region.

Nevertheless, Huang *et al's.* (2006) 3D simulation results are enormously different to the other two simulations. For example, this work and Kieviet's results produces total percentage (including all) of impacts for particles as 100%, where as, Huang *et al*'s results record the fates of only 21% of the total number of particles released. It is difficult to know the positions of the remaining particles. It seems there was some problems in Huang *et al*'s simulations, as inconsistent results are shown in their predictions of velocity, humidity and total number of particle impacts.

7.8 *Case B*: Tall-form spray dryer

Case B is concerned with the CFD simulations relating to the tall-form spray-dryer used for the experiments in this thesis (Chapter 5). The simulation methodologies used were the same for *Cases A* and *B*. However, this tall-form spray dryer was constructed almost 25 years ago and there were no options for measurements of velocity and gas/particle temperature inside the drying chamber. It was considered that the spray-dryer simulation methodology had been validated with the *Case A* study and hence may be applied with confidence to the *Case B* study. Figure (7-18) shows the geometry used in this simulation. A 30% (w/v) whey protein isolate feed concentration at 181°C inlet gas temperature (experimental trial 1) was selected for this study.

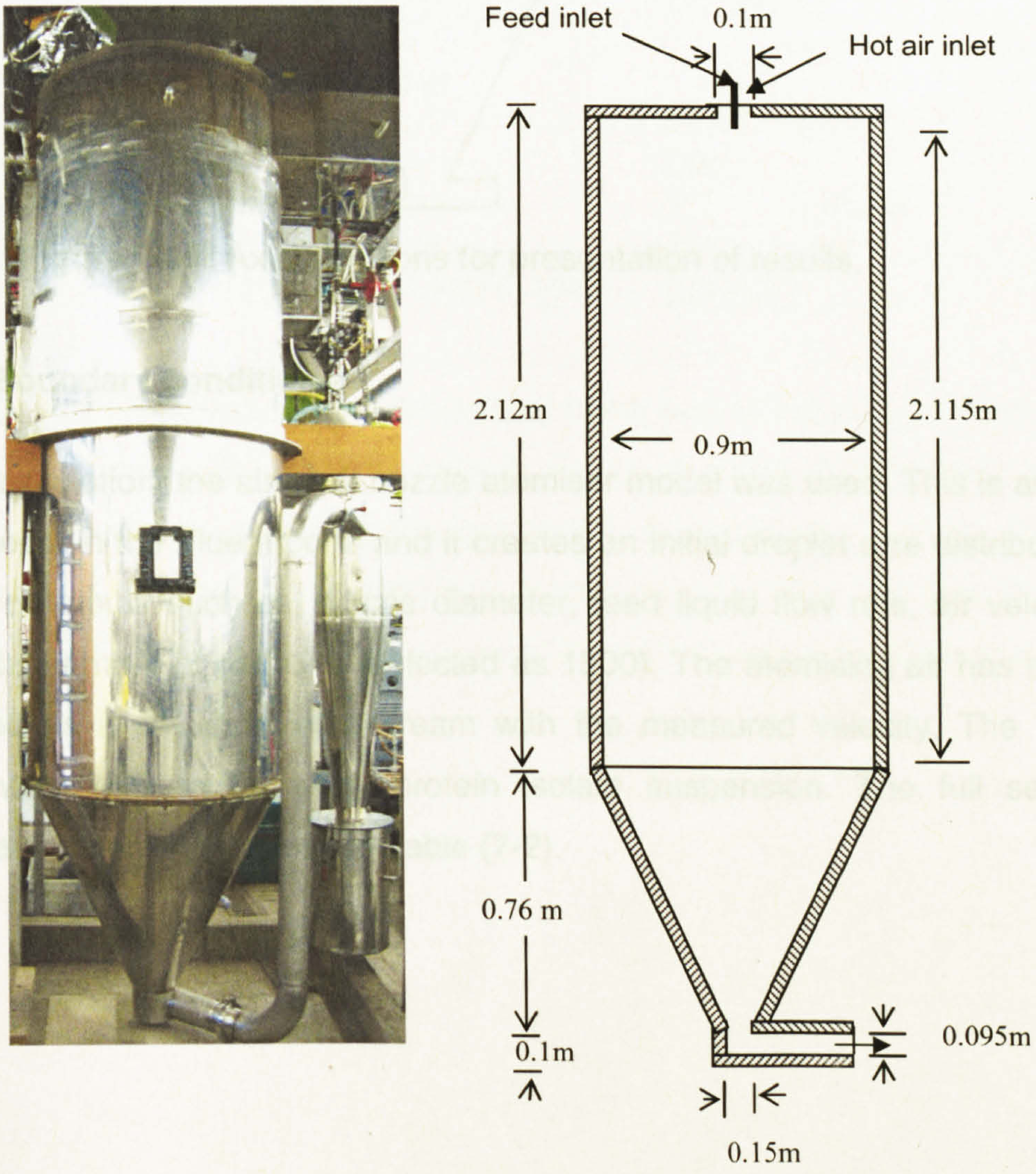

Figure 7-18: Geometry used in *Case B* simulation.

The axial positions used for the presentation of results are shown in figure (7-19).

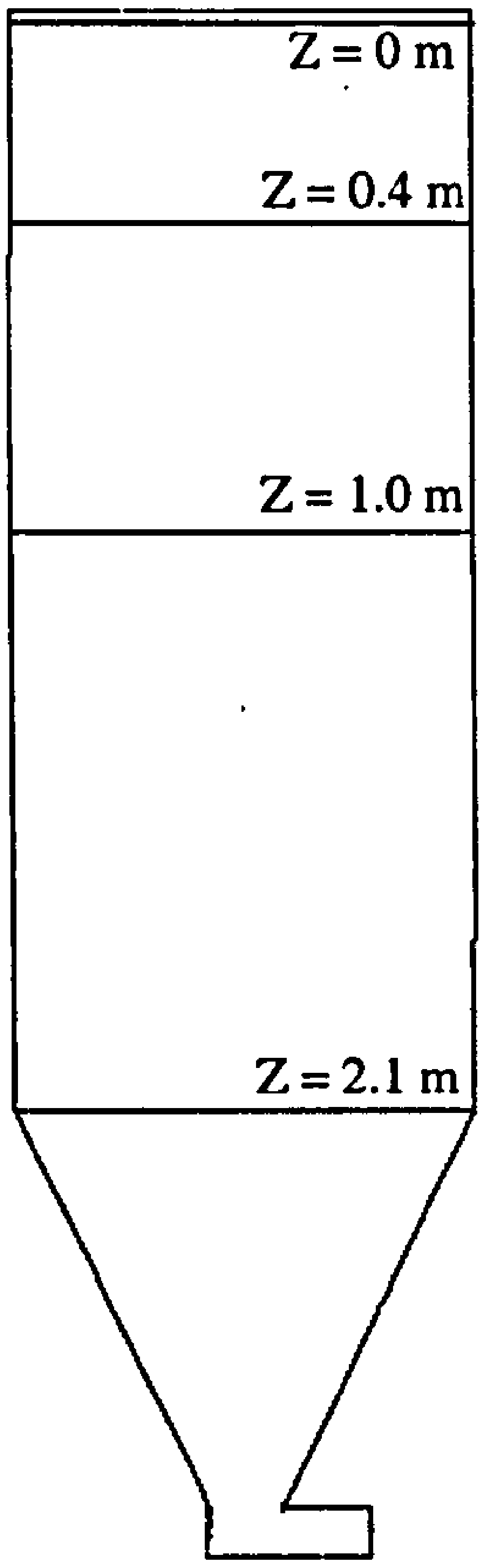

Figure 7-19: Axial positions for presentation of results.

7.8.1 Boundary conditions

In this simulation, the air blast nozzle atomiser model was used. This is an in-built model in the Fluent code and it creates an initial droplet size distribution based on inputs such as, nozzle diameter, feed liquid flow rats, air velocity and total number of particles (selected as 1500). The atomising air has been included as a separate inlet stream with the measured velocity. The feed liquid was 30% solids whey protein isolate suspension. The full set of boundary conditions is given in Table (7-2).

Table 7-2: Boundary conditions used for tall-form spray dryer simulation.

Inlet Air	
Air inlet temperature	444 (K)
Air mass flow rate	0.063 (kg/s)
Air axial velocity	8.87 (m/s)
Outlet Condition	
Outflow and reference at outlet	-100 (Pa)
Turbulence inlet condition	
Turbulence k-value	0.29 (m^2/s^2)
Turbulence ε-value	0.51 (m^2/s^3)
Liquid spray from nozzle	
Liquid feed rate (spray rate)	0.00203 (kg/s)
Feed Temperature	293 (K)
Spray half angle	9°
Injector inner diameter	0.00173 (m)
Injector outer diameter	0.00305 (m)
Atomising air velocity	29.2 (m/s)
Chamber wall conditions	
Chamber wall thickness	0.002 (m)
Wall material	Steel
Wall-heat transfer co-efficient	3.5 (W/m^2K)
Air temperature outside wall	293 (K)
Interaction between wall and droplet	Escape *

In the 3D-model a hexahedral grid (typical mesh size 0.001 m) was used with 294,237 grid cells. The grid geometry is shown in figure (7-20). The k and ε initial condition values were estimated based on equations (7-18) to (7-20). The "*escape*" wall boundary conditions were also used. The wall overall heat transfer coefficient was determined experimentally from energy balance over the dryer (see section 5.3).

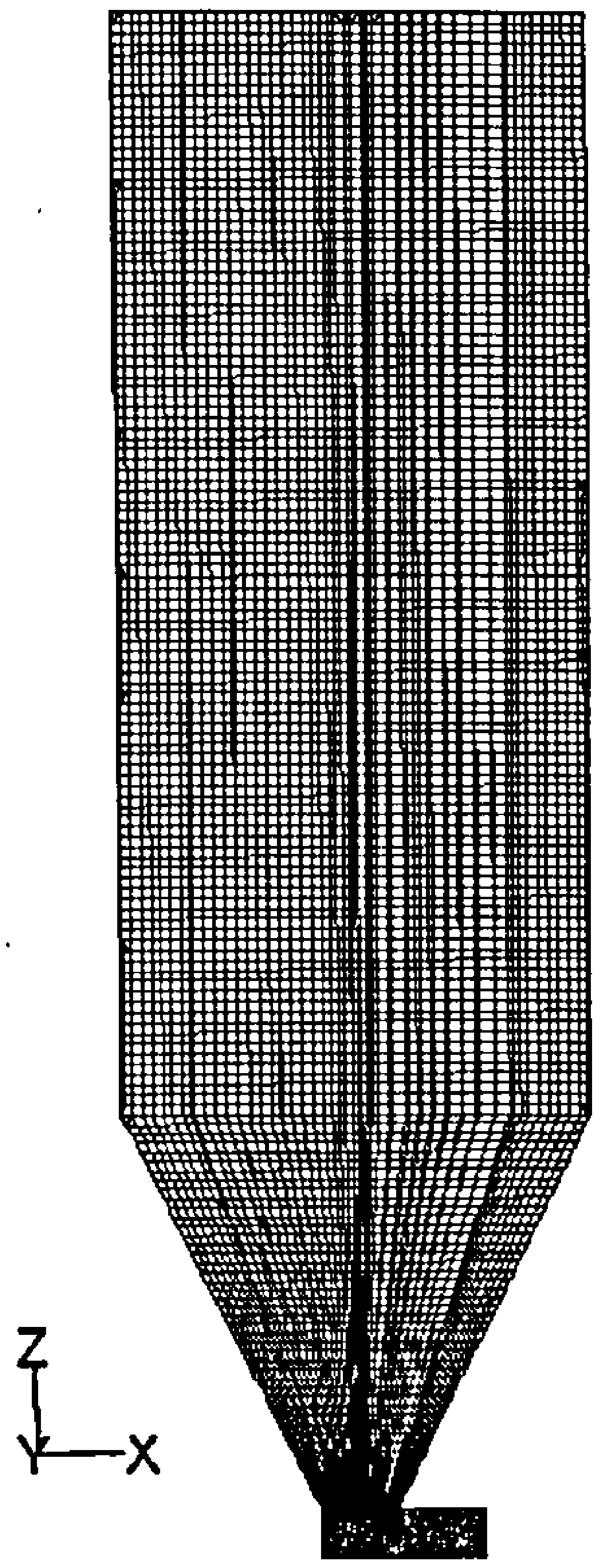

Figure 7-20: Grid used in this simulation.

7.8.2 Gas velocity and temperature profiles without the spray injection

As with *Case A*, the first step in this simulation was to obtain the gas flow field in the absence of a spray injection. Figures (7-21) shows the gas flow pattern as velocity vectors, axial velocity and temperatures. The flow pattern shows recirculation of gas shown near the wall region due to the converging outlet (figure 7-21 a). However, the air flow patterns also appears to be axisymmetric throughout the drying chamber. The contours of temperature profiles are depicted in figures (7-21 c), and shows high temperatures in the core region (454 K), because of the hot air feed entering this region. Outside the core region the temperature is lower and more uniform (409 K).

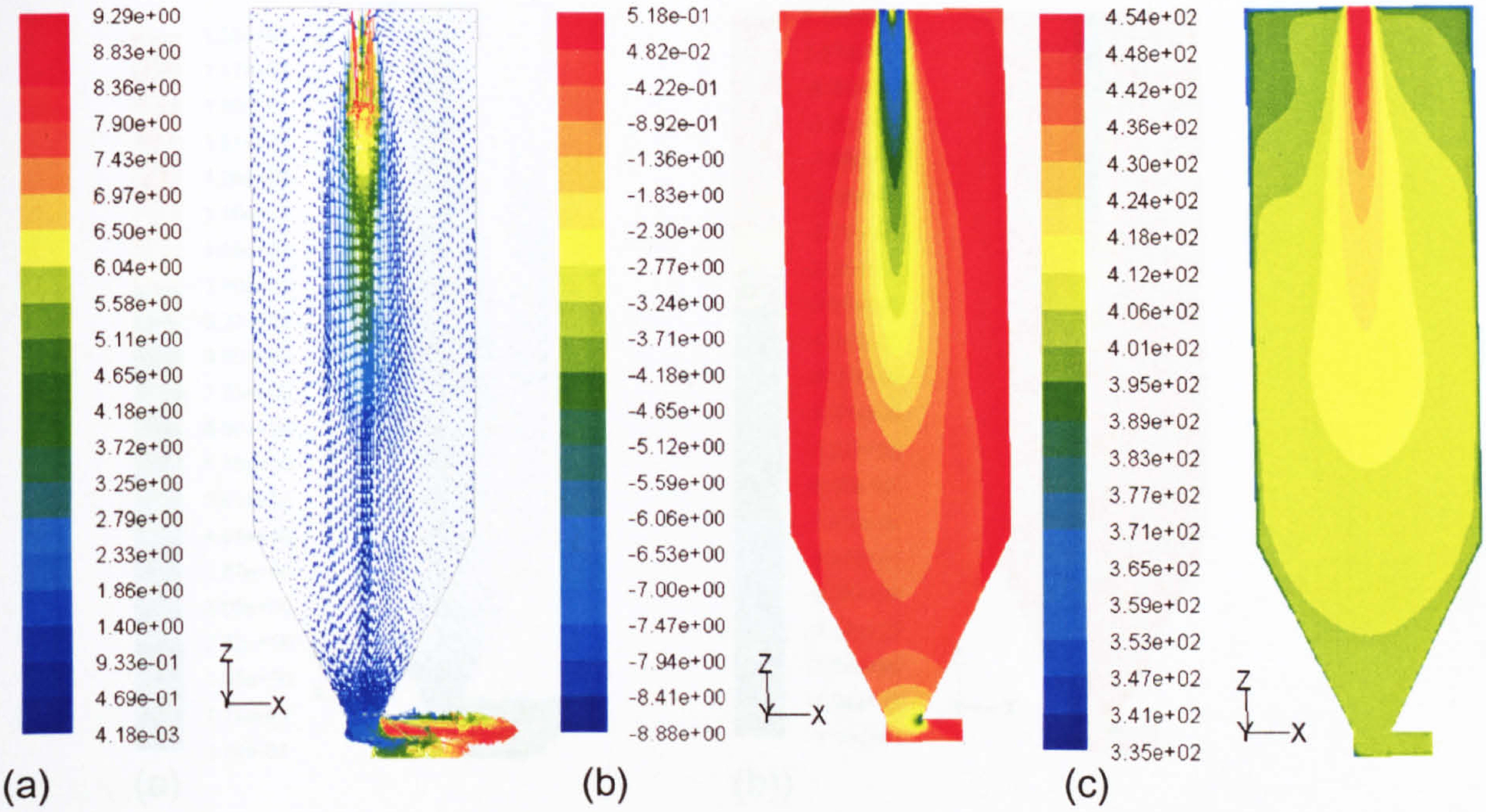

Figure 7-21: Gas profiles without spray injection: (a) velocity magnitude vector (m/s), (b) contours of axial velocity (m/s), and (c) Temperature (K).

7.8.3 Axial velocity profiles of gas with spray injection

The gas velocity magnitude vector and axial velocity profiles with spray injection are shown in figures (7-22 a-b). Figures (7-23 a-b) shows the radial profiles of gas axial velocity at axial distances from the spray nozzle of z = 0.4 m and 2.1 m. Data obtained in the X-Z planes are labeled as X and Y-Z planes are labeled as Y in the figure 7-23.

A recirculation zone is clearly shown in the figures (7-22 a) and (7-23 b) as upward axial velocities were found near to the wall region. The simulation results shows a higher axial velocity (7 m/s) in the core region at 0.4 m level (figure 7-23 a) than at z = 2.1 m. This trend was expected as a full cone spray was used in this simulation. At z = 2.1 m level the axial velocity is reduced to 0.6 m/s (see figure 7-23 b). Symmetric velocity profiles were found at z = 0.4 m, whereas, slightly asymmetric velocity profiles were found at z = 2.1 m caused by the slight asymmetry of the outlet pipe.

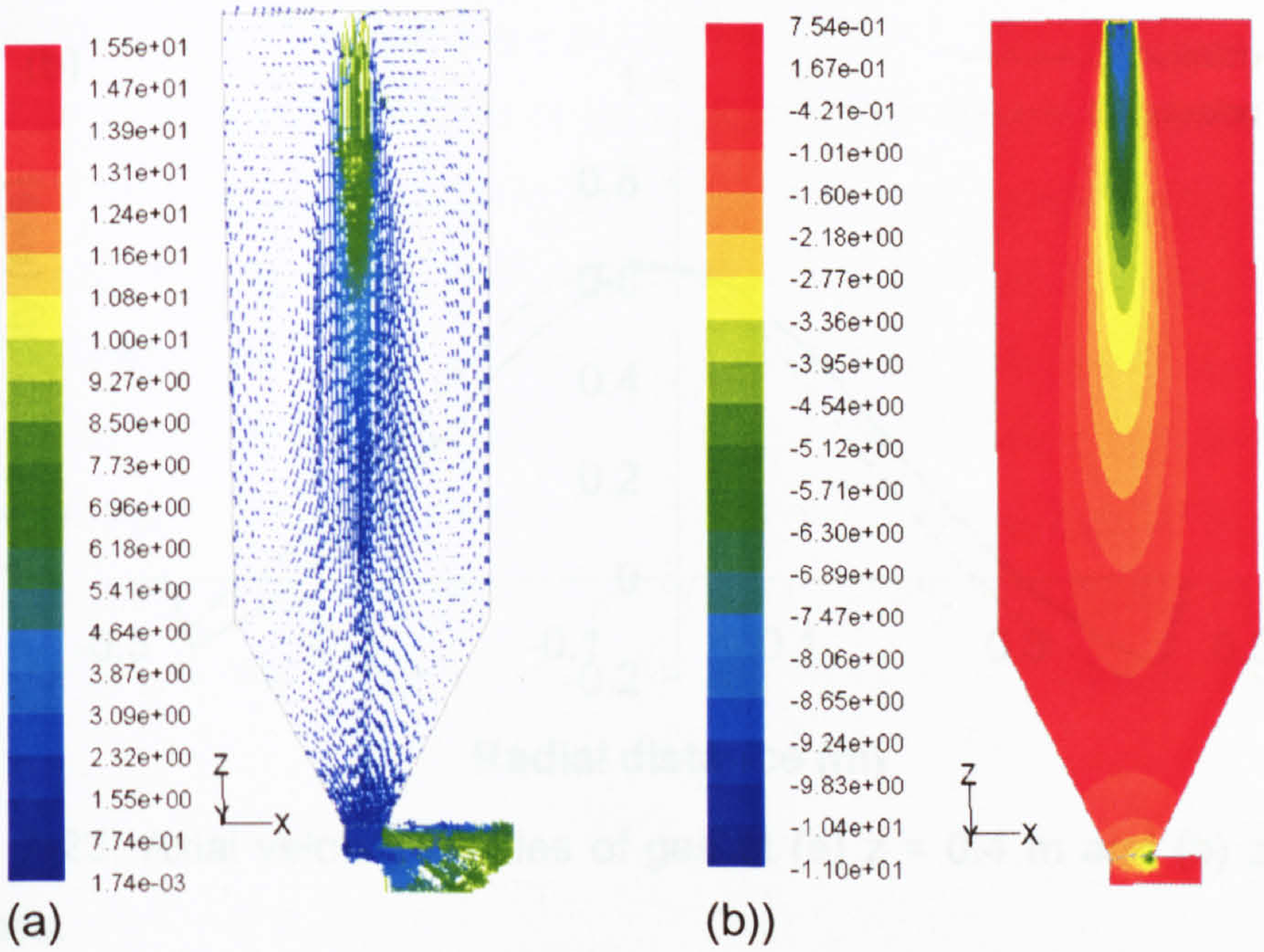

Figure 7-22: Gas velocity profiles with spray injection: (a) velocity magnitude vector (m/s), and (b) contours of axial velocity (m/s).

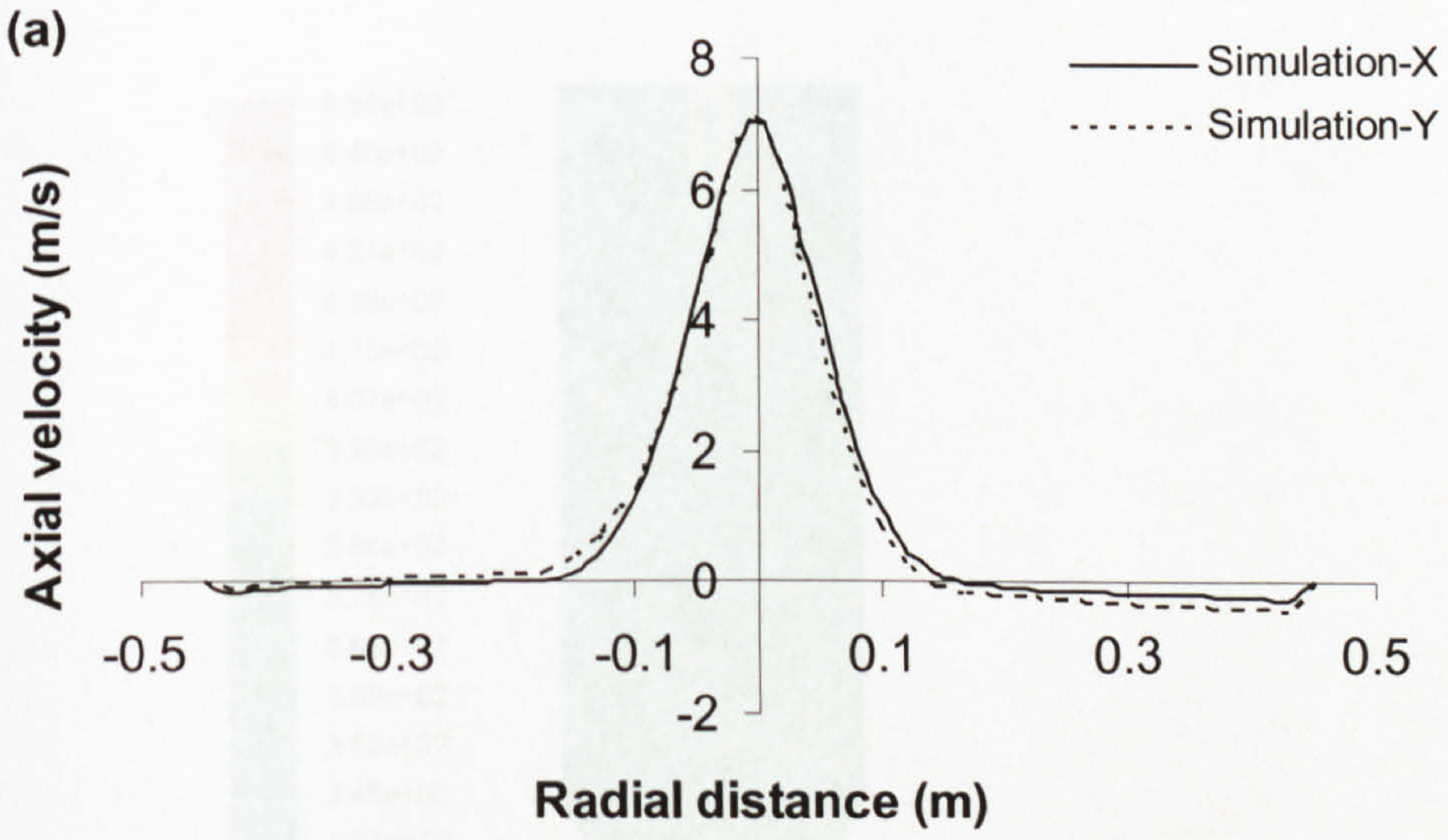

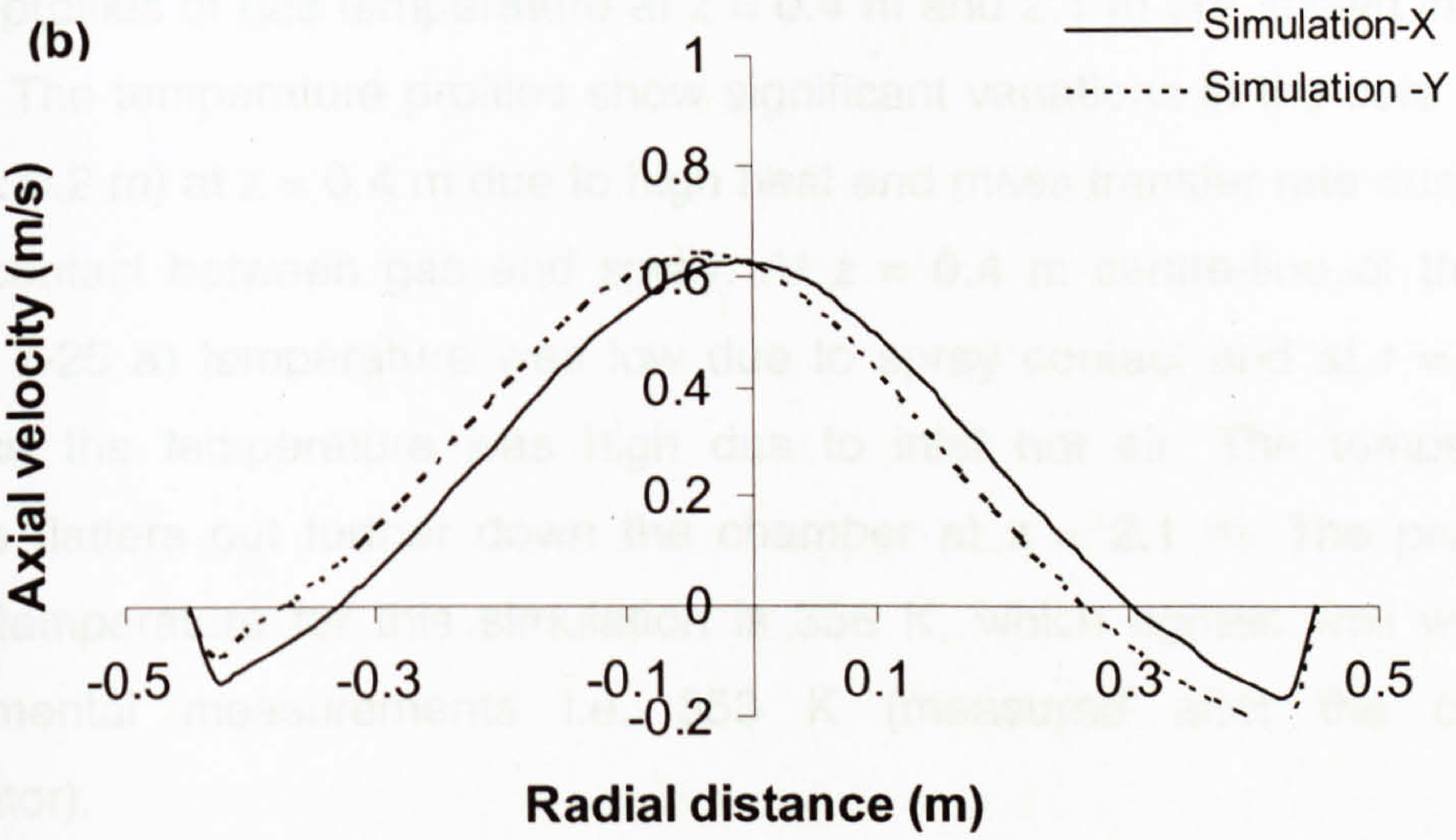

Figure 7-23: Axial velocity profiles of gas at (a) z = 0.4 m and (b) z = 2.1 m distances.

7.8.4 Temperature profile of gas with spray injection

The gas temperature contours are depicted in figure (7-24). These show that a large volume of the spray dryer outside the vicinity of the liquid spray has almost uniform temperature, similar to *Case A*.

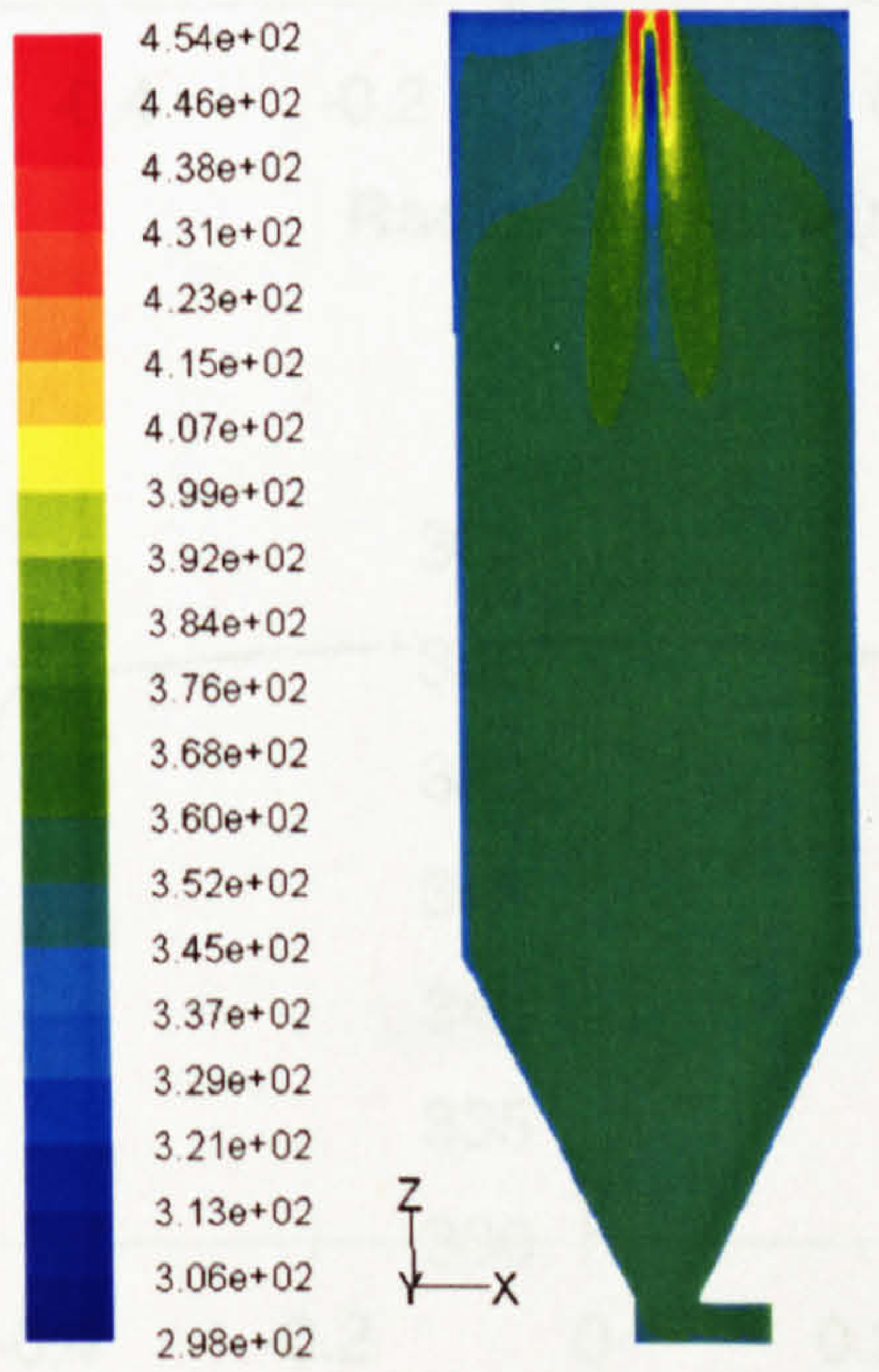

Figure 7-24: Temperature contours of gas (K).

Radial profiles of gas temperature at z = 0.4 m and 2.1 m are shown in figure (7-25). The temperature profiles show significant variations in the core region (0 < r < 0.2 m) at z = 0.4 m due to high heat and mass transfer rate during the initial contact between gas and spray. At z = 0.4 m centre-line of the axis (figure 7-25 a) temperature was low due to spray contact and at r = 0.1 m distance the temperature was high due to inlet hot air. The temperature profiles flatters out further down the chamber at z = 2.1 m. The predicted outlet temperature for this simulation is 356 K, which agrees well with the experimental measurements i.e. 353 K (measured after the cyclone separator).

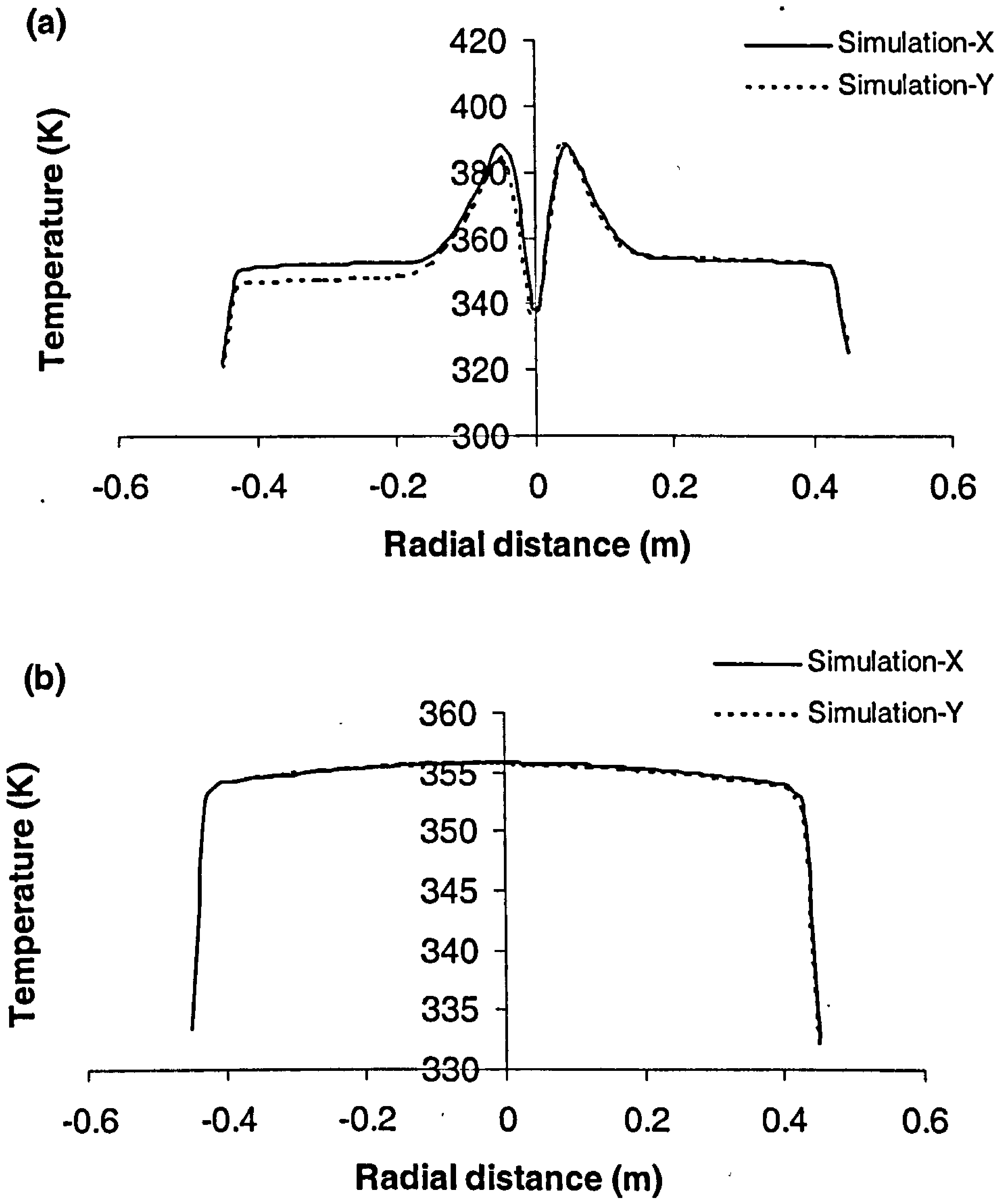

Figure 7-25: Radial temperature profiles of gas at (a) z = 0.4 m and (b) z = 2.1 m.

7.8.5 Humidity profiles of gas with spray injection

In figures (7-26 a-b), radial profiles of gas humidity, expressed as water vapour mass fraction are presented. The humidity profiles were similar in form to the temperature profiles, but inverted (see figures 7-25 and 7-26). At the z = 0.4 m level in the centre-line of the axis humidity was higher due to spray injection, whereas, at the bottom of the chamber (z = 2.1 m) the humidity was almost uniform across the chamber diameter.

Symmetric humidity profiles are shown at the z = 0.4 m and 2.1 m levels, which is different from *Case A*. In *Case B* there is no outlet pipe inside the chamber, which reduces the recirculation of gas at core region inside the chamber. This is reflected in the simulation results at z = 2.1 m showing symmetric humidity, temperature and velocity profiles. However, outside the core region (r > 0.2 m) gas humidity was shown almost similar at z = 0.4 m and 2.1 m distances. This may be due to recirculation of cold gas near to the wall region (see figure 7-21).

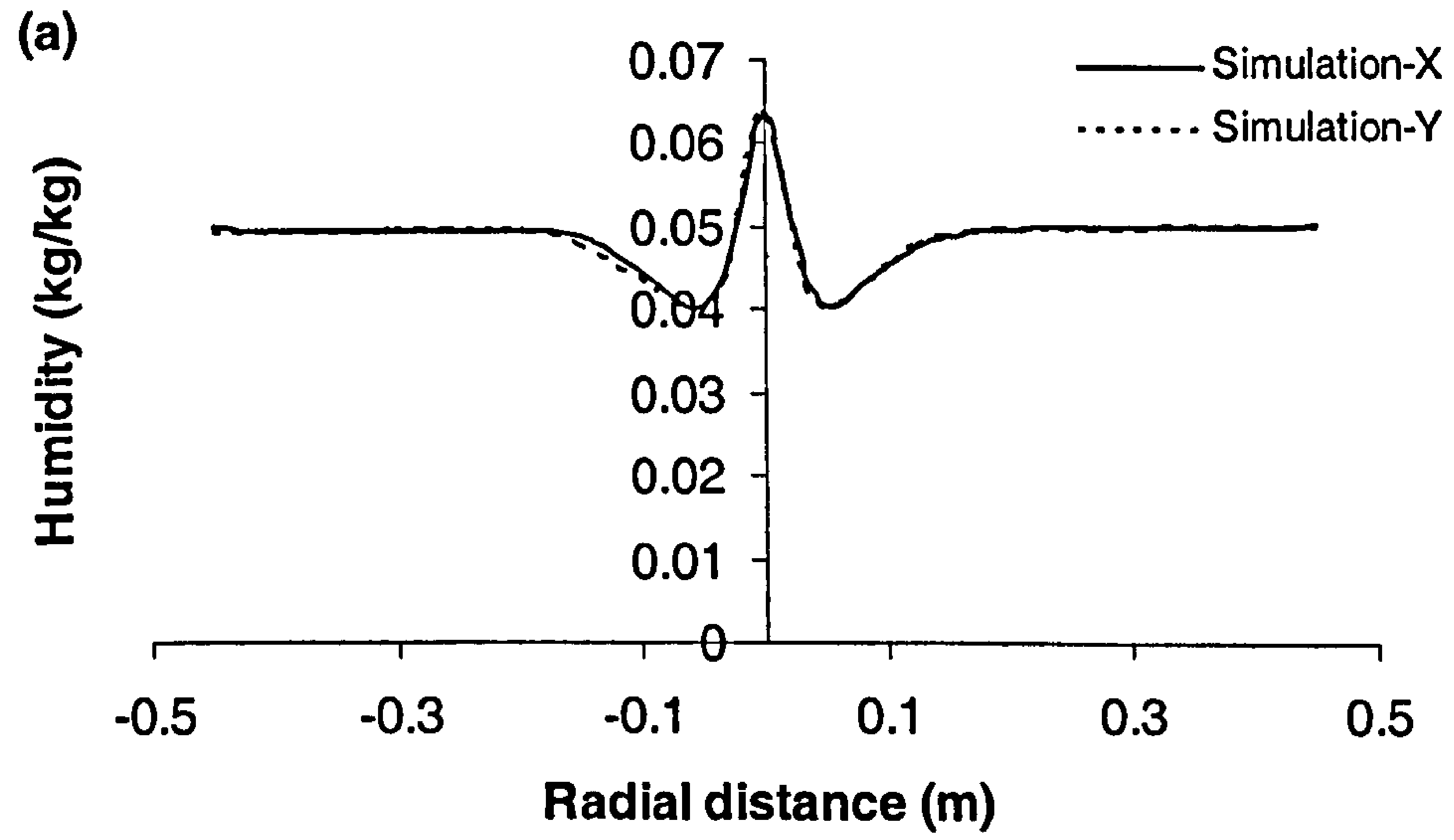

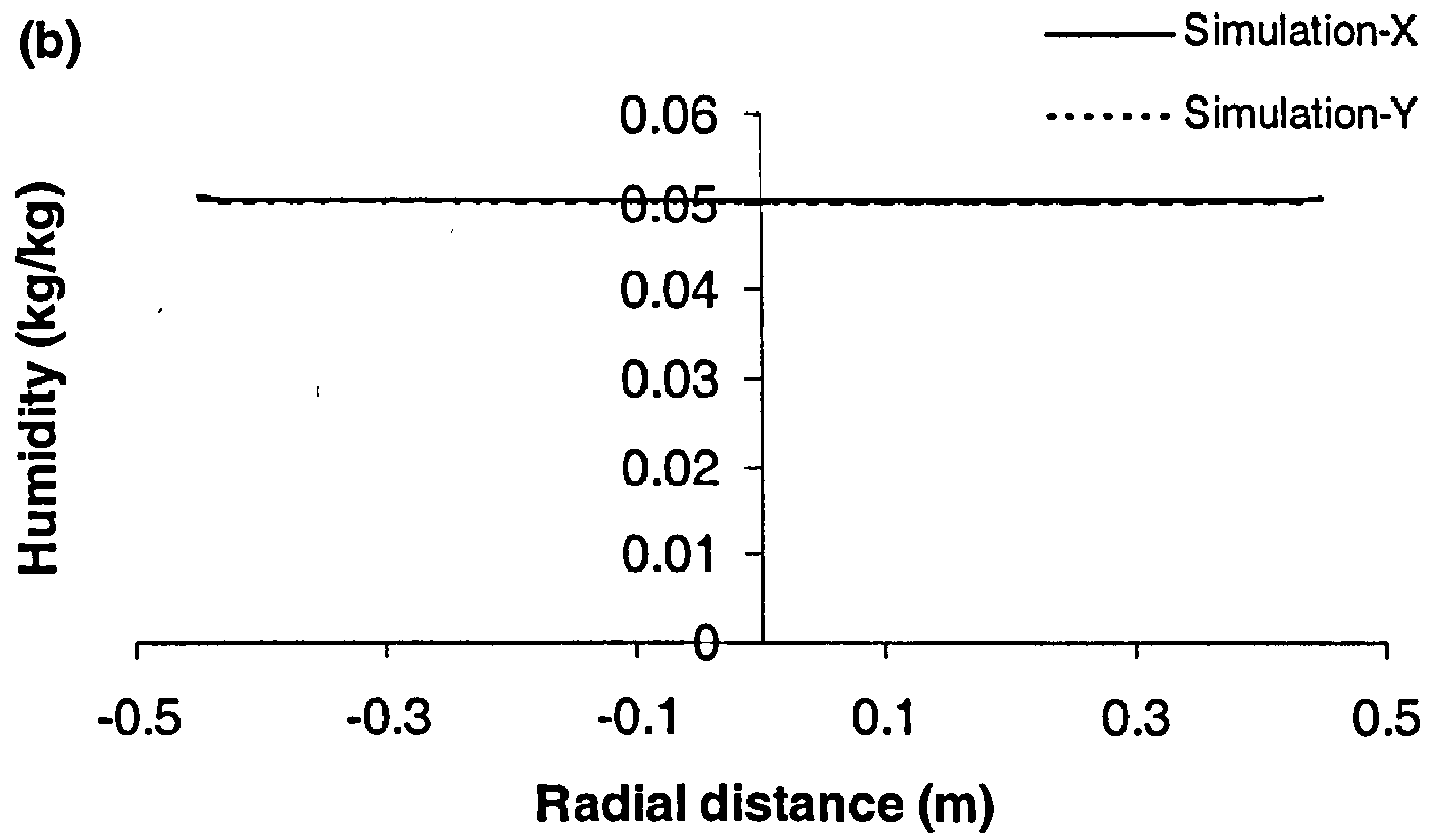

Figure 7-26: Humidity profiles of gas at (a) z = 0.4 m and (b) z = 2.1 m distance.

7.8.6 Particle histories

The particles histories for temperature and velocity, the residence time distribution (RTD) and particle impact positions on the wall in a tall-form spray dryer are described in the following sub-sections. This simulation produces wide range of particle diameters from 6 to 60 μm, but four particles size ranges of 10 μm, 20 μm, 30 μm and 40 μm were selected to represent the particle size distribution. The simulated radial profiles of particle velocity and temperatures at z = 0.4 m, 1.0 m and 2.1 m are described in the following sub-sections.

Particle history results were extracted from the simulation data by using the in-house-developed post-processor as used in this chapter.

7.8.7 Droplets axial velocity at various radial positions

The radial profiles of particle velocity at z = 0.4 m, 1.0 m and 2.1 m are shown in figures (7-27 a-c). In this simulation, the spray half angle is only 9° (solid cone), hence there are a large number of control volumes, where no droplets have passed through. The particle axial velocities were almost equal to the gas velocity profiles. At the z = 0.4, 1.0 m and 2.1 m predictions shows very similar axial velocities for all sizes of particles.

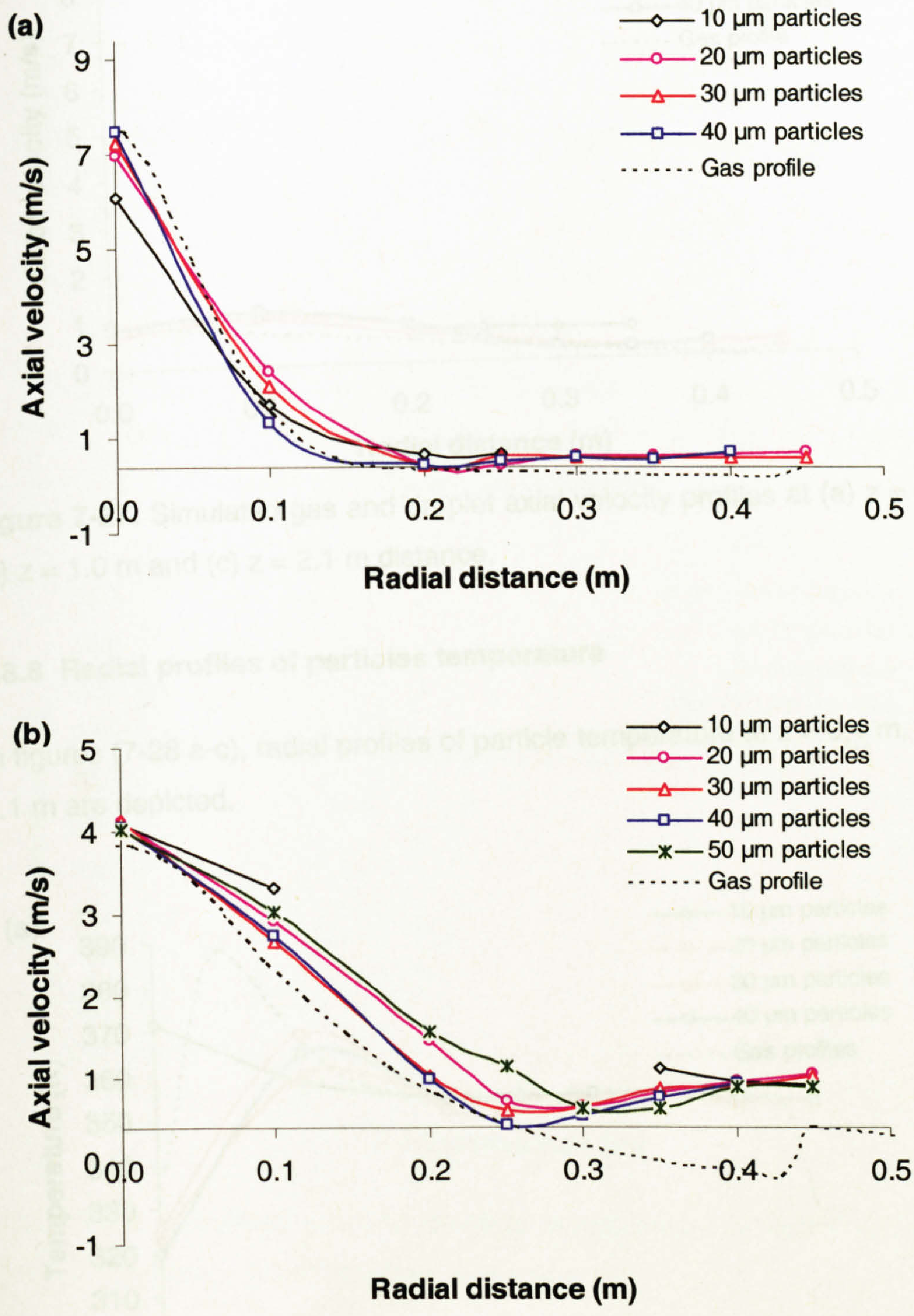

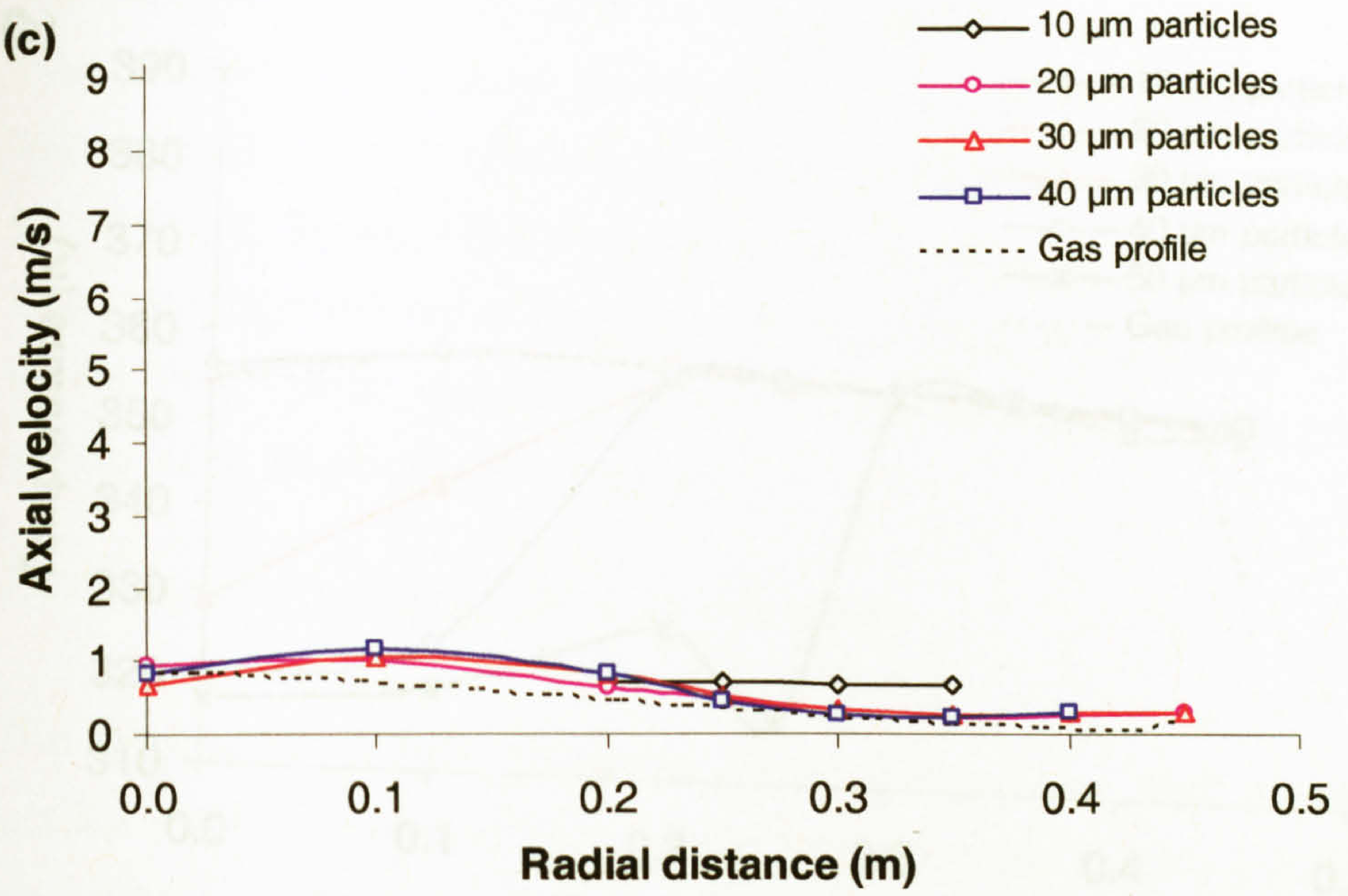

Figure 7-27: Simulated gas and droplet axial velocity profiles at (a) z = 0.4 m (b) z = 1.0 m and (c) z = 2.1 m distance.

7.8.8 Radial profiles of particles temperature

In figures (7-28 a-c), radial profiles of particle temperature at z = 0.4 m, 1.0 m, 2.1 m are depicted.

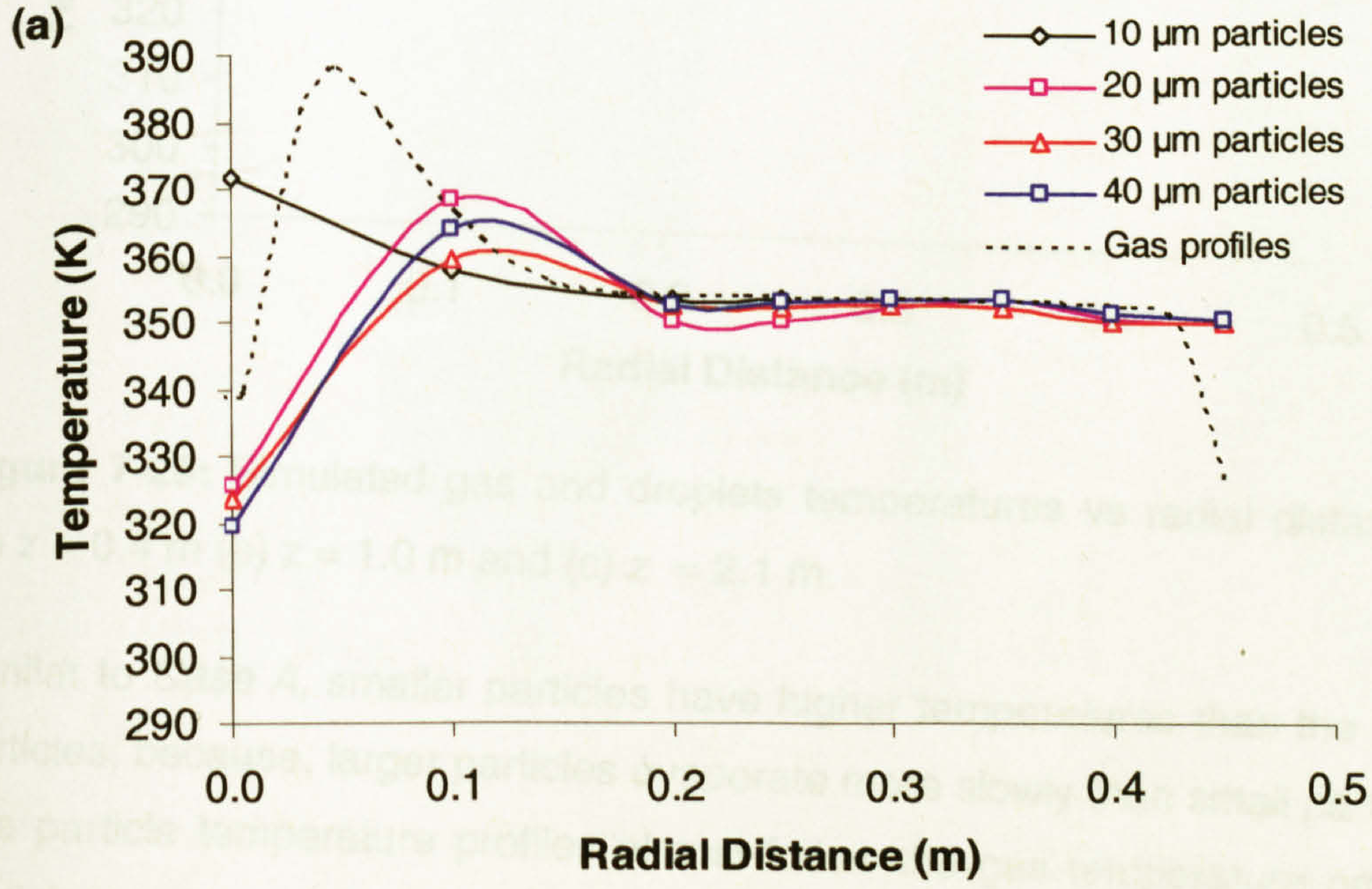

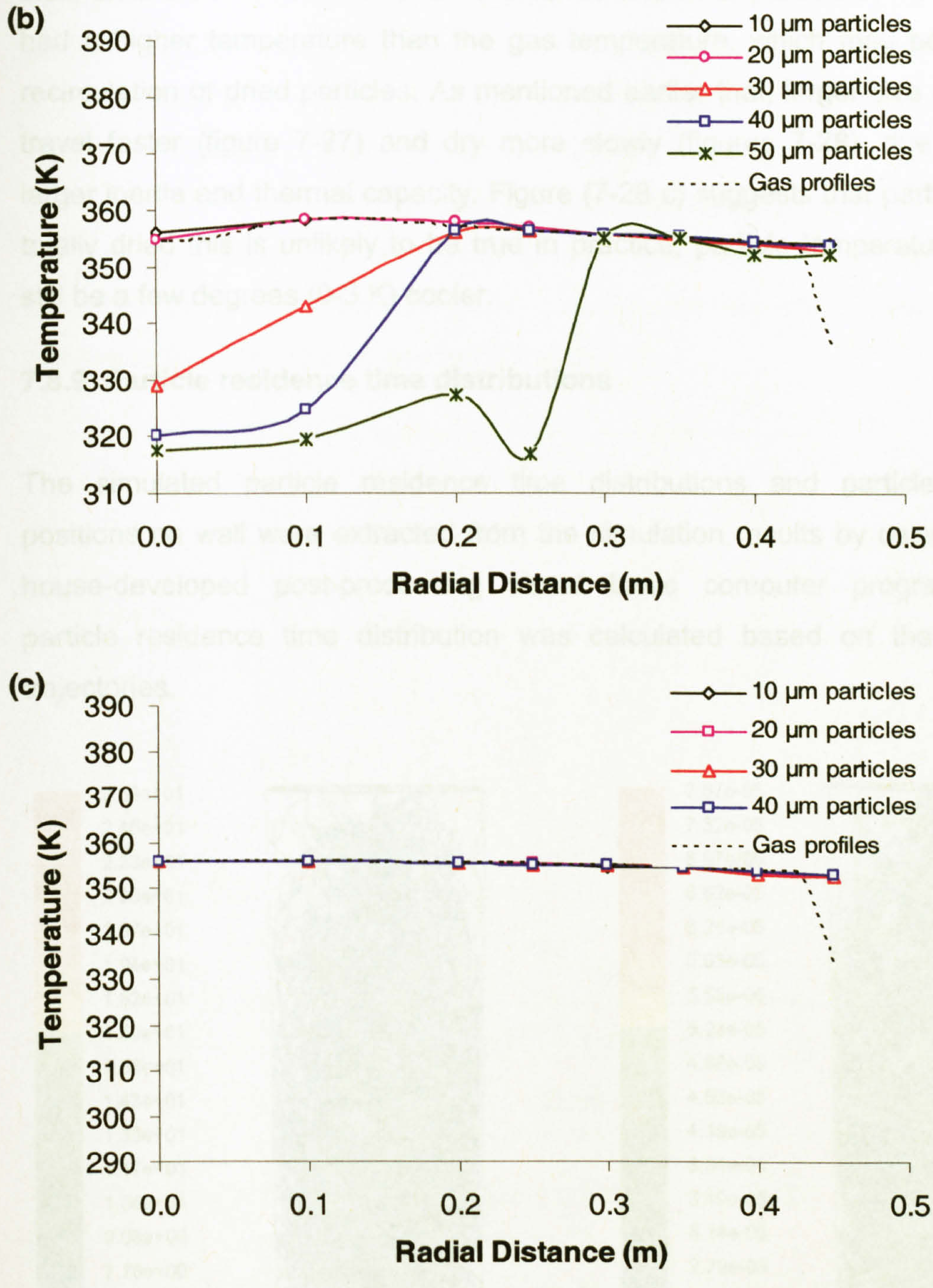

Figure 7-28: Simulated gas and droplets temperatures vs radial distance at (a) z = 0.4 m (b) z = 1.0 m and (c) z = 2.1 m.

Similar to *Case A*, smaller particles have higher temperatures than the larger particles, because, larger particles evaporate more slowly than small particles. The particle temperature profiles almost follow the gas temperature profiles, particle temperature was increasing consistently with distance down the column and finally reached the gas exit temperature of 355 K. However, at the axial distance z = 0.4 m level on the centre line axis, particle of 10 μm size had a higher temperature than the gas temperature, which may be due to recirculation of dried particles. As mentioned earlier that, larger size particles travel faster (figure 7-27) and dry more slowly (figures 7-28), due to their larger inertia and thermal capacity. Figure (7-28 c) suggests that particles are totally dried this is unlikely to be true in practice, particle temperatures may still be a few degrees (0-3 K) cooler.

7.8.9 Particle residence time distributions

The simulated particle residence time distributions and particle impact positions on wall were extracted from the simulation results by using the in-house-developed post-processing visual basic computer program. The particle residence time distribution was calculated based on the particle trajectories.

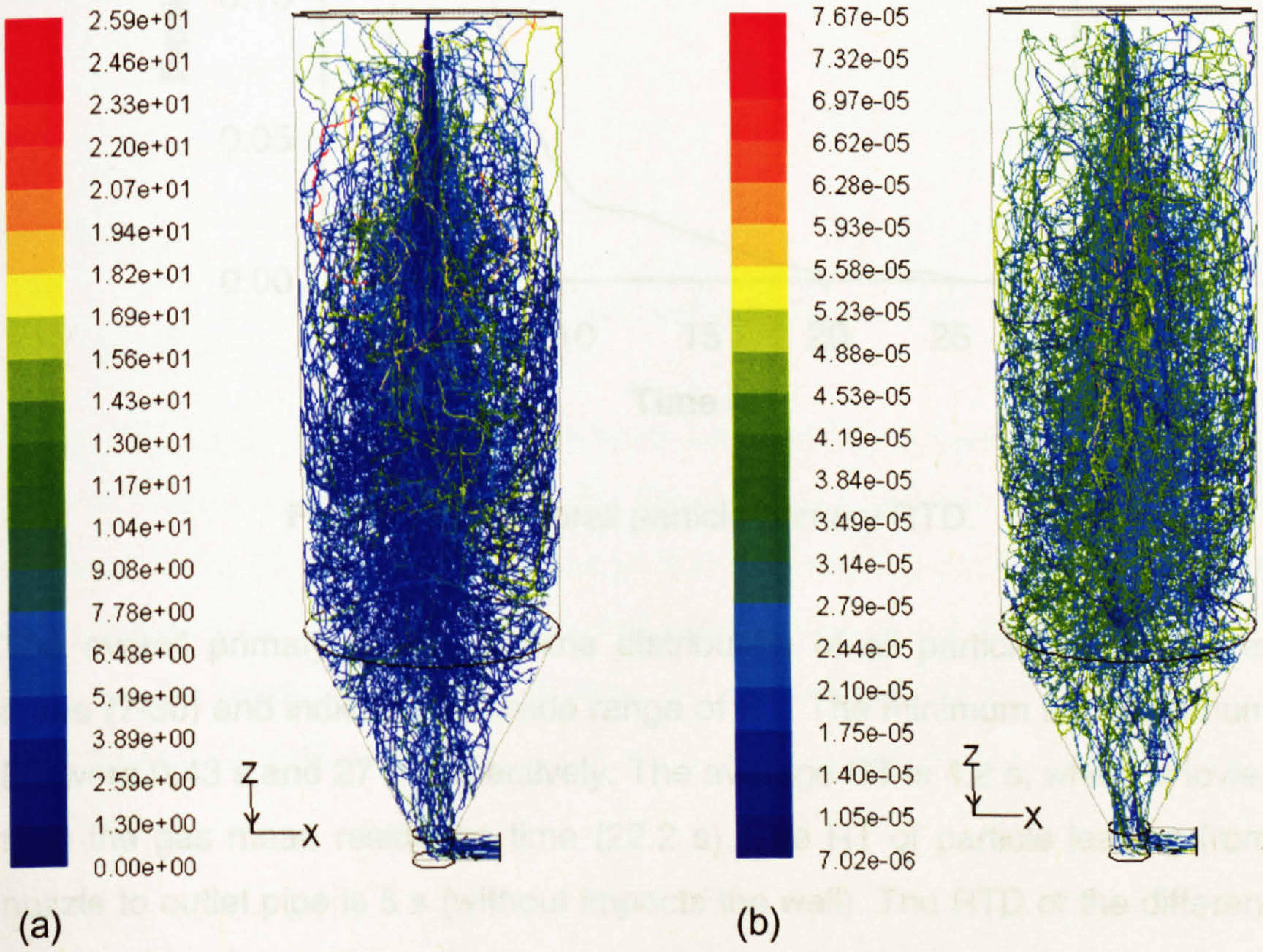

(a) (b)

Figure 7-29: Particle trajectories coloured by (a) particle residence time (s) and (b) particle diameter (m).

Figures (7-29 a-b) shows particle trajectories coloured by residence time and particle diameter respectively. Figure (7-29 a) indicates that most of the particles have a very short residence time and figures (7-29 b) reveals that change in diameter of the particles from its initial larger droplets size to its final smaller particle and it indicates that moisture was removed from the particles. Also, dried particles (smaller particles) were mostly recirculated (figures 7-29 b) by the gas phase. This may cause protein denaturation as dried particles are exposed to higher inlet gas temperatures.

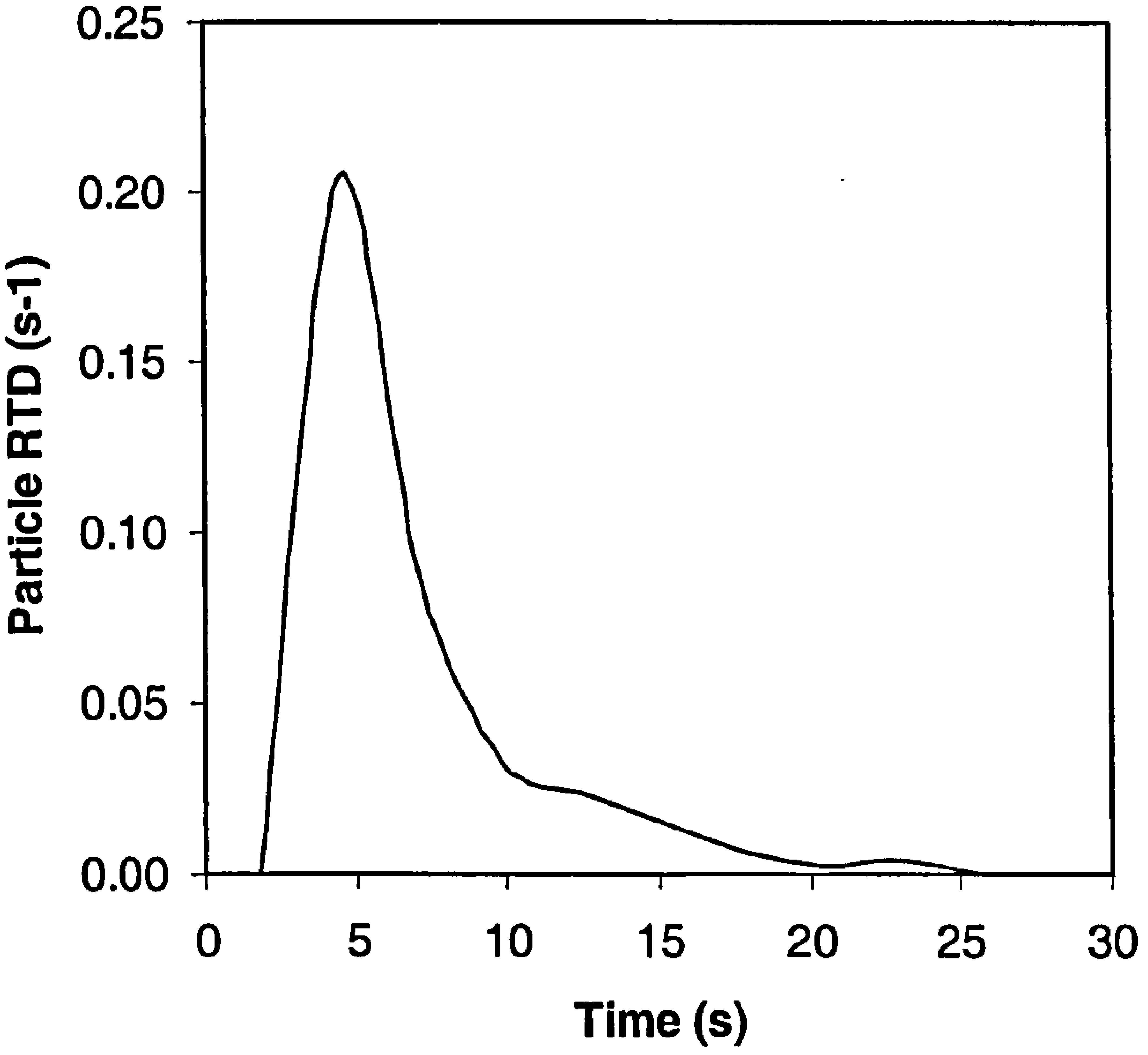

Figure 7-30: Overall particle primary RTD.

The overall primary residence time distribution of all particles is shown in figure (7-30) and indicates the wide range of RT. The minimum and maximum RT were 0.43 s and 27 s respectively. The average RT is 4.2 s, which is lower than the gas mean residence time (22.2 s). The RT of particle leaving from nozzle to outlet pipe is 5 s (without impacts the wall). The RTD of the different size particles is not shown in this simulation, because a narrow range size of particles was simulated (10 μm to 40 μm) in the air blast nozzle atomiser model.

7.8.10 Particles impact positions

In this simulation, the particles impact position on the walls are depicted in figures (7-31) and (7-32).

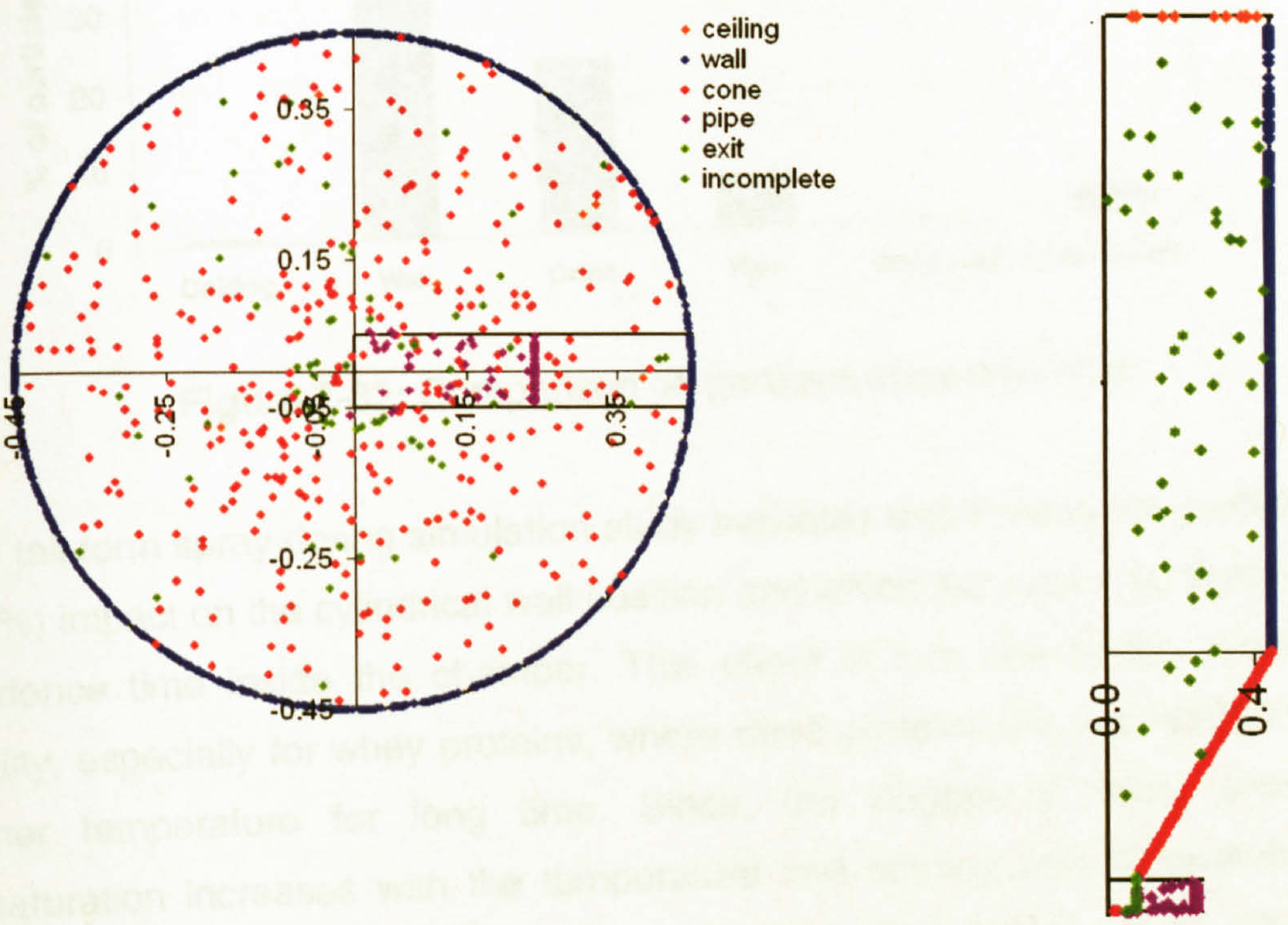

(a) Top view (b) Front view

Figure 7-31: Particles impact position on wall.

Figure (7-31 a-b) shows the top and front views of the simulated results for the particle impact on the chamber walls. These figures indicate that 65 % of the particles strike on the cylindrical part of the wall and 9.6 % of particles hit the conical part of the wall, but only a small proportion (8%) of the particles come out from the outlet pipe line. Less than 1% of particles impact the ceiling, as recirculation of gas only took place on a large scale at the bottom of the chamber.

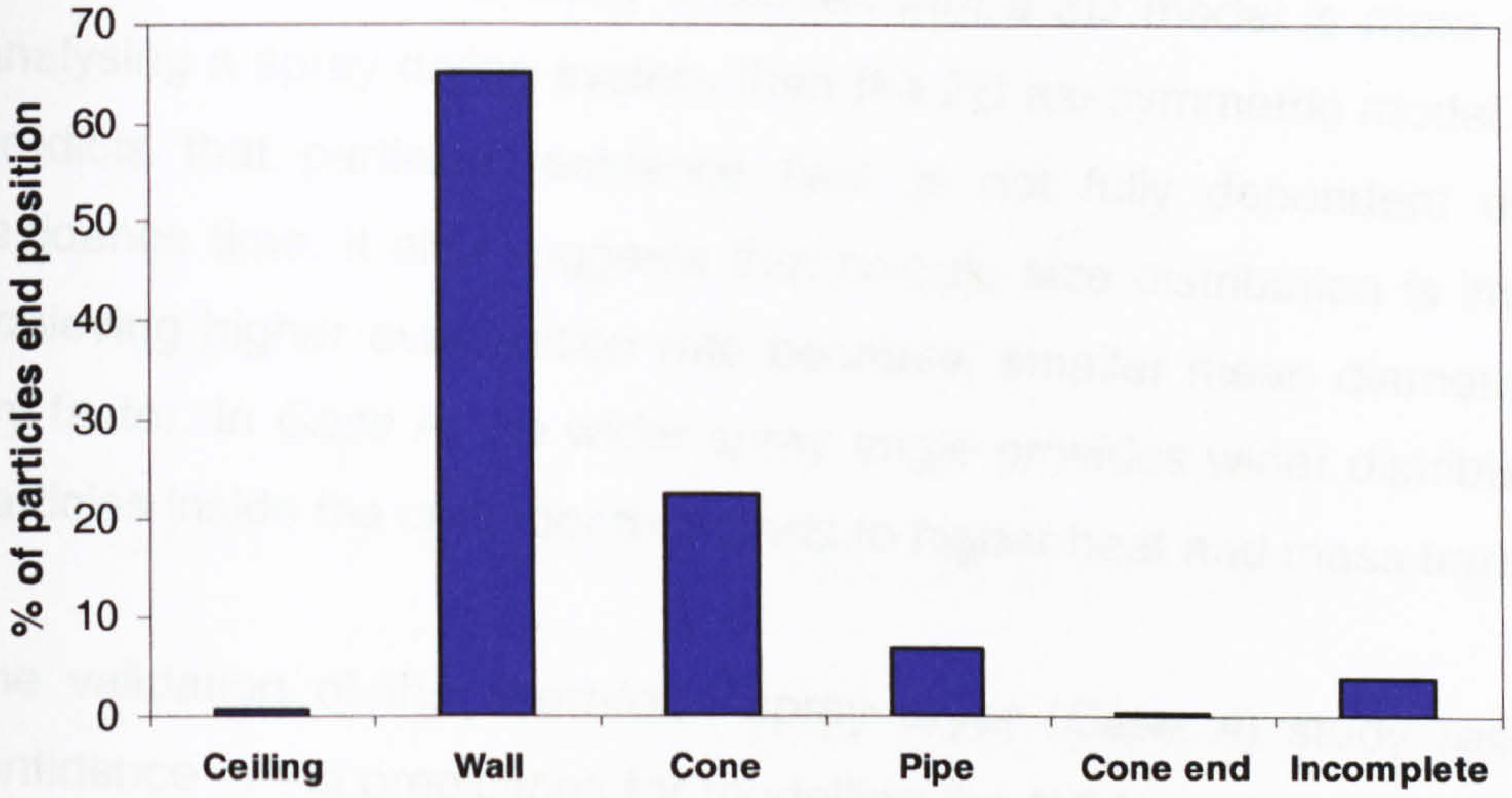

Figure 7-32: Comparison of particles impact position.

This tall-form spray drying simulation study indicates that most of the particles (65 %) impact on the cylindrical wall position and which increases the particles residence time inside the chamber. This effect in turn affects the product quality, especially for whey proteins, where dried proteins are exposed to the higher temperature for long time. Since, the degree of whey protein denaturation increases with the temperature and holding time (Dannenberg and Kessler, 1988). This findings supports the experimental results, where some denaturation of whey proteins (see chapter 5 section 5.8) was found at even low outlet temperatures.

7.9 Main findings

A three-dimensional CFD model for a short-form spray dryer was developed and compared with published experimental results and predictions. The results obtained from the CFD simulation were presented in terms of gas velocity and temperature profiles. The comparison study shows good agreement between the model and published experimental and prediction results.

This simulation results agreed well with Kieviet's (1997) experimental and simulation results, but, were slightly different to Huang *et al's* (2006) position on walls. This study indicates that a 3D model is more suitable for analysing a spray drying system than the 2D axi-symmetric model. The study predicts that particles residence time is not fully dependent on the gas residence time. It also suggests that particle size distribution is important for achieving higher evaporation rate because, smaller mean diameter particles dry faster. In *Case A*, the wider spray angle provides wider distribution of the particles inside the chamber that leads to higher heat and mass transfer.

The validation of the short-form spray dryer (*Case A*) study results gives confidence in the predictions for modelling the tall-form dryer (*Case B*), which was used in this work for protein denaturation and solubility studies. This study also helps to understand the experimental results. The *Case B* model predictions shows more than 60% of particles impacts on the cylindrical wall position and this may affect the protein denaturation and solubility. An increase in the chamber diameter may reduce the wall deposition rate. The primary residence time study also reveals that the tall-form dryer predicts longer RT (due to larger distances between the nozzle and outlet and also greater gas recirculation) and this may also leads to more denaturation and insolubility of proteins. These results indicate that outlet temperature has more influence on the particle nature than the inlet temperature. These simulation results also support results from the experimental study, where the outlet temperature was selected as a controlling variable during spray drying experiments.

This short-form and tall-form spray dryer study suggests that an increase in the chamber diameter may reduce the particle deposition on the cylindrical wall (e.g. *Case A*) and it can also accommodate the wider spray angle of atomiser. However, the bend outlet pipe inside the chamber increases the gas and particle recirculation, consequently, cold gas mixed with down flowing hot inlet gas as well as dried particles will be exposed to the higher inlet air temperature. Hence, this study concludes that a short-form dryer with bottom outlet is most likely to be suitable for the drying of heat sensitive products like proteins.

Chapter 8

Computational fluid dynamics (CFD) simulation studies of spray-freezing

8.1 Introduction

This chapter deals with the development of Computational Fluid Dynamics (CFD) simulations for the spray-freezing operation. This study will the gas flow pattern and particle histories such as temperature, velocity profiles, particle trajectories and particle impact on the wall. The aim of the simulations is to improve the spray-freezing operation by determining the distribution of particle velocities, temperatures and impact positions on the wall during the spray freezing process. Three simulation case studies will be examined as follows

Case A: Existing spray-freezing chamber design with solid cone spray
Case B: Existing spray-freezing chamber design with hollow cone spray
Case C: Modified spray-freezing chamber design with solid cone spray

The first section of this chapter is focussed on an experimental validation of spray-freezing simulations with a solid cone spray operation (*case A*). The second section will compare the two different types of spray patterns obtained from solid and hollow cone spray nozzles (*case A* and *case B*). The final section will explore the possibilities of a new spray-freezing chamber design using CFD simulation (*case C*).

8.1.1 Background

Spray-freezing in a cold gas is a complex process and involves a number of mechanisms such as

(i) the fluid mechanics of the spray, its formation and the movement of individual spray drops with respect to each other and the gas

(ii) the heat transfer between the gas phase and the droplets depends on the local conditions such as, gas temperature, droplet temperature and droplet-gas slip velocity.

(iii) the freezing mechanism itself.

Al-Hakim (2004) studied droplet size and axial velocity during the spray-freezing process, using a Phase Doppler Anemometer (PDA) system. However, the PDA measurements could only be performed at a maximum axial distance of z < 0. 2 m below the nozzle. It is difficult to obtain data at greater distance than this due to (i) droplet freezing causing a reduction in refractive scatter, (ii) fewer numbers of droplets entering the measurement volume due to the farming outwards of the spray, and (iii) greater interference of droplets not in the measurement volume due to a generally greater degree of "fog" further away from the nozzle. However, the design and operation of a spray freezing process requires information on particle behaviour (temperature, velocity and residence time) throughout the chamber. To date, no articles have been reported in the open literature on the CFD modelling of spray-freezing operations. Hence, a CFD model was developed to predict the gas and particle temperature, velocity and residence time.

8.2 Experimental procedure

The experimental verification study was performed using a co-current configuration with a solid cone spray and comparison was made with Al-Hakim's (2004) data. The geometry used in this simulation is shown in figure (8-1), with a solid cone spray pressure nozzle atomiser located at the top of the chamber; the freezing gas (liquid nitrogen) enters the through an annulus.

Spray freezing was carried out in a specially constructed cylindrical chamber (height 1.5 m and diameter 0.8 m), which included plane windows to permit PDA measurements to be made (see figures 8-2 and 8-3). The windows were removable to allow easy cleaning between experiments. The sprayed liquid was distilled water which was atomised using a hydraulic nozzle (WL 053), which is a solid (full) cone spray nozzle (details in chapter 3.4.2). The nozzle housings required exterior air heating to prevent blockage caused by freezing of the feed stream within the nozzle (discussed in chapter 3). The pressure of the liquid feed for the hydraulic nozzle was 6 bar with a corresponding liquid flow rate of 0.0125 kg/s.

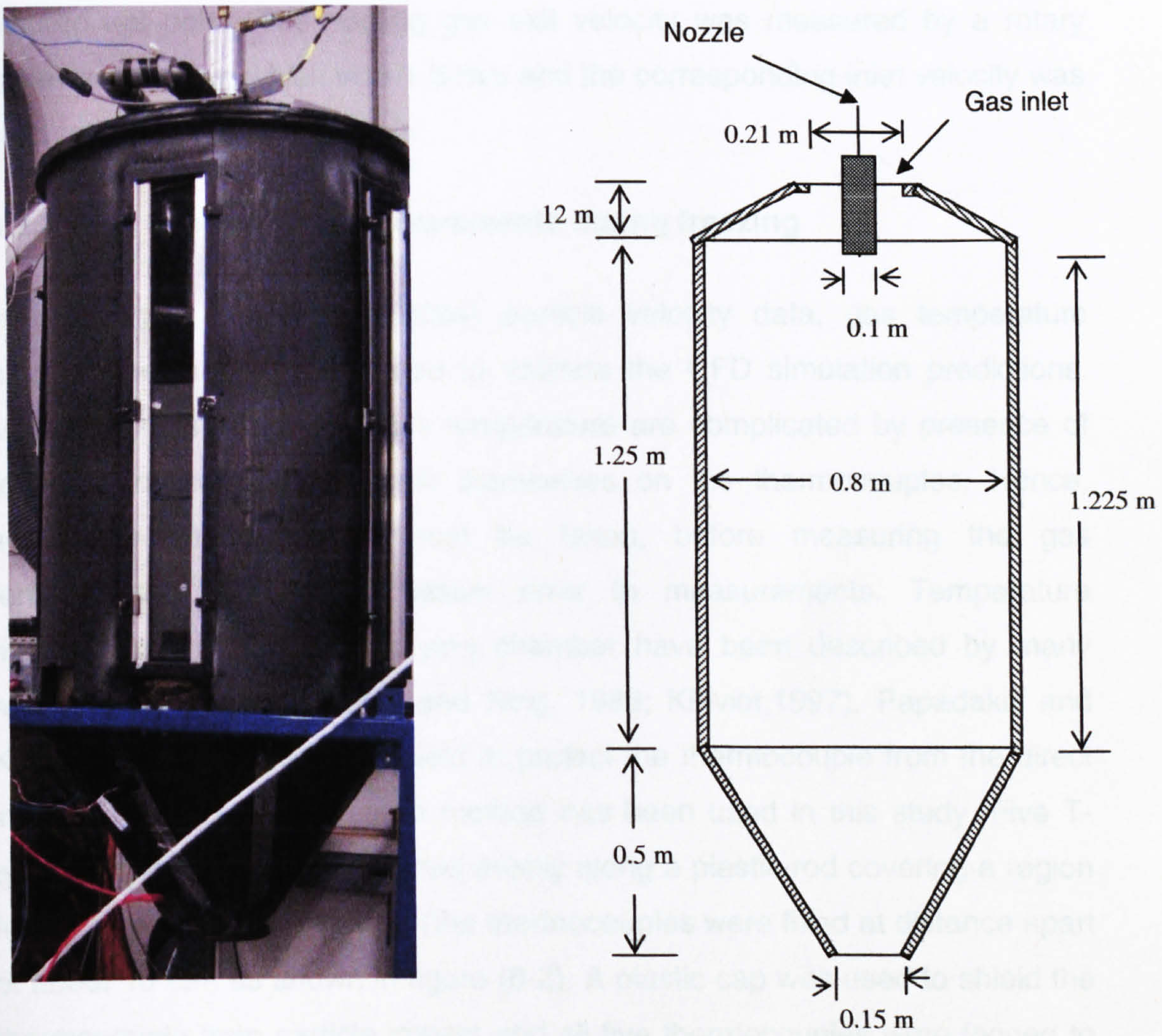

Figure 8-1: Spray-freezer geometry: Photograph of experimental apparatus (left) and cross section showing dimensions (right).

The liquid feed was supplied from a pressurized feed tank to maintain constancy of flow. All feed pressures were controlled by regulator valves which were pre-set during trial experiments to give the desired line pressures at the nozzle, and were measured using piezo transducers. The sprays were actuated on each occasion by the use of solenoid valves included in the feed lines. Before spraying took place the chamber was first purged with dry nitrogen gas from a cylinder to remove humidity from the chamber and then cooled using a liquid nitrogen supply. During spray-freezing experiments, a chamber temperature of -42°C was used, which was maintained by controlling the flows of liquid nitrogen. The temperature in the chamber was measured by a thermocouple and was checked on each occasion to be within 2°C of the desired set point. The cooling gas exit velocity was measured by a rotary vane velocimeter, which was 1.5 m/s and the corresponding inlet velocity was calculated which was 0.99 m/s.

8.2.1 Gas temperature measurements during freezing

In addition to Al-Hakim's (2004) particle velocity data, gas temperature measurements were performed to validate the CFD simulation predictions. Measurements of the cold gas temperature are complicated by presence of frozen particles which deposit themselves on the thermocouples. Hence, some preventative steps must be taken, before measuring the gas temperature, to avoid excessive error in measurements. Temperature measurements in a spray drying chamber have been described by many researchers (e.g. Papadakis and King, 1988; Kieviet,1997). Papadakis and King (1988) used a simple shield to protect the thermocouple from the direct impact of particles. The same method has been used in this study. Five T-type thermocouples were spaced evenly along a plastic rod covering a region from the centerline to the wall (the thermocouples were fixed at distance apart of about 10 cm) as shown in figure (8-2). A plastic cap was used to shield the thermocouple from particle impact and all five thermocouples were logged to data acquisition hardware (Data Scan 7321) on a PC for online temperature measurements.

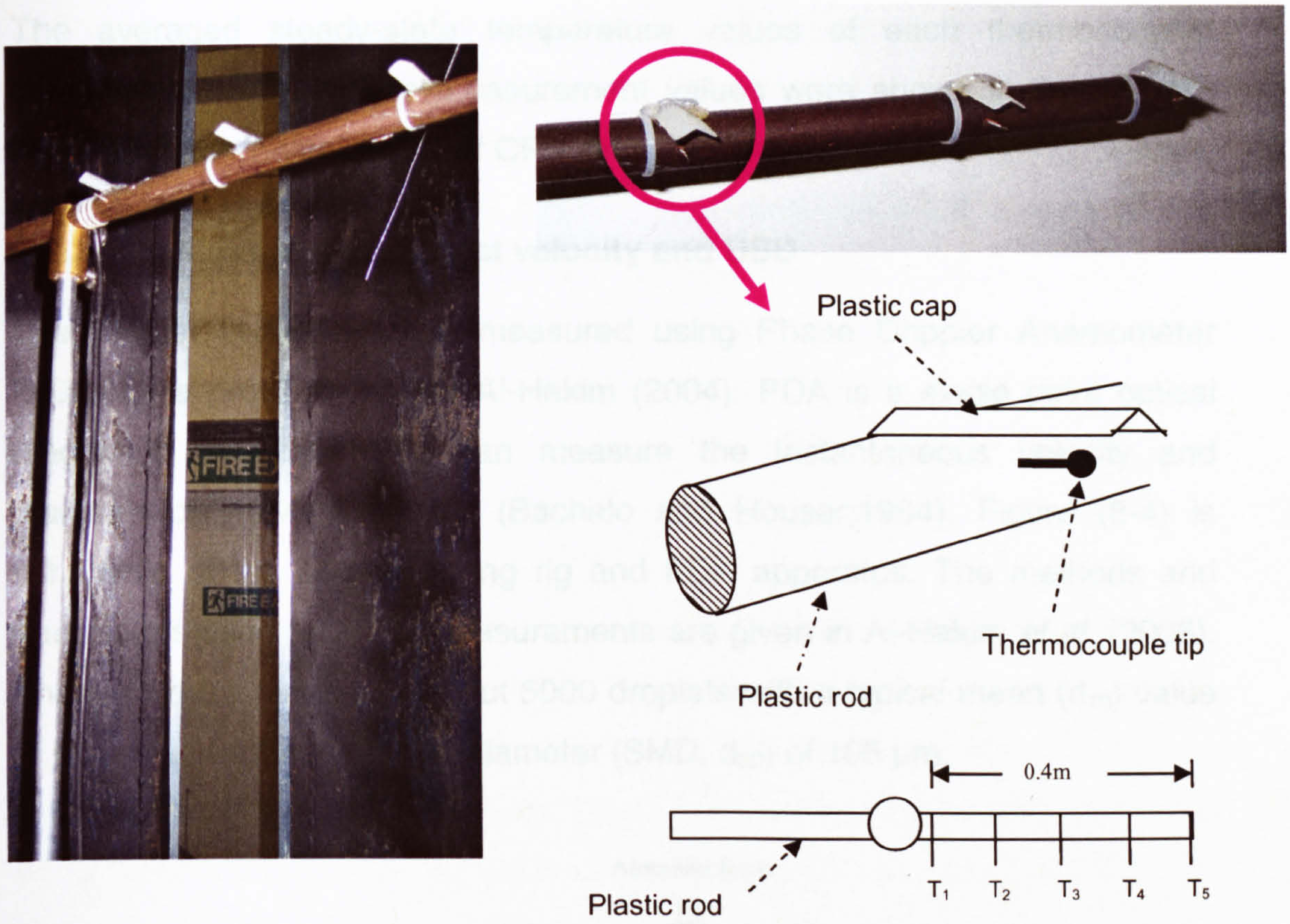

Figure 8-2: Shielded thermocouple used for temperature measurements.

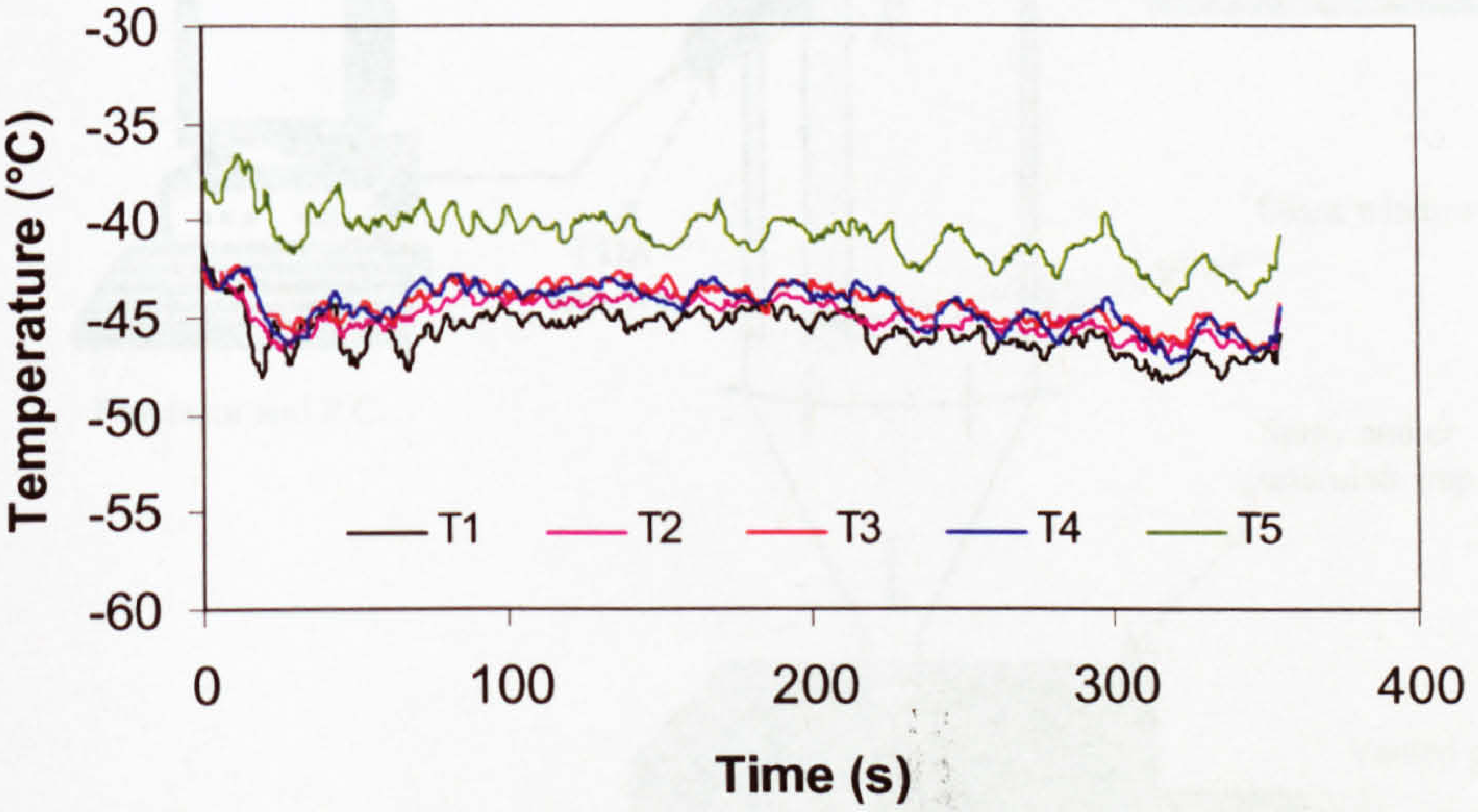

Figure 8-3: Temperature measurements during spray-freezing at -42°C chamber temperature at an axial distance z =1.23 m below the nozzle.

An example history of the gas temperature measurements from the five thermocouples is shown in figure (8-3), for a the spray-freezing operation at a chamber temperature of –42°C and an axial distance z = 1.23 m from nozzle.

The averaged steady-state temperature values of each thermocouples (steady state temperature measurement values were shown in figure 8-10) were taken for the validation of CFD simulation results.

8.2.2 Measurement of droplet velocity and DSD

The droplet velocities were measured using Phase Doppler Anemometer (PDA) by a previous worker Al-Hakim (2004). PDA is a single point optical diagnostic technique that can measure the instantaneous velocity and diameter of individual drops (Bachalo and Houser,1984). Figure (8-4) is schematic of the spray-freezing rig and PDA apparatus. The methods and parameters used for PDA measurements are given in Al-Hakim *et al.* (2006). These workers measured about 5000 droplets with a typical mean (d_{10}) value of 50 μm and a Sauter mean diameter (SMD, d_{32}) of 105 μm.

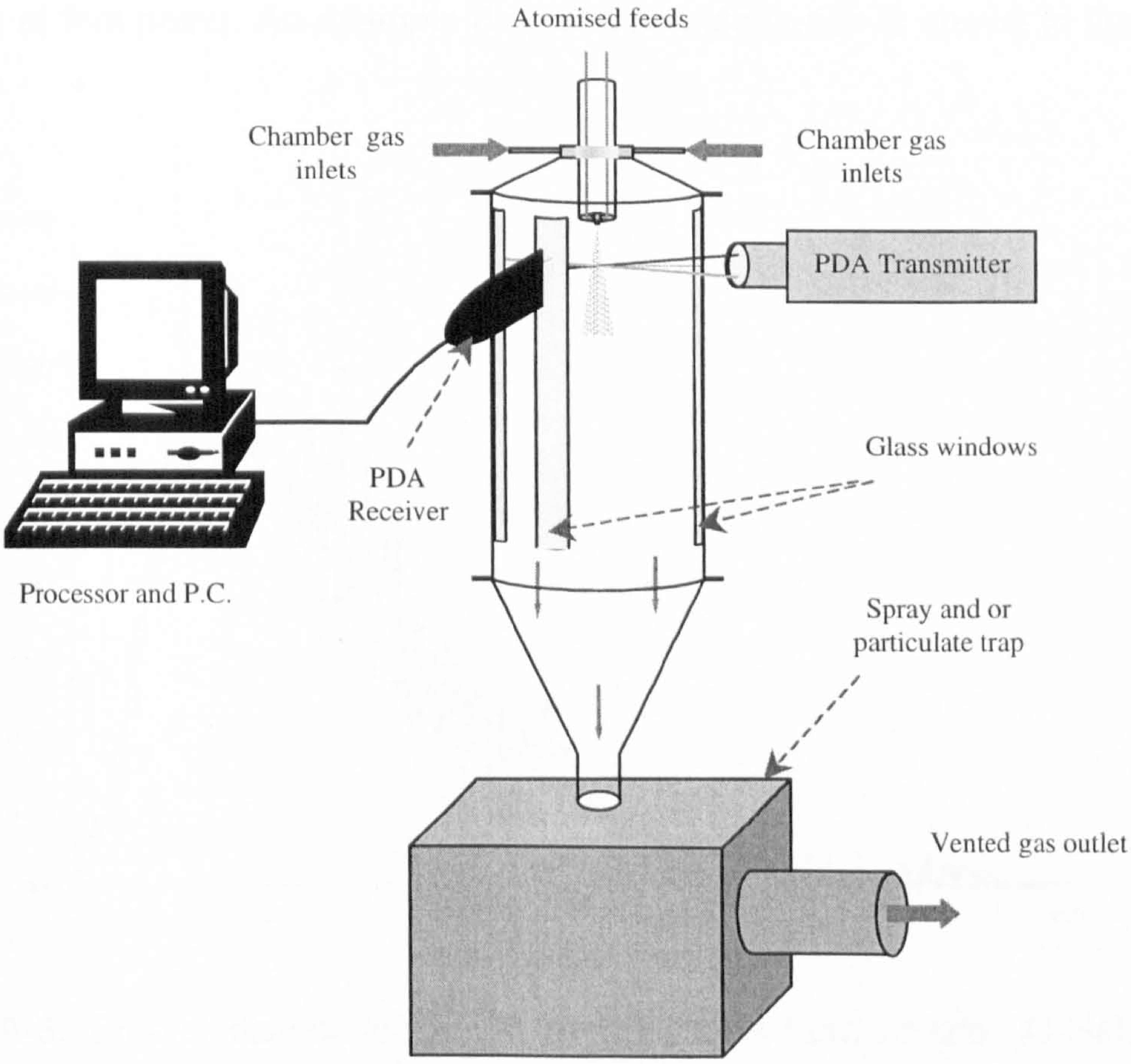

Figure 8-4: Schematic of PDA measurement system used by Al-Hakim (2004).

Drop size distributions (DSDs) were obtained by sorting the droplets into 1 μm sized bins, and normalizing these counts with respect to the total number of droplets detected by the PDA burst detector (i.e., the total spray population). The PDA software performs a system of internal validation checks on the measurements of size and velocity for each droplet. Mean velocity values and standard deviations were calculated for validated droplets in each individual size category. The Al-Hakim *et al.*'s (2006) droplet size and velocity measurements were used to validate the CFD simulation predictions performed here.

In the CFD simulations, the initial droplet size distribution needs to be set as a nozzle injection parameter. For that the Al-Hakim *et al.*'s (2006) measurements of droplet size distribution near to the nozzle (at 38 mm distance from the nozzle) was used (there is no DSD at the nozzle – it is still a liquid jet at that point). An example droplet size distribution is shown in figure (8-5).

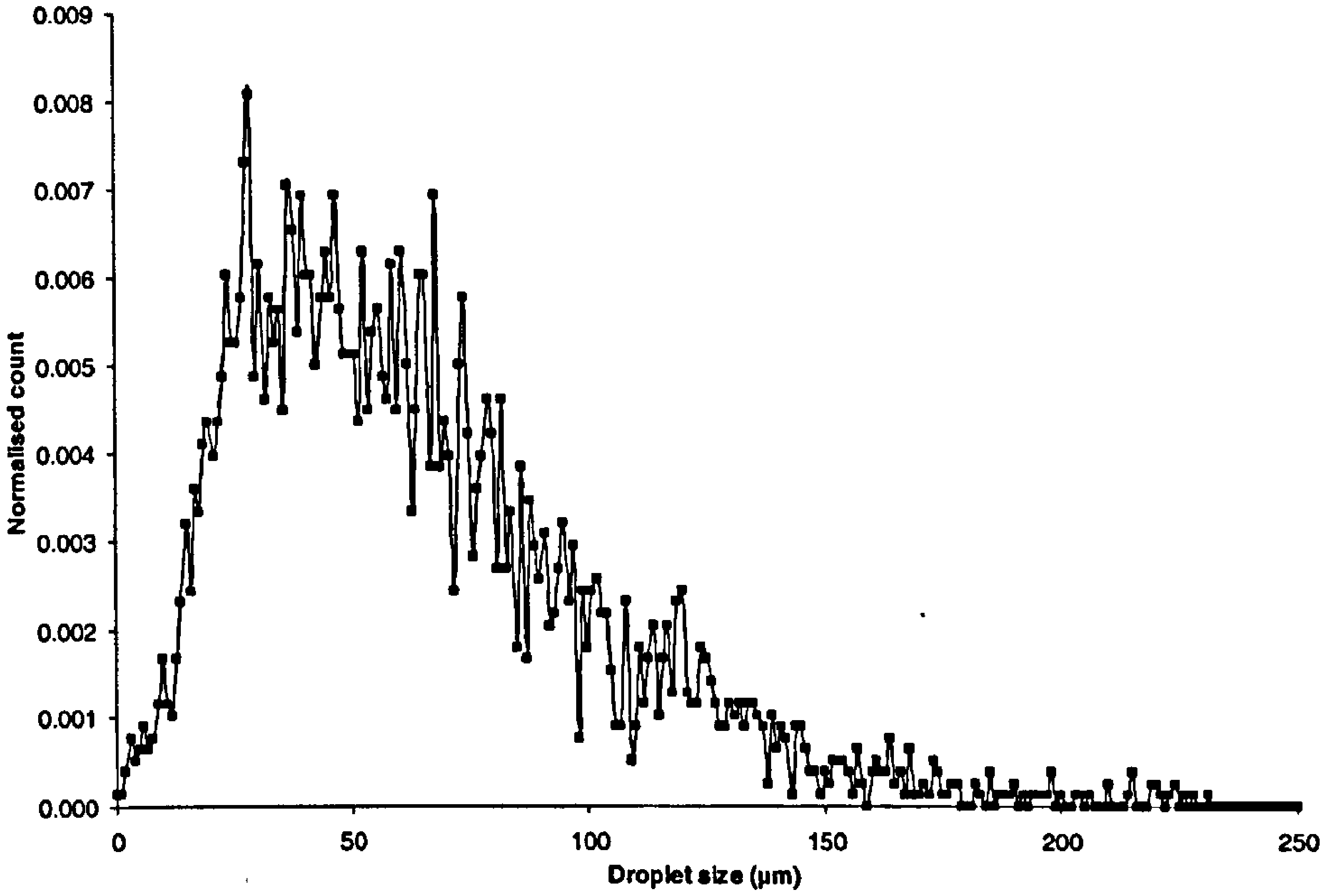

Figure 8-5: Droplet distribution at 38 mm distance from nozzle (Al-Hakim, 2004).

The Rosin-Rammler (RR) diameter distribution was used to characterise the initial spray drop size distribution in the CFD simulations. The RR distribution is based on an exponential relationship between the droplet diameter d and the mass fraction of droplets with a diameter greater than d is given by:

$$Y_d = e^{-\left(\frac{d}{\bar{d}}\right)^n} \qquad \text{Eq (8-1)}$$

where, $\bar{d}$ is the mean diameter and n is the spread parameter. These parameters were determined using the following procedure using the data collected by Al-Hakim (2004).

The complete range of measured droplet sizes was divided into discrete size ranges, each to be defined by single stream that is part of the group as given in Table (8-1).

Table 8-1: Rosin-Rammler (RR) distribution.

Diameter range (µm)	Mass fraction	Diameter (µm)	Mass fraction with diameter greater than d (Y_d)	Fitted value of $Y_d = e^{-\left(\frac{d}{\bar{d}}\right)^n}$
0-20	0.000	20	1.000	1.00
20-50	0.032	50	0.967	0.96
50-100	0.282	100	0.685	0.72
100-150	0.388	150	0.297	0.30
150-200	0.205	200	0.092	0.05
200-250	0.095	250	0.000	0.00

To determine the RR distribution parameters, droplets size data were converted and plotted as mass fraction vs. diameter as shown in figure (8-6). The $\bar{d}$ was obtained by the corresponding value of d at $Y_d = e^{-1} \approx 0.368$. From the graph (figure 8-6), $\bar{d}$ was obtained as 141 µm. The spread parameter n is estimated from the following equation for each pair of data points and the averaged n value is 3.21.

$$n = \frac{ln(-ln Y_d)}{ln\left(\frac{d}{\bar{d}}\right)} \qquad \text{Eq (8-2)}$$

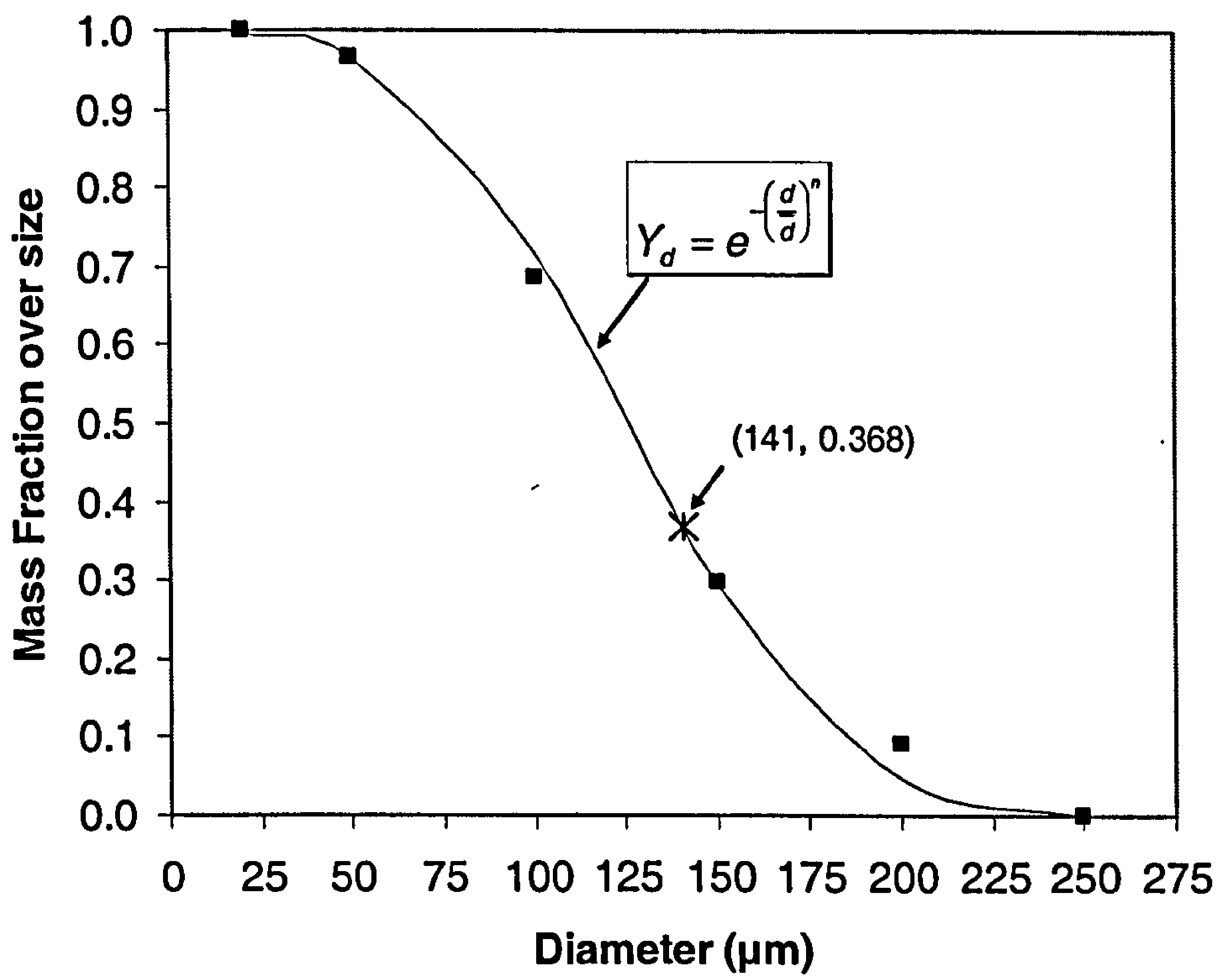

Figure 8-6: Rosin-Rammler curve fit (the astonish marks is the mean diameter).

Substituting all the calculated values into equation (8-1) will give RR exponential equation values of Y_d (Table 8-1) and this value was fitted with the particles size data as shown in graph (8-6). All these values were used to calculate the size of droplets produced by the spray injection in the CFD simulations.

8.3 CFD Simulation methodology

This CFD simulation used the same method as that described earlier for the spray drying simulations, except that an "*inert particle*" model was selected instead of an evaporating "*droplet*" model - species transport model was not used since no evaporative heating occurred in this system. Hence a simple heat transfer model could be applied.

The heat transfer between the droplet and the cold gas was computed based on the following equation.

$$m_p c_p \frac{dT_p}{dt} = hA_p(T_g - T_p) \qquad \text{Eq (8-3)}$$

where, m_p is the mass of the droplet, c_p is the droplet specific heat, T_p is the droplet temperature, A_p is the surface area of the droplet. The heat transfer coefficient (h) was obtained from the Ranz (1952) equation (Chapter 7 equation. 7-12).

The current Fluent 6.3 code (DPM model) does not include phase change during freezing (solidification). A single droplet freezing study (Hindmarsh *et al.*, 2003; MacLeod, *et al.*, 2006) indicated that the drop freezing process can be considered to comprise a number of stages: (1) initial cooling to a supercooled temperature below the normal freezing temperature, (2) nucleation, (3) recalescence, whereby rapid crystal growth occurs with a sudden temperature rise, as crystal growth liberates latent heat and the droplet warms up to the normal freezing temperature, (4) further, slower crystal growth which is limited by heat transfer from the gas, during which some freezing point depression may occur, and (5) once freezing is complete, cooling of the frozen particle down to the gas temperature.

Table 8-2: Particle specific heat values.

Point	Temperature (K)	Specific heat (c_p) J/kg K
1	0	2093 (ice)
2	262.9	2093 (ice)
3	263	35343 (phase change)
4	273	35343 (phase change)
5	273.1	4185 (water)
6	373	4185 (water)

The effect of the latent heat of fusion during the recalescence and subsequent growth (3+4) stages was included in this model by considering that solidification took place at temperatures between 0 and -10°C. Over this range the particle pseudo specific heat (c_p) value was defined to be a piece-wise linear function of temperature and hence it reflect the additional latent heat (the value of latent heat of ice was divided by 10 K) as in the table (8-2) and figure (8-7).

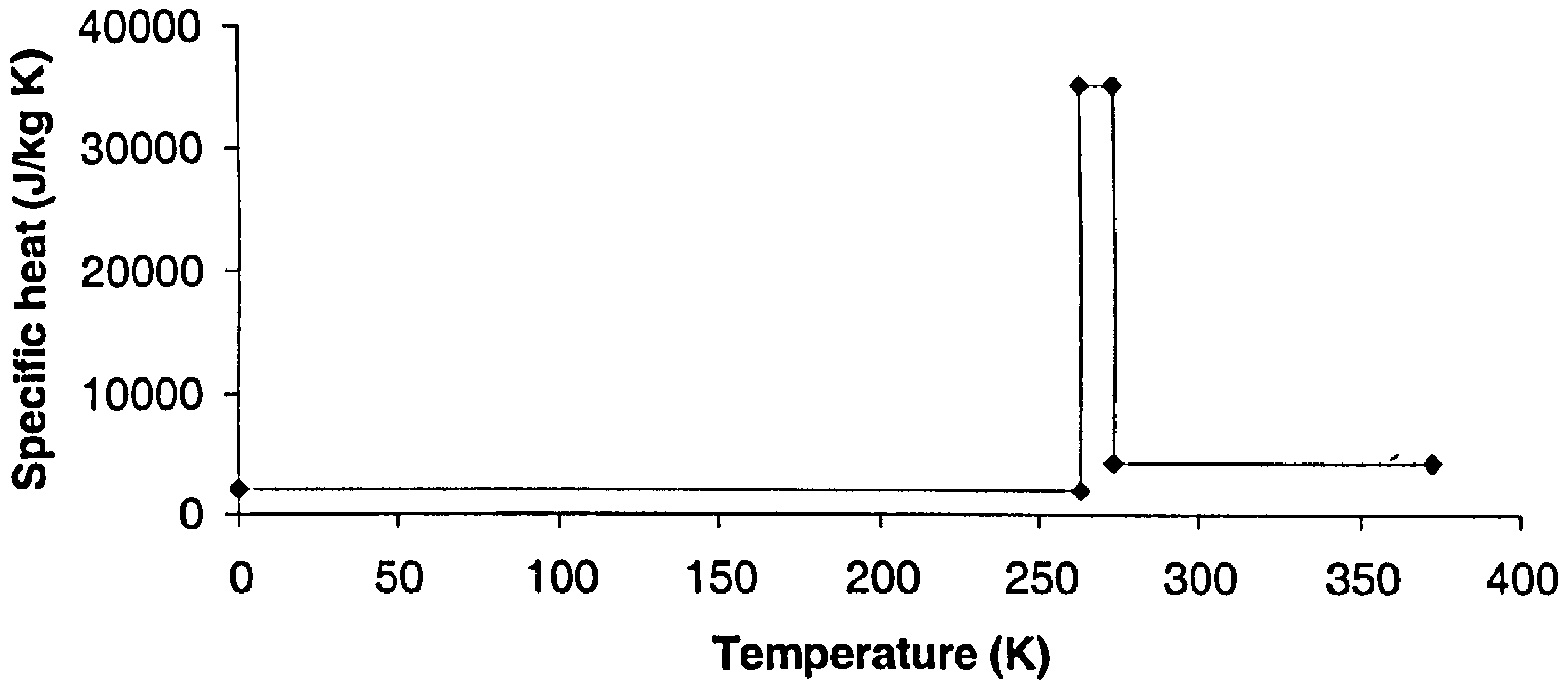

Figure 8-7: Particle specific heat function of temperature.

8.4 Boundary conditions

The full set of CFD boundary conditions is given in the Table (8-3) and reflected the experimental conditions used by Al-Hakim (2004). The initial droplet distributions and spray parameters were obtained from the Al-Hakim (2004) experimental measurements (see figure 8-4). The standard k-ε turbulence model was used. The k and ε initial condition values were estimated based on equations (7-21) to (7-23) in section (7.6). The "escape" wall boundary (the particles are lost from the calculation at the point of impact with the wall) condition was used.

Table 8-3: Boundary conditions used for spray-freezing simulation.

Inlet Air	
Air inlet temperature	203 (K)
Air mass flow rate	0.336 (kg/s)
Air velocity magnitude	0.9897 (m/s)
Outlet Condition	
outlet	Outflow
Turbulence model	
Turbulence *k*-value	3.588×10^{-3} (m^2/s^2)
Turbulence ε-value	3.21×10^{-4} (m^2/s^3)
Liquid spray from nozzle	
Liquid feed rate (spray rate)	0.0125 (kg/s)
Feed Temperature	20 (°C)
Spray angle (full angle)	30°
Minimum droplet diameter	0.5 (μm)
Maximum droplet diameter	250 (μm)
Average droplet diameter $\overline{d}$	141 (μm)
Droplet velocity at nozzle exit	28 (m/s)
Rosin-Rammler spread parameter	3.21
Chamber wall conditions	
Chamber wall thickness	0.001 (m)
Wall material	Steel
Wall-heat transfer co-efficient	0.001 (W/m^2K)
Interaction between wall and droplet	Escape

In the 3-D model, a hexahedral mesh was used (typical size is 0.001m) with 180 000 grid cells. The grid geometry is shown in figure (8-8 a). To maintain the accuracy of the solution near to the nozzle a fine mesh was used, which is also shown in figure (8-8 a). The measurement and predicted levels in axial positions below the nozzle are shown in figure (8-8 b).

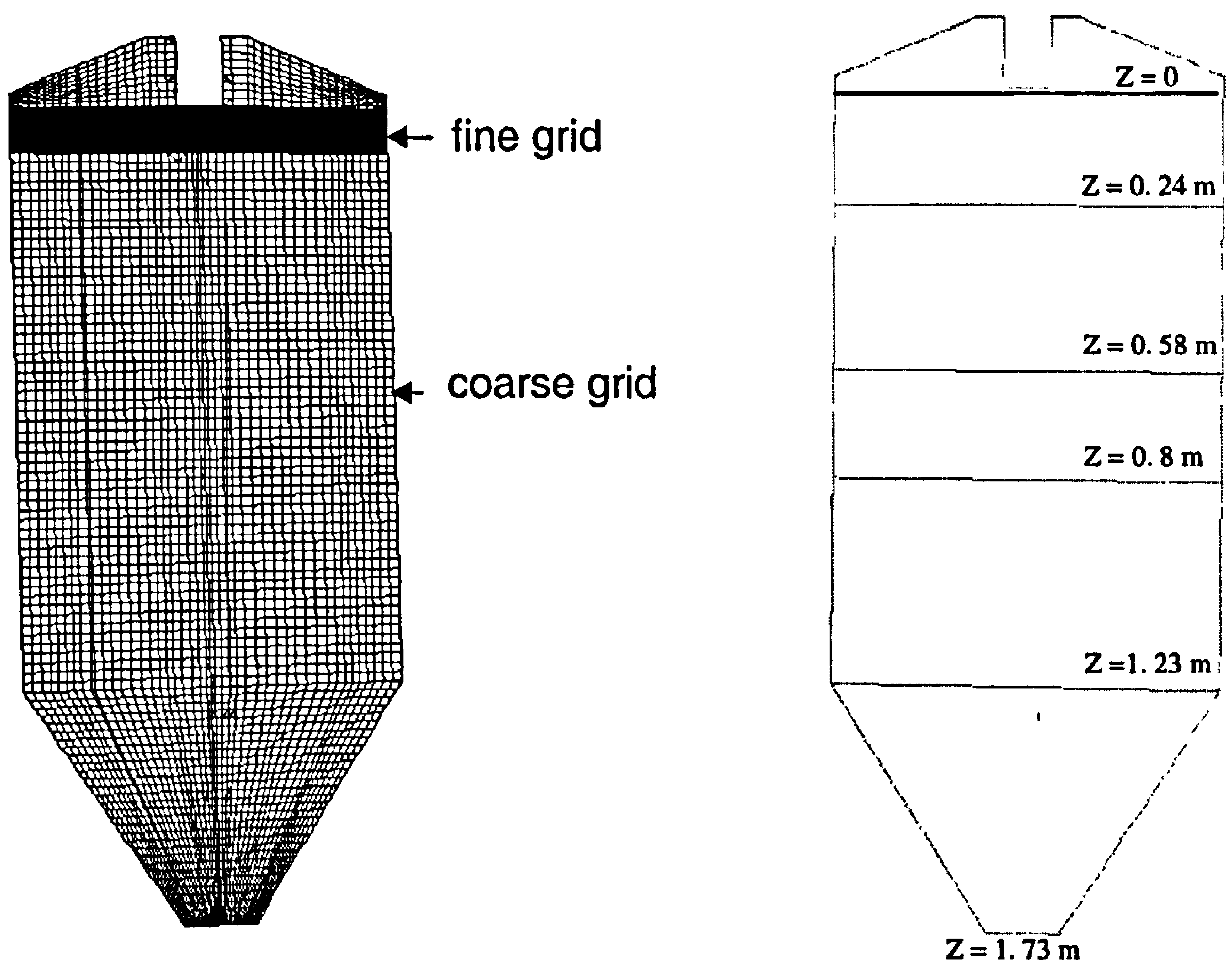

(a) (b)

Figure 8-8: (a) Grid used in the spray-freezing simulation (b) Measurement and prediction axial positions.

8.5 Simulation without spray injection

The first step in this simulation was to obtain the gas flow field in the absence of spray injection. Figures (8-9) shows the flow pattern of gas without spray. The flow pattern shows almost uniform axial velocity in the chamber, but higher velocity was observed at the bottom of the chamber due to a reduced area of the chamber cone outlet. Moreover, it was observed that no re-circulation zone was found in the spray-freezing chamber due to the low inlet gas velocity (0.09 m/s).

The gas axial velocity profiles are plotted in figure (8-10) at an axial level z = 0.24 m from the nozzle. The predicted profiles are plotted in the X-Z planes (denoted as X) and Y-Z planes (denoted as Y) in figure (8-10). The air flow patterns were almost symmetric (X and Y planes) throughout the freezing chamber. The axial velocity increased as the air stream moved goes downwards in the chamber; at the outlet (z = 1.73 m), the highest axial velocity shown as 1.5 m/s due to chamber bottom cone.

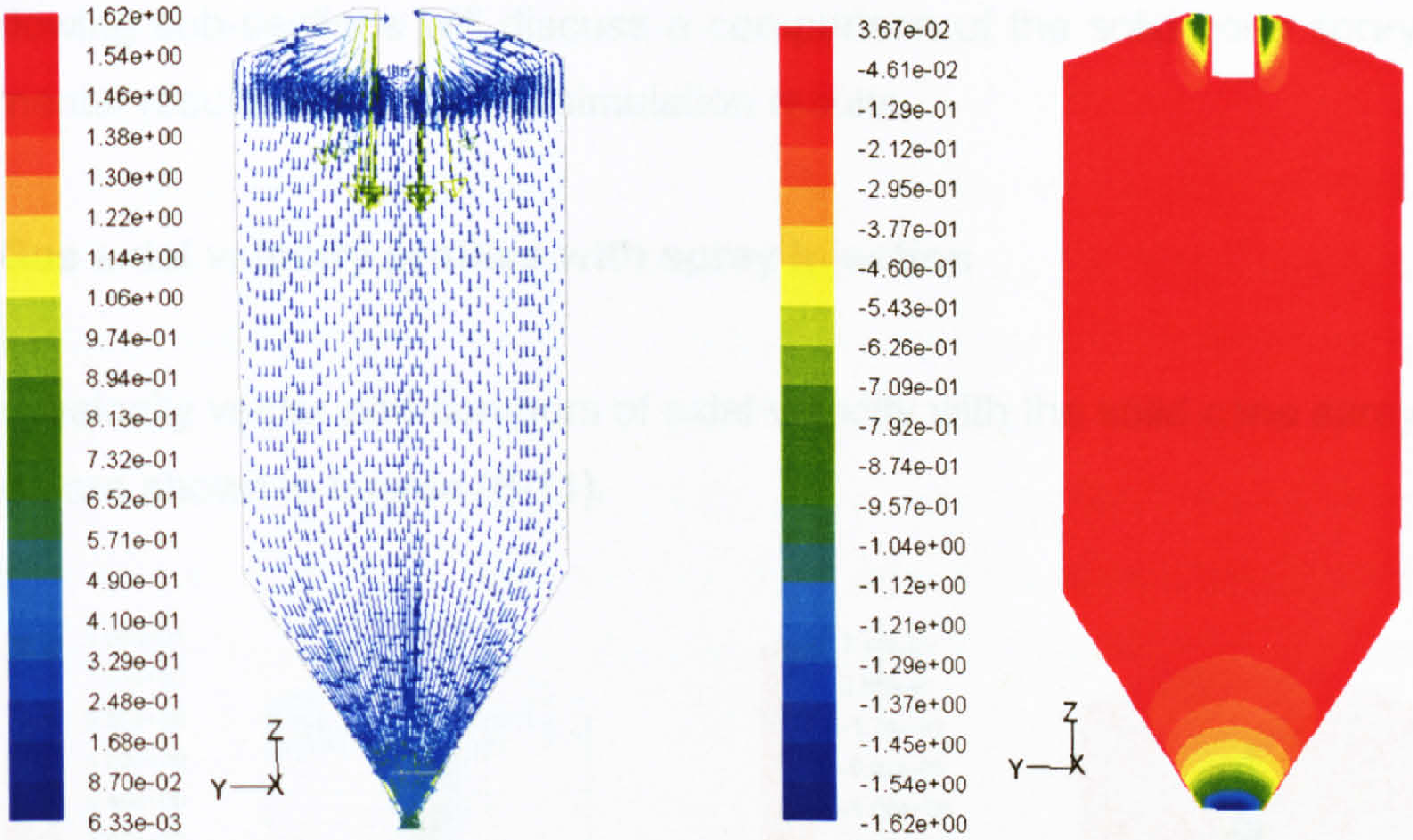

(a) (b)

Figure 8-9: Gas velocity without spray injection: (a) velocity magnitude vector (m/s) and (b) contours of axial velocity (m/s).

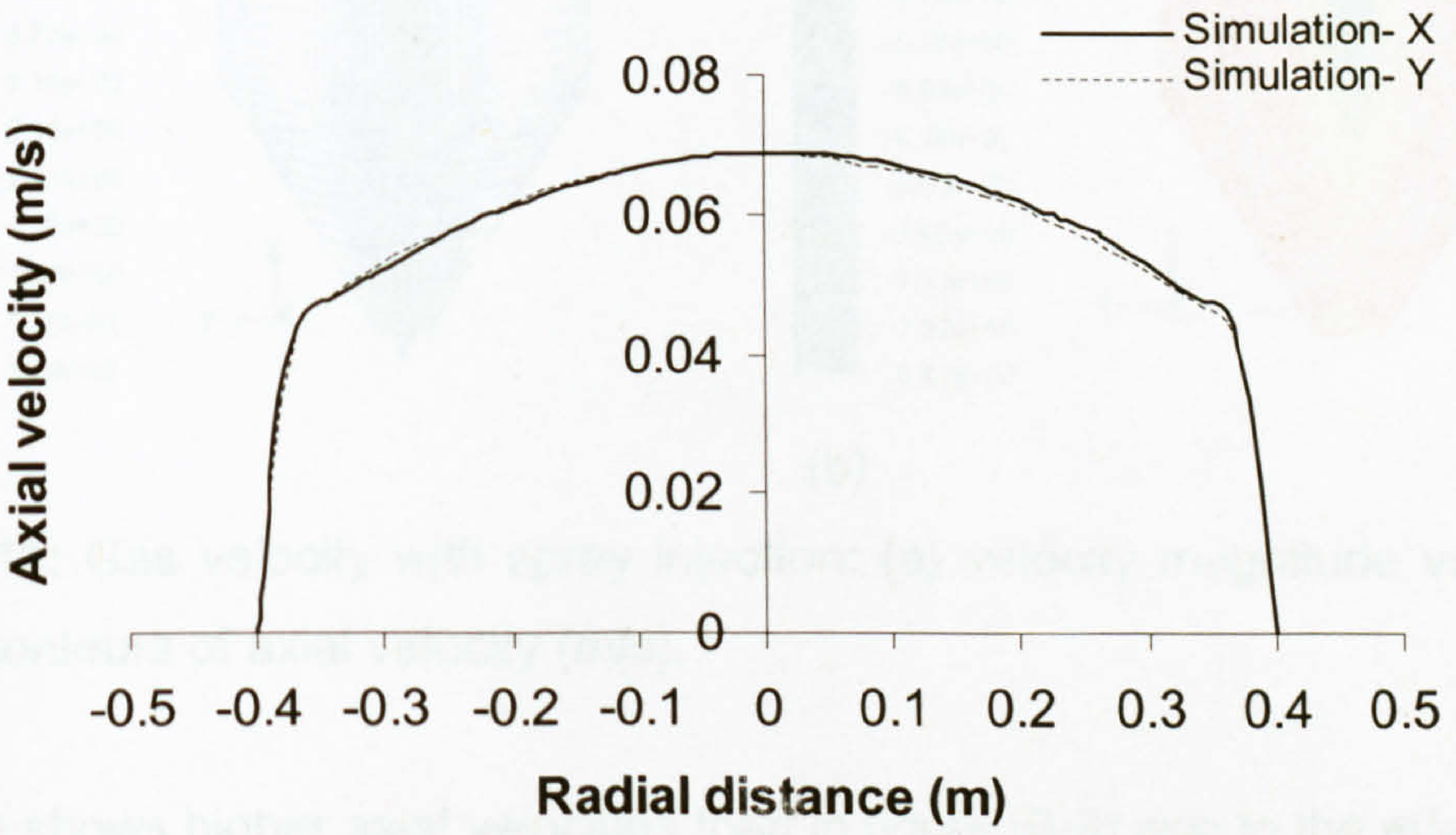

Figure 8-10: Gas axial velocity profiles without spray condition at z = 0.24 m axial distance.

In the absence of a spray, the simulated chamber temperatures remain close to the inlet gas temperature (203 K), as a very low wall heat transfer coefficient was used (the system is effectively insulated).

8.6 *Case A*: Solid cone spray predictions

A solid cone (or full cone) spray distributes the droplets over a circular area. The following sub-sections will discuss a comparison of the solid cone spray experimental results with the CFD simulation results.

8.6.1 Gas axial velocity profiles with spray injection

The gas velocity vector and contours of axial velocity with the solid cone spray condition are shown in figures (8-11).

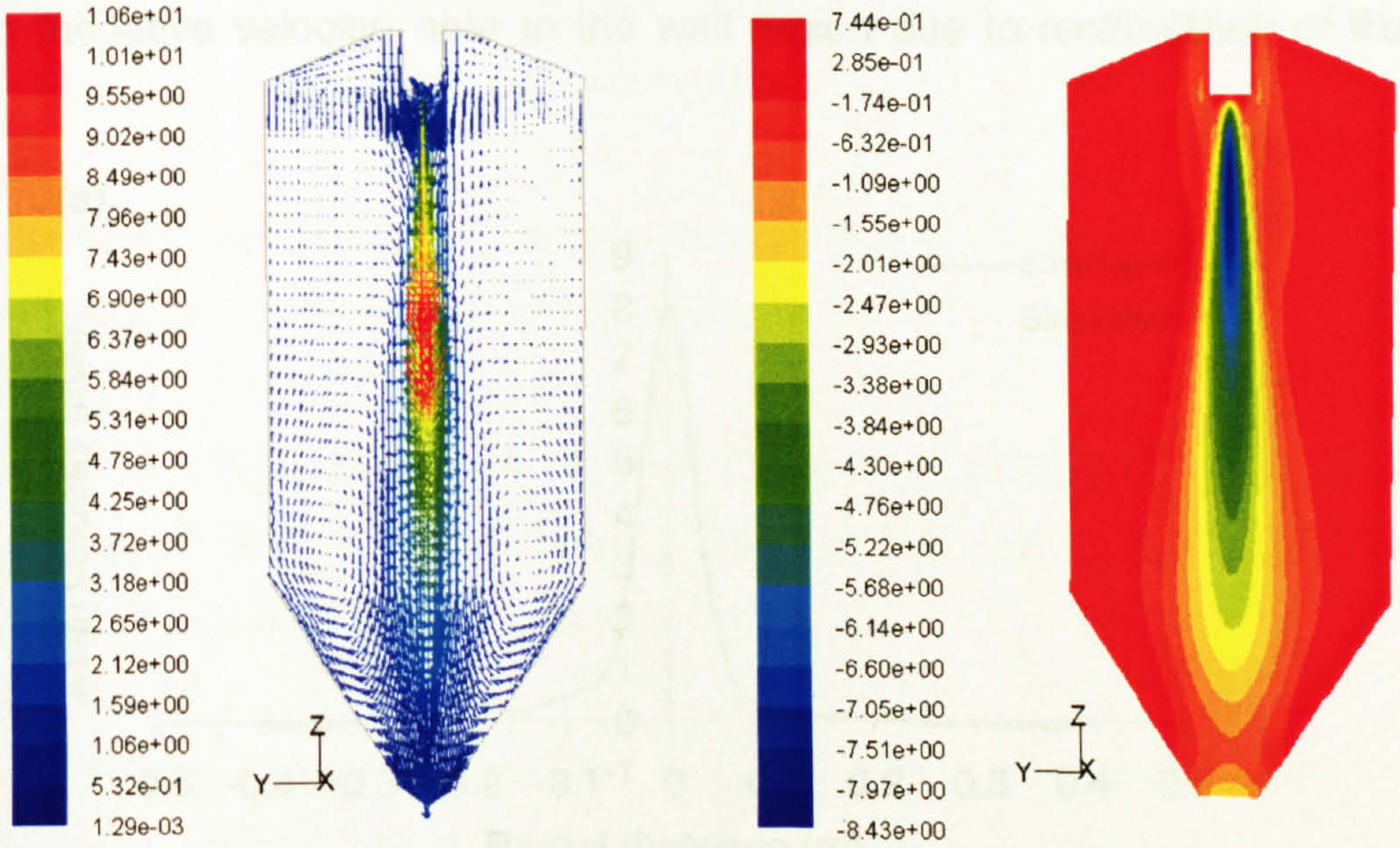

(a) (b)

Figure 8-11: Gas velocity with spray injection: (a) velocity magnitude vector (m/s) (b) contours of axial velocity (m/s).

This figure shows higher axial velocities than in figure (8-8) due to the effect of the spray injection. It was also observed that recirculation of gas occurs at the bottom of the chamber (see figure 8-11 b). This recirculation is in a region of relatively stagnant gas, which surrounds the fast moving core created by the spray, whereas, without the spray, the simulation shows no recirculation at the bottom (figure 8-9). This recirculation strongly influences the particle temperature, since it increases the residence time of some of the particles and hence reduces their temperature. Moreover, in this *case A,* recirculation occurs at the bottom of the chamber cone region and thus cold particles are transported to the cone wall or bottom of the cylindrical wall region, which results in more deposition of particles on the conical wall.

The gas axial velocity profiles are plotted in figures (8-12 a-c) at axial distances of z = 0.24 m, 0.8 m and 1.23 m below the nozzle. The simulation show a higher axial velocity (8 m/s) in the core region at z = 0.24 m (figure 8-12 a) compared to the outer regions of the chamber. This trend was expected as a solid cone spray was used in this simulation. As the spray passes down the chamber the centerline axial velocity falls, and also shows an upward motion (negative velocity) near to the wall region due to recirculation of the gas.

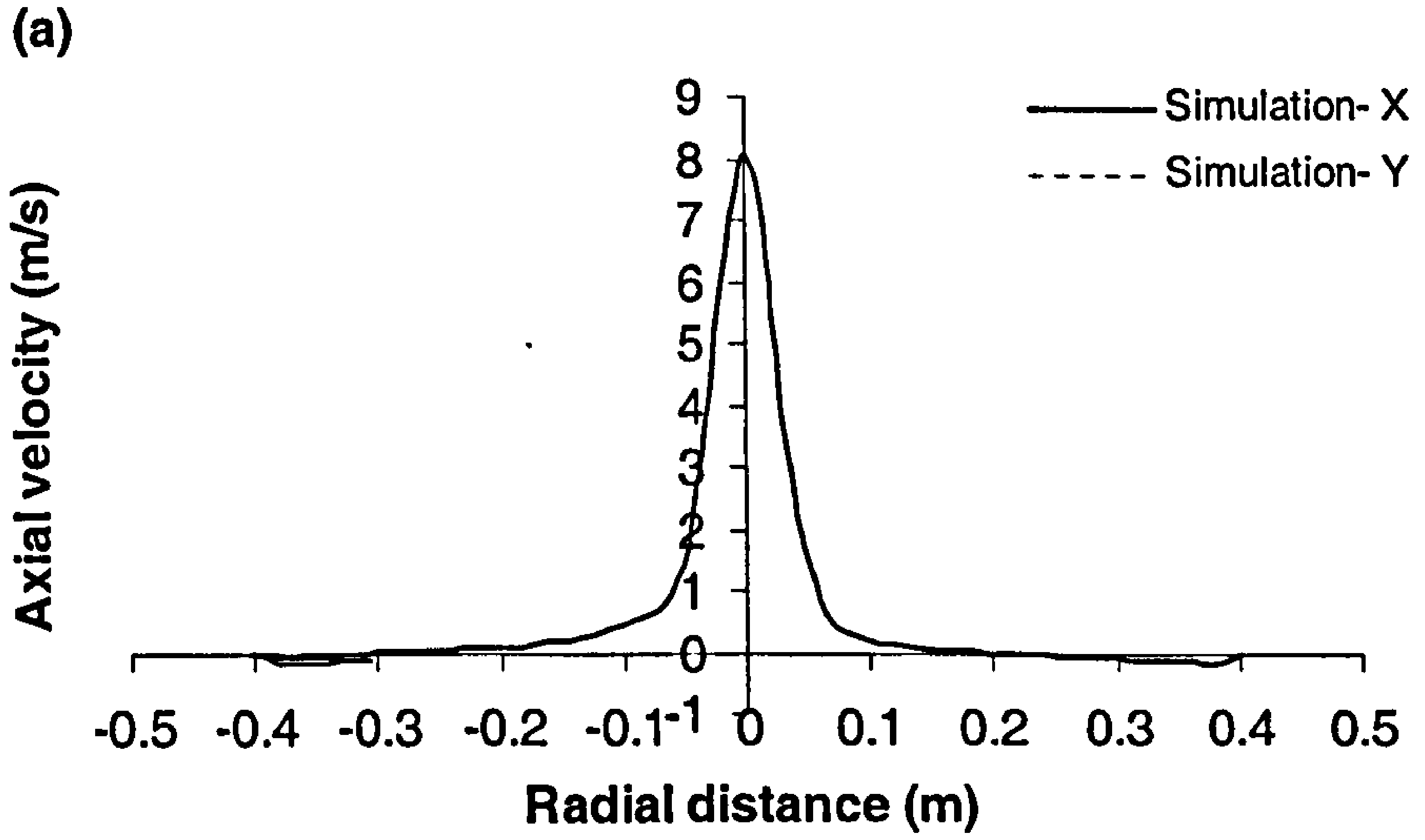

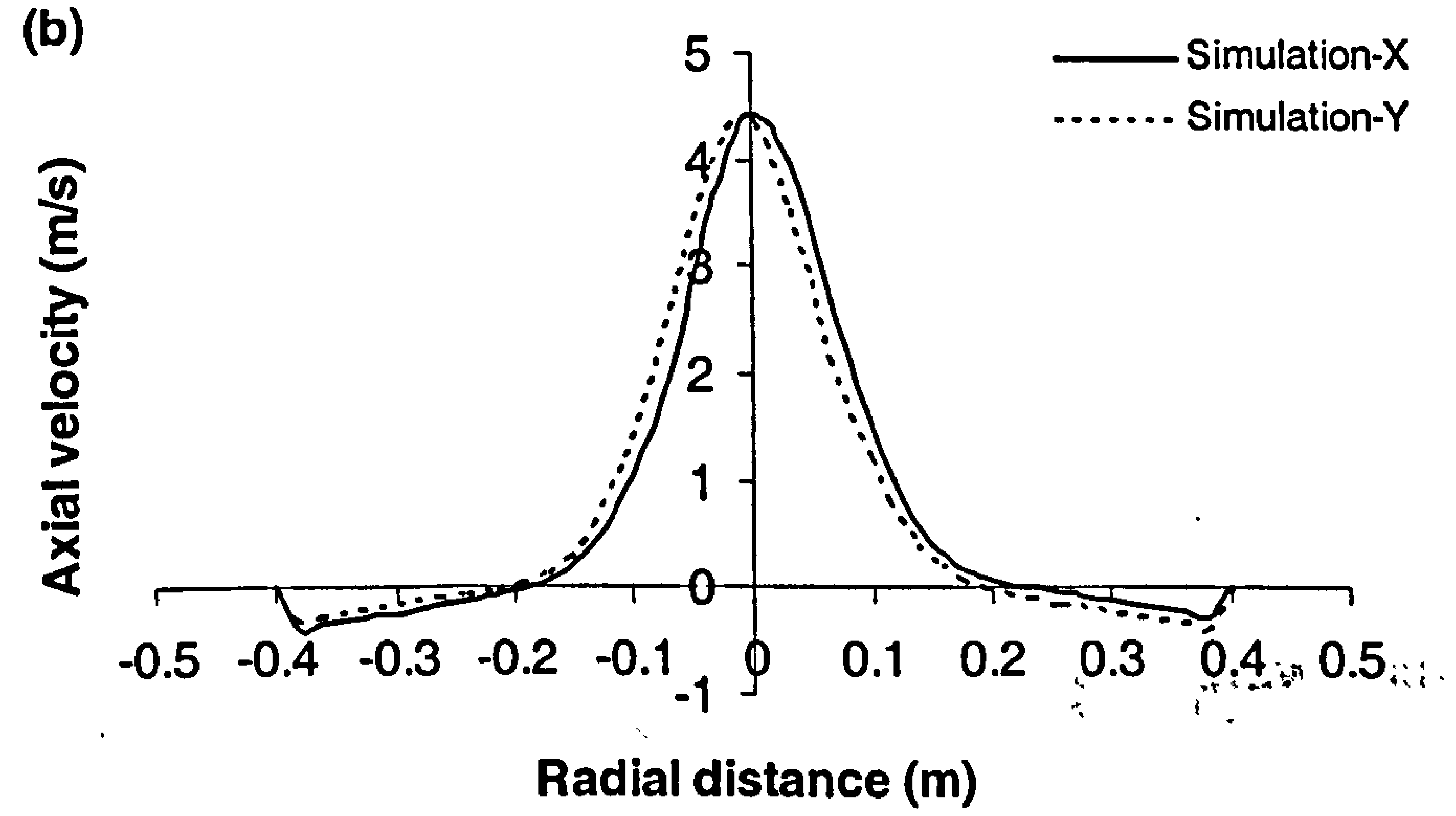

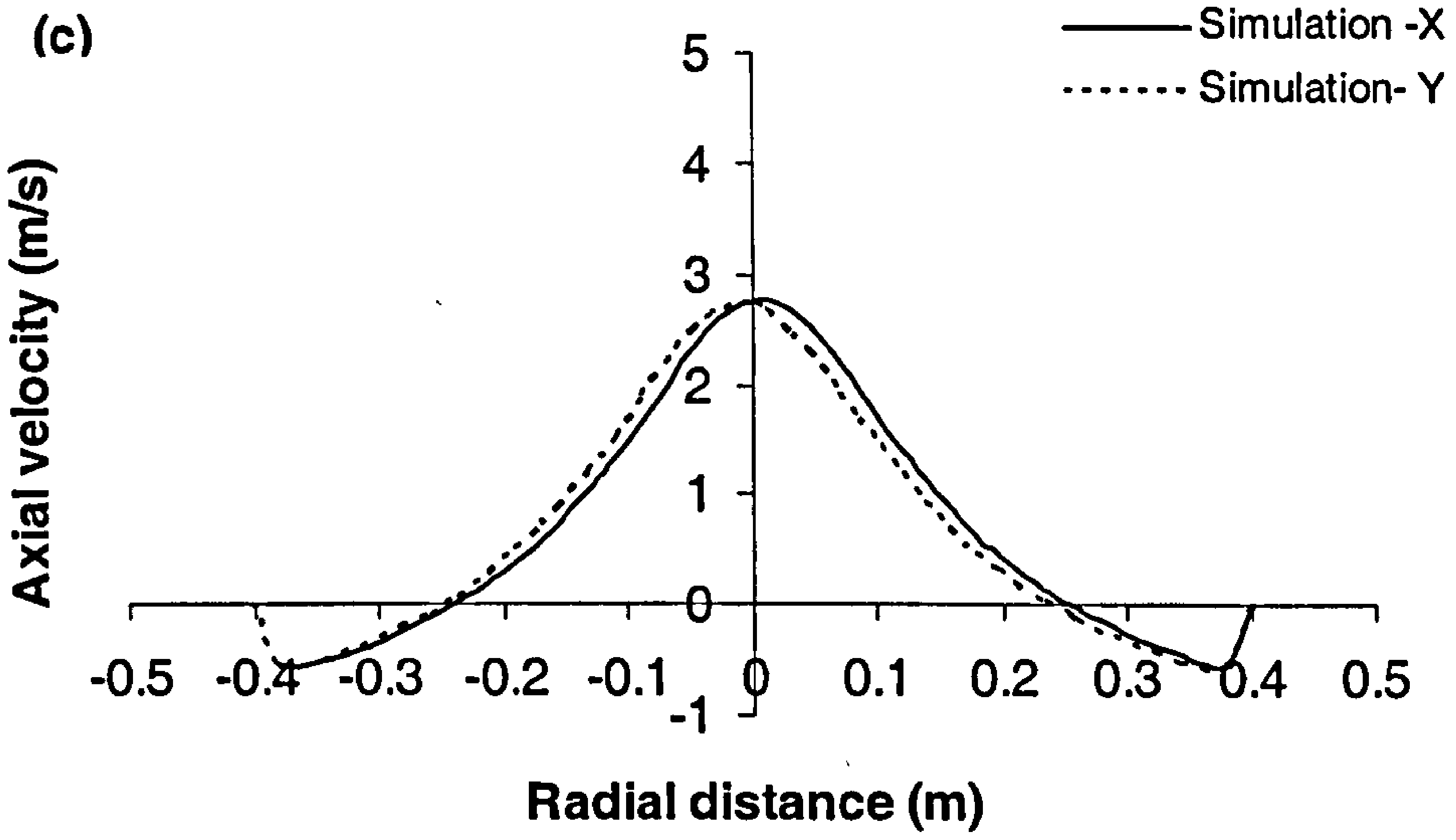

Figure 8-12: Gas axial velocity profiles at axial distances of (a) z = 0.24 m (b) z = 0.8 m and (c) z = 1.23 m below the nozzle.

8.6.2 Comparison between the measurement and the predictions of the gas temperature with the spray injection

The experimental temperature profiles of the gas are plotted in figures (8-13 a-d) at axial positions of z = 0.24 m, 0.58 m, 0.8 m and 1.23 m below the nozzle (see figure 8-7 for the positions).

In general, the prediction results were in good agreement with the experimental results, except in the main spray region. The differences in experimental results at the core region were probably due to drops of liquid nitrogen flowing into the core of the chamber from the inlet, (see figure 8-1). However, further down the chamber at z = 0.8 m and 1.23 m, the temperature profiles become flatter and core region of higher temperature broader as the spray fans out compared to z = 0.24 m and 0.58 m due to evaporation of liquid nitrogen. Also due to supercooling/recalescence which through not part of model does occur with in particle.

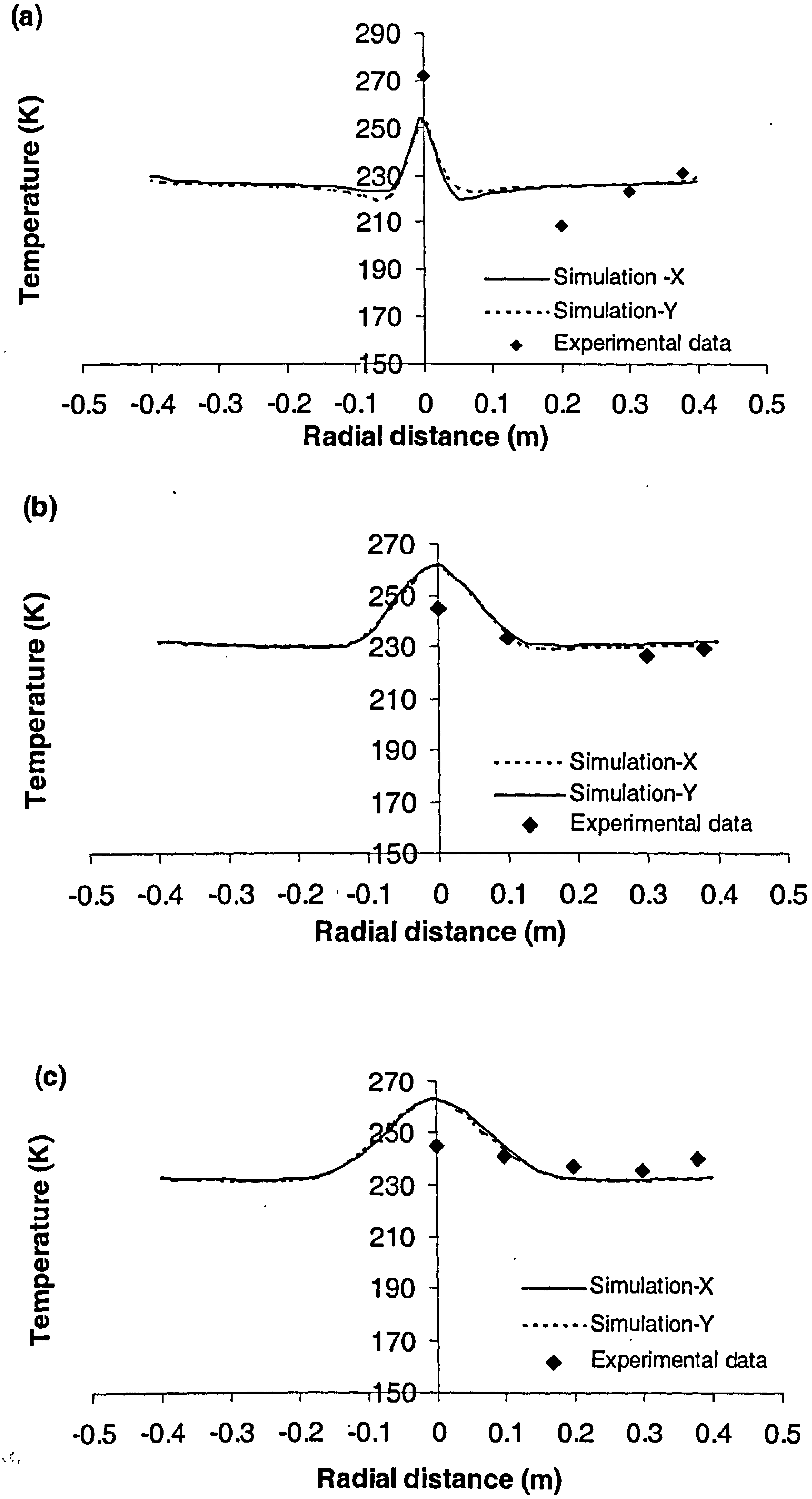
(a)
Temperature (K)
290
270
250
230
210
190
170
150
-0.5 -0.4 -0.3 -0.2 -0.1 0 0.1 0.2 0.3 0.4 0.5
Radial distance (m)
Simulation -X
Simulation-Y
Experimental data
(b)
Temperature (K)
270
250
230
210
190
170
150
-0.5 -0.4 -0.3 -0.2 -0.1 0 0.1 0.2 0.3 0.4 0.5
Radial distance (m)
Simulation-X
Simulation-Y
Experimental data
(c)
Temperature (K)
270
250
230
210
190
170
150
-0.5 -0.4 -0.3 -0.2 -0.1 0 0.1 0.2 0.3 0.4 0.5
Radial distance (m)
Simulation-X
Simulation-Y
Experimental data

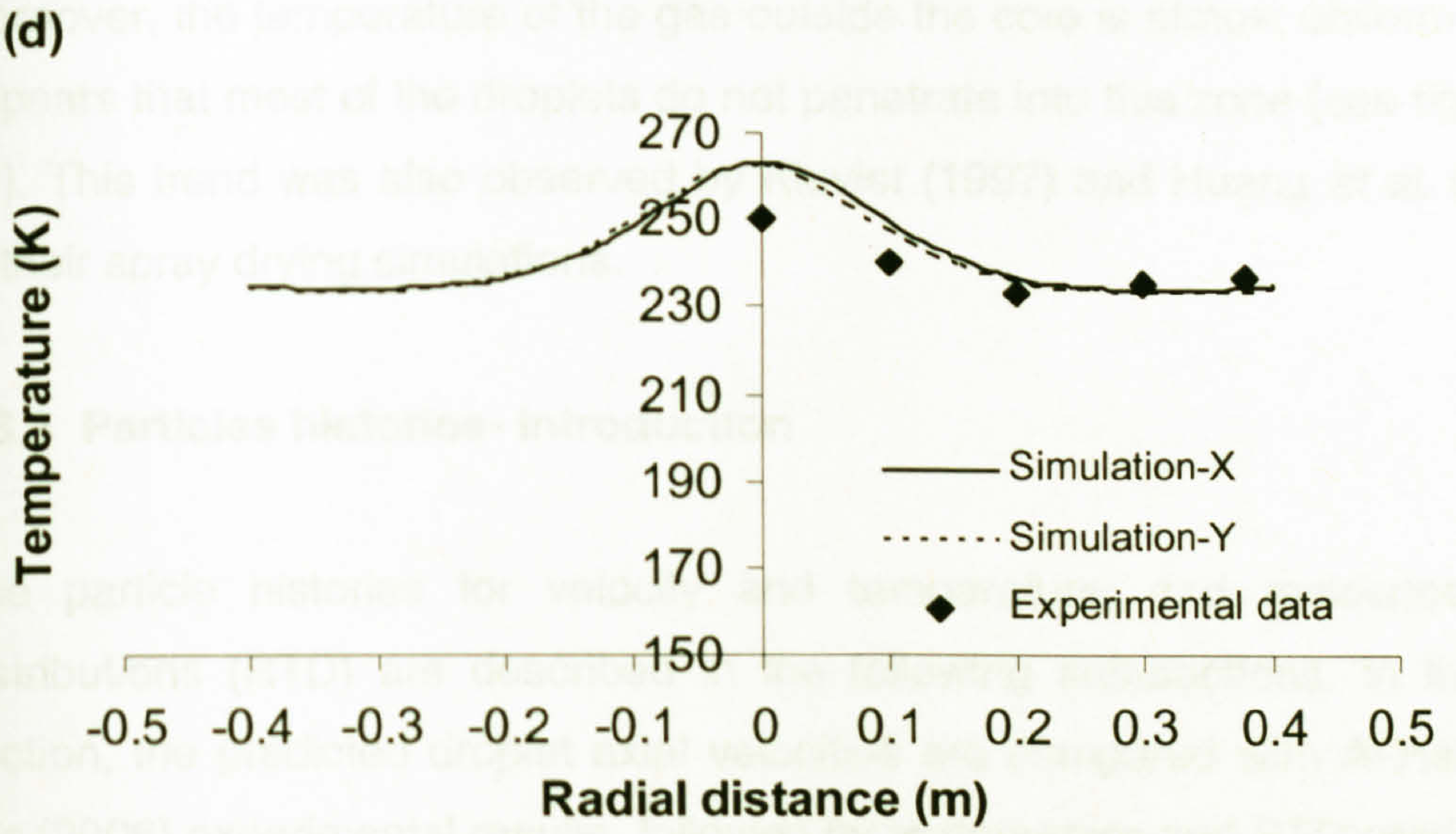

Figure 8-13: Comparison of gas temperature profiles between measurements and simulation at (a) z = 0.24 m (b) z = 0.58 m (c) z = 0.8 m and (d) z = 1.23 m from the nozzle spray point.

The temperature contours are depicted in figure (8-14), which show that most of the freezing takes place in the core region due to solid cone spray pattern.

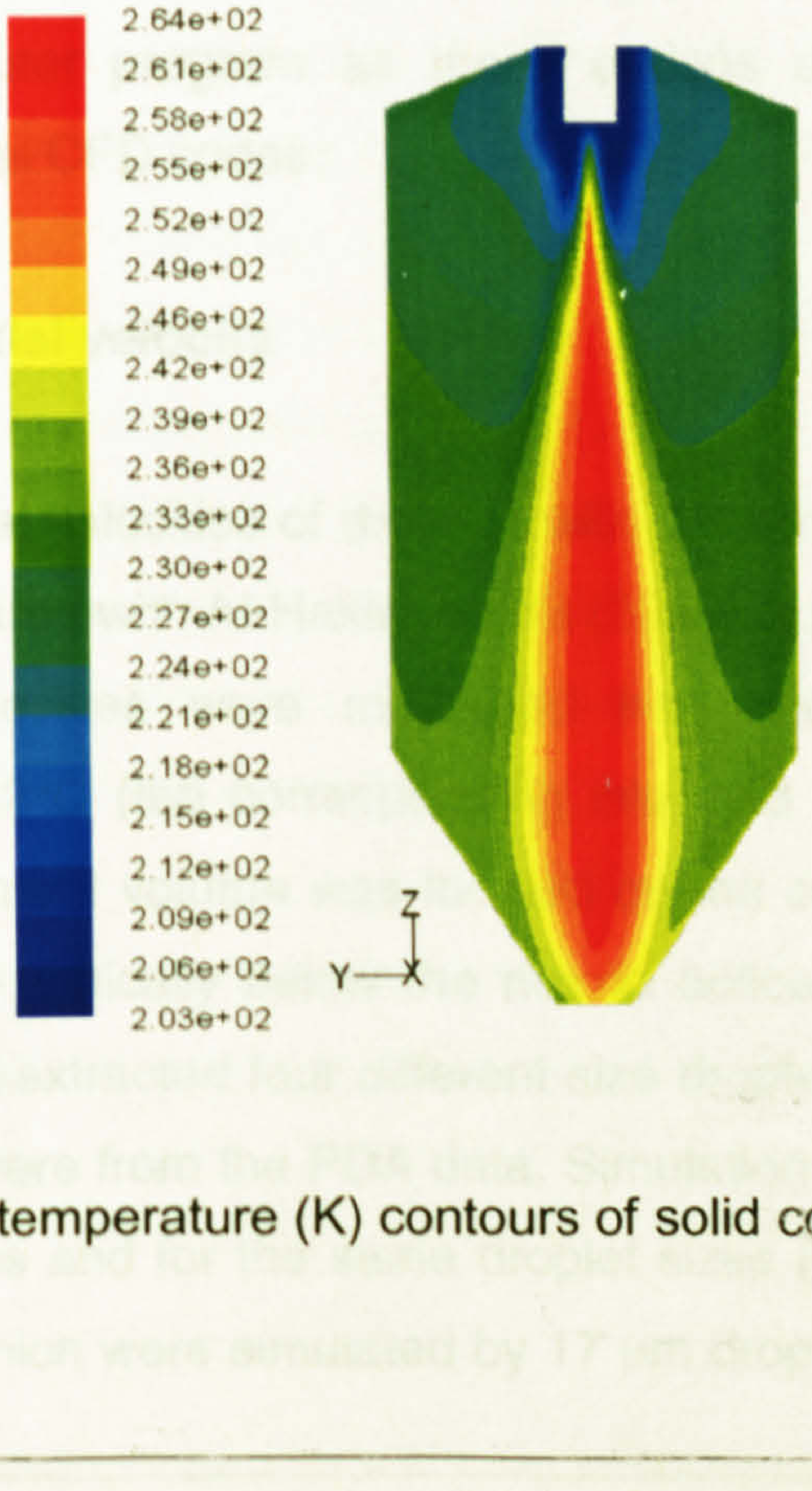

Figure 8-14: Gas temperature (K) contours of solid cone spray condition.

Moreover, the temperature of the gas outside the core is almost uniform and it appears that most of the droplets do not penetrate into this zone (see figure 8-20). This trend was also observed by Kieviet (1997) and Huang *et al.* (2006) in their spray drying simulations.

8.6.3 Particles histories- introduction

The particle histories for velocity and temperature, and residence time distributions (RTD) are described in the following sub-sections. In the first section, the predicted droplet axial velocities are compared with Al-Hakim *et al's* (2006) experimental results followed by temperature and RTD predictions are presented and discussed. In this model, Rosin-Rammler droplet distribution was used (Table 7-1) with 16 particles size ranges from 0.5 μm to 250 μm (total no of particle tracks were 1600). But, four size ranges of 17 μm, 50 μm, 100 μm and 150 μm particles are selected to represent the behaviour of different particle sizes.

The particles histories data presented in the following sub-sections were extracted from the simulation results using the in-house-developed post-processing computer program as these options are not available in the present commercial CFD codes.

8.6.4 Droplets axial velocity

The simulated axial velocities of droplets with different sizes from a solid cone spray were compared with Al-Hakim *et al's* (2006) experimental (PDA) results. Droplet axial velocities were measured from the spray at a chamber temperature of -42°C (the corresponding inlet gas temperature was -70°C) and the measurement volume was located on the centre-line of the spray at various distances vertically below the nozzle orifice: 0.038 m, 0.068 m and 0.108 m. Data for extracted four different size droplets of 20 μm, 50 μm, 100 μm and 150 μm were from the PDA data. Simulation results were extracted at the same locations and for the same droplet sizes (with the exception of the 20 μm droplets which were simulated by 17 μm droplets) and plotted together with the experimental results (mean velocities with standard deviation) in figure (8-15).

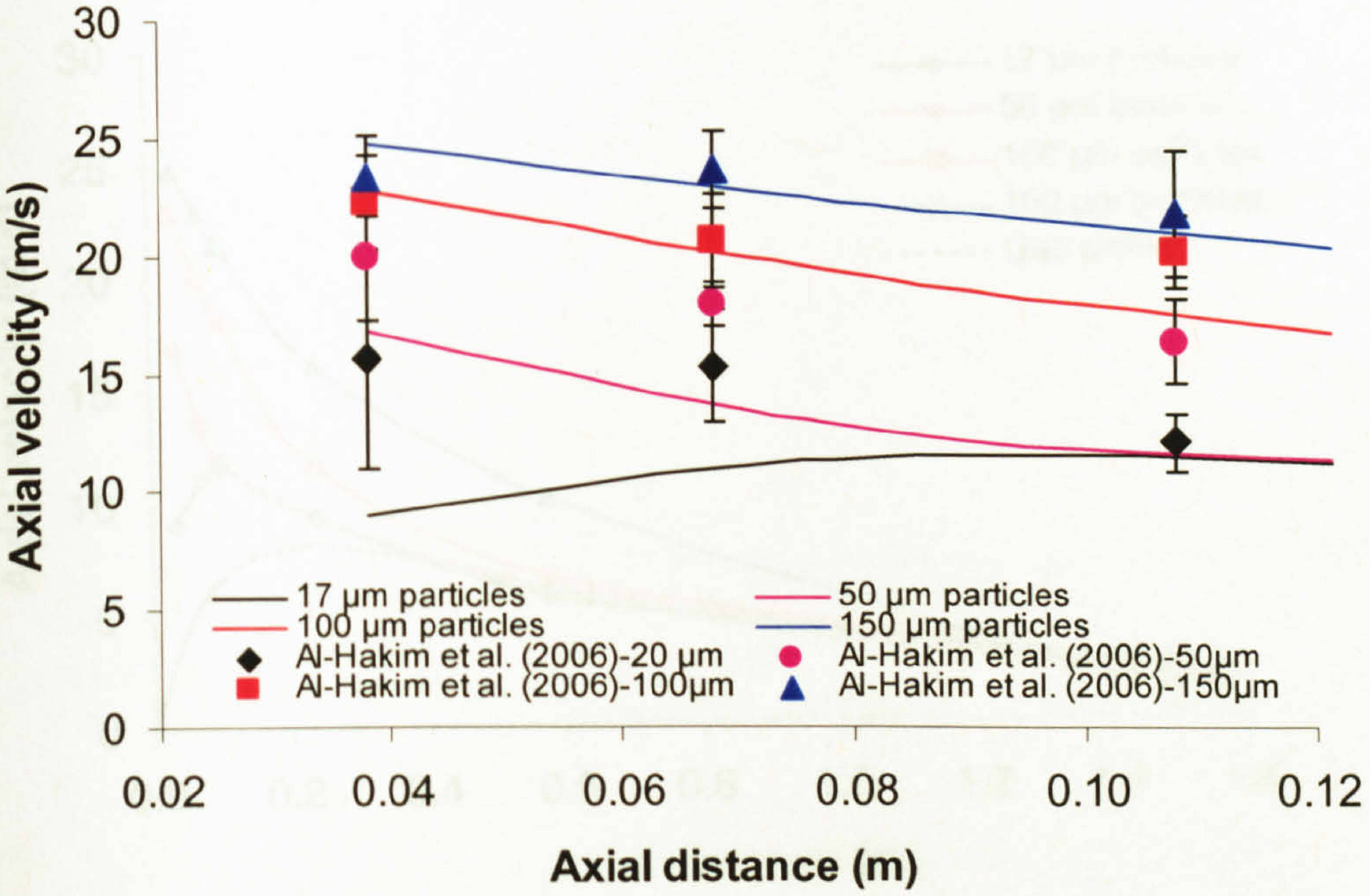

Figure 8-15: Comparison of axial velocity between measurements and simulation at an axial distances of z = 0.038 m, 0.068 m and 0.108 m from the nozzle for various particle sizes.

The predicted and experimental results indicate that the larger particles travel faster than smaller size particles. The smaller size particles decelerate more rapidly towards their terminal velocities. The terminal velocity is also approximately proportional to the square of the drop diameter (Papadakis and King, 1988). The simulation results are in reasonable agreement with the PDA experimental results. However, whereas the larger diameter particles (100 and 150 μm) are in good agreement, the smaller diameter particles (17 and 50 μm) are not. The reason may be due to small experimental measurement error (e.g. gas and liquid flow rates).

Figure (8-16) shows the simulation results for particle axial velocities along the axis of the chamber and it clearly indicates that axial velocities of all size particles decelerate during the course of flow (except 17 μm diameter particles show a slight increase in velocities after release from the nozzle as it is more influenced by the gas velocity.

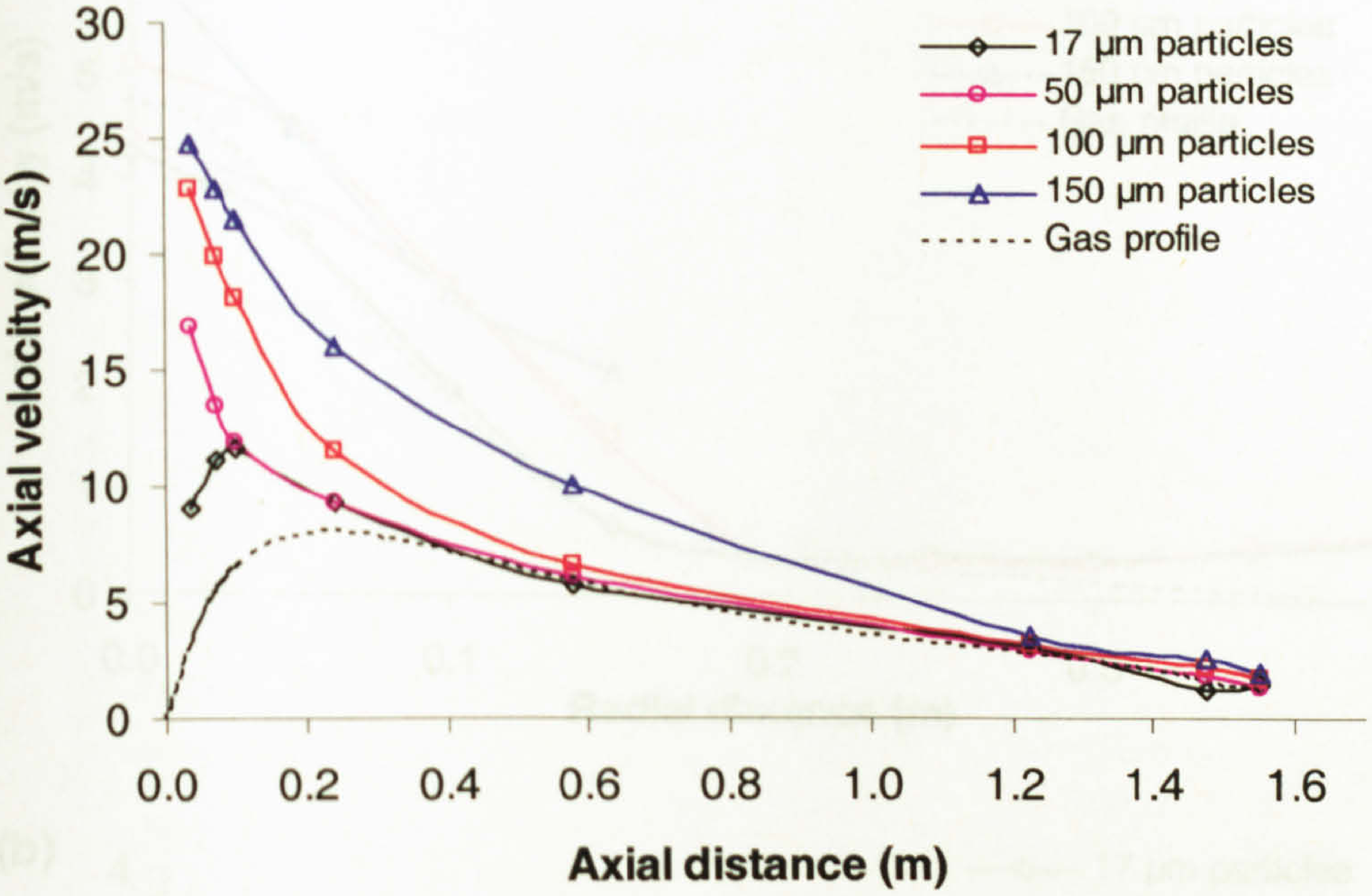

Figure 8-16: CFD simulated particle and gas axial velocities on the centre-line.

8.6.5 Radial variations of particle axial velocity

Simulated radial profiles of the particle axial velocity at axial distances of z= 0.8 m and 1.23 m below the nozzle orifice are shown in figures (8-17 a-b). The gas velocity profile is also shown in the figures (8-17). Simulation results at z = 0.8 m and 1.23 m only are presented here, because near to the nozzle, particles have not been dispersed widely enough to cover the width of the chamber (because the spray half angle is 15°). Thus no particle velocity data could be collected for these cases.

The particle axial velocities were similar in magnitude to the gas velocity profiles. Along the centre-line of the chamber, the particle velocities were higher than the gas velocities, due to higher spray feed velocity compared to that of the low gas inlet velocity (0.98 m/s). The large size particles have a higher axial velocity than the smaller ones at 0.8 m and 1.23 m distance from nozzle. Although the particles have the same initial velocities, but higher mass particles have larger momentum, hence it takes longer for them to decelerate.

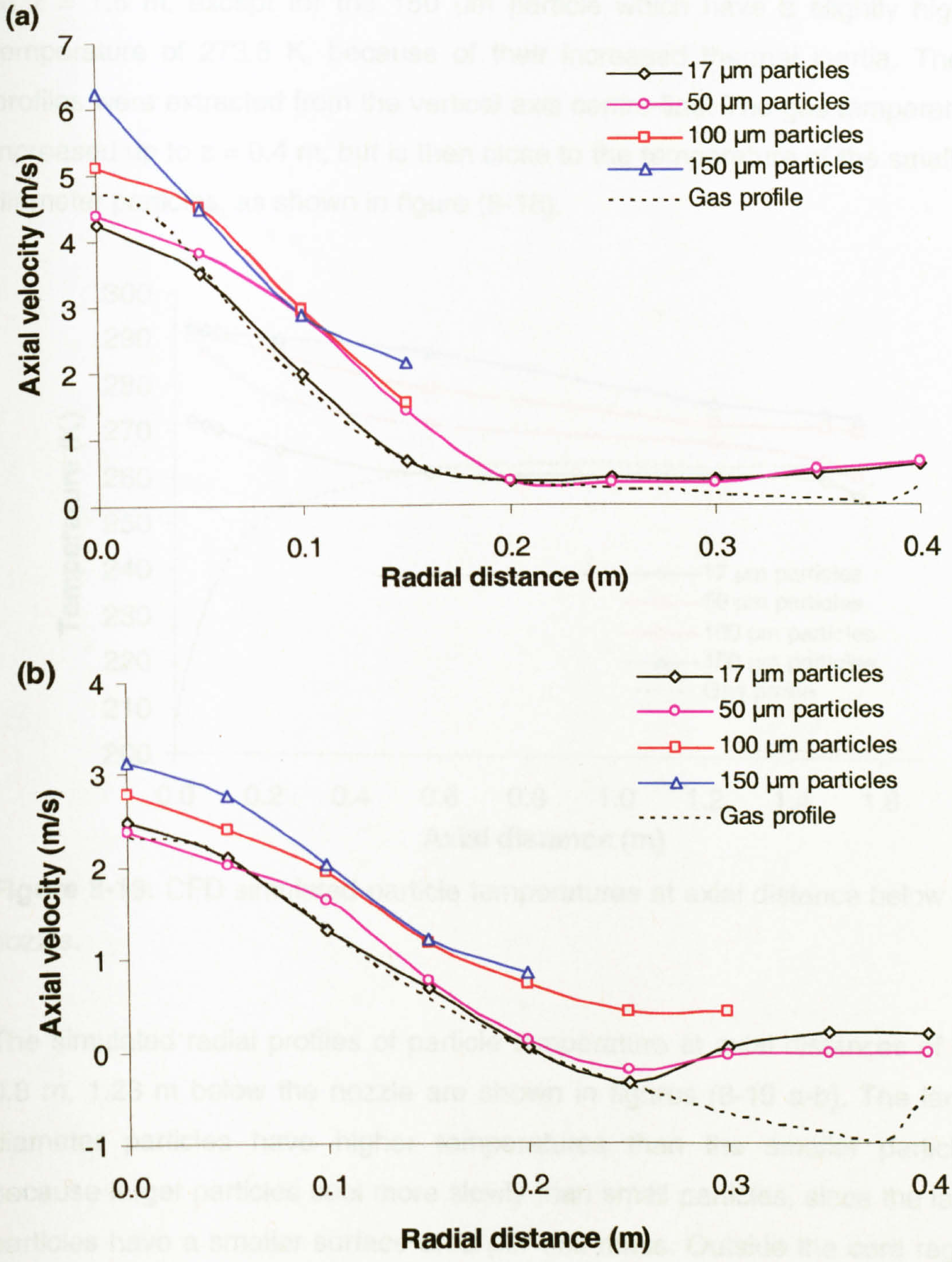

Figure 8-17: CFD simulated particle axial velocities at axial distances of (a) z = 0.8 m and (b) z = 1.23 m distance below the nozzle.

8.6.6 Temperature profiles

Particles temperatures at the centre-line of the spray are plotted in figure (8-18). Figure (8-18) shows that the smaller size particles are colder than the large size particles. All diameter particle temperatures shown are below 273 K at z = 1.6 m, except for the 150 μm particle which have a slightly higher temperature of 273.5 K, because of their increased thermal inertia. These profiles were extracted from the vertical axis centre-line. The gas temperature increased up to z = 0.4 m, but is then close to the temperature of the smallest diameter particles, as shown in figure (8-18).

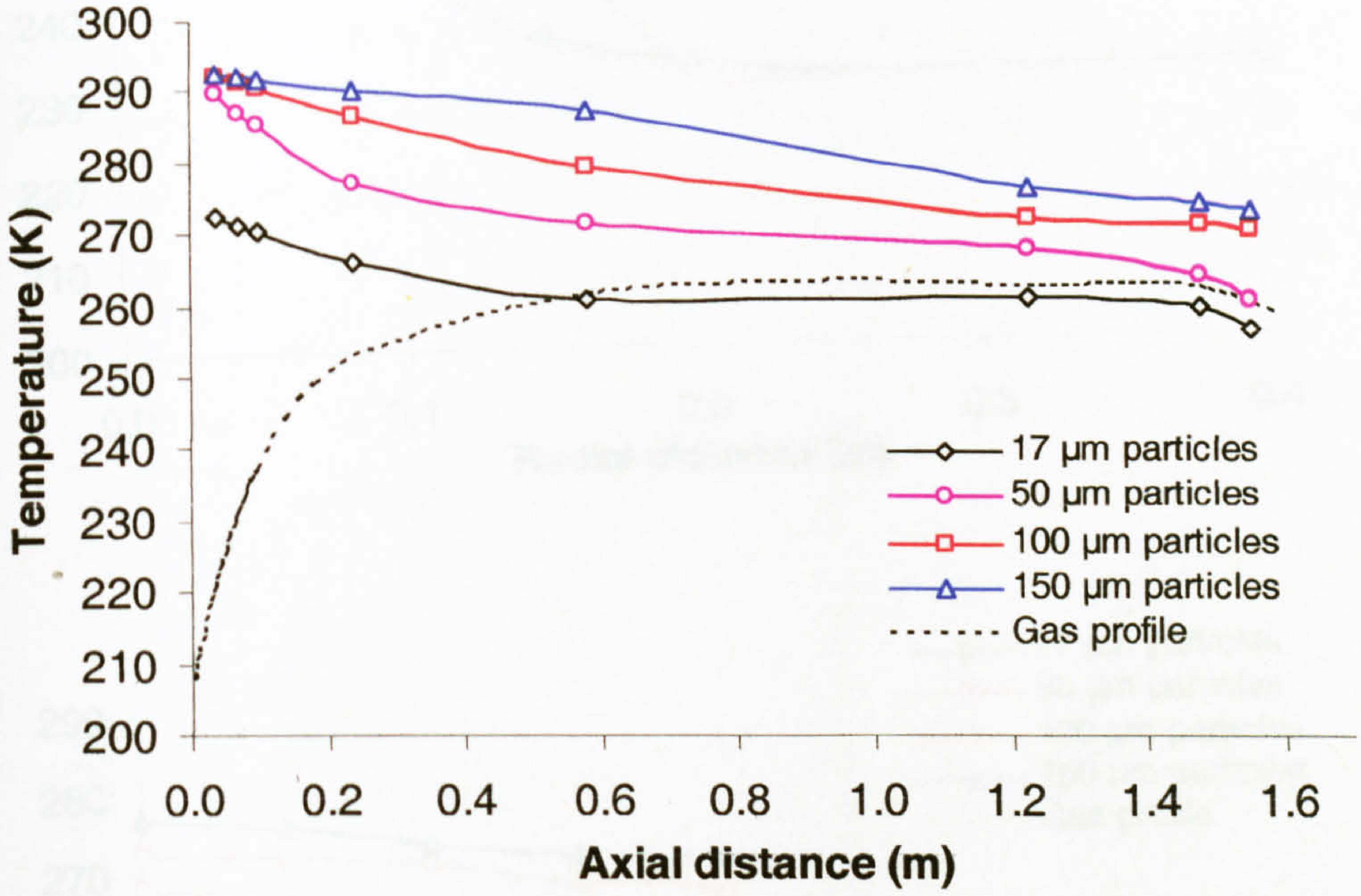

Figure 8-18: CFD simulated particle temperatures at axial distance below the nozzle.

The simulated radial profiles of particle temperature at axial distances of z = 0.8 m, 1.23 m below the nozzle are shown in figures (8-19 a-b). The larger diameter particles have higher temperatures than the smaller particles, because larger particles cool more slowly than small particles, since the large particles have a smaller surface area per unit mass. Outside the core region (0.2 m < r < 0.4 m) the droplet temperatures were low and almost equal to the gas temperatures. However, in the core region, figure (8-19) shows that the particle temperature was higher than the gas temperature and also the particle temperatures were decreasing as they travel down the chamber.

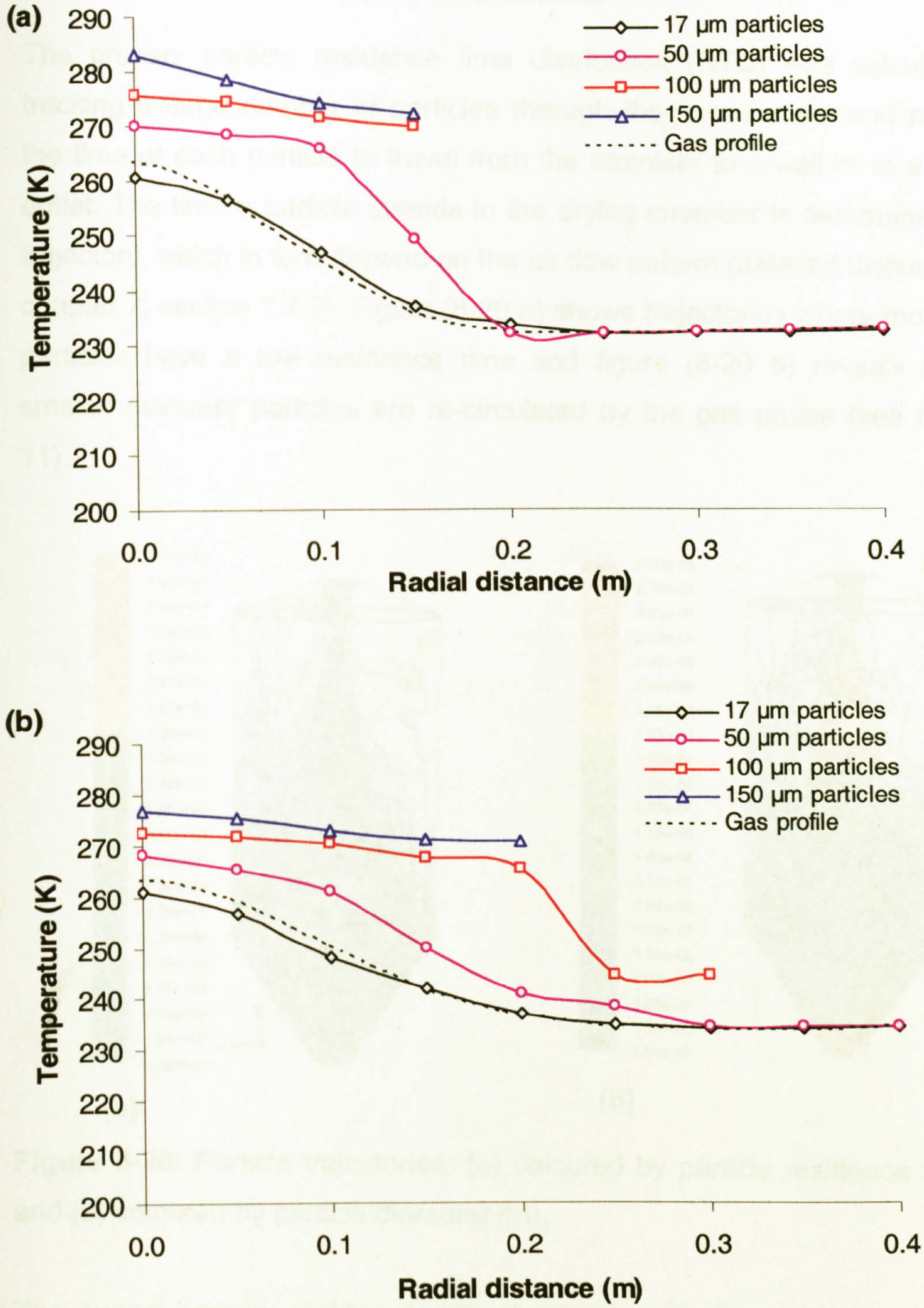

Figure 8-19: CFD simulated particle temperatures at axial distances of (a) z = 0.8 m and (b) z = 1.23 m.

8.6.7 Particle residence time distributions

The primary particle residence time distribution (RTD) was calculated by tracking a large number of particles through the flow domain and recording the time of each particle to travel from the atomiser to a wall or to a product outlet. The time a particle spends in the drying chamber is determined by its trajectory, which in turn depend on the air flow pattern (detailed discussions in chapter 7, section 7.7.9). Figure (8-20 a) shows trajectories where most of the particles have a low residence time and figure (8-20 b) reveals that the smaller diameter particles are re-circulated by the gas phase (see figure 8-11).

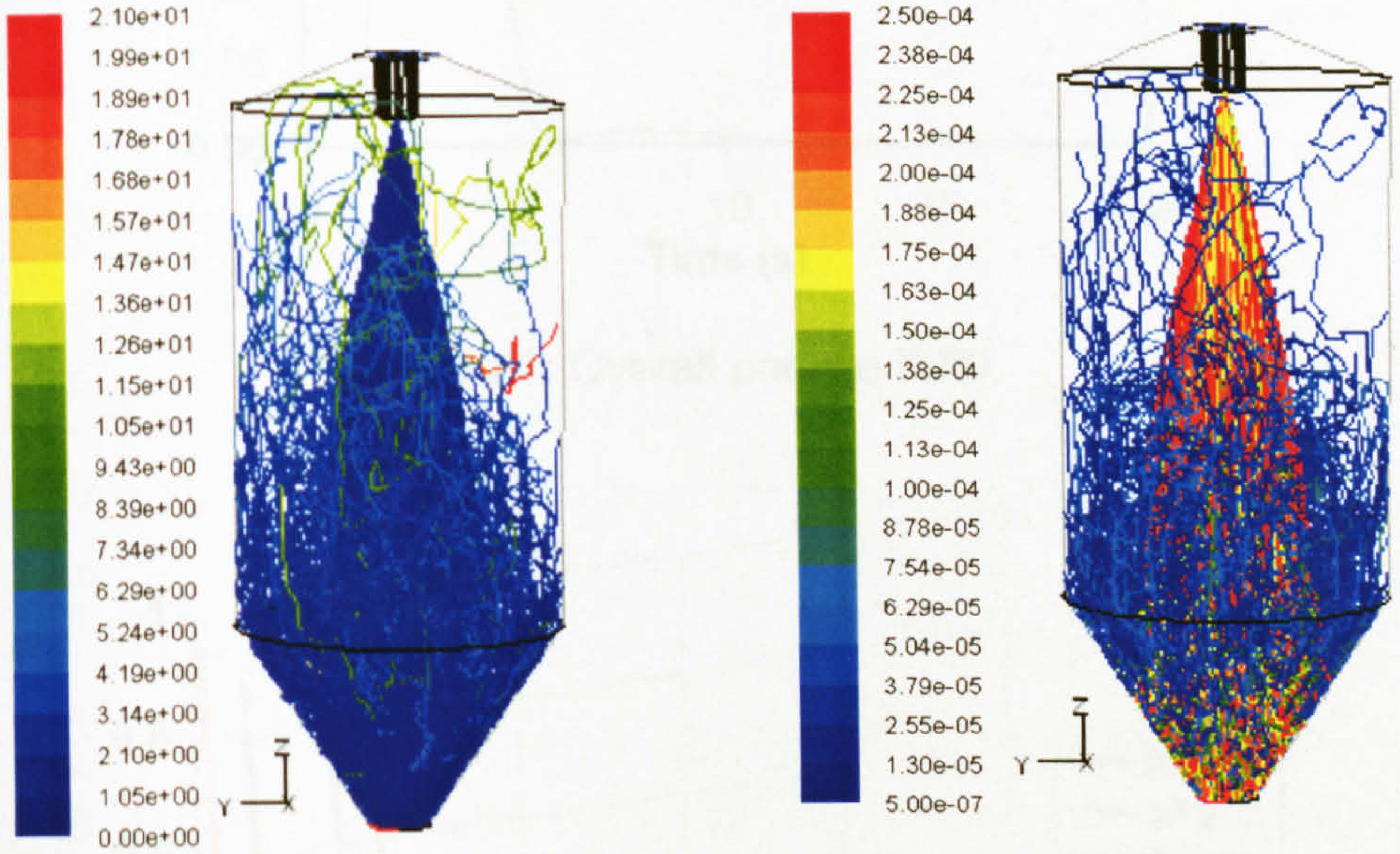

(a) **(b)**

Figure 8-20: Particle trajectories: (a) coloured by particle residence time (s) and (b) coloured by particle diameter (m).

The overall primary residence time distribution of all particles is shown in figure (8-21). The minimum and maximum particle RT is 0.19 s and 20.9 s respectively. The shape of the RTD curve, which shows that the majority of particles have a RT between 1.5 to 5.4 s and figure (8-21), also shows some of the particles having a longer RT, which may be due to re-circulation of the particles. The average RT is 1.3 s, which is much lower than gas residence time (18 s), because influence of the atomiser exit velocity on speeding up transit through chamber.

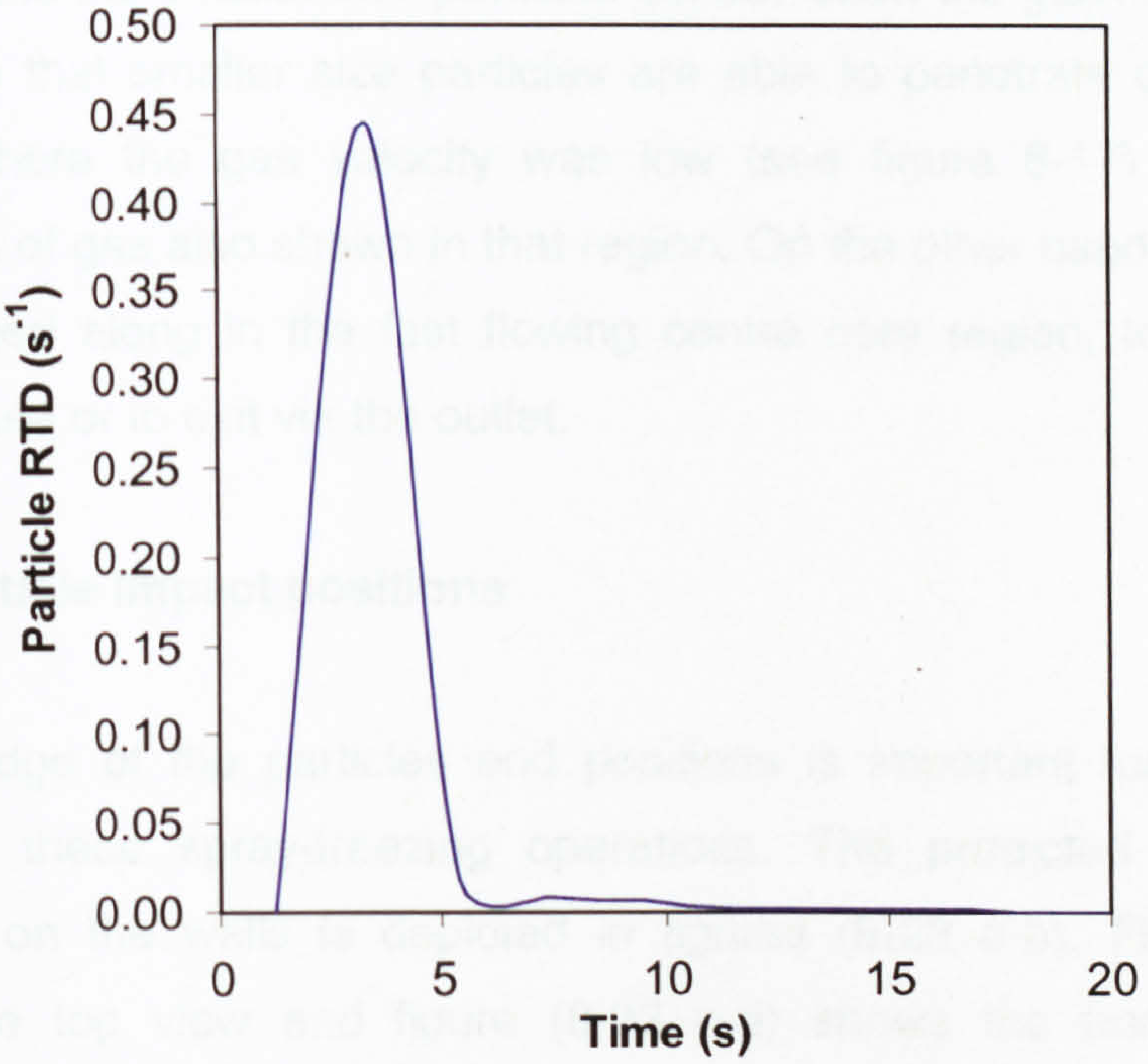

Figure 8-21: Overall particle RTD.

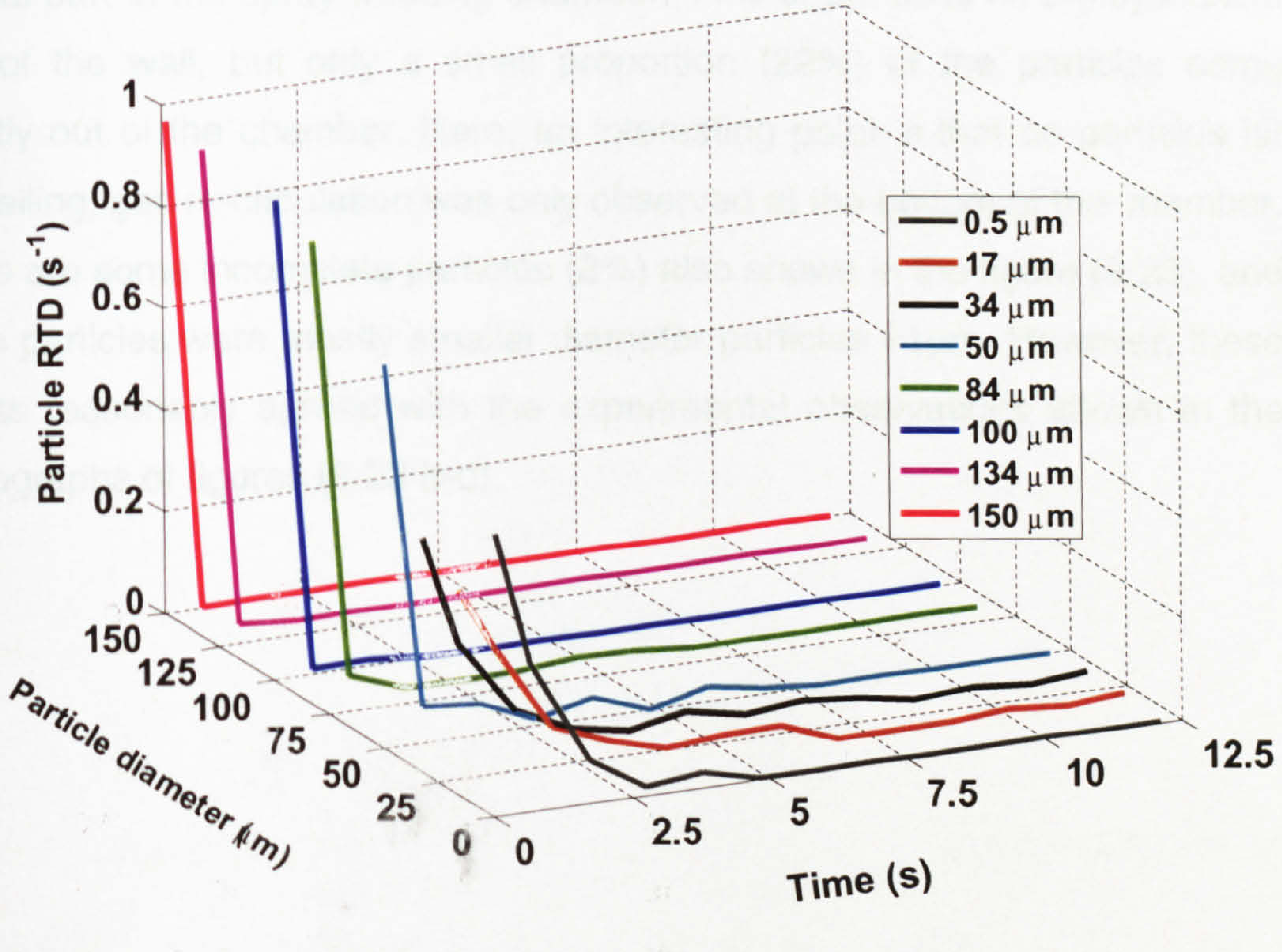

Figure 8-22: Predicted residence time distribution for different particle sizes.

The RTDs of the different size particles are shown in figure (8-22). The smaller particles have a longer residence time than the larger diameter particles and the smaller size particles almost follow the gas flow. Figure (8-20 b) reveals that smaller size particles are able to penetrate outside the core region, where the gas velocity was low (see figure 8-17) as well as re-circulation of gas also shown in that region. On the other hand, larger particles are dragged along in the fast flowing centre core region, to impact on the conical base or to exit via the outlet.

8.6.8 Particle Impact positions

A knowledge of the particles end positions is important for designing and operating these spray-freezing operations. The predicted particle impact positions on the walls is depicted in figures (8-23 a-b). Figure (8-23 a-b) shows the top view and figure (8-23 c-d) shows the front views of the simulated and experimental results for particle impacts on the chamber walls. These figures indicates that a large fraction of the particles (65%) strike on the conical part of the spray-freezing chamber; 11% of particles hit the cylindrical part of the wall, but only a small proportion (22%) of the particles come directly out of the chamber. Here, an interesting point is that no particles hit the ceiling; gas re-circulation was only observed at the bottom of the chamber. There are some incomplete particles (2%) also shown in the figure (8-23), and those particles were mostly smaller diameter particles <1µm. However, these results reasonably agreed with the experimental observations shown in the photographs of figures (8-23 b-d).

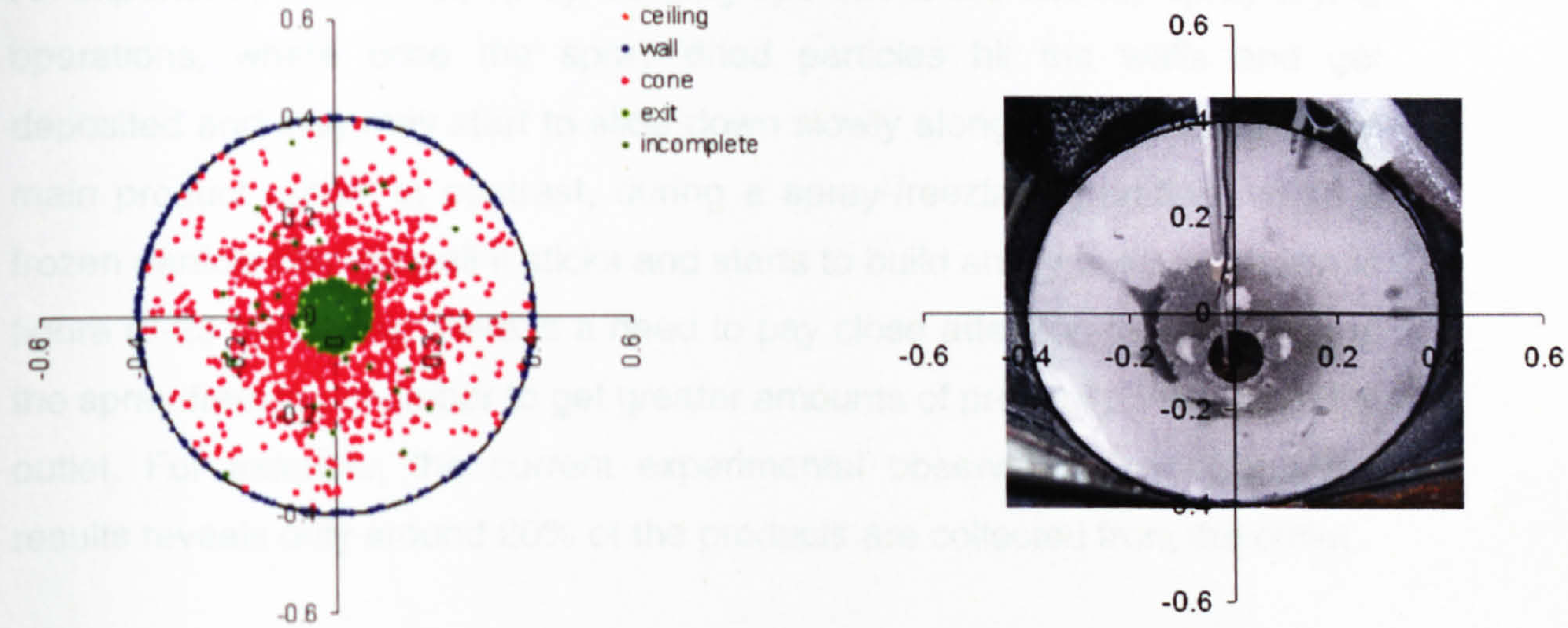

(a) Simulation (top view)

(b) Experiment (top view)

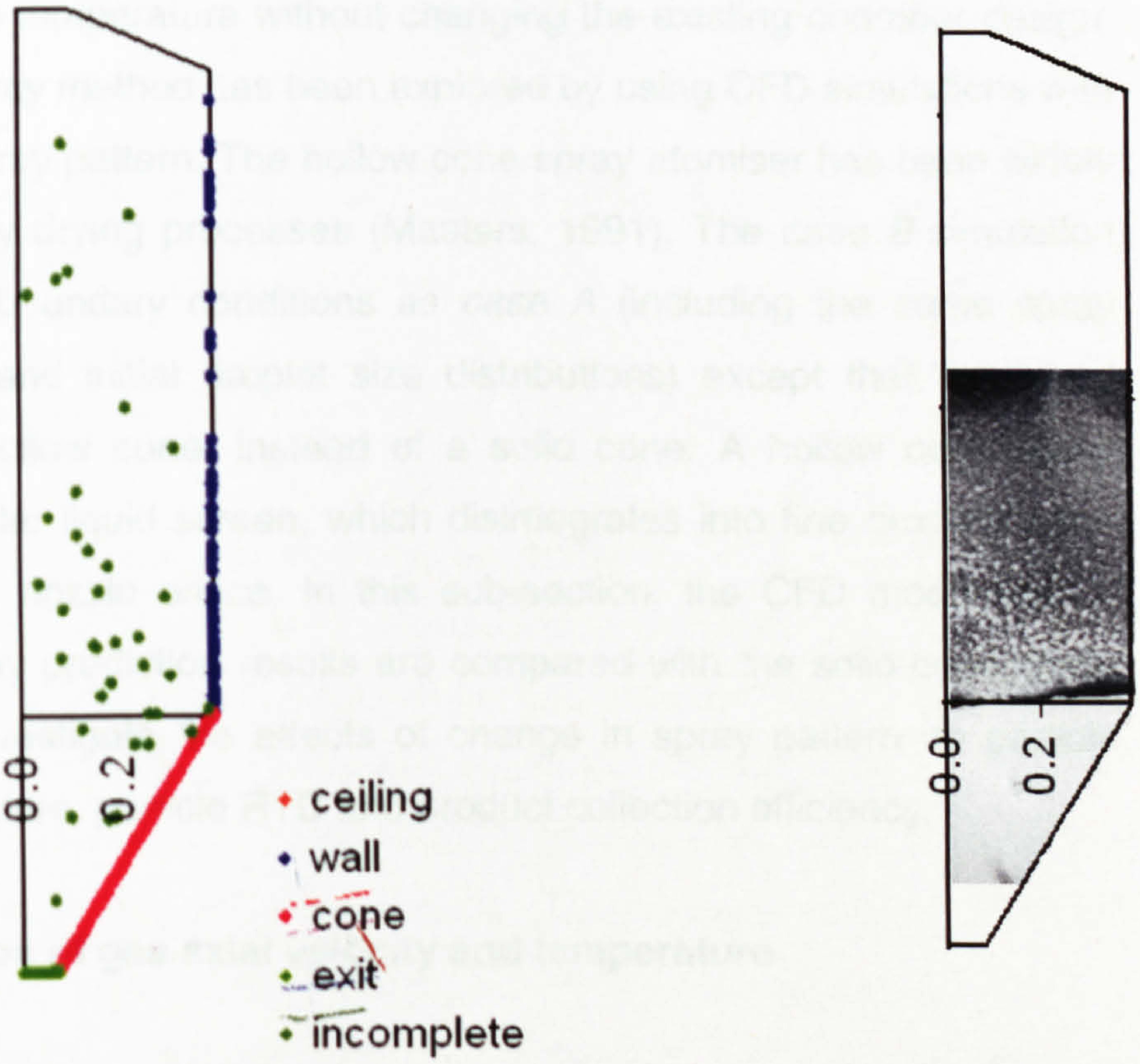

(c) Simulation (front view)

(d) Experiment (front view)

Figure 8-23: CFD simulated and experimental results of particle impact position on the walls.

An important point is that, spray-freezing operations are not like spray-drying operations, where once the spray dried particles hit the walls and get deposited and they may start to slide down slowly along the wall towards the main product outlet. In contrast, during a spray-freezing operation, when a frozen particle hits the wall it sticks and starts to build an icy layer as shown in figure (8-23 b). Hence, there is a need to pay close attention to the design of the spray-freezing chamber to get greater amounts of product conveyed to the outlet. For example, the current experimental observation and simulation results reveals only around 20% of the products are collected from the outlet.

8.7 *Case B*: Hollow cone spray

Case A study showed that higher particle temperature at the outlet. To reduce the outlet particle temperature without changing the existing chamber design, an alternative spray method has been explored by using CFD simulations with a hollow cone spray pattern. The hollow cone spray atomiser has been widely used in the spray drying processes (Masters, 1991). The *case B* simulation used the same boundary conditions as *case A* (including the same spray mass flow rate and initial droplet size distributions) except that the spray pattern was a hollow cone, instead of a solid cone. A hollow cone spray produces a circular liquid screen, which disintegrates into fine droplets soon after leaving the nozzle orifice. In this sub-section, the CFD model with a hollow cone spray prediction results are compared with the solid cone spray predictions to investigate the effects of change in spray pattern on particle velocity, temperature, particle RTD and product collection efficiency.

8.7.1 Distribution of gas axial velocity and temperature

The gas axial velocity and temperature distribution with hollow cone spray injection are depicted in figure (8-24). The axial velocity profiles were similar to the solid cone spray, but the temperature distributions were different. In the solid cone spray, at the core region/centre axial line of the chamber, the gas temperature was hotter due to more heat transfer from droplets to gas, because droplets were sprayed at the centre axial line of the chamber. In the hollow cone spray, there was no spray in the central axial line due to the spray pattern, hence it predicts a lower gas temperature.

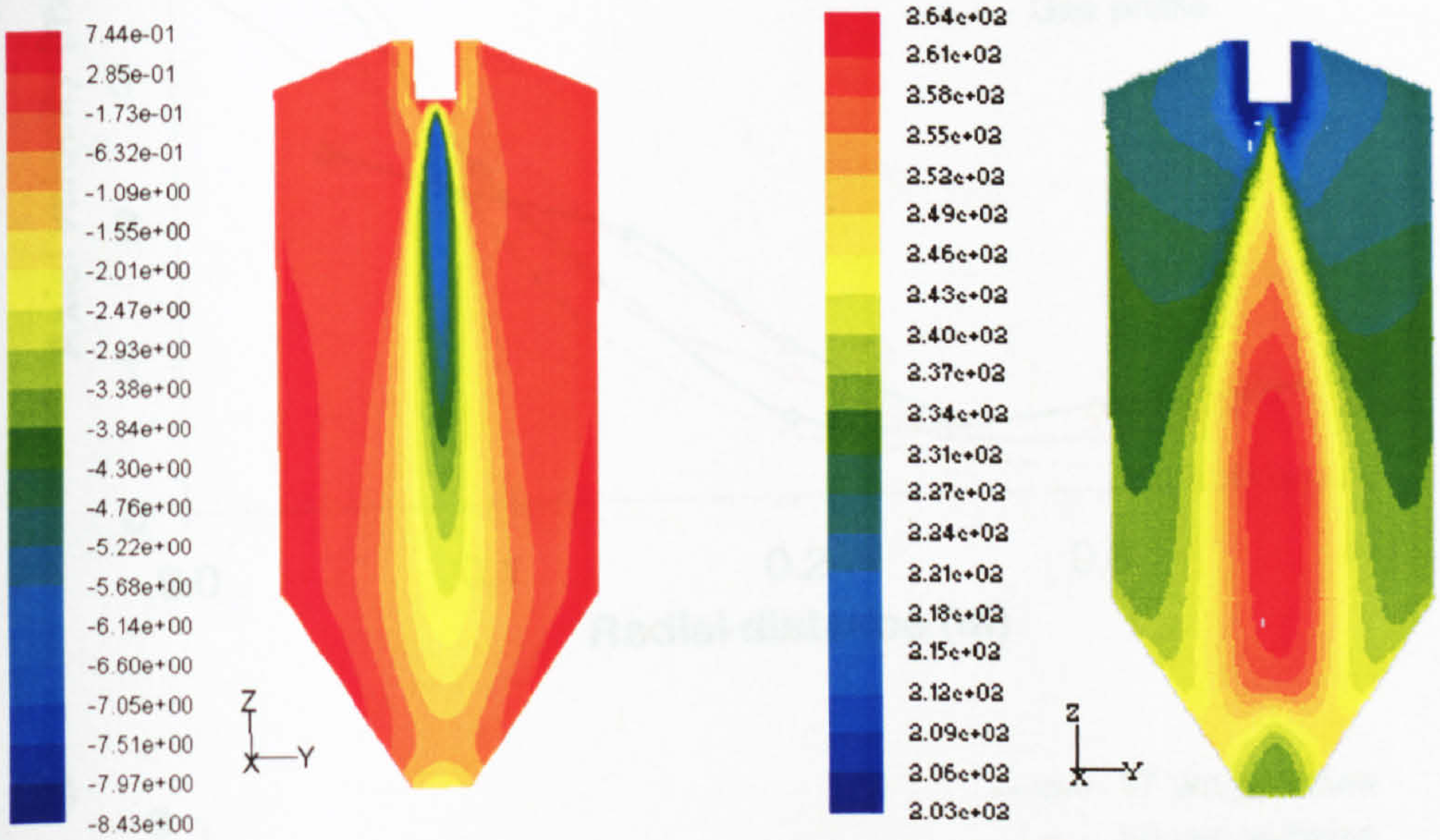

(a) (b)

Figure 8-24: Gas profile contours with hollow cone spray: (a) axial velocity (m/s) and (b) temperature (K).

8.7.2 Particles histories

The particles histories such as velocity, temperature, RTD are described in this sub-section and are followed by a comparison between the solid and the hollow cone results. The radial profiles of particle velocity at axial distances of z = 0.8 m and 1.23 m below the nozzle are shown in figures (8-25 a-b). The particle axial velocities is very similar to the gas velocities. In contrast to the solid cone spray results, the hollow cone spray shows all size particles including larger size particles penetrating outside the core region (0.1 m < r < 0.4 m). This reducing the particle velocities (due to low gas velocity) and temperatures (due to increased residence time). At z = 1.23 m level the larger particles shown highest axial velocities than the smaller particles.

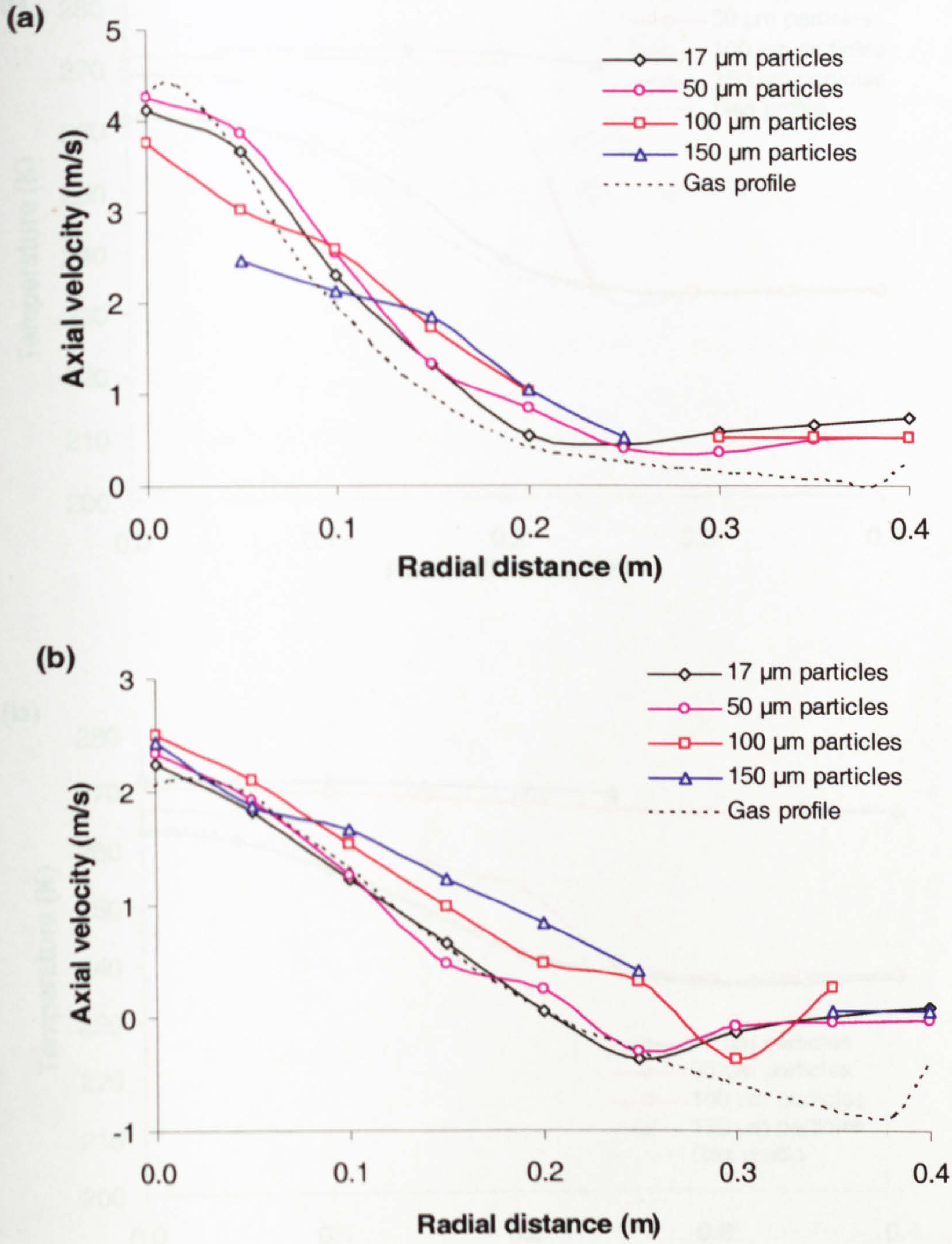

Figure 8-25: CFD simulated hollow cone spray particle axial velocities at axial position of (a) z = 0.8 m and (b) z = 1.23 m levels.

The radial profiles of particle temperatures at axial distance of z= 0.8 m and 1.23 m level below the nozzle orifice are shown in figures (8-26 a-b). These show similar results to the solid cone spray, where, the larger size particles have higher temperatures than the smaller size particles.

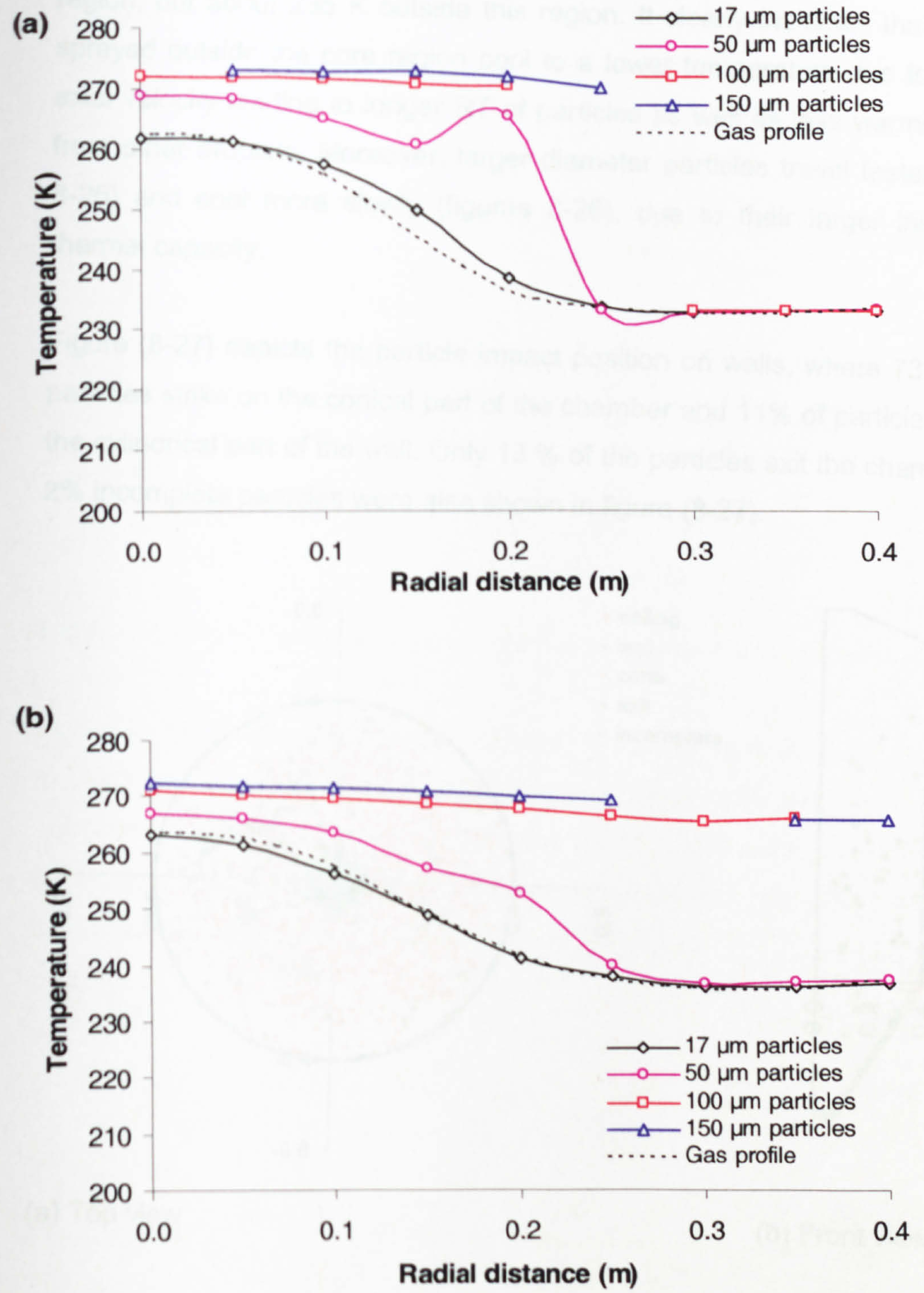

Figure 8-26: CFD simulated hollow cone spray particle temperatures at axial position of (a) z = 0.8 m and (b) z = 1.23 m levels.

In the core region (0 < r < 0.2 m) particle temperatures are almost constant, but once particles travel to the outside of the core region (0.2 < r < 0.4 m), the particle temperatures start decreasing; for example, the temperatures of the 50 μm particle at z = 0.8 m level (figure 8-26 a) were around 270 K in the core region, but about 235 K outside this region. It clearly indicates that droplets sprayed outside the core region cool to a lower temperature due to low gas axial velocity leading to longer RT of particles as well as less warming effect from other droplets. Moreover, larger diameter particles travel faster (figures 8-25) and cool more slowly (figures 8-26), due to their larger inertia and thermal capacity.

Figure (8-27) depicts the particle impact position on walls, where 73% of the particles strike on the conical part of the chamber and 11% of particles impact the cylindrical part of the wall. Only 13 % of the particles exit the chamber and 2% incomplete particles were also shown in figure (8-27).

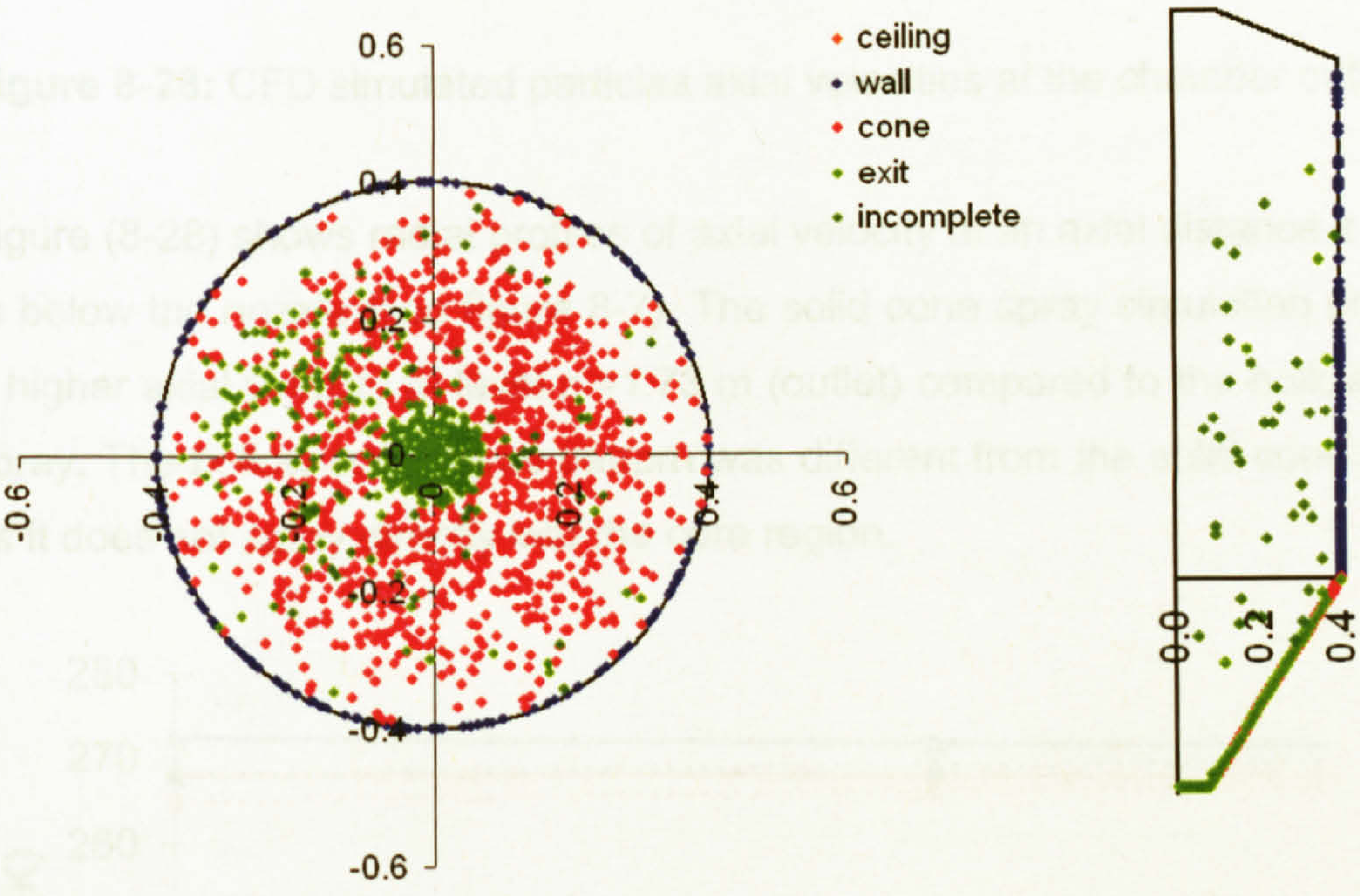

(a) Top view

(b) Front view

Figure 8-27: Predicted particle impact position on walls for *case B.*

8.7.3 Comparison of solid and hollow cone sprays

A comparison of the solid and hollow cone spray profiles at the outlet (z = 1.73 m) in terms of the particles axial velocities, temperatures, overall RTD and collection efficiency is presented in this sub-section.

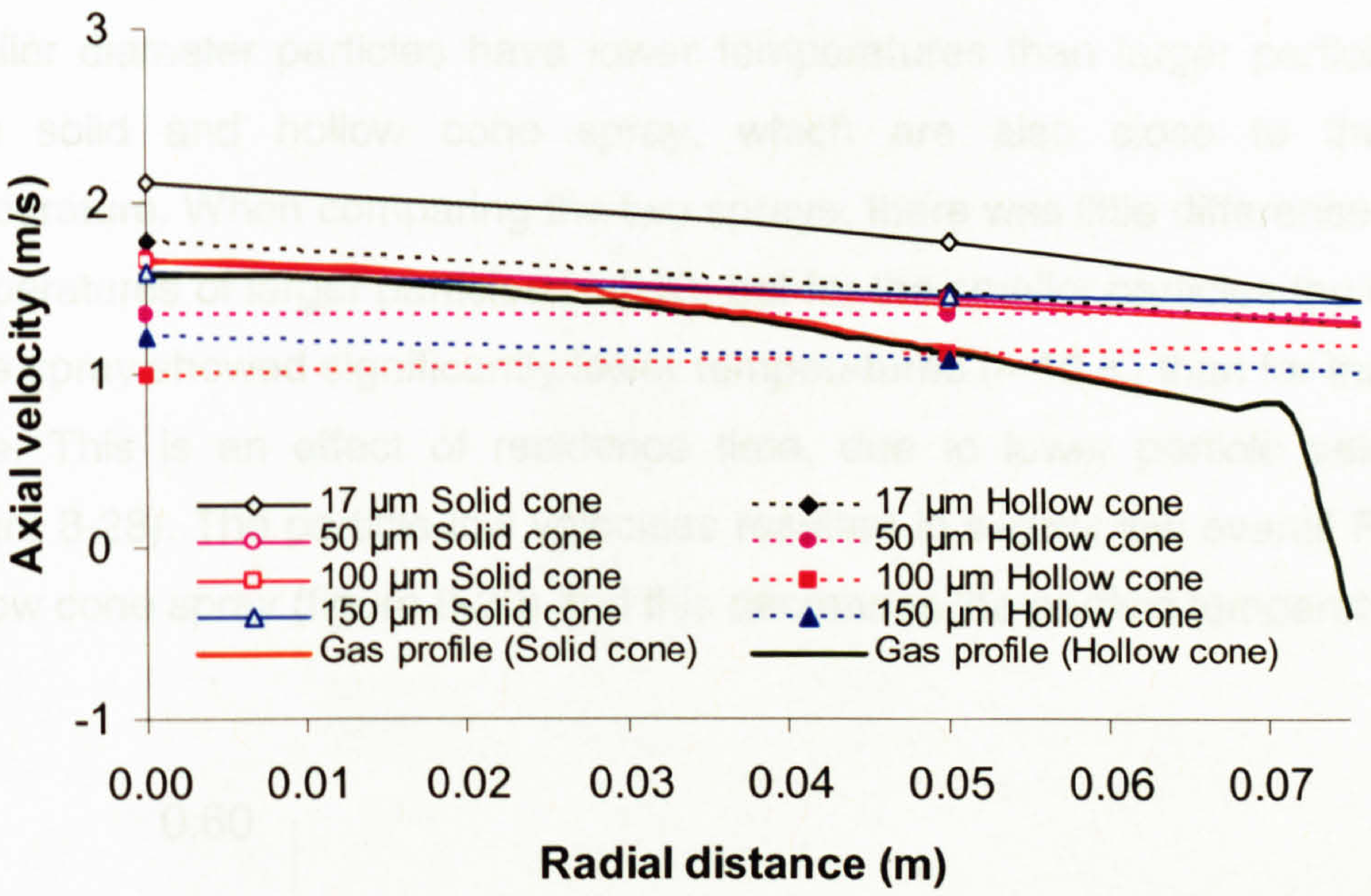

Figure 8-28: CFD simulated particles axial velocities at the chamber outlet.

Figure (8-28) shows radial profiles of axial velocity at an axial distance z =1.73 m below the nozzle (see figure 8-7). The solid cone spray simulation predicts a higher axial velocity at level z =1.73 m (outlet) compared to the hollow cone spray. The hollow cone spray pattern was different from the solid cone spray, as it does not spray directly into the core region.

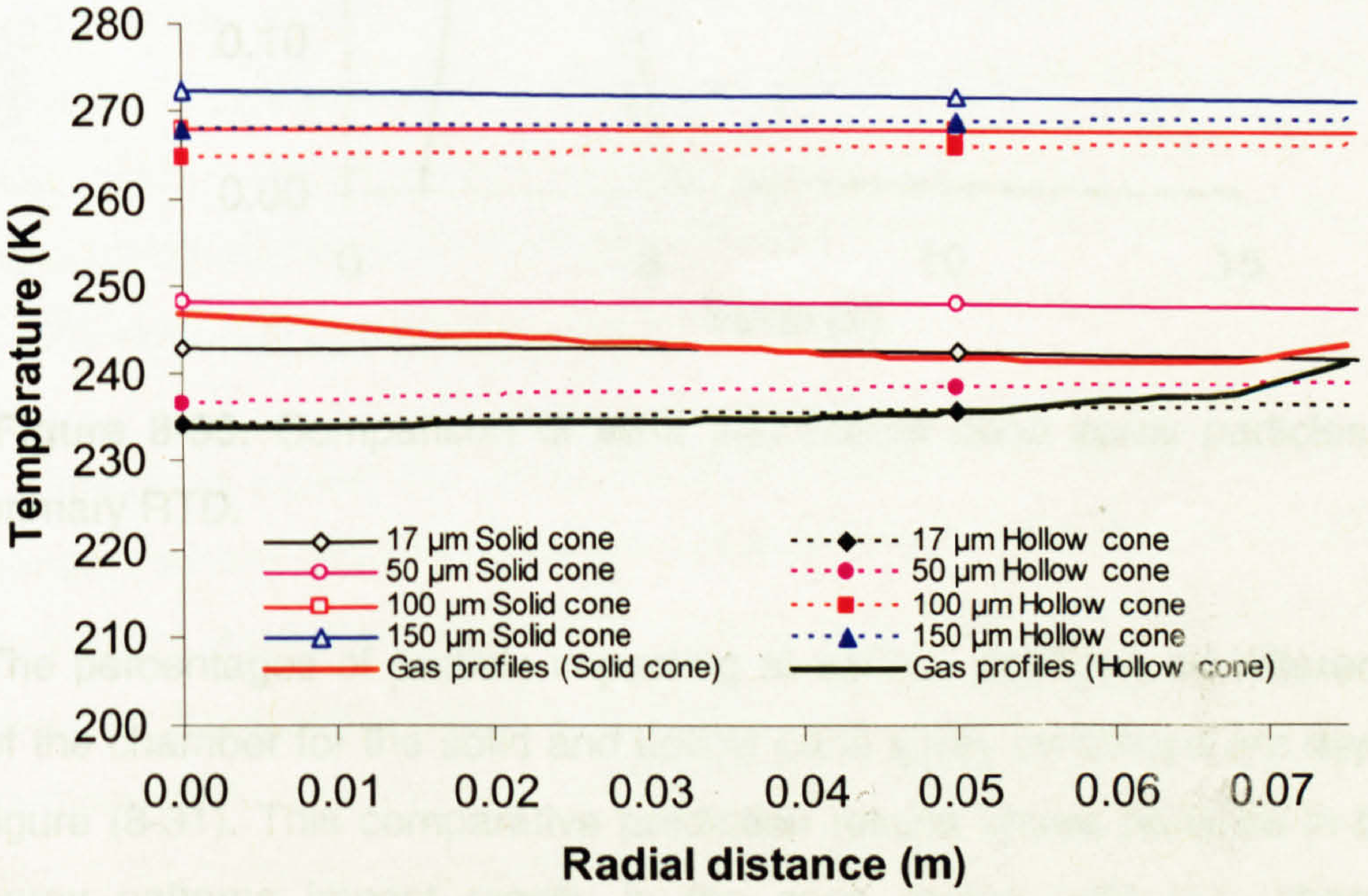

Figure 8-29: CFD simulated particles temperatures at the chamber outlet.

The outlet particle temperature prediction results (figure 8-29) shows that smaller diameter particles have lower temperatures than larger particles for both solid and hollow cone spray, which are also close to the gas temperature. When comparing the two sprays, there was little difference in the temperatures of larger particles (< 2 K), but for the smaller particles the hollow cone spray showed significantly lower temperatures (~ 10 K) than for the solid cone. This is an effect of residence time, due to lower particle velocities (figure 8-28). The particle low velocities resulted in slightly low overall RTD of hollow cone spray (figure 8-30) and this decreases the particle temperatures.

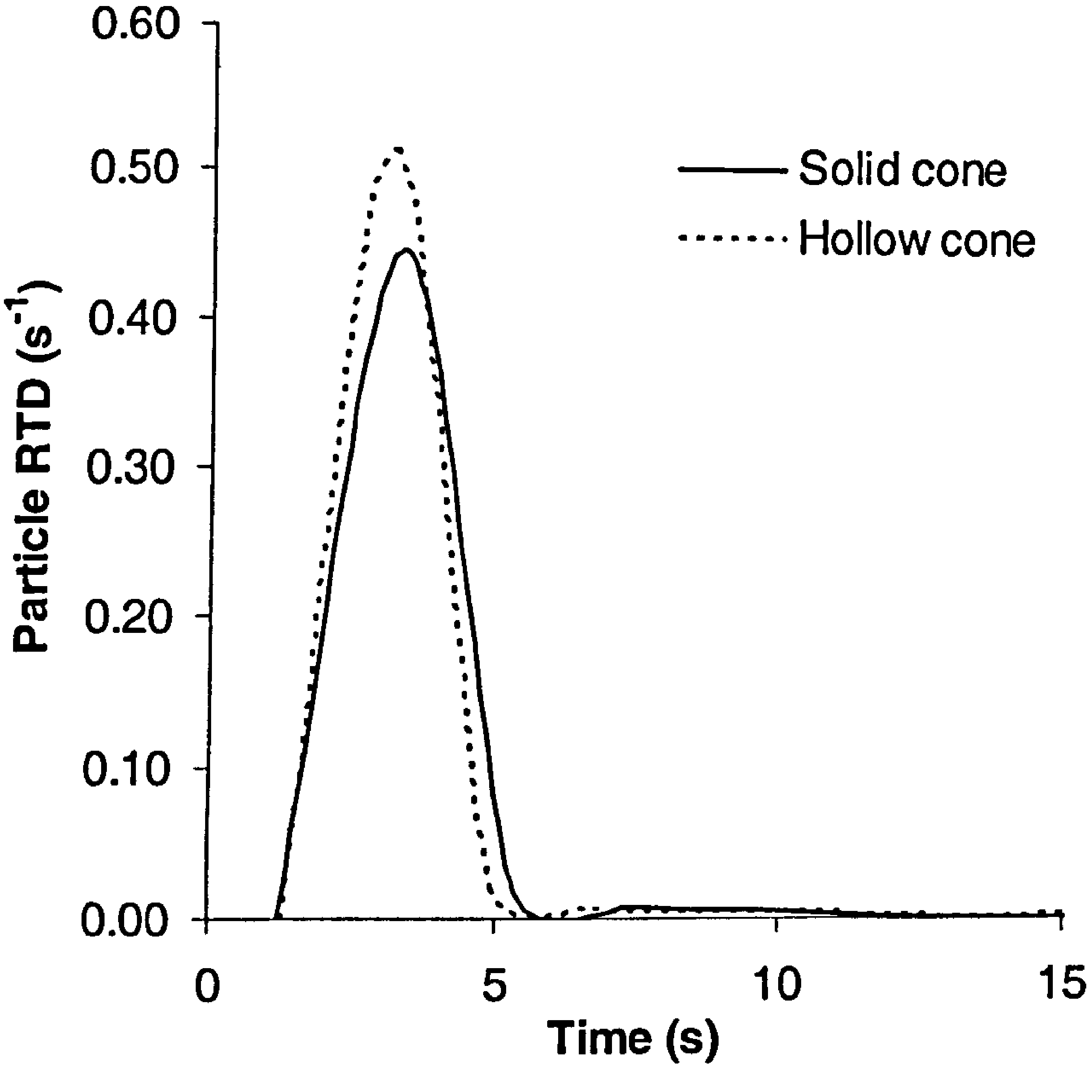

Figure 8-30: Comparison of solid and hollow cone spray particles overall primary RTD.

The percentages of particle impacting at various positions on different areas of the chamber for the solid and hollow cone spray conditions are depicted in figure (8-31). This comparative prediction results shows particles in both the spray patterns impact mostly in the cone region (>60 %), whereas the cylindrical wall region shows only 10% of impacts. However, the chamber outlet exit particles are almost 10% higher in the solid cone spray condition. Hence solid cone spray improves the outlet particles collection efficiency.

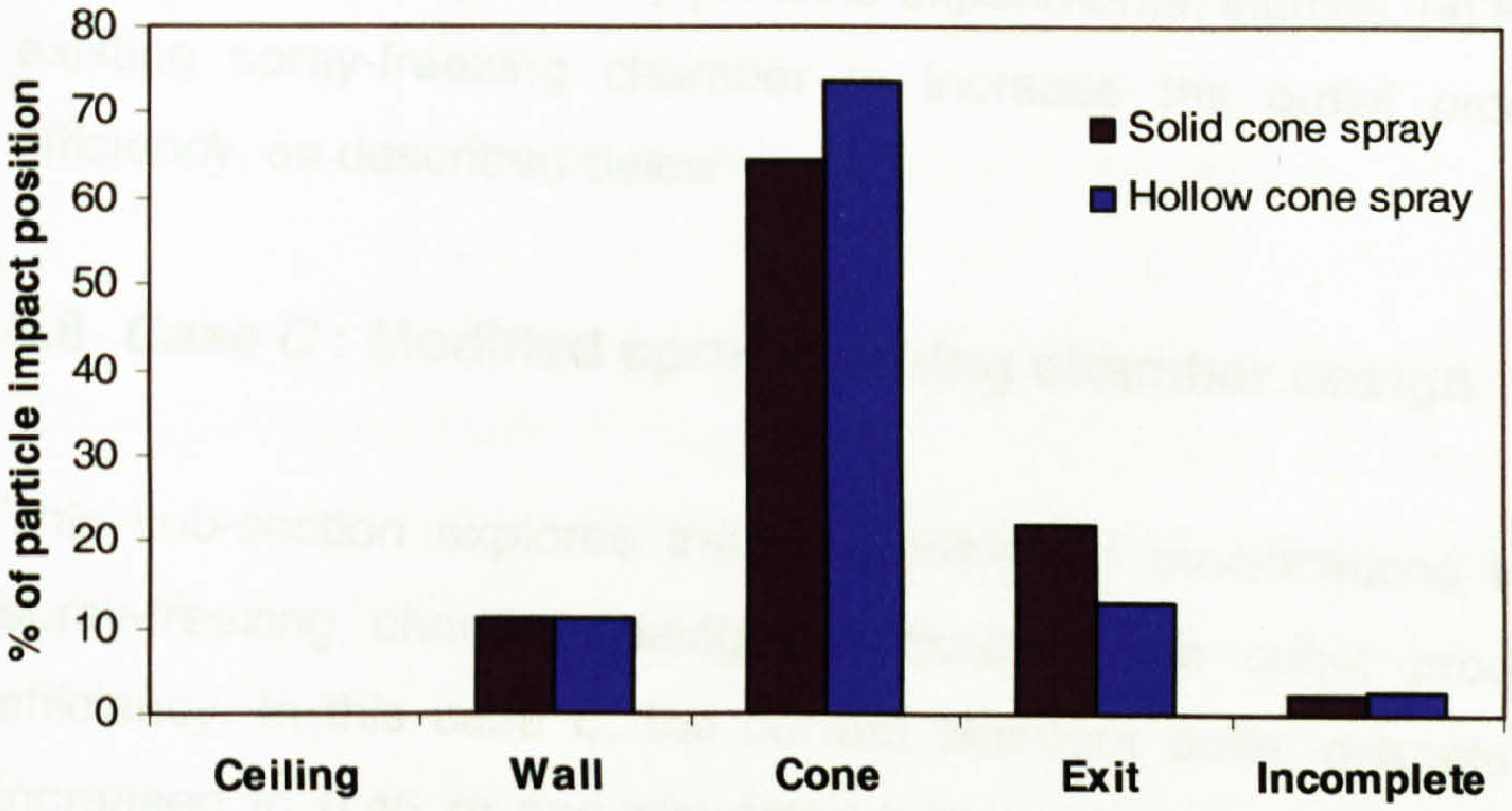

Figure 8-31: Comparison of solid and hollow cone spray particle impact position on walls.

This comparison study indicates that the hollow cone spray produces lower *particle velocities due* its spray pattern, hence it yields low particle temperatures, which is important for spray-freeze-drying *operations. The case A* (solid cone) yields particle temperature higher than 0°C and it strongly affects the freeze-drying process, where the high temperature particles start to agglomerate during the sublimation stage, resulting in larger diameter, irregularly shaped particles. In turn, this spoils the aim of spray-freeze-drying process (detail discussions in chapter 6). However, the hollow cone spray pattern yields slightly lower particle collection efficiency. In fact, both the spray patterns yield very low particle collection efficiency (less than 20%).

As mentioned earlier the spray-freezing operation is not like spray drying operation, where dried particles are collected from wall and cone by sliding on their own or under the influence of outside hammer operations. Moreover, the spray-freezing-drying operation is mainly used for high-value added food and pharmaceutical products, hence the final product collection is important to make SFD process successful as a commercial success. The following two solutions can be used to avoid higher temperature particles and low outlet particle collections: (i) Decrease the gas inlet temperature yields a lower particle temperature; the same method has been used for this work in the spray freeze drying of whey proteins experimental studies. (ii) Redesign of the existing spray-freezing chamber to increase the outlet product collection efficiency, as described below.

8.8 *Case C* : Modified spray-freezing chamber design

This sub-section explores the possibilities of modifications to the existing spray-freezing chamber design to increase the outlet product collection efficiency. In this *case C*, the current chamber outlet diameter 0.15 m was increased to 0.45 m and simulated with *case A* boundary conditions (solid cone spray). The proposed modified geometry is shown in figure (8-32).

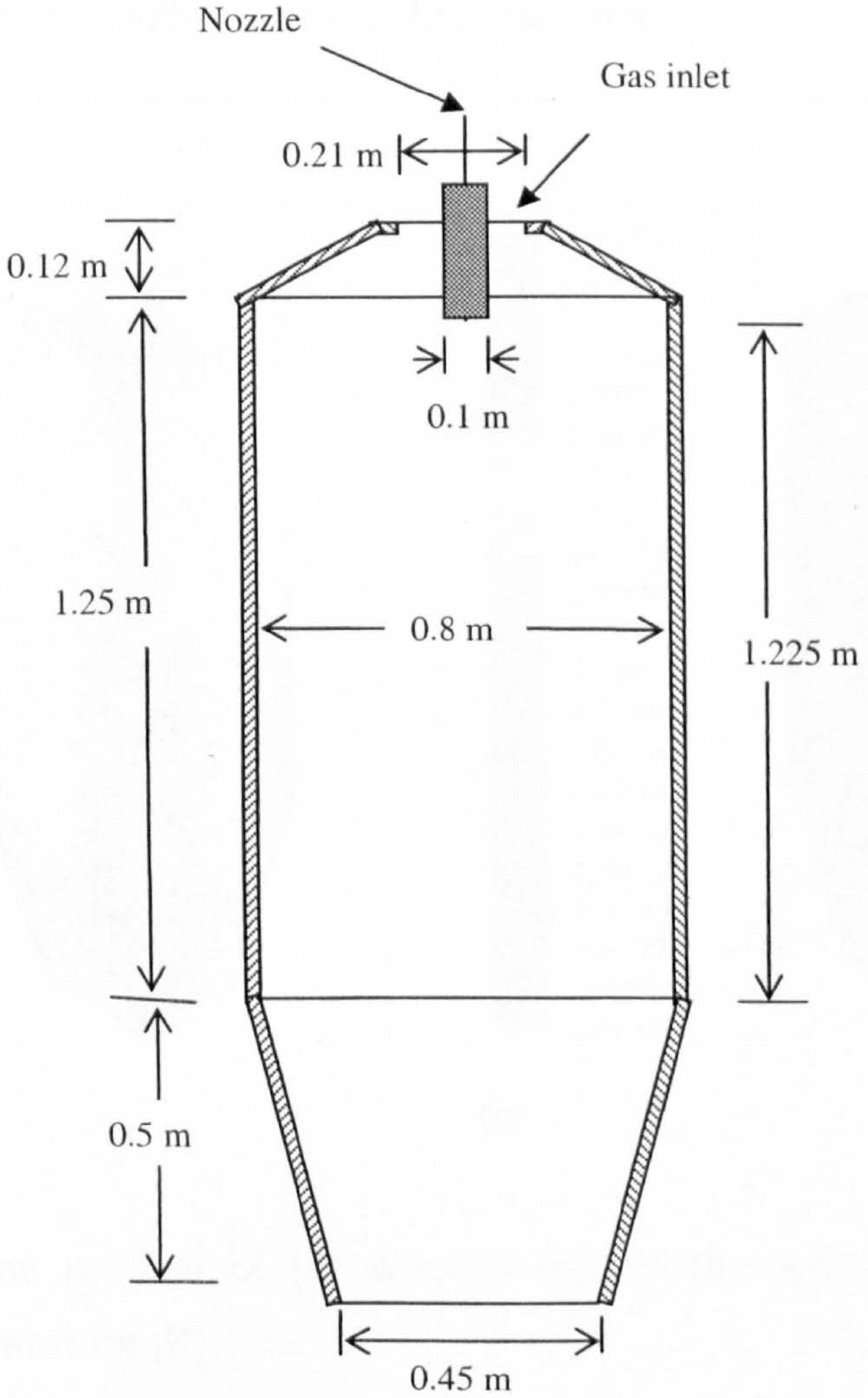

Figure 8-32: Modified spray-freezing chamber design.

The main objective of this CFD simulation is to study the effects of a change in the outlet chamber diameter on the product collection efficiency and particle temperatures.

8.8.1 Distributions of axial velocity and temperature

The gas axial velocity and temperature profiles are shown in figures (8-33). This simulation results shows almost similar trends to *case A*. The figure shows minimum gas re-circulation near the wall in the cone region of the chamber (figure 8-33 a). However, temperature profiles shows (figure 8-33 b) a slight difference near the outlet, where the gas temperature shown is slightly higher (260 K) for than the solid cone spray with the existing chamber design (*case A*). This effect is due to the narrow outlet cone (e.g. *case A*), which produces more gas recirculation (see figure 8-11), which in turn reduces the gas temperature at the outlet region of the chamber.

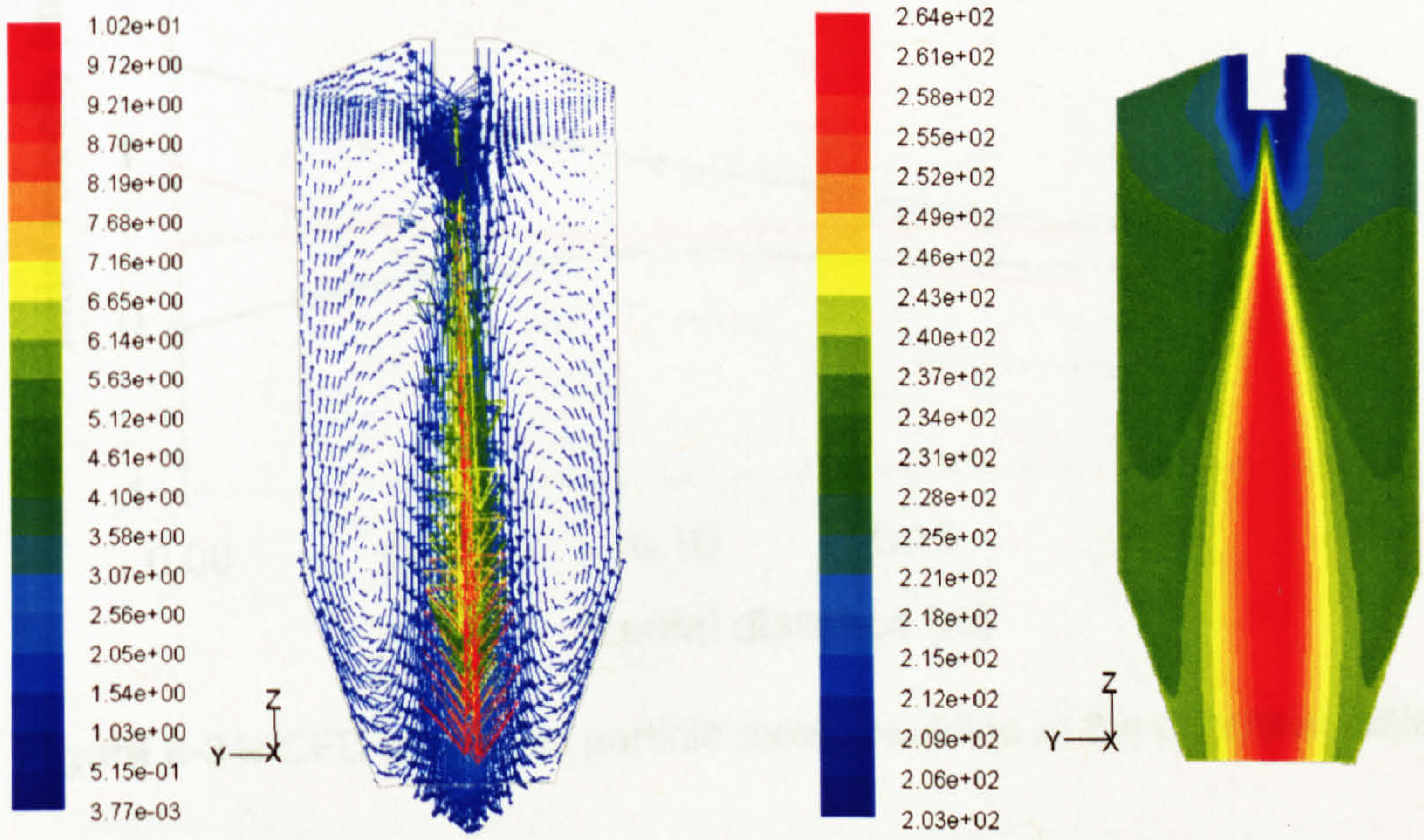

(a) (b)

Figure 8-33: Gas profiles of (a) velocity magnitude vector (m/s) and (b) contours of temperature (K).

8.8.2 Particle histories

The modification to the chamber has been made at outlet of the chamber, and hence the results at outlet (z = 1.73 m) are of most interest here. The radial profile for particle axial velocities and temperature profiles are presented in figures (8-34) and (8-35) respectively. The *case C* particle axial velocity at the outlet was lower than the *case A*, because an increase in the outlet diameter reduces the exit gas velocity. However, a mixed trend was shown in the temperature profiles, where larger particles behave in a similar way to *case A* results, but smaller particles show nearly 5K higher temperatures (figure 8-36) due to reduced degree of gas re-circulation. *Case C*, reduces the RT of small particles and results in higher particle temperatures.

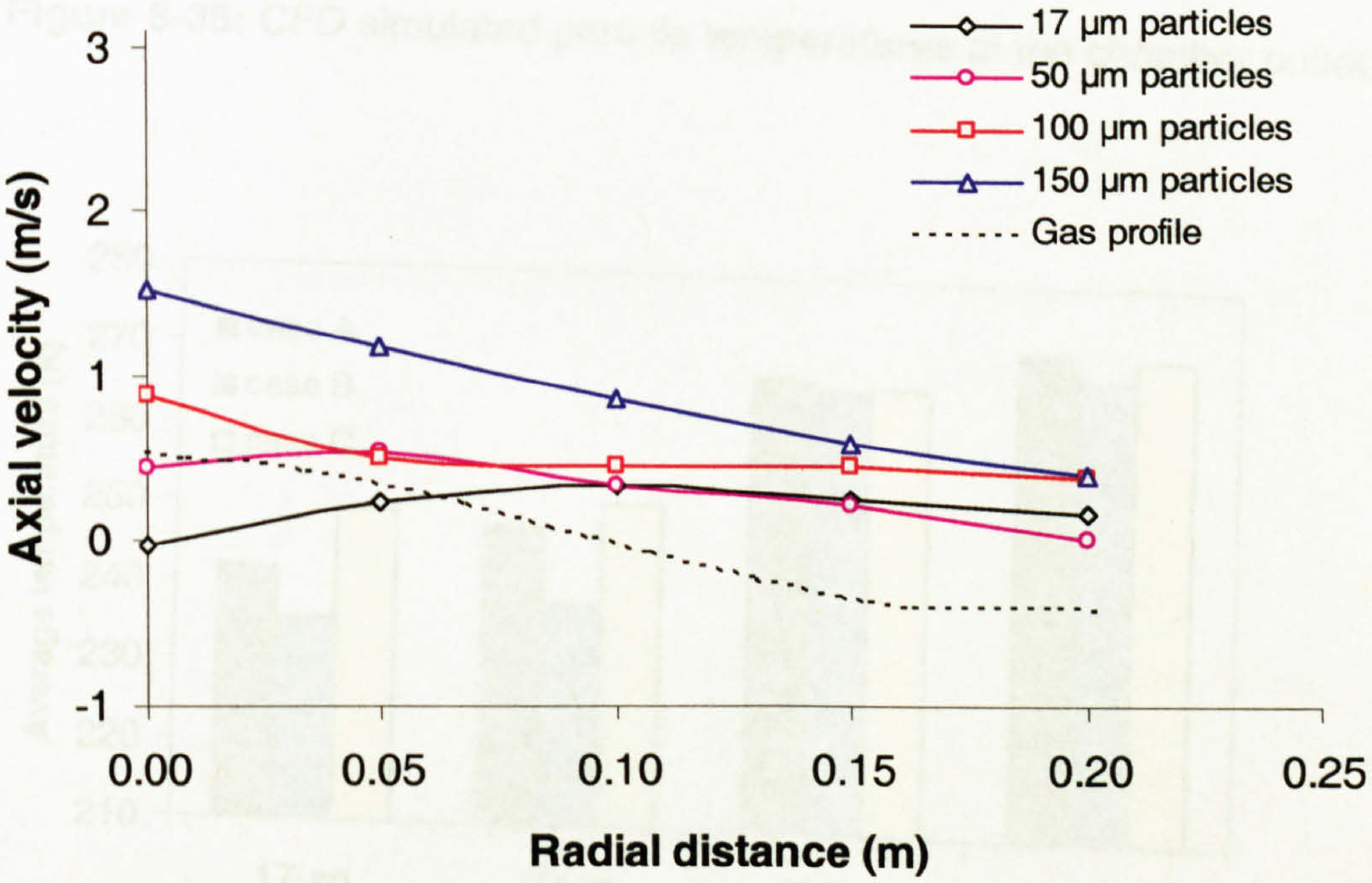

Figure 8-34: CFD simulated particle axial velocities at the chamber outlet.

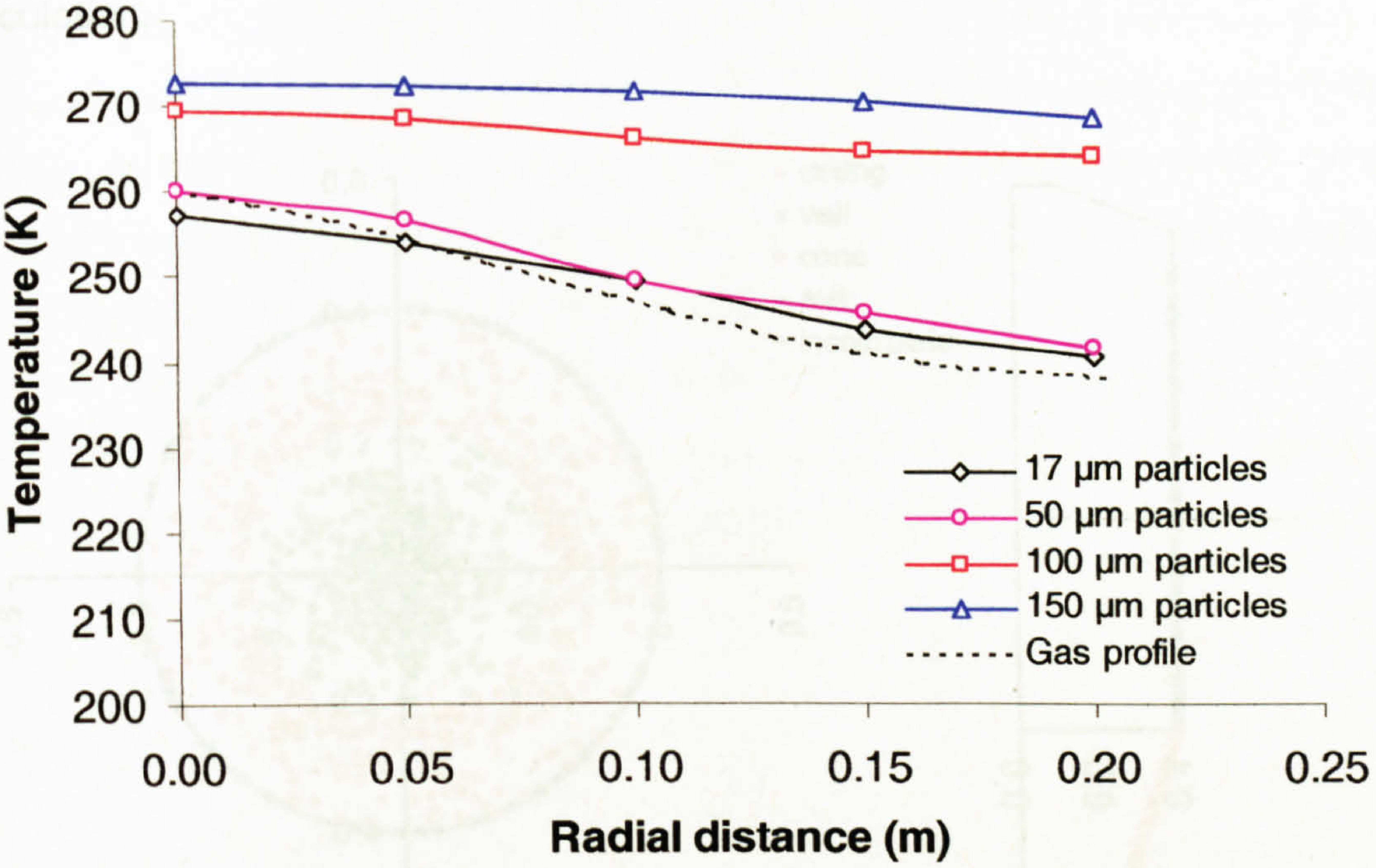

Figure 8-35: CFD simulated particle temperatures at the chamber outlet.

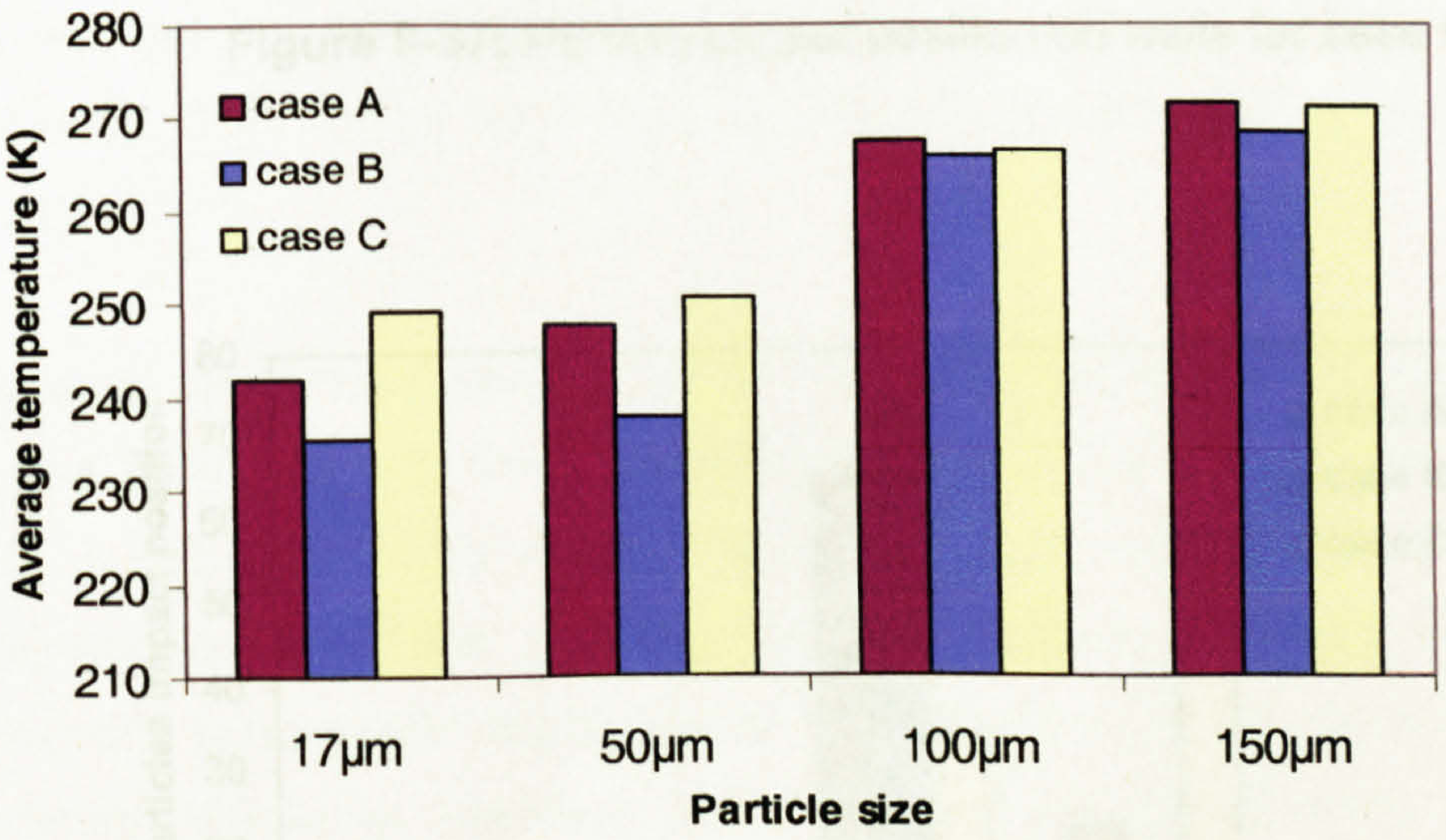

Figure 8-36: Average particle temperature at outlet (z = 1.73 m).

Figures (8-37) depicts the particles impact positions on walls for *case C.* These figures reveals that 57% of the particles exit the chamber and only 33% of particles strike the conical part of the chamber. The remaining 10% of particles impact on the cylindrical part of the wall. There were no incomplete particles in this system since the wider outlet area reduces the gas re-circulation.

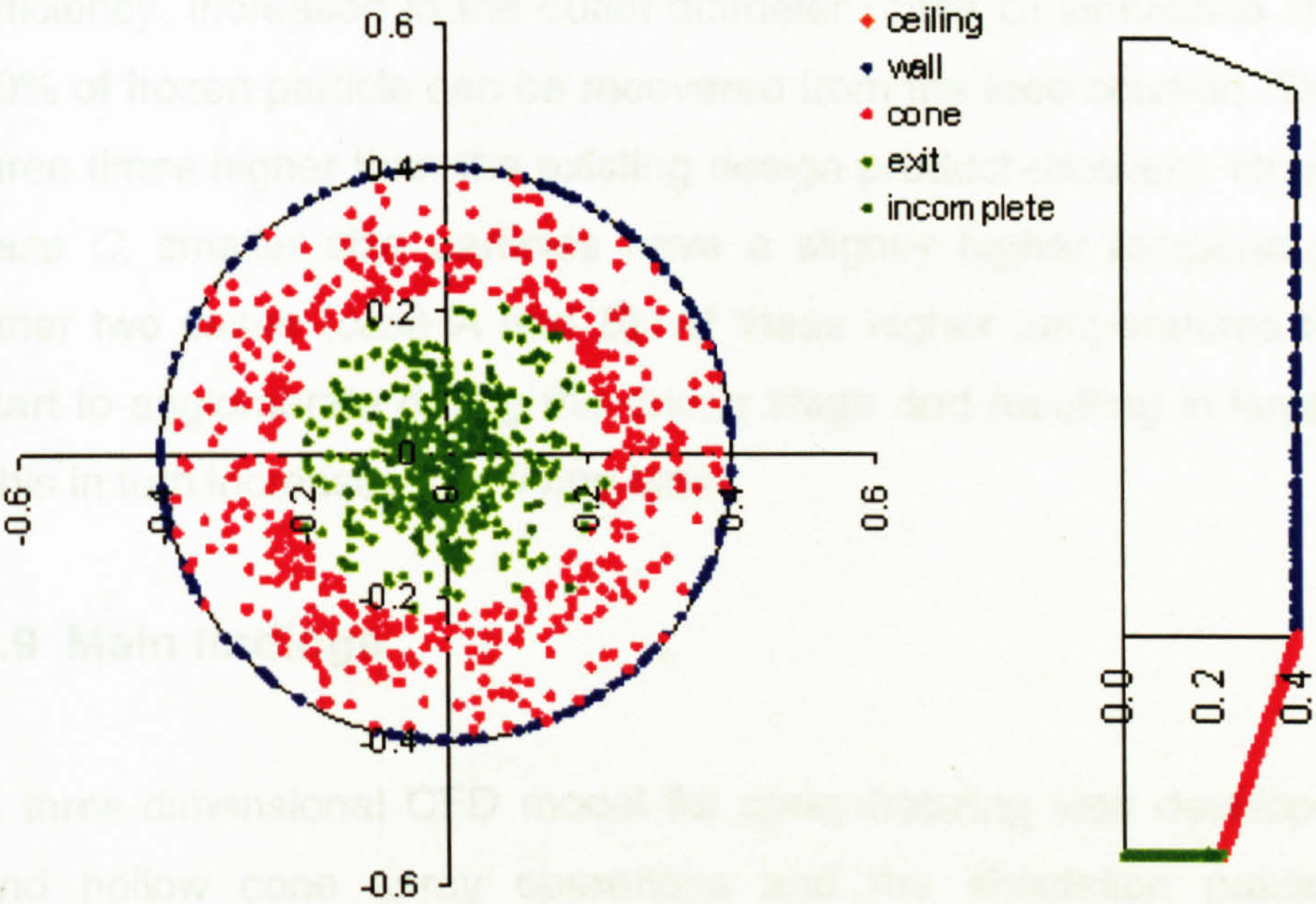

(a) Top view (b) Front view

Figure 8-37: Particle impact position on walls for *case C*.

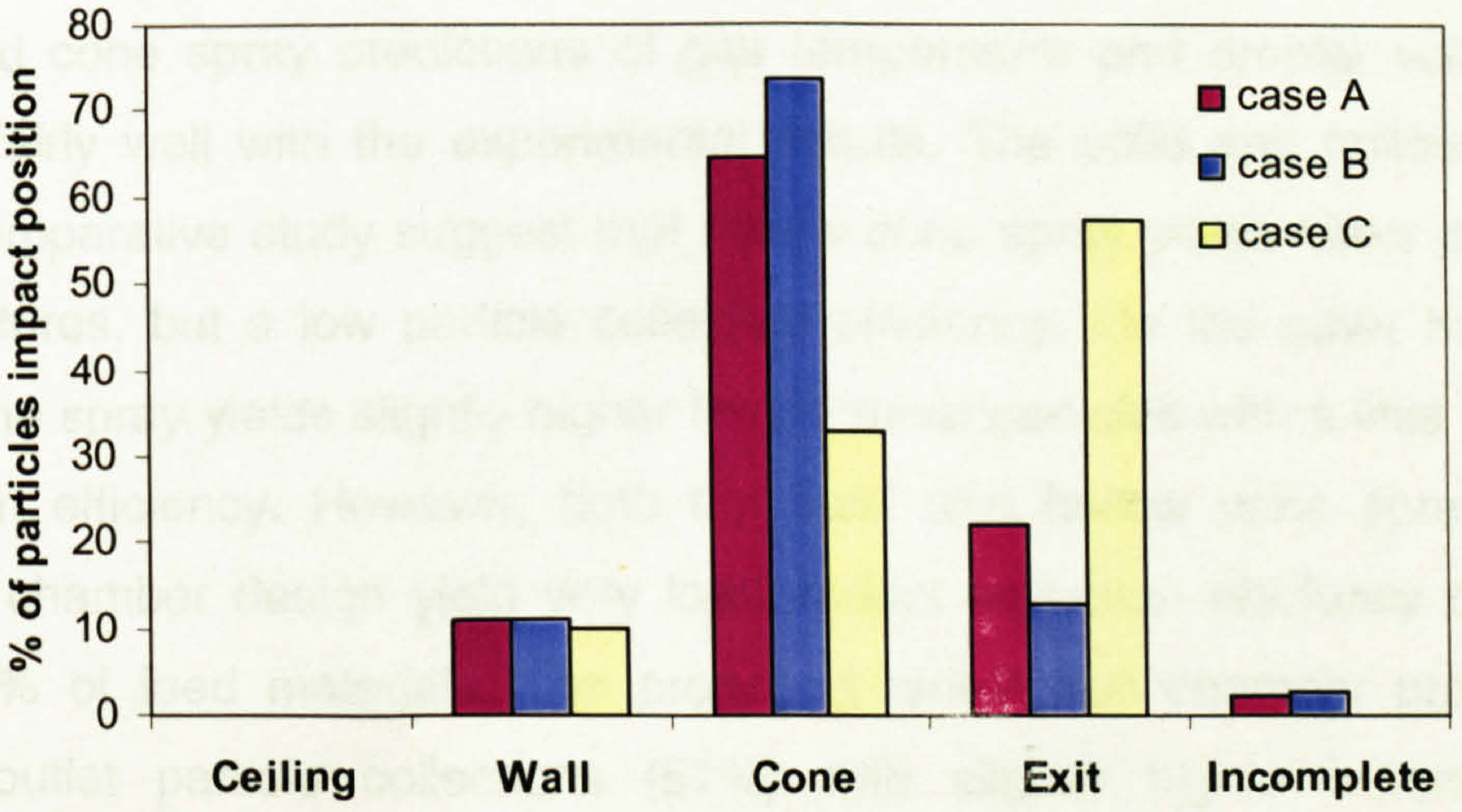

Figure 8-38: Comparison of all three cases of particle impact position on wall.

The percentages of particles impact positions on the wall in all three cases are plotted in figure (8-38), which clearly indicates that a change to the existing spray-freezing design produces higher outlet particle collection efficiency. Increased in the outlet diameter (*case C*) simulation shows nearly 60% of frozen particle can be recovered from the feed solution. This is almost three times higher than the existing design product recovery. However, in the *case C*, smaller size particles have a slightly higher temperature than the other two cases (*case A* and *B*). At these higher temperatures the particles start to agglomerate during the drying stage and resulting in larger diameter. This in turn increases the drying time.

8.9 Main findings

A three-dimensional CFD model for spray-freezing was developed for solid and hollow cone spray operations and the simulation predictions were compared with the experimental results. The results obtained from the CFD model were presented in terms of gas and particles axial velocity, temperature profiles, particle residence time distributions and outlet particles collection efficiency. This model also included the latent heat effects during phase change.

The solid cone spray predictions of gas temperature and droplet velocities agreed fairly well with the experimental results. The solid and hollow cone spray comparative study suggest that hollow cone spray yields lower particle temperatures, but a low particle collection efficiency. On the other hand, a solid cone spray yields slightly higher temperature particles with a little higher collection efficiency. However, both the solid and hollow cone spray with existing chamber design yield very low product collection efficiency of less than 20% of feed materials. The proposed redesigned chamber produces higher outlet particle collections (57%) with slightly higher temperature products. This study also suggests that increasing the outlet area may affect the particle temperature due to reduced re-circulation of gas in the cone region.

The solid cone spray would be a better option for the current spray-freezing rig in terms of product collection efficiency, but the modified chamber with a hollow cone spray may yield higher product recoveries with low particle temperatures. However, this experimental and simulation study confirm that the existing design of the spray-freezing chamber needs to be modified to have a larger outlet area to yield a higher product collection efficiency.

Chapter 9

Conclusions and future work

9.1 Conclusions

An experimental study of spray-drying and spray-freeze-drying of whey proteins has been carried out. Additionally, computational fluid dynamics (CFD) simulation studies of spray drying and spray-freezing have been performed. The findings are summarised in the following sub-sections.

9.1.1 Spray drying

The effects of varying feed concentration (20-40% w/v) and outlet temperature (60°C to 120°C) on whey protein denaturation (determined by DSC) and solubility (by Kjeldhal and RP-HPLC methods) in a pilot-scale co-current spray dryer have been studied. It was found that low outlet gas temperatures (60-80°C) were required to avoid excessive denaturation of proteins, as determined by DSC. Slightly more denaturation and loss of solubility was found with a 40% feed concentration. It was observed that α-lactalbumin is more stable than β-lactoglobulin. At higher outlet gas temperatures (120°C) and higher feed concentrations (40% w/v), there was a sharp increase in the loss of solubility of α-lactalbumin and β-lactoglobulin. There is evidence for greater crust formation at 40% feed concentration, as drier product was obtained in the experiments with 30% feed concentration. This could occur if the crust that forms dries to such an extent that water diffusion is hampered by a severe reduction in diffusivity. In the case of the 40% feed concentration, the formation of a crust may restrict bubble inflation, resulting in smaller particle sizes. Thus, to summarise, the effect of increasing the feed concentration could be to promote crust formation, which would raise particle temperatures above wet bulb conditions and lead to greater levels of denaturation and insolubility in the moist core region.

The DSC denaturation results were supported by protein solubility tests, which showed qualitatively similar results. The comparative study of RP-HPLC and Kjeldhal nitrogen content analysis suggests that the protein solubility can also be estimated from the RP-HPLC technique. Moreover, the RP-HPLC solubility analysis method is straightforward and requires less analytical time than the nitrogen content analysis method. It can also resolve individual proteins. It is the first method of its kind to be developed for whey protein powder solubility analysis.

The CFD models for short-form and tall-form spray dryers have been developed and the predictions have been validated against published experimental results and other simulations. The comparison study shows good agreement between the model and published Kieviet's (1997) experimental and some of Huang *et al's* (2006) simulation results. This study predicted that the particle residence time (RTD) was rather different from the gas RTD, because this RTD was calculated from the primary residence time and also particles travel with a high velocity for a short period after leaving the atomiser. The tall-form spray dryer model CFD predictions showed that more than 60% of the particles impacted on the cylindrical wall and this may affects the protein denaturation and solubility; particles may be stuck to the wall for appreciable times, drying out and losing their wet-bulb protection. The primary residence time CFD study also revealed that particle residence times in the tall-form dryer were longer (due to larger distances between the nozzle and outlet and also greater gas recirculation), which could lead to greater denaturation of proteins. This study also indicates that the short form dryer with a bottom outlet is suitable for drying of heat sensitive products, such as proteins, due to the low amounts of recirculated of gas and hence the shorter residence time of particles. This confirms with the wide spread use of short form spray dryers in the food industry.

9.1.2 Spray-freeze-drying

A pilot scale spray-freeze-drying (SFD) process, operating at a sub-atmospheric pressure of 0.1 bara, has been developed and investigated. This SFD process gave excellent fluidisation behaviour and freeze drying times of less than 2 h, which are far quicker than in conventional freeze drying, requiring 24 h or more. The material used in this study was whey protein; the dried product had a highly porous structure, with very little loss of protein solubility. Therefore, it has been demonstrated that spray-freezing, combined with the VFBFD technique, has the potential to produce high-value-added food and pharmaceutical products more quickly than is currently possible by commercial vacuum freeze-drying processes.

A three-dimensional CFD simulation for spray-freezing was developed and was applied in an attempt to overcome the problems during the operation such as, higher particles temperature and low particles collection efficiency. This model included the latent heat effects during phase change by increasing the effective specific heat capacity of the particles over the temperature range -10 to 0°C. The simulation predictions reasonably agreed with experimentally measured gas and droplet velocity results by Al-Hakim (2004).

The CFD model was used to investigate two different spray patterns namely, solid and hollow cone spray. This comparative study suggested that the hollow cone spray case produced low particle temperatures in the chamber, but yielded a low particle collection efficiency. The higher particle temperature strongly affects the freeze-drying process, where the high temperature particles start to agglomerate during the drying stage, resulting in larger diameter, irregularly shaped particles. In turn, this spoils the aim of spray-freeze-drying process. However, both the solid and hollow cone spray with existing chamber design yielded very low product collection efficiencies of less than 20% of feed materials. The proposed modified chamber, with a larger product outlet at the base, produced higher outlet particle collections of 57%. The solid cone spray appears to be a slightly better option for the current spray-freezing rig, in terms of product collection efficiency, but the modified chamber with hollow cone spray should yield higher product recoveries with low particle temperatures.

9.1.3 Main contributions

The main contributions from the thesis are summarised below:

- A pilot-scale spray-freezing combined with VFBFD process has been further developed for drying of whey protein solution at -30°C and 0.1 bara.

- The effects of varying feed concentration and higher outlet temperature on product quality during spray-drying have been investigated. The study recommends that low outlet gas temperature (60-80°C) and low feed concentrations (20-30% w/v) are required to avoid excessive denaturation and insolubility of whey proteins.

- A novel RP-HPLC method has been developed for proteins powder solubility analysis.

- 3D CFD simulations for tall and short form spray dryer have performed and examined the particle histories. This simulation predictions agreed with the published experimental results better than the Huang *et al* (2006) 3D simulation.

- CFD simulations were developed for spray-freezing operations with the solid and hollow cone spray patterns. A hollow cone spray is recommended and a modified spray-freezing chamber design was proposed based on CFD simulations to improve the frozen particles collection efficiency.

9.2 Scope for future work

The following interesting and challenging research areas could be further investigated.

1. CFD models were developed for various spray-drying and spray-freezing operations in this thesis work, using the DPM model to include particle-fluid and fluid-particle interactions (two-way coupling). However, particle-particle collisions, droplet breakage and agglomeration effects could not be considered within the particle tracking framework. To do this would required, a population balance model to be included, and applied as a user-defined function in the CFD code. Such a model could provide better predictions of the particles histories, which could include agglomeration during spray drying, or droplet breakage and coalescence during spray-freezing. Moreover, including the falling rate period in the existing model would produce better predictions especially for particle temperatures and gas humidity profiles.

2. A range of methods of insulin administration other than injection have been sought since the discovery of insulin in 1920. During recent years, more attention has been given to the delivery of insulin via the pulmonary route. Available clinical trial data indicates that pulmonary insulin delivery appears to be safe, efficacious and well accepted by patients. The spray-freeze-dried process can produce porous particles, with a low bulk density, this in turn reduces aerodynamic diameter (d_{ae}) of particles (d_{ae} is equal to the physical diameter multiplied by square root of the particle density). Hence, decrease in d_{ae} increases the aerosol deposition both gravitational settling and inertial impaction.. Furthermore, CFD simulation studies could provide a cost effective way to evaluate the flow patterns and deposition efficiency of spray-freeze-dried particles in the upper human airways during breathing cycles. Considering these facts, it is timely to develop such an alternative

process for production of formulated insulin inhaler powders using the SF + VFBFD process.

3. Models are available to predict the drying rates in atmospheric fluidised beds. But, there is a scope for developing a model with falling rate period to predict the drying rate during vacuum fluidised bed freeze drying (VFBFD). This work will enable to understand the effects of the process parameters such as particle size, gas velocity, and inlet gas temperature on freeze drying rate.

References

Al-Hakim, K. (2004) "*An Investigation of spray-freezing and spray-freeze-drying*", PhD thesis, Loughborough University.

Al-Hakim, K. and Stapley, A. G. F. (2004) "*Morphology of spray-dried and spray-freeze-dried whey powders*", *Drying 2004*, Vol C, 1720-1726.

Al-Hakim, K., Wigley, G and Stapley, A. G. F. (2006) "*Phase doppler anemometry studies of spray freezing*", Trans IChemE, Part A, Chemical Engineering Research and Design, **84**(A12), 1142-1151.

Anandharamakrishnan, C. (2003) "*Computational fluid dynamics (CFD) – applications for the food industry*", Indian Food Industry, **22**(6), 62-68.

Anandharamakrishnan, C., Khwanpruk, K., Rielly, C. D. and Stapley, A. G. F. (2006) "*Spray freeze drying at sub-atmospheric pressures*", Drying 2006 - Proceedings of the 15th International Drying Symposium, Budapest, Hungary, *Ed.* by I .Farkas and A.S. Majumdar, 636.

Anandharamakrishnan, C., Rielly, C. D. and Stapley, A. G. F. (2007) "*Effects of process variables on the denaturation of whey proteins during spray-drying*", Drying Technology, **25**, 799-807.

Anandharamakrishnan, C., Rielly, C. D. and Stapley, A. G. F. (2008) "*Loss of solubility of α-lactalbumin and β-lactoglobulin during spray drying of whey proteins*", LWT-Food Science and Technology, **41**, 270-277.

Anderson, J. D. (1984). "*Computational fluid dynamics- The basics with applications*", McGraw-Hill Inc, New York.

Anema, S. G. (2000). "*Effects of milk concentration on the irreversible thermal denaturation and disulfide aggregation of β-lactoglobulin*", Journal of Agricultural and Food Chemistry, **48**, 4168-4175.

Anema, S. G. (2001) "*Kinetics of the irreversible thermal denaturation and disulfide aggregation of α-lactalbumin in milk samples of various concentrations*", Journal of Food Science, **66**(1), 2-9.

Anema, S. G., Stockmann, R. and Lowe, E. K. (2005) "*Denaturation of β-lactoglobulin in pressure-treated skim milk*", Journal of Agricultural and Food Chemistry, **53**, 7783-7791.

ASAE Standards. (1998) "*Psychrometric Data*", ASAE D271.2 DEC94.

Bachalo, W. D. and Houser, M. J. (1984) "*Phase Doppler spray analyzer for simultaneous measurement of drop size and velocity distributions*", Optical Engineering, **23**(5), 583–590.

Bakker, A. (2002) "*Computational fluid mixing*", Fluent Inc. Lebanon, New Hampshire, USA

Bhandari, B. R., Datta, N. and Howes, T. (1997) "*Problems associated with spray drying of sugar-rich foods*", Drying Technology, **15**(2), 671-684.

Bhandari, B. R. and Howes, T. (1999) "*Implication of glass transition for the drying and stability of dried foods*", Journal of Food Engineering, **40**, 71-79.

Bird, B., Stewart, W. E. and Lightfoot, E. N. (1960) "*Transport phenomena*", John Wiley & Sons, New York.

Blanshard, J. M. V. and Lillford, P. J. (1993), "*The glassy state in foods*", Nottingham University Press, Loughborough.

Boeh-Ocansey, (1988) "*Freeze- drying in a fluidized-bed atmospheric dryer and in a vacuum dryer: evaluation of external transfer coefficients*", Journal Food Engineering, **7**, 127-146.

Boeh-Ocansey, O. and Wachet, J. N. (1983-84) "*A study of the freeze drying of some liquid foods in vacuum and atmospheric pressure*", Drying Technology, **2**(3), 389-405.

Boeh-Ocansey, O. and Wachet, J. N. (1986) "*A study of ice sublimation in an atmospheric dryer*", Drying Technology, **4**(3), 439-459.

Bornhardt, C. (1994) "*Particle size analysis classification and sedimentation methods*", Chapman & Hall.

Boye, J. I. and Alli, I. (2000) "*Thermal denaturation of mixtures of α-lactalbumin and β- lactoglobulin: a differential scanning calorimetric study*", Food Research International, **383**, 673-682.

Boye, J. I., Alli, I. and Ismail, A. A. (1997) "*Use of differential scanning calorimetry and infrared spectroscopy in the study of thermal and structural stability of α-lactalbumin*", Journal of Agricultural and Food Chemistry, **45**, 1116-1125.

Branden, C. and Tooze, J. (1999) "*Introduction to protein structure*", Second edition, Garland Publishing, New York.
Charm, S. E. (1971) "*The fundamentals of food engineering*", The AVI Publishing Company, Westport, Connecticut.

Cohen, J. S. and Yang, T. S. (1995) "*Progress in food dehydration*", Trends in Food Science and Technology, **6**, 20-24.

Costantino, H. R., Firouzabadian, L., Hogeland, K., Wu, C., Beganski, C., Carrasquillo, K. G., Cordova, M., Griebenow, K., Zale, S. E. and Tracy, M. A.

(2000) "*Protein spray-freeze drying. Effect of atomization condition on particle size and stability*", Pharmaceutical Research, **17**(11),1374-1380.

Costantino, H. R., Firouzabadian, L., Wu, C., Carrasquillo, K. G., Griebenow, K., Zale, S. E. and Tracy, M. A. (2002) "*Protein spray-freeze drying.2. Effect of formulation variables on particle size and stability*", Journal of Pharmaceutical Science, **91**(2), 388-95.

Coulson, J. M. and Richardson, J. P. (1983) "*Introduction to chemical engineering design*", Volume 6, Pergamon Press.

Creighton, T. E. (1992) "*Protein folding*", W. H. Freeman and Company, New York.

Crowe, C. T. (2006) "*Multiphase flow handbook*", Taylor & Francis, London.

Crowe, C. T., Sharam, M. P. and Stock, D. E. (1977) "*The particle source in cell (PSI-Cell) model for gas-droplet flows*", Journal of fluid Engineering, **9**, 325-332.

Daemen, A. L. H. and van der Stege, H.J. (1982) "*The destruction of enzymes and bacteria during the spray drying of milk and whey.2. The effect of the drying conditions*", Netherlands Milk Dairy Journal, **36**, 211-229.

Dannenberg, F. and Kessler, H. (1988) "*Reaction kinetics of the denaturation of whey proteins in milk*", Journal of Food Science, **53**(1), 258- 263.

Diaza, O., Pereira, C. D. and Cobos, A. (2004) "*Functional properties of ovine whey protein concentrates produced by membrane technology after clarification of cheese manufacture by-products*", Food Hydrocolloids, **18**, 601-610.

Elgar, D. F., Norris, C. S., Ayers, J. S., Pritchard, M., Otter, D. E. and Palmano, K. P. (2000) "*Simultaneous separation and quantisation of the* *major bovine whey protein including proteose peptone and caseinomacroptide by reversed phase high-performance liquid chorography on polystyrene-divinylbenzene*", Journal of Chromatography A, **878**, 183-196.

Etzel, M. R., Suen, S,Y., Halverson, S. L. and Budijono, S. (1996) "*Enzyme inactivation in a droplet forming a bubble during drying*", Journal of Food Engineering, **27**, 17-34.

Fachin, L and Viotto, W. H. (2005) "*Effect of pH and heat treatment of cheese whey on solubility and emulsifying properties of whey protein concentrate produced by ultrafiltration*", International Dairy Journal, **15**, 325-332.

Farid, M. (2003) "*A new approach to modelling of single droplet drying*", Chemical Engineering Science, **58**, 2985-2993.

Fellows, P. J. (1998), "*Food processing technology-Principles and practice*", Woodhead Publishing Limited, Cambridge.

Ferreira, I. M. P. L. V. O., Mendes, E. and Ferreira, M. A. (2001) "*HPLC/UV Analysis of protein in dairy products using a hydrophobic interaction chromatographic column*", Analytical Science, **17**, 499-501.

Ferreira, I. M. P. L. V. O. and Cacote, H. (2003) "*Detection and quantification of bovine, ovine and caprine milk percentage in protected denomination of origin cheese by reversed-phase high-performance liquid chromatography of beta-lactoglobulins*", Journal of Chromatography A, **1015**, 111-118.

Fletcher, A. J. (2000) "*Computational Techniques for fluid dynamics*", 2nd Edition, Springer-Verlag , New York.

Fletcher, D., Guo, B., Harvie, D., Langrish, T., Nijdam, J. and Williams, J. (2003) "*What is important in the simulation of spray dryer performance and how do current CFD models perform*", 3rd International Conference on CFD in the Minerals and Process Industries, CSIRO, Melbourne, Australia, 10-12 December 2004.

Fluent manual. (2005) (www.fluent.com)

Ford, J. L. and Timmins, P. (1989) "*Pharmaceutical thermal analysis-Techniques and applications*", Ellis Horwood Limited, UK.

Foster, K. D., Bronlund, J. E. and Paterson, A. H. J. (2005) "*The prediction of moisture sorption isotherms for dairy powders*", International Dairy Journal, **15**, 411-418.

Franks, F. (1998) "*Freeze-drying of bioproducts: putting principles into practice*", European Journal of Pharmaceutics and Biopharmaceutics, **45**, 221-229.

Gauvin, W. H. and Katta, S. (1976) "*Basic concepts of spray dryer design*", AIChE, **22**(4), 713-724.

Geldart, D. (1973) "*Types of gas fluidization* ", Powder Technology, **7**, 285-292.

Geldart, D. (1986) "*Gas fluidization technology*"; Wiley, Chichester.

Goldblith, S. A. (1975) "*Freeze drying and advance food technology*", Academic press, London.

Guy,E. J., Vettel, H. E. and Pallansch, M. J. (1967) "*Denaturation of cottage cheese whey proteins by heat*", Journal of Dairy Science, **50**, 828-832.

Guyomarc'h, F., Warin, F., Muir, D. D. and Leaver, J. (2000) "*Lactosylation of milk proteins during the manufacture and storage of skim milk powders*", International Dairy Journal, **10**, 863-872.

Heldman, D. R. and Hohner, G. A. (1974) "*An analysis of atmospheric freeze drying*", Journal of Food Science, **39**, 147-155.

Hindmarsh, J. P., Russell, A. B. and Chen, X. D. (2003) *"Experimental and numerical analysis of the temperature transition of a suspended freezing water droplet"*, International Journal Heat and Mass Transfer, **46**, 1199-1213.

Hindmarsh, J. P., Russell, A. B. and Chen, X. D. (2007) *"Fundamentals of the spray freezing of foods-microstructure of frozen droplets"*, Journal of Food Engineering, **78**, 136-150.

Hoffmann, M. A. M. and van Mil, P. J. J. M. (1997) "*Heat-induced aggregation of β-lactoglobulin: Role of free thiol group and disulfide bonds*", Journal of Agricultural and Food Chemistry, **45**, 2942-2948.

Hohne, G. W. H., Hemminger, W. F. and Flammersheim, H. J. (2003) "*Differential scanning calorimetry*", Second Edition, Springer, New York.

Holland, F. A. and Bragg, R. (1995) "*Fluid flow for chemical engineers*", 2nd Edition, Butterworth Heinemann, Oxford.

Howard, J. R. (1989) "*Fluidized bed technology –Principles and applications*", Adam Hilger, New York.

Hu, J., Johnston, K. P. and Williams, R. O. (2003) "*Spray freezing into liquid (SFL) particle engineering technology to enhance dissolution of poorly water soluble drugs: organic solvent versus organic/aqueous co-solvent systems*", European Journal of Pharmaceutical Sciences, **20**(3), 295-303.

Huang, L. X., Kumar, K. and Mujumdar, A. S. (2003) "*A parametric studu of the gas flow patterns and drying performance of co-current spray dryer: Results of a computational fluid dynamics study*", Drying Technology, **21**(6), 957-978.

Huang, L. X., Kumar, K. and Mujumdar, A. S. (2004) "*Simulation of a spray dryer fitted with a rotary disk atomizer using a three-dimentional computational fluid dynamic model*", Drying Technology, **22**(6), 1489-1515.

Huang, L. X., Kumar, K. and Mujumdar, A. S. (2006) "*A comparative study of a spray dryer with rotary disc atomizer and pressure nozzle using computational fluid dynamic simulations*", Chemical Engineering and Processing, **45**, 461-470.

Ibanoglu, E. (2005) "*Effect of hydrocolloids on the thermal denaturation of proteins*", Food Chemistry, **90**, 621-626.

Incropera, F. P., Dewitt, D. P., Bergman, T, L. and Lavine, A, S. (2007) "*Fundamentals of heat and mass transfer*", John Wiley & Sons. New York.

Jakobsen, H. A., Sannaes, B. H., Grevskott, S. and Svendsen, H. F. (1997) "*Modeling of vertical bubble-driven flows*", Industrial Engineering Chemistry Research, **36**, 4052–4074.

Jeremiah, L. E. (1995) "*Freezing effects on food quality*", Marcel Dekker, Inc. New York.

Jouppila, K and Roos, Y. H. (1994) "*Glass transitions and crystallization in milk powders*", Journal of Dairy Science, **77**, 2907-2915.

Katta, S and Gauvin, W. H. (1975) "*Some fundamental aspects of spray drying*", AIChE Journal, **27**(1),143-153.

Kay, J., Lunt, G. and Osguthorpe, D. (1990) "*Protein structure, prediction and design*", Biochemical Society Symposium. London.

Keey, R. B. (1972) "*Drying principles and practice*", Pergamon Press, Oxford.

Kessler, H. G., Plock, J. and Beyer, H. J. (1992) "*Influence of composition and concentration of milk proteins on whey protein denaturation and gel forming characteristics*", IDF Special Issue, 9303, 216-226.

Kieviet, F. G. (1997) *"Modeling quality in spray drying"*, Ph.D. thesis, Endinhoven University of Technology, Netherlands.

King, C. J. (1970) *"Freeze drying of foodstuffs"*, CRC Critical Review Food Technology, 1-379.

Knopp, S. A., Chongprasert, S. and Nail, S. L. (1998) *"The relationship between the TMDSC curve of frozen sucrose solutions and collapse during freeze-drying"*, Journal of Thermal Analysis, **54**, 659-672.

Kochs, M., Korber, C. H., Heschel, I. and Nunner, B. (1993) *"The influence of the freezing process on vapour transport during sublimation in vacuum freeze-drying of macroscopic samples"*, International Journal of Heat Mass Transfer, **36**(7), 1727-1738.

Kozanoglu, B. U., Vilchez, J. A., Casal, J. and Arnaldos, J. (2002) *"Drying of solids in vacuum fluidized bed"*, The Canadian Journal of Chemical Engineering, **80**, 376-385.

Kozanoglu, B. U., Chanes, W. J., Cuautlle, G. D. and Jean, S. J. P. (2002) *"Hydrodynamics of large particle fluidization in reduced pressure operation: an experimental study"*, Powder technology, **125**, 55-60.

Krokida, M. K., Karathanos, V. T. and Maroulis, Z, B. (1998) *"Effect of freeze-drying condition on shrinkage and porosity of dehydrated agricultural products"*, Journal of Food Engineering, **35**, 369-380.

Kudara, T. and Strumillo, C. (1998) *"Thermal processing of bio-materials"*, Gordon & Breach Science Pubublications.

Kunii, D. and Levenspiel, O. (1991) *"Fluidization engineering"*, Butterworth-Heinemann, Boston.

La Mont, C. A. *US patent.* 51263 (1865).

Langrish, T. A. G., Oakley, D. E., Keey, R. B., Bahu, R. E. and Hutchinson, C. A. (1993) "*Time-dependent flow patterns in spray dryers*", Trans I Chem E, Part A, **71**, 355-360.

Langrish, T. A. G. and Zbicinski, I. (1994) "*The effects of air inlet geometry and spray cone angle on the wall deposition rates in spray dryer*", Trans I ChemE, Part A, **72**, 420-430.

Langrish, T. A. G. and Fletcher, D. F. (2001) "*Spray drying of food ingredients and applications of CFD in spray drying*", Chemical Engineering and Processing, **40**, 345-354.

Langrish, T. A. G., Williams, J. and Fletcher, D. F. (2004) "*Simulation of the effects of swirl on gas flow patterns in a pilot-scale spray dryer*", Trans I *Chem E*, Part A, **82**(A7), 821-833.

Launder, B. E. and Spalding, D. B. (1973) "*Lectures in Mathematical Models of Turbulence*". Academic Press, London, England, 1972.

Law, A. J. R. and Leaver, J. (1997) "*Effects of protein concentration on rates of thermal denaturation of whey proteins in milk*", Journal of Agricultural and Food Chemistry, **45**, 4255-4261.

Leuenberger, L. (1986) *"Process of drying a particulate material and apparatus for implementing the process*", US Patent No. 4 608764.

Leuenberger, L. (2002) *"Spray freeze-drying- the process of choice for low water soluble drugs?"*, Journal of Nanoparticle research, **4**(1/2), 111-119.

Leuenberger, L., Plitzko, M. and Puchkov, M. (2006) "*Spray freeze drying in fluidized bed at normal and low pressure*", Drying Technology,**7** ,11-719.

Leva, M. (1959) "*Fluidization*", McGraw-Hill, London.

Levi, G. and Karel, M. (1995) *"Volumetric shrinkage (collapse) in freeze-dried carbohydrates above their glass transition temperature"*, Food Research International, **28**(2), 145-151.

Llop, M. F., Madrid, F., Arnaldos, J. and Casal. J. (1996) "*Fluidization at vacuum conditions. A generalized equation for the prediction of minimum fluidization velocity*", Chemical Engineering Science, **51**(23), 5149-5157.

Lombrana, J. I. and Villaran, M. C. (1997) "*The influence of pressure and temperature on freeze-drying in an adsorbent medium and establishment of drying strategies*", Food Research International, **30**(3/4), 213-222.

Maa, Y. F., Nguyen, P. A., Sweeney, T., Shire, S.J. and Hsu, C. C. (1999) "*Protein inhalation powders: spray drying vs spray freeze drying*", Pharmaceutical Research, **16**(2), 249-255.

Maa, Y. F., Ameri, M., Shu, C., Payne, L. G. and Chen, D. (2004) *"Influenza vaccine dry powder formulation development :spray freeze-drying and stability evaluation*", Journal of Pharmaceutical Science, **93**(7), 1912-23

MacLeod, C. S., McKittrick, J. A., Hindmarsh, J. P., Johns, M. L. and Wilson, D. I. (2006) "*Fundamentals of spray freezing of instant coffee*", Journal of Food Engineering, **74**, 451-461.

Malecki, G. J., Shinde, P., Morgan, A. I. and Farkas, D. F. (1970) "*Aatmospheric fluidized bed freeze drying*", Food Technology", **24**, 601-617.

Mann, G. W. (1998) *"Surface heat and water vapour budgets over Antarctica"* The Environment Centre, The University of Leeds, Jul 1998, Leeds - UK.

Mant, C. T and Hodges, R. S. (1991) "*High-performance liquid chromatography of peptides and proteins*", CRC Press, London.

Masters, K. (1991) *"Spray drying handbook"*, Longman Scientific and Technical, Harlow.

Matteo, Di. P., Donsi, G. and Ferrari, G. (2003) "*The role of heat and mass transfer phenomena in atmospheric freeze drying of foods in a fluidized bed*", Journal of Food Engineering, **59**, 267-275.

Matzinos, P. D. and Hall, G. M. (1993) "*Denaturation of lactate dehydrogenase during spray-drying of bovine plasma*", Journal of Food science, **58**(5), 1021-1029.

Mazza, M. G. G., Brandao, L. E. B. and Wildhagen, G. S. (2003) "*Characterization of the residence time distribution in spray dryers*", Drying Technology, **21**(3), 525-538.

McKenna, B. M. and O'Sullivan, A. C. (1971) "*Whey protein denaturation in concentrated skim milks*", Journal of Dairy Science, **54**(7),1074–1077.

McKenzie, H. A. (1971) "*Milk proteins: chemistry and molecular biology*", Volume 1 and 2, Academic Press.

Meerdink, G and van't Riet. (1995) "*Prediction of product quality during spray drying*", Food and Bioproducts Processing, **73**, 165-170.

Merymann, H. T. (1959) "*Sublimation freeze-drying without vacuum*", Science, **130**, 628-635.

Meyer, V. R. (1999) "*Practical high-performance liquid chromatography*", Third edition, John Wiley and Sons , England.

Miao, S. and Roos, Y. H. (2004) "*Nonenymatic browning kinetics of carbohydrate-based low moisture food system at temperatures applicable to spray drying*", Journal of Agricultural and Food Chemistry, **52**, 5250-5257.

Morr, C. V., German, B., Kinsella, J. E., Regenstein, J. M., Van Buren, J. P., Kilara, A., Lewis, B. A and Mangino, M. E. (1985) "*A collaborative study to* *develop a standardized food protein solubility procedure*", Journal of Food Science, **50**, 1715-1719.

Morsi, S. A. and Alexander, A. J. (1972) "*An investigation of particle trajectories in two-phase flow systems*", Journal of Fluid Mechanics, **55**(2):193-208.

Mostafa, A. A. and Mongia, H. C. (1987) "*On the modeling of turbulent evaporating sprays: Eulerian versus Lagrangian approach*", International Journal of Heat and Mass Transfer, **30**(12), 2583-2593.

Mujumdar, A. S. (1987) "*Handbook of Industrial Drying*", Marcel Dekker, New York.

Mumenthaler, M. and Leuenberger, L. (1991) *"Atmospheric spray freeze drying; a suitable alternative in freeze drying technology",* International Journal of Pharmaceutics, **72,** 97-110.

Nijdam, J. J., Guo, B., Fletcher, D. F. and Langrish, T. A. G. (2006) "*Lagrangian and Eulerian models for simulating turbulent dispersion and coalescence of droplets within a spray*", Applied Mathematical Modelling, **30**, 1196-1211.

Niven, R. W., Prestrelski, S. J., Treuheit, M. J., Anna Y. I. and Arakawa, T. (1996) "*Protein nebulization II. Stabilization of G-CSF to air-jet nebulisation and the role of protectants*", International Journal of Pharmaceutics, **127** (2), 191-201.

Norton, T and Sun, Da-Wen. (2006) "*Computational fluid dynamics (CFD) - an effective and efficient design and analysis tool for the food industry: A review*", Trends in Food Science and Technology, **17**, 600-620.

Oakley, D. E. and Bahu, R. E. (1993) "*Computational modelling of spray dryers*", Computers and Chemical Engineers, **17**, 493-498.

Oetjen, G. W. (1999) "*Freeze-drying*", Wiley-VCH, New York.

Oldfield, D. J., Singh, H., Taylor, M. W. and Pearce, K. N. (2000) "*Heat-induced interactions of β-lactoglobulin and α-lactalbumin with casein micelle in pH- adjusted skim milk*", International Dairy Journal, **10**, 509-518.

Oldfield, D. J., Taylor, M. W. and Singh, H. (2005) "*Effect of preheating and other process parameters on whey proteins reactions during skim milk powder manufacture*", International Dairy Journal, **15**, 501-511.

Papadakis, S. E. and King, C. J. (1988) "*Air temperature and humidity profiles in spray drying. 1. Features predicted by the particle source in cell model*", Industrial Engineering Chemistry Research, **27**, 2111-2116.

Parris, N. and Baginski, M. A. (1991) "*A rapid method for the determination of whey protein denaturation*". Journal of Dairy Science, **74**(1), 58–64.

Parti, M. and Palancz, B. (1974) "*Mathematical model for spray-drying*", Chemical Engineering Science, **29**, 355-362.

Pelegrine, D. H. G. and Gasparetto, C. A. (2005) "*Whey proteins solubility as function of temperature and pH*", Lebensm.-Wiss. U.-Technology (LWT), **38**, 77-80.

Permyakov, E. A. and Berliner, L. J. (2000) "*α-lactalbumin: Structure and function*", FEBS Letters, **473**, 269-274.

Perry, R. H. and Chilton, C. H. (1984) "*Perry's chemical engineers handbook*", McGraw-Hill, London.

Phillips, W. A. and Bulteel, J. G. (1910) *English Patent*:23045, Oct.5.

Ranz, W. E. (1952) "*Fixation and transfer coefficients for single particles and packed beds*", Chemical Engineering Progress, **48**, 247-253.

Roehrig, F. K. and Wright, T. R. (1972) "*Freeze drying: a unique approach to the synthesis of ultrafine powders*", Journal of Vacuum Science and Technology, **9**(6), 1368-1372.

Rogers, T. L., Hu, J., Yu, Z., Johnston, K. P. and Williams III, R. O. (2002) "*A novel particle engineering technology: spray-freezing into liquid*", International Journal of Pharmaceutics, **242**, 93-100.

Rogers, T. L., Nelsen, A. C, Sarkari, M., Young, T. J., Johnston, K. P. and Williams III, R. O. (2003) "*Enhanced aqueous dissolution of poorly water soluble drug by novel particle engineering technology: spray-freezing into liquid with atmospheric freeze-drying*", Pharmaceutical Research, **20**(3), 485-493.

Roos, Y and Karel, M. (1991) "*Amorphous state and delayed ice formation in sucrose solutions*", International Journal of Food Science and Technology, **26**, 553-566.

Rosenberg, M. and Sheu, T-Y. (1996) "*Microencapsulation of volatile by spray drying in whey protein-based wall systems*", International Dairy Journal, **6**, 273-284.

Rugg, M., Moor, U. and Blanc, B. (1977) "*A calorimetric study of the thermal denaturation of whey proteins in simulated milk ultrafiltrate*", Journal of Dairy Research, **44**, 509-520.

Samborska, K., Witrowa-Rajchert, D. and Gonçalves, A. (2005) "*Spray-drying of Amylase-The effect of process variables on the enzyme inactivation*", Drying Technology, **23**, 941-953.

Schokker, E. P., Singh, H. and Creamer, L. K. (2000) "*Heat-induced aggregation of β-lactoglobulin A and B with α-lactalbumin*", International Dairy Journal, **10**, 843-853.

Scott, G. and Richardson, P (1997) "*The application of computational fluid dynamics in the food industry*", Trends in Food Science and Technology, **8**,119-124.

Senadeera, W., Bhandari., B. R., Young, G. and Wijesinghe, B. (2000) "*Methods for effective fluidization of particulate food materials*", Drying Technology, **18**(7),1537-1557.

Sheu, T. Y. and Rosenberg, M. (1998) "*Microstructure of microparticles consisting of whey proteins and carbohydrates*", Journal of Food Science, **63**(3), 491-494.

Shilton, N. C. and Niranjan, K. (1993) "*Fluidization and its application to the food processing*", Food Structure, **12**, 199-215.

Shoyele, A. S. and Cawthorne, S (2006) "*Particle engineering techniques for inhaled biopharmaceuticals*", Advanced Drug Delivery Reviews, **58**, 1009-1029.

Sonner , C., Maa, Yuff-Fun. and Lee, G. (2002) "*Spray-freeze-drying for protein powder preparation: particle characterization and a case study with trypsinogen stability*", Journal of Pharmaceutical Science, **91**(10), 2122-2139.

Southwell, D. B., Langrish, T. A. G. and Fletcher, D. F. (1999) "*Process intensification in spray dryer by turbulent enhancement*", Trans I *Chem E*, Part A, **77**, 189-205.

Stahl, K., Claesson, M., Lilliehorn, P., Linden, H. and Backstrom, K. (2002) "*The effect of process variables on the degradation and physical properties of spray dried insulin intended for inhalation*", International Journal of Pharmaceutics, **233**, 227-237.

Stanton, C., Ross, R. P., Fitzgerald, G. F. and Sinderen, D. V. (2005) "*Fermented functional foods based on probiotics and their biogenic metabolites*", Current Opinion in Biotechnology, **16**, 198-203.

Stapley, A. G. F. (2008) "*Freeze Drying*". Frozen Food Science and Technology. Chapter 12. Ed. J.A. Evans. Blackwell, Oxford.

Straatsma, J., Van Houwelingen, G ., Steenbergen, A. E. and De Jong, P. (1999) "*Spray drying of food products: 1. Simulation model*", Journal of Food Engineering, **42**, 67-72.

Sweeney, L. G., Wang, Z., Loebenberg, R., Wong, J. P., Lange, C. F. and Finlay, W.H. (2005) "*Spray-freeze-dried liposomal ciprofloxacin powder for inhaled aerosol drug delivery*", International Journal of Pharmaceutics, **305**,180-185.

Terebiznik, M. R., Buera, M. P. and Pilosof, A. M. R. (1997) "*Thermal stability of dehydrated α-amylase in trehalose matrices in relation to its phase transitions*", Lebensm.-Wiss. U.-Technol (LWT), **30**, 513-518.

Ullum, T. (2006) "*Simulation of a spray dryer with a rotary atomizer: The appearance of vortex breakdown*", Drying 2006 - Proceedings of the 15th International Drying Symposium, Budapest, Hungary, *Ed.* by I .Farkas and A.S. Majumdar, 251-257.

Vanarsdel, W. B. and Copley, M. J. (1963) "*Food dehydration*", The Avi Publishing Company, Westport, Connecticut.

Versteeg, H. K. and Malalasekera, W. (1995) "*An introduction to computational fluid dynamics*", Pearson Education Ltd, Essex, England.

Walsh, G. (2002) "*Proteins-Biochemistry and biotechnology*", John Wiley, England.

Wang, Z. L., Finlay, W. H., Peppler, M. S. and Sweeney, L. G. (2006) "*Powder formation by atmospheric spray-freeze-drying*", Powder Technology, **170**, 45-52.

Wolff and Gibert. (1990) "*Atmospheric freeze drying Part 1: Design, experimental investigation and energy-saving advantages*", Drying Technology, **8**(2), 385-404.

Woodward, H. T. (1963) *"Freeze-drying without vacuum (commercial feasibility of carrier-gas process verified for low-sugar foods) good quality and cost",* H. teynham Woodward, (Jun), 96-97.

Xia, B. and Da-Wen Sun. (2002) "*The application of computational fluid dynamics (CFD) in the food industry: a review",* Computers and Electronics in Agriculture, **34**, 5-24

Yamul, D. K. and Lupano, C. E. (2005) *"Whey protein concentrate gels with honey and wheat flour*", Food Research International, **38**, 511-522.

Yates, J. G. (1983) "*Fundamentals of fluidized bed chemical processes*", Butterworth, London.

Yu, Z., Garcia, A. S., Johnston, K. P. and Williams, R. O. (2004) "*spray freezing into liquid nitrogen for highly stable protein nanostructured microparticles",* European Journal of Pharmaceutics and Biopharmaceutics, **58**(3), 529-37.

Yu, Z., Garcia, A. S., Johnston, K. P. and Williams, R. O. (2006) "*Spray freezing into liquid versus spray-freeze drying: influence of atomization on protein aggregation and biological activity",* European Journal of Pharmaceutics and Biopharmaceutics, **27**(3), 9-18.

Zbicinski, I. (1995) "*Development and experimental verification of momentum, heat and mass transfer model in spray drying*", The Chemical Engineering Journal, **58,** 123-133.

Zbicinski, I., Strumillo, C. and Delag, A. (2002) "*Drying kinetics and particle residence time in spray drying*", Drying Technology, **20**(9), 1751-1768.

Appendix A

Mass and heat balance over spray dryer

I. Material balance for furnace

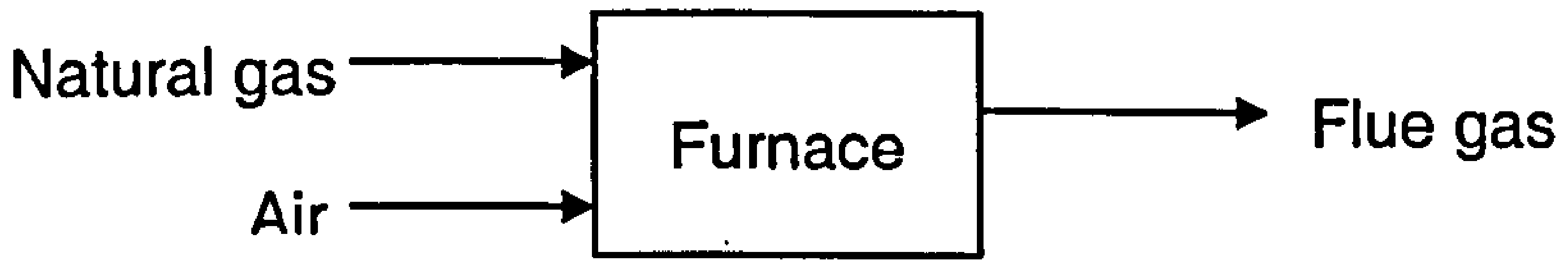

The combustion reaction for CH_4 is

$$CH_4 + 2O_2 \rightarrow CO_2 + 2H_2O$$

Let x be the amount of O_2 that reacts with 1 kmol of CH_4 in the above combustion reaction. Y_1 is the absolute humidity of the air entering the furnace.

Component	**kmol**	**RMM**	**kg**
		Reactants	
CH_4	1	16	16
O_2	x	32	$32x$
N_2	$3.76x$	28	$105.3x$
H_2O	$7.63xY_1$	18	$137.3xY_1$
		Total =	**$16+137.3(1+Y_1)x$**
		Products	
CO_2	1	44	44
N_2	$3.76x$	28	$105.33x$
H_2O	$2+7.63xY_1$	18	$137.3xY_1+36$
O_2	$x-2$	16	$32(x-2)$
		Total =	**$16+137.3(1+Y_1)x$**

Reactants:

Mass of gas = 32 x+105.3 x = 137.3 x kg

Mass of water = 0.01×137.3 x = 1.37 x kg

Absolute inlet air humidity (measured), Y_1 = 0.01 kg/kg dry air

Products:

Mass of gas= 32 (x-2)+44+105.3 x =137.3 x-20

Mass of water = 1.37x+36

Furnace outlet air humidity (Y_2)= $\dfrac{1.37x+36}{137.3x-20}$ Eq (1)

Excess air (x)

Heat to raise gas from 25°C (T_o) to T_{g1} (see Chapter 5, figure 5-2)

$$-\Delta H_R = \sum_{out} n_i C_{pi} \Delta T_{out} - \sum_{in} n_i C_{pi} \Delta T_{in} \quad \text{Eq (2)}$$

$$-\Delta H_R = \sum_{out} n_i C_{pi} (T_{g2} - T_o) - \sum_{in} n_i C_{pi} (T_{g1} - T_o) \quad \text{Eq (3)}$$

Solution

Datum temperature T_o = 25°C and gas inlet temperature T_{g1}= 20°C then equation (3) becomes,

$$-\Delta H_R = \sum_{out} n_i C_{pi} (T_{g2} - 25) - \sum_{in} n_i C_{pi} (20 - 25) \quad \text{Eq (4)}$$

Heat of combustion (ΔH_R) = -802310 kJ/kmol at 298 K

Mean specific heats (C_{pi}) (300-500K)

$CH_4 = 2.5$ kJ/kg K
$CO_2 = 0.92$ kJ/kg K
$O_2 = 0.92$ kJ/kg K
$N_2 = 1.1$ kJ/kg K
$H_2O = 1.9$ kJ/kg K

$$802310=\{(T_{g2}-25)[(x-2)32(0.92)O_2+44(0.92)CO_2+105.3x(1.1)N_2+(1.37x+36)1.9H_2O]\}-$$
$$\{(20-25)[16(2.5)CH_4+32(x)(0.92)O_2+105.3(x)(1.2)N_2+1.37(x)(1.9)H_2O]\}$$

$$x=\frac{(803349.5-49.6T_{g2})}{(142.3T_{g2}-2844)} \qquad \text{Eq (5)}$$

II. Example

An example 30 %(w/v) WPI concentration at 120 °C outlet temperature experimental trial of mass and energy balance calculations are given below

(i) Mass balance

(a) Dryer outlet gas temperature T_{g2}= 250 °C substitute in equation (5)

$$x = 24.18$$

(b) Substitute x value in equation (1)

Furnace outlet air humidity (Y_2)= $\frac{1.37(24.18)+36}{137.3(24.18)-20}$

= 0.021 kg/kg dry air

(c) Moisture content of the feed = W_{si} = 70/30
= 2.3 kg/kg dry solid

(d) Moisture content of the final product = W_{so} = 5/95
= 0.053 kg/kg dry solid

(e) Mass flow rate of natural gas = 0.109 kg/h
Mass flow rate of air (M_a) = 227.84 kg/h

(f) Mass flow rate of dry solid in the feed liquid/slurry (M_s) = 4.8 x 30%
= 1.451 kg/h

(g) Absolute outlet gas humidity $Y_3 = Y_2 + \left[\frac{M_s}{M_a}\right](W_{si} - W_{so})$

Y_3 = 0.035 kg/kg dry air

(ii) Energy Balance:

(h) Enthalpy of inlet air = $Q_{ai} = (C_g + C_{wv}Y_2)(T_{g2} - T_o) + h_{fg}Y_2$

T_o = reference temperature = 273 K

C_g = specific heat of gas = 1012 J/kg K

C_{wv} = specific heat of water vapour = 1914 J/kg K

h_{fg} = latent heat of vaporization of water = 2502000 J/kg

Q_{ai} = 3.15 x10^5 J/kg

(i) Enthalpy of inlet air = $Q_{ao} = (C_g + C_{wv}Y_3)(T_{g3} - T_o) + h_{fg}Y_3$

C_s = specific heat of solid particles =2500 J/kg dry solid K

Q_{ao} = 2.18 x10^5 J/kg

(j) Enthalpy of liquid/slurry feed entering dryer = $Q_{si} = C_s(T_{p1} - T_o) + W_{si}C_w(T_{g2} - T_o)$

C_w = specific heat of water = 4185 J/kg K

T_{p1} = initial particle temperature =293 K

Q_{si} = 2.43 x10^5 J/kg

(k) Enthalpy of dried product leaving the dryer = $Q_{so} = C_s(T_{p2} - T_o) + W_{so}C_w(T_{g3} - T_o)$

T_{p3} = outlet particle temperature = 355 K

Q_{so} = 2.23x10^5 J/kg

(l) Heat loss from the dryer = $Q_L = M_a(Q_{ai} - Q_{ao}) + M_s(Q_{si} - Q_{so})$

(i) Q_L = 22282819 J/hr
(ii) Q_L = (22282819 J/hr)/ (M_a = 227.84 kg/h)

Q_L = 97.8 x10^3 J/kg

Appendix B: Psychrometric chart

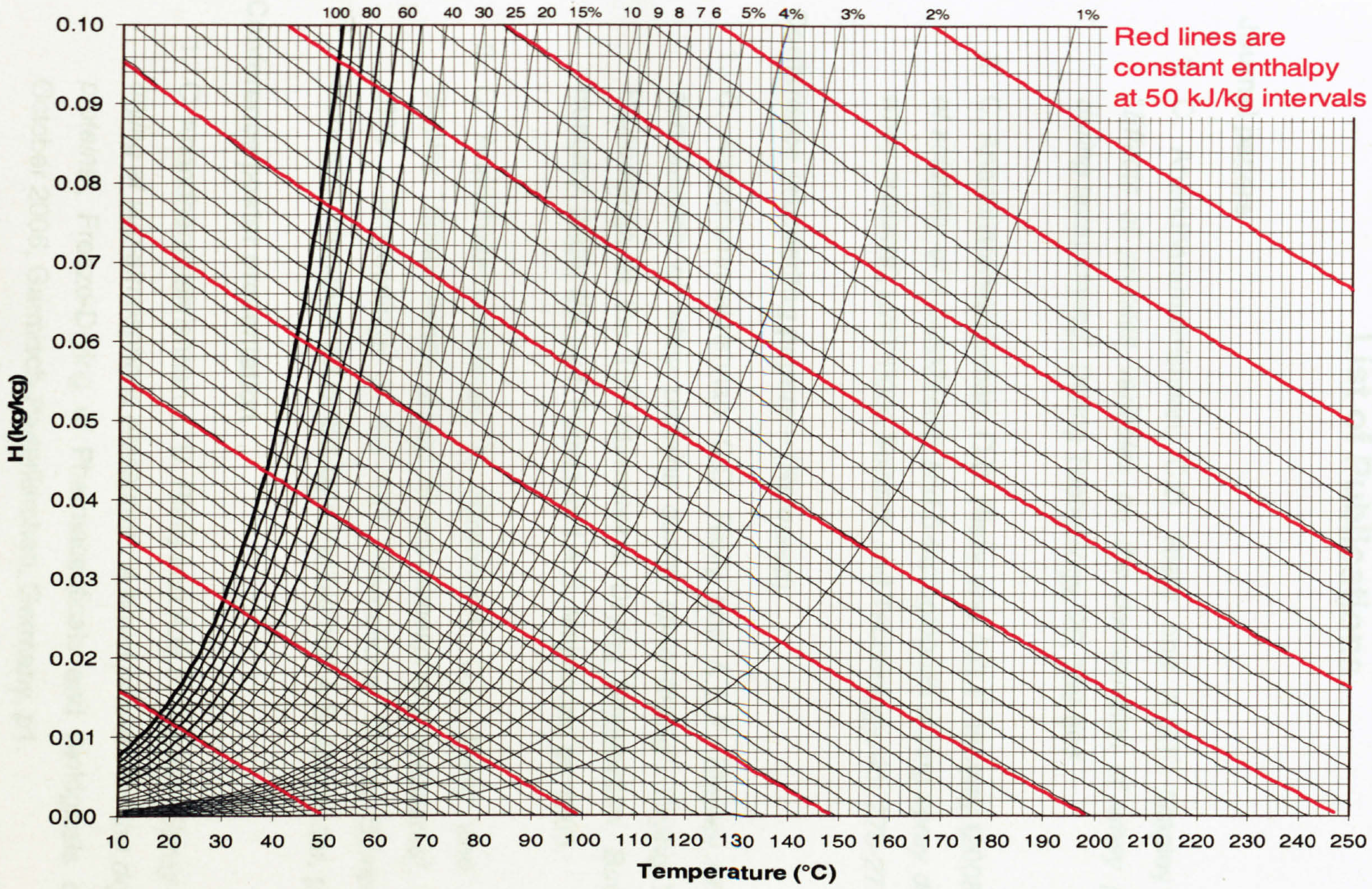

Appendix C

List of Publications

Journal papers

1. C. Anandharamakrishnan, C.D. Rielly and A.G.F. Stapley (2007) "*Effects of process variables on the denaturation of whey proteins during spray-drying*", Drying Technology, 25, 799-807.

2. C. Anandharamakrishnan, C.D. Rielly and A.G.F. Stapley (2008) "*Loss of solubility of α-lactalbumin and β-lactoglobulin during spray drying of whey proteins*", LWT-Food Science and Technology, 41, 270-277.

Conference proceeding papers – (*Refereed*)

1. C. Anandharamakrishnan, C.D. Rielly and A.G.F. Stapley "*Thermal denaturation of whey proteins during spray-drying*", Drying 2006 - Proceedings of the 15th International Drying Symposium, Budapest, Hungary, 2006, *Ed.* by I .Farkas and A.S. Majumdar, pp 1265.

2. C. Anandharamakrishnan, K. Khwanpruk, C.D. Rielly and A.G.F. Stapley "*Spray freeze drying at sub-atmospheric pressures*", Drying 2006 - Proceedings of the 15th International Drying Symposium, Budapest, Hungary, 2006, *Ed.* by I .Farkas and A.S. Majumdar, pp 636.

Conference poster presentation

1. C. Anandharamakrishnan, C.D. Rielly and A.G.F. Stapley "*Spray freeze drying at sub-atmospheric pressures : A novel process for the drying of proteins*", Freeze-Drying of Pharmaceuticals and Biologicals on 4-6 October 2006, Garmisch-Partenkirchen, Germany, p1.